DTIC FILE COPY

ISBN 0-85432-2298

AFWAL-TR-88-3034

AD-A197 307

PROCEEDINGS OF THE
THIRD INTERNATIONAL CONFERENCE
ON

RECENT ADVANCES

IN

STRUCTURAL DYNAMICS

VOLUME 1

DTIC
ELECTE
JUL 2 2 1988
S D
E

APPROVED FOR PUBLIC RELEASE; DISTRIBUTION UNLIMITED

88 7 21 058

INSTITUTE OF SOUND &
VIBRATION RESEARCH
UNIVERSITY OF SOUTHAMPTON
ENGLAND S09 5NH

FLIGHT DYNAMICS LABORATORY
AIR FORCE WRIGHT
AERONAUTICAL LABORATORIES
WRIGHT-PATTERSON AFB, OH 45433

NOTICE

When Government drawings, specifications, or other data are used for any purpose other than in connection with a definitely related Government procurement operation, the United States Government thereby incurs no responsibility nor any obligation whatsoever; and the fact that the government may have formulated, furnished, or in any way supplied the said drawings, specifications, or other data, is not to be regarded by implication or otherwise as in any manner licensing the holder or any other person or corporation, or conveying any rights or permission to manufacture, use or sell any patented invention that may in any way be related thereto.

This report has been reviewed by the Information Office (OI) and is releasable to the National Technical Information Service (NTIS). At NTIS, it will be available to the general public, including foreign nations.

This technical report has been reviewed and is approved for publication.

Howard F. Wolfe
HOWARD F. WOLFE, Tech Mgr
Acoustics & Sonic Fatigue Group
Structural Dynamics Branch
Structures Division

Jerome Pearson
JEROME PEARSON, Chief
Structural Dynamics Branch
Structures Division

FOR THE COMMANDER

R M Bader
ROBERT M. BADER, Asst Chief
Structures Division

If you address has changed, if you wish to be removed from our mailing list, or if the addressee is no longer employed by your organization please notify AFWAL/FIBG, W-PAFB, OH 45433 to help us maintain a current mailing list.

Copies of this report should not be returned unless return is required by security considerations, contractual obligations, or notice on a specific document.

DISCLAIMER NOTICE

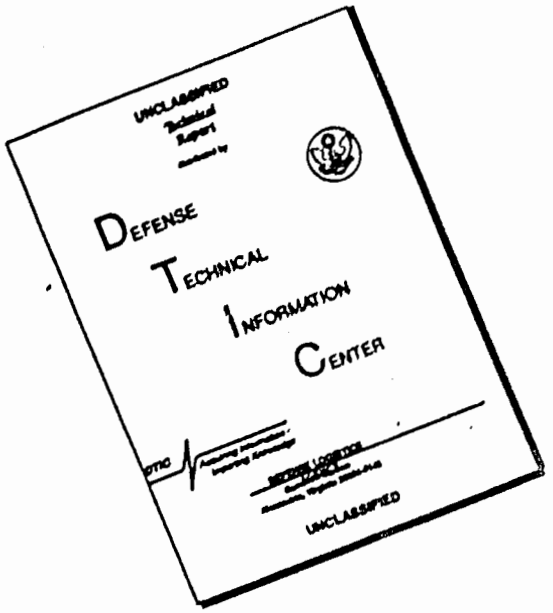

THIS DOCUMENT IS BEST QUALITY AVAILABLE. THE COPY FURNISHED TO DTIC CONTAINED A SIGNIFICANT NUMBER OF PAGES WHICH DO NOT REPRODUCE LEGIBLY.

UNCLASSIFIED
SECURITY CLASSIFICATION OF THIS PAGE

AD-A197 807

REPORT DOCUMENTATION PAGE

Form Approved OMB No. 0704-0188

1a. REPORT SECURITY CLASSIFICATION UNCLASSIFIED	1b. RESTRICTIVE MARKINGS
2a. SECURITY CLASSIFICATION AUTHORITY	3. DISTRIBUTION/AVAILABILITY OF REPORT Approved for public release; distribution unlimited
2b. DECLASSIFICATION/DOWNGRADING SCHEDULE	
4. PERFORMING ORGANIZATION REPORT NUMBER(S) AFWAL-TR-88-3034	5. MONITORING ORGANIZATION REPORT NUMBER(S)
6a. NAME OF PERFORMING ORGANIZATION Acoustics & Sonic Fatigue Group	6b. OFFICE SYMBOL (If applicable) AFWAL/FIBGD
6c. ADDRESS (City, State, and ZIP Code) Wright-Patterson Air Force Base, OH 45433	7a. NAME OF MONITORING ORGANIZATION
8a. NAME OF FUNDING/SPONSORING ORGANIZATION	8b. OFFICE SYMBOL (If applicable)
8c. ADDRESS (City, State, and ZIP Code)	9. PROCUREMENT INSTRUMENT IDENTIFICATION NUMBER
	7b. ADDRESS (City, State, and ZIP Code)

10. SOURCE OF FUNDING NUMBERS			
PROGRAM ELEMENT NO.	PROJECT NO.	TASK NO.	WORK UNIT ACCESSION NO.
62201F	2401	04	42

11. TITLE (Include Security Classification)
Third International Conference on Recent Advances in Structural Dynamics (Unclassified)

12. PERSONAL AUTHOR(S)

13a. TYPE OF REPORT	13b. TIME COVERED	14. DATE OF REPORT (Year, Month, Day)	15. PAGE COUNT
Conference Proceedings	FROM 84 TO 88	1988 July	

16. SUPPLEMENTARY NOTATION

17. COSATI CODES			18. SUBJECT TERMS (Continue on reverse if necessary and identify by block number)
FIELD	GROUP	SUB-GROUP	Major topics in Volume I omitted

19. ABSTRACT (Continue on reverse if necessary and identify by block number)

Individual papers of the Third International Conference on Recent Advances in Structural Dynamics to be held 18-22 July 1988 at the Institute of Sound and Vibration Research in Southampton, England are presented. The subjects include: Analytical methods, finite element methods, testing techniques and correlation, ~~shock, failure~~ and fatigue, vibration control and damping, nonlinear techniques, random vibration of nonlinear systems, parameter excitation, composites, ~~large space structures~~, structural/acoustic interaction, civil engineering. materials

Aerospace structures; Structural analysis; Fracture; Dynamic response; Structural response; Wave propagation; Algorithms; Structural components; Vibration; Laminates; Structural shells; Buckling; Determination; Loading; Structures; Structural damping; Friction; damping

20. DISTRIBUTION/AVAILABILITY OF ABSTRACT	21. ABSTRACT SECURITY CLASSIFICATION
☒ UNCLASSIFIED/UNLIMITED ☐ SAME AS RPT. ☐ DTIC USERS	UNCLASSIFIED
22a. NAME OF RESPONSIBLE INDIVIDUAL HOWARD F. WOLFE	22b. TELEPHONE (Include Area Code) 513-255-5229
	22c. OFFICE SYMBOL AFWAL/FIBGD

DD Form 1473, JUN 86 — Previous editions are obsolete. — SECURITY CLASSIFICATION OF THIS PAGE
UNCLASSIFIED

D Structural engineering: Aerospace engineering (code)

PROCEEDINGS OF THE
THIRD INTERNATIONAL CONFERENCE
ON

RECENT ADVANCES

IN

STRUCTURAL DYNAMICS

18-22 JULY 1988

University of Southampton, England

Accession For
NTIS GRA&I
DTIC TAB
Unannounced
Justification
By
Distribution/
Availability Codes
Dist | Avail and/or Special
A-1

Edited by

M. Petyt , H.F. Wolfe and C. Mei

VOLUME I

ORGANISATION

The Conference was organised by the

Institute of Sound and Vibration Research

with the support of the following bodies:

Air Force Wright Aeronautical Laboratories
Wright Patterson Air Force Base
European Office of Aerospace Research and Development
Institute of Mechanical Engineers
Institute of Civil Engineers
The Society for Earthquake and Civil Engineering Dynamics

ORGANISING COMMITTEE

Dr. M. Petyt
Professor R.G. White
Dr. F.J. Fahy
Mr. R.C. Drew
Mr. M.J.B. Shelton

Mr. H.F. Wolfe
Lt.Col. J.G.R. Hansen
Dr. R.J. Pinnington
Mr. S.C.P. Galea
Mrs. M.Z. Strickland

Dr. C. Mei
Professor H. Tottenham
Mr. N.S. Ferguson
Miss J.L. Horner

CONTENTS

Page No.

1. ANALYTICAL METHODS

1. D.J. GORMAN
A general computational technique for the free vibration analysis of rectangular plates with classical edge support based on the superposition method — 3

2. P. HAMMER and B. PETERSSON
Minimised input power by line force excitation — 13

3. O.A. FETTAHLIOGLU
Exact solutions for wave propagation in rings and arches on elastic foundations — 21

4. D.J. MEAD and Y. YAMAN
Vibration analysis of finite uniform structures using the harmonic response functions of the infinite structure — 35

5. G.J. KISSEL
Randomly disordered periodic structures — 45

6. J. WEI and M. PETYT
Free vibration of ring stiffened cylindrical shells — 55

7. T.N. SHIAU and C.C. PAN
Sensitivity analysis and dynamic behaviors of rotating pretwisted tapered blade — 65

8. I. ELISHAKOFF, C.D. HETTEMA and E.L. WILSON
Direct superposition of Wilson trial functions by computerized symbolic algebra — 75

9. I-CHEN CHANG
Problems of structural dynamics solved by Chinese remainder algorithm — 87

2. FINITE ELEMENT METHODS

10. E. HINTON and B. AL JANABI
Vibration of plates with concentrated masses and plates with point supports — 101

11. D.J. MEAD, D.C. ZHU and N.S. BARDELL
Free vibration of an orthogonally stiffened flat plate — 111

12. R.P. LEAL and C.A. MOTA SOARES
Mixed elements in design sensitivity analysis of plates with dynamic and stability constraints — 123

13. A. POTIRON
A new finite element for the dynamical study of pretwisted beams — 133

14. S.S. GUPTA 147
A complex vibration analysis of a three-shaft geared, compressor set mounted on a steel entablature

15. Y.A. KHULIEF and H.T. CHIU 159
Transient dynamics of rotating flexible bodies with base motion excitations

3. COMPOSITES

16. E.R. BAYLIS and W.A. GREEN 171
Impact stress waves in fibre reinforced laminated plates

17. W.A. GREEN and E.R. BAYLIS 185
The contribution of high-harmonics to transient waves in plates and laminates

18. G. CEDERBAUM, L. LIBRESCU and I. ELISHAKOFF 199
Response of laminated composite plates to non-stationary random excitation

19. S.P. LIM, K.H. LEE and N.R. SENTHILNATHAN 211
Nonlinear vibrations of antisymmetric angle-ply laminates using a simple higher-order theory

20. MALLIKARJUNA and T. KANT 219
On transient response of laminated composite plates based on higher-order theory

21. L. LIBRESCU, A.A. KHDEIR and D. FREDERICK 229
Free vibration and buckling of cross-ply laminated shear deformable shallow shell-type panels

22. N. SANKARANARAYANAN, K. CHANDRASEKARAN and G. RAMAIYAN 241
On the free vibrations of laminated conical shells of variable thickness

4. TESTING TECHNIQUES AND CORRELATION

23. D.L. BROWN 253
Invited Paper - Future trends in modal analysis

24. G.R. TOMLINSON and P. MILAS 265
Impulse testing techniques applied to large vibration isolators

25. H.G.D. GOYDER 279
Three methods for determining natural frequencies and damping ratios from vibration spectra

26. T.K. TEE, J.E. MOTTERSHEAD, R. STANWAY, and D.J. BROOKFIELD 289
Application of filtering techniques for system identification of vibrating structures

27. K. WORDEN and G.R. TOMLINSON 299
Identification of linear/nonlinear restoring force surfaces in single and multi-mode nonlinear systems

28. F. BENEDETTINI, D. CAPECCHI and F. VESTRONI 309
On identification of linear and nonlinear structural systems

29. J. BRANDON 319
On the use of oversized models for modal identification in structural dynamics

30. H.G.D. GOYDER and A.P. LINCOLN 329
An experimental technique for investigating nonlinear structures

31. H.R. LO and J.K. HAMMOND 339
Nonlinear system identification using the surface of nonlinearities form: discussion on parameter estimation and some related problems

32. L. GAZDAG and G.T. ENDROCZI 349
Multilevel substructuring and mode superposition for complex structures

33. P.O. LARSSON 363
Methods using frequency-response functions for the analysis of assembled structures

34. J. ZEISCHKA, M. BRUGHMANS and O. STORRER 377
LMS/LINK correlating and validating Finite Element Analysis (FEA) for dynamic structure behaviour with experimental modal analysis

35. J.L. HORNER and R.G. WHITE 387
Vibrational power transmission through discontinuities

36. B.A.T. PETERSSON 397
Giant magetostrictive devices in structural acoustics

5. VIBRATION CONTROL AND DAMPING

37. D.I.G. JONES 409
Invited Paper - Recent advances in structural damping

38. C.U. BRUER and J.S. BOLTON 429
Damping of continuous structures by the use of elastic porous materials

39. S.N. SHOUKRY 437
Assessment of frictional damping in tangentially loaded metallic interfaces

40. J.M. CUSCHIERI and V.R. DESAI 449
Friction damping due to interfacial slip

41. E. SEMERCIGIL and N. POPPLEWELL 459
The sean bag impact damper

42. M.A. CUTCHINS, J.E. COCHRAN, K. KUMAR, N.G. FITZ-COY, and M.L. TINKER 469
Analysis of coils of wire rope arranged for passive damping

43. A. PREUMONT, E. CZAJKOWSKI, and R.T. HAFTKA
Stabilizing the neglected dynamics in active control of vibration 481

44. R. UHRIG
Vibration problems in coalmine hauling systems 491

45. W. D'AMBROGIO and A. SESTIERI
Altering the vibrational behavior of an I.E. engine as a preliminary step for noise reduction 499

6. SHOCK

46. D.L. ANDERSON and M.D. OLSON
Recent progress in analyzing the nonlinear response of beams and stiffened plates 511

47. XI DECHANG and PEN NANLING
Nonlinear responses of a rigid block with a simply supported beam subjected to shock excitation 521

48. W.P. SCHONBERG
Dynamic impact of beams - a correlation of experimental and theoretical results 527

49. D.H. TREPESS and R.G. WHITE
Shock testing with electrodynamic exciters using oscillatory transient excitation 537

50. S.J.C. DYNE, J.K. HAMMOND and P. DAVIES
A method for finding an upper bound for the response of structures to blast waves 551

51. D.K. ANDERSON
Impact coupled oscillator systems 561

7. FAILURE AND FATIGUE

52. J.S. MIXSON
Invited Paper - Overview of acoustic fatigue activities at NASA Langley Research Center 573

53. R. VAICAITIS and S.T. CHOI
Acoustic fatigue of stiffened structures 593

54. N.S. FERGUSON
An analytical investigation into the behaviour of composites 605

55. C.F. NG
The influence of snap-through motion on the random response of curved panels to intense acoustic excitation 617

56. S.C. GALEA and R.G. WHITE
Effect of temperature on acoustically induced stresses in some CFRP plates 629

57. P. DAVIES and J.K. HAMMOND
Two methods for the detection of failure in mechanical systems 641

8. NONLINEAR TECHNIQUES

58. A.H. NAYFEH — 653
Invited Paper - Modal interactions in the nonlinear response of structural elements - theory and experiment

59. C. HOFF — 671
Dissipative step by step integration methods in nonlinear structural dynamics

60. F. BRANCALEONI and C. VALENTE — 683
On some aspects of operational error distribution and propagation in direct integration for nonlinear dynamics

61. C.E. TEH and H.G.D. GOYDER — 693
Nonlinear vibration of a loosely supported beam

62. P.B. GONCALVES and R.C. BATISTA — 705
Nonlinear vibrations of fluid loaded cylindrical shells

9. RANDOM VIBRATION OF NONLINEAR SYSTEMS

63. Y.K. LIN — 717
Invited Paper - Recent advances in nonlinear random vibration

64. H.J. PRADLWARTER, G.I. SCHUELLER and X.-W. CHEN — 737
Consideration of non-Gaussian response properties by use of stochastic equivalent linearization

65. G. TSIATAS and H. SADID — 753
Random vibration of hysteretic systems

66. M.J.H. FOX — 759
A method for the dynamic analysis of randomly excited structures with frictional constraints

67. C.K. CHIANG and CHUH MEI — 769
A finite element large deflection multiple-mode random response analysis of beams subjected to acoustic loading

68. F. CASCIATI, L. FARAVELLI — 781
Non linear stochastic dynamics of frames

10. PARAMETRIC EXCITATION

69. C.W.S. TO — 793
Recent advances in vibration analysis of systems with parametric random excitations

70. D.A. STREIT, A.K. BAJAJ and C.M. KROUSGRILL — 809
Parametric instabilities and chaotic amplitude modulations in a system with two degrees of freedom

71. G. OSTIGUY and H. NGUYEN — 819
Combination resonances of parametically excited rectangular plates

11. STRUCTURAL/ACOUSTIC INTERACTION

72. A. FRID — 833
Fluid vibration in piping systems - a structural mechanics approach

73. J.S. POLLARD — 845
Application of statistical energy analysis to helicopter cabin type structures

74. H. CARLSSON and G. SANDBERG — 857
Finite element analysis of structure acoustic interaction

75. P. GORANSSON — 869
Analysis of the transmission of sound into the passenger compartment of a propeller aircraft using the Finite Element Method

12. LARGE SPACE STRUCTURES

76. S. ABRATE — 881
Modelling of latticed structures for dynamic analyses

77. H.V. PANOSSIAN — 891
An assessment of model order reduction techniques

78. G.A. BECUS and C.W. CHENG — 901
Energy methods for model reduction in the dynamics and control of large structural systems

79. S.E. LAMBERSON and C.A. FISHER — 911
Structural dynamic analysis and tests of a planar large space truss subcomponent

80. S. MAHANIAN — 921
The effects of cable suspension on bending vibration of large beams

81. G.L. SLATER, M.D. MCLAREN, V.B. VENKAYYA and V.B. TISCHLER — 933
Robustness and positive real control design for large space structures

13 CIVIL ENGINEERING

82. L. FRYBA — 945
Invited Paper - Dynamics of bridges

83. J. RAVINGER — 963
Dynamic post-buckling of slender webs

84. H-J ZHOU — 973
Determination of dynamic behavior of thin arch dams using spline semi-analytic method

85. L.A. DE BEJAR — 981
Effect of the gradient of elastic eccentricity on the lateral-torsional effective earthquake forces on building systems

86. R.K.N.D. RAJAPAKSE and A.H. SHAH 993
Torsional oscillations of flexible inclusions in a layered elastic half-space

87. J.R. MAGUIRE 1003
A frequency/damping database for tall chimneys

88. S. TSANG and C. WILLIAMS 1009
Application of experimental modal analysis to full scale civil engineering structures

89. L. FARAVELLI 1021
Source-to-site seismic models in structural dynamics

90. F. LOPEZ-ALMANSA, J. RODELLAR, A.H. BARBAT and J.A. CANAS 1033
An assessment of digital active tendon control of building structures

91. G. HIRSCH and A. KLEINE-TEBBE 1043
Semi-active control of earthquake induced oscillations in structures - mechanical qualification by means of the SAMSON shaking table.

1. ANALYTICAL METHODS

A GENERAL COMPUTATIONAL TECHNIQUE FOR THE FREE VIBRATION ANALYSIS OF RECTANGULAR PLATES WITH CLASSICAL EDGE SUPPORT BASED ON THE SUPERPOSITION METHOD

by

D.J. Gorman
Department of Mechanical Engineering
University of Ottawa
Ottawa, Canada K1N 6N5

1. INTRODUCTION

One of the most fundamental problems in the history of mechanical vibration is that of obtaining free vibration frequencies and mode shapes for thin rectangular plates with combinations of classical, i.e., simply supported, clamped, or free edge conditions. It is well known that such plates fall into two distinct categories, or groups, the first group containing only those plates which have at least one pair of opposite edges simply supported and the second group containing all of the remaining plates.

Free vibration analysis of plates of the first group, referred to hereafter as Group 1, is easily conducted in an exact analytical fashion. Lévy-type solutions are obtained in each case, except the case with simple support along all edges, and enforcement of the boundary conditions leads to development of a transcendental equation for the eigenvalues which can be solved to any desired degree of accuracy. Eigenvalues for plates with simple support along all edges are available in closed form.

The obtaining of solutions for plates of the second group above, referred to hereafter as Group 2, has presented researchers with much greater difficulty. This is because such problems are not amenable to solution by means of a simple Lévy-type solution. Warburton was the first to perform a comprehensive study of these problems employing the Rayleigh method [1]. He represented the mode shapes by pairs of appropriate beam eigenfunctions thereby satisfying the boundary conditions exactly, except in the case of free edges. Later, these problems were explored further by Leissa who used several beam functions to represent the mode shapes [2].

At an even later date, the author analyzed all of the plates of Group 2 by means of a superposition method he developed for this purpose. The method and computed results are to be found in Ref. [3]. It is not intended to discuss this latter method in detail here, however, it is pointed out that among its advantages is the fact that no functions need be selected to represent the mode shapes and all boundary conditions, free or otherwise, are satisfied to any desired

degree of accuracy. It is re-emphasized that beam eigenfunctions when used to represent the shape of plate vibration modes as discussed above, do not completely satisfy plate free edge conditions.

The object of this paper is to describe a general computational procedure which allows immediate establishment of accurate eigenvalues and mode shapes for any rectangular plate of Groups 1 or 2. Eigenvalues for plates of Group 1 are obtained by solving the appropriate transcendental equation. Those of Group 2 are solved by the superposition method. Each displacement mode is normalized so that its maximum dimensionless displacement is equal to unity. The dimensionless bending moment is made available throughout the plate for any angular orientation and it is shown how this information is utilized to obtain the distribution of principal stresses.

2. MATHEMATICAL PROCEDURE

2.1 Plates of Group 1

Little need be said about the frequency and mode shape analysis for plates of this group. It is known that with correct orientation of the axis the solution can always be written in the form (Fig. 1) [3]

$$W(\xi,\eta,\tau) = W(\xi,\eta) \sin \omega\tau \tag{1}$$

where

$$W(\xi,\eta) = Y(\eta) \sin m\pi\xi \tag{2}$$

$$Y_m(\eta) = A_m \cosh \beta_m\eta + B_m \sinh \beta_m\eta + C_m \sin \gamma_m\eta + D_m \cos \gamma_m\eta \tag{3}$$

for $\lambda^2 \leq (m\pi)^2$

and

$$Y_m(\eta) = A_m \cosh \beta_m\eta + B_m \sinh \beta_m\eta + C_m \sinh \gamma_m\eta + D_m \cosh \gamma_m\eta \tag{4}$$

for $\lambda^2 \geq (m\pi)^2$

where $\beta_m = \phi\sqrt{\lambda^2+(m\pi)^2}$, $\gamma_m = \phi\sqrt{\lambda^2-(m\pi)^2}$

or $\phi\sqrt{(m\pi)^2 - \lambda^2}$, whichever is real, and m equals the number of half sine waves running across the plate in a direction normal to the simply supported edges. The coefficients A_m, B_m, etc., are adjusted to satisfy the boundary conditions.

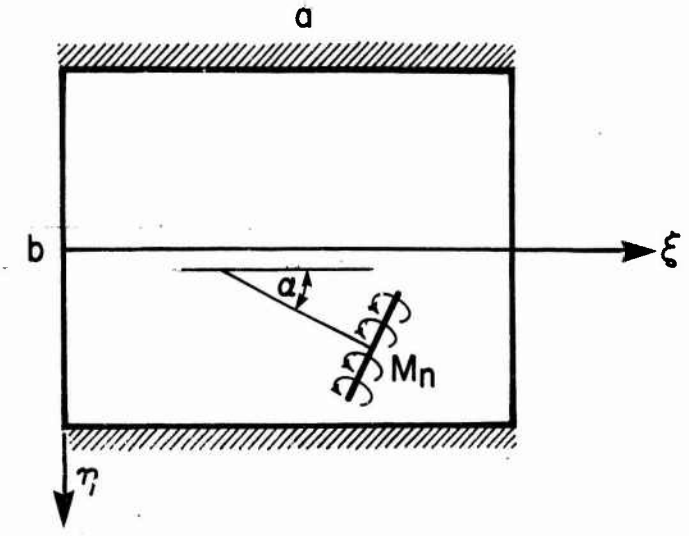

Fig. 1 View of rectangular plate of Group 1 with two opposite edges clamped and the other two simply supported. Choice of coordinate axis is shown as well as angular orientation of computed bending moment.

A typical plate of Group 1 is shown in Figure 1. This is a plate which has two opposite edges clamped and the other two simply supported. In this case, as in all cases of Group 1 where the edges running parallel to the ξ axis as shown in Figure 1 are identical, i.e., clamped, free or simply supported, it is advantageous to let the ξ axis run along the center of the plate. It is immediately obvious that all vibration modes of such plates will fall into two families, one family with modes symetric about the ξ axis and another family with modes antisymmetric about this axis. It is best to treat each family as a separate case of Group 1. For each of these families, as a result of symmetry or antisymmetry, two of the coefficients of equations (3), or (4), can be eliminated immediately by inspection. The analysis is, thereby, simplified significantly. Of course, if the edges running parallel to the ξ axis do not have identical boundary conditions, it is better to let the ξ axis run along the upper edge of the plate (Fig.1). Regardless of the type of problem, the appropriate transcendental equation is easily written on enforcing the boundary conditions and exact solutions for the eigenvalues and mode shapes are computed following steps as described in Ref. [3]. In the case of a plate with simple support along all edges, no computation is required to obtain the eigenvalues. Beyond this problem, there is found to be seven separate cases to be handled in Group 1.

Dimensionless bending moments along the plate edges are discussed in Ref.[3]. It can be easily shown [4] that for any angular orientation, α, (see Fig.1), a dimensionless bending moment can be

written as

$$\frac{M_n b^2}{a^2 D} = \{\theta_1 \phi^2 \frac{\partial^2 W}{\partial \xi^2} + \theta_2 \frac{\partial^2 W}{\partial \eta^2} + \theta_3 \phi \frac{\partial^2 W}{\partial \xi \partial \eta}\} \qquad (5)$$

where

$$\theta_1 = \cos^2\alpha + \nu \sin^2\alpha \qquad \theta_2 = \sin^2\alpha + \nu \cos^2\alpha$$

$$\theta_3 = (1-\nu) \sin 2\alpha$$

With the eigenvalue obtained the mode shape and bending moment can be readily coputed for a rectangular grid of points distributed throughout the plate. Computation of the principal stresses for this grid of points will be discussed later.

2.2 Plates of Group 2

All plate vibration problems of this group are solved by means of the superposition method as described in Refs. [3] and [5], although the selection of building blocks may differ slightly in order to minimize the computation work required. Again, advangage will be taken of symmetry where such symmetry exists. Only one case of Group 2 will be discussed in any detail in order to economize on space.

We consider a rectangular plate with clamped support along all edges. It will be appreciated that all possible modes of free vibration for this plate will fall into one of three categories. Modes which are fully symmetric about a central axis taken through the plate, modes which are fully antisymmetric about the same axis, and modes which are symmetric about one axis and antisymmetric about the other. In view of these observations, we need analyze one quarterof the plate only, provided the correct boundary conditions are enforced [3].

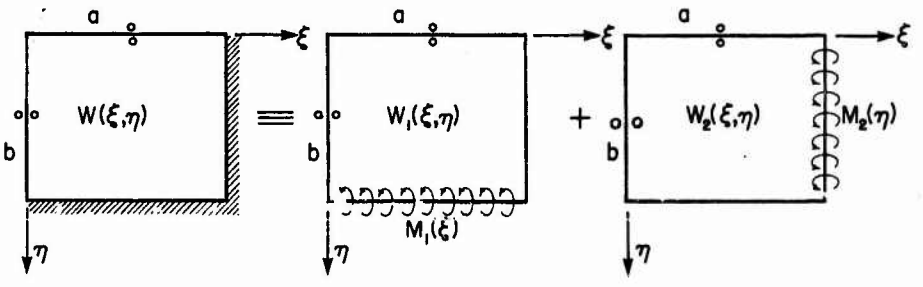

Fig. 2. Building blocks utilized in analyzing the fully symmetric modes of the rectangular plate with all outer edges clamped.

We choose to discuss, in a minimum of detail, the analysis of the fully symmetric modes. Reference is made to the quarter plate as shown on the left hand side of Figure 2. Boundary conditions which must be enforced along the axes are denoted as slip shear conditions. This implies that there is no vertical edge reaction along these edges and that slope, taken normal to the edge is everywhere zero. These conditions are designated by two small circles adjacent to the edges.

In order to solve this problem, we develop solutions for the two forced vibration plate problems appearing on the right hand side of Figure 2. The first forced vibration problem, or building block, involves a plate given simple support along the edge, $\xi=1$, and with a condition of zero lateral displacement enforced along the edge, $\eta=1$. Along this latter edge we enforce a harmonic distributed bending moment of circular frequency ω. Its spacial distribution is expanded in series form as,

$$\left.\frac{M_1 b^2}{a D}\right|_{\eta=1} = \sum_{m=1,3,5}^{\infty} E_m \cos \frac{m\pi\xi}{2} \tag{6}$$

In view of the boundary conditions enforced along the edges running parallel to the η axis, it is known that a Lévy-type solution for the forced response of this building block can be written as [3],

$$W(\xi,\eta) = \sum_{m=1,3,5}^{\infty} Y_m(\eta) \cos \frac{m\pi\xi}{2} \tag{7}$$

where the expression for $Y_m(\eta)$ is of the form given by Equations (3) and (4). Two of the coefficients in these equations (the second and third) can be immediately set equal to zero in view of the boundary conditions enforced along the edge, $\eta=0$. The remaining two coefficients can be evaluated as a result of the condition of zero displacement to be enforced along the edge, $\eta=1$, as well as the condition expressed by Equation (6). Following procedures as outlined in Ref. [3] we obtain,

$$W_1(\xi,\eta) = \sum_{m=1,3,5}^{K^*} \left\{\theta_{11_m} \frac{\cosh \beta_m\eta}{\sinh \beta_m} + \theta_{13_m} \frac{\cos \gamma_m\eta}{\sin \gamma_m}\right\} \cos \frac{m\pi\xi}{2}$$

$$+ \sum_{m=K^*+2}^{\infty} \left\{\theta_{22_m} \frac{\cosh \beta_m\eta}{\sinh \beta_m} + \theta_{23_m} \frac{\cosh \gamma_m\eta}{\sinh \gamma_m}\right\} \cos \frac{m\pi\xi}{2} \tag{8}$$

where $\beta_m = \phi\sqrt{\lambda^2+(m\pi/2)^2}$, $\gamma_m = \phi\sqrt{\lambda^2-(m\pi/2)^2}$, or $\phi\sqrt{(m\pi/2)^2-\lambda^2}$ whichever is real,

and the first summation includes only those terms for which $\lambda^2 \geq (m\pi/2)^2$

$$\theta 11_m = \frac{-1}{(\beta_m^2 + \gamma_m^2)\cosh \beta_m/\sinh \beta_m}$$

$$\theta 13_m = \frac{1}{(\beta_m^2 + \gamma_m^2)\cos \gamma_m/\sin \gamma_m}$$

$$\theta 22_m = \frac{-1}{(\beta_m^2 - \gamma_m^2)\cosh \beta_m/\sinh \beta_m}$$

$$\theta 23_m = \frac{1}{(\beta_m^2 - \gamma_m^2)\cosh \gamma_m/\sinh \gamma_m}$$

Groupings for the parameters $\theta 11_m$, etc., are quite different from those used in Ref. [3]. This constitutes a significant advantage since computer overflow problems encountered with the earlier formulations are eliminated here.

It will be obvious that the solution for the second building block, $W_2(\xi,\eta)$, can be extracted from that of the first. It is only necessary to interchange the variables ξ and η of Eqn. (8) and replace the aspect ratio by its inverse.

Having obtained the solutions for the two building blocks of Fig. 2, construction of the eigenvalue matrix can proceed following the procedure described in Ref. [3]. One expands the slope along the driven edges of these blocks in cosine series of the type employed in Equn..(6). Requiring that the net slope of the superimposed building blocks must vanish, necessitates that the coefficients of each term in the above pair of series must equal zero. This gives rise to a set of 2K homogenous linear albegraic equations for the coefficients E_m,etc., and hence construction of a 2K by 2K eigenvalue matrix, where K equals the total number of terms employed in each building block solution. Solutions for the eigenvalues and mode shapes are obtained by following standard procedures [3]. It is also required here to obtain bending moment distributions throughout the plate, according to Equation 5, for all points in the rectangular grid used for storing displacement data. Of course, in the cases of Group 2, one must enter the sum of derivatives taken from each of the superimposed building blocks when computing the bending moment at a point, according to Eqn. 5.

It will be appreciated that the other two cases of plate vibration related to the fully clamped plate can also be solved by using pairs of building blocks slightly modified from those described

above. The same general analytical procedure is applicable to the completely free rectangular plate provided proper building blocks are selected. There will be some problems which are completely lacking in symmetry and some which have only one plane of symmetry, the cantilever plate for example. In this latter case one half of the plate, only, will be analyzed.

It is appropriate at this time to enumerate the major differences between the analysis described in Ref. (3) for plates of Group 2, and the more advanced analysis described here.

(1) It is characteristic of the method of superposition that numerous different combinations of building blocks can be employed to analyze any of the 30 distinct vibrations problems, or cases, which make up those of Group 2. In fact, 30 different computer programs were developed in order to perform the analysis reported in Ref. [3]. Each one of the earlier programs generated its own matrix from which the associated eigenvalues were generated.

In the computations reported here, a much more judicious selection of building blocks has been made. It is found, in fact, that only 20 unique building block solutions are required and that many of these are easily extracted from others in the set. As indicated above, 30 different matrices had to be generated to obtain the results reported in Ref. [3]. These matrices varied in size from 2K by 2K to 4K by 4K, where K equals the number of terms in each series. In the work reported here a new approach is taken. One master matrix of 10K by 6K only, is generated and it is found that all of the 30 matrices of interest can be extracted from this one master matrix. It has, therefore, been possible to replace the earlier set of 30 computer codes by a single one.

(2) Formualtion of the building block solutions as shown in Eqn. (8) rather than as formulated in the earlier publications has contributed vastly toward simplifying the computations. It will be seen that the quantities θ_{22_m}, etc., now involve ratios of the hyperbolic functions. These ratios can be replaced by the quantity, unity, for high values of the arguments. All of the integrations required in expanding the slopes, etc., along the plate edges are now called through computer subroutines. Again, because of the ratios of the hyperbolic functions involved (Equn. (8)), it is possible to arrange the integrals within the subroutines so that for high values of arguments of the functions, overflow or underflow problems are avoided.

(3) A persistent problem that characterized the earlier computations was the uncovering of false eigenvalues as well as the genuine ones [3]. This came about because in the analysis of certain problems involving free edges (doubly symmetric mode vibration of the completely free plate, for example) it was possible to obtain non-trivial solutions for the fourier coefficients with the net displacement of the combined building blocks equal to zero. In such a case, the displacement represented by one building block was equal and opposite to that represented by the other. This left the boundary conditions satisfied. Fortunately, these false eigenvalues could easily be

predicted before computation began and they were rejected. This problem has been eliminated by prescribing forced edge rotation rather than distributed bending moment along the driven edge. In fact, one eliminates the problem of false eigenvalues entirely by a judicious choice of prescribed edge rotations or bending moments along the driven edges.

3. COMPUTATION OF PRINCIPAL STRESSES

In order to compute the dimensionless normal stress, σ_ξ, at the various points in the grid, it is only necessary to compute the bending moment as discussed earlier, with the orientation angle α equal to zero, and extract the value σ_ξ therefrom. A repitition of these computations with α equal $\pi/2$ permits establishment of the normal stress σ_η.

Finally, repeating the computations with $\theta_1=\theta_2=0$, and $\theta_3=\nu-1$, one obtains the dimensionless twisting moment

$$\frac{M_{\xi\eta} b}{a D} = (1-\nu)\,\phi\,\frac{\partial^2 \omega}{\partial\xi\partial\eta} \qquad (9)$$

from which the dimensionless shear stress $\tau_{\xi\eta}$ is obtained.

With the normal and shear stresses known at each point, the two principal stresses lying in the plane of the plate surface, as well as their orientation are easily obtained. The third principal stress, normal to the surface is, of course, equal to zero. With the three principal stresses know for all points in the grid the maximum shear stress is readily obtained.

4. SOME CHARACTERISTICS OF THE DIGITAL COMPUTER CODE ANALDYNE-1

This digital computer code (analytical dynamics-1) has been developed to form a complete, highly accurate, free vibration analysis of all plates of Groups 1 and 2 as discussed above. It is easy to employ in that one need only choose the group and case numbers for their plate of interest from a prepared list and enter the required plate properties. One can demand an eigenvalue search with a prescribed increment between prescribed limits, or, if the eigenvalue is known, it may be entered and a complete analysis of the mode shape, bending moment, and stress distribution is carried out. An additional and important feature of the code is its ability to conduct a mode shape and stress analysis in dimensional form if the maximum anticipated displacement of the plate, while vibrating in the mode of interest, is prescribed. Highly accurate computation of the fatigue stress amplitudes are performed and fatigue life can be predicted. At present, the dimensions are in English units.

The code generates the master matrix when solving problems of Group 2. Despite its broad capabilities, its running time is very short and storage requirements are a minimum. Numerous verification runs have been performed on a large I.B.M. computer as well as a much smaller Vax machine.

5. SUMMARY AND CONCLUSIONS

In this paper an analytical procedure has been outlined whereby a highly accurate free vibration analysis of rectangular plates of any aspect ratio, and any combination of classical boundary conditions, is achieved. The most remarkable aspect of this procedure is that it has permitted the preparation of a single and relatively compact digital computer code which has the capacity to perform all of the computations. In addition to computing mode shapes the code also has the capacity to compute principle stress distributions as well as maximum shear stress distributions throughout the plate. This latter aspect is of critical importance when fatigue stresses and fatigue life are under study. Because mode shape solutions are available in analytical form the differentiation required for stress computation does not present the difficulties characteristic of numerical methods such as the finite element method. Advances reported here have permitted development of a compact computer code which, for the first time, has the capability to provide analytical typesolutions for all of the classical rectangular plate free vibration problems.

NOMENCLATURE

a,b	edge lengths of plate being analyzed
D	plate flexural rigidity $= Eh^3/(12(1-\nu^2))$
E	Young's modulus of plate material
h	plate thickness
K^*	upper subscript limit for terms of first summation
K	upper subscript limit for terms of series
M	plate bending moment
W	plate lateral displacement divided by edge length a
α	angle of orientation of bending moment
ξ	distance along edge divided by edge length a
η	distance along edge divided by edge length b
τ	time
λ^2	eigenvalue $= \omega a^2\sqrt{\rho/D}$
ω	circular frequency of vibration
ρ	mass of plate per unit area
ϕ	plate aspect ratio $= b/a$
ν	poisson's ratio of plate material

REFERENCES

1. G.B. WARBURTON 1954 Proceedings of the Institution of Mechanical Engineers, Ser.A, 168, 371-384. The vibration of rectangular plates.

2. A.W. LEISSA 1973 Journal of Sound and Vibration 31(3), 257-293. The free vibration of rectangular plates.

3. D.J. GORMAN Free Vibration Analysis of Rectangular Plates. Elsevier North Holland, Inc.

4. S. TIMOSHENKO and S. WOINOWSKY-KRIEGER 1959 Theory of Plates and Shells. McGraw-Hill Book Co. 2nd edition.

5. D.J. GORMAN and R.K. SHARMA 1976 Journal of Sound and Vibration 47, 126-128. A comprehensive approach to the free vibration analysis of rectangular plates by use of the method of superposition.

MINIMISED INPUT POWER BY LINE FORCE EXCITATION

P. Hammer and B. Petersson

Department of Engineering Acoustics
Lund Institute of Technology

1. INTRODUCTION

It is customary to couple the two subsystems, source and receiver, in a number of discrete points and the sound and vibration power transmission is thereby conveniently treated by means of mobility theory. A basic condition for such an approach is that the point - thereby used in a somewhat extended meaning - can be regarded as an area of dimensions smaller than a fraction of the governing wavelength. Consequently, some complications arise in the theoretical treatment when an installation is suggested where the coupling is constituted by large line footings. Such a coupling however, can be appropriate e.g. for static reasons or due to strict requirements on alignment. Hence, it is important to study the alterations in the mobility approach that are necessary in order to incorporate large contact areas.

The concept of strip mobility has been introduced [1], [2]. To complement this studies concerning strip-coupled subsystems the aim of the present work has been to seek the force distribution along a strip attached to an infinite plate which minimises the power transmission.

The reason for choosing an infinite plate is due to the fact that common parts of built-up systems are plate-like. For systems found in practice the dimensions are finite. However, valuable qualitative insight can be gained by simplifying the analysis by considering the plate as infinite.

2. THEORY

The analysis is restricted to comprise small displacements, hence linear theory is valid. Only sinusoidal motion is considered wherefore the time-base is chosen to be $e^{j\omega t}$. However, throughout this text the time factor will be omitted.

The infinite plate is considered to be homogeneous and thin which implies that the thickness is only a fraction of the governing wavelength. Rotational inertia and shear deformation will be neglected. Hence, simple bending theory for thin plates is valid.

Internal and radiation losses in the plate will be neglected, as well as the influence of the local contact phenomena including a possible portion of viscous damping at the excited region. Taking into account the external forces, the governing equation in phasor notation becomes [3],

$$\Delta\Delta\underline{v} - k^4 \underline{v} = \frac{j\omega}{B'} \underline{\sigma}(x,y) \quad , \qquad (2.1)$$

where, $\underline{v}$ is the spatial transverse velocity of the plate, k the bending wavenumber, B' the bending stiffness per unit width, $\underline{\sigma}$ the normal force per unit area due to the source that acts normal to the plate i.e. the receiving structure and Δ the two-dimensional Laplace operator.

The solution to equation (2.1) is a combination of two cylindrical Hankel functions of the second kind [3]. Thus,

$$\underline{v}(x,y) = \int_S \int \underline{\sigma}(x,y)\, Y_0\, \Pi(kr)\, dx\, dy \quad , \tag{2.2}$$

where Y_0 is the input point mobility and $\Pi(kr)$ is the combination of the cylindrical Hankel functions

$$\Pi(kr) = H_0^{(2)}(kr) - H_0^{(2)}(-jkr) \quad .$$

It must be noted that in the present case the surface on which the force distribution $\underline{\sigma}(x,y)$ acts is herein defined as a long narrow strip where the width of the strip is assumed to be only a fraction of the governing wavelength and the length of the strip may comprise several wavelengths. Hence, the force distribution formally may be written as

$$\underline{\sigma}(x,y) = \underline{\sigma}(x) \cdot \delta(y)$$

Moreover, the spatial distribution of the force is chosen to be real and the net force

$$F = \int_{-\ell/2}^{\ell/2} \sigma(x)\, dx \tag{2.3}$$

and symmetric, i.e.

$$\sigma(x) = \sigma(-x) \tag{2.4}$$

A reason for presuming a real, spatial distribution is that such a distribution may be realised by combining simple, passive components. Secondly, the symmetry is a condition for no net moment.

2.1 Minimisation of the input power

Consider the configuration sketched in Figure 2.1.

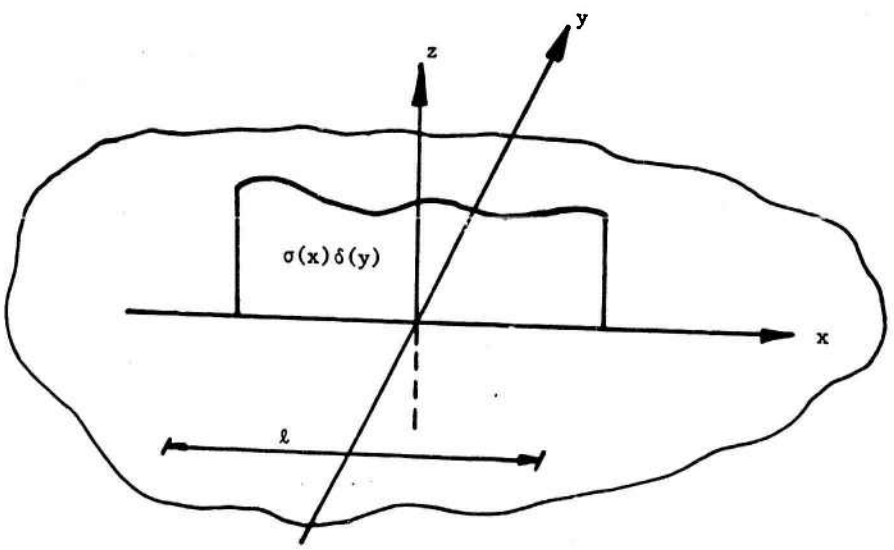

Figure 2.1. An infinite plate excited by a line force distribution $\sigma(x)\delta(y)$.

The complex input power may be written

$$Q = \frac{1}{2} \int_{-\ell/2}^{\ell/2} \int_{-\infty}^{\infty} \underline{\sigma}(x)\, \delta(y)\, \underline{v}^*(x,y)\, dxdy \quad . \qquad (2.5$$

By using equation (2.2) one may rewrite equation (2.5) as

$$Q = \frac{Y_0}{2} \int_{-\ell/2}^{\ell/2} \underline{\sigma}(x)\, dx \left(\int_{-\ell/2}^{\ell/2} \underline{\sigma}(x_0)\, \Pi(k(x - x_0))\, dx_0 \right)^* . \qquad (2.6)$$

Principally this is the equation underlying the minimisation. For engineering practice however, the active power transmitted often is of primary concern, wherefore the real part of equation (2.6) is chosen for the minimisation.

Thus, with the limitations introduced above, equation (2.6) is developed to yield

$$W = \frac{Y_0}{2} \int_{-\ell/2}^{\ell/2} \sigma(x)\, dx \int_{-\ell/2}^{\ell/2} \sigma(x_0)\, J_0(k(x - x_0))\, dx_0 \qquad (2.7)$$

where, W is the real part of Q and J_0 is the zero order Bessel function.

A more tractable formulation is obtained by setting $\xi = \frac{2x}{\ell}$ and $\eta = 2x_0/\ell$.

Thereby, a modified force distribution of $\sigma(x)$ may be written as,

$$\sigma(\xi) = 2F/\ell \cdot p(\xi) \quad ,$$

where $p(\xi)$ is a dimensionless spatial distribution. Hence, with a change of integration variables, equation (2.7) becomes

$$W = \frac{Y_0}{2} F^2 \int_{-1}^{1} p(\xi)\, d\xi \int_{-1}^{1} p(\eta)\, J_0 \left(\frac{k\ell}{2} (\xi - \eta) \right) d\eta \qquad (2.7a)$$

Introducing another force distribution $p_0(\xi)$ which has the property of minimising the active input power, the latter denoted W_0, a variational technique can be applied. Hence, the problem may be summarised as

$$W = W_0 \qquad \text{if} \quad p(\xi) = p_0(\xi)$$

and (2.8)

$$W > W_0 \qquad \text{if} \quad p(\xi) \neq p_0(\xi)$$

With the constraints in equations (2.3) and (2.4) and the conditions in equation (2.8) imposed on equation (2.7a) one obtains the infinite system of integral equations, [4],

$$\int_{-1}^{1} p_0(\xi)\,\frac{d}{dx}\,J_1\left(\frac{k\ell}{2}\,\xi\right)\,d\xi = 0$$

$$\int_{-1}^{1} p_0(\xi)\,\left(\frac{d}{d\xi}\right)^3 J_1\left(\frac{k\ell}{2}\,\xi\right)\,d\xi = 0 \qquad n=1,2,3\ldots \qquad (2.9)$$

$$\int_{-1}^{1} p_0(\xi)\,\left(\frac{d}{d\xi}\right)^{2n-1} J_1\left(\frac{k\ell}{2}\,\xi\right)\,d\xi = 0$$

where J_1 is the first order Bessel function.

Finally, the choise of $p_0(\xi)$ remains. An admissible choice for a power series to describe $p_0(\xi)$ is

$$p_0(\xi) = \frac{1}{2} - \sum_{m=1}^{n} \frac{a_{2m}}{2m+1} + \sum_{m=1}^{n} a_{2m}\,\xi^{2m} \quad ,$$

since it fulfils the constraints stated in equations (2.3) and (2.4). The set of integral equations (2.9) is solved numerically.

Knowing the force distribution, the strip mobility may be determined. This quantity is proportional to the power present at the excited region and may be interpreted as a transition from the continuous case to the equivalent, single point case.

From the definition of the complex strip mobility, [1] and [2],

$$Y_Q = \frac{Y_0}{|F|}\int_{-1}^{1} \underline{q}(\xi)d\xi \int_{-1}^{1} \underline{q}(\eta)^*\,\Pi\left(\frac{k\ell}{2}(\xi-\eta)\right)^* d\eta \qquad (2.10)$$

where $\underline{q}$ is an arbitrary spatial distribution.

However, in the present case where $q_0(\xi)$ is real and $|F| = 1$ one may find that the real part of the strip mobility is

$$\mathrm{Re}[Y_Q] = Y_0 \int_{-1}^{1} p(\xi)d\xi \int_{-1}^{1} p(\eta)\,J_0\left(\frac{k\ell}{2}(\xi-\eta)\right)\,d\eta \qquad (2.11)$$

Inserting the power series for $p_0(\xi)$ in equation (2.11) and using the binomial theorem one may rewrite equation (2.11) in the form,

$$\mathrm{Re}[Y_Q] = Y_0 \sum_{s=0}^{\infty} \frac{(-1)^s}{(s!)^2}\left(\frac{k\ell}{4}\right)^{2s} \cdot \sum_{t=0}^{2s}\binom{2s}{t} \int_{-1}^{1} \xi^{2s-t}\cdot\left(\frac{1}{2} - \sum_{m=1}^{n}\frac{a_{2m}}{2m+1} + \right.$$

$$\left. + \sum_{m=1}^{n} a_{2m}\xi^{2m}\right)d\xi \cdot \int_{-1}^{1} (-y_0)^t\left(\frac{1}{2} - \sum_{m=1}^{n}\frac{a_{2m}}{2m+1} + \sum_{m=1}^{n} a_{2m}\,y^{2m}\right)\,dy_0$$

3. NUMERICAL RESULTS

3.1 Force distribution in the case of minimised input power

The force distribution minimising the input power is shown in Figure 3.1.

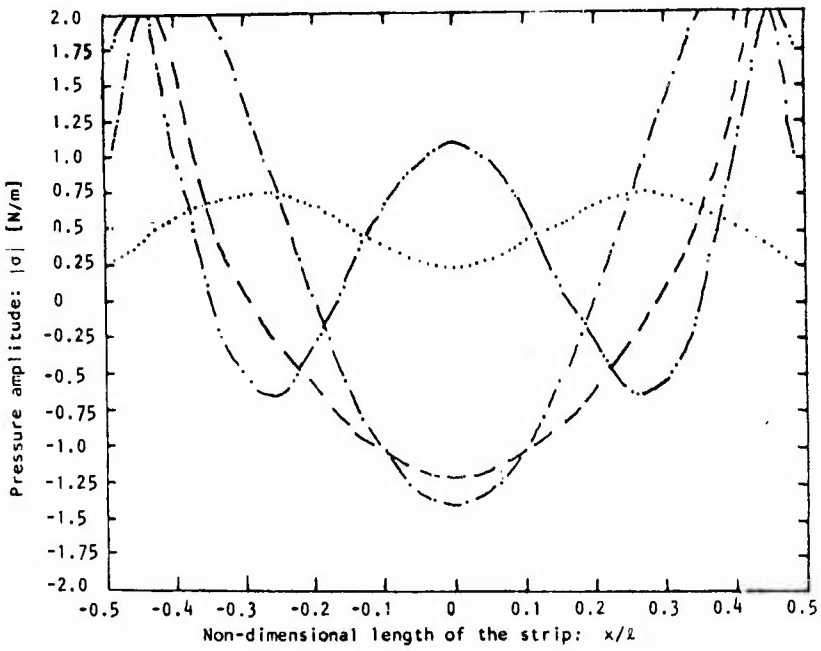

Figure 3.1. The spatial variation of the force distribution minimising the active power transmitted for some Helmholtz numbers. (---): kℓ=3, (-•-•-): kℓ=4, (••••): kℓ=7, (-••-••-): kℓ=10.

For low Helmholtz number, kℓ < 1.5, the numerical unstability in order to solve eq. (2.9) heavily affect the solutions. However, this is with respect to power transmission of minor interest, since the excited region may be considered to be point-like.

Increasing the Helmholtz number, one may note that maxima and minima come closer and closer. The distance between the peaks and troughs is approximately half a wavelength. Comparing this case with the simpliest discretice case, namely two point forces, where the distance between the forces is d. The minimum input power would be obtained when $d \approx \lambda/2$, [5]. Finally, the curves in Figure 3.1 indicate that the spatial distribution is periodic, but the variation of the amplitude versus kℓ is irregular.

3.2 Normalised strip mobility

In Figure 3.2 the real part of the normalised strip mobility for the two, real, excitation conditions - the force distribution giving the minimum input power and the uniform force distribution - are compared. In addition, the input power for the case of a cosecant shaped force distribution, [1], is included. The latter distribution resembles that found from half-space theory, [6].

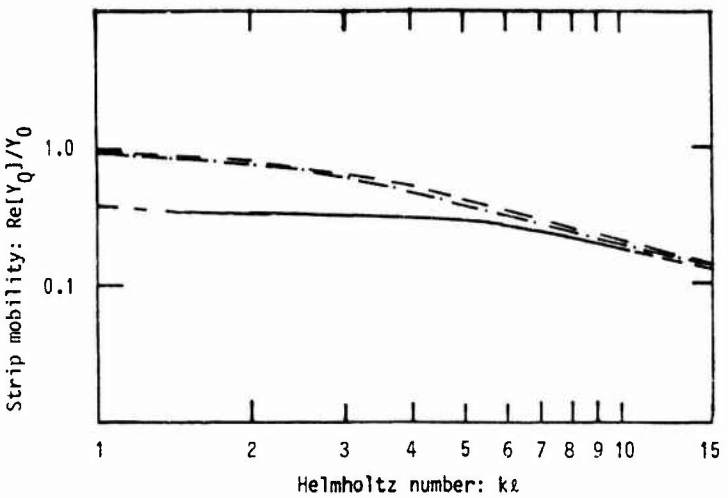

Figure 3.2. Normalised strip mobility versus Helmholtz number. (——): minimising force, (---): uniform force and (-·-): cosecant shaped force.

It is seen from Figure 3.2 that for low Helmholtz numbers the real parts of the strip mobilities are equal to the ordinary point mobility for the two force distributions, uniform and cosecant respectively. Naturally, for kℓ low enough this, also may be found to be valid for the minimising force distribution. In the region of kℓ inbetween 1.5 and 4 one may note that the real part of the normalised strip mobility decreases more for the minimising force distribution than for other cases.

However, as kℓ increases the difference in real parts between the different cases diminishes. This trend may also be found valid in the cases of other force distributions, [7].

4. CONCLUSIONS

It is found from a variational approach that there exists a real-valued force distribution which, in a certain range of Helmholtz numbers, reduces the input power in comparison with other force distributions. Furthermore the input power by strip excitation is significantly less than in the point excitation case at high Helmholtz numbers. Hence, by a proper design of the strip interface (including some transmission elements) between the source and receiver structures, the power transmission may be minimised, given a net force.

For high Helmholtz numbers in the strip excitation cases investigated, the input power tends to be independent of the excitation distribution. The asymptote is that of an equivalent point excited, infinite beam.

The constraints on the force distribution, hence, whether it is set to be complex or real with regards to its spatial variation, is of importance. Thus, reformulating the constraints to incorporate a complex distribution of the force will give a different input power compared with that obtained for a real-valued force distribution.

Finally, for the special case of a real and positive force distribution, the minimum is obtained with the distribution derived above, superposed on a uniform distribution. The magntiude of the uniform part is equal to the minimum stress of the alternating part. This distribution is realisable simply by a continuous bed of springs with varying stiffness.

5. ACKNOWLEDGEMENT

The financial support received from the Swedish Council for Building Research is gratefully acknowledged.

6. REFERENCES

1. P. HAMMER 1986 Dept. of Engineering Acoustics, Lund Institute of Technology, Report TVBA-3034. Structural Acoustics in Built-up Systems; Part I: Strip mobility.

2. B. PETERSSON 1983 Dept. of Building Acoustics, Chalmers University of Technology, Report S83-04. Structure-Borne Sound Power Transmission between Line-Coupled Source and Receiver Systems; Part I: An introductory study.

3. L. CREMER, M. HECKL and E.E. UNGAR 1973 Structure-Borne Sound. Springer Verlag.

4. P. HAMMER 1987 Dept. of Engineering Acoustics, Lund Institute of Technology. Report TVBA-3045. Structural Acoustics in Built-up Systems; Part IV: Minimised input power.

5. Dept. of Engineering Acoustics, Lund Institute of Technology 1987 Short course on ordinary and effective mobility.

6. G.N. BYCROFT 1956 Phil. Trans. Roy. Soc., A248, 327-368. Forced vibrations of a rigid circular plate on a semi-infinite elastic space and on an elastic stratum.

7. P. HAMMER 1987 Dept. of Engineering Acoustics, Lund Institute of Technology, Report TVBA-3044. Structural Acoustics in Built-up Systems; Part III: Uniform velocity distribution along a finite strip.

EXACT SOLUTIONS FOR WAVE PROPAGATION IN RINGS AND ARCHES ON ELASTIC FOUNDATIONS

Omer A. Fettahlioglu
New York Institute of Technology

1. INTRODUCTION

The purpose of this paper is to present closed-form solutions for the characteristics of traveling elastic waves in circularly curved thin rings and arches on elastic foundations, and then to exhibit the effects of extensional and shearing deformations and elastic foundations on the frequencies, phase and group velocities of the propagating waves in rings and arches with various boundary conditions.

The present treatise which deals with the problem in its general form has been developed previously in [1] from variational considerations using Hamilton's principle to derive the exact equations of motion for thin circularly curved beams and rings, together with consistent boundary, discontinuity and initial conditions in terms of the radial and tangential midsurface displacements and the rotation of the normal. The theory accounts for the effects of extensional, flexural and shearing deformations, and rotatory inertia. The effects of distributed elastic foundations in the radial, tangential and rotational directions are also incorporated into the equations of motion.

The vibration and wave propagation analysis on which the present investigation is based properly begins with the resolution of the foregoing equations of motion given in [2] into three-uncoupled sixth order homogeneous differential equations in terms of radial and tangential midsurface displacements, and the rotation. Using the classical form for the traveling wave solution, the exact equations for the frequency, phase and group velocities are derived herein for closed rings in terms of flexural, transverse shearing and extensional stiffnesses as well as the three spring constants of the elastic foundations as precisely identifiable parameters. The frequency equation reduces to that found by Lamb [3] neglecting the effects of extensional and shearing deformations, and elastic foundations. The governing dispersion relations are derived and exhibited in terms of short and long wave lengths, cutoff frequencies and standing waves. The effects of extensibility and/or shearing deformation and elastic foundations are also examined.

With the exception of Graff [4], little attention has been given to wave propagation in rings with or without the effects of extensional and shearing deformations. Dispersion curves and frequency spectra wherein the effects of elastic foundations, curvature, extensibility, shearing deformation and rotatory inertia on the wave propagation characteristics of rings and arches of various boundary conditions may be assessed, are not available in the literature. Moreover, Graff's frequency and phase velocity equations which neglected elastic foundations, the shearing deformation and the rotatory inertia do not reduce to the classical inextensional solution. This is due to the fact that the effect of the tangential displacement on the rotation of the normal was not included in his strain-displacement relation which yields inconsistency in the resulting equations of motion. Furthermore, Graff's study is confined to phase velocity only, thus in fact leaving out the group velocity with which the energy propagates.

Exact solutions for the midsurface displacements in the radial and tangential directions, the rotation and the stress resultants are also derived for steep arches in terms of six independent constants of integration. The frequency spectra for the steep arches with elastic foundations (fixed-fixed, fixed-hinged and hinged-hinged) are then developed by means of the exact deformations and stress resultants.

2. GOVERNING EQUATIONS

A thin circular ring element (Fig. 1) that is symmetrical about the plan of its centroidal axis is considered to be deformed in the plane of its initial curvature with normals preserved in the process (Bernoulli - Euler hypothesis).

The present treatise properly begins with the steady-state solution of the deformation equations of motion of the following form given in [1]:

$$\begin{aligned} a(v'-w)+c(w''+v'-R\varphi')-k_1Rw &= \rho AR\ddot{w} \\ a(v''-w')-c(w'+v-R\varphi)-k_2Rv &= \rho AR\ddot{v} \\ bR^2\varphi''+cR(w'+v-R\varphi)-k_3R\varphi &= \rho IR\ddot{\varphi} \end{aligned} \qquad (1)$$

in which dots and primes denote differentiation with respect to time and θ, respectively, and ρ is the mass density of the ring. The spring constants of the elastic foundations k_1 , k_2 and k_3 indicate their resistances in the radial, tangential and rotational directions. The stiffness constants are defined as

$$a = EA/R \;\; ; \;\; b = EI/R^3 \;\; ; \;\; c = fAG/R \qquad (2)$$

where A, I and f are the area, the moment of inertia of the cross section and the form factor for shear, respectively.

The propagation characteristics of rings and arches are developed by considering the solutions of (1) for the dimensionless vector of deformations of the form

$$\underline{Y}(\theta,\tau) = \underline{Y}(\theta).\exp(i\omega^*\tau) \qquad (3)$$

where,

$$\underline{Y} = [w/R,\; v/R,\; \varphi]^T \qquad (4)$$

$$\underline{Y} = [W,\; V,\; \Phi]^T = \underline{A}\exp(-i\lambda\theta) \qquad (5)$$

in which $\underline{A}$ is the eigenvector whose components are the maximum amplitudes of the deformations. The dimensionless wave number and the phase velocity are

$$\lambda = Rm \;\; ; \;\; \gamma = \Omega^*/\lambda \qquad (6)$$

in which m is the dimensional wave number; and Ω^* is related to the dimensional circular frequency, ω as follows:

$$\Omega^* = \tilde{\Omega}Z^{1/4} = (t/\tau)\omega = \omega R(\rho/E)^{1/4} \qquad (7)$$

The term $(E/\rho)^{1/4}$ is the bar velocity. The dimensionless time, τ in terms of the dimensional time, t is chosen to be: $\tau=(t/R)(E/\rho)^{1/4}$

3. SOLUTION FOR CLOSED RINGS

The substitution of (3) into the normalized form of (1) and the elimination of W,V and ϕ successively (considering the operational coefficients of the variables W, V and ϕ) with the notation of $D=d/d\theta$ yields a system of homogeneous equations whose nontrivial solution exist, if and only if the determinant of its coefficient matrix is equal to zero.

$$[D\delta+\alpha_1 D^4+\alpha_2 D^2+\alpha_3] \begin{Bmatrix} V(\theta) \\ W(\theta) \\ \phi(\theta) \end{Bmatrix} = 0 \qquad (8)$$

where, letting $\tilde{\Omega}^2=\Omega=\omega^2 R^4(\rho A/EI)$ (9)

$$\alpha_1 = 2+\Omega Z(2+X)-Z(\delta_1 X+\delta_2)-\delta_3/Z$$

$$\alpha_2 = (\Omega Z)^2(1+2X)+\Omega(Z-XZ-1)+1+\delta_1(1-2\Omega XZ^2+Z)+\delta_2 Z(X-\Omega XZ-\Omega Z)-\delta_3(\Omega+\Omega X+2/Z)+$$
$$\delta_1\delta_2 XZ^2+\delta_2\delta_3+\delta_3\delta_1 X$$

$$\alpha_3 = (\Omega Z)^3 X-(\Omega Z)^2(1+X)-\Omega^2 Z+\Omega(1+Z)+\delta_1(\Omega Z)(1+Z-\Omega XZ^2)+\delta_2[-1+\Omega Z(1+ZX)-$$
$$\Omega^2 Z^3 X]+\delta_3[\Omega(1+X)-\Omega^2 ZX-1/Z]+\delta_1\delta_2 Z+(\Omega Z^2 X-1)+\delta_2\delta_3 X(\Omega Z-1)+$$
$$\delta_3\delta_1(\Omega ZX-1)-\delta_1\delta_2\delta_3 ZX$$

The dimensionless spring constants of the foundations are defined in the form

$$\delta_1 = K_1 R^4/EI \quad ; \quad \delta_2 = K_2 R^4/EI \quad ; \quad \delta_3 = K_3/EA \qquad (10)$$

The dimensionless quantities Z and X are the measures of extensibility and shearing deformation, respectively, and are given by the relations

$$X = a/c = E/fG \quad \text{and} \quad Z = b/a = I/AR^2 \qquad (11)$$

3.1 Frequencies

The subsequent substitution of (5) into (8) gives the frequency equation

$$B_1\Omega^3+B_2\Omega^2+B_3\Omega+B_4 = 0 \qquad (12)$$

where,

$$B_1 = XZ^3;$$

$$B_2 = -[\lambda^2 Z^2(1+2X)+Z^2(1+X)+Z+XZ(\delta_1 Z^2+\delta_2 Z^2+\delta_3)]$$

$$B_3 = \lambda^4 Z(2+X)+\lambda^2[1-Z(1-X)]+1+Z+\delta_1 Z(2\lambda^2 XZ+1+Z)+\delta_2 Z[Z\lambda^2(1+X)+1+ZX]+$$
$$\delta_3(1+\lambda^2)(1+X)+ZX(\delta_1\delta_2 Z^2+\delta_2\delta_3+\delta_1\delta_3)$$

$$B_4 = -\lambda^2(\lambda^2-1)^2-\delta_1\lambda^2(\lambda^2 XZ+1+Z)-\delta_2(\lambda^4 Z+\lambda^2 ZX+1)-\delta_3(1/Z)(\lambda^2-1)^2-$$
$$\delta_1\delta_2 Z(\lambda^2 ZX+1)-\delta_2\delta_3(\lambda^2+X)-\delta_1\delta_3(1+X\lambda^2)-\delta_1\delta_2\delta_3 ZX$$

The frequency polynomial (12) rewritten in terms of wave number is:

$$\lambda^6-\alpha_1\lambda^4+\alpha_2\lambda^2-\alpha_3 = 0$$

For the special case of inextensibility (Z=0) and δ_3=0, the frequency polynomial (12) takes the form

$$\tilde{\Omega}^2 = [\lambda^2(\lambda^2-1)^2+\delta_1\lambda^2+\delta_2]/(1+\lambda^2) \qquad (13)$$

which reduces to the form given by Lamb [3] in the absence of elastic foundations. Cutoff frequencies are obtained at λ=0 for the three branches of the frequency spectra as follows:

$$\tilde{\Omega}_1^2=0 \; ; \quad \tilde{\Omega}_2^2=(1+Z\delta_1)/Z \; ; \quad \tilde{\Omega}_3^2=(1+Z)/XZ^2 \qquad (14)$$

Computer results clearly indicate in Fig.2 and Table 1 that the elastic foundation, δ_1 has a pronounced effect on the frequencies for wave numbers less than about 10, that is for long wave lengths; however, this effect attenuates as the wave number increases beyond 10. It is also clear that the effect of extensibility increases significantly as the wave number increases from about five. The shearing deformation has also a considerable effect on the fundamental frequency, only for wave numbers greater than about five.

An enlargement of the frequency of the first mode in the long wavelength region of Fig. 2 (in the absence of elastic foundations) would reveal that the fundamental frequency increases from zero at λ=0 to a maximum of small magnitude, 0.34 at λ=0.5; then it decreases to become zero at λ=1, Table 1. In the absence of elastic foundation the phase velocity is also zero at λ=1 given later by equation (21).

3.2 Velocities

The roots of the frequency equation (12) give the solutions of the propagating waves of the following form for the vector of deformations (3) by means of (6) and (7):

$$\underline{Y} = \underline{A}\, \exp[i(\gamma\tau-\theta)\lambda] \qquad (15)$$

Consequently, (12) is transformed into a cubic in γ^2 or a quadratic polynomial in λ^2 neglecting δ_2 and δ_3

$$\lambda^4(XZ)\gamma^6-\lambda^2[\lambda^2Z(1+2X)+Z(1+X)+1+XZ^2\delta_1]\gamma^4+(\lambda^4Z(2+X)+\lambda^2[1-Z(1-X)]+1+Z+$$

$$\delta_1Z(2\lambda^2XZ+1+Z)]\gamma^2-Z[(\lambda^2-1)^2+\delta_1(\lambda^2XZ+Z+1)] = 0 \qquad (16)$$

The group velocity, V_g which is the velocity of energy propagation is determined from either the slope of the tangent to the frequency diagram or the slope of the tangent to the phase velocity diagram by the formula

$$V_g = \partial\Omega^*/\partial\lambda = \gamma+\lambda\partial\gamma/\partial\lambda \qquad (17)$$

From the former point of view using (7)

$$V_g = \partial\Omega^*/\partial\lambda = C/D \qquad (18)$$

$$C = Z\lambda^4[\gamma^4(1+2X)-2\gamma^2(2+X)+3]-\lambda^2[\gamma^2(1-Z+XZ+2XZ^2\delta_1)+2Z(2-XZ\delta_1)]$$

$$+Z[1+\delta_1(1+Z)]$$

$$D = Z\lambda^4\gamma[3X\gamma^4-2\gamma^2(1+2X)+2+X]+\lambda^2\gamma[-2\gamma^2(Z+ZX+Z^2X\delta_1+1)+1-Z(1-X)$$

$$+2XZ^2\delta_1]+\gamma(1+Z)(1+Z\delta_1)$$

For the special case of inextensibility (Z=0), (16) and (18) reduce to the forms

$$\gamma_1^2 = 0 \; ; \; \gamma_2^2 = (\lambda^2+1)/\lambda^2 \quad \text{and} \quad V_{g1} = 0 \; ; \; V_{g2} = 1/\gamma_2 \qquad (19)$$

Analytic solutions for certain limiting and special cases of the preceding equations are easily obtained as follows:

1) Short wave length limit. For $\lambda \to \infty$, two horizontal asymptotes shown in Fig.3 are obtained from (16) and (18) associated with the phase and group velocities

$\gamma = V_g = 1$ gives $v_p = v_g = (E/\rho)^{1/2}$, bar velocity

$\gamma = V_g = X^{-1/2}$ gives $v_p = v_g = (fG/\rho)^{1/2}$, shear velocity

where, v_p and v_g are dimensional phase and group velocities, respectively.

2) Long wave length limit. For $\lambda \to 0$, the resulting limits are of the form

$$\gamma^2 = V_g^2 = Z[1+\delta_1(1+Z)]/(1+Z)(1+Z\delta_1) \qquad (20)$$

3) Standing waves. Substitution of $\gamma=0$ in (16) gives the corresponding value of the wave number to be determined from the equation:

$$\lambda^4-\lambda^2(2-XZ\delta_1)+1+\delta_1(1+Z) = 0 \qquad (21)$$

which yields $\lambda=1$ neglecting the elastic foundation. With the inclusion of the elastic foundation, however, (21) has no roots. In fact the phase velocity (16) has a minimum

$$\gamma^2_{min} \approx Z[(\lambda^2-1)^2+\delta_1]/(\lambda^2+1) \qquad (22)$$

at a wave number

$$\lambda^2 \approx [2(\delta_1+4)^{1/2}-2-XZ\delta_1]/2 \qquad (23)$$

These special cases provide useful checks for the numerical computations of the various dispersion curves. The group velocity has a jump discontinuity when the phase velocity is zero at $\lambda=1$; however, with the inclusion of the elastic foundation it becomes a continuous function exhibiting a minimum lower than the minimum phase velocity, at a wave number greater than two, Fig. 4. Indeed, for the first mode $\gamma<V_g$ when $\partial\gamma/\partial\lambda>0$ on the short wave length branch, which is referred to as anomalous dispersion; conversely, $V_g<\gamma$ when $\partial\gamma/\partial\lambda<0$ on the long wave length branch, for which the normal dispersion occurs, Fig. 3 and 4. Moreover, for very long waves the first mode has negative group velocity. This implies that energy is propagated in the direction opposite to that of traveling waves as also was shown by Lamb [5] and Crandall [6,7] on straight wires and beams, respectively. The lowest mode phase and group velocities are asymptotic to the shear velocity, $X^{-1/2}$ for very large wave numbers; however, the higher phase and group velocities of the second and third modes are asymptotic to the bar velocity at very large wave numbers. For the second and third modes the group velocity is always less than the phase velocity. Table 2 presents exact numerical values of the phase velocities corresponding to various levels of X and Z effects for numerous wave numbers.

The present steady-state solution indicates that there are three "critical" load speeds. These are equal to (1) the speed of propagation in a bar, (2) the speed of shear waves, and (3) the substantially lower minimum phase velocity.

4. SOLUTION FOR ARCHES

The general solution of (8) gives the auxiliary equation

$$r^6+a_1r^4+a_2r^2+a_3 = 0 \qquad (24)$$

The roots of this polynomial (24) are functions of $\tilde{\Omega}$; and the elimination of the arbitrary constants from the six boundary conditions (three for each end) gives the frequency values. The behavior of the roots of (24) is determined by substituting the value of $\tilde{\Omega}$ calculated from Lamb's "classical" inextensional solution [3]; the result is 3 pairs of complex-conjugate roots. Therefore, the general solution of (8) for steep arches (α > 180) is

$$W = (\exp p_1\theta)(C_1\cos q_1\theta+C_2\sin q_1\theta)+(\exp p_2\theta)(C_3\cos q_2\theta+C_4\sin q_2\theta)$$

$$+(\exp p_3\theta)(C_5\cos q_3\theta+C_6\sin q_3\theta) \qquad (25)$$

The expressions for V and Φ are similarly written in terms of constants F and H, respectively. The eighteen constants of integration are not all independent. The conditions that insure that the equations of motion (1) are identically satisfied by the substitution of the foregoing deformations (25) yield after substantial algebra the admissible deformations in terms of six independent constants of integration: C_i, i=1,... 6. The relations which connect the twelve dependent constants to the six independent constants are given in the Appendix. The stress resultants are then obtained from their general expressions given in [1, 2].

Arches of any boundary conditions can then be analyzed in a consistent manner accounting for the effects of extensional and shearing deformations, and the elastic foundation in the radial direction. The conditions yield six simultaneous homogeneous algebraic equations in terms of the frequency, the roots of the auxiliary equation (24) and the six independent constants of integration, C_i (i=1... 6). The determinant of the coefficient matrix must vanish for a nontrivial solution of the boundary equations. In this analysis a trial frequency is calculated from Lamb's inextensional formula; thus permitting the explicit solution of the auxiliary equation. With the assumed value of frequency and the calculated values of the roots of (24), the determinant is solved using the "regula falsi" method (rule of false position).

The effect of the elastic foundation on the fundamental frequency with respect to the angular span is exhibited in Fig. 5 for fixed-fixed, fixed-hinged and two-hinged arches. The effects of extensibility and transverse shear are illustrated in Table 3 for the fixed arch, wherein, an increase in each of the measures of extensional and shearing deformations causes a decrease in frequencies.

The calculations were performed usiong ADA computer program [8] which is written in FORTRAN IV. ADA runs presently on VAX 11/780 supermini computer of New York Institute of Technology under operating system VMS 4.6 , and is currently being revised for implementation on IBM-PC compatible hardware.

5. ACKNOWLEDGEMENT

The author would like to express his appreciation to Dr. Heskia Heskiaoff, Director of Graduate Studies in Computer Science at NYIT for his support. Special thanks are also due to graduate student: Mr. Jeffrey Lloyd for his computer generated graphics and undergraduate M.E. student Mr. Guillermo Guzman-Barron E. for performing numerical analyses and for the preparation of the manuscript.

6. REFERENCES

1. O.A. FETTAHLIOGLU and T.K. STEELE May 19-23, 1980. Proceedings of the Fourth International Conference on Pressure Vessel Technology 2, NO C85/80, 185-192. Thermal Deformations and Stresses in Circularly Curved Thin Beams and Rings.

2. O.A. FETTAHLIOGLU and G.M. YEHODIAN 1984 Proceedings of the Second International Conference on Recent Advances in Structural Dynamics 1, 3-13. Wave Propagation in Circularly Curved Beams and Rings.

3. H. LAMB 1889 Proceedings of the London Mathematical Society 19, 365-376. On the Flexure and Vibrations of a Curved Bar.

4. K.F. GRAFF 1971 International Journal of Mech. Sciences: Pergamon Press, 13, 107-111. On Dispersion of Elastic Waves in Rings.

5. H. LAMB 1904 Proceedings of the London Mathematical Society 1, 473-479. On Group Velocity.

6. S.H. CRANDALL 1956 Proceedings of the Third Midwestern Conference on Solid Mechanics, 146-159. The Timoshenko Beam on an Elastic Foundation.

7. S.H. CRANDALL 1957 Journal of Applied Mechanics, 24, 622-623. Negative Group velocities in Continuous Structures.

8. O.A. FETTAHLIOGLU 1987 New York Institute of Technology. Arch and Ring Dynamic Analysis Program - ADA.

7. APPENDIX

The deformations in arches are

$$W = (\exp p_1\theta)(C_1\cos q_1\theta + C_2\sin q_1\theta) + (\exp p_2\theta)(C_3\cos q_2\theta + C_4\sin q_2\theta) + (\exp p_3\theta)(C_5\cos q_3\theta + C_6\sin q_3\theta)$$

$$V = (\exp p_1\theta)(C_1Y_1 + C_2Y_2) + (\exp p_2\theta)(C_3Y_3 + C_4Y_4) + (\exp p_3\theta)(C_5Y_5 + C_6Y_6)$$

$$\phi = (\exp p_1\theta)(C_1Y_7 + C_2Y_8) + (\exp p_2\theta)(C_3Y_9 + C_4Y_{10}) + (\exp p_3\theta)(C_5Y_{11} + C_6Y_{12})$$

The bending moment [1, 2] takes the form

$$M^* = -(R/EI)M = (d\phi^*/d\theta)$$

$$M^{H} = (\exp p_1\theta)[C_1(q_1Y_8-p_1Y_7)-C_2(q_1Y_7+p_1Y_8)]$$
$$+(\exp p_2\theta)[C_3(q_2Y_{10}-p_2Y_9)-C_4(q_2Y_9+p_2Y_{10})]$$
$$+(\exp p_3\theta)[C_5(q_3Y_{12}-p_3Y_{11})-C_6(q_3Y_{11}+p_3Y_{12})]$$

where,

$$Y_1 = D_1\cos q_1\theta+D_2\sin q_1\theta \quad ; \quad Y_7 = D_7\cos q_1\theta-D_8\sin q_1\theta$$
$$Y_2 = -D_2\cos q_1\theta+D_1\sin q_1\theta \quad ; \quad Y_8 = D_8\cos q_1\theta+D_7\sin q_1\theta$$
$$Y_3 = D_3\cos q_2\theta+D_4\sin q_2\theta \quad ; \quad Y_9 = D_9\cos q_2\theta-D_{10}\sin q_2\theta$$
$$Y_4 = -D_4\cos q_2\theta+D_3\sin q_2\theta \quad ; \quad Y_{10} = D_{10}\cos q_2\theta+D_9\sin q_2\theta$$
$$Y_5 = D_5\cos q_3\theta+D_6\sin q_3\theta \quad ; \quad Y_{11} = D_{11}\cos q_3\theta-D_{12}\sin q_3\theta$$
$$Y_6 = -D_6\cos q_3\theta+D_5\sin q_3\theta \quad ; \quad Y_{12} = D_{12}\cos q_3\theta+D_{11}\sin q_3\theta$$

$$D_1=[-p_1(K_1^2+K_2^2)-h_4(K_1H_{11}-K_2H_{12})+h_7Z(K_1H_{12}+K_2H_{11})]/(K_1^2+K_2^2)$$
$$D_2=[q_1(K_1^2+K_2^2)+h_4(K_1H_{12}+K_2H_{11})+h_7Z(K_1H_{11}-K_2H_{12})]/(K_1^2+K_2^2)$$
$$D_3=[-p_2(K_3^2+K_4^2)-h_5(K_3H_{33}-K_4H_{34})+h_8Z(K_3H_{34}+K_4H_{33})]/(K_3^2+K_4^2)$$
$$D_4=[q_2(K_3^2+K_4^2)+h_5(K_3H_{34}+K_4H_{33})+h_8Z(K_3H_{33}-K_4H_{34})]/(K_3^2+K_4^2)$$
$$D_5=[-p_3(K_5^2+K_6^2)-h_6(K_5H_{55}-K_6H_{56})+h_9Z(K_5H_{56}+K_6H_{55})]/(K_5^2+K_6^2)$$
$$D_6=[q_3(K_5^2+K_6^2)+h_6(K_5H_{56}+K_6H_{55})+h_9Z(K_5H_{55}-K_6H_{56})]/(K_5^2+K_6^2)$$
$$D_7=[K_1H_{11}-K_2H_{12}]/(K_1^2+K_2^2) \quad ; \quad D_8=[K_1H_{12}+K_2H_{11}]/(K_1^2+K_2^2)$$
$$D_9=[K_3H_{33}-K_4H_{34}]/(K_3^2+K_4^2) \quad ; \quad D_{10}=[K_3H_{34}+K_4H_{33}]/(K_3^2+K_4^2)$$
$$D_{11}=[K_5H_{55}-K_6H_{56}]/(K_5^2+K_6^2) \quad ; \quad D_{12}=[K_5H_{56}+K_6H_{55}]/(K_5^2+K_6^2)$$

$$K_1 = 1-h_1h_4+Zh_7^2 \; ; \; K_2 = h_4h_7+Zh_1h_7 \; ; \; K_3 = 1-h_2h_5+Zh_8^2$$
$$K_4 = h_5h_8+Zh_2h_8 \; ; \; K_5 = 1-h_3h_6+Zh_9^2 \; ; \; K_6 = h_6h_9+Zh_3h_9$$
$$H_{11}=h_1p_1-h_7q_1+h_{10}; \; H_{12}=h_1q_1+h_7p_1+h_{11}; \; H_{33}=h_2p_2-h_8q_2+h_{12}$$
$$H_{34}=h_2q_2+h_8p_2+h_{13}; \; H_{55}=h_3p_3-h_9q_3+h_{14}; \; H_{56}=h_3q_3+h_9p_3+h_{15}$$
$$h_1=X(p_1^2-q_1^2)+l_1 \; ; \; h_2=X(p_2^2-q_2^2)+l_1 \; ; \; h_3=X(p_3^2-q_3^2)+l_1$$
$$h_4=XZ(p_1^2-q_1^2)+l_2; \; h_5=XZ(p_2^2-q_2^2)+l_2; \; h_6=XZ(p_3^2-q_3^2)+l_2$$
$$h_7=2p_1q_1X \; ; \; h_8=2p_2q_2X \; ; \; h_9=2p_3q_3X \; ; \; h_{10}=(X+1)p_1$$
$$h_{11}=(X+1)q_1 \; ; \; h_{12}=(X+1)p_3 \; ; \; h_{13}=(X+1)q_2 \; ; \; h_{14}=(X+1)p_3$$
$$h_{15}=(X+1)q_3 \quad ; \quad l_1=XZ(\Omega-\delta_2)-1 \quad ; \quad l_2=X(\Omega Z^2-\delta_3)-1$$

Table 1. Effects of Shearing and Extensional Deformations and Elastic Foundations on Frequencies of a Free Ring

	$\tilde{\Omega}_1$								$\tilde{\Omega}_2$	
X	0.0				3.0				3.0	
Z	0.0		0.001		0.0		0.001		0.001	
λ \ δ_1	0	500	0	500	0	500	0	500	0	500
0	0.0	0.0	0.0	0.0	0.0	0.0	0.0	0.0	31.62	38.72
1	0.0	15.81	0.0	14.80	0.0	15.81	0.0	14.80	44.69	47.73
2	2.68	20.17	2.68	19.93	2.68	20.18	2.66	19.92	70.68	71.44
3	7.58	22.53	7.55	22.37	7.58	22.52	7.45	22.34	99.98	100.2
4	14.55	26.12	14.43	25.89	14.55	26.12	14.10	25.73	130.3	130.5
8	62.50	66.30	60.60	64.30	62.50	66.30	55.97	60.02	255.0	255.0
12	142.5	144.2	133.2	134.8	142.5	144.2	115.0	117.0	381.0	381.0
16	254.5	255.5	227.0	227.9	254.5	255.5	183.5	184.7	507.0	507.0
32	1023	1023	718.5	718.7	1023	1023	488.5	489.0	1013	1013

Table 2. Effects of Shearing and Extensional Deformations and Elastic Foundations on Phase Velocities of a Free Ring

	γ_1								γ_2			
X	3.0				10.0				3.0			
Z	0.0001		0.001		0.0001		0.001		0.0001		0.001	
λ \ δ_1	0	500	0	500	0	500	0	500	0	500	0	500
0.2	.009	.214	.029	.572	.009	.214	.029	.572	5.098	5.217	5.099	6.178
1	0	.157	0	.468	0	.157	0	.468	1.414	1.423	1.414	1.509
2	.013	.010	.042	.315	.013	.100	.0415	.315	1.117	1.119	1.117	1.130
10	.096	.099	.265	.273	.094	.096	.217	.228	1.004	1.004	1.004	1.005
20	.185	.185	.406	.408	.167	.167	.279	.281	1.001	1.001	1.001	1.001
100	.481	.481	.564	.564	.300	.300	.314	.315	1.00	1.00	1.00	1.00

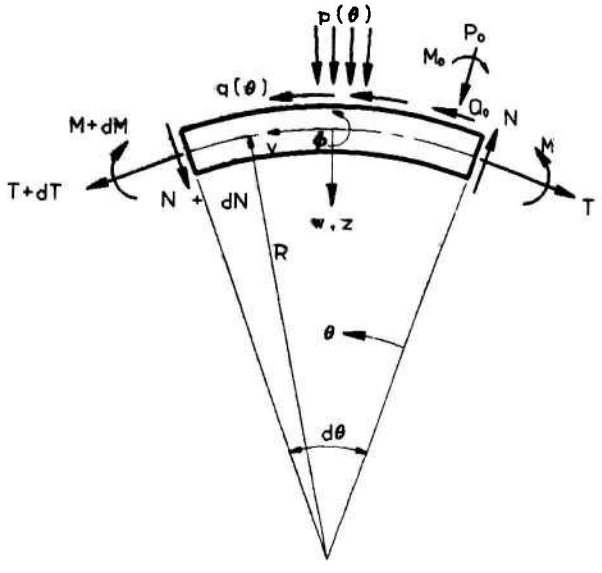

Fig. 1. Geometry of a Ring Element

Table 3. Effects of Extensional and Shearing Deformations and Elastic Foundations on Frequencies of Fixed-Arches

$\tilde{\Omega}_1$								
α	200°					260°		
X	0		3			3		
Z \ δ_1	0	50	0	30	50	0	30	50
.0000	3.308	6.281	3.308	5.301	6.281	1.562	3.940	4.897
.0007	3.299	6.233	3.266	5.247	6.210	1.551	3.908	4.840
.0050	3.242	5.931	3.039	4.946	5.800	1.488	3.718	4.505

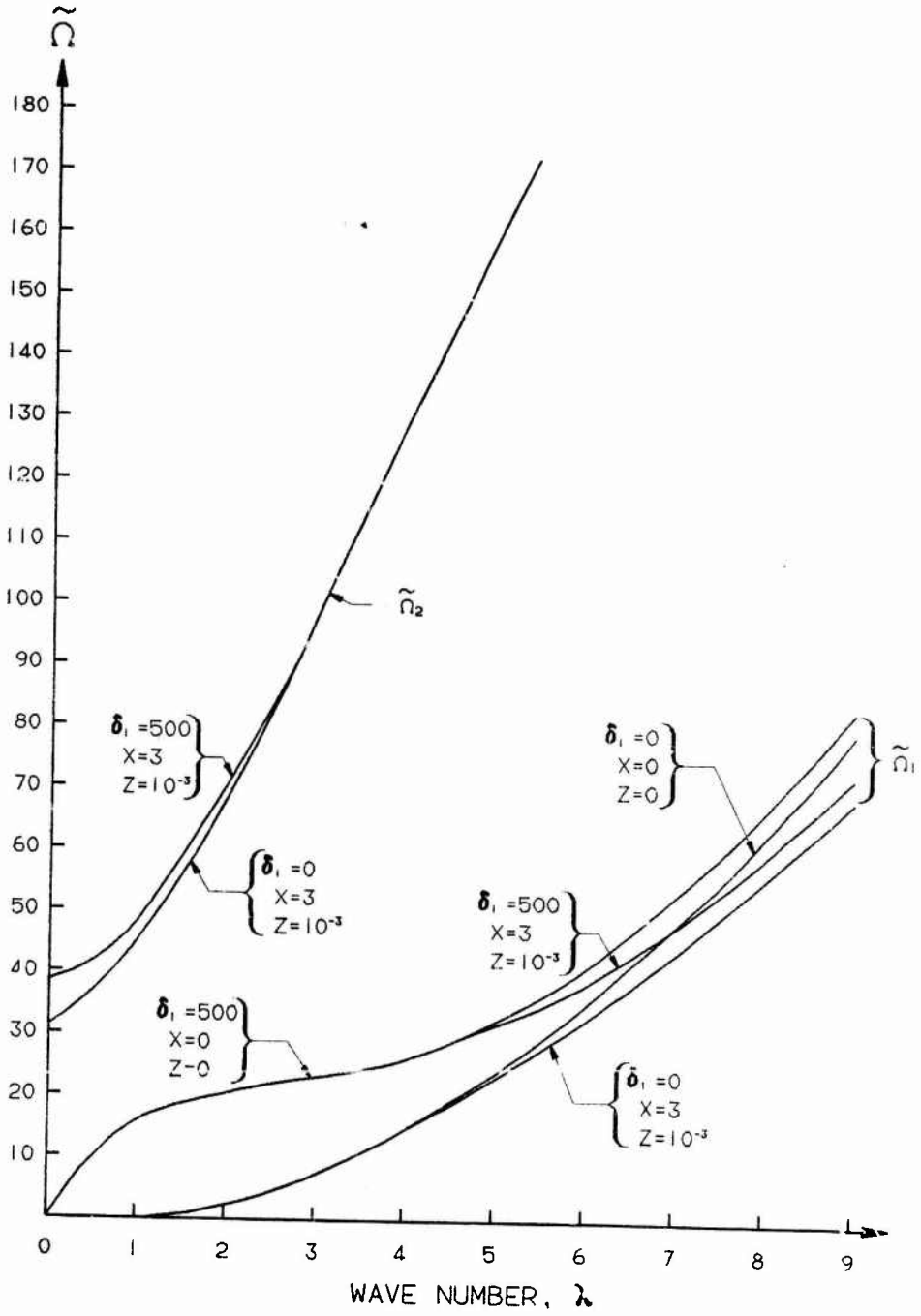

Fig. 2 Effect of the elastic foundation on the frequencies of a free ring.

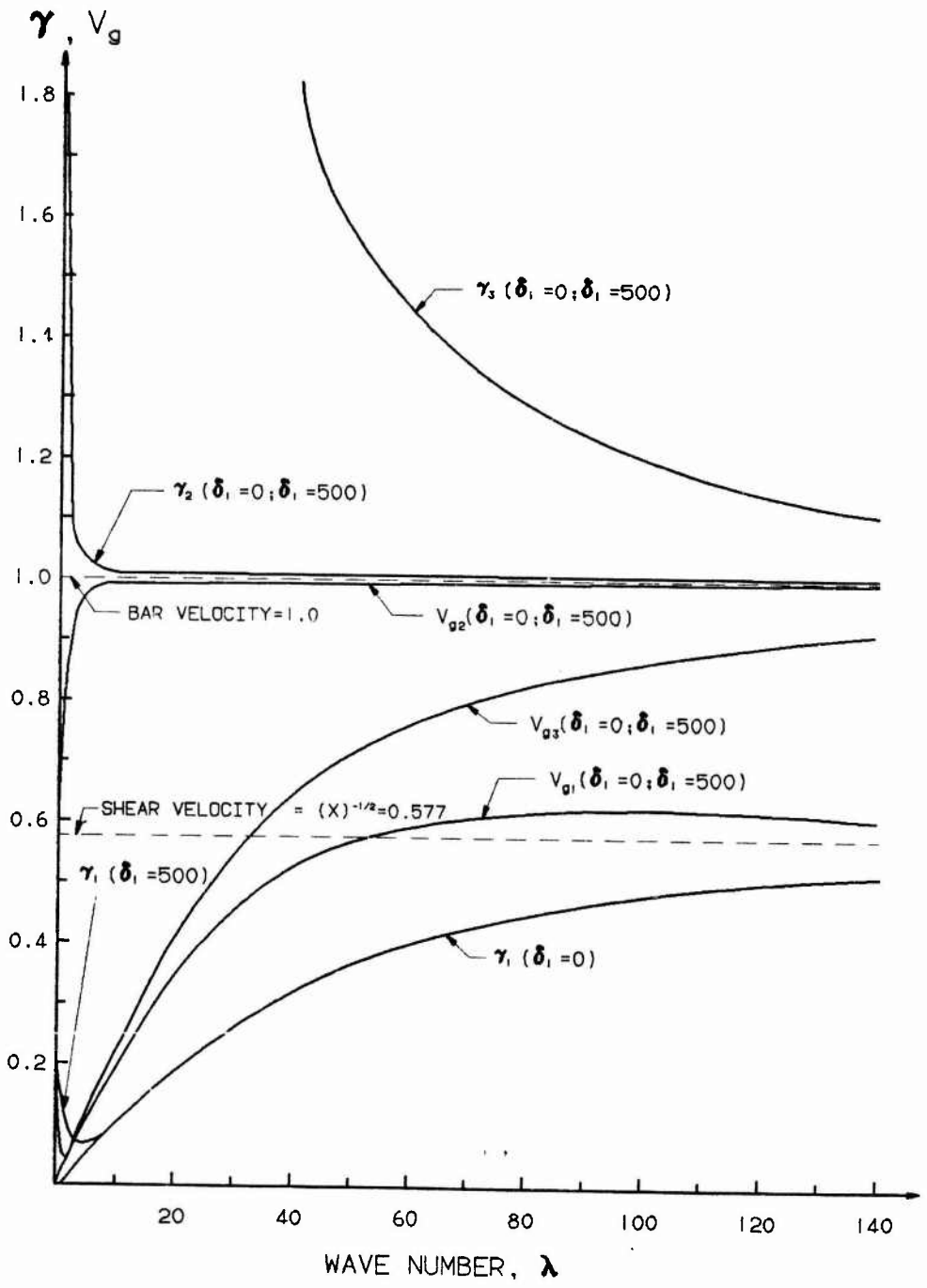

Fig. 3 Variation of phase and group velocities with wave number for a free ring and short wave lengths (ν=.3 ; Z=0.0001).

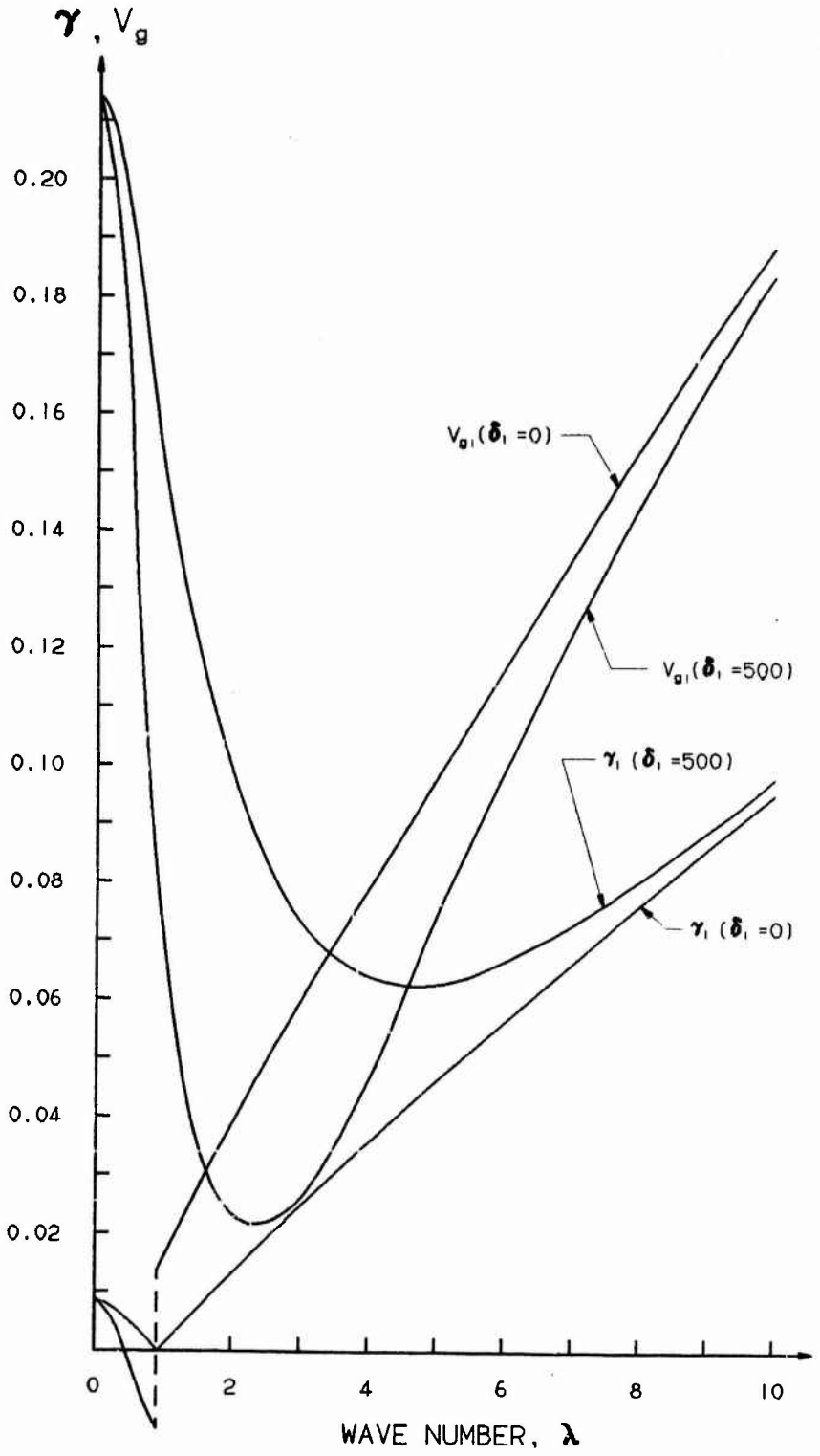

Fig. 4 Enlargement of long wavelength region of first mode of Fig. 3 (X=3 ; Z=0.0001).

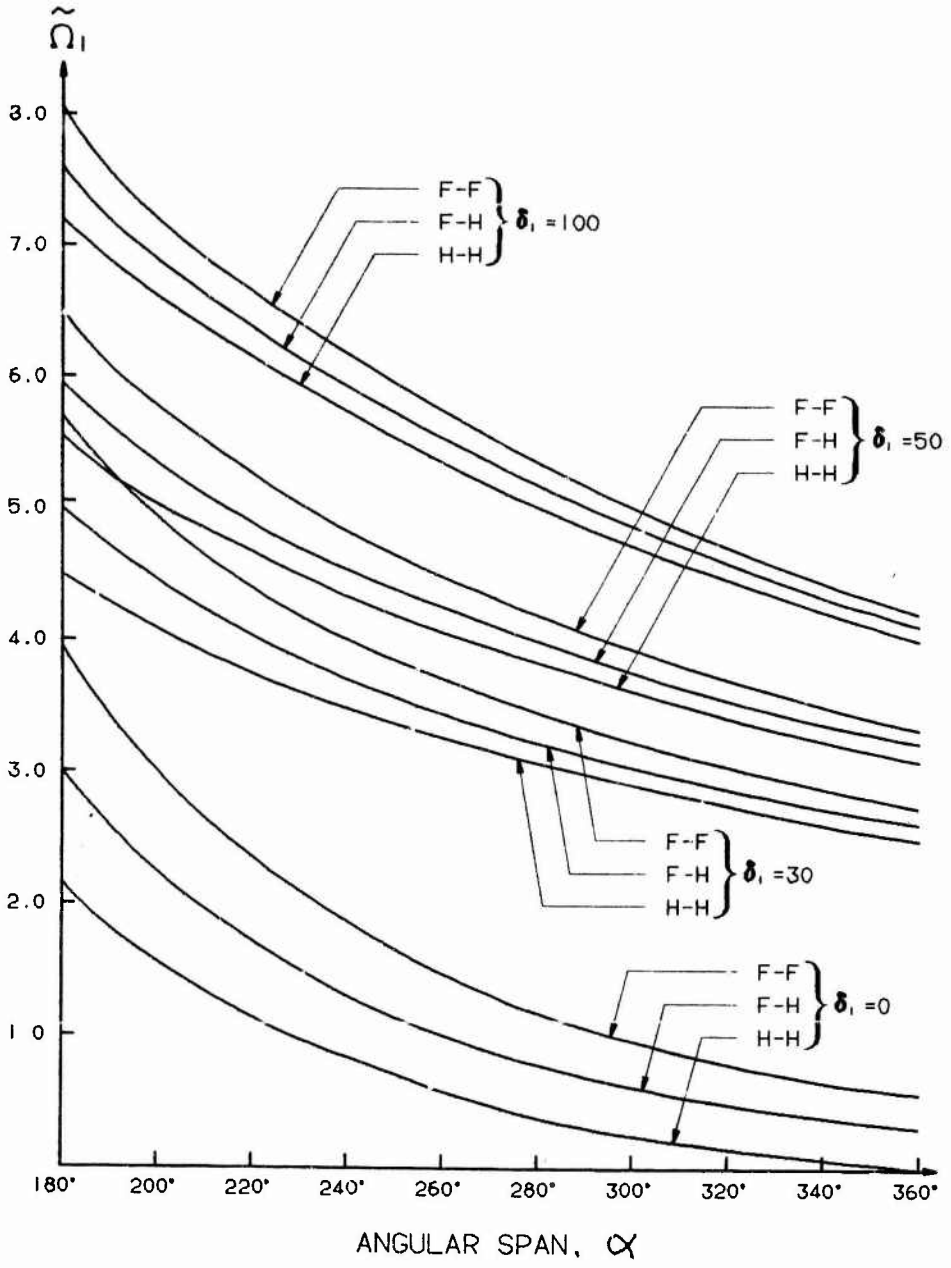

Fig. 5 Variation of the fundamental frequency of arches with angular span (X=3 ; Z=0.005); F-fixed; H-hinged.

VIBRATION ANALYSIS OF FINITE UNIFORM STRUCTURES USING THE HARMONIC RESPONSE FUNCTIONS OF THE INFINITE STRUCTURE

D.J. Mead and Y. Yaman

Department of Aeronautics & Astronautics
University of Southampton
Southampton SO9 5NH, England

Summary

The harmonic response of a uniform infinite structure (e.g. a beam, flat plate, sandwich plate etc) to a point force or moment can usually be found in closed form by solving the corresponding wave equation. The motion of the infinite structure can then be easily understood in terms of the wave motion generated by the source. The harmonic transfer function so obtained can very easily be incorporated in an analysis to study the forced harmonic response of a finite structure to a point force when that structure is on multiple supports having elastic and inertial properties. The method has already been applied by one of the authors to determine the propagation constants of infinite periodic structures. This paper shows how the concepts may be applied to finite uniform structures. As an introductory example Euler-Bernoulli beams on multiple irregular supports are studied. Harmonic responses are easily found. Both single-point and multi-point harmonic excitation can be studied with equal facility. The forced response of a single-point-excited infinite periodic beam is also demonstrated, this having application to railway lines on their flexible sleepers. Damping is easily included in the system. An example is also shown of the response of a heavily-damped sandwich plate which is stiffened at regular intervals and is excited by a line force. The superiority of this method over other methods of analysis described.

1. INTRODUCTION

In a previous study [1], Mead analysed the wave propagation in periodic uniform beams and plates. The systems were infinite in extent and had harmonic phased arrays of forces and moments imposed upon them by the supports at regular intervals. The concept of an 'Infinite system point receptance function' was used. This function gives the response of the infinite uniform structure to just one harmonic force or moment and is easy to calculate.

The method of [1] has subsequently been applied to the study of free wave propagation in a uniform three-layered sandwich plate and has been found to yield satisfactory results. The forced response of the three-layered plate when forced in one of its bays by a harmonic force or moment has also been studied. It was found that the total response due to each of the supports and external forces can conveniently be analysed by considering their appropriate individual infinite system point receptance functions.

These results encouraged further analyses of multibay finite structures using these functions. The conventional methods of analysis, such as finite structrue receptance approaches, can be very long and often tedious. The analysis gets further complicated if one wants to include both inertial and elastic properties of the supports (e.g. stiffeners on the plate). The purpose of the current study is therefore to develop this easy-to-apply and accurate analystical method.

In finite uniform structures, each external excitation sends out waves in both directions as in the case of infinite structures and these outgoing waves are reflected from the ends. The magnitudes of the reflected waves and the magnitudes of any intermediate reactions which may exist constitute the unknowns. They can be found by satisfying the relevant boundary conditions of the total structure at each end and at each intermediate support and forming these boundary conditions into a matrix equation for the unknowns. These equations enable one to analyse different external loading conditions with great ease.

This paper basically illustrates the method by applying it to the simple cases of uniform Euler-Bernoulli beams having various support conditions. Damping was introduced through the complex flexural rigidity, in the form of $EI(1+i\eta)$. Some results obtained from these beams are

presented together with some results from the more complicated case of sandwich plates supported on stiffeners.

2. THEORY

Consider the infinite beam of Figure 1(a). When a harmonic force $F_o e^{i\omega t}$ acts on the beam at $x = 0$ the transverse motion to the right or left of the force can be expressed in the form;

$$w(x,t) = \sum_{n=1}^{N} a_n e^{-k_n x} e^{i\omega t} \tag{1}$$

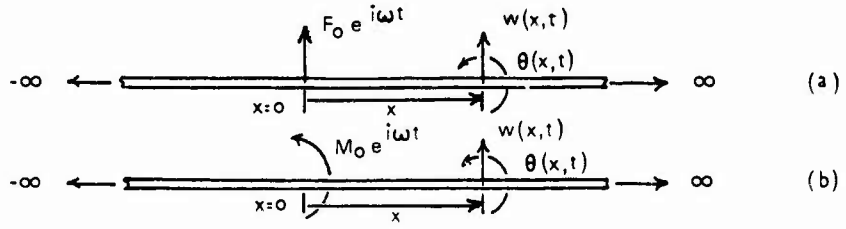

Figure 1. Diagram of Forcing, Response and Sign Conventions
(a) Infinite Beam with a Harmonic Force
(b) Infinite Beam with a Harmonic Moment.

The k_n's are the wave numbers of the N free waves which can travel in the positive direction in the beam. A purely real wave number implies a decaying motion, whereas a purely imaginary one defines a propagating motion with constant amplitude. N depends on the number of degrees of freedom of the cross-section of the beam. For an Euler-Bernoulli beam $N = 2$, the freedoms being transverse motion and rotation. In this case $k_1 = k$ and $k_2 = ik$, where $k = (\rho\omega^2/EI)^{\frac{1}{4}}$. In the case of three layered uniform sandwich plate $N = 3$ at low frequencies.

Figure 1(b) shows an infinite uniform beam subjected to a harmonic moment. In this case the transverse motion to the right of the moment can be written as,

$$w(x,t) = M_o \sum_{n=1}^{2} b_n e^{-k_n x} e^{i\omega t} \tag{2}$$

Similar expressions can be written for the rotations $\theta = dw/dx$ as follows:

$$\theta(x,t) = F_o \sum_{n=1}^{2} c_n e^{-k_n x} e^{i\omega t} \tag{3}$$

$$\theta(x,t) = M_o \sum_{n=1}^{2} d_n e^{-k_n x} e^{i\omega t} \tag{4}$$

Expressions for the coefficients a_n, b_n, c_n, d_n can easily be found by considering the relevant equilibrium conditions at the point of application of the force or moment. For a uniform Euler-Bernoulli beam they are determined as [1]

$$
\begin{aligned}
a_1 &= -1/4EIk^3 & a_2 &= ia_1 \\
b_1 &= -1/4EIk^2 & b_2 &= -b_1 \\
c_1 &= 1/4EIk^2 & c_2 &= -c_1 \\
d_1 &= 1/4EIk & d_2 &= id_1
\end{aligned} \tag{5}
$$

In all the subsequent work, it will be asumed that all the forces and displacements are harmonic, so the e^{iwt} term will usually be omitted.

2.1 The Forced Response of a Finite Beam

When a finite structure is harmonically forced at a point, the wave motion generated by the applied force propagates outwards to the ends where the waves are reflected. In the case of uniform beams, one propagating and one near-field wave are reflected from each end and these travel back to the other end of the beam. Total motion in the beam is therefore the sum of the motion generated by the applied force as if it was acting on an infinite beam plus the motion due to the four reflected waves. Figure 2 illustrates this total wave system for an Euler-Bernoulli beam.

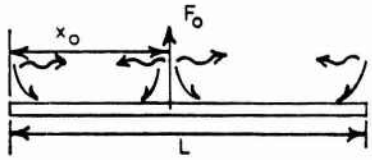

Figure 2. The Generated and Reflected Waves of a Finite Uniform Beam Under the Influence of a Single Applied Force

Within the context of the current study the reflected waves will be called 'free waves' whereas the motion generated by the applied forces will be referred to as 'forced wave'. Hence by considering the Figures 1 and 2 it can be seen that the forced wave responses are given by the relevant infinite system point receptance functions of equations (1) to (4). On the other hand the free wave response of the Euler-Bernoulli beam is given by,

$$
w(x) = \sum_{n=1}^{4} A_n e^{k_n x} \tag{6}
$$

where the A_n's are the coefficients yet to be determined from the boundary conditions. As an introductory example assume that the two extreme ends are simply-supported. By satisfying the appropriate boundary conditions the following equations can be obtained.

$$
\begin{aligned}
w(o) = 0 &: \sum_{n=1}^{4} A_n + F_o \sum_{n=1}^{2} a_n e^{-k_n x_0} = 0 \\
w''(o) = 0 &: \sum_{n=1}^{4} k_n^2 A_n + F_o \sum_{n=1}^{2} k_n^2 a_n e^{-k_n x_0} = 0 \\
w''(L) = 0 &: \sum_{n=1}^{4} k_n^2 A_n e^{k_n L} + F_o \sum_{n=1}^{2} k_n^2 a_n e^{-k_n (L - x_0)} = 0 \\
w(L) = 0 &: \sum_{n=1}^{4} A_n e^{k_n L} + F_o \sum_{n=1}^{2} a_n e^{-k_n (L - x_0)} = 0
\end{aligned} \tag{7}
$$

where '"' indicates $\partial^2/\partial x^2$

These simultaneous equations can be put into a matrix form and the resultant equation for the 4 unknown A_n's becomes:

$$\begin{bmatrix} 1 & 1 & 1 & 1 \\ k^2 & k^2 & -k^2 & -k^2 \\ k^2e^{kL} & k^2e^{-kL} & -k^2e^{ikL} & -k^2e^{-ikL} \\ e^{kL} & e^{-kL} & e^{ikL} & e^{-ikL} \end{bmatrix} \begin{bmatrix} A_1 \\ A_2 \\ A_3 \\ A_4 \end{bmatrix} = - \begin{bmatrix} F_o \sum_{n=1}^{2} a_n e^{-k_n x_0} \\ F_o \sum_{n=1}^{2} k_n^2 a_n e^{-k_n x_0} \\ F_o \sum_{n=1}^{2} k_n^2 a_n e^{-k_n (L-x_0)} \\ F_o \sum_{n=1}^{2} a_n e^{-k_n (L-x_0)} \end{bmatrix} \quad (8)$$

2.2 The Response of a Finite Beam to Multiple Forces

Consider the beam of Figure 2 and assume that another force with a magnitude of F_1 acts at x_1. If the ends are simply-supported, the matrix equation can be shown to be:

$$\begin{bmatrix} 1 & 1 & 1 & 1 \\ k^2 & k^2 & -k^2 & -k^2 \\ k^2e^{kL} & k^2e^{-kL} & -k^2e^{ikL} & -k^2e^{-ikL} \\ e^{kL} & e^{-kL} & e^{ikL} & e^{-ikL} \end{bmatrix} \begin{bmatrix} A_1 \\ A_2 \\ A_3 \\ A_4 \end{bmatrix} = - \begin{bmatrix} F_o \sum_{n=1}^{2} a_n e^{-k_n x_0} + F_1 \sum_{n=1}^{2} a_n e^{-k_n x_1} \\ F_o \sum_{n=1}^{2} k_n^2 a_n e^{-k_n x_0} + F_1 \sum_{n=1}^{2} k_n^2 a_n e^{-k_n x_1} \\ F_o \sum_{n=1}^{2} k_n^2 a_n e^{-k_n (L-x_0)} + F_1 \sum_{n=1}^{2} k_n^2 a_n e^{-k_n (L-x_1)} \\ F_o \sum_{n=1}^{2} a_n e^{-k_n (L-x_0)} + F_1 \sum_{n=1}^{2} a_n e^{-k_n (L-x_1)} \end{bmatrix} \quad (9)$$

Again, as in the previous section, the terms relating to the known external forces appear on the right hand side and those relating to the free (reflected) response are contained within the matrix on the left-hand side. One can easily and conveniently incorporate any number of external forces and/or any combination of external loadings. Notice that the left hand side of Equation (9) is identical to that of Equation (8).

Once the unknown A_n's are found the total response 'w' at any point x_r can be determined as:

$$w(x_r) = \sum_{n=1}^{4} A_n e^{k_n x_r} + F_o \sum_{n=1}^{2} a_n e^{-k_n |x_r - x_0|} + F_1 \sum_{n=1}^{2} a_n e^{-k_n |x_r - x_1|} \qquad (10)$$

2.3 The Response of Finite Multi-Supported Beam

2.3.1 The Beam on Simple Supports

Now consider a six bay finite uniform beam on simple supports. Figure 3 represents the model. The intermediate supports supply unknown transverse forces each of which generates its own 'forced wave field' identical in form to the forced waves of the external forces, but porportional to the unknown reaction force. There are still four 'free waves' reflected back from the extreme ends. Hence the total number of unknowns are the magnitudes of four 'free waves' plus the magnitudes of the reactions R at the intermediate supports. This requires further equations which are found by satisfying the boundary conditions at each intermediate support location.

Consider the condition at the support $x = x_2$. The displacement at this point due to all the intermediate support reactions R x p (p = 1, 5), the external force Fo and the waves reflected from the ends is,

$$w(x_2) = \sum_{n=1}^{4} A_n e^{k_n x_2} + R_{x1} \sum_{n=1}^{2} a_n e^{-k_n (x_2 - x_1)} + R_{x2} \sum_{n=1}^{2} a_n e^{-k_n (x_2 - x_2)} + R_{x3} \sum_{n=1}^{3} a_n e^{-k_n (x_3 - x_2)}$$

$$+ R_{x4} \sum_{n=1}^{2} a_n e^{-k_n (x_4 - x_2)} + R_{x5} \sum_{n=1}^{2} a_n e^{-k_n (x_5 - x_2)} + F_o \sum_{n=1}^{2} a_n e^{-k_n (x_0 - x_2)} \qquad (11)$$

Similar expressions can be written down for the other intermediate supports. If these supports do not deflect, the corresponding vertical displacements should be set to zero. This yields 5 equations. Another 4 can be written down to express zero displacement and curvature at the beam ends. Altogether we now have 9 equations for the 9 unknowns (5 R x p's and 4 A_n's) and they are found by numerical solution of the equation.

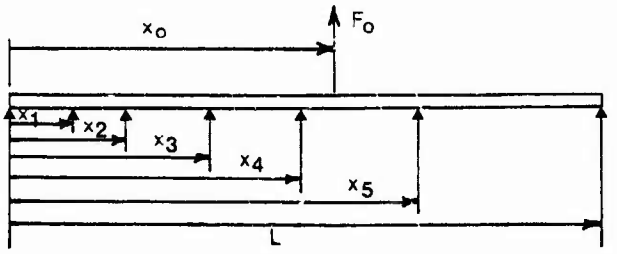

Figure 3. 6 Bay Uniform Beam on Simple Supports

The response at any point x_r on the beam is now found from,

$$w(x_r) = \sum_{n=1}^{4} A_n e^{k_n x_r} + F_o \sum_{n=1}^{2} a_n e^{-k_n |x_o - x_r|} + \sum_{p=1}^{5} R_{xp} \sum_{n=1}^{2} a_n e^{-k_n |x_p - x_r|} \qquad (12)$$

2.3.2 The Finite Beam on Transversely Elastic Supports

Now suppose the support at x_j is elastic, requiring a transverse force of s_j to produce unit $w(x_j)$. The reaction force R_j is given by $R_j = -s_j w(x_j)$. Using Equation (11) for $w(x_j)$ one then finds the modified boundary condition for support x_j (after some rearrangement) to be,

$$\sum_{n=1}^{4} A_n e^{k_n x_j} + \sum_{\substack{m=1 \\ m \neq j}}^{5} R_m \sum_{n=1}^{2} a_n e^{-k_n |x_m - x_j|} + R_j \left(\sum_{n=1}^{2} a_n e^{-k_n (x_j - x_j)} + \frac{1}{s_j} \right)$$

$$= -F_o \sum_{n=1}^{2} a_n e^{-k_n |x_o - x_j|} \qquad (13)$$

Five such equations exist for five elastic intermediate supports and four other equations exist which represent the boundary conditions at the extreme ends of the beam (as before). If those ends are elastically supported, the corresponding equations must be modified to allow for the support flexibility. The nine equations in all are easily solved for the unknown A_n's and R x p's, allowing the response $w(x_r)$ to be calculated.

3. COMPUTED RESULTS AND DISCUSSION

In order to verify the validity of the method, it was first applied to some simple cases where results from previous investigations are available. The above equations have been programmed for computer and have been studied for a number of cases. In the case of uniform Euler-Bernoulli beams the following non-dimensional parameters have been used.

ND Frequency Ω : $\omega XL^2 (\rho/EI)^{1/2}$

ND Receptance: $\dfrac{w}{F}\left(\dfrac{EI}{XL^3}\right)$

ND Transverse Stiffness K: $s_t\left(\dfrac{XL^3}{EI}\right)$

where E – Young's modulus $[N/m^2]$, I = Second moment of Area of the beam section $[m^4]$, XL = Bay Length $[m]$, ρ = mass per unit length $[kg/m]$, ω = Angular Frequency $[rad/s]$, s_t = Translational Stiffness $[N/m]$.

3.1 Finite Beam on Simple Supports

A six bay uniform beam having equal bays was considered. The intermediate supports were taken as simple ones, whereas the outer edge conditions were in turn made i) Simply-Supported, ii) Clamped-Clamped, iii) Free-Free. Very low damping (η = 0.000001) was assigned to the beams, and the frequency response curves were generated by using equation (12). Resonance frequencies were very precisely located by an iterative procedure. Figure 4 shows the frequency response curves (i.e. receptances vs frequency). The resonance frequencies obtained from these are compared in Table 1 with the natural frequencies of the beams quoted in [2]. It

can be seen that on the whole the agreement reached is impeccable, with a maximum difference of 0.2%.

	Simply-Supported		Clamped-Clamped		Free-Free	
Nat. Freq	Ref. 2	Present Work	Ref. 2	Present Work	Ref. 2	Present Work
1	9.87	9.87	10.63	10.63	2.36	2.36
2	10.63	10.63	12.65	12.65	2.38	2.38
3	12.65	12.65	15.42	15.42	10.69	10.69
4	15.42	15.42	18.47	18.47	12.73	12.73
5	18.43	18.47	21.18	21.17	15.42	15.42
6	21.18	21.17	22.37	22.37	18.36	18.36

Table 1. Comparison of Uniform Beam Natural Frequencies (Ω's)

The modes of vibration of the beam with free ends have been computed from equation (12) for two particular frequencies and these are presented in Figure 5. As can be seen they represent the fundamental symmetric and antisymmetric modes.

3.2 Infinite Beam on Periodic Transversely Flexible Supports

Space has not permitted the presentation of the theory for this beam, so this must be the subject of a future publication. However, a combination of this approach already outlined, together with the use of phased-array receptance functions [1] has permitted the calculation of the response in an infinite beam to a single point force acting at x from the left-hand end of the excited bay (Bay length = XL). Figure 6 shows the ND response at the loading point, for different values of x. This particular problem can be applied to railway line vibration theory, the line being supported on periodic flexible sleepers.

Figure 6 shows that at low frequencies the response increases as the loading point moves towards the centre of the bay. At higher frequencies, the response may be highest when the load acts elsewhere. As the beam is now periodic, the peak responses occur in the characteeristic 'frequency pass-bands', with much lower responses in the intermediate 'attenuation bands'.

3.3 Finite Three-Layered Sandwich Plate on Periodic Stiffeners

A uniform sandwich plate having two equal face plates has next been considered. A sinusoidal line force excitation was assumed to act in the middle of the second bay. The plate rested on simple supports along the length whereas across the width the stiffeners having elastic and inertial properties provided the constraints. The coupling between the tranverse and torsional motions of the stiffener was included in the analysis. Damping β was introduced through the complex core shear modulus, in the form of $Gc = Gc\,(1 + i\beta)$. The plate consisted of 6 equal bays each with a length of XL = 0.17 $[m]$ and an aspect ratio of 2 The thicknesses of face plates and core were taken as h = 0.87 $[mm]$ and hc = 1.1 $[mm]$ respectively. The responses of heavily and lightly damped six-bay plate are shown in Figure 7.

As the structure is periodic, resonances are bunched together in the bands indicated by the lightly damped curve. With heavy damping the resonance peaks merge together to form, low humps in the same bands. Using the current method of analysis, the computational effort required to calculate the response and corresponding modes is less when the damping is heavy than when it is light, even though the modes are heavily complex. This is because fewer frequency points are required to define the response curve for the heavily damped structure. Scarcely any extra effort would be required to calculate the responses and modes if extra harmonic forces or distributed pressures acted on the plate.

4. CONCLUSIONS

It has been demonstrated that the use of infinite system point receptance functions greatly simplifies the vibrational analysis of uniform beam structures. Those functions depend only on one set of wave numbers and a corresponding set of coefficients. They are very easily obtained for the structures considered in this paper.

Using these functions a simple and analytically exact method has been presented for the determination of the response of uniform multi-span beams and plates which are under point and line excitations respectively. The method is very easily developed to determine the response due to distributed loadings which have simple analytical forms. The superiority of the proposed method over the other traditional methods lies in the fact that any number and any combination of the possible loading conditions can easily be dealt with. Furthermore the bays need not to be equal and elastic and inertial characteristics of the supports can conveniently be included.

5. REFERENCES

1. D.J. MEAD 1986 Journal of Sound and Vibration 104 (1), 9-27 'A New Method of Analyzing Wave Propogation in Periodic Structures; Applications to Periodic Timoshenko Beams and Stiffened Plates'.

2. R.D. BLEVINS 1979 Formulas for Natural Frequency and Mode Shape. Van Nostrand Reinhold.

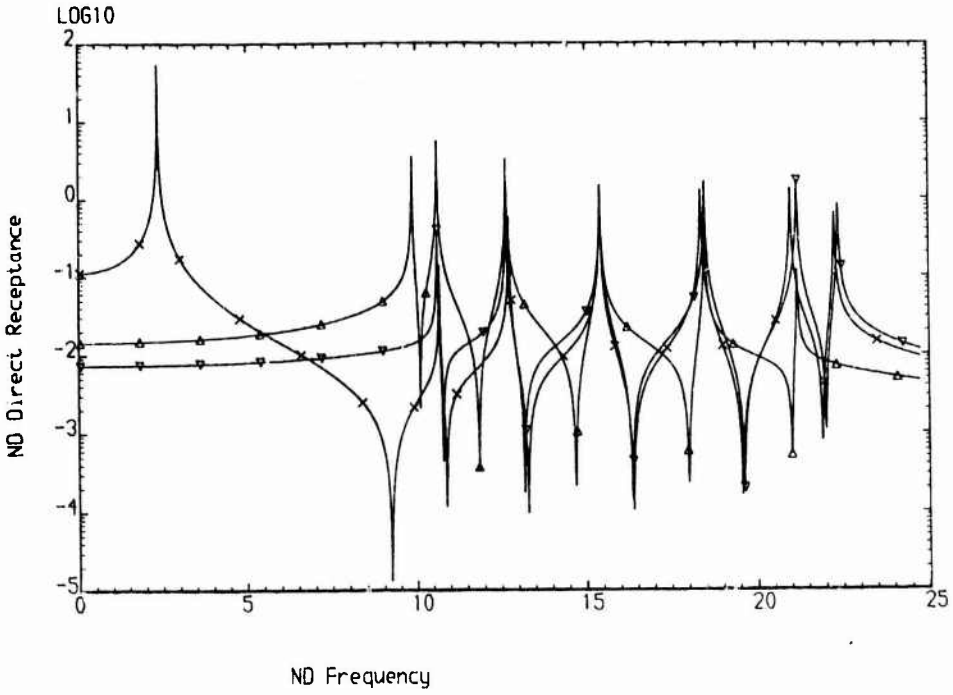

Figure 4. 6 Bay Uniform Simply-Supported Beam (η = 0.001, —△— Simply-Supported Ends, —▽— Clamped Ends, —×— Free ends)

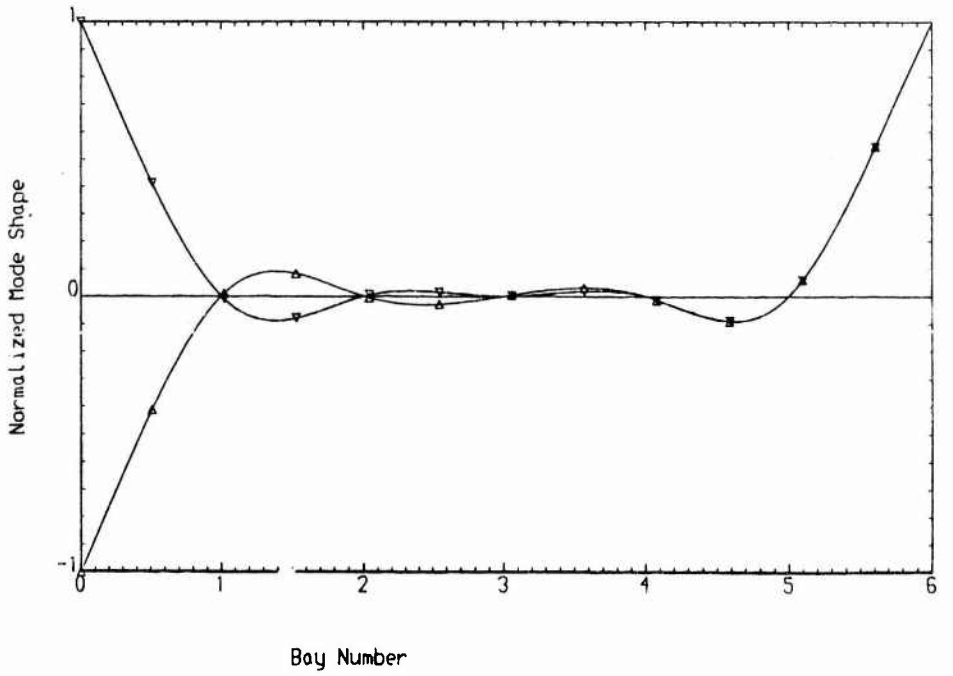

Figure 5. 6 Bay Uniform Simply-Supported Beam with Free Ends (η = 0, —△— Ω = 2.36, —▽— Ω = 2.38)

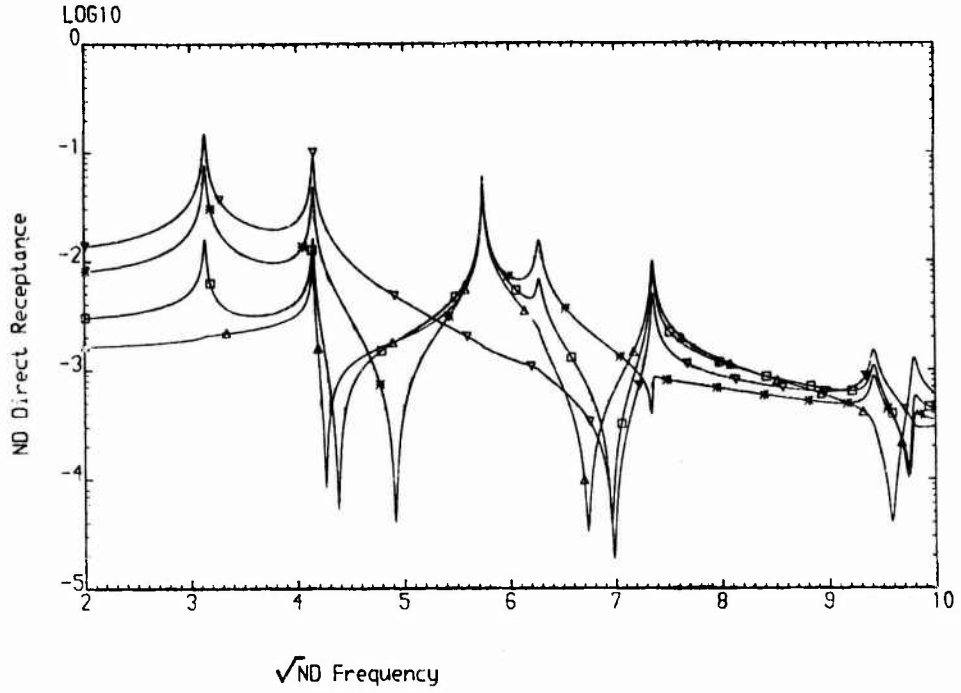

Figure 6. Infinite Uniform Beam on Transversely Elastic Supports (η = 0.01, K = 600, —△— x = 0, —□— x = 0.1XL, —✱— x = 0.25XL, —▽— x = 0.5XL)

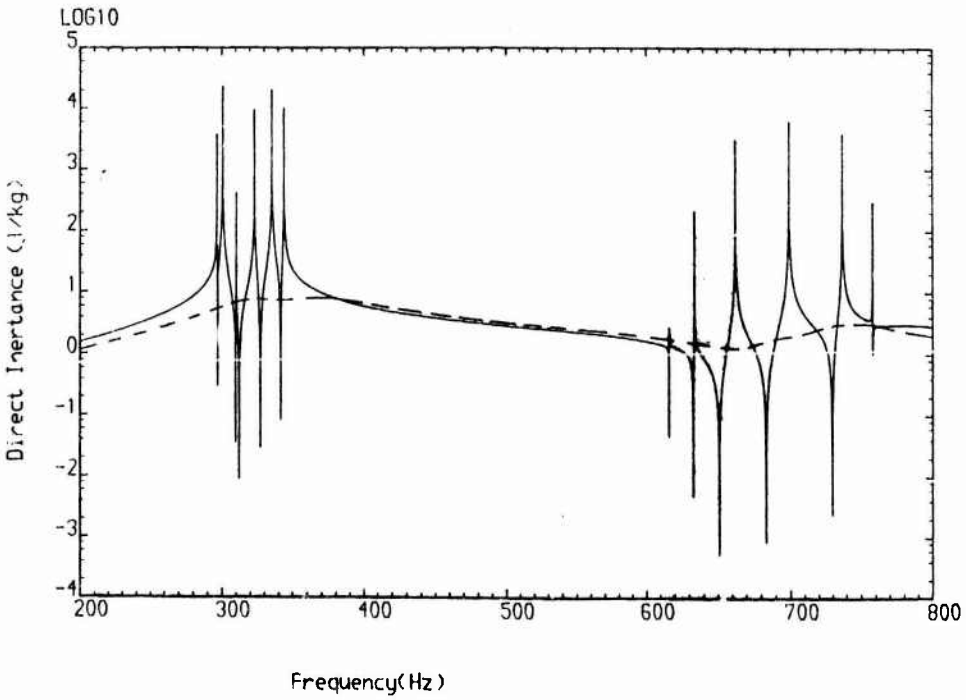

Figure 7. 6 Bay Uniform Sandwich Plate on Stiffeners (x_f = L/4, —— β = 0.0001, – – – – β = 1)

RANDOMLY DISORDERED PERIODIC STRUCTURES

G. J. Kissel
Jet Propulsion Laboratory
California Institute of Technology

1 INTRODUCTION

Spatially periodic systems occur in many engineering and physical contexts. Here we consider periodic structures in one linear dimension, like the skin-stringer panels of an airplane or a periodic truss structure to be deployed in space. Dynamically, periodic structures are characterized by mode shapes which are themselves periodic (see Figure 1), or equivalently, from a traveling wave perspective, by frequency bands which alternately pass and stop traveling waves. This is the familiar passband/stopband property characteristic of all periodic systems.

Because of manufacturing and assembly defects no structure will be perfectly periodic. The disorder in periodicity is assumed to be distributed among all the bays of the structure and not sprinkled in a few. Disordered periodic structures have been examined in [1], [2] and [3]. The paper [1] considered a beam on up to six randomly spaced supports and numerically averaged frequency response functions when the beam was under point loading and convected loading. In [2] wave propagation was investigated for a section of beam on supports with spacing deterministically disordered between supports. The disordered segment was inserted between two perfectly periodic segments. Unfortunately, there was not a clear description of the underlying physics for the observed results in any of the above papers.

Probably the most successful paradigm used to study the effects of disorder in periodic systems is the *localization* paradigm. Hodges in [3] was the first to identify the analogy between the localization phenomenon studied for the past 30 years in solid state physics and the same effect manifesting itself in disordered periodic structures of interest to the engineer. Philip Anderson [4] was the first person to explain the localization phenomenon; this was in the context of electron propagation in disordered crystals. He was later awarded the Nobel Prize for Physics in 1977 in part for his work on localization. The appellation "localization" specifically refers to the fact that

mode shapes are now spatially localized in disordered periodic systems (see Figure 2). Equivalently, from a traveling wave perspective, waves are attenuated in all frequency bands, even in what had been the passbands of the corresponding perfectly periodic system.

Once we have decided to rely on the localization paradigm to study the dynamic effects of disorder in periodic structures, we still have a surprising array of methods from which to begin our analysis. We might, for example, choose to study, numerically and analytically, the localized mode shapes of the disordered system. This has not proven to be a particularly fruitful approach. More success has come from using a traveling wave perspective. But even at this juncture there are several perspectives to take. Hodges used a heuristic wave approach in [3] to study localization effects in a beam on randomly spaced supports. His approach is not easily adaptable to other disordered structures and did not even give localization effects as a function of frequency. Anderson et al [5] used an approach based on the scattering matrix of each bay of the disordered system. This methodology can be cumbersome and again has not given localization effects as a function of frequency. Apparently the most successful approach to localization studies utilizes the *transfer matrix* formalism. Here each bay of the disordered periodic system is modeled via a random transfer matrix, and, as a result, the entire disordered periodic structure is modeled via a product of random transfer matrices. This in turn allows us to appeal to theories on products of random matrices from which we can infer asymptotically (as the number of bays becomes very large) the transmission properties of the disordered system. In addition, analytical equations are available from which frequency dependent localization effects can be readily calculated. Such an approach has been used successfully in [6], [7] and [8]. It is the purpose of this paper to describe the dynamic effects of disorder in normally perfectly periodic structures using the localization paradigm along with the transfer matrix formalism and theories on products of random matrices.

2 PREVIEW

In the remaining sections, after discussing the modeling of disordered periodic structures with transfer matrices, we will first consider the problem of localization in disordered periodic systems carrying a single pair of waves. We will use the theorem of Furstenberg on products of random matrices to show that waves decay exponentially in a disordered system. We will then state a formula to approximate localization effects as a function of frequency and demonstrate this approximation in Section 5 on a Bernoulli-Euler beam on simple supports with random lengths between supports. In Section 6 we will examine the localization phenomenon in disordered periodic structures carrying a multiplicity of wave types at a given frequency. Here we make use of the theorem of Oseledets on products of random matrices to derive a localization factor as a function of the transmission properties of the disordered multiwave system. Concluding remarks are made in the final section.

3 MODELING OF PERIODIC AND DISORDERED PERIODIC STRUCTURES

Each bay of a periodic structure can be modeled with a transfer matrix, $\mathbf{T}$, which relates a state vector, in physical coordinates, of one cross-section to the state vector of the succeeding cross-section

$$\mathbf{x}_j = \mathbf{T}\mathbf{x}_{j-1}$$

Because each bay is identical, the state vector after n bays is simply related to the state vector at the beginning

$$\mathbf{x}_n = \mathbf{T}^n\mathbf{x}_0$$

When a periodic structure is disordered it can no longer be modeled with $\mathbf{T}^n$, but can be modeled with a product of random transfer matrices

$$\prod_{j=1}^{n} \mathbf{T}_j = \mathbf{T}_n \cdots \mathbf{T}_1$$

Here we assume that the transfer matrix is a function of a random variable, α. So $\mathbf{T} = \mathbf{T}(\alpha)$. Because the disorder is distributed among all the bays, the random variables are independent and identically distributed.

We want to concentrate on the effects disorder has on propagating waves. Because strong wave attenuation already occurs in the stopbands, our focus is on the effects of disorder at the frequencies in the passbands of the normally perfectly periodic structure, which is where propagating waves exist. Our wave analysis is possible if we transform each transfer matrix into a *wave transfer* matrix, $\mathbf{W}_j$. This is done by using the average transfer matrix's eigenvector transformation, $\mathbf{X}$, which makes a transformation from physical coordinates to wave coordinates. For the time being we look at a single disordered segment in the middle of a perfectly periodic structure. The perfectly periodic structure corresponds to the mean of the disordered segment. We have

$$\mathbf{W}_j = \mathbf{X}^{-1}\mathbf{T}_j\mathbf{X}$$

where

$$\mathbf{W}_j = \begin{bmatrix} \frac{1}{t_j} & -\frac{r_j}{t_j} \\ -\frac{r_j^*}{t_j^*} & \frac{1}{t_j^*} \end{bmatrix}$$

So waves traveling along the perfectly periodic structure are either transmitted or reflected by the disordered segment j. Here t_j is the transmission coefficient, r_j is the reflection coefficient and $*$ is complex conjugate. Physically $|t_j|^2$ represents the ratio of transmitted energy to incident energy and $|r_j|^2$ represents the ratio of reflected energy to incident energy for this disordered segment. Because we include no damping in our models, energy conservation implies that $|t_j|^2 + |r_j|^2 = 1$. (Note that in the passbands of the perfectly periodic structure $t_j = e^{-ik}$ and $r_j = 0$ for all j, where $i^2 = -1$ and k is the wave number.) So the wave transfer matrix for the n disordered bays, again with a perfectly periodic structure on either side, is

$$\mathbf{W}_n \cdots \mathbf{W}_1 = \begin{bmatrix} \frac{1}{\tau_n} & -\frac{\rho_n}{\tau_n} \\ -\frac{\rho_n^*}{\tau_n^*} & \frac{1}{\tau_n^*} \end{bmatrix} \tag{1}$$

where τ_n is the transmission coefficient and ρ_n is the reflection coefficient. Here $|\tau_n|^2$ is the ratio of transmitted energy to incident energy for the n bay disordered system.

4 CALCULATION OF LOCALIZATION EFFECTS VIA FURSTENBERG'S THEOREM

While it is difficult for us to make a rigorous statement about the transmission properties of a disordered periodic system with a finite number of bays, we are able to come to some rigorous conclusions when the number of bays becomes very large. We come to these conclusions by appealing to a theorem of Furstenberg [9,10] on products of random matrices. His theorem says that

$$\lim_{n\to\infty} \frac{1}{n} \ln \|\mathbf{W}_n \cdots \mathbf{W}_1\| = \gamma, \quad w.p.\ 1$$

where $\gamma > 0$, and $w.p.\ 1$ means the result holds with probability one.

The physical interpretation of this limiting behavior can be seen by taking any matrix norm of the random matrix product in Equation (1) and by performing the indicated limiting operation. Doing this we find

$$\gamma = -\lim_{n\to\infty} \frac{1}{n} \ln |\tau_n| \quad w.p.\ 1 \tag{2}$$

which tells us that

$$|\tau_n|^2 \sim (e^{-\gamma n})^2$$

the transmitted energy decays exponentially with the number of bays. This is the localization effect manifesting itself from a wave perspective. Here γ is called the *localization factor*. This result holds for any level of disorder and even though no damping is present in our model. Note here that we are not taking an ensemble average in Equation (2). The result holds asymptotically. Variables that behave in this way are called self-averaging. It has been argued elsewhere [11] that the degree of spatial localization of the mode shapes is governed by an envelope of the form $e^{-\gamma n}$.

Clearly we do not want to take the above limits in order to find the localization factor γ. Fortunately we can use further results of Furstenberg to derive an approximation to γ to first order in the variance of the random variable of the disordered periodic structure. Here we state that approximation; the motivated reader can consult [7] and [8] for the details of the derivation. Letting α be the random variable, σ_α^2 its variance and $\frac{1}{t(\alpha)}$ the (1,1) term in the random wave transfer matrix we find

$$\gamma = \frac{1}{2}\sigma_\alpha^2 \frac{\partial^2 \ln \left|\frac{1}{t(\alpha)}\right|}{\partial \alpha^2}\Big|_{<\alpha>} + o(\sigma_\alpha^2) \tag{3}$$

Note that the second partial derivative is evaluated at $< \alpha >$, the mean value of α.

5 CALCULATION OF LOCALIZATION EFFECTS FOR A BEAM ON SIMPLE SUPPORTS

With Equation (3) we can now calculate localization effects as a function of frequency in the passbands of what is normally a periodic structure. To illustrate these calculations we examine a Bernoulli-Euler beam on simple supports (see Figure 3) where the distance between supports is randomized. Here we take the random variable to be a nondimensional length, $\frac{l}{<l>} = \hat{l}$, where it is randomized $\pm.1\%$ from its average value of 1. The necessary calculations are quite involved and the interested reader should consult [8] for details. Here it will suffice to present the results graphically. In Figure 4 we plot $\log_{10}(\gamma)$ versus a nondimensional frequency $\bar{\omega} = \omega\sqrt{\frac{\rho l}{EI}}$ for the first eight passbands of the periodic system. Localization would add a small amount of extra attenuation to the huge amount already existing in the stopbands. The results are confirmed with a Monte Carlo simulation which involved averaging $-\ln|t(\alpha)|$ over an ensemble of 1001 realizations. Note that we did not have to take a product of random matrices to get good Monte Carlo results. From Figure 4 we see that the localization factor is most pronounced at the edges of the passbands, near the stopbands, while it is diminished in the middle of the passbands. Clearly, the localization factor is a strongly varying function of frequency and contrary to the result of [3], the localization effects do not become constant at high frequency.

The attenuation caused by the disorder is unlike that of dissipation. Here localization prevents the wave from traveling along the structure, unlike the case for a perfectly periodic system, where the wave would travel without attenuation. Localization tends to confine the wave near its point of origin, where it is eventually dissipated by the damping that exists in all real structures. The implication of these results is that experimental measurements made on a beam of supposedly evenly separated supports could be most susceptible to the inevitable disorder that exists at frequencies near the stopbands.

6 LOCALIZATION IN MULTIWAVE DISORDERED PERIODIC STRUCTURES

Most real structures do not carry a single pair of waves, but carry a multiplicity of wave types at a given frequency. This implies that their transfer matrices are of dimension $2d \times 2d$ with $d > 1$. This higher dimensionality greatly complicates the analysis of the localization phenomenon. Multiwave localization has received no attention in the engineering literature and only recently have researchers looked at the corresponding problem in solid state physics. Our goal in this section is to provide the multiwave analog to our single wave result of Equation (2) showing explicitly how the transmission properties are disrupted.

Again, we model our disordered periodic system via a product of random transfer matrices, and we will rely on a theory for products of random matrices to guide our work. We use the theorem of Oseledets [12,10] on products of random matrices. In

addition, we will make two assumptions about our wave transfer matrices, $\mathbf{W}$. First we assume that $\mathbf{W}$ is symplectic. A matrix is symplectic if

$$\mathbf{W}^T \mathbf{J} \mathbf{W} = \mathbf{J}$$

where

$$\mathbf{J} = \begin{bmatrix} \mathbf{0} & \mathbf{I} \\ -\mathbf{I} & \mathbf{0} \end{bmatrix}$$

An important property of symplectic matrices is that their eigenvalues occur in reciprocal pairs, λ and $\frac{1}{\lambda}$. Note that we take a matrix transpose in the above even though $\mathbf{W}$ is a complex matrix. The symplecticity of $\mathbf{W}$ is a consequence of its corresponding scattering and impedance matrices being symmetric.

We also assume that $\mathbf{W}$ is an element of the special unitary group $SU(d,d)$. The word special means that the matrix has determinant equal to one. A matrix $\mathbf{W}$ is an element of $SU(d,d)$ if

$$\mathbf{W}^H \mathbf{\Delta} \mathbf{W} = \mathbf{\Delta}$$

where

$$\mathbf{\Delta} = \begin{bmatrix} \mathbf{I} & \mathbf{0} \\ \mathbf{0} & -\mathbf{I} \end{bmatrix}$$

This group theoretic property follows from the corresponding scattering matrix being unitary, which in turn follows from our assuming no dissipation in the system and excluding any evanescent waves that exist simultaneously with the traveling waves.

The wave transfer matrix for the n bay disordered periodic structure is

$$\mathbf{W}_n \cdots \mathbf{W}_1 = \begin{bmatrix} \tau_n^{-1} & -\tau_n^{-1}\rho_n \\ -\tau_n^{-1*}\rho_n^* & \tau_n^{-1*} \end{bmatrix}$$

where τ_n is the transmission matrix and ρ_n is the reflection matrix. The special form of the wave transfer matrix above is a consequence of it being both symplectic and an element of $SU(d,d)$.

The theorem of Oseledets says

$$\lim_{n\to\infty} [(\mathbf{W}_n \cdots \mathbf{W}_1)^H (\mathbf{W}_n \cdots \mathbf{W}_1)]^{\frac{1}{2n}} = \mathbf{B} \quad w.p.\ 1$$

where $\mathbf{B}$ is a random matrix, whose eigenvalues are nonrandom. The $2d$ eigenvalues of $\mathbf{B}$ are $e^{\gamma_1}, \cdots, e^{\gamma_d}, e^{-\gamma_d}, \cdots, e^{-\gamma_1}$ where $\gamma_1 \geq \cdots \geq \gamma_d > 0$. The γ_is are known as Lyapunov exponents of the random matrix product.

The eigenvalues physically represent d pairs of waves traveling in both directions. The theorem of Furstenberg allows us to calculate γ_1, the uppermost Lyapunov exponent. However, in this multiwave case with $\gamma_d \leq \gamma_1$, γ_d represents the wave with the least amount of decay and so it carries energy along the structure farther than any other wave. Thus, the dth Lyapunov exponent, γ_d, is the quantity of interest when calculating multiwave localization effects.

The derivation of γ_d as a function of the transmission matrix takes a number of pages, so the interested reader is directed to [8] for the details. The derivation depends

heavily on the fact that the wave transfer matrices are symplectic and elements of $SU(d,d)$. We find

$$\gamma_d = -\lim_{n\to\infty} \frac{1}{n} \ln |\tau_{nij}|_{max} \quad w.p.\ 1$$

This tells us that the wave which propagates the farthest is governed by the element of the transmission matrix, τ_n, with the maximum absolute value, which makes perfect sense. Our result corrects the work of a few solid state physicists, including Anderson [13], who have studied multiwave localization.

An analytical approximation for γ_d, analogous to Equation (3), is at least theoretically possible [8,10]. The actual derivation of the approximation is left as a future research topic.

7 CONCLUSION

In this paper we have explored the effects disruption in periodicity has on the transmission properties of normally perfectly periodic structures. Disorder is known to spatially localize mode shapes and attenuate traveling waves in all frequency bands. This "localization" in disordered periodic systems was first discovered in solid state physics, and we have chosen to exploit the analogy between localization occuring in disordered crystals and conductors and the corresponding effect manifesting itself in disordered periodic structures.

We modeled our disordered periodic structures via a product of random wave transfer matrices, then, appealing to appropriate theorems on products of random matrices, explicitly showed the disruption of wave transmission. For structures carrying a single pair of waves (those modeled with 2×2 transfer matrices) we also presented an analytical approximation for calculating the intensity of the localization effect. This approximation was applied to a beam on unevenly spaced supports. The results showed that the localization effects are most pronounced at frequencies at the edges of the passbands (near the stopbands).

We also examined the localization phenomenon in disordered periodic systems carrying a multiplicity of wave types at a given frequency (those modeled with transfer matrices of dimension $2d \times 2d$ with $d > 1$). A new result was presented - the multiwave localization factor as a function of the transmission properties of the disordered system.

ACKNOWLEDGMENT

This paper is derived from the author's doctoral thesis which was written at the Massachusetts Institute of Technology. The doctoral research was supported in part by the Air Force Office of Scientific Research with Dr. Tony Amos as contract monitor.

References

[1] J. N. YANG and Y. K. LIN 1975 Journal of Sound and Vibration 38, 317-340. Frequency Response Functions of a Disordered Periodic Beam.

[2] A. S. BANSAL 1980 Journal of the Acoustical Society of America 67, 377-389. Free-wave Propagation Through Combinations of Periodic and Disordered Systems.

[3] C. H. HODGES 1982 Journal of Sound and Vibration 82, 411-424. Confinement of Vibration by Structural Irregularity.

[4] P. W. ANDERSON 1958 Physical Review 109, 1492-1505. Absence of Diffusion in Certain Random Lattices.

[5] P. W. ANDERSON, D. J. THOULESS, E. ABRAHAMS and D. S. FISHER 1980 22, 3519-3526. New Method for a Scaling Theory of Localization.

[6] V. BALUNI AND J. WILLEMSEN 1985 Physical Review A 31, 3358-3363. Transmission of Acoustic Waves in a Random Layered Medium

[7] G. J. KISSEL 1987 28th AIAA Structures, Structural Dynamics and Materials Conference, Monterey, CA. Localization in Disordered Periodic Structures.

[8] G. J. KISSEL 1988 Ph.D. Thesis, Department of Aeronautics and Astronautics, Massachusetts Institute of Technology. Localization in Disordered Periodic Structures.

[9] H. FURSTENBERG 1963 Transactions of the American Mathematical Society 108, 377-428. Noncommuting Random Products.

[10] P. BOUGEROL and J. LACROIX 1985 Products of Random Matrices with Applications to Schrödinger Operators. Boston: Birkäuser.

[11] H. MATSUDA and K. ISHII 1970 Supplement of the Progress of Theoretical Physics 45, 56-86. Localization of Normal Modes and Energy Transport in the Disordered Harmonic Chain.

[12] V. I. OSELEDETS 1968 Transactions of the Moscow Mathemetical Society 19, 197-231. A Multiplicative Ergodic Theorem.

[13] P. W. ANDERSON 1981 Physical Review B 23, 4828-4836. New Method for Scaling Theory of Localization. II. Multichannel Theory of a "Wire" and Possible Extension to Higher Dimensionality.

Figure 1: Mode of a perfectly periodic structure.

Figure 2: Mode of a disordered periodic structure.

Figure 3: Bernoulli-Euler beam on simple supports.

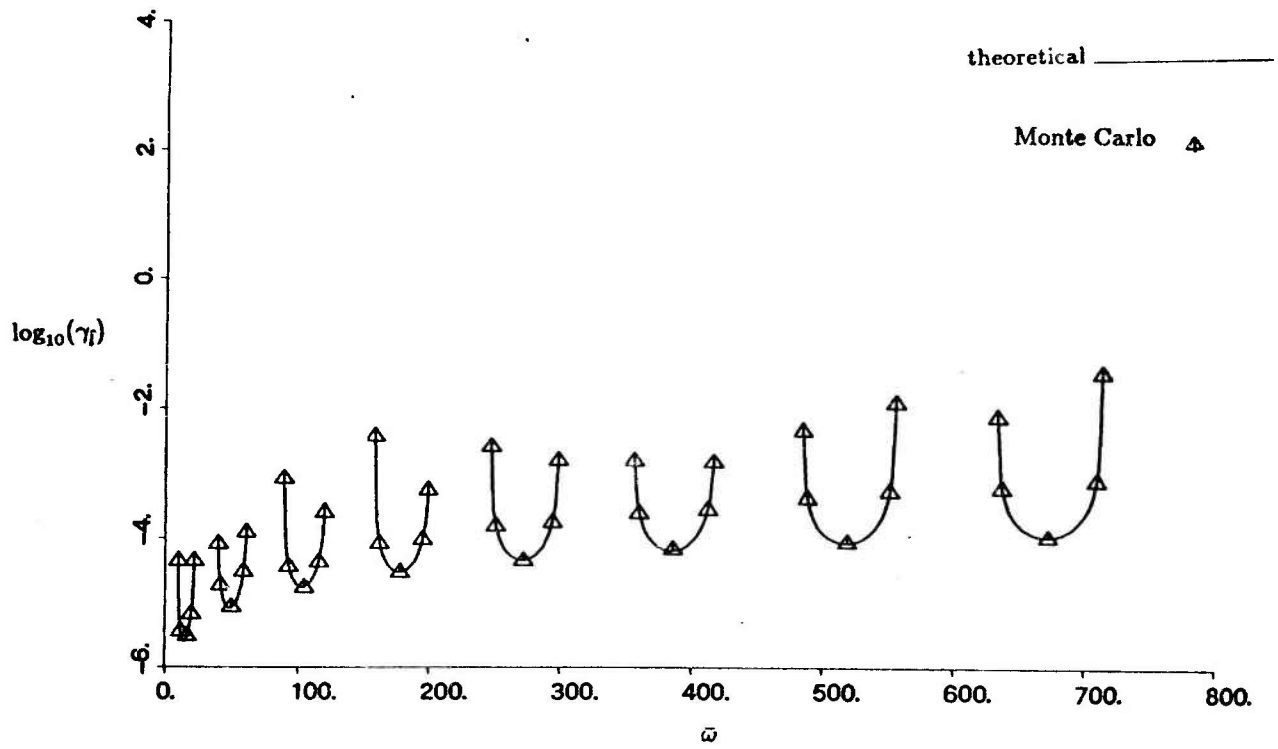

Figure 4: Localization factor for beam on simple supports with nondimensional lengths between supports disordered ±.1% from their average value.

FREE VIBRATION OF RING STIFFENED CYLINDRICAL SHELLS

J. Wei and M. Petyt

Institute of Sound and Vibration Research
University of Southampton

1. INTRODUCTION

Cylindrical shells reinforced with rings, stringers, or both, have been widely used in structural design by many industries. Various methods have been developed for analysing the free vibration of such structures. These methods can be divided into two main types: those where the properties of the stiffeners are averaged over the surface of the shell and those that consider the stiffeners to be discrete. The first of these two approaches is only applicable if there are a large number of closely and equally spaced, identical stiffeners. A comprehensive survey of these methods can be found in reference [1] by Rosen and Singer.

This paper is concerned with the analysis of ring stiffened cylindrical shells where the stiffening rings are considered to be discrete. One of the more popular methods of analysing discretely stiffened shells is the Rayleigh-Ritz method. Egle and Sewall [2] and Egle and Soder [3] have used this method to analyse orthogonally stiffened cylindrical shells. However, Egle and Soder observe that using the solutions for the unstiffened shell as the assumed displacement functions produces "erratic or, at least, unusual" convergence. In the present paper this approach is re-examined and applied to ring stiffened cylindrical shells. A modification is proposed which overcomes the difficulties with the convergence. Indeed, accurate frequencies are produced using far fewer terms than in reference [3]. It is also shown that the proposed method is an extension of the method of Galletly [4] who used a one-term solution which accounted for the inter-ring deformation.

2. THEORETICAL ANALYSIS

The structure to be analysed is a uniform cylindrical shell of length L, radius R and thickness h, having freely supported ends. It is stiffened by means of thin-walled, open-section rings which are identical and equally spaced. The strain energy of the shell is derived using Flugge's theory and that of the rings by Vlasov's thin-walled beam theory. Full details may be found in reference [5].

The circumferential modal displacements of a ring stiffened cylinder are either symmetric or anti-symmetric about a diameter of a cross-section. In order to illustrate the method, only the symmetric modes are considered. In this case the assumed displacements are:

$$u = \sum_m u_{mn} \cos \frac{m\pi x}{L} \cos n\theta \sin \Omega t$$

$$v = \sum_m v_{mn} \sin \frac{m\pi x}{L} \sin n\theta \sin \Omega t \qquad (1)$$

$$w = \sum_m w_{mn} \sin \frac{m\pi x}{L} \cos n\theta \sin \Omega t$$

where u, v and w are the axial, circumferential and radial displacement components of the shell middle surface. x is the axial coordinate and m the half-wave number in the axial direction. θ is the circumferential coordinate and n the circumferential wave number. Ω is the circular frequency and t denotes time.

The expressions in (1) are not summed over n as ring stiffeners do not create any coupling between the circumferential assumed functions. When (1) are substituted into the strain and kinetic energy expressions for the cylinder alone there is no coupling between the axial assumed functions. This is because the assumed functions are the exact solution for the cylinder. However, when the expressions (1) are substituted into the strain and kinetic energy expressions for the rings there is coupling between the axial assumed functions. The coupling terms are functions of the following quantities:

$$c_i\, c_j = \sum_k \cos \frac{m_i \pi x_k}{L} \cos \frac{m_j \pi x_k}{L} \tag{2a}$$

$$c_i\, s_j = \sum_k \cos \frac{m_i \pi x_k}{L} \sin \frac{m_j \pi x_k}{L} \tag{2b}$$

$$s_i\, s_j = \sum_k \sin \frac{m_i \pi x_k}{L} \sin \frac{m_j \pi x_k}{L} \tag{2c}$$

in which x_k is the x-coordinate of the k^{th} ring and the summation is taken over the number of rings. i,j = 1,2,3 ...etc. and m_i, m_j are the corresponding axial half-wave numbers.

It is difficult to obtain explicit expressions for the values of the summations in (2), except when the rings are equally spaced. In this case, let N_b represent the total number of bays between rings and between rings and the shell ends, then it can be shown that

$$c_i c_j = \begin{cases} \frac{N_b}{2} \pm 1 & \text{if } |m_i - m_j| = 2pN_b \text{ or } |m_i + m_j| = 2qN_b \quad (3a) \\ N_b \pm 1 & \text{if } |m_i - m_j| = 2pN_b \text{ and } |m_i + m_j| = 2qN_b \quad (3b) \\ 0 & \text{if } |m_i - m_j| \text{ is odd} \quad (3c) \\ \pm 1 & \text{otherwise} \quad (3d) \end{cases}$$

$$s_i s_j = \begin{cases} \frac{N_b}{2} & \text{if } |m_i - m_j| = 2pN_b \quad (4a) \\ -\frac{N_b}{2} & \text{if } |m_i + m_j| = 2qN_b \quad (4b) \\ 0 & \text{if } |m_i - m_j| = 2pN_b \text{ and } |m_i + m_j| = 2qN_b \text{ or otherwise} \quad (4c) \end{cases}$$

$$c_i s_j = \begin{cases} 0 & \text{if } |m_i - m_j| \text{ is even} \quad (5a) \\ \dfrac{\sin \frac{m_j \pi}{N_b}}{\cos \frac{m_i \pi}{N_b} - \cos \frac{m_j \pi}{N_b}} & \text{if } |m_i - m_j| \text{ is odd} \quad (5b) \end{cases}$$

where p and q are any integer or zero. The positive sign in Eq. (3) stands for the cases with rings on both ends of the shell ($N_b = N_r - 1$, where N_r is the number of the rings) while the negativs sign is for the cases where there are no rings on both ends of the shell ($N_b = N_r + 1$).

The coupling between even and odd axial terms is caused by $c_i s_j$ (see Eq. (5b)), where even or odd terms mean the terms having even or odd axial half wave-number. However, the elements associated with $c_i s_j$ in both mass and stiffness matrices of the ring mainly contain the products of products of inertia of the ring cross-section, the coordinates of the shear centre and the ratio of the eccentricity to the radius of the attachment point. These quantities are usually small compared with others. Thus, the coupling due to these elements may be less important and negligible. This is especially true if the ring cross-section has one symmetric axis passing through the attachment point. This kind of coupling may be called secondary coupling. Another secondary coupling is due to $c_i c_j$ shown in Eq. (3d). It causes the coupling between even or odd modes, and becomes relatively small if the number of the rings increases. It is interesting to notice that if only one end of the shell has a ring, this coupling will vanish.

However, if these two kinds of secondary coupling are neglected, the coupling relations between the axial terms are simple.

For a given m, if $m < N_b$, the coupling exists only between the terms having

$$m_1 = m, \; m_2 = 2N_b - m, \; m_3 = 2N_b + m, \; m_4 = 4N_b - m, \; \ldots \quad (6a)$$

with

$$c_i c_j = \frac{N_b}{2} \pm 1$$

$$s_i s_j = \begin{cases} \dfrac{N_b}{2} & \text{if } |m_i - m_j| = 2pN_b \\ -\dfrac{N_b}{2} & \text{if } |m_i + m_j| = 2qN_b \end{cases}$$

If $m = N_b$, the coupling exists only between

$$m_1 = N_b, \; m_2 = 3N_b, \; m_4 = 5N_b, \; \ldots; \quad (6b)$$

If $m = 0$, then

$$m_1 = 0, \; m_2 = 2N_b, \; m_3 = 4N_b, \; \ldots; \quad (6c)$$

For the latter two cases,

$$c_i c_j = N_b \pm 1 \; ;$$

$$s_i s_j = 0 \; .$$

It is only necessary to solve an eigenvalue problem which is formed by retaining only the terms which are coupled to one another. The resulting generalised eigenvalue problem has been solved by first reducing it to a standard eigenvalue problem. This eigenvalue problem was then solved using a combined Householder/QL algorithm.

3. APPLICATIONS

Initially, calculations were carried out neglecting the secondary coupling terms. Thus, for a given $m < N_b$, only the coupling terms indicated by equations (6) were retained.

3.1 Comparison with an exact solution

The present method is first applied to the shell analysed by Forsberg [6]. Only the example which assumes that the rings are attached to the shell along a line is considered. It is a four-bay shell which is stiffened by three rings. The material properties and geometrical data are given in column A of Table 1. The natural frequencies for symmetric, external and internal rings are given in Table 2.

The agreement between the two methods is good. For an eccentricity, $h_c = 0$, the present method predicts frequencies which are very close to the exact solution, the maximum difference being 0.4% for n = 4, m = 3. The ones predicted by the present method are greater than those predicted by Forsberg except for low values of m. For $h_c = \pm 4.572$ mm, the predicted frequencies are also generally greater than the exact ones (except for two modes in each case), the maximum difference being 2.3% for n = 4, m = 1.

Table 3 shows the convergence of the n = 2, m = 1 mode with increasing number of terms. Nine terms have been used for the results in Table 2.

3.2 Comparison with the finite element method

Al-Najafi and Warburton [7] have used axi-symmetric shell finite elements to analyse a six-bay shell stiffened by five external rings. The rings have rectangular cross-sections. Three different depths have been considered. The geometric and material properties are given in column B of Table 1. They compare their predicted frequencies with experimentally measured ones. The frequencies obtained with the present method (rows marked (b)) are compared with both these sets in Table 4. It can be seen that the present method produces frequencies which are lower than those predicted by the finite element method. The differences are greatest for the largest ring depth and the larger values of m and n. For example, when d = 25.4 mm, n = 4 and m = 6, the difference is 10%. All but one of the predicted frequencies are greater than the measured frequencies.

3.3 Comparison with the conventional Rayleigh-Ritz method

Egle and Soder [3] have used the Rayleigh-Ritz method to calculate the natural frequencies of a 12-bay cylindrical shell stiffened by 13 rings having rectangular cross-sections. The geometrical and material properties are given in column C of Table 1. They used symmetry about x = L/2 to uncouple the odd and even axial modes. Their calculations were carried out using 19 odd terms. Frequencies have been calculated using both 3 and 9 terms in the present method. They are compared with the results of Egle and Soder in Table 5. The 3 term solution produces frequencies which are lower than reference [3] for low values of n and similar frequencies for high values of n. The 9 term solution produces frequencies which are lower than those of reference [3] for all values of n. The modes corresponding

to high values of n are dominated by inter-ring motion. The present analysis used the same shell analysis as reference [3], but a more accurate ring analysis.

Using equation (6a), it is not difficult to explain what Egle and Soder called "the erratic or unusual convergence". For m = 1, the first 9 coupled terms are those having m = 1, 23, 25, 47, 49, 71, 73, 95 and 97. The terms between 1 and 23, 25 and 47, and 49 and 71 contribute little to the convergence and give a false impression until the next coupled term is included.

The advantage of the present method is obvious. To include the effect of the ninth coupled term in the conventional Rayleigh-Ritz method requires, for this example, the solution of an eigenproblem of order 147, whilst the present method generates one of order 27.

3.4 The effect of the secondary coupling due to $c_i c_j$

If the ring-stiffeners have a rectangular cross-section, the secondary coupling due to $c_i s_j$ (equation (5b)) does not exist. Therefore, such stiffeners can be used to investigate the effect of secondary coupling due to $c_i c_j$ (equation (3d)). This causes coupling between even or odd terms only.

Forsberg's shell was analysed using 36 terms which included secondary coupling due to $c_i c_j$. It was also analysed without this secondary coupling. In this case, only 18 terms are coupled. The difference between the two sets of frequencies was less than 1%.

Warburton's shell was analysed using 27 terms with secondary coupling and 9 terms without the coupling. The results are indicated by rows (c) and (b) respectively in Table 4. In the case of the stiffeners with depths of 6.35 mm and 17.78 mm the differences are less than 0.5%. But for d = 25.4 mm, the differences are quite large for some values of n and m. For example, when n = 2 and m = 5, the difference is 10%. In this case, the mode of vibration is dominated by the rings. The neglect of secondary coupling can be considered to be the same as applying some restraint in the rings. When the vibration of the shell is dominated by the rings, it is more sensitive to such restraints. Studies which investigate the effect of the secondary coupling $c_i s_j$ for thin-walled open-section rings are given in reference [5].

4. INTER-RING MOTION

Inter-ring motion has been shown to be important by many investigators, especially when the shell is vibrating in the frequency region in which its dynamic behaviour is dominated by the shell between the rings. Galletly has used an additional cosine term to his one term displacement function to account for its effect [4]. Wah and Hu [8] argued that the inter-ring displacement pattern may have the shape of a slightly modified half-sine wave in their example. Al-Najafi and Warburton [7] discussed that in practice the ring usually is not stiff enough to provide a clamped end condition for the shell between the rings and that the inter-ring displacement may be between the above two forms, but the latter is more likely the case. Thus, it is hard to use one term to describe inter-ring motion.

Considering the displacement function used in the present method, for a given $m < N_b$, the radial component of displacement is

$$W = \cos n\theta \left[W_{m_1 n} \sin\frac{m\pi x}{L} + W_{m_2 n} \sin\frac{(2N_b - m)\pi x}{L} + W_{m_3 n} \sin\frac{(2N_b + m)\pi x}{L} + \ldots \right] \tag{7}$$

Letting $W_{m_2 n} = -W_{m_3 n} = -W_{2n}$,

$W_{m_4 n} = -W_{m_5 n} = -W_{4n}$; ..., ... etc.

Equation (7) becomes

$$W = \cos n\theta \left[W_{m_1 n} + \sum_{k=2,4,6\ldots} W_{kn} \cos\frac{kN_b\pi x}{L} \right] \sin\frac{m\pi x}{L} \tag{8}$$

The first two terms in equation (8) are those used by Galletly, which is a special combination of the first three terms in the present method. This gives some understanding of how inter-ring motion can be expressed in the present method. The coupling relations combine the terms which are important for inter-ring motion in a given axial mode m. In this sense, the present method can be considered as an extension of Galletly's method.

Table 6 shows a comparison between the natural frequencies of Warburton's shell calculated using Galletly's method and also the present method with 3 coupled terms only. Compared with Table 4, it can be seen that Galletly's method becomes unsuitable as the rings become stiffer and also as m and n increase, which is towards the region dominated by the inter-ring motion. The present method with three terms provides more flexibility for inter-ring motion than Galletly's method. Therefore, better results are obtained which are also better than the FEM results in the region dominated by the inter-ring motion. It should also be noted that Galletly's method is not suitable for calculating the frequencies when $m > N_b$.

5. CONCLUSIONS

The free vibration of cylindrical shells with equally spaced ring-stiffeners and freely-supported end conditions have been analysed using the Rayleigh-Ritz method. The coupling relationships produced by the stiffeners are discussed and a method of selecting the terms in the assumed series presented. The results obtained are compared with those obtained by other methods found in the literature. It is shown that the proposed method is an extension of Galletly's method which allows for inter-ring motion.

ACKNOWLEDGEMENT

This research has been carried out under the sponsorship of the Department of Trade and Industry.

REFERENCES

1. A. ROSEN and J. SINGER 1974 TAE Report No. 162. Vibration of axially loaded stiffened cylindrical shells. Part I: Theoretical analysis.

2. D.M. EGLE and J.L. SEWALL 1968 AIAA Jnl. 6, 518-526. An analysis of free vibration of orthogonally stiffened cylindrical shells with stiffeners treated as discrete elements.

3. D.M. EGLE and K.E. SODER Jr. 1969 NAS CR-1316. A theoretical analysis of the free vibration of discretely stiffened cylindrical shells with arbitrary end conditions.

4. G.D. GALLETLY 1955 Proc. 2nd U.S. Nat. Congr. Appl. Mec . Soc. Mech. Engr., 225. On the in-vacuo vibration of simpl. ..pported ring-stiffened sylindrical shells.

5. J. WEI and M. PETYT (To be published) Vibration of freely-supported ring-stiffened cylindrical shells.

6. K. FORSBERG 1969 AIAA/ASME 10th Structures, Structural Dynamics and Materials Conference, Volume on Structures and Materials, 28. Exact solution for natural frequencies of ring-stiffened cylinders.

7. A.M.J. AL-NAJAFI and G.B. WARBURTON 1970 Journal of Sound and Vibration, 13(1), 9-25. Free vibration of ring-st' .fened cylindrical shells.

8. T. WAH and W.C.L. HU 1968 Jnl. Acoust. Soc. Am., 43, 1005-1016. Vibration analysis of stiffened cylinders including inter-ring motion.

Table 1. Data for numerical examples.

	A	B	C
Material properties			
E Young's modulus; x 10^9 Nm^{-2}	72.4	204.1	206.9
ρ Mass density; kg m^{-3}	2713	7833	7822
ν Poisson's ratio;	0.32	0.29	0.3
Shell data = mm			
L Length	411.5	457.2	609.6
R Radius	77.57	108.0	152.4
h Thickness	1.524	3.861	0.381
Ring data = mm			
N_b Number of bays	4	6	12
N_r Number of rings	3	5	13
b Width	5.08	6.35 6.35	3.05
d Depth	4.572	17.78 25.4	9.55

A = Forsberg's shell [6]
B = Warburton's shell [7]
C = Egle and Soder's shell [3]

Table 2. Comparison with Forsberg's exact solution [6].

		Symmetric ring h_c = 0.0 mm		External ring h_c = 4.572 mm		Internal ring h_c = 4.572 mm	
n	m	Forsberg	Present	Forsberg	Present	Forsberg	Present
2	1	788	787	854	858	999	999
	2	2219	2220	2280	2274	2254	2272
	3	3796	3798	3915	3899	3710	3745
3	1	1155	1149	1392	1424	2087	2090
	2	1661	1659	1840	1862	2397	2407
	3	2617	2617	2806	2817	3073	3092
4	1	1988	1979	2187	2237	3161	3127
	2	2132	2132	2296	2338	3085	3071
	3	2535	2545	2644	2679	3014	3049

* Present results are calculated with 9 terms.

Table 3. Convergence of solution.

n	m	Forsberg	Present	1 term	3 terms	5 terms	9 terms	13 terms	18 terms
2	1	854	External	958	897	872	858	855	854
2	1	999	Internal	1107	1050	1019	999	995	993

Table 4. Comparison with FEM.

Unit = Hz

d mm	n	m	1	2	3	4	5	6
6.35	2	a	834	2317	3767	4895	5715	–
		b	832	2302	3734	4853	5673	6404
		d	809	2132	3421	–	–	–
	5	a	2908	3014	3303	3795	4417	4903
		b	2904	3011	3298	3780	4382	4837
		d	2882	2985	3260	3741	4314	–
17.78	2	a	1031	2257	3605	4701	5512	6038
		b	1031	2245	3574	4655	5453	5798
		d	996	1615	4265	–	–	–
	5	a	4596	4558	4596	4710	4850	4927
		b	4551	4512	4534	4632	4746	4799
		d	–	4518	4585	–	4780	–
25.4	2	a	1223	2279	3528	4509	5105	5209
		b	1222	2265	3480	4388	4836	4492
		c	1222	2263	3447	4171	4383	4415
		d	1187	2082	3074	4285	–	–
	4	a	4006	3983	4113	4357	4610	4651
		b	3963	3902	3975	4141	4285	4200
		c	3905	3864	3960	4052	4300	4299
		d	3881	3811	3883	–	–	4126

a = FEM's results from [7]
b = present results using 9 terms (without $c_i c_j$)
c = calculated with 27 odd or even terms (including $c_i c_j$)
d = experimental results from [7]

Table 5. Comparison with Egle and Soder's results.

m = 1	External ring			Symmetric ring		
n	a	b	c	a	b	c
2	518	462	459	491	454	453
4	1208	1171	1085	1226	1157	1155
6	2277	2187	1997	2556	2514	2464
10	2695	2682	2501	2995	2998	2842
14	2507	2507	2373	2601	2605	2476

a = Egle and Soder's result calculated with 37 odd terms [3]
b = present results with 3 terms
c = present results with 9 terms

Table 6. Comparison with Galletly's method (Warburton's shell).

d mm	n	m	1	2	3	4	5	6
6.35	2	a	884	2303	3736	4858	5685	6405
		b	833	2303	3735	4856	5677	6404
	5	a	2998	3114	3413	3913	4559	4839
		b	2981	3082	3360	3831	4416	4837
17.78	2	a	1050	2257	3597	4706	5550	5973
		b	1045	2252	3587	4682	5502	5872
	5	a	4829	4951	5223	5665	6251	4800
		b	4748	4678	4654	4699	4766	4800
25.4	2	a	1257	2298	3562	4638	5462	5232
		b	1247	2289	3522	4525	5182	4767
	4	a	4245	4367	4712	4271	5956	4314
		b	4143	4066	4116	4260	4382	4247

a = calculated by using Galletly's method [4]
b = calculated by using the present method with 3 terms

SENSITIVITY ANALYSIS AND DYNAMIC BEHAVIORS OF ROTATING PRETWISTED TAPERED BLADE

T.N. Shiau and C.C. Pan

Institute of Aeronautics and Astronautics
National Cheng Kung University
Taiwan

1. INTRODUCTION

Turbomachine blade failures are normally attributed to fatigue which usually occurs when the blade vibrates at or near resonant conditions. Hence, the major goals of modern engine blade designs are to minimize the noise and vibration, to assure structural integrity, and to increase the overall performance of engine system. To achieve these goals, many factors that influence the dynamic motion of a rotating blade must be taken into account. For examples, the parameters of cross section asymmetry, pretwist angle, taper, rotation, disc radius, setting angle, the acceleration of rotor center, interblade coupling, elastic support stiffness, shrouding, and aerodynamic forces can significantly affect the motion of the blades. In addition, turbomachine blades will experience instabilities caused by the gyroscopic motion. This precessional motion is often encountered in cases such as flight through severe atmospheric turbulence, taxing over rough runways, and turn maneuvers. Practically, it has been found impossible to determine the blade characteristics fully with taking account of all the parameters.

The vibration analysis of nonrotating pretwisted tapered blade has been studied by Carnegie and Thomas [1], and Rao [2]. A parametric study of vibration of rotating pretwisted and tapered plate was investigated by Sreenivasamurthy and Ramamurti [3] using finite element approach. The effect of two types of precessional velocity on the dynamic behavior of rotating uniform straight blades was studied: (1) the constant angular velocity case, Sisto [4], (2) the harmonic time dependent angular velocity case, Sisto [5]. The effect of Coriolis acceleration was also investigated by Sisto [6] using perturbation method. Shiau and Tong [7] studied these two types of precessional velocity on the dynamic behavior of rotating tapered blade case using both a perturbation method and Floquet theory.

In the present paper, the effect of both constant and harmonic precessional angular velocity on the dynamic stability and response of a pretwisted tapered blade is studied using both a perturbation method and Floquet theory. In most cases, the rotor spinning speed is very high so that the blade can be assumed to be cantilevered at the hub and beam theory is applied to analyze the motion of high aspect ratio blade. The forshortening effect of Vigneron [8], is considered for the displacement along the longitudinal direction of the blade.

2. FORMULATION OF EQUATION OF MOTION

The rotating blade system considered in the present study is shown in Figure (1a–1c) and simplified with the following assumptions: the rotor disc is very rigid, the spin speed of rotor is fixed, the magnitude of precessional velocity is very small compared

to the rotor spin speed but its direction is fixed, the acceleration of rotor center and the aerodynamic forces are neglected. To derive the system governing equation, two reference frames are used. The XYZ:F (xyz:R) triad is a fixed (rotation) reference with the X and x axes being colinear and coincident with undeformed rotor centerline. R is defined relative to F by a single rotation ωt about X with ω denoting the spinning speed of the rotor. The total angular velocity of the blade can be expressed as

$$\begin{aligned}\vec{\omega} =& \omega\,\vec{i} + \Omega[\cos(1+r)\theta + \cos(1-r)\theta]/2\,\vec{j} \\ &+ \Omega[\sin(1+r)\theta + \sin(1-r)\theta]/2\,\vec{k} \end{aligned} \tag{1}$$

where $r \equiv -\omega^*/\omega$ is a nondimensional frequency and Ω and ω^* are the magnitude and frequency of precessional velocity, respectively, r is a nondimensional frequency. In addition, $\theta \equiv \gamma - \omega t$ is a nondimensional time and γ is the angle between precessional axis and Y axis. For the convenience, the local frame η, ξ, z is utilized for the calculation of velocity $(\dot{\vec{r}})$ and strain (ϵ_{zz}) at any point of the blade. The total kinetic energy (T) and potential energy (V) can be expressed as

$$T = \frac{1}{2}\int_R^{R+L}\iint_A \rho(\dot{\vec{r}}\cdot\dot{\vec{r}})\,d\eta\,d\xi\,dz, \quad V = \frac{1}{2}\int_R^{R+L}\iint_A E(\epsilon_{zz})^2\,d\eta\,d\xi\,dz \tag{2}$$

where E is the Young's modulus and R and L are the radius of disc and the length of the blade. The expressions of velocity $\dot{\vec{r}}$ and strain $\epsilon_{zz})$ in equation (2) are written as

$$\begin{aligned}\dot{\vec{r}} =& \left\{(\omega\cos\beta + \Omega\cos\theta_1\,\sin\beta)(z + S_z + \eta u\beta' - \xi u') - \Omega(\xi+u)\sin\theta_1\right\}\vec{e}_\eta \\ &+ \left\{u + \eta\Omega\sin\theta_1 - (\omega\sin\beta - \Omega\cos\theta_1\,\cos\beta)(z + S_z + \eta u\beta' - \xi u')\right\}\vec{e}_\xi \\ &+ \left\{\dot{S}_z + \eta\dot{u}\beta' - \xi\dot{u}' + (\omega\cos\beta - \Omega\cos\theta_1\,\cos\beta)(\xi+u) - \eta(\omega\cos\beta\right. \\ &\left. + \Omega\cos\theta_1\,\sin\beta)\right\}\vec{e}_z \end{aligned} \tag{3}$$

$$\epsilon_{zz} = \xi(u\beta'^2 - u'') + \eta(u\beta'' + \beta' u') \tag{4}$$

where u and S_z are the displacements of the center of cross-section in ξ and z direction respectively. The parameter β is the angle of ξ-axis and x-axis at $z = z$. The derivatives $(')$ and $(\dot{})$ are defined as $\frac{d}{dz}$ and $\frac{d}{d\theta}$ respectively. Let α be the taper constant and κ be the pretwist. One can express the width of blade (b) and pretwist angle (β) at any cross-section as

$$b = b_R\,[1 - \alpha(z-R)/L]\,, \qquad \beta = \beta_R + \kappa(z-R)/L \tag{5}$$

where $\alpha = (b_R - b_T)/b_R$ and $\kappa = \beta_T - \beta_R$. The subscripts R and T represent the position of blade root and tip.

Using the assumed mode method, which is of the form:

$$u(z,t) = \overline{u}(t)[1 - \cos\pi(z-R)/2L] \tag{6}$$

where $\overline{u}(t)$ is the displacement of blade tip, and the Largrangian approach, the nonlinear equation governing the blade tip motion is derived for the harmonic precessional case. It can be expressed as

$$\frac{d^2\overline{u}}{d\theta^2} + [a_0 + \epsilon^2 a_1 + \epsilon q_1 \cos\theta_1 + \epsilon^2 q_2 \cos 2\theta_1]\,\overline{u}$$
$$- \epsilon[3\sin\theta_1 - \sin\theta_2]q_3\overline{u}^2 + q_4[-\overline{u}^3 + 2\overline{u}^2\frac{d^2\overline{u}}{d\theta^2} + 2\overline{u}(\frac{d\overline{u}}{d\theta})^2]$$
$$= \epsilon^2 F_1 \sin\theta_1 \cos\theta_1 + \epsilon F_2 \sin\theta_2 + \epsilon F_3 \sin\theta_1 \qquad (7)$$

where
$$\cos\theta_1 \equiv [\cos(1+r)\theta + \cos(1-r)\theta]/2$$
$$\sin\theta_1 \equiv [\sin(1+r)\theta + \sin(1-r)\theta]/2$$
$$\sin\theta_2 \equiv [(1+r)\sin(1+r)\theta + (1-r)\sin(1-r)\theta]/2$$
$$\cos 2\theta_1 \equiv [-1 + 0.5\cos 2(1+r)\theta + 0.5\cos 2(1-r)\theta + \cos 2\theta + \cos 2r\theta]/2 \qquad (8)$$

and the parameters a_0, a_1, q_1, q_2, q_3, and q_4 are functions of taper constant, pretwist, and blade geometry. The forcing terms in the R. H. S of equation (7) are due to the contributions of gyroscopic effect. The gyroscopic factor ϵ is defined as the ratio of magnitude of precessional motion to the rotor spin speed, i.e. $\epsilon = \Omega/\omega << 1$. The parameter a_0 represent the nondimensional frequency without the gyroscopic effect. The parameters a_1 and q_2 imply the centrifugal effect. The parameters q_1 and q_3 are the linear and nonlinear term due to the Coriolis effect respectively. The term of q_4 represent the high order effect of displacement which can be neglected for high aspect ratio blade compared to other terms. The equation (7) can be reduced to the form :

$$\frac{d^2\overline{u}}{d\theta^2} + [a_0 + \epsilon^2 a_1 + \epsilon q_1 \cos\theta_1 + \epsilon^2 q_2 \cos 2\theta_1]\,\overline{u} - \epsilon[3\sin\theta_1 - \sin\theta_2]q_3\overline{u}^2$$
$$= \epsilon^2 F_1 \sin\theta_1 \cos\theta_1 + \epsilon F_2 \sin\theta_2 + \epsilon F_3 \sin\theta_1 \qquad (9)$$

The solution of the linearized nonlinear differential equation system, described by equation (9) is assumed of the form:

$$\overline{u} = u_L + \epsilon u \qquad (10)$$

where u_L satisfies the eqation

$$\frac{d^2 u_L}{d\theta^2} + a_0\, u_L = 0 \qquad (11)$$

which has the solution:

$$u_L = A_L \cos\sqrt{a_0}\,\theta + B_L \sin\sqrt{a_0}\,\theta \qquad (12)$$

And u satisfies the following equation by neglecting the $(\epsilon u)^2$ term:

$$\frac{d^2 u}{d\theta^2} + k(\theta)u = f(\theta) \qquad (13)$$

where the coefficient k and forcing term f are both time dependent periodic functions i.e. $k(\theta + T) = k(\theta)$, $f(\theta + T) = f(\theta)$, and there are of the forms:

$$k(\theta) = [a_0 + \epsilon^2 a_1 + \epsilon q_1 \cos\theta_1 + \epsilon^2 q_2 \cos 2\theta_1 - 2\epsilon(3\sin\theta_1 - \sin\theta_2)\, q_3 u_L] \quad (14)$$

$$f(\theta) = (3\sin\theta_1 - \sin\theta_2)\, q_3 u_L^2 - (\epsilon a_1 + q_1 \cos\theta_1 + \epsilon q_2 \cos 2\theta_1)\, u_L + \epsilon^2 F_1 \sin\theta_1 \cos\theta_1 + \epsilon F_2 \sin\theta_2 + \epsilon F_3 \sin\theta_1 \quad (15)$$

3. STABILITY ANALYSIS

The instability of linearized differential equation system, described by the Mathieu type equation (13) with time dependent coefficients, is investigated using a perturbation method and also the Floquet transition matrix method. The analysis procedures for the pretwisted tapered blade case using the perturbation method are very similar to those used in Sisto [6] for the uniform straight blade case. For the Floquet transition matrix method, one can convert equation (13) into first order differential equation system by setting

$$y_1 = u, \quad y_2 = \frac{du}{d\theta} \quad (16)$$

The result is given by

$$\{\dot{y}\} + [D(\theta)]\{y\} = \{G(\theta)\} \quad (17)$$

where $(\dot{}) \equiv \frac{d}{d\theta}$, $\{y\} = \{y_1, y_2\}$, $\{G(\theta)\} = \{0, f\}^t$, $[D(\theta)] = \begin{bmatrix} 0 & -1 \\ k(\theta) & 0 \end{bmatrix}$, $[D(\theta+T)] = [D(\theta)]$, t is the transpose of a matrix, and T is the period of the system.

The stability of the linearized system, equation (17), is governed by the homogeneous part:

$$\{\dot{y}\} + [D(\theta)]\{y\} = \{0\} \quad (18)$$

Based on Magnus and Winkler [5], Bogolinbor and Mitropolsky [10], and Peters and Hohenemser [11], the instability region can be determined by the condition

$$|\Lambda_k| > 1 \qquad \text{unstable} \quad (19)$$

where Λ_k, $k = 1, 2$, are the eigenvalues of Floquet transition matrix $[Q(T)]$ which satisfies

$$\{y(T)\} = [Q(T)]\{y(0)\} \quad (20)$$

The Floquet transition matrix (FTM) is of the form:

$$[Q(T)] = [\{y^{(1)}\}\{y^{(2)}\}] \quad (21)$$

where $\{y^{(1)}\}$ and $\{y^{(2)}\}$ are the solutions of equation (18) at $\theta = T$ with initial conditions $y_1(0) = 1$, $y_2(0) = 0$ and $y_1(0) = 0$, $y_2(0) = 1$, respectively.

4. RESPONSE ANALYSIS

The steady state periodic response of the linearized time varying system, equation (17), can be obtained by directly solving the gyroscopically induced vibratory system. For most cases, it is very time-consuming to obtain the steady state periodic response for any arbitrary initial condition.

In this paper a technique shown by Peters and Hohenemser [11] and Shiau [12] based on the Floquet theory, is presented to find the initial conditions for steady state periodic response by integrating over one period. The solution of equation (17) is taken to be of the form:

$$\{y\} = \{y_H\} + \{y_P\} \tag{22}$$

where $\{y_H\}$ satisfies equation (18). The periodic response $\{y\}$ of equation (17) can be written as

$$\{y(\theta)\} = [Q(\theta)\{y(0)\} + [Q(\theta)] \int_0^\theta [Q(\tau)]^{-1} \cdot \{G(\tau)\}\, d\tau \tag{23}$$

where $[Q(\theta)]$ satisfies the equation

$$[\dot{Q}(\theta)] + [D(\theta)][Q(\theta)] = 0 \tag{24}$$

with the initial conditions $[Q(0)] = I$. From the periodicity condition, i.e. $\{y(T)\} = \{y(0)\}$, one can find the initial condition $\{y(0)\}$ for the periodic response from equation (23), and it is of the form:

$$\{y(0)\} = [I - [Q(T)]]^{-1} [Q(T)] \int_0^T [Q(\theta)]^{-1} \{G(\theta)\} d\theta \tag{25}$$

where T is the period of the response and $[Q(T)]$ is the FTM calculated in the stability analysis. To calculate the initial condition, one can defining the above integral as follow

$$\{v(T)\} \equiv \int_0^T [Q(\theta)]^{-1} \{G(\theta)\} d\theta \tag{26}$$

The differentiation of last equation yields

$$\{\dot{v}(\theta)\} = [Q(\theta)]^{-1} \{G(\theta)\} \tag{27}$$

with the initial condition $\{v(0)\} = \{0\}$.

To obtain the Floquet transition matrix $[Q(T)]$ and the vector $\{v(T)\}$, one can integrate equations (24) and (27) over the interval zero to T with corresponding initial values, simultaneously. By substituting $[Q(T)]$ and {v(T)} into equation (25), the initial conditions for the periodic response is obtained. Therefore, the periodic response can be established by integrating one more cycle. Note that the total response of the balde tip motion is the sum of the response u_L and the response of gyroscopic effect u.

5. EXAMPLES AND RESULTS

Using the perturbation method introduced by Sisto [6], the stability transition curves are obtained for the constant precessional velocity case and the harmonic precessional velocity case. For the constant precessional velocity case, $r = 0$, the emanating points (a_0, ϵ) are $(\frac{1}{9}, 0)$, $(\frac{1}{4}, 0)$, and $(1, 0)$ and the corresponding stability transition curves are expressed as equation (28)-(30) respectively.

$$a_0 = \frac{1}{9} \pm \epsilon q_3 \sqrt{A_L^2 + B_L^2} - \epsilon^2 \left(a_1 + \frac{9}{10} q_1^2 \pm \frac{9}{2} q_3^2 B_L \sqrt{A_L^2 + B_L^2}\right) \tag{28}$$

$$a_0 = \frac{1}{4} - \frac{\epsilon}{2} q_1 + \epsilon^2 \left[-a_1 - \frac{q_1^2}{8} + \frac{q_3^2}{15}\left(116 B_L^2 - 84 A_L^2\right)\right]$$

$$a_0 = \frac{1}{4} - \frac{\epsilon}{2} q_1 + \epsilon^2 \left[-a_1 + \frac{q_1^2}{8} + \frac{q_3^2}{15}\left(116 A_L^2 - 84 B_L^2\right)\right] \tag{29}$$

$$a_0 = 1 + \epsilon q_3 \left(2B_L \pm \sqrt{B_L^2 + A_L^2}\right) - \epsilon^2 \left[a_1 + \frac{q_3^2}{8}\left(A_L^2 + B_L^2\right)\right] \tag{30}$$

Similarly for the harmonic precessional case, $r = 1$, the emanating points (a_0, ϵ) are $(\frac{4}{9}, 0)$ $(1, 0)$ and $(4, 0)$ and the corresponding stability transition curves are expressed as equation (31–33), respectively.

$$a_0 = \frac{4}{9} + \epsilon\left(-\frac{1}{2} q_1 \pm \frac{q_3}{4}\sqrt{A_L^2 + B_L^2}\right) - \epsilon^2 \left(a_1 + \frac{9}{160} q_1^2 - \frac{q_2}{4} \pm \frac{9}{128} q_3^2 B_L \sqrt{A_L^2 + B_L^2}\right) \tag{31}$$

$$a_0 = 1 - \frac{3}{4}\epsilon q_1 - \epsilon^2 \left[a_1 + \frac{q_1^2}{128} - \frac{1}{4} q_2 + \frac{q_3^2}{120}\left(21 A_L^2 - 29 B_L^2\right)\right]$$

$$a_0 = 1 - \frac{1}{4}\epsilon q_1 - \epsilon^2 \left[a_1 + \frac{q_1^2}{128} - \frac{1}{4} q_2 + \frac{q_3^2}{120}\left(29 A_L^2 - 21 B_L^2\right)\right. \tag{32}$$

$$a_0 = 4 + \epsilon \left[-\frac{q_1}{2} + \frac{q_3}{4}\left(2B_L \pm \sqrt{A_L^2 + B_L^2}\right)\right] - \epsilon^2 \left(a_1 + \frac{q_3^2}{512}\left(A_L^2 + B_L^2\right)\right] \tag{33}$$

Two parameter values chosen by Sisto [6] are used for the stability analysis and they are $L = 25.4cm$, $\frac{R}{L} = 1.384$. The effects of pretwist angle on the stability of blade tip motion are shown in Figures 2 and 3 for the constant precessional case with the emanating points $(a_0, \epsilon) = (\frac{1}{9}, 0)$ and $(\frac{1}{4}, 0)$ respectively. Similary for the harmonic precessional case, the effect of pretwist angle on the blade tip motion are shown in Figures 4 and 5 with $\beta_R = 30°$ and $45°$, and the emanating point $(a_0, \epsilon) = (\frac{4}{9}, 0)$ and $(1, 0)$ respectively. The steady state periodic response exists only for certain parameter values. Figure 6 shows the effect of initial conditions on the periodic response. The effect of pretwist angle on the periodic response is shown in Figure 7.

6. CONCLUSIONS

The sensitivity of pretwist angle on the dynamic stability and response of a rotating tapered blade under the gyroscopic effect induced by precession of the rotor spin axis is investigated. It can be concluded that the instability region will decrease with the increasing of pretwist for the constant precessional case and also for the harmonic precessional case. The increase of pretwist angle will result in small amplitude of response for the pretwisted tapered blade motion.

REFERENCES

1. W. CARENGIE and J. THOMAS 1972 Journal of Engineering for Industry, Transactions of ASME 94, 255–266. The Coupled bending-bending vibration of pretwisted tapered blading.

2. J.S. RAO 1972 Journal of Engineering for Industry, Transactions of ASME, 94, 343-346. Flexural vibration of pretwisted tapered cantilevered beams treated by Galerkin method.

3. S. SREENIVASAMURTHY and V. RAMAMURTI 1981 Journal of Sound and Vibration 76, 311-328. A parametric study of vibration of rotating pretwisted and tapered low aspect ratio cantilever plates.

4. F. SISTO and A.T. CHANG 1981 The Fifth International Symposium on Air-breathing Engines Bangolone, India. The influence of gyroscopic forces on the dynamic behavior of rotating bodies.

5. F. SISTO, A.T. CHANG and M. SUTCU 1982 Proceeding of the IFTO MM Conference on Rotor-Dynamic Problem in Power-plants, Rome. Blade excitation due to gyroscopic forces.

6. F. SISTO, A.T. CHANG and M. SUTCU 1983 Journal of Engineering for Power, Transactions of ASME 105, 342–347. The influence of Coriolis forces on gyroscopic motion of spinning blades.

7. T.N. SHIAU and J.S. TONG 1987 AIAA/ASME/ASCE/AHS 28th Structures, Structural Dynamic and Material Conference 76–83. The effect of gyroscopic forces on dynamic stability and response of spinning taper blades.

8. F.R. VIGNERON 1975 AIAA Journal No. 1 126–127. Comment on mathematical modeling of spinning elastic bodies for model analysis.

9. W. MAGNUS and S. WINKLER 1979 Basic Concepts, Hill's equation Dover Edition, Dover.

10. N.N. BOOGOLINBOR and Y. A. MITROPOLSKY 1963 Gordon and Breach Science Publishers, New York. Influence of external period forces asympototic methods in the theory of nonlinear oscillations.

11. D.A. PETERS and K.H. HOHENEMSER 1971 Journal of Americal Helicopter Society 25-33. Application of the Floquet transition matrix to problems of lifting rotor stability.

12. T.N. SHIAU 1984 Ph.D. Thesis, University of Illinois at Urbana-Champaign. Rotor blade flap-lag stability and response in forward flight in turbulent flow.

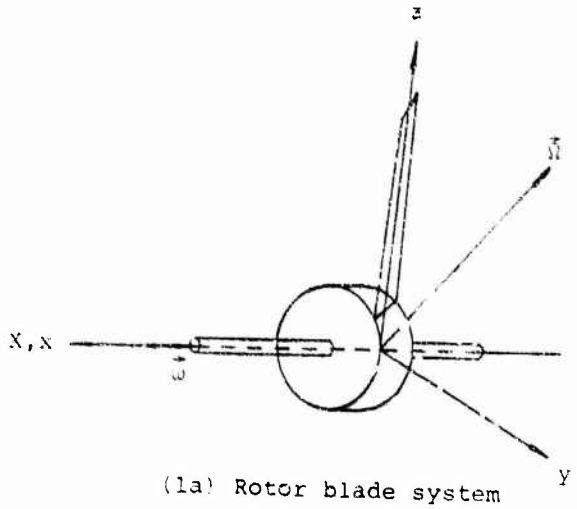

(1a) Rotor blade system

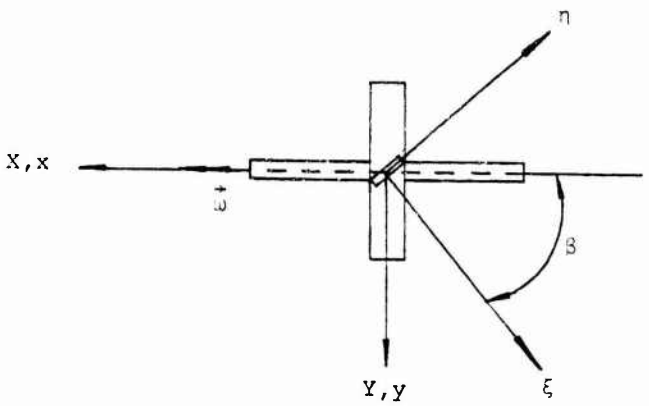

(1b) Top view of blade at any cross section

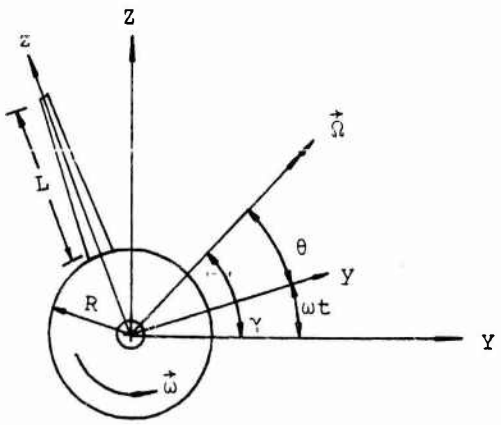

(1c) Side view

Fig. 1 The configuration of rotating blade system (1a) Rotor blade system (1b) Top view of blade at any cross section (1c) Side view

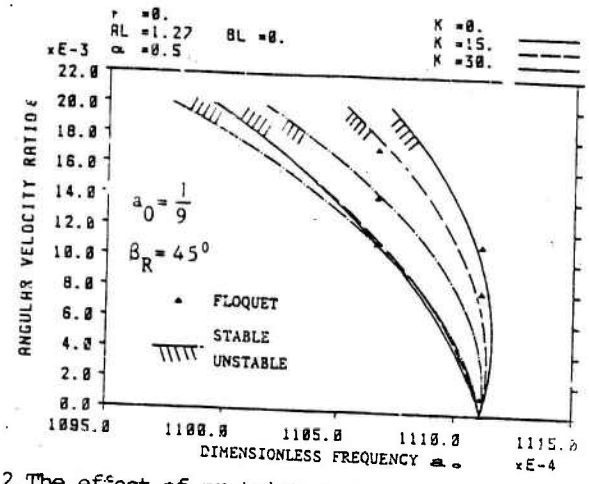

Fig. 2 The effect of pretwist angle on the system stability

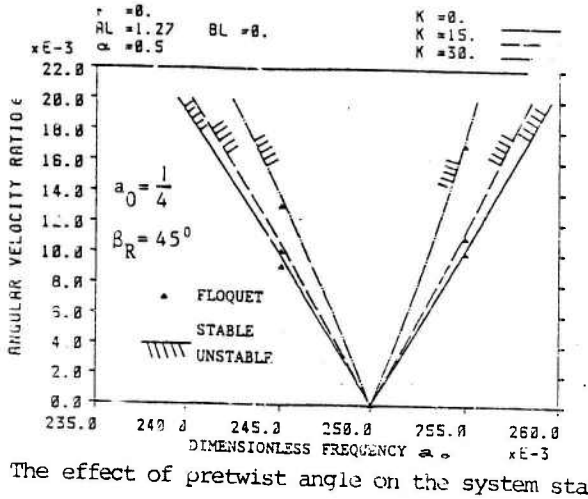

Fig. 3 The effect of pretwist angle on the system stability

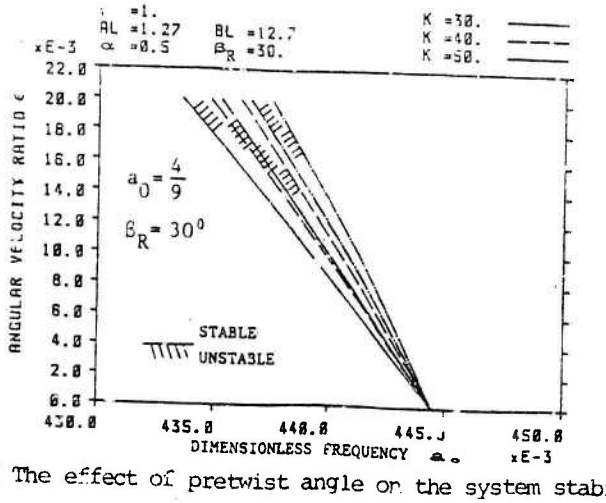

Fig. 4 The effect of pretwist angle on the system stability

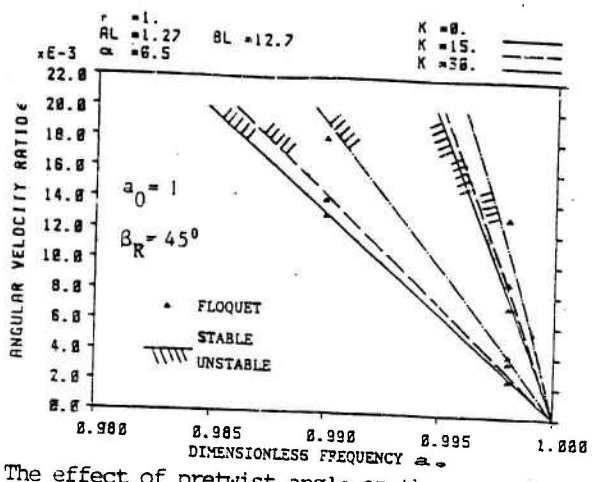

Fig. 5 The effect of pretwist angle on the system stability

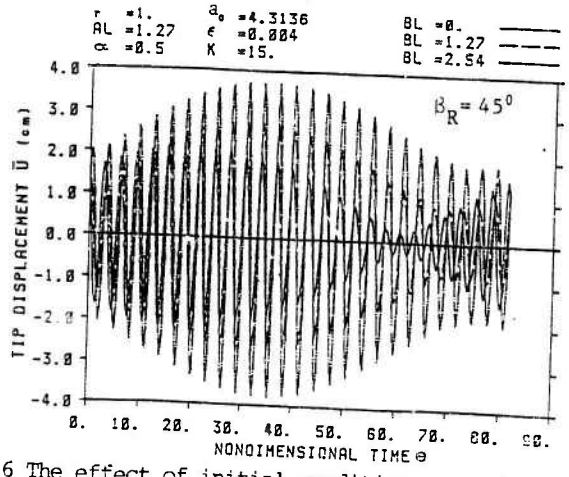

Fig. 6 The effect of initial condition on periodic response

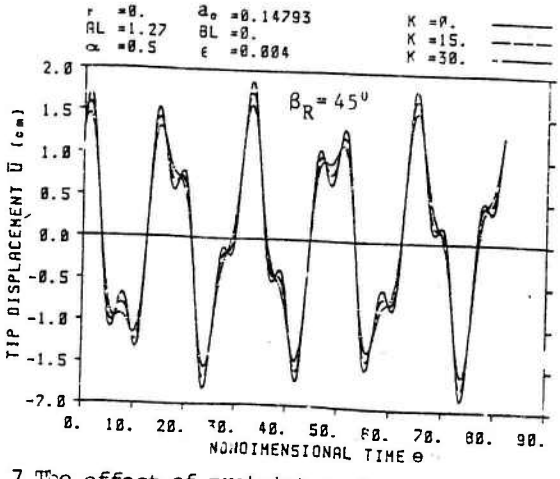

Fig 7 The effect of pretwist angle on the periodic response

DIRECT SUPERPOSITION OF WILSON TRIAL FUNCTIONS BY COMPUTERIZED SYMBOLIC ALGEBRA

Isaac Elishakoff*, Charles D. Hettema† and Edward L. Wilson††

SUMMARY

The method of direct superposition of trial vectors, proposed by Wilson, is elucidated for the forced vibration analysis of systems. possessing damping, by the computerized symbolic algebra. The essence of the method is using a specific set of trial functions (Wilson trial functions) derived in a special manner from the appropriate static solution, rather than performing a mode superposition analysis by the exact eigenvectors of the system. Immediate advantage of the method is that the static solution, to which a dynamic solution should tend for the vanishing excitation frequency, is obtained automatically, by using a single vector, whereas within the exact eigenvectors, an infinite number of eigenvectors are involved to obtain a static solution. A specific example is numerically evaluated and it is clearly demonstrated that the superposition of the Wilson trial functions yields extremely accurate results with fewer vectors than using the conventional set of trial functions, utilized within the Rayleigh-Ritz method.

1. INTRODUCTION

Usually the analysis of the forced vibration of the damped system is preceded by the free vibration study, namely by the evaluation of the natural frequencies and the mode shapes. Then mode superportion analysis is performed, where the given (excitation) and sought (response) functions are expanded in terms of the mode shapes of the undamped structure. As is well recognized, the numerical determination of the exact natural frequencies and mode shapes can require a large numerical effort. The usefulness of the prior knowledge of the natural frequencies lies in that one can forecast the possible resonant conditions, since in the vicinity of natural frequencies the magnification ratios assume considerable values. Modal superposition techniques may require however large amounts of modes to be taken into account to accurately predict the structural response. For example, it is well recognized that to capture the static load effects, especially for concentrated loads, a considerable amount of eigenvectors can be required [1,2]. Wilson et al. [3,4] proposed a new method which overcomes the above predicament which may arise with using the exact eigenvectors. The use of the

* Professor of Aeronautical Engineering, Technion, I.I.T., Haifa 32000, Israel.

† Graduate Student, Department of Mechanical Engineering, Naval Postgraduate School, Monterey, CA 93943, U.S.A.

†† Professor of Civil Engineering, University of California, Berkeley, CA 94720, U.S.A.

alternative set of orthogonal vectors, which are not eigenvectors of the system, provides accurate solution at a reduced computational cost. The main idea of Wilson's method is as follows. The equations of motion of the system (written in terms of finite elements) read

$$M\ddot{u} + C\dot{u} + Ku = f(s)r(t) \tag{1}$$

where M,C and K are the mass, damping and stiffness matrices respectively. The vector f(s) represents the spatial distribution of the loading for fixed t, whereas r(t) is a temporary distribution for fixed s. The first Ritz vector is found from the solution of the static problem $Ku_1^* = f(s)$.

We perform then the normalization with respect to the mass matrix:

$$u_1 = u_1^* / \sqrt{u_1^{*T} M u_1^*} \tag{2}$$

so that $u_1^T M u_1 = 1$.

The subsequent vectors are generated from the following recurrence relationship

$$Ku_i^* = Mu_{i-1} \quad , \quad i = 2,3,\ldots,N \tag{3}$$

where N is a number of terms taken into consideration. The vectors are orthogonalized at each step by the use of the procedure

$$u_i^{**} = u_i^* - \sum_{j=1}^{i-1} c_j u_j \quad , \quad c_j = u_j^T M u_i^* \tag{4}$$

The vectors are then normalized, in perfect analogy with Eq. (3):

$$u_1 = u_1^{**} / \sqrt{u_i^{**T} M u_i^{**}} \tag{5}$$

As a result the set of functions u_i is orthonormal $u_i^T M u_j = \delta_{ij}$ where δ_{ij} is Kronecker's delta.

The vectors so generated are used for the solution of the forced vibration problem. Such a procedure automatically captures the static response problem, since the first vector is derived from the static solution. We will use the Wilson trial functions for the forced vibration problem of the cantilever beam, previously treated by Leissa and Young [5] within the extended Ritz-Galerkin method for the forced damped vibration (one may also consult with the related papers by Leissa [6,7] and discussion by Warburton [8] of Ref. 6).

2. BASIC EQUATIONS

Consider a beam of length L subjected to a distributed transverse load q, sinusoidally varying in time

$$q(x,t) = q(x)\exp(i\Omega t) \tag{6}$$

where Ω is an excitation frequency and x is an axial coordinate. The kinetic and strain energies are, respectively

$$T = \frac{1}{2}\int_0^L \rho A(\partial w/\partial t)^2 dx \ , \ T = \frac{1}{2}\int_0^L EI(\partial^2 w/\partial x^2)^2 dx \tag{7}$$

Leissa and Young [5] generalize the functional T_{max}-V_{max} used in free undamped vibrations by minimizing the following functional

$$L_{max} = (T_{max} - D_{max}) - (V_{max} - W_{max}) \tag{8}$$

where D is a dissipation functional and W is the work done by the force:

$$D = (1/2)\int_0^L cw(\partial w/\partial t)dx \ ; \ W = \int_0^L wq(x,t)dx \tag{9}$$

Further, to apply the Ritz method, assume that the vibratory motion w(x,t) may be expressed as

$$w(x,t) = W\exp(i\Omega t) = \sum_{j=1}^{N} C_j \psi_j(x)\exp(i\Omega t) \tag{10}$$

where $\psi_j(x)$ are the trial functions which satisfy at least the geometric boundary conditions and C_j are the complex coefficients $C_j = C_j^R - iC_j^I$ where and C_j^R is a vector component of the response in phase of the exciting force and C_j^I is the response component which lays the exciting force by 90 degrees; in Eq. (15) j denotes the number of terms retained in the series. In Eq. (13) the index "max" implies maximum value (in time) of the functional, so that

$$T_{max} = (\Omega^2/2)\int_0^L \rho AW^2 dx \ , \ V_{max} = (1/2)\int_0^L EI(d^2w/dx^2)^2 dx \tag{11}$$

$$D_{max} = (i\Omega/2)\int_o^L cW^2 dx \ , \quad V_{max} = \int_o^L qW dx \tag{12}$$

The Ritz method requires L_{max} to attain minimum so that

$$\partial L_{max}/\partial C_j = 0 \ , \ (j = 1,2,\ldots,N) \tag{13}$$

where N is the number of terms taken into account. This yields in N linear simultaneous equations for C_j or 2N equations for C_j^R and C_j^I.

For the trial functions, in Ref. 5, the functions

$$\psi_j(x) = x^j \ (j = 2,3,\ldots,N) \tag{14}$$

were used, with numerical results reported for 2, 4 and 7 term approximations. In addition an exact solution of the problem wasreported. Here following Refs. [3]-[4] we will use the Wilson trial functions, in complete analogy with Ritz vectors described in the Introduction.

3. GENERATION OF WILSON TRIAL FUNCTIONS

The static solution for the cantilever is readily obtainable

$$w(x) = (q_o/24EI)u_1^*(x) \ , \ u_1^*(x) = x^4 - 4x^3L + 6x^2L^2 \tag{15}$$

where, for the similarity with the matrix notation in the Introduction, we denote by u_j^* the unorthonormal set of Wilson trial functions, whereas by u_j^{**} the orthogonalized set; and by u_j the orthonormal set. The analogue of the normalization equation is

$$u_1(x) = u_1^*(x)/\int_o^L \rho A(u_1^*)^2 dx \tag{16}$$

and results in

$$u_1(x) = (3\sqrt{5}/2\sqrt{26})(1/\rho\sqrt{AL})(1/L^4)(x^4-4x^3L+6x^2L^2) \tag{17}$$

The first approximation of the natural frequency squared is

$$\omega_1^2 = \int_o^L u_1 EI(d^4u_1/dx^4)dx = 12.461538 \qquad (18)$$

which is 0.80% higher than the "exact" natural frequency $1.8741041943^4\ EI/\rho AL^4 = 12.3623642\ EI/\rho AL^4$ [5].

For generation of further trial functions the computerized symbolic algebraic code REDUCE [9] was used. For applications of computerized symbolic algebra in various engineering problems one may consult the book by Pavelle [10]; applied mechanics applications are given in Refs. 11-13. In our circumstances, the Eq. (5) for subsequent trial functions is replaced by

$$EI\ d^4u_i^*/dx^4 = \rho A u_{i-1} \qquad (19)$$

supplemented by boundary conditions (22).

Once u_i^* is found, the orthonormalization procedure is performed with the following algorithm

Algorithm	Comments
FOR I: = 2: N DO	
FOR J: = 1: (I-1) DO	
<<CA: = INT(RO*A*U(J)*USTAR(I), X);	
C(J): = SUB (X-L,CA) - SUB (X=0,CA>>;	Finding cj (Eq. 7)
UD: = J: =1: (I-1) SUM C(J)*U(J);	Finding $\sum_{j=1}^{i-1} c_j u_j$
UDSTAR(I): = USTAR(I) - UD	Evaluation of Eq. (6)
UA: = INT(RO*A*(UDSTAR(I)**2), X);	Calculation of
UD1: = SUB(X-L,UA) - SUB(X=0,UA);	the denominator Eq. (8)
U(I): = UDSTAR(I)/(UD1**(1/2);	Obtaining the new trail function Eq. (8)

The so constructed three subsequent trial functions are listed as follows, with $\xi = x/L$:

$$u_1(\xi) = (1/\sqrt{\rho AL})\xi^2\,(-30.61273645 - 72.8225909\xi - 47.6885789\xi^2 + 9.82764375\xi^4 - 2.80789821\xi^5 + 0.33509872768\xi^6) \quad (20)$$

$$u_2(\xi) = (1/\sqrt{\rho AL})\xi^2\,(115.8769233 - 524.670645\xi + 698.9829412\xi^2 + 753.370\,1876\xi^4 + 661.5679963\xi^5 - 208.2233227\xi^6 + 13.947\,48035\xi^8 - 2.535905519\xi^9 + 0.2113254599\xi^{10}) \quad (21)$$

$$u_3(\xi) = (1/\sqrt{\rho AL})\xi^2\,(-291.61499 + 2052.590181\xi - 4317.372131\xi^2 + 12586.1589\,9\xi^4 - 19350.20111\xi^5 + 11405.15083\xi^6 - 3707.9871\,21\xi^8 - 2038.397555\xi^9 + 425.6576594\xi^{10} + 14.054461\,34\xi^{12} - 1.87392818\xi^{13} + 0.1171205112\xi^{14}) \quad (22)$$

Interestingly, using one term Rayleigh or Galerkin methods for the fundamental vibration frequency yields

$$\omega_1^2 = \int_0^L u_i\, EI(d^4u_1/dx^4)dx \;,\; i = 1,2,\ldots,N. \quad (23)$$

Now we turn to the forced vibration problem. Instead of arbitrary trial functions in Eq. (15), we resort to the Wilson trial functions, $u_j(x)$; so that Eq. (15) is replaced by

$$w(x,t) = \sum_{j=1}^{N} C_j u_j(x)\exp(i\Omega t) \quad (24)$$

It is instructive to report the results obtained for one and two term approximations. It is appropriate to quote here Leissa [8] "... the author is especially excited about the capabilities of using the method with only one or two trial functions on many problems to obtain adequate results by means of ordinary hand calculator". We will demonstrate that this is even "more true" using the computerized symbolic algebra, allowing us to obtain explicit expression for the response characteristics.

4. ONE TERM APPROXIMATION

In this case $w(x,t) = C_1u_1(x)$.

The Equation $dL_{max}/dC_1 = 0$ reads

$$[130(\rho AL^4\Omega^2 - i\Omega^4) - 1620EI]\, C_1 = -9\sqrt{130}\,\sqrt{\rho AL}\, qL^4 \quad (25)$$

so that

$$C_1^R = \frac{\sqrt{130}(-11.7\alpha + 145.8)Q\sqrt{\rho AL}}{169(\alpha^2+\beta^2) - 4212\alpha + 26244}$$

$$C_1^I = \frac{-11.7\sqrt{130}Q\beta}{169(\alpha^2+\beta^2) - 4212\alpha + 26244} \quad (26)$$

where

$$\alpha = \frac{\rho AL^4\Omega^2}{EI} \quad , \quad \beta = \frac{c\Omega^4}{EI} \quad , \quad Q = \frac{qL^4}{EI} \quad (27)$$

The response of the beam at the cross-section x may be obtained by adding the in-phase and out-of-phase components and combining them vectorially [5]. This implies that

$$w(x,t) = \bar{W}(x)\exp[i(\Omega-\psi)] \quad (28)$$

where $\bar{W}(x)$ is the amplitude of the response

$$\bar{W}(x) = \sqrt{(C_1^R)^2 + (C_1^I)^2}\, u_1(x) \quad (29)$$

This amplitude is nondimensionalized with respect to the tip's static displacement $w_{st}(L) = qL^4/8EI$. Additionally, the damping c is expressed in terms of the critical damping corresponding to the first natural frequency $c_{cr,1} = 2\rho A\omega_1$ and is taken as $c/c_{cr}=\delta$. For the nondimensional tip displacement amplitude response $\bar{W}(L)/W_{st}(L)$ we obtain the following analytical formula

$$R=\bar{W}(L)/W_{st}(L)=(1.01610\gamma^4+ 4.064436\gamma^2\delta^2- 2.048521\gamma^2+ 1.032477)/$$
$$(\gamma^8 + 8\gamma^6\delta^2 - 4.032089\gamma^6 + 16\gamma^4\delta^4 - 16.128356\gamma^4\delta^2$$
$$+ 6.096653\gamma^4 + 8.128871\gamma^2\delta^2 - 4.097042\gamma^2 + 1.032477) \quad (30)$$

where $\gamma = \Omega/\omega_i$ is the excitation-frequency-to-first-natural

frequency ratio. For the damping coefficient, used by Leissa and Young [5], $\delta = 0.01$, we obtain a simple formula

$$\bar{W}(L)/W_{st}(L) = 1.016109/(\gamma^4 - 2.015645\gamma^2 + 1.0166109) \qquad (31)$$

The numerical values listed in the table clearly demonstrate that this formula compares very well with the two term approximation used in Ref. 5. As is seen, computerized symbolic algebra allows one to obtain explicit analytical expressions.

5. MULTITERM APPROXIMATION AND DISCUSSION

Under new circumstances

$$T_{max} = (\Omega^2/2)(C_1^2 + C_2^2)$$

$$V_{max} = 6.230769C_1^2 - 7.015022C_1C_2 + 254.286828C_2^2)(EI/\rho AL^4)$$

$$D_{max} = (ic\Omega/2\rho AL)(C_1^2 + C_2^2) \qquad (32)$$

$$W_{max} = (0.789352\ C_1 - 0.444353\ C_2)q\sqrt{L/\rho A}$$

Equations (19) read

$$C_1(\rho AL^4\Omega^2 - i\Omega L^4 - 12.461538EI) + C_2 7.015022EI = -0.789352/L^4\sqrt{\rho AL} \qquad (33)$$

$$C_1 7.015022EI + C_2(\rho AL^4\Omega^2 - i\Omega L^4 - 508.573656EI) = 0.444353L^4\sqrt{\rho AL}$$

The nondimensional tip-displacement amplitude response becomes

$$R = \bar{W}(L)/W_{st} = M/N$$

where

$$\begin{aligned} M = {} & 0.215269\gamma^{12} + 2.583230\gamma^{10}\delta^8 - 56.327795\gamma^{10} + 10.332921\gamma^8\delta^4 \\ & - 450.622356\gamma^8\delta^2 + 5311.677892\gamma^8 + 13.777229\gamma^6\delta^6 - 901.24473\gamma^6\delta^4 \\ & + 29477.70047\gamma^6\delta^2 - 214428.6689\gamma^6 + 32923.95559\gamma^4\delta^4 - 832577.5833\gamma^4\delta^2 \\ & + 3279621.37\gamma^4 + 11474129.24\gamma^2\delta^2 - 5936923.794\gamma^2 + 2866475.528 \end{aligned} \qquad (34)$$

$$N = \gamma^{16}+16\gamma^{14}\delta^2-168.587556\gamma^{14}+96\gamma^{12}\delta^4-2023.050668\gamma^{12}\delta^2$$
$$+10822.74905\gamma^{12}+256\gamma^{10}\delta^6-8092.202673\gamma^{10}\gamma^4$$
$$+100134.5241\gamma^{10}\delta^2-320282.7948\gamma^{10}+256\gamma^8\delta^8-10789.60356\gamma^8\delta^8$$
$$+281584.2381\gamma^8\delta^4-2451272.69\gamma^8\delta^2+4042714.61\gamma^8$$
$$+216840.5066\gamma^6\delta^6-4680566.041\gamma^6\delta^4+27555491.34\gamma^6\delta^2$$
$$-13178642.26\gamma^6+45971956.75\gamma^4\delta^4-48147688.89\gamma^4\delta^2$$
$$+18323638.19\gamma^4+22945342.77\gamma^2\delta^2-11744558.43\gamma^2+2866475.528 \quad (35)$$

For the damping ratio $\delta = 0.01$, utilized in Ref. 7 we arrive at

$$R =(0.215269\gamma^{12}-56.327536\gamma^{10}+5311.63283\gamma^8-214425.7212\gamma^6$$
$$+3279538.112\gamma^4-5935776.381\gamma^2+2866475.528)/(\gamma^{16}-168.585956\gamma^{14}$$
$$+10822.5675\gamma^{12}-320272.7815\gamma^{10}+4042469.485\gamma^8-13175886.76\gamma^6$$
$$+18318823.88\gamma^4-11742263.89\gamma^2+2866475.528) \quad (36)$$

Results of the two-term, as well as four term approximations are listed in the table, along with the numerical values reported by Leissa and Young [5]. The last column is associated with the exact solution, derived and evaluated in Ref. 5. This exact solution turns out to be practically coincident with the seven-term approximation using conventional Ritz method [5]. Comparison of the present one-, two- and four-term approximations with the exact solution, demonstrates that utilizing Wilson's trial function method allows to converge to the exact solution much faster, than by applying the conventional Ritz method.

6. CONCLUSION

By utilizing computerized symbolic algebra it is demonstrated that application of the trial functions, generated from the appropriate static solution, represents an improved approximation for the response of structures, possessing damping. It turns out to be a far superior procedure than the conventional Rayleigh-Ritz method, since it yields extremely accurate results faster.

7. ACKNOWLEDGEMENT

The financial support provided by the Research Foundation of the Naval Postgraduate School and the direct funding through the Office of Naval Research to I. Elishakoff is sincerely appreciated. The study wasinitiated when E.L. Wilson was the NAVSEA Chair Professor at the Department of Mechanical Engineering, Naval Postgraduate School during the Winter and Spring quarters of the 1986/87 academic year. This financial aid and the kind and warm hospitality is gratefully recorded.

8. REFERENCES

1. O.E. HANSTEEN 1979 Earthquake Engineering and Structural Dynamics, 7, 405-411. On the accuracy of mode superposition analysis in structural dynamics.

2. R.G. SCHENDLER and R.H. MACNEAL 1962 Aeronautical Systems Division, W-PAEB Ohio ASD-TR-61-680. Optimum Structural Representation in Aeroelastic Analysis.

3. E.L. WILSON, M.-W. YUAN and J.M. DICKENS 1982 Earthquake Engineering and Structural Dynamics, 10, 813-821. Dynamic analysis by direct superposition of Ritz vectors.

4. E.P. BAYO and E.L. WILSON 1984 Earthquake Engineeirng and Structural Dynamics, 12, 499-505. Use of Ritz vectors in wave propagation and foundation response.

5. A.W. LEISSA and T.H. YOUNG 1981 Proceedings of the Vibration Damping Workshop, Long Beach, California, Feb. 27-29. Extension of the Ritz-Galerkin Method for the forced, damped vibrations of structural elements.

6. A.W. LEISSA 1978 Journal of Sound and Vibration, 56(3), 313-324. A direct method for analyzing the forced vibrations of continuous systems having damping.

7. A.W. LEISSA 1978 Development in Theoretical and Applied Mechanics, Proceedings of the 9th Southeastern Conference on Theoretical and Applied Mechanics, 9, 183-193. The analysis of forced vibrations of plates having damping.

8. G.B. WARBURTON 1978 Journal of Sound and Vibration, 60(4), 591-595. A direct method for analyzing the forced vibrations of continuous systems having damping.

9. A.C. HEARN (Ed.) 1984 Rand Publication Cp78. REDUCE, User's Manual, Version 3.1.

10. PAVELLE, R. (Ed.) 1984 Application of Computer Algebra, Kluwer Academic Publishers, Boston.

11. I. ELISHAKOFF and B. COUCH 1987 Solid Mechanics Archives, 12, 379-389. Nonuniform Leipholz's column on elastic foundation - instability study of symbolic algebra.

12. I. ELISHAKOFF and J. HOLLKAMP 1987 Computer Methods in Applied Mechanics and Engineering, 62, 27-46. Computerized symbolic solution for a nonconservative system in which instability occurs in one range of parameter and by divergence in another.

13. L.M. REHAK, F.L. DIMAGGIO, H. BENAROYA and I. ELISHAKOFF 1987 Computer Methods in Applied Mechanics and Engineering, 61, 61-70. Random vibrations with MACSYMA.

$\gamma = \frac{\Omega}{\omega_1}$	N = 1		N = 2		N = 4
	Present	Ref. [5]	Present	Ref. [5]	Present
0.0	1.00000	1.00000	1.00000	1.00000	1.00000
0.5	1.32969	1.33134	1.33758	1.33759	1.33759
0.9	5.06955	5.06759	5.29609	5.29609	5.29622
0.99	29.44850	28.65560	36.08840	36.08700	36.09010
1.0	46.77830	45.88600	50.66940	50.66970	50.67030
1.01	42.83020	44.49840	35.57050	35.57440	35.57130
1.1	4.96141	5.04832	4.81290	4.83250	4.81315
1.5	0.81139	0.82658	0.82457	0.82473	0.82472
2.0	0.33688	0.34731	0.35254	0.35276	0.35276
6.267	0.02634	0.03837	0.31930	1.27647	3.71133
17.547	0.00328	0.00001	0.00124	0.02056	0.42110

N = 4		N = 7	Exact
Ref. [5]	Present	Ref. [5]	Ref. [5]
1.00000	1.00000	1.00000	1.00000
1.33759	1.33759	1.33759	1.33759
5.29609	5.29622	5.29622	5.29622
36.08700	36.09010	36.08960	36.08960
50.66970	50.67030	50.66940	50.66940
35.57440	35.57130	35.57130	35.57150
4.83250	4.81315	4.81315	4.81315
0.82473	0.82472	0.82472	0.82472
0.35276	0.35276	0.35276	0.35276
1.27647	3.71133	4.48085	4.48085
0.02056	0.42110	0.83682	0.93829

PROBLEMS OF STRUCTURAL DYNAMICS SOLVED BY CHINESE REMAINDER ALGORITHM

I-Chen Chang

Associate Professor, Department of Mathematics
College of Staten Island, City University of New York, USA

1. INTRODUCTION

Because there is no Chinese alphabet, ancient Chinese mathematicians could not express their ideas by formulas. As a result, the style of Chinese mathematics is very different from its Western counterpart. In recent years books have been written in the English language concerning Chinese mathematics before and during the 13th century [1,2,3]. These works, however, are limited to issues of historical and philosophical interest without technical application for modern times. After the 13th century, the Chinese made no progress in their type of mathematics beyond the promotion of the abacus to their neighboring countries. With the advance of modern computers, however, the abacus has become obsolete in the eyes of Westerners as well as Chinese, and it has come to appear that Chinese mathematics has been dead for 700 years and that there is little prospect for its revival. Nonetheless, from studying the biographies of ancient Chinese mathematicians and from conducting the research for two short papers [4,5] on Chinese mathematics, the author has come to believe that the situation may not be entirely hopeless. This conclusion is based on the following observations:

(i) In the year 1970, a young Russian mathematician, Y.B. Matiyasevic solved one of 23 important unsolved problems suggested by the great German mathematician D. Hilbert. This solution indicated that the Chinese algorithm is still useful.

(ii) In recent years the textbooks on design and analysis of computer algorithms [6] have been teaching the Chinese remainder algorithm.

(iii) In Chinese mathematics, the emphasis is on algorithms rather than on proofs, and while the abacus served as device to store numbers, the tabulated diagrams (the Chinese type of mathematics) served as flow diagrams for processing. Now, the abacus has been replaced by personal computers since computing and graphing can be carried out without formula translation. Therefore, the Chinese type of mathematics may be found useful for modern computer applications.

(iv) The tabular form of Chinese algorithm can produce decimal numbers to any degree of accuracy [7] and can produce the values of special functions.

(v) The modular representation of huge integers by sets of relative prime numbers can avoid long and tedious computation of multiplication and division operations.

In this paper, the attempt is made to solve some typical vibration problems of continuous structures by using ancient Chinese algorithm techniques. Since Chinese mathematics has fallen behind 700 hundred years, this present scheme should be viewed as only a beginning effort and as being very primitive. Nonetheless, its purpose is to stimulate the interest of engineers so that they might be able to develop an entirely different type of mathematics—a mathematics without formulas.

2. FOUR DIFFERENT METHODS OF STRUCTURAL ANALYSIS

That most modern engineering analysis requires higher mathematics does not mean that simple numerical computations have no use for solving practical problems. In

the year 1932, for example, Professor H. Cross proposed a procedure known as the method of Moment Distribution [8] (Method I of the four approaches considered in this section). Although this method was not developed in a rigorous mathematical way, it was very effective for solving practical problems. This method has come to be known by structural engineers all over the world and has maintained its popularity for over a quarter of a century. Before 1932, most structural computations had to be carried out by the method of virtual work, which required at least a working knowledge of integration. Mathematically speaking, Cross's procedure is a method of successive approximation [9]. The beauty of this method is that its operation is based on a set of well-defined structural terms such as the fixed end moment, M^F_{AB}, the stiffness factor K_{AB}, the carry-over factor from A to B, ρ_{AB}, and the distribution factor r_{AB} at the end A of member AB. The well-known example of Professor Cross is shown by Fig. 1, and its detailed explanation can be found in References 8 and 9.

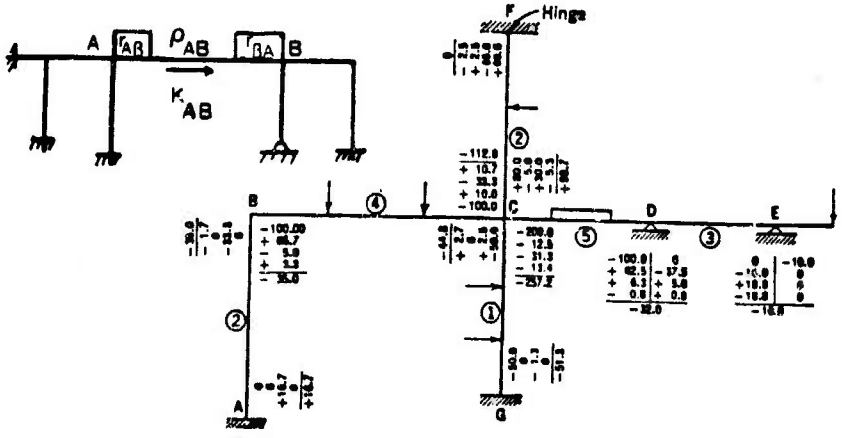

Fig. 1. Professor Cross's well-known example of continuous frame.

In 1937 T.Y. Lin proposed a technique called the direct method of moment distribution [10]. Although his method is well-accepted by some of the Chinese writers [11], most American writers have been inclined to use the v-value method of L.E. Grinter [12].

By making use of the idea of Professor T.Y. Lin, the author was able to reduce a complicated structural system to a simpler network and to emphasize distribution factors r_{AB} instead of stiffness factors K_{AB} in the process of analysis [13,14]. The reason for this shift in emphasis is that moment distribution depends on the "relative" magnitude of the stiffness factors, i.e. K_{AJ}. Mathematically speaking, the distribution factors r_{AB} serve as a "weight" of distribution. An example of this is shown in Fig. 2, and a detailed explanation can be found in References 13 and 14.

In eastern Europe and East Germany, making use of continued fraction [15], Dr. Kloucek developed a method known as distribution of deformation (Method II). Although one of his papers was published in the United States in 1951 [16], it received little attention from American structural engineers and writers.

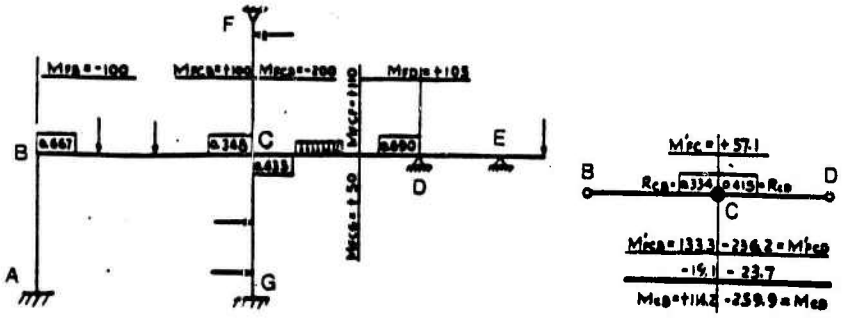

Fig. 2. Simplified rigid frame analysis with distribution factors.

From 1960 to 1980 most structural analysis work was done by large computer programs, and as a result, slope deflection equations and the matrix method (Method III) took the place of the method of moment of distribution. Only in recent years because of the use of the method of recurrence formula on personal computers (Method IV), has the investigation of the relation between the four methods come once again to writers' attention.

The main formula of the Kloucek's method is expressed if expressed in the terminology of H. Cross's method is

$$\theta_1 = \frac{\sum M_1^F}{2\sum K_1[1-\sum a_{1-n}]} \qquad \text{----------(2.1)}$$

where θ_1 is the angular deformation at joint 1

$\sum M_1^F$ is the sum of fixed moment at joint 1.

$$\sum a_{1-n} = \cfrac{a_{12}}{1-\cfrac{a_{23}}{1-\cfrac{a_{34}}{1-\text{ect}}}} \qquad \text{.....(2.2)}$$

and $a_{ij} = c_{ij}c_{ji}r_{ij}r_{ji}$ (2.3)

$c_{ij} = c_{ji} = 1/2$ is the carry-over factor from end i to end j of member ij.

r_{ij} is the distribution factor at the end i of the member ij. If it is expressed in terms of slope-deflection formulation, then

$$\theta_1 = \frac{\sum M_1^F}{2(\sum K_1)B_n} \qquad \text{----------(2.4)}$$

and

$$B_n = \begin{vmatrix} 1 & -a_1 & 0 & 0 & 0 & - & - & 0 \\ -a_1 & 1 & -a_2 & 0 & 0 & - & - & 0 \\ 0 & -a_2 & 1 & -a_3 & 0 & - & - & 0 \\ - & - & - & - & - & - & - & - \\ - & - & - & - & - & - & - & - \\ 0 & 0 & - & - & 0 & -a_{n-2} & 1 & -a_{n-1} \\ 0 & 0 & - & - & 0 & 0 & -a_{n-1} & 1 \end{vmatrix} \qquad \text{.....(2.5)}$$

It can be shown that the determinants B_n satisfy the recurrence formula

$$B_n = B_{n-1} - (a_{n-1})^2 B_{n-2} \quad \text{.....(2.6)}$$

$$n = 1, 2, 3 \text{ .,...}$$

3. TWO DIFFERENT MATHEMATICAL MODELS FOR STUDYING VIBRATION OF RIGID FRAME STRUCTURES

There are commonly two different mathematical models used in the dynamic analysis of rigid frame structures. One of these is the continuous system model and the other is the discrete system model, i.e. the mass-spring model. In 1955, the author was studying the buckling strength of structures [17] under Dr. E.F. Masur [18] and discovered the similarity between the stability analysis and the vibration analysis of rigid frames from a paper by Prof. T.C. Looney [19]. This however, was only a roughly formulated idea which crystallized later on, in reading the authoritative book of Prof. Bishop [20] and the brilliant paper (which then became a book) of Dr. Marguerre [21,22], both in 1960.

In 1962, by making use of characteristic functions, the author formulated the slope-deflection equations for structural dynamics and simplified them by taking advantage of the basic idea of moment and direct moment distribution method, for example, the stiffness factor

$$K = \frac{2EI}{L}\lambda\left(\frac{\cosh\lambda\sin\lambda - \sinh\lambda\cos\lambda}{1 - \cosh\lambda\sin\lambda}\right) = \frac{EI\lambda}{L}\left(\frac{F_5}{F_2 - 1}\right) \text{.....(3.1)}$$

and the carry-over factor

$$\rho = \frac{\sinh\lambda - \sin\lambda}{\cosh\lambda\sin\lambda - \sinh\lambda\cos\lambda} = \frac{F_8}{F_5} \text{ .....(3.2)}$$

where

$$\lambda^4 = \frac{\omega^2 \mu L^4}{EI}$$

ω = natural frequency

μ = mass/unit length of the structural member
L = length of the member I = moment inertia of the member
E = Young's modulus

$$F_2 = \cos\lambda \cosh\lambda .$$

$$F_5 = \cos\lambda \sinh\lambda - \sin\lambda \cosh\lambda .$$

$$F_8 = \sin\lambda - \sinh\lambda .$$

are the characteristic functions used by Professor Bishop in his tables of flexural vibration of beams [20].

Since all problems have to be solved by the trial and error process, this method is not very practical in comparison with the matrix method used by large computer programs. In 1982, when hand-held calculators became widely used by students, the author decided to let engineers know of his long suffering endeavor [23,24]. An example is given in Fig. 3 and for detailed explanation, please see References 23 and 24.

Example. Find the first natural frequency of the frame shown in Fig. 3.

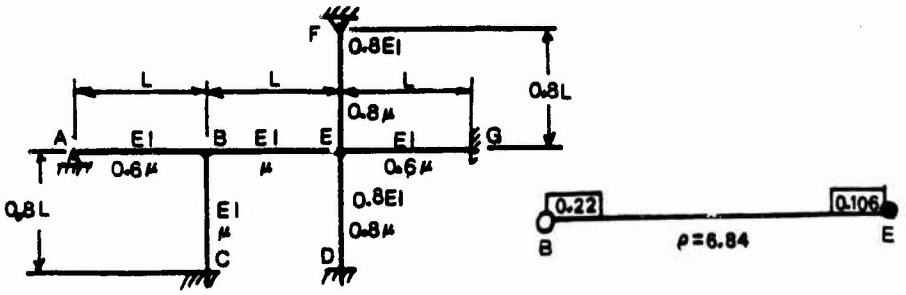

Fig. 3. A simple model of dynamic analysis of rigid frame.

Solution: By using an estimated value λ_o of member BE and the equation

$$\lambda_i = \left(\frac{L_i}{L_o}\right)\sqrt{\frac{\mu_i}{\mu_o}\left(\frac{E_o I_o}{E_i I_i}\right)}\,\lambda_o$$

we obtain all the values of λ_i, (i=1,2,3) at B, i=1 to 4

	Joint B				Joint E				Carry-Over factor ρ
i	Member		K	r	Member		K	r	
1	BE	*3.820	0.698	0.220	EB	3.820	0.698	0.106	6.84
2	BC	3.056	0.474	0.149	EF	3.056	0.474	0.072	
3	BA	3.362	1.997	0.631	EG	3.362	2.433	0.367	
4					ED	3.056	3.014	0.455	
		$\sum$	3.169	1.000		$\sum$	6.619	1.000	

Table 1. Calculation of Dynamic Distribution Factors

*After trying a few values of λ_{BE}, $\Longrightarrow$ $\lambda_{BE} = \lambda_o = 3.82$ $\lambda_{AB} = 3.362$ and $\lambda_{BC} = 3.056$

Error $\epsilon = 1 - \rho^2 r_{BE} r_{EB} = 1 - (6.84)^2(0.22)(0.106) = -0.091$

Theoretically, the continued fraction approach yields a very elegant formula for calculating the fundamental frequency of a continuous structure, according to equation (2.4)

$$B_n(\lambda) = 0 \quad \text{.....(3.4)}$$

When n = 2, we have

$$1 - \rho_{AB}\rho_{BA} r_{AB} r_{BA} = 0$$

as one may see from the given example, where ρ's and r's are functions of frequency.

To the discrete model (mass-spring model) of rigid frames, this approach also can easily be applied. To illustrate this, we will take the example from a well-known book of advanced engineering mathematics of A.C. Bajpai [25].

The characteristic equation for the frame is shown by Fig. 4.

$$B_n = \begin{vmatrix} (K_1+K_2)-\omega^2 M_1 & -K_2 & 0 \\ -K_2 & (K_2+K_3)-\omega^2 M_2 & -K_3 \\ 0 & 0 & K_3-\omega^2 M_3 \end{vmatrix} \qquad \text{----------(3.5)}$$

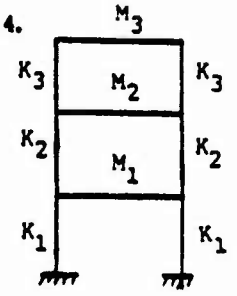

Fig. 4. A three-story rigid frame

If we express Eq. (3.5) in terms of continued fraction, we have $B_n(\omega) = 0$

where

$$B_n = b_1 + Z_1 - \cfrac{a_1^2}{b_2 + Z_2 - \cfrac{a_2^2}{b_3 + Z_3 - \ddots}}$$

$$a_i = K_{i+1}, \qquad b_i = K_i + K_{i+1} \quad \text{and} \quad z_i = -\omega^2 M_i$$

In the dynamics of robot manipulator we have a similar equation [26]. For example, in studying the trajectory of manipulator, the spline segment equation takes the form: $[m]\ [F'] = [a]$

$$[m] = \begin{bmatrix} t_4 & 2(t_3+t_4) & t_3 & 0 & 0 & 0 \\ 0 & t_5 & 2(t_4+t_5) & \cdots & 0 & 0 \\ 0 & \cdots & \cdots & \cdots & \cdots & \cdots \\ 0 & 0 & 0 & t_{n-1} & 2(t_{n-2}+t_{n-1}) & t_{n-2} \end{bmatrix}$$

$[a]$ = acceleration matrix, $[F']$ = coordinate matrix of points

Therefore, the determinant of the matrix [m] can also be treated as .

All this, however, is not surprising because many more general cases in the theory of oscillations can be treated by the method of continued fraction. One of the well-known examples is an alternative to Routh-Hurwitz criterion given by Prof. H.S. Wall [27,28]. We shall present a simplified version of his case for the practical use.

Consider $f(\lambda) = a_0 \lambda^n + a_1 \lambda^{n-1} + a_2 \lambda^{n-2} + \ldots\ldots + a_n = 0 \quad (3.8)$

as the characteristic equation

and let

$$g(\lambda)=a_1\lambda^{n-1}+a_3\lambda^{n-3}+a_5\lambda^{n-5}+\cdots\cdots \quad (3.9)$$

then $\frac{f(\lambda)}{g(\lambda)}$ can be expressed as the expansion algorithm of a special case of J-function as follows:

$$\frac{f(\lambda)}{f(\lambda)} = b_1x + 1 + \cfrac{1}{b_2x + \cfrac{1}{b_3x + \ddots}} \quad (3.10)$$

where $b_i = \frac{\alpha_{i-1}}{\alpha_5}$, if $n \geq 5$. then we have: $\alpha_{-1} = a_0$, $\alpha_1 = a_1$ $\alpha_2 = a_2 - b_1a_3$, $\alpha_3 = a_3 - b_2(a_4 - b_1a_5)$, $\alpha_4 = a_4 - (b_1+b_3)a_5$, and $\alpha_5 = a_5$

The theorem is ; "All roots of Eq.(3.8) will have negative real parts if and only if all $b_i > 0$ We will not prove the theorem but work out the condition for n=4.

$$f(\lambda) = \lambda^4 + a_1\lambda^3 + a_2\lambda^2 + a_3\lambda + a_4 = 0$$

The result is: $b_i > 0$ (i=1 to 4) where $b_1 = 1/a_1$, $b_2 = a_1^2/(a_1a_2 - a_3)$ $b_3 = (a_1a_2 - c_3)^2/a_1(a_1a_2a_3 - a_3^2 - a_1^2a_4)$ and $b_4 = (a_1a_2a_3 - a_3^2 - a_1^2a_4)/a_4$.

4. FROM CONTINUED FRACTION BACK TO ANCIENT CHINESE ALGORITHM

Continued fraction without analytic theories and deep theory of convergence [29,30] is a low level mathematics of the kind that used to be taught in high school algebra courses 30 years ago [31]. For the past 30 years practical engineers have no longer been interested in this topic. Since it is so useful in discrete mathematics, however, we can now make use of it once more to enhance our understanding of Chinese algorithm.

In a large history chart of mathematicians from the 10th to the 19th centuries prepared by IBM [32], the only Chinese mathematician represented was Chin chiu-shao. In studying Chin's process of Ta-yen Chiu-i-shu (method of finding unity), I find that his tabulated form of mathematics is nothing but a flow-diagram of continued fraction.

In solving the problem of Shang-yuan-chi-nien, Chin suggested a mathematical form of drill to obtain an answer for the following question:

What is the value of "a" such that $a(79) = 1 \pmod{325}$

Solution: $c_0 = 1$, $c_2 = q_1$

$c_i = c_{i-1}q_i + c_{i-2}$

$r_1 = 9$, $q_1 = \frac{325}{79} = 4$

k	0	1	2	3	4
c_k	1	4	33	37	$c_L = 144 = a$
q_k	325	4	8	1	3
r_k	79	9	7	2	1

Just like the old master of kung-fu, what an old master of ancient Chinese mathematics like Chin did, was to offer a form of drill for his followers. Making use of his form, the following three examples are given as illustrations for putting Western mathematics of continued fraction in the framework of the ancient Chinese type of mathematics

Form 1 Trivial case-Fibonacci numbers ($p_i=q_i=1$) $c_i=c_{i-1}+c_{i-2}$

i	0	1	2	3	4	5	6	7	8	9	10
c_i	1	1	2	3	5	8	13	21	34	55	89
q_i	1	1	1	1	1	1	1	1	1	1	1

Form 2

$$p_i = \begin{cases} N-2k & \text{if } i = 1 \pmod 3 \quad k=0,1,2,3,\ldots\ldots \\ 1 & \text{otherwise} \end{cases}$$

$$c_i = p_i c_{i-1} + c_{i-2}, \qquad c_0 = 1, \quad c_{-1} = 0$$

i	0	1	2	3	4	5	6	7	8	9	10	11
c_i	1	8	9	17	111	128	239	1084	1323	2407	6137	8544
p_i	1	8	1	1	6	1	1	4	1	1	2	1

$$e = 2 + \frac{6137}{8544} = 2.71828183$$

Form 3

$$B_n = \cfrac{a_0}{b_0 + \cfrac{a_1}{b_1 + \cfrac{a_2}{b_2 + \cfrac{a_3}{b_3 + \ddots + \cfrac{a_n}{b_n}}}}}$$

$B_i = b_i + B_{i-1} + a_i B_{i-2}$
$B_{-1} = 0, \quad B_{-2} = 0$

If we use $\frac{1}{4} = \text{Arctan } x$

$x = 1$ as an example

$a_i = (2i-1)^2, \quad i=0,1,2,\ldots$

$b_0 = 1, \quad b_i = 2$

all are known, then

i	0	1	2	3	4	5	6	7
b_i	1	2	2	2	2	2	2	2
B_i	1/0	1	2/1	3	6/9	13	30/75	105	210/735	945	1890/8505	10395	20 790/114345	135 135	2,027,025
a_{i+1}	1		9		25		49		81		121		144		169

$$B_0 = b_0 B_{-1} + a_0 B_{-2} = 1 + 0 = 1$$

$$B_1 = b_1B_0 + a_1B_{-1} = 2(1) + (1)(1) = 3$$

$$B_2 = b_2B_1 + a_2B_0 = 2(3) + 9(1) = 15$$

$$B_3 = b_3B_2 + a_3B_1 = 2(15) + 25(3) = 30 + 75 = 105 \text{ etc.}$$

Also $q_i = -\frac{a_{i+1}B_{i-1}}{B_{i+1}}$, $p_o = \prod_{j=1}^{i} q_j$, $c_i = \sum_{j=-1}^{i} p_j$

i	-1	0	1	2	3	4	5	6	7
a_{i+1}	1	1	9	25	49	81	121	169	
B_i	1	1	3	15	105	945	10,395	135,135	2,027,025
q_i	1	$-\frac{1}{3}$	$-\frac{3}{5}$	$-\frac{5}{7}$	$-\frac{7}{9}$	$-\frac{9}{11}$	$-\frac{11}{13}$	$-\frac{13}{15}$	$-\frac{15}{17}$
p_i	1	$-\frac{1}{3}$	$\frac{1}{5}$	$-\frac{1}{7}$	$\frac{1}{9}$	$-\frac{1}{11}$	$\frac{1}{13}$	$-\frac{1}{15}$	

$$\frac{\Pi}{4} = \text{Arctan } x = \sum_{j=1}^{6} p_i = 1 - \frac{1}{3} + \frac{1}{5} - \frac{1}{7} + \ldots\ldots - \frac{1}{15}$$

5. CONCLUSION

With the wide use of microcomputers, more and more calculations are performed on computers directly. In order to reduce the work of formula translation, effort is made to carry out the vibration analysis of structures by recurrence formulas which are based on the theory of continued fraction and the tabulated form of ancient Chinese algorithm.

References

1. J. NEEDHAM and L. WONG 1971 Science and Civilization in China, Mathematics and Science of Heavens and Earth, Vol. 3. Cambridge, England: Cambridge University Press.

2. U. LIBBRECHT 1975 Chinese Mathematics in the Thirteenth Century. Cambridge, MA: The MIT Press.

3. Y. LI and S. DU 1976 Chinese Mathematics, A Concise History (in Chinese) Peking, China: Comm Press. (English translation by J.N. CROSSLEY and A.W. LUN, in press, New York: Clarendon.)

4. I.C. CHANG and P. MULLER 1980 International Journal of Mathematical Education in Science and Technology 11. The Ancient Chinese Pearl in Number Theory—the Chinese Remainder Theory.

5. J. NEWMARK and I.C. CHANG 1986 International Journal of Mathematics Education in Science and Technology 17. The Billiard Ball Problem Solved by the Ancient Chinese Concept of Pairing.

6. A.V. AHO, J.E. HOPCROFT, and J.D. ULLMAN 1974 The Design and Analysis of Computer Algorithms. Reading, MA: Addison-Wesley.

7. T.D. DWYER and M. CRITCHFIELD 1985 A Bit of IBM Basic. Reading, MA: Addison-Wesley.

8. H. CROSS 1932 Transaction ASCE, 96. Analysis of Continuous Frames by Distributing of Fixed-end Moments.

9. L.E. GRINTER ET AL. 1949 Numerical Method of Analysis in Engineering. New York: Macmillan Company.

10. T.Y. LIN 1937 Transaction ASCE. A Direct Method of Moment Distribution.

11. Y.Y. KU 1958 Scientia Sinica 2, Civil Engineering, Peking. Simplification of Rigid Frame Analysis.

12. L.E. GRINTER 1949 Theory of Modern Steel Structures, Vol. II. New York: Macmillan Company.

13. I.C. CHANG 1957 Proceedings of the ASCE 20, St. 3. Discussion of "Simplified Analysis of Rigid Frames."

14. I.C. CHANG 1958 Proceedings of the ASCE 84, St. 7. Discussion of "Lateral Load Analysis of Two Column Bents."

15. C.V. KLOUCEK 1949 Distribution of Deformation, Prague III-157.

16. C.V. KLOUCEK 1951 Quarterly of Applied Mathematics, IX. Structural Analysis by Distribution of Deformation.

17. F. BLEICH 1952 Buckling Strength of Metal Structures. New York: McGraw-Hill.

18. E.F. MASUR, I.C. CHANG, and L.H. DONNEL 1962 Transaction of ASCE, 127. Stability of Frames in the Presence of Primary Bending Moments.

19. L.C. CHANG 1955 Proceedings of ASCE, No. 589. Discussion of "Behavior of Structures Subjected to Forced Vibration," by T.C. Looney.

20. R.E.D. BISHOP and D.C. JOHNSON 1960 Mechanics and Vibration. Cambridge, England: Cambridge University Press.

21. K. MARGUERRE 1960 Progress in Solid Mechanics, 1. Matrices of Transmission in Beam Problems.

22. K. MARGUERRE and K. WOLFEL 1979 Mechanics of Vibration. The Netherlands: Sijthoff and Noordhoff.

23. L.C. CHANG 1982 Proceedings of the First International Model Analysis Conference, Orlando, Florida. Dynamic Analysis of Rigid Frame Structures Subjected to Non-linear Earthquake Vibration.

24. L.C. CHANG 1984 Proceedings of the Second International Model Analysis Conference, Orlando, Florida. Non-linear Vibration Analysis of Stacklike Structure by Perturbation Method.

25. A.C. BAJPAI, L.R. MUSTOE, and D. WALKER 1977 Advanced Engineering Mathematics. New York: John Wiley & Sons.

26. P.G. RANKY and C.Y. HO 1985 Robot Modeling, Control and Application with Software. IFS Ltd, UK.

27. H.S. WALL 1945 American Mathematics, 52. Polynomials Whose Zero Have Negative Real Parts.

28. H.S. WALL 1984 Analytic Theory of Continued Fractions. New York: D. Van Nostrand.

29. G.H. HARDY and E.M. WRIGHT 1960 An Introduction to Theory of Numbers, 4th Edition. Oxford, England: Oxford University Press.

30. A. YA. KHINTCHINE 1963 Continued Fractions. The Netherlands: P. Noordhoff.

31. H.S. HALL and S.R. KNIGHT 1957 High Algebra. London: Macmillan & Company.

32. R. RADHEFER 1966 Men of Modern Mathematics—a History Chart of Mathematicians from 1000 to 1900. Armonk, New York: IBM.

2. FINITE ELEMENT METHODS

VIBRATIONS OF PLATES WITH CONCENTRATED MASSES AND PLATES WITH POINT SUPPORTS

E. Hinton and B.S. Al Janabi
Dept. of Civil Engineering, University College of Swansea

Summary

This paper deals with vibrations of square plates carrying concentrated masses. To analyse these problems, a nine noded, quadrilateral Mindlin plate element is adopted. The effects of the ratio of the concentrated mass to the plate mass and the postion of the concentrated mass on the vibrational characteristics of the square plates is discussed. Skew plates resting on point supports are also considered

1. INTRODUCTION

Recently, Huang and Hinton [1] developed a new nine noded Mindlin plate bending element which provides superior performance when compared with earlier elements — i.e. no locking or mechanisms, patch test satisfaction and good convergence characteristics.

In the present paper the new element is used to study the vibrational characteristics of square plates carrying concentrated masses and skew plates resting on point supports. Comparisons are provided with solutions from a comprehensive set of studies carried out using a spline element method based on thin plate theory [2].

2. VIBRATIONS OF SQUARE PLATES CARRYING CONCENTRATED MASSES

General comments

The studies in this section all involve square plates with side length a, thickness h, density ρ, flexural rigidity D, added mass intensity M and mass location $\xi = x/a, \eta = y/a$ — note that the origin of the x, y coordinate system coincides with the bottom left hand corner of the plate.

All finite element solutions are obtained using a 10×10 mesh of 9-node, Huang/Hinton, Mindlin plate elements. A lumped mass representation is adopted using a 3×3 Lobatto rule to evaluate the matrix — since the sampling points coincide with the nodal points a diagonal matrix results.

The eigenvalues are extracted using the subspace iteration algorithm with Sturm sequence check described by Bathe and Wilson [3]. The finite element program used in the studies is listed and documented by Hinton [4].

To simulate thin plate behaviour, a thickness/span ratio $h/a = 0.01$ is adopted throughout these studies.

Simply supported and clamped square plates

The vibrations of square, thin plates carrying a concentrated mass are considered. Table 1 shows the first five natural frequency parameters, $\Omega_i = \omega_i a^2(\rho h/D)^{1/2}$ of square plates with various boundary conditions, and each carrying a concentrated mass at its centre (i.e. at $\xi = \eta = 0.5$). The mass ratio, $\mu = M/\rho h a^2$ varies from 0.0 to 1.0.

For the simply supported and clamped plates comparsions are provided with results obtained by Mizusawa [2] using the spline element method. Excellent agreement between the spline and finite element solutions is obtained. For the simply supported, square plate with mass ratio $\mu = 0.25$, further comparsions are provided with Mindlin plate solutions obtained by Nicholson and Bergman [5] using Green's functions. Again, excellent correlation with the results from the finite element solution is observed.

For modes with nodal lines (i.e. contours of zero amplitude) passing through the location of the added concentrated mass, the resulting frequency parameter is independent of the mass ratio.

Square plate simply supported on two parallel edges and free on the remaining edges

A similar study is also undertaken for a square plate with two opposite edges simply supported and the remaining edges free. Thus, Table 2 shows the first five natural frequency parameters of square plates carrying a central concentrated masses with mass ratios varying from 0.0 to 1.0. Excellent agreement with the results from the spline element solutions presented by Mizusawa [2] is obtained.

Influence of location of concentrated mass

Table 3 shows the influence of the location of the concentrated mass on the frequency parameters of the plate considered in the previous section. A mass ratio of $\mu = 0.5$ is assumed. The last column of the table provides the frequency parameters for the case where no concentrated mass is added. The greatest effects on the frequencies occurs when the added mass is positioned at the midpoint of a free edge. Again, comparisons with the spline element solutions of Misuzawa [2] are excellent.

Square cantilever plate

Table 4 shows the effect of varying the mass ratio on the first five frequency parameters of a cantilevered square plate carrying a concentrated mass at the acute corner of the free edge (i.e. at $\xi = 1.0, \eta = 1.0$). Excellent correlation between the frequency parameters obtained using the spline and finite element solutions is again observed.

Table 1 Natural frequency parameter Ω_i of square plates carrying central mass with simple supports (SSSS) and clamped supports (CCCC): finite and spline element methods

mass ratio	modes	simple supports		clamped supports	
		fin. el. soln.	spline el. soln.	fin. el. soln.	spline el. soln.
0.0	1	19.74	19.74	35.98	35.99
	2	49.35	49.35	73.40	73.39
	3	49.35	49.36	73.40	73.39
	4	78.95	78.96	108.20	108.20
	5	98.75	98.70	131.70	131.60
0.25	1	13.73	13.74	21.87	21.92
		*13.73**	—	—	—
	2	49.35	49.35	73.40	73.39
		49.35	—	—	—
	3	49.35	49.35	73.40	73.39
		49.35	—	—	—
	4	64.99	65.64	89.52	90.70
		65.01	—	—	—
	5	78.95	78.96	108.20	108.20
		78.96	—	—	—
0.50	1	11.07	11.09	16.96	17.02
	2	49.35	49.35	73.40	73.39
	3	49.35	49.35	73.40	73.39
	4	59.60	60.32	84.52	85.78
	5	78.95	78.96	108.20	108.20
1.00	1	8.475	8.492	12.63	12.69
	2	49.35	49.35	73.40	73.39
	3	49.35	49.35	73.40	73.39
	4	56.36	57.08	81.72	82.98
	5	78.95	78.96	108.20	108.20

* Results obtained by Nicholson and Bergman [5]

3. VIBRATIONS OF PLATES WITH POINT SUPPORTS

General comments

The studies presented in this section all involve skew plates with side length a, skew angle ϕ (N.B. $\phi = 0°$ represents a square plate), thickness h, denisty ρ and flexural rigidity D.

Table 2 The effect of the mass ratio $\mu = M/\rho ha^2$ on the first five frequency parameters Ω_i of a square plate with two opposite edges simply supported and the other two edges free: finite and spline element solutions

	μ =			
modes	0.0	0.25	0.50	1.00
1	9.630	7.905	6.815	5.514
	*9.631**	*7.909*	*6.820*	*5.520*
2	16.12	16.12	16.12	16.12
	16.13	*16.13*	*16.13*	*16.13*
3	36.68	28.59	36.00	24.08
	36.73	*28.62*	*26.11*	*24.21*
4	38.92	38.92	38.92	38.92
	38.95	*38.95*	*38.95*	*38.95*
5	46.69	46.69	46.69	46.69
	46.74	*46.74*	*46.74*	*46.74*

* Results given by Mizusawa [2]

Table 3 Influence of location (ξ, η) of the concentrated mass M on frequency parameters Ω_i of square plate with two opposite edges simply supported and two edges free: finite and spline element solutions

	ξ, η =					no added
modes	0.5,1.0	0.5,0.75	0.25,1.0	0.25,0.75	0.25,0.5	mass
1	5.224	6.506	6.357	7.587	7.810	—
	*5.232**	*6.510*	*6.364*	*7.590*	*7.814*	*9.631*
2	11.99	14.17	11.95	14.38	16.12	—
	12.00	*14.18*	*11.96*	*14.39*	*16.13*	*16.13*
3	27.58	36.22	23.36	28.39	23.54	—
	27.66	*36.27*	*23.40*	*28.44*	*23.62*	*36.73*
4	38.92	38.92	37.84	36.74	37.78	—
	38.95	*38.95*	*37.87*	*36.78*	*37.81*	*38.95*
5	46.69	46.69	42.35	43.51	46.69	—
	46.74	*46.74*	*42.39*	*43.56*	*46.74*	46.74

* Results obtained by Misuzawa [2]

Table 4 The effect of the mass ratio $\mu = M/\rho h a^2$ on the first five frequency parameters Ω_i of a square cantilevered plate: finite and spline element solutions

	μ =			
modes	0.0	0.25	0.50	1.00
1	3.471	2.299	1.799	1.345
	*3.467**	*2.297*	*1.798*	*5.520*
2	8.498	5.961	5.657	5.492
	8.462	*5.946*	*5.645*	*5.481*
3	21.27	16.96	16.45	16.17
	21.19	*16.94*	*16.42*	*16.15*
4	27.18	21.87	21.83	21.81
	27.18	*21.79*	*21.75*	*21.73*
5	30.91	29.41	29.39	29.37
	30.77	*29.33*	*29.31*	*29.30*

* Results given by Mizusawa [2]

As with the previous study, all finite element solutions are obtained using a 10×10 mesh of 9 node Huang/Hinton, Mindlin plate elements using a lumped mass matrix. To simulate thin plate behaviour a thickness/span ratio of $h/a = 0.01$ is adopted throughout these studies.

Plates with point supports

A series of point supported skew plates are analysed for skew angles $\phi = 0°, 15°, 30°, 45°$ and $60°$. In all cases the lowest five frequency parameters $\Omega_i = \omega_i a^2 (\rho h/D)^{1/2}$ are evaluated. The following plates are considered:

(a) corner supported plates, see Figure 1,

(b) plates supported at mid-side points, see Figure 2, and

(c) plates supported at corner and mid-side points, see Figure 3.

The frequency parameters Ω_i for plates (a), (b) and (c) are listed in Tables 5, 6 and 7 respectively. In all cases excellent correlation is obtained with the results presented by Mizusawa and Kajita [6] who used the spline element method.

4. CONCLUSIONS

The Huang/Hinton, Mindlin plate element has been used to study various square plates carrying concentrated masses and also skew plates on point supports. The results are

Table 5 First five frequency parameters Ω_i for skew plates with corner supports: finite and spline element solutions

	ϕ =				
modes	0°	15°	30°	45°	60°
1	7.103	7.573	9.089	10.20	9.424
	*7.111**	*7.583*	*9.104*	*10.20*	*9.433*
2	15.74	13.15	11.39	11.79	14.63
	15.77	*13.17*	*11.40*	*11.82*	*14.66*
3	15.74	19.54	22.63	27.73	36.20
	15.77	*19.59*	*22.65*	*27.76*	*36.29*
4	19.59	20.28	25.11	29.73	39.22
	19.60	*20.29*	*25.18*	*29.78*	*39.52*
5	38.34	33.90	30.25	33.22	39.88
	38.43	*33.97*	*30.29*	*33.34*	*39.94*

* Results given by Mizusawa and Kajita [2]

Table 6 First five frequency parameters Ω_i for skew plates with supports at mid-side points: finite and spline element solutions

	ϕ =				
modes	0°	15°	30°	45°	60°
1	13.45	12.17	10.58	9.449	8.718
	*13.47**	*12.19*	*10.59*	*9.458*	*8.718*
2	17.81	18.53	19.28	19.17	18.58
	17.91	*18.62*	*19.37*	*19.21*	*18.61*
3	18.75	19.31	19.52	21.85	24.02
	18.84	*19.40*	*19.59*	*21.97*	*24.12*
4	18.75	20.09	22.84	23.84	28.67
	18.84	*20.23*	*23.02*	*23.99*	*28.87*
5	26.87	28.27	35.48	48.02	47.50
	26.96	*28.33*	*35.51*	*48.49*	*47.79*

* Results given by Mizusawa and Kajita [2]

in excellent agreement with results obtained by Misuzawa [2], [6] using a spline element method.

Table 7 First five frequency parameters Ω_i for skew plates with supports at corners and mid-side points: finite and spline element solutions

	ϕ =				
modes	0°	15°	30°	45°	60°
1	17.81	18.23	19.87	24.30	35.31
	*17.91**	*18.32*	*19.94*	*24.37*	*35.41*
2	34.82	36.45	41.84	42.81	39.51
	34.99	*36.71*	*42.21*	*42.88*	*39.57*
3	34.82	37.18	42.67	47.71	52.54
	34.99	*37.33*	*42.96*	*48.13*	*52.94*
4	38.34	39.33	44.80	51.22	57.77
	38.43	*39.48*	*44.98*	*51.98*	*58.46*
5	59.91	56.64	48.85	61.09	80.82
	60.27	*56.91*	*49.10*	*61.39*	*81.24*

* Results given by Mizusawa and Kajita [2]

5. REFERENCES

1. HUANG, H.C. and HINTON, E. 1984 *Eng. Comput.* **1**,369-379. A nine node Lagrangian Mindlin plate element with enhanced shear interpolation.

2. MIZUSAWA, T. 1987 *J. Sound Vib.* **116**, 561-572. Vibrations of skew plates carrying a concetrated mass.

3. BATHE, K.J. and WILSON, E.L. 1976 *Numerical methods in finite element analysis*. Prentice-Hall, New Jersey.

4. HINTON, E. (Ed.) 1988 *Numerical methods and software for dynamic analysis of plates and shells. Pineridge Press, Swansea.*

5. NICHOLSON, J.W. and BERGMAN, L.A. 1985 *J. Sound Vib.* **103**, 357-369. Vibration of thick plates carrying concentrated masses.

6. MIZUSAWA, T. and KAJITA, T. 1987 *J. Sound Vib.* **115**, 243-251. Vibration of skew plates resting on point supports.

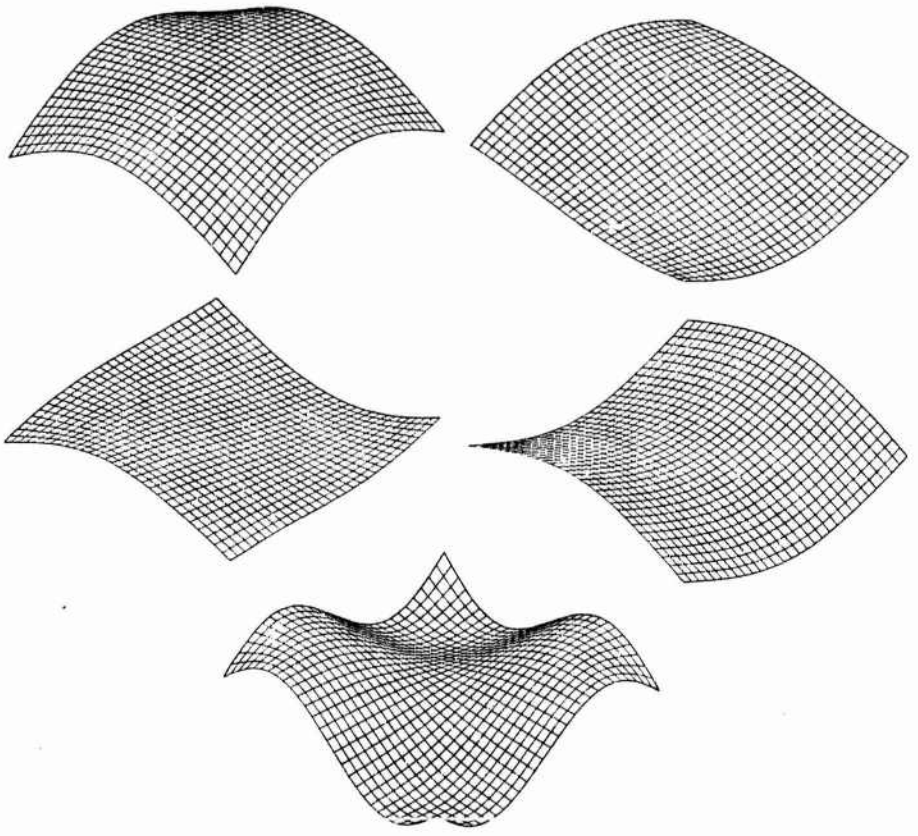

Figure 1 Mode shapes for corner supported square plate

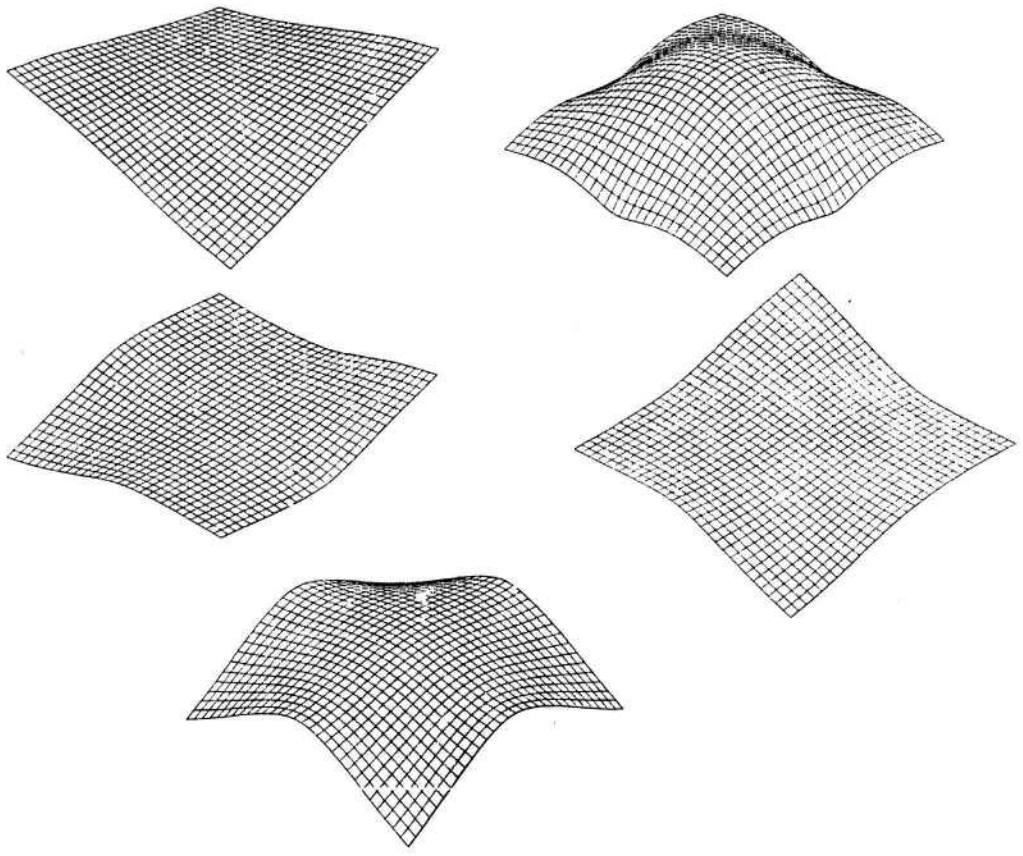

Figure 2 Mode shapes for plate supported at mid-side points

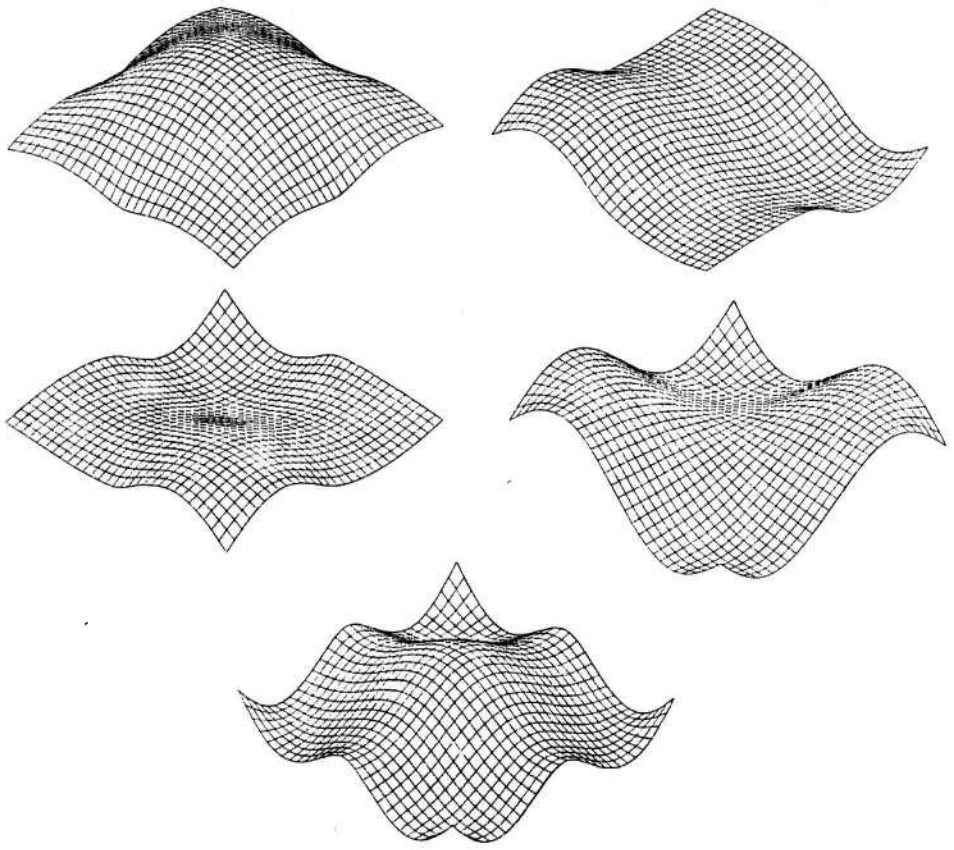

Figure 3 Mode shapes for plate supported at corners and mid-sides

FREE VIBRATION OF AN ORTHOGONALLY-STIFFENED FLAT PLATE

By D J Mead, D C Zhu & N S Bardell

Department of Aeronautics & Astronautics, University of Southampton, Highfield, Southampton, SO9 5NH, England.

SUMMARY

A flat plate, reinforced by a regular orthogonal array of uniform beams, is analysed using techniques developed for studying wave propagation in two-dimensional periodic structures. A "plane-wave" type of motion is considered which may be characterised by different propagation phase constants in the x- and y-directions. The Hierarchical Finite Element Method is used to set up the governing equations of free wave motion, and these are then solved as an eigenvalue problem for the frequencies at which particular waves will propagate.

1. INTRODUCTION

Reinforced flat plates are used extensively in aerospace and marine structures where both vibration-induced fatigue and excessive noise radiation can cause serious problems. The scant attention paid to the dynamic analyses of such structures in the past is clearly in need of rectification.

The specific problem of a flat plate resting on equi-spaced elastic beams is addressed in this paper. The Hierarchical Finite Element Method is used to formulate the problem and also to improve the accuracy and economy of the computational processes. The frequencies at which waves will propagate with specified phase constants are sought from a matrix eigenvalue problem which contains the mass and stiffness matrices of the periodic element. The frequencies of attenuating waves have not been obtained.

2. THE MATHEMATICAL MODEL

2.1 Outline of the Method

The plate itself is assumed to be isotropic, homogenous, elastic and of uniform thickness. The stiffeners are assumed to be uniform beams possessing both flexural and torsional stiffness and inertia. In flexure, they are assumed to satisfy the Euler-Bernoulli equations of motion. Damping has not been included in this work, but its effect is easily incorporated via the Correspondence Principle and the complex elastic modulus.

The mathematical analysis combines the periodic structural approach of Mead[1] with the Hierarchical Finite Element Method. The basic periodic element of the structure (a rectangular plate with a beam along adjacent edges) is itself considered as just three finite elements. In the x-direction, the plate and the x-wise beam are allowed to deflect in the conventional four cubic polynomial modes of the standard finite element approach. The Hierarchical Finite Element method allows these finite structural elements to deform in additional prescribed modes. The displacements of these additional modes are represented by the "interior coordinates" of Mead's generalised theory of periodic structure analysis. Similar modes of deflection are assigned to the plate and beam in the y-direction. When these modes are used, mass and stiffness matrices can be formed for the whole periodic element and these are then used to set up equations which govern so-called "plane" wave motion through the whole periodic structure. These are solved to yield the frequency at which waves of known wave-numbers will propagate. Much the same approach was adopted by Abdel-Rahman and Petyt who used conventional Finite Elements to solve a similar problem [2]. Examples are included which verify the work of Mead and

Parthan[3] and demonstrate the power of the Hierarchical Finite Element Method in dealing with the dynamic analysis of periodic structures.

2.2 Formulation of the Problem

Consider an infinite flat plate resting on an orthogonal beam grillage as shown in Figure 1. The beams are pitched at equal intervals, a, in the x-direction and b in the y-direction.

Figure 2 illustrates a typical periodic element or bay of this structure and Figure 3 shows its idealisation for compatibility with the Hierarchical Finite Element Method. Each bay is modelled with interior and boundary degrees of freedom and is coupled to its neighbours on all sides and corners. q_I, F_I denote the internal displacement coordinates and internal forces of the bay, q_L, F_L, q_R, F_R, q_B, F_B and q_T, F_T denote the left, right, bottom and top side displacement coordinates and side forces of the bay: q_{LB}, F_{LB}, q_{RB}, F_{RB}, q_{LT}, F_{LT}, q_{RT}, F_{RT} denote the left bottom, right bottom, left top, and right top corner displacement coordinates and corner forces of the bay. The linear equations of motion of the undamped bay are then given by

$$([K] - \omega^2[M])\{q\} = \{F\} \tag{1}$$

[K] and [M] are the stiffness and mass matrices for the bay, and {q} and {F} are the coordinates and generalised force vectors given by

$$\{q\} = [q_{LB}\ q_{LT}\ q_{RT}\ q_{RB}\ q_L\ q_R\ q_B\ q_T\ q_I]^T \tag{2}$$

and

$$\{F\} = [F_{LB}\ F_{LT}\ F_{RT}\ F_{RB}\ F_L\ F_R\ F_B\ F_T\ F_I]^T$$

It is convenient to partition the [K] and [M] matrices according to the corner, left, right, bottom, top and internal displacement coordinates hence

$$[K] = \begin{bmatrix}
K_{LB,LB} & K_{LB,LT} & K_{LB,RT} & K_{LB,RB} & K_{LB,L} & K_{LB,R} & K_{LB,B} & K_{LB,T} & K_{LB,I} \\
K_{LT,LB} & K_{LT,LT} & K_{LT,RT} & K_{LT,RB} & \multicolumn{4}{c}{\cdots\cdots\ \text{etc}} & \\
K_{RT,LB} & K_{RT,LT} & K_{RT,RT} & K_{RT,RB} & & & & & \\
K_{RB,LB} & K_{RB,LT} & K_{RB,RT} & K_{RB,RB} & & & & & \\
K_{L,LB} & & & & K_{L,L} & & & & \\
K_{R,LB} & & & & & K_{R,R} & & & \\
K_{B,LB} & & & & & & K_{B,B} & & \\
K_{T,LB} & & & & & & & K_{T,T} & \\
K_{I,LB} & & \text{etc} & & & & & & K_{I,I}
\end{bmatrix}$$

A similar expression can be written for [M].

For free wavemotion, no external forces act on the bay apart from those on its boundaries from adjacent bays. Hence $\{F_I\} = 0$. The forces on the bay's boundaries are those which transmit the wave motion from that bay to its immediate neighbours. This wavemotion is characterised by the relationships between the edge displacement coordinates and their corresponding generalised forces in one bay to the corresponding coordinates and forces in adjacent bays.

The left, right, top and bottom coordinates are related through

$$\{q_R\} = e^{\mu_x}\{q_L\} \quad and \quad \{q_T\} = e^{\mu_y}\{q_B\} \tag{3 a, b}$$

and the left, right, top and bottom corner coordinates through

$$\{q_{RB}\} = e^{\mu_x}\{q_{LB}\}, \{q_{LT}\} = e^{\mu_y}\{q_{LB}\} \quad and \quad \{q_{RT}\} = e^{\mu_x + \mu_y}\{q_{LB}\} \tag{4 a, b}$$

The forces along the left, right, top and bottom edges are related through

$$\{F_R\} = -e^{\mu_x}\{F_L\} \quad and \quad \{F_T\} = -e^{\mu_y}\{F_B\} \tag{5 a, b}$$

and the left, right, top and bottom corner forces through

$$\{F_{RB}\} = -e^{\mu_x}\{F_{LB}\}, \{F_{LT}\} = -e^{\mu_y}\{F_{LB}\} \quad and \quad \{F_{RT}\} = e^{\mu_x + \mu_y}\{F_{LB}\} \tag{6 a, b}$$

By substituting equations (3a-6b) into equation (1) and setting $\{F_I\} = 0$, the condensed matrix equation of wave propagation through the structure is given by

$$([K'(\mu_x, \mu_y)] - \Omega^2[M'(\mu_x, \mu_y)]) \begin{matrix} q_{LB} \\ q_L \\ q_B \\ q_I \end{matrix} = 0 \tag{7}$$

where $[K'(\mu_x, \mu_y)] =$

$$\begin{matrix} K'_{LB,LB} & K'_{LB,L} & K'_{LB,B} & K'_{LB,I} \\ K'_{L,LB} & K'_{L,L} & K'_{L,B} & K'_{L,I} \\ K'_{B,LB} & K'_{B,L} & K'_{B,B} & K'_{B,I} \\ K'_{I,LB} & K'_{I,L} & K'_{I,B} & K'_{I,I} \end{matrix}$$

and

$$K'_{LB,LB} = K_{LB,LB} + K_{LB,LT}e^{\mu_y} + K_{LB,RB}e^{\mu_x} + K_{LB,RT}e^{\mu_x+\mu_y}$$
$$+ K_{LT,LB}e^{-\mu_y} + K_{LT,LT} + K_{LT,RB}e^{\mu_x-\mu_y} + K_{LT,RT}e^{\mu_x}$$
$$K_{RB,LB}e^{-\mu_x} + K_{RB,LT}e^{\mu_y-\mu_x} + K_{RB,RB} + K_{RB,RT}e^{-(\mu_x+\mu_y)}$$
$$+ K_{RT,LB}e^{-(\mu_x+\mu_y)}K_{RT,LT}e^{-\mu_x} + K_{RT,RB}e^{-\mu_y} + K_{RT,RT}$$

$$K'_{LB,L} = K_{LB,L} + K_{LB,R}e^{\mu_x} + K_{LT,L}e^{-\mu_y} + K_{LT,R}e^{\mu_x-\mu_y} + K_{RB,L}e^{-\mu_x}$$
$$+ K_{RB,R} + K_{RT,L}e^{-(\mu_x+\mu_y)} + K_{RT,R}e^{-\mu_y}$$

$$K'_{LB,B} = K_{LB,B} + K_{LB,T}e^{\mu_y} + K_{LT,B}e^{-\mu_y} + K_{LT,T} + K_{RB,B}e^{-\mu_x}$$
$$+ K_{RB,T}e^{\mu_y-\mu_x} + K_{RT,B}e^{-(\mu_x+\mu_y)} + K_{RT,T}e^{-\mu_x}$$

$$K'_{LB,I} = K_{LB,I} + K_{LT,I}e^{-\mu_y} + K_{RB,I}e^{-\mu_x} + K_{RT,I}e^{-(\mu_x+\mu_y)}$$

$$K'_{L,LB} = K_{L,LB} + K_{L,LT}e^{\mu_y} + K_{L,RB}e^{\mu_x} + K_{L,RT}e^{\mu_x+\mu_y}$$
$$+ K_{R,LB}e^{-\mu_x} + K_{R,LT}e^{\mu_y-\mu_x} + K_{R,RB} + K_{R,RT}e^{\mu_y}$$

$$K'_{L,L} = K_{L,L} + K_{L,R}e^{\mu_x} + K_{R,L}e^{-\mu_x} + K_{R,R}$$

$$K'_{L,B} = K_{L,B} + K_{L,T}e^{\mu_y} + K_{R,B}e^{-\mu_x} + K_{R,T}e^{\mu_y-\mu_x}$$

$$K'_{L,I} = K_{L,I} + K_{R,I}e^{-\mu_x}$$

$$K'_{B,LB} = K_{B,LB} + K_{B,LT}e^{\mu_y} + K_{B,RB}e^{+\mu_x} + K_{B,RT}e^{\mu_x+\mu_y}$$
$$+ K_{T,LB}e^{-\mu_y} + K_{T,LT} + K_{T,RB}e^{\mu_x-\mu_y} + K_{T,RT}e^{\mu_x}$$

$$K'_{B,I} = K_{B,L} + K_{B,R}e^{\mu_x} + K_{T,L}e^{-\mu_y} + K_{T,R}e^{\mu_x-\mu_y}$$

$$K'_{B,B} = K_{B,B} + K_{B,T}e^{\mu_y} + K_{T,B}e^{-\mu_y} + K_{T,T}$$

$$K'_{B,I} = K_{B,I} + K_{T,I}e^{-\mu_y}$$

$$K'_{I,LB} = K_{I,LB} + K_{I,LT}e^{\mu_y} + K_{I,RB}e^{\mu_x} + K_{I,RT}e^{\mu_x-\mu_y}$$

$$K'_{I,L} = K_{I,L} + K_{I,R}e^{\mu_x}$$

$$K'_{I,B} = K_{I,B} + K_{I,T}e^{\mu_y}$$

$$K'_{I,I} = K_{I,I}$$

The elements of the condensed M' matrix have the same form as the elements of the K' matrix, but with the K' replaced by M'. Ω is a non-dimensional frequency factor given by $\Omega^2=\omega^2a^4(m/D)$ where $m=\rho h$. The above formulation is a completely general result for a two-dimensional periodic structure.

The condition described above is satisfied if a so-called "plane wave" of frequency ω propagates across the reinforced plate at an angle θ to the x-axis. Each rectangular element then vibrates in the same complex mode $w(x, y)\, e^{-j\omega t}$, but there is a phase difference of ε_x between adjacent elements in the x-direction and of ε_y between adjacent elements in the y-direction. These quantities are related through

$$\tan\theta = (\varepsilon_y/\varepsilon_x)(a/b) \qquad (8)$$

2.3 Energy Expressions for the Periodic Element

Use will be made of the standard expressions for the energies of a flat plate and beam expressed in terms of non-dimensional coordinates ξ, η which are related to the x- and y-coordinates by $x/a=(\xi+1)/2$ and $y/b=(\eta+1)/2$. (See Figure 2). The

total energy expressions are

$$U = bD/2a^3\left[4\int_{-1}^{+1}\int_{-1}^{+1}\left\{\left(\partial^2 w/\partial\xi^2\right)^2 + \frac{1}{(b/a)^2}\left(\partial^2 w/\partial\eta^2\right)^2 + \frac{2\nu}{(b/a)^2}\left(\partial^2 w/\partial\xi^2\right)\left(\partial^2 w/\partial\eta^2\right)\right.\right.$$

$$\left.\left. + \frac{2(1-\nu)}{(b/a)^2}\left(\partial^2 w/\partial\xi\partial\eta\right)^2\right\} d\xi d\eta + \frac{8(EI)_x}{Db}\int_{-1}^{1}\left(\partial^2 w/\partial\xi^2\right)^2 d\xi$$

$$+ \frac{8(GJ)_x a^2}{Db^3}\int_{-1}^{1}\left(\partial^2 w/\partial\xi d\eta\right)^2 d\xi + \frac{32(E\Gamma)_x}{Db^3}\int_{-1}^{1}\left(\partial^3 w/\partial\xi^2 d\eta\right)^2 d\xi$$

$$+ \frac{8(EI)_y a^3}{Db^4}\int_{-1}^{1}\left(\partial^2 w/\partial\eta^2\right)^2 d\eta + \frac{8(GJ)_y a}{Db^2}\int_{-1}^{1}\left(\partial^2 w/\partial\xi d\eta\right)^2 d\eta$$

$$\left. + \frac{32(E\Gamma)_y a}{Db^4}\int_{-1}^{1}\left(\partial^2 w/\partial\eta^2\partial\xi\right)^2 d\eta\right] \qquad (9)$$

$$T = \rho h a b/2\left[\tfrac{1}{4}\int_{-1}^{1}\int_{-1}^{1}\left(\partial w/\partial t\right)^2 d\eta d\xi + \tfrac{1}{2}\frac{A_x}{hb}\int_{-1}^{1}\left(\partial w/\partial t\right)^2 d\xi\right.$$

$$+ \frac{2I_{px}}{hb^3}\int_{-1}^{1}\left(\partial^2 w/\partial\eta\partial t\right)^2 d\xi + \tfrac{1}{2}\frac{A_y}{ha}\int_{-1}^{1}\left(\partial w/\partial t\right)^2 d\eta$$

$$\left. + \frac{2I_{py}}{ha^3}\int_{-1}^{1}\left(\partial^2 w/\partial\xi\partial t\right)^2 d\eta\right] \qquad (10)$$

2.4 The Hierarchical Finite Element Method

The Hierarchical Finite Element Method adopts the reverse procedure to the ordinary Finite Element Method in that it keeps the size of the element constant, but allows an increased number of polynomial functions to describe its displacement mode. (The Hierarchical mode order p is related to the highest order polynomial with order p-1 used to describe a displacement mode of the structure). This is particularly well suited to the kind of problem described in this paper. The ascending hierarchy of functions used in this work are derived from Legendre orthogonal polynomials, and are given by

$$f_r(\xi) = \sum_{n=0}^{r/2}\frac{(-1)^n}{2^n n!}\cdot\frac{(2r-2n-7)!!}{(r-2n-1)!}\xi^{r-2n-1} \qquad r>4 \qquad (11)$$

where r!! = r(r-2) (r-4). . . .(2 or 1), 0!! = (-1)!! = 1, and r/2 denotes its own integer part only. These hierarchical modes have zero displacement and rotation at each end, and hence only contribute to the internal displacement field of the finite element. Table 1 presents the first ten out-of-piane hierarchical shape functions calculated from Equation 11. The first four of these are standard Hermite cubic functions which are independent of Equation 11. Then, the plate displacement is given by the product of both x- and y-modes as

$$w(\xi,\eta) = \sum_{r=1}^{p}\sum_{s=1}^{p}\Phi_{r,s} f_r(\xi) g_s(\eta) \qquad (12)$$

This double series (in non-dimensional form) is firstly substituted into the strain and kinetic energy expressions (equations 9 and 10) for the complete element. The resulting expressions are then used in Lagrange's equations of motion to yield the stiffness and mass matrices for the periodic element. Referring to Equations 1 and 12, it can be seen that if p is chosen to be 10, then the [K] and [M] matrices are each of order 100 x 100.

All of the non-vanishing integral products within [K] and [M] and related to the higher order modes can easily be calculated by using the following unified and explicit integral formula[4]

$$\int_{-1}^{+1} f_r^s(\xi) f_{r+n}^t(\xi)\, d\xi = \frac{G}{\prod_{k=0}^{4-s-t} (2r+n-1-s-t-2k)} \qquad r>4 \tag{13}$$

where G is the integration coefficient shown in Table 2, and s and t are the differential orders of the function

This method yields exact fractional answers, and thus keeps the numerical error to an absolute minimum, which is very important when high order modes are used. In general, the size of matrix which has finally to be used in the eigenvalue problem is conveniently reduced in size, i.e. for [K] and [M] of order $p^2 x p^2$, [K'] and [M'] of Equation 7 are of order $(p-2)^2$ x $(p-2)^2$. This is a result of the condensation process mentioned in Section 2.2.

2.5 The Eigenvalue Problem

By supplying the propagation constants μ_x and μ_y, Equation (7) may be solved as an eigenvalue problem to determine Ω^2. Results are presented in this paper for the case when μ_x and μ_y are purely imaginary, i.e. $\mu_x=j\varepsilon_x$, and $\mu_y=j\varepsilon_y$. This ensures that the [K'] and [M'] matrices in Equation 7 are Hermitian and the eigenvalues (Ω^2) will always be real.

3. THE COMPUTED PHASE CONSTANT SURFACES

3.1 Flat Plate Stiffened by an Orthogonal Array of Line Simple Supports

Figures 4, 5 and 6 show the frequency plotted against ε_x, ε_y for periodically simply-supported plates with support-spacing aspect ratios (a/b) of 1.0, 0.5 and 0.25 respectively. The lines which are drawn correspond to (ε_x=0 or π and ε_y) or (ε_x and ε_y=0 or π) and constitute the boundaries of "phase-constant surfaces" of the form first presented by Mead and Parthan[3]. The upper and lower bounding frequencies of these surfaces define the pass bands of the structure - i.e. the frequency bands in which "plane" wave motion can freely propagate. The upper and lower bounding frequencies of a particular phase constant surface also correspond to the natural frequencies of a single periodic element with all its edges clamped and simply-supported respectively.

With a hierarchical mode order of 8, the bounding frequencies of the first band agree to within 1% with the results of Leissa[5]. Very close agreement is also observed for the bounding frequencies of some of the subsequent bands.

The phase constant surfaces of Figures 4 to 6 have been generated by using hierarchical modes up to the order 8, the highest of which is a seventh order polynomial function with four maxima. The phase constant surfaces so obtained can therefore only include those surfaces whose upper and lower bounding frequencies correspond to the natural frequencies of a single periodic element vibrating with m and/or n≤4. The inclusion of hierarchical modes of still higher order would permit more accurate computation of surfaces, corresponding to the higher order natural modes of the single element.

3.2 Flat Plate Stiffened by an Orthogonal Beam Grillage

The simple supports are now replaced by a general beam grillage having non-dimensional flexural and torsional stiffnesses characterised by

$$KT_x = EI/bD, KT_y = EIa^3/Db^4 \quad and \quad CR_x = GJa^2/Db^3 \; and \; CR_y = GJa/Db^2$$

respectively. The effects of torsional and transverse inertia can be included by assigning specific values to the beam non-dimensional areas A_x/hb and A_y/ha and to the non-dimensional torsional inertias I_{px}/hb^3 and I_{py}/ha^3. It is assumed that the beam neutral axes coincide with the neutral surface of the plate so that in-plane wave motion of the plate itself is not coupled to the beam flexural motion.

Two examples are now considered, and the structural properties of each are summarised in Table 3. The first case (structure "A") is a plate on ideal massless stiffeners. The second case (structure "B") represents the more realistic example of a section of flat aircraft skin, stiffened in the x-direction by integrally-machined flangeless stringers and stiffened in the y-direction by I-section frames. Flexural and torsional inertia effects are fully included, but the coupled in-plane motions of the plate which would result are neglected.

Figure 7 shows the phase constant surfaces for configuration "A". The first phase constant surface now dips to zero at $\varepsilon_x=\varepsilon_y=0$. The severity of the dip on the faces $\varepsilon_x=0$ and $\varepsilon_y=0$ is determined solely by the beam flexural stiffness in the y- and x-directions respectively. If either of these stiffnesses were increased, the gradient of the dip would increase, until as KT_x and $KT_y \to \infty$, it would become vertically discontinuous. When $\varepsilon_x=\varepsilon_y=0$ and $\Omega=0$, the whole structure moves as a rigid body, with every bay in phase with its neighbour. This corresponds to a motion of infinite wavelength and zero frequency existing in the beams. As the frequency increases slightly, waves with non-zero values ε_x and/or ε_y can exist. The motion of the structure is dominated in this region by the flexural stiffness of the beams together with the mass of the beams and plate. Such wave motion of course, can propagate from zero frequency as shown by Heckl[6].

The curves on the face $\varepsilon_x=\pi$ and $\varepsilon_y=\pi$ are straighter than those obtained for the plate on line simple-supports. (Figure 4). This is due to the torsional restraint introduced by the stiffeners, which raises the torsionally-dependent bounding frequencies.

The higher surfaces (Figure 7) are affected in a manner similar to the first surface. That the higher surfaces appear to pass through one another is of interest, though the full significance of this is not understood at present. The frequency stop/pass-band behaviour of the structure is preserved, although in this particular case it commences with a pass band. Heckl [6] showed this to be the case for periodic beam grillages, and it is clearly also true for periodically stiffened plates.

The phase constant surfaces for configuration "B" are shown in Figure 8. These are seen to be rather complicated! Multiple intersections of each surface now occur, and no frequency attentuation bands are in evidence. Free wavemotion can propagate at any frequency, and there are no stop bands for this structure which can be used to control the vibration levels. The high value of the frame flexural stiffness, KT_y, is seen to cause a very steep dip in the first phase constant surface on the face $\varepsilon_x=0$, whereas the lesser value of KT_x causes the curve on the face $\varepsilon_y=0$ to vary in a far gentler manner.

4. THE NATURAL FREQUENCIES OF A FINITE ORTHOGONALLY-STIFFENED PLATE

Mead and Parthan [3] showed that the natural frequencies of a finite plate with N_x bays in the x-direction and N_y bays in the y-direction occur at frequencies at

which

$\varepsilon_x = m\pi/N_x$ & $\varepsilon_y = n\pi/N_y$ if the extreme edges are clamped

and $\varepsilon_x = (m+1)\pi/N_x$ & $\varepsilon_y = (n+1)\pi/N_y$ if the extreme edges are simply-supported. (m=0, 1, 2, 3,. . . N_x-1 and n=0, 1, 2, 3, . . . N_y-1).
Given one of the phase constant surfaces between two bounding frequencies, all of the natural frequencies of the finite plate structure in that frequency range can be found from the intersections on that surface of the planes $\varepsilon_x = m/N_x$ and $\varepsilon_y = n/N_y$. These frequencies can be found in practice by assigning the above values of ε_x and ε_y, and then by computing the corresponding frequencies from Equation 7.

This has been done for the first phase constant surface of Structure "A" in Section 3.2. A finite structure of ten bays in both the x-y-directions was considered. The construction grid to locate these frequencies is shown in Figure 9, and the natural frequencies so obtained are tabulated in Table 4. If all the extreme edges are clamped, the last column and bottom row should be disregarded. If all the extreme edges are simply-supported, the first column and top row should be disregarded.

This method of finding the natural frequencies is a computational generalisation for two dimensional structures of Sen Gupta's geometrical construction [7].

5. CONCLUSIONS

A mathematical model has been developed to represent the most general case of a flat plate stiffened by an orthogonal array of beams. The pass/stop band nature of this type of periodic structure has been observed from the stacks of phase constant surfaces. These also assist in explaining certain dynamic features. The first surface has been used in one case to determine the natural frequencies of a finite periodic 100 bay plate with particular boundary conditions. The dynamic behaviour of the stiffened plate at low frequencies bears a marked resemblance to that of a periodic beam grillage.

REFERENCES

1. D J MEAD, 1973, Journal of Sound and Vibration 27(2) pp235-260.. A general theory of harmonic wave propagation in linear periodic systems with multiple coupling.

2. A Y A ABDEL-RAHMAN & M PETYT, 1980, Proceedings of the First Conference - Recent Advances in Structural Dynamics, pp 361-373.

3. D J MEAD & S PARTHAN, 1978, Journal of Sound and Vibration 64(3) pp325-348. Free wave propagation in two-dimensional periodic plates.

4. D C ZHU, 1986, Proceedings of the International Conference on Computational Mechanics, Vol 1 pp123-128, Tokyo. Development of Hierarchical Finite Element Methods at BIAA.

5. A W LEISSA, 1973 NASA SP-160. Vibration of plates.

6. M A HECKL, 1964, Journal of the Acoustical Society of America vol 36 no. 7. Investigations on the vibrations of grillages and other simple beam structures.

7. G SEN GUPTA, 1970, PhD Thesis, University of Southampton. Dynamics of periodically stiffened structures using a wave approach.

TABLE 1
The first ten Hierarchical Shape Functions

$f_1(\xi) = \frac{1}{2} - \frac{3}{4}\xi + \frac{1}{4}\xi^3$	f_1	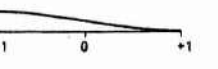
$f_2(\xi) = \frac{1}{8} - \frac{1}{8}\xi - \frac{1}{8}\xi^2 + \frac{1}{8}\xi^3$	f_2	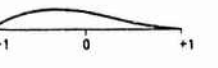
$f_3(\xi) = \frac{1}{2} + \frac{3}{4}\xi - \frac{1}{4}\xi^3$	f_3	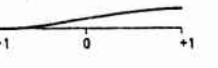
$f_4(\xi) = -\frac{1}{8} - \frac{1}{8}\xi + \frac{1}{8}\xi^2 + \frac{1}{8}\xi^3$	f_4	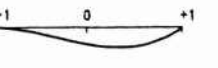
$f_5(\xi) = \frac{1}{8} - \frac{1}{4}\xi^2 + \frac{1}{8}\xi^4$	f_5	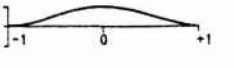
$f_6(\xi) = \frac{1}{8}\xi - \frac{1}{4}\xi^3 + \frac{1}{8}\xi^5$	f_6	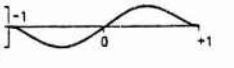
$f_7(\xi) = -\frac{1}{48} + \frac{3}{16}\xi^2 - \frac{5}{16}\xi^4 + \frac{7}{48}\xi^6$	f_7	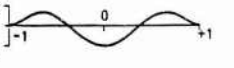
$f_8(\xi) = -\frac{3}{48}\xi + \frac{5}{18}\xi^3 - \frac{7}{16}\xi^5 + \frac{9}{48}\xi^7$	f_8	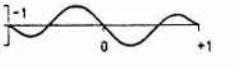
$f_9(\xi) = \frac{3}{384} - \frac{15}{96}\xi^2 + \frac{35}{84}\xi^4 - \frac{83}{96}\xi^6 + \frac{99}{384}\xi^8$	f_9	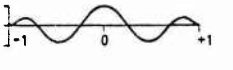
$f_{10}(\xi) = \frac{15}{384}\xi - \frac{35}{98}\xi^3 + \frac{63}{64}\xi^5 - \frac{99}{98}\xi^7 + \frac{143}{384}\xi^9$	f_{10}	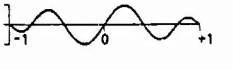

TABLE 2
The non-vanishing integration coefficient G

s, t	2, 2	1, 2	1, 1	0, 2	0, 1	0, 0	otherwise
n	0	+1	0 +2	0 +2	+1 +3	0 +2 +4	0
G	2	+2	4 -2	-4 2	+6 +2	12 -8 2	0

TABLE 3
Details of the parameters characterising structures "A" and "B" and the corresponding figure numbers for the phase constant surfaces

Structure	Figure	a/b	KT_x	KT_y	CR_x	CR_y	A_x/hb	A_y/ha	I_{xx}/hb^3	I_{yy}/ha^3
A	7	1.0	800.0	400.0	4.0	2.0	0.0	0.0	0.0	0.0
B	8	4.0	125.0	287×10^3	26.0	27.0	0.66	1.42	0.006	0.001

TABLE 4
Natural frequencies Ω in the first propagation band for structure "A".

Plate aspect ratio a/b = 1.0: $KT_x = 800.0$, $KT_y = 400.0$, $CR_x = 4.0$, $CR_y = 2.0$											
c_x c_y	0	π/10	2π/10	3π/10	4π/10	5π/10	6π/10	7π/10	8π/10	9π/10	π
0	0.0	2.79	10.90	22.06	30.16	33.22	34.18	34.46	34.52	34.53	34.52
1π/10	3.94	4.83	11.54	22.23	30.19	33.20	34.13	34.41	34.46	34.46	34.46
2π/10	15.02	15.24	17.98	24.77	30.69	33.19	34.01	34.48	34.29	34.28	34.27
3π/10	27.31	27.36	27.98	29.82	32.02	33.33	33.86	34.02	34.03	34.01	33.99
4π/10	32.57	32.56	32.60	32.81	33.19	33.53	33.70	33.74	33.70	33.67	33.65
5π/10	33.85	33.83	33.76	33.68	33.62	33.58	33.52	33.45	33.36	33.30	33.28
6π/10	34.06	34.03	33.93	33.79	33.63	33.46	33.30	33.15	33.03	32.95	32.92
7π/10	33.98	33.94	33.84	33.68	33.48	33.26	33.06	32.87	32.73	32.63	32.60
8π/10	33.85	33.81	33.70	33.53	33.31	33.08	32.85	32.65	32.49	32.39	32.35
9π/10	33.74	33.70	33.59	33.41	33.19	32.95	32.72	32.50	32.34	32.23	32.19
π	33.71	33.67	33.55	33.37	33.15	32.91	32.67	32.45	32.28	32.18	32.14

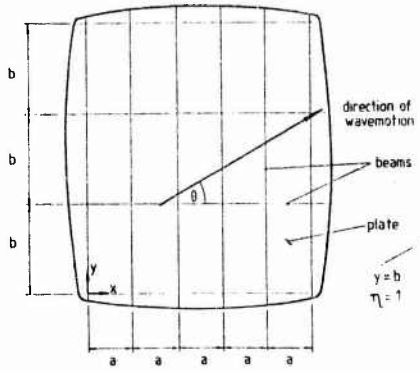

Figure 1 The two-dimensional periodic structure.

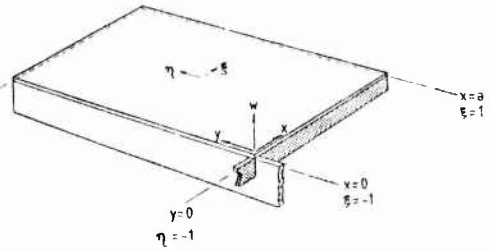

Figure 2 Diagram showing the periodic element - a flat plate with a beam along two adjacent edges.

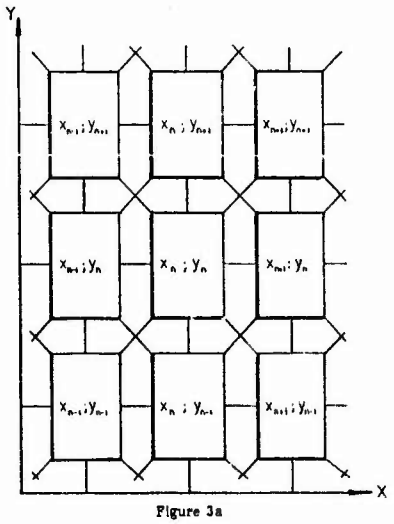

Figure 3a

Idealisation of a two-dimensional periodic flat plate as an assembly of bays joined together on all sides and corners.

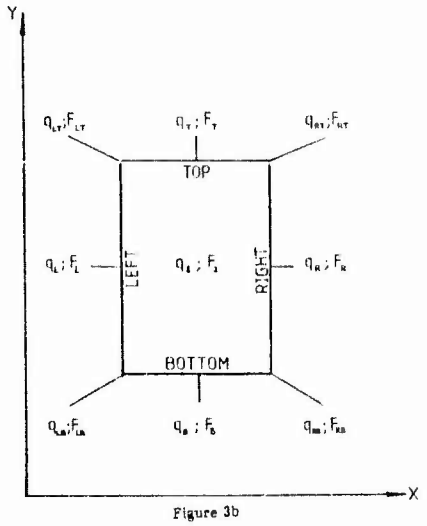

Figure 3b

The displacement coordinates and forces acting on a single bay of the periodic structure.

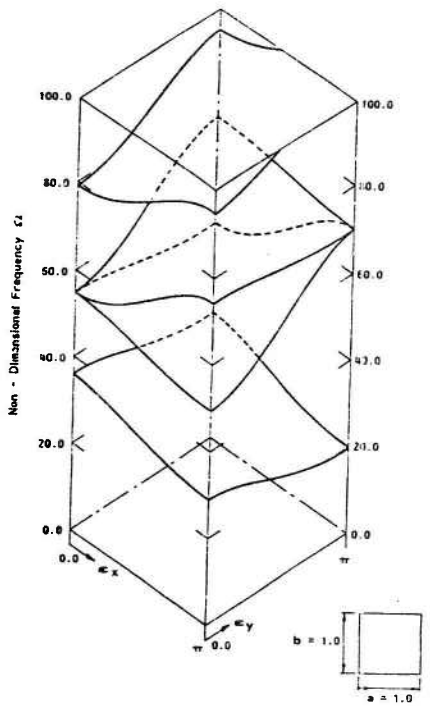

Figure 4

Phase constant surfaces for an orthogonally stiffened flat plate of aspect ratio 1.0. The hierarchical mode order is 8, and the stiffener parameters are KT_x=S.S, KT_y=S.S, CR_x=0.0, CR_y=0.0.

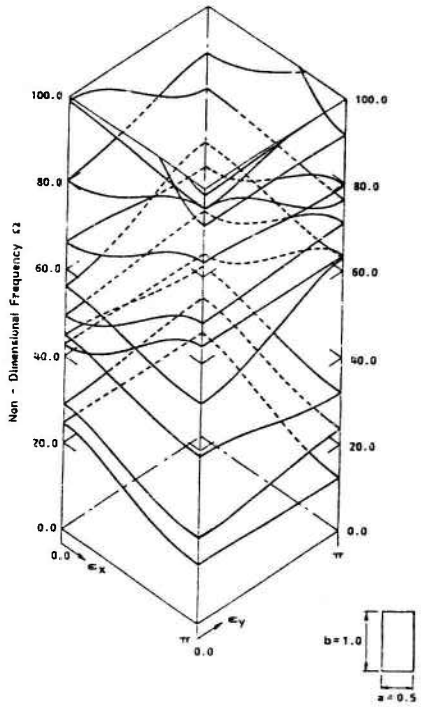

Figure 5

Phase constant surfaces for an orthogonally stiffened flat plate of aspect ratio 0.5. The hierarchical mode order is 8, and the stiffener parameters are KT_x=S.S,KT_y=S.S,CR_x=0.0, CR_y=0.0.

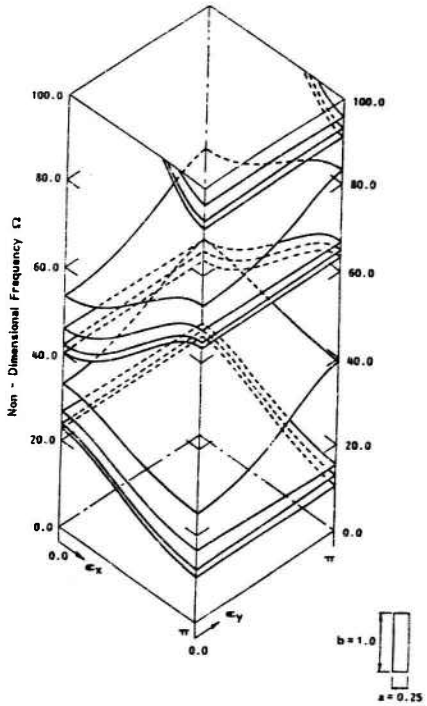

Figure 6

Phase constant surfaces for an orthogonally stiffened flat plate of aspect ratio 0.25. The hierarchical mode order is 8, and the stiffener parameters are KT_x=S.S, KT_y=S.S, CR_x=0.0,CR_y=0.0.

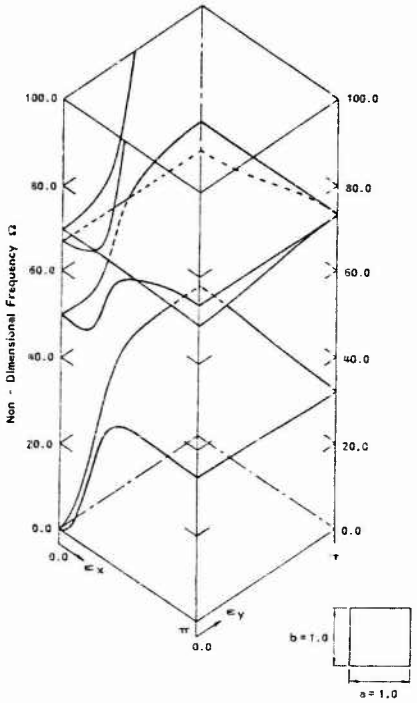

Figure 7

Phase constant surfaces for an orthogonally stiffened flat plate of aspect ratio 1.0. The hierarchical mode order is 8, and the stiffener parameters are KT_x=800.0, KT_y=400.0, CR_x=4.0, CR_y=2.0.

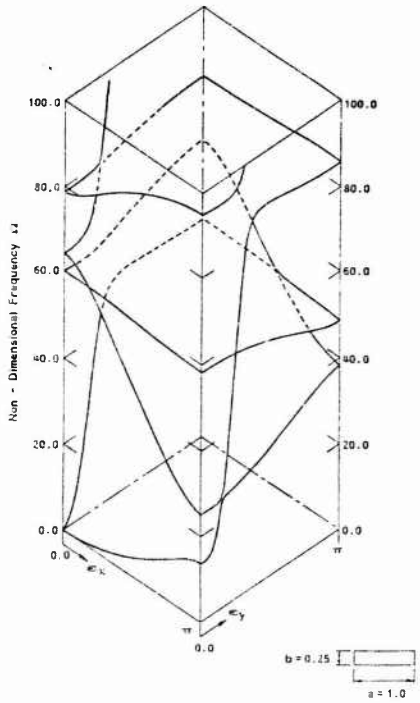

Figure 8

Phase constant surfaces for an orthogonally stiffened flat plate of aspect ratio 4.0. The hierarchical mode order is 8, and the stiffener parameters are KT_x=125.0, KT_y=2.87x10^5, CR_x=26.0, CR_y=27.0.

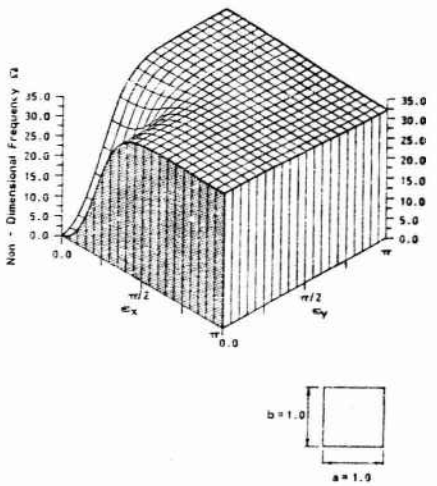

Figure 9

A complete phase constant surface for an orthogonally stiffened flat plate of aspect ratio 1.0. The hierarchical mode order is 8 and the stiffener parameters are KT_x=800.0, KT_y=400.0, CR_x=4.0, CR_y=2.0 (This corresponds to the first surface in Figure 7).

MIXED ELEMENTS IN DESIGN SENSITIVITY ANALYSIS OF PLATES WITH DYNAMIC AND STABILITY CONSTRAINTS

R.P. Leal*
Secção Autónoma de Engenharia Mecânica
Faculdade de Ciências e Tecnologia da Universidade de Coimbra
3000 COIMBRA, PORTUGAL

C.A. Mota Soares
Centro de Mecânica e Materiais da Universidade
Técnica de Lisboa (CEMUL), Instituto Superior Técnico
Av. Rovisco Pais, 1096 LISBOA CODEX, PORTUGAL

ABSTRACT

In this paper is developed the theory of design sensitivity analysis of structures subjected to dynamic and stability constraints, based on mixed finite element models. The theory is applied to the sensitivity and analysis of natural frequencies and critical stresses of plates. The results are compared with analytical and finite differences solutions. The advantages and disadvantagens of the mixed elements in sensitivity analysis of plates are discussed with reference to applications.

1. INTRODUCTION

Sensitivity analysis of structures is the most important stage in the optimal structural design of structures [1]. The combination of sensitivity analysis, an adequate choice of objective function and constraints, with the correct selection of design variables and optimization algorithms are the basic requirements for the efficient optimal structural design.

In this paper, the theory of the design sensitivity analysis of structures subjected to dynamic and stability constraints, based on mixed finite element models, is developed. The sensitivity analysis of beams based on mixed formulation has been presented recently [2]. The theory is now applied to the sensitivity of natural frequencies and critical stresses of plates due to thickness variation. The models are based on an isoparametric quadratic mixed finite element with eight nodes and thirty two degrees of freedom presented by Mota Soares et al. [3].

In finite element dynamic and stability analysis of plate structures, mixed models offer some advantages over displacement models. The mixed models calculate the displacements and moments with the same degree of accuracy snd the reduction of degrees of freedom of the eigenproblem is an exact operation. In sensitivity analysis of plates the advantages and disadvantages of the mixed elements are discussed with reference to application and the results are compared with analytical and finite difference solutions.

*Sponsored by Instituto Nacional de Investigação Científica (INIC).

2. MIXED ELEMENTS IN PLATES

Mixed elements are based on the Reissner's variational principle. Using the nomenclature defined in Fig. 1 the Reissner functional for plates is 4

$$V_R = \int_A [m_{ij} r_{j,i} + s_j (r_j + w_{,j}) - U^* + \Omega] dA - \int_{\Gamma_t} (\bar{m}_{nn} r_n + \bar{m}_{ns} r_s + \bar{s}_n w)\, d\Gamma - \\ - \int_{\Gamma_u} [m_{nn} (r_n - \bar{r}_n) + m_{ns} (r_s - \bar{r}_s) + s_n (w - \bar{w})]\, d\Gamma \qquad (1)$$

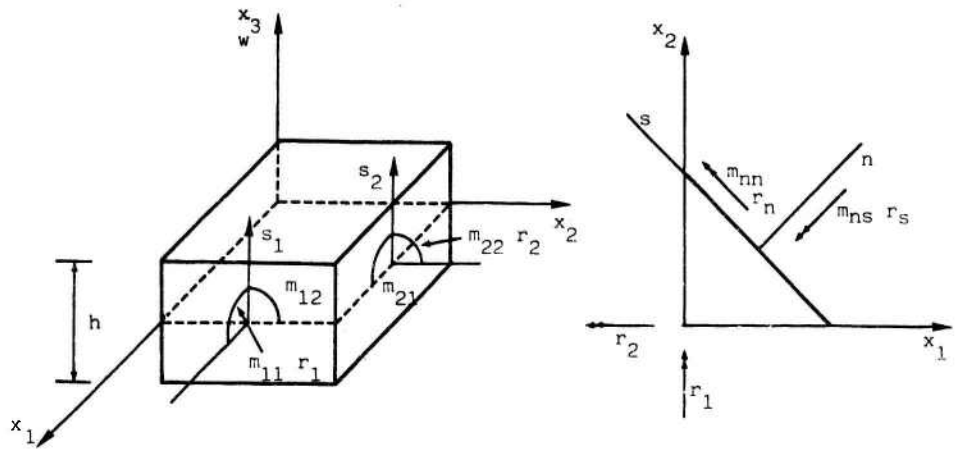

Figure 1. Notation

where A is the domain, that is, the area of the midsurface of plate, Γ_t is the boundary with known forces, Γ_u is the boundary with prescribed displacements and the superscript bar indicates the prescribed forces and displacements in the boundary. U* is the complementary energy per unit area and Ω is the potential of external forces. For a plate of thickness h subjected to lateral and axial loads we have

$$\Omega = -\int_A \left(pw + \frac{h}{2} \sigma_{ij} w_{,i} w_{,j}\right) dA \qquad (2)$$

where σ_{ij} are the stress components and p is the lateral distributed load.

In finite element analysis it is necessary to use a discretised form of the Reissner's functional. Assuming that there is continuity of variables between elements and that the boundary conditions are satisfied, then by integrating by parts the first term of equation (1) we obtain:

$$V_R = \sum_e \int_{A_e} [r_j (s_j - m_{ij,i}) + s_j w_{,j} - U^* + \Omega] dA \qquad (3)$$

where A_e is the area of element e. Assuming that

$$s_j = m_{ij,i} \tag{4}$$

then equation (3) becomes

$$V_R = \sum_e \int_{A_e} (s_j w_{,j} - U^* + \Omega)\, dA \tag{5}$$

In the theory of moderatly thick orthotropic plates, the complementary energy per unit area is

$$U^* = \frac{1}{2} n^T C n + \frac{1}{2} s^T D s \tag{6}$$

where

$$n^T = [m_{11} \quad m_{22} \quad m_{12}]$$

$$s^T = [s_1 \quad s_2]$$

$$C = \frac{12}{h^3} \begin{bmatrix} 1/E_1 & -\nu_{12}/E_2 & 0 \\ -\nu_{12}/E_2 & 1/E_1 & 0 \\ 0 & 0 & 1/G_{12} \end{bmatrix}$$

$$D = \frac{6}{5h} \begin{bmatrix} 1/G_{13} & 0 \\ 0 & 1/G_{23} \end{bmatrix}$$

where E_1, E_2, ν_{12}, G_{12}, G_{13} and G_{23} are the elastic properties of orthotropic plates.

Representing displacement and moment fields by

$$w = N q_e \tag{7}$$

$$n = L m_e \tag{8}$$

where q_e and m_e are the displacement and moment degrees of freedom of the element and N and L are the shape function matrices (see Appendix) the slope and shear force fields are expressed by

$$r = \begin{bmatrix} \partial w/\partial x_1 \\ \partial w/\partial x_2 \end{bmatrix} = \begin{bmatrix} \partial/\partial x_1 \, N \\ \partial/\partial x_2 \, N \end{bmatrix} q_e = N^* q_e \tag{9}$$

$$s = \begin{bmatrix} \partial/\partial x_1 & 0 & \partial/\partial x_2 \\ 0 & \partial/\partial x_2 & \partial/\partial x_1 \end{bmatrix} \quad n = L^* m_e \,. \tag{10}$$

Introducing equations (2) and (6) in the functional (5) we obtain, in material form

$$V_R = \sum_e \int_{A_e} [s^T r - \frac{1}{2} (n^T C n + s^T D s) - pw - \frac{h}{2} r^T Z r]\, dA \,. \tag{11}$$

were

$$Z = \begin{bmatrix} \sigma_{11} & \sigma_{12} \\ \sigma_{21} & \sigma_{22} \end{bmatrix}$$

Using equations (7) to (10) in the Reissner's functional (11) we obtain

$$V_R = \sum_e \left(-\frac{1}{2} m_e^T G_e m_e + m_e^T H_e q_e - q_e^T f_e - \frac{1}{2} q_e^T S_e q_e\right) \tag{12}$$

where

$G_e = \int_{A_e} (L^T C L + L^{*T} D L^*)\, dA$ Flexibility matrix

$H_e = \int_{A_e} L^{*T} N^*\, dA$ Flexibility/stiffness matrix

$S_e = \int_{A_e} (h N^{*T} Z N^*)\, dA$ Geometric matrix

$f_e = \int_{A_e} N^T p\, dA$ Element force vector

The kinetic energy of a plate in a discretized form is

$$T = \sum_e \frac{1}{2} \int_{A_e} \rho \left\{ h \left(\frac{\partial w}{\partial t}\right)^2 + \frac{h^3}{12} \left[\left(\frac{\partial^2 w}{\partial t\, \partial x_1}\right)^2 + \left(\frac{\partial^2 w}{\partial t\, \partial x_2}\right)^2 \right] \right\} dA \tag{13}$$

where ρ and t are the density and time, respectively. Applying equations (7) and (9) this equation can be written as

$$T = \sum_e \frac{1}{2} \dot{q}_e^T M_e \dot{q}_e \tag{14}$$

where

$M_e = \int_{A_e} \rho [\, h N^T N + (h^3/12) N^{*T} N^*]\, dA$ Mass matrix

and $\dot{q}_e$ is the velocity vector.

The stationary condition of the Reissner's functional (12) without lateral load p leads to an equation at element level that, after assembling in the usual way, gives the global equation for the stability of plates

$$\begin{bmatrix} -G & H \\ H^T & 0 \end{bmatrix} \begin{Bmatrix} m \\ q \end{Bmatrix} - \begin{bmatrix} 0 & 0 \\ 0 & \lambda S \end{bmatrix} \begin{Bmatrix} m \\ q \end{Bmatrix} = \begin{Bmatrix} 0 \\ 0 \end{Bmatrix} \tag{15}$$

where λ is the instability coefficient.

Applying Hamilton's principle and constructing the global equations, we obtain for the dynamic of plates without inplane loads the following equation

$$\begin{bmatrix} -G & H \\ H^T & 0 \end{bmatrix} \begin{Bmatrix} m \\ q \end{Bmatrix} + \begin{bmatrix} 0 & 0 \\ 0 & M \end{bmatrix} \begin{Bmatrix} m \\ \ddot{q} \end{Bmatrix} = \begin{Bmatrix} 0 \\ f \end{Bmatrix} \tag{16}$$

where $\ddot{q}$ is the acceleration vector. Considering that

$$m = G^{-1} H q \tag{17}$$

these equations can be transformed to

$$K q - \lambda S q = 0 \tag{18}$$

$$K\,q + M\,\ddot{q} = f \tag{19}$$

where

$$K = H^T\,G^{-1}\,H \tag{20}$$

is the stiffness matrix of the system. It should be noticed that the reduction of degrees of freedom (equations (15)-(16) to (18)-(19) is an exact operation and that the moments are calculated (equation (17)) by a matrix transformation of the displacements.

For free harmonic vibrations, equation (19) becomes

$$K\,q = \omega^2\,M\,q \tag{21}$$

where ω are the natural frequencies of the system.

3. SENSITIVITY ANALYSIS IN FREE VIBRATIONS AND STABILITY OF PLATE STRUCTURES

The equilibrium/compatibility equation for free and harmonic vibration (21) can be represented by the eigenproblem

$$K\,q - \mu\,M\,q = 0 \tag{22}$$

where μ represents the square of natural frequency of the plate. Considering an eigenvalue

$$\mu_k = \mu_k(q_k,\ b) = \omega_k^2 \tag{23}$$

where b is the vector of design variables and q_k is the eigenvector which is normalized

$$q_k^T\,M\,q_k = 1 \tag{24}$$

the sensitivity of the eigenvalue due to the variation of the design variable b_i is obtained deriving equation (22) and using equation (24)

$$\frac{d\mu_k}{db_i} = q_k^T\left(\frac{\partial K}{\partial b_i} - \mu_k\,\frac{\partial M}{\partial b_i}\right)q_k \tag{25}$$

Using equation (20) and the symmetry of G the sensitivity can be written as

$$\frac{d\mu_k}{db_i} = q_k^T\left(E^T\,\frac{\partial(-G)}{\partial b_i}\,E + 2\,E^T\,\frac{\partial H}{\partial b_i} - \mu_k\,\frac{\partial M}{\partial b_i}\right)q_k \tag{26}$$

where

$$E = G^{-1}\,H$$

In the case where the design variables are thickness of the plate, tne previous equation can be simplified

$$\frac{d\mu_k}{db_i} = q_k^T\left(E^T\,\frac{\partial(-G)}{\partial b_i}\,E - \mu_k\,\frac{\partial M}{\partial b_i}\right)q_k \tag{27}$$

Using equation (23) we have for free and harmonic vibration the following equation

$$\frac{d\omega_k}{db_i} = \frac{1}{2\omega_k}\,q_k^T\left(E^T\,\frac{\partial(-G)}{\partial b_i}\,E - \omega_k^2\,\frac{\partial M}{\partial b_i}\right)q_k \tag{28}$$

By analogy, sensitivity of the eigenvalue in the stability problem is

$$\frac{d\lambda}{db_i} = q_k^T \left(E^T \frac{\partial(-G)}{\partial b_i} E - \lambda \frac{\partial S}{\partial b_i}\right) q_k \qquad (29)$$

4. APPLICATIONS

The mixed formulation derived in this paper is applied to the design sensitivity analysis of natural frequencies and critical stresses of a simple supported plate due to thickness variation. The plate, represented by Fig.2, is discretized into nine mixed quadratic elements and the model has sixteen displacements and ninety-two moment degrees of freedom.

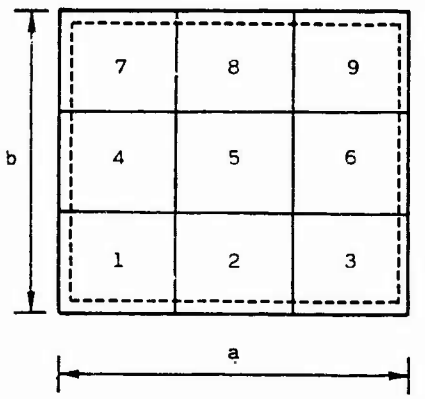

a = 1.20 m
b = 1.00 m
h = 0.01 m
$E_1=E_2=2.00\times10^{11}$ Nm^{-2}
$\nu_{12}= 0.30$
$G_{12}=G_{13}=G_{23}=8.077\times10^{10}$ Nm^{-2}
$\rho = 7.80\times10^{3}$ $Kg\ m^{-3}$

Figure 2. Simple supported rectangular plate with discretization used

First, we consider the thickness as the single design variable. For this case, the results for the sensitivity of the lowest six natural frequencies are presented in Table 1. The results for the sensitivity of the critical stress in x_1 direction are presented in Table 2. For comparison we present the exact values obtained by derivation of the analytical expression of the natural frequencies [5] and critical stress [6] of a simple supported rectangular plate. Tables 1 and 2 also present the errors of the mixed model for the natural frequencies, critical stress and their sensitivity due to thickness change.

As a second example, we consider the thickness of each element as a design variable. In this case, there are nine design variables that can be reduce to four considering the symmetry. The results for the sensitivity of the first natural frequency due to the element thickness are presented in Table 3. For comparison, the same table has the results obtained by Rayleigh-Ritz and finite difference solutions. Table 4 shows the results for the sensitivity of the critical stress in X-direction due to the element thickness variation

Table 1 - Natural frequencies and its sensitivities due to the thickness variation of a simple supported rectangular plate: comparison of the mixed model with analytical results.

Mode shape - half waves in x_1 and x_2 directions.	Natural frequency (rad/seg)		Sensitivity to thickness	
	Exact values	Mixed model (% Error)	Exact values	Mixed model (% Error)
1 - 1	256.26	258.83 (1.00%)	25626.16	25866.76 (0.94%)
2 - 1	571.34	587.36 (2.80%)	57133.72	58649.53 (2.65%)
1 - 2	709.97	727.13 (2.42%)	70997.05	72588.11 (2.24%)
2 - 2	1025.05	1086.24 (5.97%)	102504.62	108320.04 (5.67%)
3 - 1	1096.46	1135.47 (3.56%)	109646.34	113215.73 (3.26%)
1 - 3	1466.15	1495.54 (2.00%)	146615.22	149024.99 (1.64%)

Table 2 - Critical stress in x_1 direction and its sensitivity due to tickness variation of a simple supported rectangular plate: comparison of the mixed model with analytical results.

Critical stress (x E7 Nm^{-2})		Sensitivity to thickness (x E10)	
Exact values	Mixed model (% Error)	Exact values	Mixed model (% Error)
7.473	7.611 (1.84%)	1.496	1.522 (1.74%)

and, for comparison, it contains a finite difference solution.

The finite difference are obtained by finite element analysis of two slightly perturbed designs of the structure. The difference in the value of the natural frequency or critical stress divided by the total design perturbation Δh is the approximate derivative. Tables 3 and 4 also show the error of the proposed model relatively to the alternative results.

The results obtained in this paper show that sensitivity analysis of the stability and dynamical behaviour can be accurately and efficiently calculated with the mixed element model developed. The errors in natural frequencies or critical stresses and in the respective sensitivities due to the thickness

Table 3 - Sensitivity of the first three natural frequency due to the thickness variation of each element of a simple supported rectangular plate discretized with nine elements: comparison of the mixed model with Rayleigh-Ritz and finite difference results.

Design variable (thickness of element...)	Natural frequency number...	Sensitivity to thickness		
		Mixed model	Rayleigh-Ritz (% Error)	Finite Difference ($\Delta h = \pm 0.01xh$) (% Error)
1	1	3432.2	3371.5 (1.80%)	3432.4 (0.00%)
	2	5912.8	-	5913.4 (0.01%)
	3	6741.5	-	6742.0 (0.00%)
2	1	1860.0	1855.0 (0.27%)	1860.3 (0.01%)
	2	6166.5	-	6167.0 (0.00%)
	3	13899.6	-	13899.0 (0.00%)
4	1	1845.1	1855.0 (0.54%)	1845.3 (0.01%)
	2	9070.4	-	9070.3 (0.00%)
	3	5776.9	-	5777.8 (0.02%)
5	1	4727.6	4720.0 (0.16%)	4727.5 (0.00%)
	2	4524.6	-	4525.8 (0.03%)
	3	6296	-	6270.9 (0.03%)

Table 4 - Sensitivity of the critical stress due to the tickness variation of each element of a simple supported rectangular plate discretized with nine elements: comparison of the mixed model with finite difference results.

Design variable: (thickness of element ...)	Sensitivity to thickness	
	Finite Difference ($\Delta h = \pm 0.01xh$)	Mixed model (% Error)
1	.16076	.16074 (0.01%)
2	.19171	.19169 (0.01%)
4	-.02135	-.02140 (0.26%)
5	.54130	.53798 (0.62%)

are of the same order shows that an adequate discretization for critical stresses or natural frequencies is an acceptable model for their sensitivities.

REFERENCES

1. C.A. MOTA SOARES (editor) 1987 Computer Aided Optimal Design: Structural and Mechanical Systems, Springer-Verlag.

2. C.A. MOTA SOARES and R. PEREIRA LEAL, 1987 Engineering Optimization 11, 227-237 Mixed elements in the sensitivity analysis of structures.

3. C.A. MOTA SOARES, L.M. TRABUCHO CAMPOS and A.F. VIEGAS GAGO 1980 Recent Advances in Structural Dynamics (Editor M. Petyt). Institute of Sound and Vibration Research. Dynamic analysis of plates by mixed elements.

4. J. CONNOR 1970 Finite Element Techniques in Structural Mechanics (editor H. Tottenham and C. Brebbia). Southampton: Stress Analysis Publishers. Mixed models for plates.

5. A.W. LEISSA 1969 Vibration of plastes NASA SP-160.

6. P.S. BULSON 1970 The stability of Flat Plates London: Chato & Windus.

ACKNOWLEDGEMENT

This research has been supported by the Advisory Group for Research and Development (Project AGARD-SMP-31, JNICT (Junta Nacional de Investigação Científica e Tecnologia) and INIC (Instituto Nacional de Investigação Científica).

APPENDIX ISOPARAMETRIC MIXED QUADRATIC ELEMENT FOR PLATES

The mixed element used is an isoparametric quadratic element based on moderatly thich ortotropic plate theory. The element has 8 nodes and 32 degrees of freedom, and it is represented in Fig. 3. The nodal degrees of freedom are the transverse displacement and the three moments.

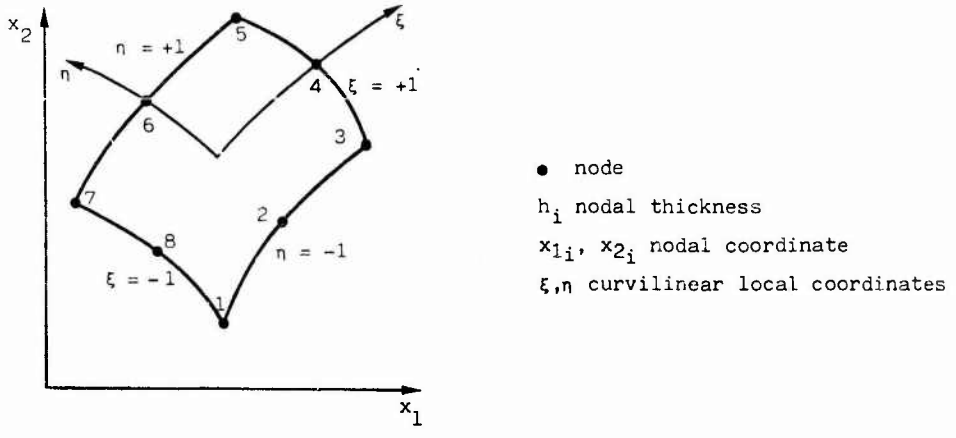

Figure 3. Isoparametric quadratic element.

The geometric, displacement and moment fields for mixed elements are represented by

$$\begin{aligned} x &= N\, x_e \\ h &= N\, h_e \\ w &= N\, q_e \\ n &= L\, m_e \end{aligned} \tag{30}$$

where x_e, h_e, q_e and m_e are the coordinates, thickness, displacement degree of freedom and moment degress of freedom of the element and N and L are the shape function matrices.

$$\begin{aligned} N &= [N_1\ N_2\ N_3\ \ldots\ N_8] \\ L &= [L_1\ L_2\ L_3\ \ldots\ L_8] \end{aligned} \tag{31}$$

with

$$L_i = \begin{bmatrix} N_i & 0 & 0 \\ 0 & N_i & 0 \\ 0 & 0 & N_i \end{bmatrix} \tag{32}$$

The shape functions can be represented by:

$$N_i = \frac{1}{4}\,(1 + \xi_o)\,(1 + \eta_o)\,(\xi_o + \eta_o - 1) \tag{33}$$

for the nodes 1, 3, 5 and 7,

$$N_i = \frac{1}{2}\,(1 - \xi^2)\,(1 + \eta_o) \tag{34}$$

for the nodes 4 and 8,

$$N_i = \frac{1}{2}\,(1 + \xi_o)\,(1 - \eta^2) \tag{35}$$

for the nodes 2 and 6.

In these expressions we have

$$\begin{aligned} \xi_o &= \xi_i \xi \\ \eta_o &= \eta_i \eta \end{aligned} \tag{36}$$

where ξ_i and η_i are the local coordinates of the node i.

The element matrices are calculated substituting equations (30-36) into equations (12) and (13). All the matrices are integrated numerically using 3x3 Gaussian mesh.

A NEW FINITE ELEMENT FOR THE DYNAMICAL STUDY OF PRETWISTED BEAMS

POTIRON Alain

Département de Génie Mécanique
INSTITUT NATIONAL DES SCIENCES APPLIQUEES
Avenue de Rangueil
31077 TOULOUSE CEDEX
FRANCE

ABSTRACT

The method of integrated displacement parameters is applied to the study of pretwisted straight beams. With the use of curvilinear coordinates, the formulation leads to a basic theory inlighting the couplings between torsion, longitudinal extension and warping. A new finite element of pretwisted beam is deduced allowing for the numerical computation of eigenfrequencies and modes.

1. INTRODUCTION

As pointed out by LEISSA and JACOB [1] , the vibrations of naturally pretwisted beams have received considerable attention because this one dimensional formulation represents a first approximation of turbomachinery blade analysis.

The static case of Torsion and Extension of pretwisted beams has been widely investigated by means of the "helical fibers" concept or in recent works by means of curvilinear coordinates formulations. In [2] ROSEN shows that the initial twist increases the torsional stiffness of such beams subjected to uniform torsion and warping. Considering the influence of axial loading on the torsion of slender beams, HODGES [3] concludes that they untwist. A more general linear theory including non uniform warping has been developped by KRENK in [4] . It leads to the same conclusions especially in the study of the coupling between torsion and extension.

In the dynamical case, the three dimensional analysis [1] of vibrations of twisted parallelepipeds shows clearly that natural frequencies and modes are split in two sets which are uncoupled from each other ; the flapwise, edgewise and symmetric chordwise bendings are coupled in one class, whereas the torsion, the longitudinal extension and the antisymmetric chordwise bending are coupled together forming another class . Thus, the aim of the present work is to set up a simple preliminary tool for the prediction of the coupled Torsion-Extension natural oscillations of pretwisted straight beams, independantly from the bending vibrations.

It has been shown [5] that an accurate formulation of the torsional vibrations of beams should involve the non uniformity of torsion and warping of the cross sections. This is done here through a new warping parmeter Ⓗ defined by means of the SAINT VENANT warping function of the associated prismatic beam with the same cross section shape. The leading

features of the paper are obtained through the use of integral parameters defined over the cross section, associated with the corresponding generalized beam forces. In the general case seven parameters are defined for the study of beams vibrations but here, due to the uncoupling with bendings, only three are necessary if the secondary effects of warping are neglected. The numerical investigations will be conducted further by means of a new beam finite element with three degrees of freedom at each node.

2. BASIC THEORY

The beam under consideration is of constant doubly symmetric cross-section, the center G of which lies on the X_1° axis. A schematic of the coordinate systems is shown in Fig 1. The fixed reference frame is $OX_1^\circ X_2^\circ X_3^\circ$. Y and Z with unit vectors $\vec{Y}$, $\vec{Z}$, are the principal axis of the cross section. The beam is uniformly twisted along the center line the rate of twist χ being a constant. We denote by x the longitudinal coordinate describing the position of G, and by $\mathcal{X}(x)$ the pretwist angle. Thus we have

$$\mathcal{X}'(x) = \chi \tag{1}$$

where the prime represents the derivative with respect to x.

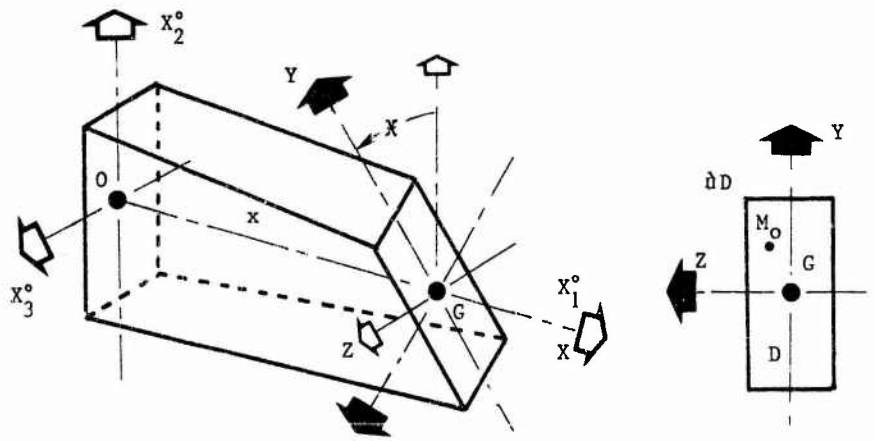

Fig. 1 - Pretwisted Beam

The cross section occupies the domain D with boundary ∂D and the position vectors of an arbitrary point in D before and after deformation are denoted by $\vec{OM}o$ and $\vec{OM}$ with

$$\vec{GM} = y\,\vec{Y} + z\,\vec{Z} \tag{2}$$

The displacement vector $\vec{U}_{Mo}$ of the point initially at Mo is deduced in the form of

$$\vec{U}_{Mo} = \vec{OM} - \vec{OMo} \tag{3}$$

In the undeformed state, at each point Mo a local cartesian frame with units vectors $\vec{J}_i$ is associated. It is deduced by translation from GXYZ. The displacement vector $\vec{U}_{Mo}$ is then written in its component forms

$$\vec{U}_{Mo} = u_i \vec{J}_i \qquad \text{or altenatively } \vec{U}_{Mo} = u_x \vec{X} + u_y \vec{Y} + u_z \vec{Z} \tag{4}$$

because the unit vectors $\vec{J}_i$ and $\vec{X}\,\vec{Y}\,\vec{Z}$ are identical.

Let us now define the tangential vectors $\vec{t}_.$ by

$$d\vec{Mo} = \vec{t}_x\, dx + \vec{t}_y\, dy + \vec{t}_z\, dz \tag{5}$$

where x y z form a set of non orthogonal curvilinear coordinates. By use of the FRENET differential formulas and recalling that in the local cartesian system we write $d\vec{Mo}$

$$d\vec{Mo} = \vec{J}_i\, d\,Xi \tag{6}$$

we are led to the following expression for $d\vec{U}_{Mo}$

$$d\vec{U}_{Mo} = \begin{vmatrix} u'_1 + X\,D(u_1) & u_{1,y} & u_{1,z} \\ u'_2 + X\,D(u_2) & u_{2,y} & u_{2,z} \\ u'_3 + X\,D(u_3) & u_{3,y} & u_{3,z} \end{vmatrix} \times \begin{vmatrix} dX_1 \\ dX_2 \\ dX_3 \end{vmatrix} \tag{7}$$

where D is the differential operator $D = z()_{,y} - y()_{,z}$ and $()_{,y}$ $()_{,z}$ are the partial derivatives with respect to y and z.
Comparison of the infinitesimal elements of length $d\mathcal{S}_o$ and $d\mathcal{S}$ before and after deformation

$$d\mathcal{S}_o^2 = \vec{OMo} \cdot \vec{OMo} \qquad d\mathcal{S}^2 = \vec{OM} \cdot \vec{OM} \tag{8}$$

leads to Green's strain tensor e_{ij} in the Lagrangian description

$$d\mathcal{S}^2 - d\mathcal{S}_o^2 = 2\, e_{ij}\, dX_i\, dX_j \tag{9}$$

The next step in the formulation is the definition of the displacement parameters.

3. DISPLACEMENT PARAMETERS

In order to set up a one dimensional theory, the displacement parameters are defined by means of weighted integration of $\vec{U}_{Mo}$ over the cross section. Thus, we obtain in the GXYZ system, the generalized displacement vector $\vec{V}$ of the cross section

$$\vec{V}(x,t) = \frac{1}{S}\int_D \vec{U}_{Mo}\, dS \tag{10}$$

and the generalized rotation vector $\vec{\theta}$

$$\vec{\theta}(x,t) = \frac{1}{I_\alpha} \int_D G \vec{Mo} \times \vec{U}_{Mo} \, dS \qquad (11)$$

The I_α are the polar and transverse quadratic moments of the cross section and S the area of the cross section. In GXYZ the components of $\vec{V}$ and $\vec{\theta}$ are denoted by (u, v, w) and $(\theta_x , \theta_y , \theta_z)$.

In order to provide a good beam approximate theory, the non uniform torsion and the non uniform warping should be taken into account. This will be done by introducing a new displacement parameter defined through the SAINT-VENANT warping function $\emptyset$ (y,z) deduced from the classical homogeneous torsion problem of the uniform beam with the same cross section shape.

Thus, the warping parameter Ⓗ is defined by the weighted integral

$$Ⓗ(x,t) = \frac{1}{I\emptyset} \int_D \emptyset(y,z) \cdot \vec{U}_{Mo} \cdot \vec{X} \, dS \qquad (12)$$

$I_\emptyset = \int_D \emptyset^2 \, dS$ is the quadratic warping moment of the cross section.

From the aforementioned definitions there follows that the displacement field can be written in the form of the "functional developement" :

$$\vec{U}_{Mo} = \begin{cases} u_x = u - y\,\theta_z + z\,\theta_y + \emptyset\,Ⓗ + \pi_x \\ u_y = v - z\,\theta_x + \pi_y \\ u_z = w + y\,\theta_x + \pi_z \end{cases} \qquad (13)$$

4. TECHNICAL FORMULATION

The technical beam formulation is done through two hypotheses.

H1 - The lateral surface of the beam being free of any forces, we suppose that the stresses σ_{22}, σ_{33} and σ_{23} are negligible compared to σ_{11}, σ_{12} and σ_{13}. Therefore $\sigma_{22} = \sigma_{33} = \sigma_{23} = 0$

H2 - The complementary warping vector $\vec{\pi}$ is neglected

It has been shown in [6] that taking $\vec{\pi}$ into account leads to couplings between shearing forces and torsion in the case of a uniform straight beam ; so it can be expected that in the case of a pretwisted beam bending, torsion and longitudinal extension should be coupled. In order to avoid too complicated a study, we shall suppose that $\vec{\pi} = 0$. In consequence, the cross section remains undeformed in its own plane.

Making use of H1 and H2 we deduce from (4), (9) and (13) the following

expressions for infinitesimal strains ε_{ij} in the cartesian system.

$$\left|\begin{array}{l} \varepsilon_{xx} = u' + z(\theta'_y - \chi\theta_z) - y(\theta'_z + \chi\theta_y) - \chi\,\textcircled{H}\,\mathfrak{D}(\emptyset) + \emptyset\,\textcircled{H}' \\ 2\,\varepsilon_{xy} = v' - \theta_z - \chi w - z\,\theta'_x + \textcircled{H}\emptyset_{,y} \\ 2\,\varepsilon_{xz} = w' + \theta_y + \chi v + y\,\theta'_x + \textcircled{H}\emptyset_{,z} \\ \varepsilon_{yy} = \varepsilon_{zz} = \varepsilon_{yz} = 0 \end{array}\right. \qquad (14)$$

with the subscripts 1, 2, 3 replaced by a "beam notation" x, y, z.

It is now necessary to turn to the internal forces in the beam acting through each cross section. They are defined in the same way as the displacement parameters by means of generalized weighted integrals of stresses over the domain D of the cross section. Then the three generalized forces of interest are the axial force N, the twisting moment M and the bimoment B

$$N(x,t) = \int_D \sigma_{xx}\, dS \;;\; M(x,t) = \int_D (y\sigma_{xz} - z\sigma_{xy})dS \;;\; B = \int_D \emptyset\,\sigma_{xx}\, dS \qquad (15)$$

For an isotropic elastic body with YOUNG's modulus E and shear modulus G, making use of the stress strains relations in (15) leads to the following force - deformation relations

$$\left|\begin{array}{l} N = ES\,u' + E\,\chi\,(I_x - J)\;\textcircled{H} \\ (M - GJ\theta'_x) = G(I_x - J)(\theta'_x - \textcircled{H}) \\ B = E\,I_\emptyset\;\textcircled{H}' \end{array}\right. \qquad (16)$$

J is the SAINT VENANT constant of uniform torsion and I_x the polar moment of inertia of the cross section. In view of (16) it is clear that the three beam forces are coupled through the warping parameter $\textcircled{H}$ and the rate of twist χ . As pointed out by LEISSA and JACOB [1] , the other bending and shear forces are uncoupled from torsion, warping and longitudinal extension. It is seen that the second relation (16) connects the non-uniform torsion moment

$$M_{nuf} = (M - GJ\theta'_x)$$

to the rate of twist θ'_x not necessarily linked with $\textcircled{H}$ as it would be in the homogeneous torsion of the beam.

5. EQUATIONS OF MOTION

They are derived by use of the principle of virtual work with a virtual displacement field analogous to (13) in which $\vec{\pi}$ is set to zero.

Among the seven equations of motion which are deduced, we shall retain a set of three because they are coupled together and uncoupled from the bendings and shear forces set. Thus, the dynamical behaviour of pretwisted beams is governed by

$$\left|\begin{array}{l} N' = \mu S \ddot{u} \\ M' = \mu I_x \ddot{\theta}_x \\ B' - x \frac{I_x - J}{S} N + (M - GJ\theta_x') - E x^2 K_2 H = \mu I_\phi \ddot{\textcircled{H}} \end{array}\right. \qquad (17)$$

The last equation is the dynamical equation of bimoment and it traduces in term of beam forces the coupling between the bimoment B, the non uniform torsion moment M_{nuf} and the axial force N. This equation can be compared to equation (24), of [7] and it can be seen that for non rotating beams (17.c) and (24), are strictly identical if we suppose that the kinematical constraint $\theta_x' = \textcircled{H}$ links the two parameters. In (17.b) a coefficient K_2 appears ; it depends on the cross section shape and is calculated by means of ϕ (y,z) as follows :

$$K_2 = J_2 - \frac{(I_x - J)^2}{S}$$

$$\text{and } J_2 = \int_D \mathfrak{D}(\phi)^2 \, dS \qquad (18)$$

In the case of a rectangular section h x b , ϕ (y,z) is known and J_2 can be calculated. For a thin walled rectangular section beam we have the following approximations

$$S = b \times h \; ; \; I_x \sim \frac{bh^3}{12} \; ; \; J \sim \frac{hb^3}{12} \; ; \; J_2 \sim \frac{bh^5}{80} \; ; \; K_2 \sim \frac{bh^5}{180} \qquad (19)$$

The Fig. 2 shows the evolution of the ratio J_{2TW}/J_{2ex} of the two values of J_2 evaluated respectively by (19) and by the exact function $\phi(y,z)$.

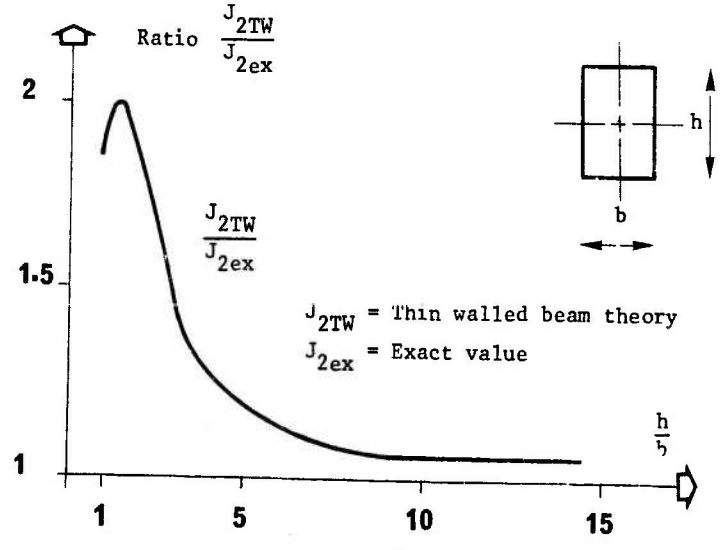

Fig. 2 - Ratio $\frac{J_{2TW}}{J_{2ex}}$ for a rectangular section

In view of Fig. 2 we can conclude that J_{2TW} is always overestimated and when h/b = 5 the error is about 20 % ; this value of h/b seems to be a limit for a correct evaluation of K_2 which is the leading coefficient in the prediction of the Torsion-Extension coupling. Having developed a beam theory for the analysis of pretwisted straight beams described by three displacement parameters, let us now turn to the Finite Element Formulation (F.E.F.).

6. FINITE ELEMENT FORMULATION (F.E.F.)

The two node finite element of the pretwisted beam is depicted Fig. 3. At each end point G_1 and G_2 the nodal displacements vectors $q_i (i=1,2)$ are defined

$$q_i(t) = \left| u_i(t) \quad \theta_{xi}(t) \quad \textcircled{H}_i(t) \right|^T$$

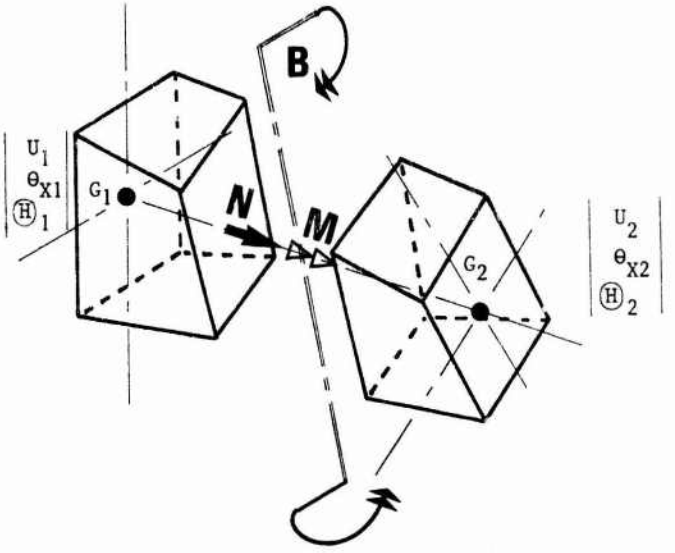

Fig. 3 - Finite Element of Pretwisted Beam

An approximate displacement field $U_e(x,t)$ is deduced in the form of

$$U_e(x,t) = A_e(x) \cdot q(t) \tag{20}$$

with $$q(t) = \left| q_1(t) \quad q_2(t) \right|^T$$

The interpolation matrix $A_e(x)$ is obtained by the resolution of the static equilibrium system deduced from (17), associated with the relations (16). The static and kinematic admissibility of the displacement field $U_e(x,t)$ thus derived insures the improvement of the formulation and consequently a large finite element discretization will not be necessary. The

internal beam forces are the aforementioned axial force N, Torsion moment M and generalized bimoment B.

The setting up of the F.E.F. involves previous formulations of technical expressions for the potential and kinetic energies and this will be examined now.

If we consider an infinitesimal beam length dx and accounting for the technical hypotheses H1 and H2, the elementary strain energy $W'(x,t)$ reduces to the integral over the cross section

$$W'(x,t) = \frac{1}{2}\int_D (\sigma_{xx}\, \varepsilon_{xx} + 2\,\sigma_{xy}\, \varepsilon_{xy} + 2\,\sigma_{xz}\, \varepsilon_{xz})dS \qquad (21)$$

The constitutive stress - strains relations holding for an isotropic homogeneous material together with the expressions (14) defining the strains, lead to the following form of W'

$$W'(x,t) = \frac{1}{2} E\left[Su'^2 + 2X(I_x - J)\,\textcircled{H}\,u' + I_\varnothing\,\textcircled{H}'^2 + x^2\,\textcircled{H}^2\,J_2\right] + \ldots$$
$$\ldots + \frac{1}{2} G\left[I_x\theta_x'^2 - 2(I_x - J)\theta_x'\,\textcircled{H} + (I_x - J)\,\textcircled{H}^2\right] \qquad (22)$$

The integration of (22) over the whole beam element of length 1 and the use of (20) allow for the derivation of the element strain energy $W_e(t)$ by means of the modal vector $q_e(t)$

$$W_e(t) = \frac{1}{2}\, q_e^T\, K_e\, q_e \qquad (23)$$

where K_e is the element stiffness matrix, terms of which are detailed in Appendix 1.

The derivation of the element mass matrix M_e is deduced from the kinetic energy T_e of the element. The elementary kinetic energy $T'(x,t)$ defined by

$$T'(x,t) = \frac{1}{2}\int_D \mu\, \dot{U}_{Mo} \cdot \dot{U}_{Mo}\, dS \qquad (24)$$

is evaluated by means of (13) in the form of :

$$T'(x,t) = \frac{1}{2}\,\mu\left[S\,\dot{u}^2 + I_x\,\dot{\theta}_x^2 + I_\varnothing\,\textcircled{H}^2\right] \qquad (25)$$

where the dot denotes the derivative with respect to time and μ is the mass per unit volume.

Performing the integration of (25) over the whole element by means of (20) leads to the element kinetic energy $T_e(t)$

$$T_e(t) = \frac{1}{2}\, \dot{q}_e^T\, M_e^c\, \dot{q}_e \qquad (26)$$

where M_e^c is the so called consistent mass matrix of the element ; due to its complexity the terms of M_e^c are not detailed herein but can be found in [9] .

However, in finite element analysis, the lumped mass matrix can give good results in the estimation of natural frequencies of beams, and for that reason we have defined the following diagonal matrix M_e^d

$$M_e^d = \mathrm{diag}\left[\ \tfrac{1}{2}S1\quad \tfrac{1}{2}I_x 1\quad \tfrac{1}{2}I_\varnothing 1\quad \tfrac{1}{2}S1\quad \tfrac{1}{2}I_x 1\quad \tfrac{1}{2}I_\varnothing 1\ \right] \qquad (27)$$

If the terms of M_e^d are obviously independant of the rate of pretwist χ , M_e^c consistently accounts for and leads to a full symmetric matrix. In order to evaluate the consistency of the theory and accuracy of the F.E.F., several pretwisted beams have been experimented and the numerical eigenfrequencies computed were compared to those of the experiments.

7. CANTILEVER BEAM

For the experimental purpose a pretwisted slender beam of thick rectangular cross section was machined and welded at one end on a thick flange. The numerical investigations were conducted by a discretization of the beam into twenty elements allowing for an accurate computation of the natural frequencies. The relative error between calculated and experimentally determined eigenfrequencies is shown Fig. 4

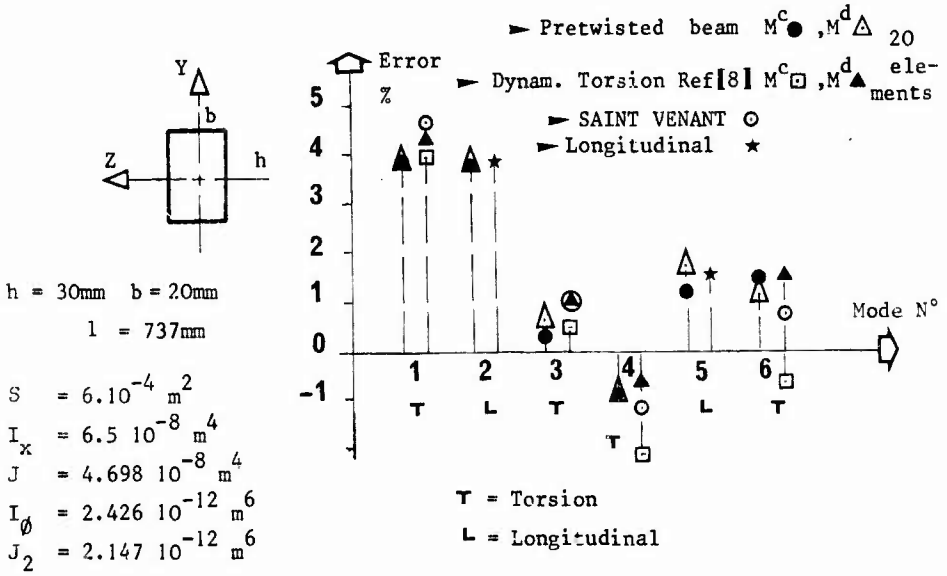

Fig. 4 - Cantilever Beam (F.E.F.)

The influence of pretwist on computed natural torsional oscillations of the beam has been evaluated through the comparison of the aforementioned results and those deduced from the SAINT VENANT theory of uniform torsion and from a F.E.F. of dynamical torsion of straight uniform beams [8] .

The error values resulting from each of the three approaches are plotted Fig. 4 where it is seen that they are of the same order of magnitude. Thus, it can be concluded that due to the thick cross section and the slenderness of the beam, the moderate rate of pretwist provides no change in the prediction of torsional frequencies. The relative bad results obtained for the first two modes are certainly a consequence of an imperfect encastre root fixing. In the other hand it can be shown, in view of (12) and

(13), that the greatest influence of pretwist is obtained for thin cross sections because the coefficients (I_x-J). χ and K_2. χ^2 which are the leading terms of the couplings between Torsion, Extension and Warping have the largest relative values.

So a thin rectangular steel strip was tested in the case of free-free ends conditions.

8. FREE-FREE RECTANGULAR THIN WALLED BEAM

The beam selected for this investigation was a flat strip of steel initially pretwisted on a lathe. A linear rate χ = 13,65 rad/m was produced over the central part (0.202 m) of a beam that was originally 0.4 m long. As shown in Fig. 5 a rather good accuracy of the predicted eigenfrequencies is obtained for the five torsional mode. In this study the beam is discretized into ten elements. Any information about the values of the natural frequencies can be deduced either from the SAINT VENANT theory or from F.E.F. of dynamical torsion [8] .

The lumped mass matrix leads to greater errors than those obtained by use of the consistent mass matrix. The mean values between the two results seem to be good approximations of the eigenfrequencies.

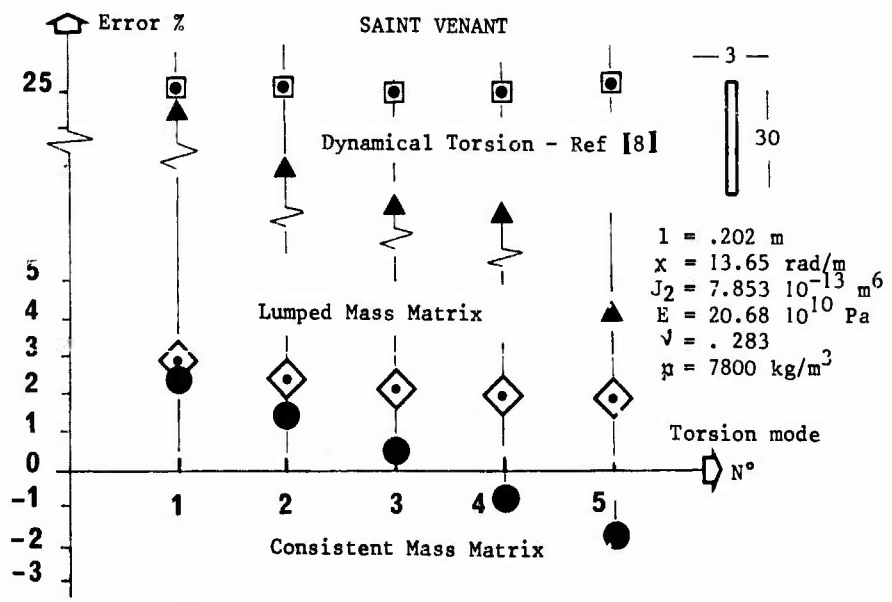

Fig. 5 - Pretwisted Thin Walled beam (F.E.F)

9. CONCLUSION

The present study of the dynamical behaviour of turbomachinery blades which can be modeled by pretwisted beams, shows the necessity to account for the non uniformity of torsion and warping of the cross section. This was achieved here by the definition of weighted displacement parameters including a warping parameter varying independantly of the twist angle. The coupling between torsion, longitudinal extension, warping and uncoupling with bending and shear forces allow for the statement of a theory of pretwisted beams by means of three displacement parameters and three generalized associated beam forces.

The study deduced from the 3-dimensional elasticity using curvilinear coordinates leads to the definition of new cross section coefficients the influence of which is shown to be essential for the accurate prediction of the dynamical behaviour of the beams. The new finite element defined here allows for the computation of eigenfrequencies of pretwisted beams with a straight center line. The numerical results obtained by use of the F.E.F. show the accuracy of the present formulation.

Obviously, in the case of beams for which the center line is not a straight line, all the beam forces are geometrically and structurally coupled and a new approach must be developped for which the use of integral parameters seems to be well suited.

REFERENCES

1. A. LEISSA and K.I. JACOB 1986 Journal of Applied Mechanics 53, 614-618. Three-dimensional vibrations of twisted cantilevered parallelepipeds.

2. A. ROSEN 1980 Journal of Applied Mechanics 47, 389-392 The effect of initial twist on the torsional rigidity of beams - Another point of view.

3. D.H. HODGES 1980 Journal of Applied Mechanics 47 , 393-397. Torsion of pretwisted beams due to axial loading.

4. S. KRENK 1983 Journal of Applied Mechanics 50, 137-142. A linear theory for pretwisted elastic beams.

5. D. GAY and R. BOUDET 1980 Journal of Mechanical Design 102, 627-632 A technical theory of dynamical torsion for beams of any cross-section shapes.

6. A. POTIRON - D. GAY and C. CZEKAJSKI 1984 University of Southampton. ISVR. Proceedings of the Second Internation Conference on Recent Advances in Structural Dynamics 1, 109-117 A new beam finite element with seven degrees of freedom at each node for the study of coupled bending-torsion vibrations

7. K.R.V. KAZA and R.E. KIELB 1984 New-Orleans Winter annual Meeting of the ASME paper 84 - WA/APM 41 Effects of warping and pretwist on torsional vibration of rotating beams.

8. A. POTIRON and D. GAY 1983 Journal of vibrations, Ac., Str., Rel. in Design 105, 476-483 On a finite element formulation of dynamical torsion of beams including warping inertia and shear deformation due to nonuniform warping.

9. A. MANGIAPAN 1986 INSA Technical Report Mémoire de D.E.A. - INSA Département de Mécanique, Avenue de Rangueil 31077 TOULOUSE CEDEX Matrice de masse cohérente pour l'étude des poutres vrillées.

APPENDIX 1

STIFFNESS MATRIX K_e FOR A PRETWISTED BEAM

We denote by a, $\tilde{z}$, ν the coefficients

$$a = \frac{I_x}{I_x - J} \cdot \frac{1}{1 + \frac{E}{G}\frac{I_x}{I_x - J} x^2 K_2} \quad ; \quad \tilde{z} = l\sqrt{\frac{G}{E}\frac{J}{a I_\phi}} \quad ; \quad \nu = J_2 \frac{S}{(I_x - J)^2}$$

and by Δ the following expression :

$$\Delta = \frac{G}{\tilde{z}E} \cdot \frac{I_x - J}{I_x}\left[2(\cosh\tilde{z} - 1) - \frac{I_x}{I_x - J}\tilde{z}\sinh\tilde{z}\right] + x^2 \frac{I_x - J}{\tilde{z}S} l\left[2(\cosh\tilde{z} - 1) - \nu\tilde{z}\sinh\tilde{z}\right]$$

Thus, the terms K_{ij} of K_e are found in the form of :

$$\Delta K_{11} = \frac{GS}{\tilde{z}}\left[2\frac{I_x - J}{I_x}(\cosh\tilde{z} - 1) - \tilde{z}(1 + \nu)\sinh\tilde{z}\right]$$

$$\Delta K_{12} = G\frac{(I_x - J)}{\tilde{z}} x\left[2(\cosh\tilde{z} - 1) - \tilde{z}\sinh\tilde{z}\right]$$

$$\Delta K_{13} = \frac{\tilde{z}}{l} x\, EI_\phi\,(\cosh\tilde{z} - 1)$$

$$K_{14} = -K_{11} \quad ; \quad K_{15} = -K_{12} \quad ; \quad K_{16} = K_{13}$$

$$\Delta K_{22} = -G\frac{I_x - J}{\tilde{z}}\left[\frac{G}{E}\frac{I_x}{I_x - J}\tilde{z}\sinh\tilde{z} - x^2\frac{I_x}{J}\,2(\cosh\tilde{z} - 1) - \nu\,\tilde{z}\sinh\tilde{z}\right]$$

$$\Delta K_{23} = -G\frac{\tilde{z}}{l} I_\phi(\cosh\tilde{z} - 1) \quad ; \quad K_{24} = -K_{12} \quad ; \quad K_{25} = -K_{22} \quad ; \quad K_{26} = K_{23}$$

$$\Delta K_{33} = E\, I_\phi\left[x^2\frac{I_x - J}{S}(\sinh\tilde{z} - \nu\tilde{z}\cosh\tilde{z}) + \frac{G}{E}\frac{I_x - J}{I_x}(\sinh\tilde{z} - \frac{I_x}{I_x - J}\tilde{z}\cosh\tilde{z})\right]$$

$$K_{34} = -K_{13} \quad ; \quad K_{35} = -K_{23}$$

$$\Delta K_{36} = -E\, I_\phi\left[x^2\frac{I_x - J}{S}(\sinh\tilde{z} - \nu\tilde{z}) + \frac{G}{E}\frac{I_x - J}{I_x}(\sinh\tilde{z} - \frac{I_x}{I_x - J}\tilde{z})\right]$$

$$K_{44} = K_{11} \quad ; \quad K_{45} = K_{12} \quad . \quad K_{46} = -K_{13} \quad ; \quad K_{55} = K_{22}$$

$$K_{56} = -K_{23} \quad ; \quad K_{66} = K_{33}$$

A COMPLEX VIBRATION ANALYSIS OF A THREE SHAFT GEARED COMPRESSOR SET MOUNTED ON A STEEL ENTABLATURE

S.S. Gupta

GEC Engineering Research Centre
Whetstone, Leicester, UK

SYNOPSIS :

Analytical and Computer Techniques developed for the prediction of the whirling response of multi-flexible-shafts in a response-prone entablature have been applied to the prediction of the dynamic unbalance vibration level for a three-shaft, geared compressor set mounted on steel foundations which have natural frequencies well within the machine's running range. Such foundations are generally referred to as being 'low-tuned' and have raised some concern as to the validity of representing machines as flexible shafts supported to earth. It was necessary to include in this analysis the hydrodynamic bearing behaviour, gyroscopic couples, shaft and structural damping and other standard features relevant to whirling analysis. The shafts which had axisymmetric rigid discs can be assumed to be torsionally infinitely stiff and interconnected at constant drive speed. In the low-tuned system, the bearing was considered as being built-in, and forming an integral part of a multi-degree-of-freedom vibration system as well as being the means of location of the rotating vibration system. The vibration of points on the shaft must affect, via the bearings, the motion of points over the foundation. Whilst there are many papers and reports related to the whirling response and stability of shafts, none deal with the general case of a rotating shaft mounted via three or more flexible bearings in a heavy, flexible structure. The purpose of the paper is to establish a mathematical approach capable of dealing with the above dynamic system, without the use of over simplifying assumptions, and without damaging either its generality or realism. The approach, as it is based upon matrix algebra, should benefit directly from the ready availability of stiffness matrices which can be output from present day computer structural analysis programs at the same time as the stresses, strains and displacements of static load cases. The results of a complex analysis of the system are presented on the basis of vibration levels over the rotors and the structure caused by unbalances placed on each rotor in turn. The calculations were made by using MELDA 'The Mechanical Engineering Laboratory Dynamic Analysis' Suite of Computer Programs. The calculated vibration levels were shown to be acceptable.

1. INTRODUCTION

1.1 Machinery

The power drive was a GEC 4-pole 21MW induction motor running at 1492 RPM, integral with a deep underslung cooler. The unit was mounted in a rectangular box-section frame for ease of on-site installation. The bearings were of oil-lubricated tilting-pad design. Drive was taken off both ends of the rotor by means of MAAG gear couplings to two MAAG gearboxes. Both gearboxes were of the step-up type. The first gearbox was GN90, with a ratio of 1:6.686, driving the high pressure compressor via a Bendix type diaphragm coupling and layshaft assembly. The second gearbox was GN70 with a ratio of 1:4.135 driving the low-pressure compressor through a similar coupling arrangement. The compressors were of GHH

manufacture and each incorporated a power recovery turbine mounted on the extreme outer end of its rotor. The casings of the turbines rested on separate stools. The turbines were of partial admission design, therefore there was a varying lateral thrust on the outer bearing of each compressor according to the degree of power recovery. All bearings in the compressors were of tilting pad design. The effect of the varying lateral force on the outer bearings was to change their stiffness and damping characteristics, which in turn affected the response-to-unbalance characteristics of the whole set.

1.2 Foundation

The machinery was mounted on a fabricated box type steel foundation of GHH design via various fabricated stools which were integral with it. An isoparametric exploded view is shown in Fig. 1. The 'Table top' of the foundation was supported on ten special columns each of which consisted of three coaxial square-section columns to form a longer and more flexible route for axial loads without giving rise to undue sway flexibility. This was done by joining the top of the outer tube to the top of the intermediate tube, and the bottom of the intermediate tube to the bottom of the innermost tube. The table top was supported on the top of the innermost tube and the base of the outer tube was fixed to the foundation slab. The top of outer tube was linked directly to the table top by simple flat springs which allowed up and down motion of the innermost tube relative to the outermost tube, but no lateral relative motion.

1.3 Other Components

The two most important items in this category were the coolers, referred to as cooler I and II, each hung by two brackets from the underside of the table top. The coolers were served by a system of water pipes and air ducts which added to a fairly extensive network of similar items on the underside of the foundation. The lube-oil system consisted of a tank and pumps which were supported on a platform, in turn supported by the foundation four end columns, but very close to the ground. The oil coolers and filters were situated on the table top, at the HP compressor end.

2. OUTLINE OF METHOD OF ANALYSIS

The program (MELDA) was developed at GEC Engineering Research Centre to specifically solve the complex whirling problems associated with the rotating and non-rotating parts of an overall structure, the important factor being the dynamic inter-play of spinning shafts with a resonance-prone steel structure. Expressions are obtained in matrix form for the kinetic energy, potential energy and energy dissipation of the rotating and non-rotating structures. For the non-rotating structure, energy expressions are in terms of displacements referred to a fixed set of axes. The energy expressions for the rotating system are, when necessary, initially in terms of displacements referred to a set of axes located within the shaft. These energy expressions are then transformed into the stationary set of coordinates by the known geometric relationship between the two sets of axes. As each type of energy expression is formed, it is then substituted in the relative term, or terms of Lagrange's equation of motion, ie.

$$\frac{d}{dt}\left(\frac{\delta T}{\delta \dot{q}_i}\right) - \frac{\delta T}{\delta q_i} + \frac{\delta D}{\delta \dot{q}_i} + \frac{\delta V}{\delta q_i} = Q_i \qquad (1)$$

to give a series of equations which are then summed at the end of the analysis to form the final equations of motion of the system under consideration.

The oil film system is, in general, non-conservative; hence to avoid involvement with complex energy functions, it is incorporated in the analysis as generalised forces Qi of Lagrange's equation. These forces are assumed linear functions of the relative displacements and velocities of the journal and housing, and after suitable transformation, they are assembled on the LHS of the final equation of motion.

The program calculates the steady-state response to unbalance at every speed specified. Unbalance may be distributed along, and at any point around the axis of the shaft. The response of the shaft is expressed in terms of the ellipses of motion of the freedom datum-points and the amplitude and phase of the projection of the orbits onto the x and y planes. The motion of the bearing housings is described in the same manner. Journal run-outs relative to their bearing housings are also described in terms of ellipses. The response of the structure, other than at the bearings, is expressed in terms of amplitude and phase of the normal mode coordinates (eigenvectors) used to describe the motion.

The purpose of the calculations was to predict the pattern of response of the three shaft-lines and the associated machinery and foundation structure due to unbalances placed on each of the three rotors in turn. A range of speeds around operating speed (1492 RPM at the drive motor, 9974 RPM at the HP compressor) was considered. The method is described in ref. [1]. It treats the system as being made up of three components: rotor; rotor support sub-structure; journal bearing lubricant film stiffness and damping characteristics. These are treated by a program suite MELDA of which the main components are shown in Fig. 2.

The program searches the data produced at each speed and finds the maximum shaft run-out and the degree-of-freedom on the shaft at which it occurs and the maximum structural deflection and the degree-of-freedom at which it occurs.

3. IDEALISATION

3.1 Rotor

The rotors were idealised as an assemblage of finite elements of the beam type, with shear distortion effects included. The size of the elements was chosen to give a close description of their elastic properties. The inertial and elastic properties of the rotors as represented by the finite elements models were reduced by a condensation process ref. [2] to a coarser mesh, which still has an adequate description of the dynamic distortion. The choice of elements and degrees-of-freedom for the three shaft-lines is shown in Fig. 4 to 6. The total number of nodes in the shaft system was 313, with 264 beam elements and 66 dynamic degrees of freedom in each plane.

3.2 Sub-structure

Each of the seven sub-structures shown in Fig. 3 was idealised as an assemblage of finite elements of the type plate, shell, beam etc. The

finite element idealisation is shown in Figs. 7 to 11. The link degrees-of-freedom were selected to link each sub-structure to its adjoining substructure and to describe its dynamic properties. A total of 3307 finite elements were deployed amongst the seven sub-structures using 7415 nodes, to give a total of 31,166 structural degrees-of-freedom (structural analysis stage). Seventy-four common link freedoms were required to join the sub-structures together. After linking the sub-structures together and eliminating the unwanted link freedoms there remained 180 degrees-of-freedom to define the dynamic motion.

4. STATIC REDUCTION

A process of condensation [2] was used to produce a stiffness matrix relating load and displacement at the selected points. Two types of freedom, dynamic and link, were considered in this analysis.

The link freedoms defined the motion at the interface between a sub structure and the sub-structure to which it was to be attached. The sub-structure to which it was to be attached had a similar matching set. Once all sub-structure stiffness and inertia matrices had been linked together by the MERGE program, the interface freedoms were not required as dynamic freedoms and were eliminated leaving only the dynamic freedom.

5. JOURNAL BEARING COEFFICIENT

The calculation of bearing characteristics was carried out using the MELBA (MEL Bearing Analysis) ref. [7] program suite. Assuming linear behaviour about the steady running condition, the bearing oil film stiffness and damping properties can be expressed by a pair of 2 X 2 matrices:

$$\begin{bmatrix} F_X \\ F_Y \end{bmatrix} = \begin{bmatrix} K_{11} & K_{12} \\ K_{21} & K_{22} \end{bmatrix} \begin{bmatrix} X \\ Y \end{bmatrix} + \begin{bmatrix} D_{11} & D_{12} \\ D_{21} & D_{22} \end{bmatrix} \begin{bmatrix} \dot{X} \\ \dot{Y} \end{bmatrix} \qquad (2)$$

5.1 Pivoted Pad Compressor Bearings

There are four bearings of this type: two in the high pressure and two in the low pressure compressor. Each bearing has five centrally-pivoted 60° pads. Two clearances are specified for each bearing: the pivoted clearance C_{piv} and the pad clearance C. The radial pivot clearance is the clearance at each pivot when the journal is central in the bearing. The pad clearance is the difference between the pad's radius of curvature and the radius of the journal.

5.2 Motor Bearings

These were partial arc bearings, the diameter, D = 280mm, length, L = 200mm, radial clearance, C = 0.24mm and the inlets are 8mm deep and have side lands 17mm wide. The circumferential length gutterways is 70mm which implies an arc of 151°. The bearings were centrally loaded.

5.3 Gearbox Bearings

Only the wheel bearings were considered. The geometry of the arc was specified by MAAG as being from -45° to 60° and from 135° to 240° from bottom dead centre. The direction of the load is relative to bottom dead centre in the direction of rotation of the journal.

6. METHOD OF BEARING ANALYSIS

6.1 Pivoted Pad Bearings

Under steady loads the oil force on each pad was taken to act through the pivot. Each pad was therefore treated as a partial arc bearing with a specified load direction. It was assumed that the leading edge temperatures were the same for all the pads. These temperatures were calculated by assuming no external load on the bearing and 100% carry over of hot oil from one pad to the next. The analysis was performed using the MELBA multi-arc journal bearing program which considered a single pad with automatic heat balance facility. A series of load cases were run and film thickness at the pivot was calculated at each load. A small FORTRAN program was used to determine the journal position, power loss, oil flow, and maximum temperature for a given load.

6.2 Motor and Gearbox Bearings

The MELBA multi-arc journal bearing program was again used to analyse the bearing. The program provides a combined solution of the energy and Reynold's equation and carries out balances to allow for mixing in the inlet wash away.

7. UNBALANCE MOMENT

7.1 Rotor Out-of-Balance Values and Standards as for Assessment of Predicted Response

The amount of out-of-balance applied to each shaft and its location was decided using ISO 1940 ("Balance quality of rotating rigid bodies") [4], and draft ISO proposal (ISO/DP5343, "Criteria for evaluating flexible rotor unbalance") [5]. It was not possible to say prior to the start of the calculations what could be classed (in terms of the above standards) as "rigid bodies" and which could be classed as "flexible rotors". A policy was therefore adopted of choosing an unbalance distribution which met the residual unbalance requirements of both cases.

The unbalance moment is controlled by paragraphs 3.3 and 3.4 of ISO 1940. Clearly all three rotors must be classified as the "two correction plane type". The unbalance could be applied as a simple unbalance at the centre of gravity of each rotor, or as two anti-phase unbalances at the rotor balancing phases. To reduce the number of computing cases it was decided to combine the two effects (lateral forcing and pitching) by applying the whole of the unbalance at a point. The lateral shaking forces and pitching moments would be produced by off-setting the bearing mid-span in this way.

Table 1 - Structural Vibration Limits, Microns O-PK

Unbalance Locations	Good	Satisfactory	Just Satisfactory	Unsatisfactory
Motor	0-25.5	25.5-63.0	63.0-160.0	>160
LP Compressor	0-6.0	6.0-15.0	15.0-38.0	>38
HP Compressor	0-3.95	3.95-9.5	9.5-23.0	>23

International Standard ISO2372 has been considered but unfortunately it did not state explicitly what could be considered as "Good", "Satisfactory", etc.

8. RESULTS AND DISCUSSION

Two forms of results are represented in this paper. Firstly, a graph of maximum shaft run out vs. rotor speed, showing the locations of peak responses and, secondly deflected shapes at the instant of maximum shaft radial run-out at the peaks.

8.1 Unbalance on the L.P. Compressor Rotor

The amplitude vs. speed curves are given in Fig. 12 for the full power and zero recovery cases. Comparison of the two show negligible differences due to power recovery. A lower resonance occurs at 3800 RPM (all speeds are referred to the HP rotor shaft speed), well below the operating speed. The shaft shape - or 'snapshots' - for this speed are plotted in Fig. 15 where it can be seen that the mode is a fundamental bending of the L.P. rotor with all significant activity confined to it with very close investigations in the speed range near the peak. These show that the orbit is very nearly circular and that very rapid phase changes occur. The level of power recovery introduces sufficient differences in phase angle to affect the 'snapshot' when these are taken at the same speed. The 12000 RPM resonance does not represent any significant danger to its design. The structural vibration levels peak at 2.6 microns O-PK at 12100 RPM. This is well within the "good" standard of Table 1.

8.2 Unbalance on the H.P. Compressor Rotor

The resonance characteristics of the H.P. and L.P. rotor are very similar. The maximum amplitude vs. speed curves and mode shape are plotted in Figs. 13 and 16 for the full power and zero power recovery cases. It can be seen that the results are virtually identical. The peak rotor vibration levels reach 40 microns O-PK at 11760 RPM. The peak bearing run-out at this speed is 3.60 microns at the drive-end, which is 5 percent of the pivot clearance - a very acceptable case.

8.3 Unbalance on the Motor Rotor

A no power recovery run was carried out for the motor unbalance case. The rotor amplitude vs. speed curve is presented in Fig. 14. The significant peak is 7 microns at 23000 RPM - well within the "Good" band of Table 1 and at over twice the operating speed. The mode shape at this speed, Fig. 17, shows it to be more in the nature of a fundamental free-free flexural vibration rather than simply supported (the deflections at the bearings are anti-phase relative to the motor centre). This case was repeated by assuming that the rigid and flexible structure, symmetrised bearing stiffness and damping cross-terms were divided by 100, an increase in response level of 30 microns was found as shown in Fig. 14 The peaks are at 9000 and 16000 RPM. The mode shapes at these peaks have been plotted as shown in Fig. 17. The conclusion of these runs are that the main source of damping was due to the non-symmetric nature of the bearing stiffness coefficients and due to the coupling of the motor rotor to the gearbox shaft via the structure.

9. CONCLUSIONS

The response levels for both the rotors and the support structure - which includes items such as the coolers and the machine casings - appear to be very acceptable, certainly the structural vibration levels are well within the limits laid down in VDI 2056. There is a slight doubt, however, that both the LP and HP compressor rotors may have second-flexural critical speeds slightly below the operating speed plus 20 percent bound. The results of the motor unbalance case have shown that motor bearing characteristics which lead to very high levels of damping and that the dynamic coupling of the motor rotor to the gears shaft via the support structure also has a significant, and similarly beneficial damping effect.

ACKNOWLEDGEMENTS

The author wishes to thank the Imperial Chemical Industries Plc and The General Electric Company plc for permission to publish this paper. The author acknowledges the contribution of J.N. Ramsden and F. Suess, both of whom are no longer with ERC and also the assistance from Mr. E.W. Cowking of the Tribology Group of ERC in preparing the bearing coefficients.

REFERENCES

1 J.N. RAMSDEN 1969 International journal of numerical methods in engineering vol.1, 225-245. A matrix method for the solution of mixed rotating and non-rotating vibration systems.

2 J.N. RAMSDEN and J.R. STOKER 1969 International journal for numerical methods in engineering vol.1, 333-349. Mass condensation: a semi-automatic method for reducing the size of vibration problems.

3 J.N. RAMSDEN, G.S. RITCHIE and S.S. GUPTA 1974 Fluid machinery group and nuclear energy group convention, pumps for nuclear power plant, I.Mech.E. Bath. The vibrational response characteristics of a design for the sodium pumps of the commercial fast reactor.

4 ISO 1940 International Standard. Balance quality of rotating rigid bodies.

5 ISO/DP5343 1979 Third draft ISO proposal. Criteria for evaluating flexible rotor unbalance - document ISO/TC 108/TC 108/SC 1/WE2.

6 VDI 2056 Verein Deutscher Ingenieure. Criteria for assessing mechanical vibrations of machines.

7 E.W. COWKING 1985 General Electric Engineering Research Centre Report No. ERC(W)46.0658. THD journal bearing computer programs user's guide.

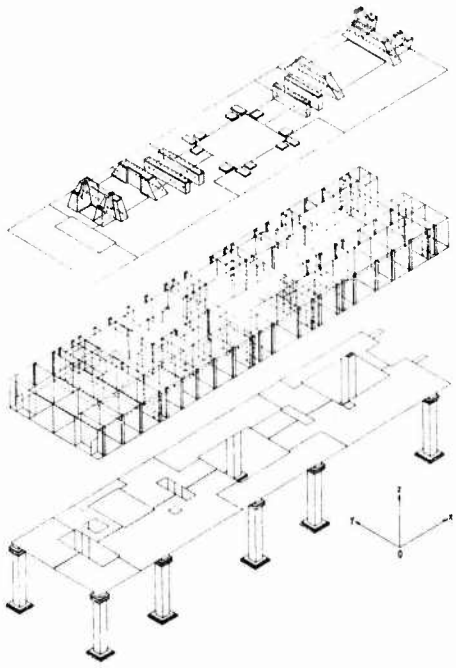

FIG 1. EXPLODED VIEW

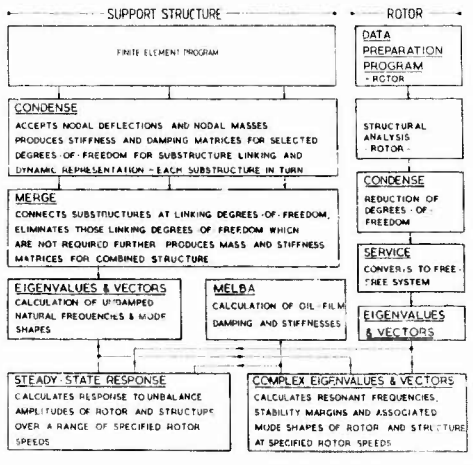

FIG 2. MELDA

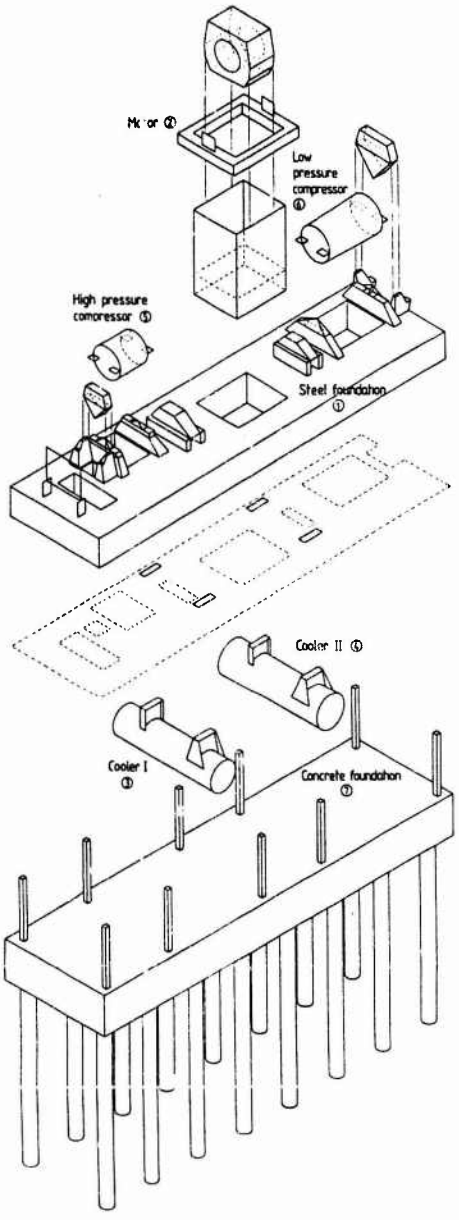

FIG 3. SUPPORT STRUCTURE

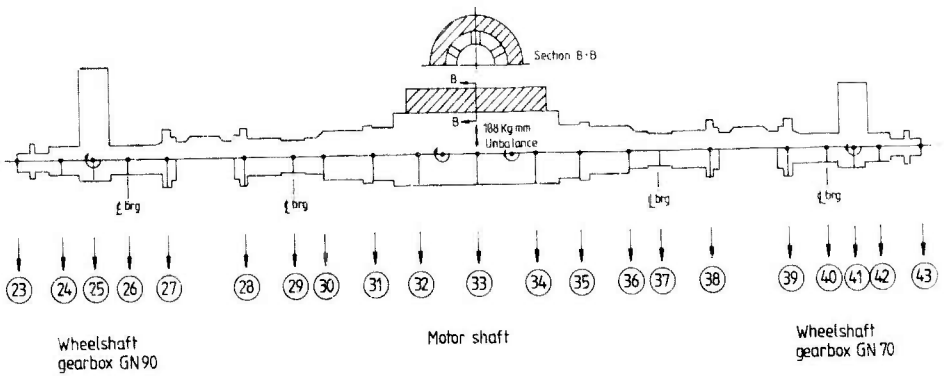

FIG 4. MOTOR SHAFT

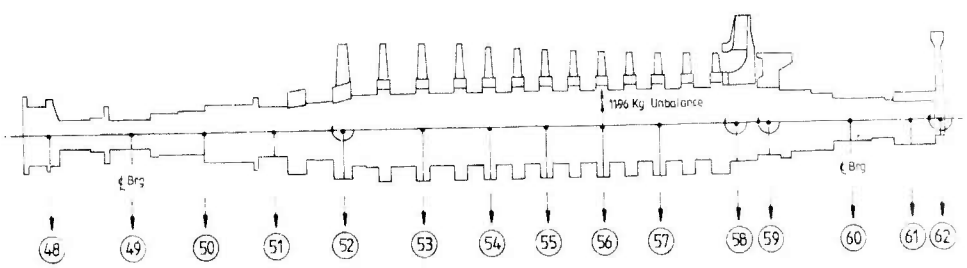

FIG 5. LP COMPRESSOR SHAFT

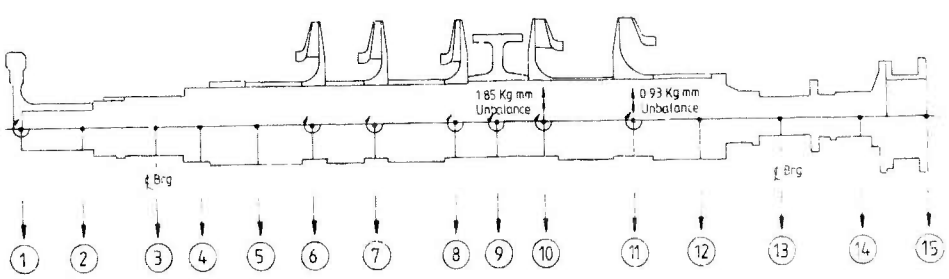

FIG 6. HP COMPRESSOR SHAFT

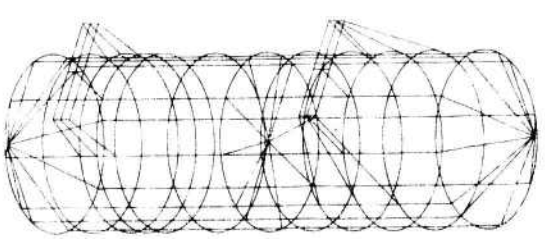

FIG 7. COOLER FINITE ELEMENT
MODEL (no. of freedoms = 2156)

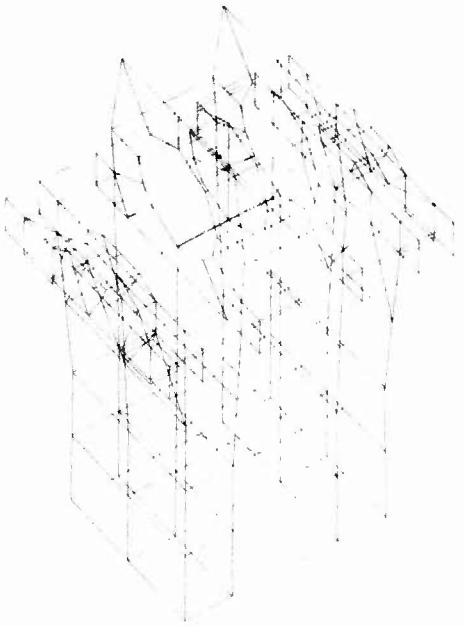

FIG 8. MOTOR FINITE ELEMENT MODEL
(no. of freedoms = 2252)

FIG 9. HP CASING FINITE ELEMENT MODEL
(no. of freedoms = 8000)

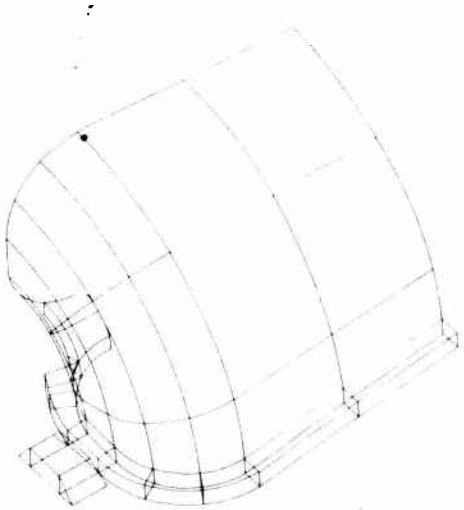

FIG 10. LP CASING FINITE ELEMENT MODEL
(no. of freedoms = 6800)

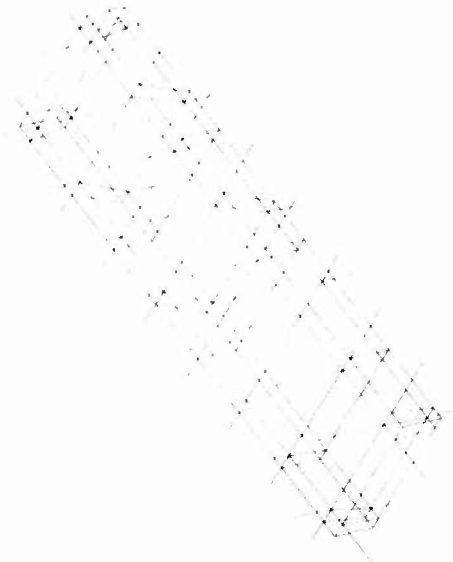

FIG 11. FOUNDATION SLAB FINITE ELEMENT MODEL

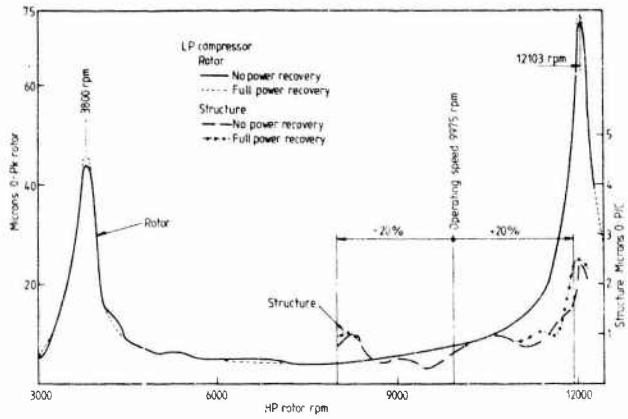

FIG 12. LP ROTOR. AMPLITUDE VS SPEED

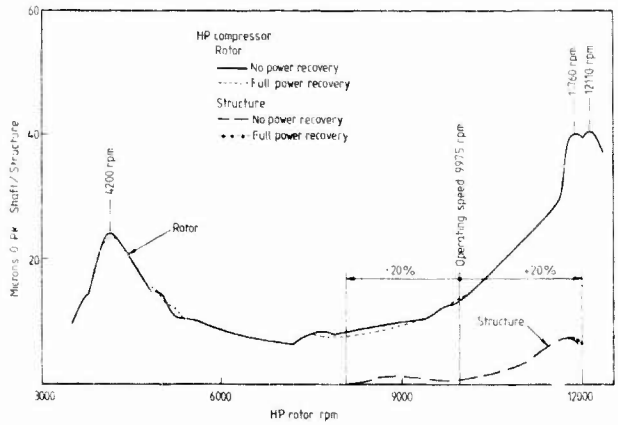

FIG 13. HP ROTOR. AMPLITUDE VS SPEED

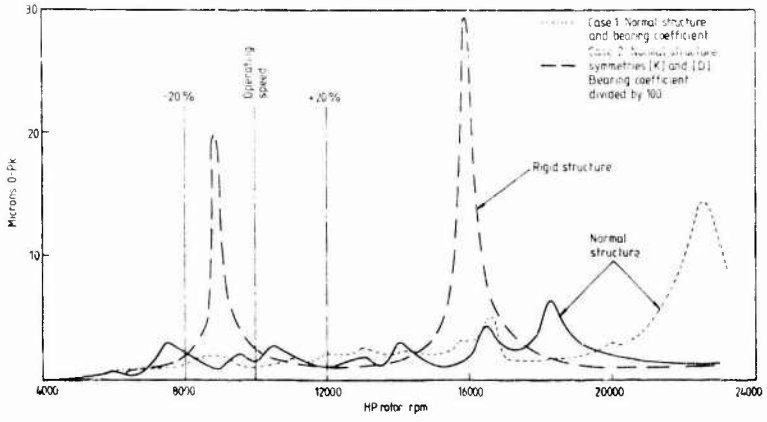

FIG 14. MOTOR ROTOR. AMPLITUDE VS SPEED

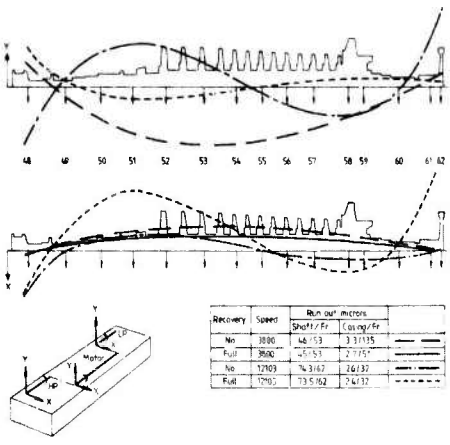

Recovery	Speed	Run out, microns	
		Shaft / Fr	Casing / Fr
No	3800	48 / 53	3 3 / 135
Full	3800	45 / 53	2 7 / 57
No	12700	74 / 162	26 / 32
Full	12700	73 5 / 62	24 / 32

FIG 15. LP ROTOR MODE SHAPE

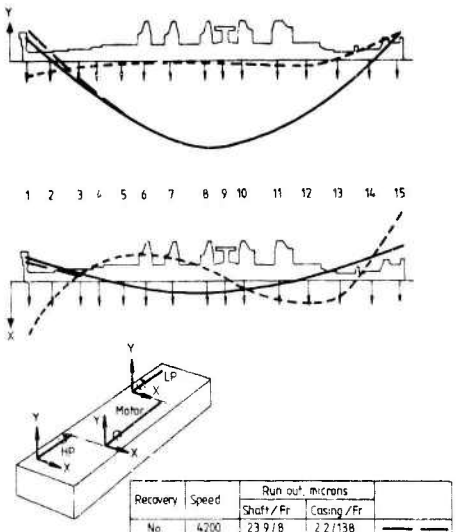

Recovery	Speed	Run out, microns	
		Shaft / Fr	Casing / Fr
No	4200	23 9 / 8	2 2 / 138
Full	4200	24 / 8	2 2 / 62
No	11760	40 / 15	7 7 / 32
Full	11760	40 /	7 7 / 32

FIG 16. HP ROTOR MODE SHAPE

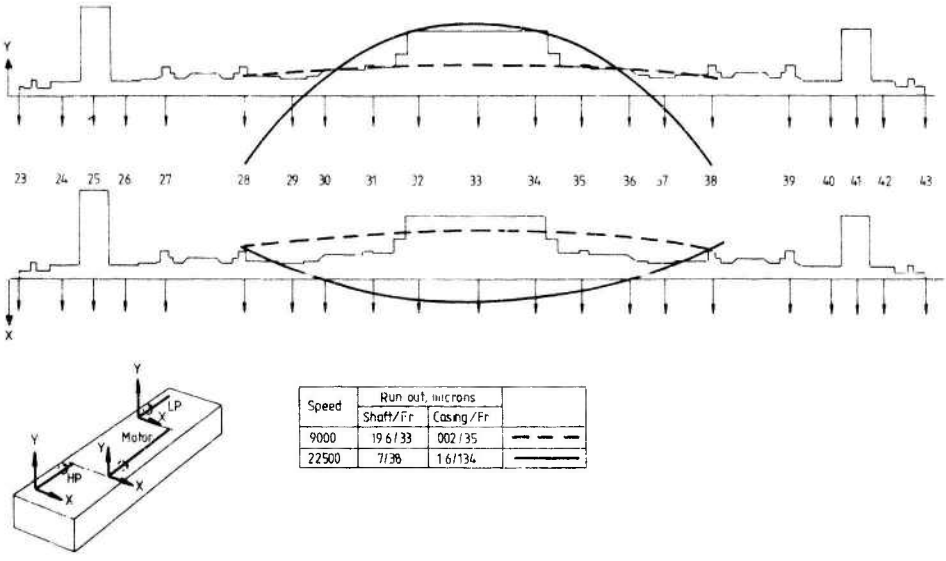

Speed	Run out, microns	
	Shaft / Fr	Casing / Fr
9000	19 6 / 33	002 / 35
22500	7 / 36	1 6 / 134

FIG 17. MOTOR MODE SHAPE

TRANSIENT DYNAMICS OF ROTATING FLEXIBLE BODIES WITH BASE MOTION EXCITATIONS

Y. A. Khulief and H. T. Chiu

Department of Mechanical Engineering
University of Alabama at Birmingham
Birmingham, AL 35294, U. S. A.

ABSTRACT

A method for modeling transient dynamics of rotating flexible components is presented. Such dynamic models are of practical importance for both design and control of several engineering applications. Examples are flexible links of high-speed mechanisms, manipulator arms, airplane propellers, and flexible appendages of spinning spacecrafts. This method is based on a nonlinear formulation of the Lagrangian form in conjunction with the finite element technique. A mixed set of generalized coordinates that accounts for inertia coupling between reference motions and local elastic deformations is employed. Component mode substitution techniques are used for generating a finite set of selected modal coordinates. The formulation accounts for component mode changes due to the effect of reference rotational speed of the elastic component. Base motion excitations, including impulsive forces, are taken into consideration. Numerical results are presented for a beam with its midpoint fixed to a rotating base which is subjected to sinusoidal pulse excitation.

1. INTRODUCTION

The dynamic behavior of rotating flexible components is an important part of the dynamic analysis of interconnected multibody systems. Examples of such mechanical systems are turbomachines, propellers, high-speed flexible mechanisms, and space stations.

In this analysis, the configuration space of the flexible component is modeled by a mixed set of reference and local elastic generalized coordinates, [1]. The finite element method is employed to generate a set of elastic coordinates that represents degrees of freedom of a selected set of discrete points in the structure. Utilization of such nodal coordinates results in a large dimensionality that often causes numerical difficulties. An alternative representation suggests the use of a truncated set of modal coordinates, [2]. A modal transformation is, therefore required to perform a transformation from the nodal space to the modal space. The precision of this transformation depends on the accuracy of the estimated modal characteristics of the elastic component.

Modal substitution techniques were employed by previous investigators [3-5], in modeling rotating flexible components. These methods, however, have relied upon modal characteristics of a non-rotating structure undergoing free vibrational motion. Rotating flexible components are known to experience centrifugally induced tensile forces that tend to increase the effective torsional and flexural stiffness. A few investigators [6-10] have conducted studies to estimate such rotational stiffening effects. The results reported in [11] show that the centrifugally induced stiffness has greater influence on lower modes, which are significant to the dynamic response of such systems. Therefore, a proper set of elastic modal coordinates must account for modal changes induced by the centrifugal force field.

In this paper, a computer-based dynamic analysis scheme is developed. A detailed two dimensional analysis based on a nonlinear Lagrangian formulation is performed. The finite

element is used to generate modal characteristics that account for the effect of rotation. Modal truncation techniques are applied in order to obtain a reduced order model. The rotating flexible components are treated as members of a multibody system. Base excitations are permitted by the dynamic model. The dynamic behavior of a rotating flexible body is then examined under the influence of basc motion excitations that give rise to primary shock loading conditions at different phase angles.

2. DESCRIPTION OF ELASTODYNAMIC MODEL

In this formulation a general flexible body i is considered. The body is deforming elastically while executing a general reference motion.

2.1 Generalized Coordinates and Velocities

The configuration of thc elastic body can be described by defining the global position of an arbitrary point in the body. For this purpose three sets of axes are introduced as shown in figure 1; the inertial frame XYZ, the body reference frame $x^i y^i z^i$, and the element coordinate frame $x^{ij} y^{ij} z^{ij}$. The global position of an arbitrary point p^{ij} in element ij can be expressed as

$$r_p^{ij}=r_o^i+R^i(\Theta^i)R^{ij}(\beta^{ij})N^{ij}\bar{R}^{ij}(\beta^{ij})e^{ij} \tag{1}$$

where R is a coordinate transformation matrix, $\bar{R}^{ij}(\beta^{ij})=diag[R^{ij}(\beta^{ij}),1,R^{ij}(\beta^{ij}),1]$ is a block diagonal matrix, N^{ij} is the shape function of the assumed displacement field of element ij, and e^{ij} is a vector of nodal coordinates defined with respect to an intermediate system of axes; located at the body origin and parallel to element axes. The rotation β^{ij} defines the orientation of element axes with respect to the body reference frame, and Θ^i defines the orientation of the body reference with respect to the initial frame. Equation (1) can simply be written as

$$r_p^{ij}=r_o^i+R^i(\Theta^i)\bar{N}^{ij}e^i \tag{2}$$

where e^i is the vector of nodal coordinates of the flexible body i, and $\bar{N}^{ij}$ is a modified shape function that accounts for a coordinate transformation from the element coordinates to the body-fixed frame, as well as a Boolean matrix transformation.

The generalized velocity expression can be obtained by differentiating equation (2) with respect to time. This will result in

$$\dot{r}_p^{ij}=\left[\, I \;,\; D^{ij} \;,\; R^i\bar{N}^{ij} \,\right]\dot{q}^i \tag{3}$$

where the term $\dot{R}^i\bar{N}^{ij}e^i$ is given by $D^{ij}\dot{\Theta}^i$, and $D^{ij}(\Theta^i,e^{ij})$ is a function of the reference rotational coordinates of body i and the elastic coordinates of element ij. The generalized coordinate vector q^i is given by

$$q^i=\left\{r_o^{iT},\Theta^{iT},e^{iT}\right\}^T \tag{4}$$

2.2 The Constrainted Lagrangian Equation

Mechanical systems, in general, can be represented by a collection of bulky rigid as well as flexible structural components, that are interconnected by typical mechanical joints; e.g. universal, prismatic, revolute, etc. The kinematics of such joints can be expressed in terms of a set of nonlinear algebraic equations of the form

$$C(q,t)=0 \tag{5}$$

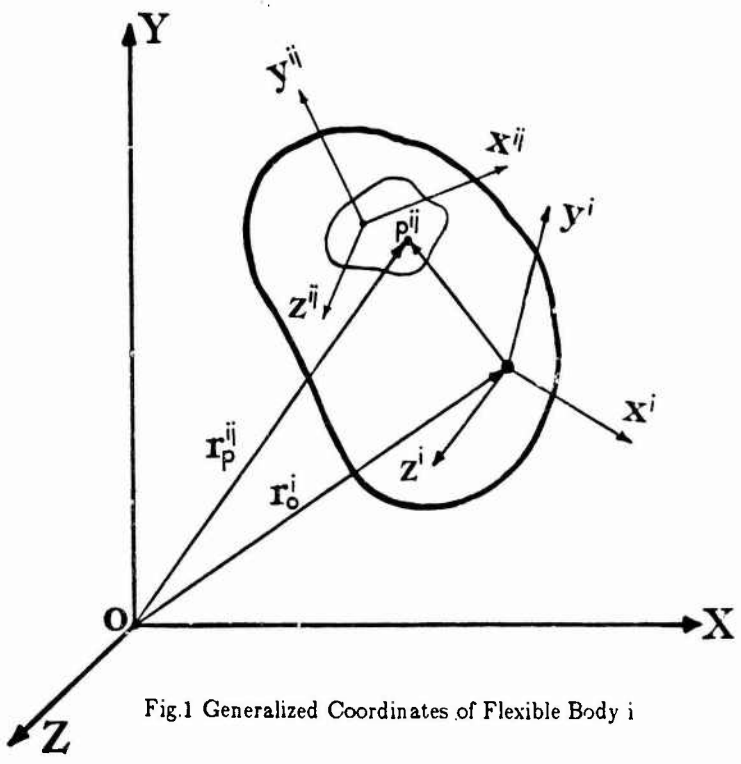

Fig.1 Generalized Coordinates of Flexible Body i

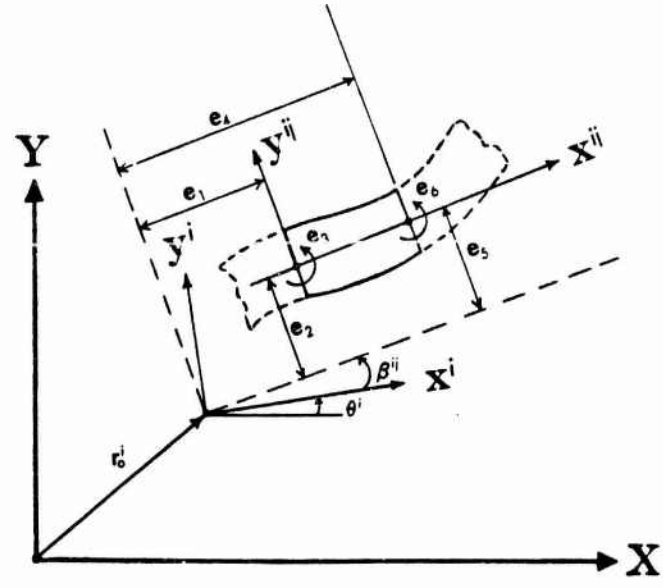

Fig.2 Nodal Coordinates of Element j

where $q = \{ q^{1T}, q^{2T}, \ldots, q^{Nb\,T} \}^T$ is the generalized coordinate vector of a mechanical system with Nb bodies. A virtural displacement δq of the system generalized coordinates, that is consistent with the constraints, can be written as

$$\left[\frac{\partial C}{\partial q}\right]\delta q = J\delta q = 0 \tag{6}$$

where J is the Jacobian matrix of the constraints equation. The Lagrangian form of the equation of motion is given by

$$M^i \ddot{q}^i + K^i q^i + J^{iT}\lambda = Q_E^i + Q_G^i \tag{7}$$

where λ is the vector of Lagrange multipliers, M^i is the mass matrix, and K^i is the stiffness matrix of body i. The vector Q_E^i represents externally applied forces, and Q_G^i represents force expressions that are functions of quadratic velocity terms, which account for Coriolis, gyroscopic and centripetal contributions.
The vector Q_E^i represents externally applied forces, and Q_G^i represents force expressions that are functions of quadratic velocity terms, which account for Coriolis, gyroscopic and centripetal contributions.

3. TWO-DIMENSIONAL ANALYSIS

In this analysis, flexible bodies are assumed to be represented by straight beam elements. There are no restrictions, however, made on the type of element which can be used to generate the coefficient matrices of equation (7).

3.1 Inertia Properties of Flexible Bodies

Utilizing the velocity expression of equation (3), the kinetic energy of the flexible body i can be written as

$$T^i = \frac{1}{2}\sum_{j=1}^{j=a^i} \int_{v^{ij}} \rho^{ij}\, \dot{r}_p^{ij\,T}\, \dot{r}_p^{ij}\, dv^{ij} \tag{8}$$

where a^i is the number of elements in the finite element mesh of body i, ρ^{ij} is the mass density, and v^{ij} is the volume of element ij. The general form of Lagrange's equation of motion is given by

$$\frac{d}{dt}\left\{\frac{\partial T^i}{\partial \dot{q}^i}\right\}^T - \left\{\frac{\partial T^i}{\partial q^i}\right\}^T + \left\{\frac{\partial U^i}{\partial q^i}\right\}^T + J^{iT}\lambda = Q_E^i \tag{9}$$

where U^i is the strain energy stored in body i. Performing the differentiation of the first two terms of equation (9), one can write

$$\frac{d}{dt}\left\{\frac{\partial T^i}{\partial \dot{q}^i}\right\}^T - \left\{\frac{\partial T^i}{\partial q^i}\right\}^T = M^i \ddot{q}^i - Q_G^i \tag{10}$$

where the mass matrix M^i is given by

$$M^i = \begin{bmatrix} m^i I & & & \\ & & & \text{Symmetric} \\ e^{i\,T} S^{i\,T} R_\Theta^{i\,T} & e^{i\,T} m_e^i e^i & & \\ S^{i\,T} R^{i\,T} & \tilde{S}^{i\,T} e^i & m_e^i & \end{bmatrix} \tag{11}$$

and Q_G^i is defined as

$$Q_G^i = \begin{Bmatrix} \dot{\Theta}^{i2} R^i S^i e^i - 2\dot{\Theta}^i R_\Theta^i S^i \dot{e}^i \\ -2\dot{\Theta}^i \dot{e}^{iT} m_e^i e^i - \dot{e}^{iT} \tilde{S}^i \dot{e}^i \\ \dot{\Theta}^{i2} m_e^i e^i - 2\dot{\Theta}^i \tilde{S}^{iT} \dot{e}^i \end{Bmatrix} \tag{12}$$

The matrix R_Θ^i is the derivative of R^i with respect to Θ, and $m^i I$ is the inertia properties associated with translational reference coordinate. Expressions for m_e^i, S^i and $\tilde{S}^i$ are given in the appendix.

3.2 Stiffness Properties of Rotating Flexible Bodies

The third term in the left side of equation (9) can be expressed as

$$\left\{\frac{\partial U^i}{\partial q^i}\right\}^T = \begin{bmatrix} 0 & & \\ 0 & 0 & \text{Symmetric} \\ 0 & 0 & K_f^i \end{bmatrix} \begin{Bmatrix} r_o^i \\ \Theta^i \\ e^i \end{Bmatrix} = K^i q^i \tag{13}$$

where K_f^i is the elastic stiffness matrix defined with respect to the local elastic coordinates in order to satisfy the uniqueness of the assumed displacement field. If the local coordinate vector of point p^{ij}, with respect to element axes, is given by

$$\begin{Bmatrix} u^{ij} \\ w^{ij} \end{Bmatrix} = \bar{N}^{ij} e^i \tag{14}$$

where deformations are confined to the plane of rotation as shown in figure 2, and the elastic body is assumed to rotate about a fixed axis in the space. Neglecting shear deformations, the strain energy expression is given by [12],

$$U^i = \frac{1}{2} \sum_{j=1}^{j=n_i} \int_0^{l^{ij}} \left\{ E^{ij} A^{ij} \left\{ \frac{\partial u^{ij}}{\partial x^{ij}} \right\}^2 + E^{ij} I^{ij} \left\{ \frac{\partial^2 w^{ij}}{\partial x^{ij2}} \right\}^2 + E^{ij} A^{ij} \left\{ \frac{\partial u^{ij}}{\partial x^{ij}} \right\} \left\{ \frac{\partial w^{ij}}{\partial x^{ij}} \right\}^2 \right\} dx^{ij} \tag{15}$$

The first two integrals of equation (15) represent linear strain energy, while the third term is a contribution of the nonlinear component of the strain. Therefore the stiffness matrix in equation (13) can be defined as

$$K_f^i = K_e^i + K_r^i \tag{16}$$

where K_e^i represents the linear elastic stiffness of body i. The matrix K_r^i is found by performing the third integral of equation (15), where the term $E^{ij} A^{ij} \{ \partial u^{ij} / \partial x^{ij} \}$ accounts for axial stress resulting from the centrifugal force field. Expression for stiffness matrices K_e^i and K_r^i are included in the appendix.

3.3 Reduced Order Model

The dynamic relation expressed by equation (9), is written in terms of reference coordinates and elastic nodal coordinates of flexible body i. This type of representation often results in large dimensionality which gives rise to numerical solution problems. In order to reduce the dimension of the dynamic model, a transformation from the nodal space to the

modal space may be invoked. Considering the expressions given by equtations (11)-(13), one can describe the free vibrational motion, associated with equation (9), in the form

$$m_e^i \ddot{e}^i + \left[K_e^i + K_\tau^i - \dot{\Theta}^{i^2} m_e^i\right] e^i = 0 \tag{17}$$

where the flexible body deformations are confined to the plane of rotation. Solving the generalized eigenvalue problem associated with equation (17), the modal transformation can be established in the form

$$\alpha^i = \Gamma e^i \tag{18}$$

where Γ is the modal matrix representing a selected finite set of mode shapes, and α^i is the corresponding set of modal coordinates. The truncated set of modal coordinates is selected to include all modes that are significant to the elastic response of the flexible component, [2].

The equation of motion of the flexible body i can be written in the modal form as

$$\bar{M}^i \ddot{d}^i + \bar{K}^i d^i + \bar{J}^{i^T} \lambda = \bar{Q}_E^i + \bar{Q}_G^i \tag{19}$$

where $d^i = \{ r_o^{i^T}, \Theta^{i^T}, \alpha^{i^T} \}^T$ is the generalized coordinate vector in the modal form, and the bar (—), refers to a transformed modal form. The composite equation of motion for a multibody system can be assembled in the form

$$\bar{M}\ddot{d} + \bar{K}d + \bar{J}^T \lambda = \bar{Q}_E + \bar{Q}_G \tag{20}$$

where $d = \{ d^{1^T}, d^{2^T}, \ldots, d^{Nb^T} \}^T$ is the generalized coordinate vector of the whole system.

4. NUMERICAL RESULTS AND CONCLUSIONS

Numerical results are obtained for a rotating beam configuration defined in figure 3. The beam is 2 meter long with its midpoint fixed to a hub rotating at 2400 rpm. The beam is made of Aluminum alloy 2014 T6 with modulus of elasticity 73 Gpa. The cross-sectional area is $0.16 \times 0.02m$ rectangular shape. The beam is modeled by 8 finite beam elements of equal lengths. Modal characteristics of the rotating beam are generated using the numerical scheme developed in [11], and compared with modal frequencies of the non-rotating beam. This comparison is presented in table 1, which shows the stiffening effect of the beam rotation.

Base motion excitation is modeled by a modified sinusoidal pulse of duration 0.04 times the time period of the fourth frequency of the beam. The pulse delivers a force of maximum peak amplitude 100 times the total weight of the beam system. The lateral deflection of the tip point (node 1) of the beam is monitered at different beam excitations. A nondimensional parameter Ψ represents the deflection at node 1 divided by the length of the element. Figure 4 displays the response of the tip point using the first four modes of the beam. This figure shows the effect of using the centrifugally stiffened mode shapes on the beam dynamic response. Figure 5 represents the effect of the nature of the primary impulsive force on the excitation of higher modes. It is noteworthy to mention that when the pulse is applied at Θ=180°, the primary generated impulsive force will be purely transversal and therefore the flexural deflection of the beam will approach its maximum amplitude. Figure 6 shows the same behavior for the beam with centrifugally stiffened mode shapes when excited at two different orientations; Θ=45° and Θ=180°. As anticipated, a pulse applied at Θ=90° will produce an axial impulsive force that has minimal contribution to the flexural deflection of the beam (figure 7).

The numerical results presented in this paper emphasize two important observations. The first is concerned with the significance of using the actual modes of a rotating beam to the evaluation of its dynamic response. The second conclusion is related to the nature of the

primary generated impulsive force. As depicted from figures 6 and 7, the direction of the primary impulsive force is relevant to the type of modes that are significant to this excitation.

REFERENCES

1. A. SHABANA and R. WEHAGE 1983 J. Structural Mechanics, 11, 401-431. A Coordinate Reduction Technique for Dynamic Analysis of Spatial Structures with Large Angular Rotations.

2. R. GRAIG 1981 Structural Dynamics. New York: John Wiley.

3. W. SUNADA and S. DUBOWSKY 1983 J. Mechanisms, Transmission, and Automation in Design, 105, 42-51. On the Dynamic Analysis and Behavior of Industrial Robot Manipulator.

4. W. J. BOOK 1984 J. Robotic Research, 3, 87-101. Recursive Lagrangian Dynamics of Flexible Manipulators.

5. Y. KHULIEF and A. SHABANA 1986 J. Sound and Vibrations, 104(2), 187-207. Impact Responses of Multibody Systems with Consistent and Lumped Masses.

6. D. A. PETERS 1973 NASA N78-33289. An Approximate Solution for the Free Vibrations of Rotating Uniform Cantilever Beams.

7. D. H. HODGES 1979 J. Helicopter Society, 24(5), 43-50. Vibration and Response of Nonuniform Rotating Beams with Discontinuities.

8. S. V. HOA 1979 J. Sound and Vibrations, 67(3), 369-381. Vibration of a Rotating Beam with Tip Mass.

9. A. WRIGHT, C. SMITH, R. THRESHER and J. WANG 1982 J. Applied Mechanics, 49, 197-202. Vibration Modes of Centrifugally Stiffened Beams.

10. R. B. BHAT 1986 J. Sound and Vibrations, 105(2), 199-210. Transverse Vibrations of Rotating Uniform Beam with Tip Mass as Predicted by Using Beam Characteristic Orthogonal Polynomials in the Rayleigh-Ritz Method.

11. Y. KHULIEF and L. YI 1988 J. Computers and Structures, to appear. Lead-Lag Vibrational Frequencies of a Rotating Beam with End Mass.

12. J. S. PRZEMIENIECKI 1968 Theory of Matrix Structural Analysis. New York : McGraw-Hill.

APPENDIX

The inertia and stiffness coefficient matrices of the flexible body i can he established using the standard finite element sequential assemhly procedure as applied to the following element matrices:

$$m_e^{ij} = \int_{v^{ij}} \rho^{ij}\ \bar{N}^{ij^T}\ N^{ij}\ dv^{ij} \tag{A.1}$$

$$S^{ij} = \int_{v^{ij}} \rho^{ij}\ \bar{N}^{ij}\ dv^{ij} \tag{A.2}$$

$$\tilde{S}^{ij} = \int_{v^{ij}} \rho^{ij} \bar{N}^{ij^T}\ \tilde{I}\ N^{ij}\ dv^{ij} \qquad ; \qquad \tilde{I} = R_0^{i^T}\ R^i \tag{A.3}$$

$$K_e^{ij} = \int_{v^{ij}} \left[G^{ij} \bar{N}^{ij}\right]^T\ E^{ij}\ G^{ij}\ \bar{N}^{ij}\ dv^{ij} \tag{A.4}$$

where R^i_θ is the derivative of R^i with respect to θ, and G^{ij} is a differential operator relating strains to displacements, [12].

The stiffness matrix K^{ij}_r can be derived from the strain energy generated by the centrifugal force field. This portion of strain energy can be expressed as

$$U^{ij}_r = \frac{1}{2}\int_{v^{ij}} \sigma^{ij}_x \left(\frac{\partial w^{ij}}{\partial x^{ij}}\right)^2 dv^{ij} \tag{A.5}$$

where the axial stress σ^{ij}_x is generated by the centrifugal force. One can express the centrifugal force associated with a differential element located at point p^{ij} of the finite element j, as

$$F^{ij}_r = \int_{o^{ij}_r}^{L} \rho^{ij} A^{ij} \dot{\Theta}^{i2} x^{ij} dx^{ij} \tag{A.6}$$

where the integration in equation (A.6) is carried out over the span between point p^{ij} and the free end of the beam. A^{ij} is the cross sectional area of element j.

Table 1. Bending Frequencies of a Beam Fixed at its Midpoint

Frequency (rad/s)		Non-rotating Beam	Beam rotating at 251 rad/s
First	Type Value	Bending 828.635	Bending 874.644
Second	Type Value	Bending 828.635	Bending 874.644
Third	Type Value	Bending 5193.82	Bending 5231.22
Fourth	Type Value	Bending 5193.82	Bending 5231.22
Fifth	Type Value	Axial 8072.13	Axial 8072.13
Sixth	Type Value	Axial 8072.13	Axial 8072.13

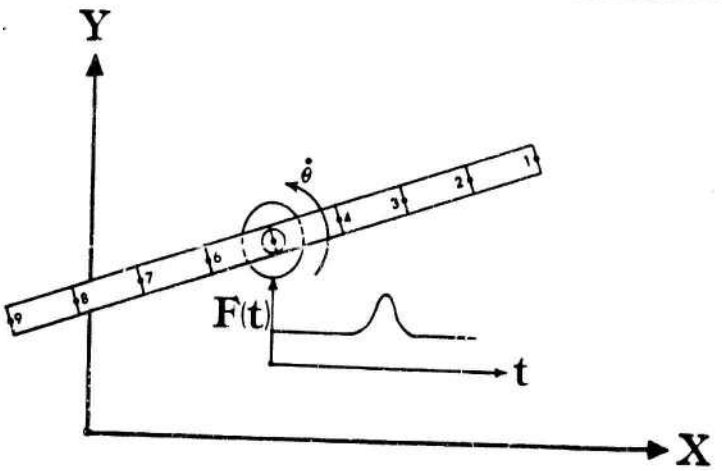

Fig.3 Base Excitation of a Rotating Beam

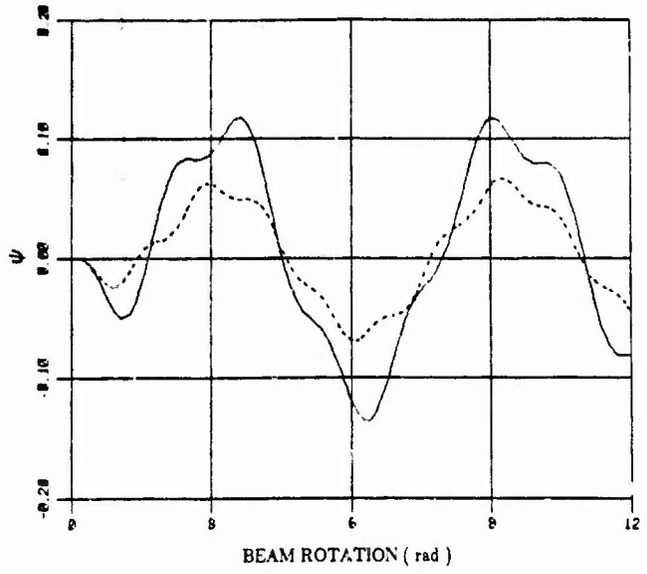

Fig.4 Deflection of the Tip Point; ——— Free Vibrational Modes;
- - - - - - - centrifugally stiffened modes

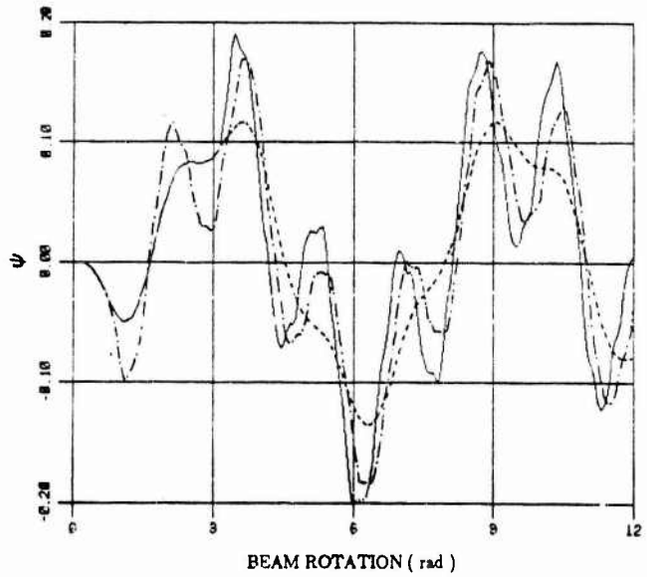

Fig.5 Response of Tip Point using Free Vibrational Modes;
- - - - - - without pulse excitation; —·—·— pulse excitation at Θ=45°;
——— pulse excitation at Θ=180°

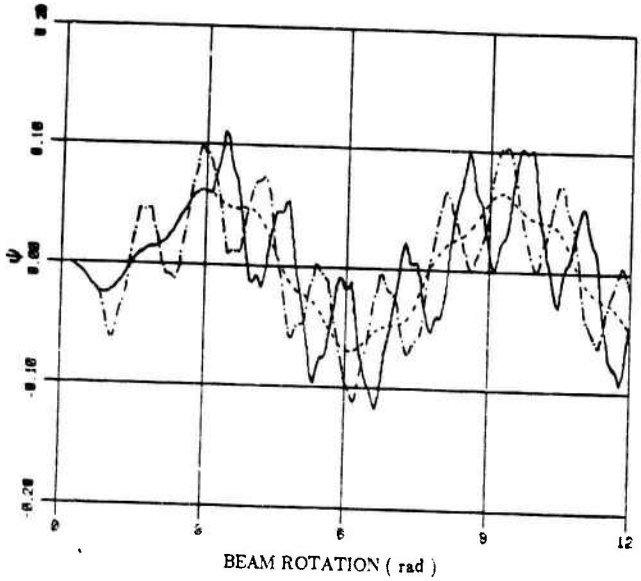

Fig.6 Response of Tip Point using Centrifugally Stiffened Modes;
- - - - - - without pulse excitation; —·—·— pulse excitation at Θ=45°;
——— pulse excitation at Θ=180°

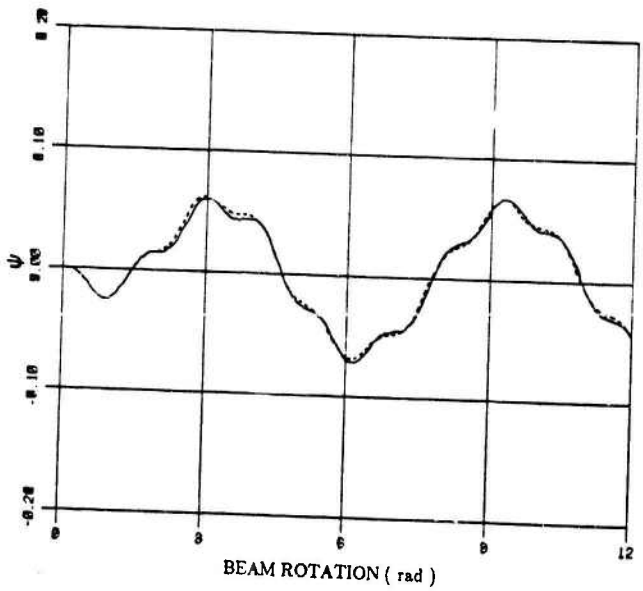

Fig.7 Response of Tip Point using Centrifugally Stiffened Modes;
- - - - - - without pulse excitation; ——— with pulse excitation at Θ=90°

3. COMPOSITES

IMPACT STRESS WAVES IN FIBRE-REINFORCED LAMINATED PLATES

E. Rhian Baylis and W. A. Green

Department of Engineering,
University of Leicester,
Leicester, LE1 7RH

Department of Theoretical Mechanics,
The University,
Nottingham, NG7 2RD

Research sponsored by the Air Force Office of Scientific Research,
Air Force Systems Command, USAF under Grant Number AFOSR-86-0330.
The U.S. Government is authorised to reproduce and distribute
reprints for governmental purposes.

1. INTRODUCTION

This paper is concerned with a theoretical and numerical investigation of the propagation of stress waves induced by surface impact on a laminated plate of finite depth and infinite lateral extent. Attention is focussed on the problem of an impulsive line load acting on the upper surface of the plate and generating plane wave disturbances travelling in the laminate along the direction normal to the line load. The plate is constructed of an arrangement of layers (or plies) of fibre-reinforced material in which the reinforcement of each layer is a family of parallel fibres lying in the plane of the layer. The plies are assembled in a periodically repeating configuration of N unit cells, the configuration being defined in terms of the angles between the fibre direction in each ply and some specified reference direction. For the present we have concerned ourselves with a simple 0/90 configuration. Here the unit cell consists of two inner layers, each of thickness h, with the fibres running along the reference direction, and bounded above and below by a layer of thickness h of the same material with fibre direction orthogonal to the reference direction. This choice of unit cell is made purely for simplicity and the techniques that we use are applicable to any configuration of the unit cell.

We model the fibre reinforced material as a homogeneous continuum of transversely isotropic elastic material with the axis of transverse isotropy along the fibre direction. This means that we look at waves whose wavelengths are an order of magnitude greater than the fibre diameter and inter-fibre spacing so that on the scale of the wavelength the continuum theory might be expected to be valid. Typical of the materials we have in mind is the ICI product PEEK, formed of carbon fibres embedded in a thermoplastic resin, for which typical dimensions are $h \simeq 125\ \mu m$ with the fibre diameter and inter-fibre spacing of the order of $6\ \mu m$. Thus we are thinking in terms of wavelengths of the order of 1/2 to 1/3 the ply thickness or greater for which the non-dimensional wave number $kh = 2\pi h/\Lambda$ (where Λ is the wavelength) varies from zero at infinite wavelength to a value of approximately 18 at $\Lambda = h/3$. For smaller wavelengths, of the order of h/10 or less, the continuum model will break down due to diffraction and scattering by the individual fibres.

There is a considerable simplification in the mathematics to be gained by treating the composite as inextensible in the direction of transverse isotropy. This is an idealization of the fact that the extensional modulus of the continuum along the fibre direction can be of the order of 100 times that in the cross fibre direction. Mathematically, the effect of the idealization is to reduce the order of the differential equations and this leads to solutions involving fewer parameters. A consequence of this reduction in the order of the equations, however, is that it is no longer possible to satisfy all the interface continuity conditions between the plies. This leads to a singular perturbation problem, in which it is necessary to allow the tangential component of traction along the fibre direction to be discontinuous across the interface, with a consequent singularity in the stress component along the fibres, associated with a finite load carried by the surface layer of fibres. This singular perturbation problem has been

examined in detail for static problems by Everstine and Pipkin [1] and for dynamic problems by Green [2], Green and Milosavljević [3] and Baylis and Green [4],[5]. In particular, Baylis and Green [4],[5], dealing with a four ply laminate, derive an expression relating the singularity along the fibre direction to the discontinuity in shear stress. They present detailed comparisons of the stresses in the inextensible laminate with those in a strongly anisotropic but not inextensible material. These comparisons show that the inextensible theory provides an acceptable approximation to the stress variation through the laminate except in the very long wavelength region and the dispersion curves for the two material models are also shown to be in good agreement, again with the exception of the very long wavelength limit. As with singular perturbation problems generally, the shear stress discontinuities are to be interpreted in terms of very narrow bands (boundary layers) adjacent to the interfaces, through which there exist high stress gradients, giving large changes in stress across the bands. The associated singular stresses along the boundary fibres are to be interpreted as high stress levels in the boundary layers, which contribute finite loads in the fibre directions when integrated through the boundary layers. It is with these interpretations in mind, that we adopt the idealization of inextensibility to give a mathematically simple model of our fibre reinforced material.

We make no assumptions about the variation of displacements and stresses through the laminate, such as is done in engineering theories of plates and shells. Our method is to solve exactly the system of governing equations appropriate to each layer, matching the solutions across the interfaces and satisfying the appropriate boundary conditions at the upper and lower surfaces of the laminate. This analytical solution is carried out in the paper by Green and Baylis [6] which appears in these proceedings. The method of solution involves taking Laplace transforms in time and Fourier transforms in the in-plane spatial coordinates, of the governing equations of the model, and yields the exact solution for the variation of the transforms with depth throughout the laminate. The approximations arise only in the numerical methods for inverting the transforms. The solutions for the displacements at the upper and lower surfaces are reproduced in Section 2. In this Section we also present the transforms of the in-plane displacement and the stress components both at the bounding surfaces and in the interior of the laminate.

The problem of inverting the transforms is considered in Section 3. There we show that it is necessary to solve the dispersion equation (relating frequency to wavelength) for plane waves travelling in the plate under traction free boundary conditions at the upper and lower surfaces. Inversion also requires that we evaluate the residue of the inversion integral along each branch of the dispersion equation and we must perform an integration along each branch and a summation over all branches to obtain the solution.

The numerical solution of the dispersion equation and the subsequent numerical integration over the branches of the dispersion curves is outlined in Section 4. It is here that the approximations come into play, since the solutions are necessarily limited to a finite number of branches and the integrations over each branch must be limited to a finite range of values of the wave number, k. We have chosen as an upper value $k = 20$, corresponding to wavelength of the order of 1/3 the ply thickness but 6 times the fibre diameter and inter-fibre spacing, which we estimate as being the limit at which the continuum model would be valid. We show that restricting the integral to a finite range of values of k gives rise to the phenomenon of "windowing" and we apply the technique due to Hamming [7] in an attempt to reduce this effect.

Graphs which show the variation of displacements and stresses, at the upper and lower surfaces, as functions of position at various times are presented in Section 5.

2. TRANSFORM SOLUTIONS

We choose a Cartesian coordinate system of axes with the x_1-axis normal to the

plane of the layers, the x_2-axis parallel to the fibre directions in the two outer layers of the unit cell and the x_3-axis parallel to the fibre directions in the two inner layers of the unit cell. We designate the layers with the fibre direction parallel to x_3 as material *1* and the layers with fibre directions parallel to x_2 as material *2* and denote stress and displacement components in the layers with the corresponding suffix. The line load which produces the disturbance is assumed to act on the upper surface of the plate, along a line making an angle $(\pi/2 - \gamma)$ with the x_3-axis giving rise to waves travelling in the plane at an angle $-\gamma$ with the x_3-axis. The displacement components $u_i(x_1,x_2,x_3,t)$, (i=1,2,3), and stress components $t_{ij}(x_1,x_2,x_3,t)$, (i,j= 1,2,3) in each layer of the laminate then become functions $u_i(x_1,x,t)$ and $t_{ij}(x_1,x,t)$ of x_1,t and $x = x_2 \sin\gamma + x_3 \cos\gamma$, only. The stress components are related to the displacement components through the stress-strain relations appropriate to each layer, and these relations are given in detail by Baylis and Green [4]. These involve the density ρ, and squared wave speeds c_1^2, c_2^2, c_3^2 derived from the elastic constants of the continuum (Green [2]), and employ the abbreviations $c = \cos\gamma$ and $s = \sin\gamma$. The stress components and displacement components must satisfy the equations of motion in each layer, together with continuity conditions at the interfaces between layers, traction free conditions on the bottom surface of the plate and the specified loading conditions on the upper surface.

In order to solve the problem, it is convenient to work with the quantities U,V,W,T_{ij}, which are obtained from the displacement components u_1,u_2,u_3 and the stress components t_{ij} respectively by taking Laplace transforms with respect to time t and Fourier transforms with respect to the variable x. Thus, U,V,W, and T_{ij} are functions of the coordinate x_1 normal to the plane of the plate only, but they also involve the Laplace transform parameter $\hat{s}$ and the Fourier transform parameter k. The equations of motion and stress-strain relations in each layer then reduce to a system of ordinary differential equations and algebraic relations to determine the transformed displacements and stresses within the layer as functions of x_1 and the interface continuity conditions become a system of algebraic equations relating the transformed quantities between one layer and the next. The solution of these equations using the propagator method is given in detail by Green and Baylis [6]. Here we quote their results for the transformed normal displacement components at the surfaces and derive expressions for the other transformed quantities, both at the surface and in the interior of the laminate. For a line load P(t) acting normal to the surface of an n-cell laminate (overall depth 4nh), the transformed normal displacement $U^{(0)}$ at the lower surface and $U^{(n)}$ at the upper surface are given by

$$U^{(0)} = \frac{\bar{P}(\hat{s})}{m_{12}(k,\hat{s})} \quad , \qquad U^{(n)} = \frac{m_{22}(k,\hat{s})}{m_{12}(k,\hat{s})}\,\bar{P}(\hat{s}) \tag{1}$$

where $\bar{P}(\hat{s})$ is the Laplace transform of P(t) and $m_{12}(k,\hat{s})$, $m_{22}(k,\hat{s})$ are known functions of the transform parameters $k,\hat{s}$, the number n, layer thickness h and elastic properties of the composite material. The elements m_{rs} (r,s=1,2) are expressed in terms of the components p_{ij} and q_{ij} (i,j=1,..4) of the propagator matrices in materials *1* and *2* respectively. For a tangential line load Q(t) on the upper surface, acting in the direction parallel to the x_2-axis, the corresponding displacement components are given by

$$U^{(0)} = \frac{\bar{Q}(\hat{s})}{n_{12}(k,\hat{s})} \quad , \qquad U^{(n)} = \frac{n_{22}(k,\hat{s})}{n_{12}(k,\hat{s})}\,\bar{Q}(\hat{s}) \quad . \tag{2}$$

Here $\bar{Q}(\hat{s})$ is the Laplace transform of Q(t), and n_{12} and n_{22} are related to m_{12}, m_{22} and the elements $p_{ij}(k,\hat{s})$ of the propagator matrix defined by Green and Baylis [6], by the equations

$$n_{12} = -\frac{p_{22}m_{12}}{p_{12}} \quad , \qquad n_{22} = m_{22} - \frac{p_{32}m_{12}}{p_{12}} \quad . \tag{3}$$

Equation (1) gives the transform of the normal component of displacement at the upper surface due to the specified normal line load. From the propagator solution it is possible to obtain expressions for the transform of the tangential displacement $V_1^{(n)}$ at the upper surface and the transformed components of stress. These are given by

$$V_1^{(n)} = \frac{p_{43}U_1^{(n)} - p_{41}\bar{P}(\hat{s})}{p_{44}} , \qquad (p_{44} \neq 0)$$

$$T_{22}^{(n)} = \rho c_2^2\left\{\left[1 - \frac{2c_2^2}{c_1^2}\right]\bar{P}(\hat{s}) + iks\left[1 - \frac{c_2^2}{c_1^2}\right]V_1^{(n)}\right\} ,$$

$$T_{23}^{(n)} = \rho c_3^2 ikcV_1^{(n)} , \qquad T_{13}^{(n)} = \rho c_3^2 ikcU_1^{(n)} , \tag{4}$$

$$T_{33}^{(n)} = -\rho c_3^2\left\{\frac{c_2^2}{c_1^2}\left[\bar{P}(\hat{s}) + 2iksV_1^{(n)}\right] - U_1^{(n)}\delta(x_1 - 2nh)\right\} .$$

In equation (4) the component $T_{13}^{(n)}$ relates to the limiting value approaching the surface from within the material and this stress component jumps discontinuously to zero on crossing the surface. The Dirac delta function term in the expression for $T_{33}^{(n)}$ gives the singularity in the reaction stress along the fibres in the surface, which is required in order to balance the shear stress discontinuity. (In the argument of the delta function, the origin of coordinates has been taken to be in the middle surface of the 2n ply laminate.) Results appropriate to the lower surface of the laminate may be derived from equations (4) on replacing $U_1^{(n)}$ by $U_1^{(0)}$, $V_1^{(n)}$ by $V_1^{(0)}$ and suppressing all the terms involving $\bar{P}(\hat{s})$.

It is possible to derive the displacement and stress transforms at any value of x_1 throughout the laminate. As an illustration of the application of these methods we calculate the transforms of both displacements and stresses at the interface between the top layer of material *1* and the remainder of the laminate. Writing $T = T_{11}/\rho c^2$, the propagator solution gives T_1 and U_1 at the interface as

$$T_1 = \left[s_{22} - \frac{s_{12}m_{22}}{m_{12}}\right]\bar{P}(\hat{s}) ,$$

$$U_1 = -\left[s_{21} - \frac{s_{11}m_{22}}{m_{12}}\right]\bar{P}(\hat{s}) , \tag{5}$$

where s_{ij} (i,j=1,2) are known functions of the parameters. Then the interface continuity conditions give $T_2 = T_1$, $U_2 = U_1$, together with $V_1 = V_2 = 0$ and $W_1 = W_2 = 0$. The tangential components of traction in material *1* at the interface are then given by

$$T_{12}^{(1)} = -\rho c_2^2\left[\frac{p_{21}T_1 + p_{23}U_1}{p_{22}}\right], \qquad (p_{22} \neq 0)$$

$$T_{13}^{(1)} = \rho c_3^2 ikcU_1 , \tag{6}$$

and the corresponding components in material *2* are

$$T_{12}^{(2)} = \rho c_3^2 iksU_1 ,$$

$$T_{13}^{(2)} = \rho c_2^2\left[\frac{q_{41}T_1 - q_{43}U_1}{q_{42}}\right], \qquad (q_{42} \neq 0) . \tag{7}$$

The discontinuities in these traction components across the interface are balanced by

singularities at the interface along the fibre direction in each material and combining these with the results derived from the transformed stress strain relations gives the in-plane stress components in the two materials. The results are

$$T_{22}^{(1)} = \rho c_2^2\left[1 - \frac{2c_2^2}{c_2^2}\right]T_1, \quad T_{23}^{(1)} = 0, \quad T_{33}^{(1)} = \frac{\rho c_3^2 c_2^2}{c_1^2} T_1 - \left[\frac{T_{13}^{(1)} - T_{13}^{(2)}}{ikc}\right]\delta(x^*),$$

$$T_{22}^{(2)} = -\frac{\rho c_3^2 c_2^2}{c_1^2} T_1 - \left[\frac{T_{12}^{(1)} - T_{12}^{(2)}}{iks}\right]\delta(x^*), \quad T_{23}^{(2)} = 0, \quad T_{33}^{(2)} = \rho c_2^2\left[1 - \frac{2c_2^2}{c_1^2}\right]T_1, \tag{8}$$

where the argument of the δ function is $x^* = x-(2n-1)h$, corresponding to the origin at the middle surface of the laminate. Results similar to those detailed in equations (5) - (8) may be obtained at any other interface of the laminate whilst at any interior point in any layer it is also possible to determine the non-zero in-plane displacement (V_1 or W_2). In the next section we consider the problem of inverting these transforms to give the required solutions.

3. TRANSFORM INVERSION

The techniques developed in Section 2 yield the transforms of the displacements and stresses throughout the laminate as known functions of the transform parameters k and $\hat{s}$ at any value of x_1. In order to determine the displacements and stresses as functions of the coordinate $x = x_3 \cos\gamma + x_2 \sin\gamma$, normal to the line load and of the time t, it is necessary to invert these transforms. Typical of the quantities to be considered is the transform of the normal displacement at the upper surface due to a normal line load, which is given by equation (1) in the form

$$\bar{U}^{(n)} = \frac{m_{22}(k,\hat{s})}{m_{12}(k,\hat{s})}\,\bar{P}(\hat{s}) \ .$$

Letting $u_1(2nh,x,t)$ denote the normal displacement on the upper surface $x_1 = 2nh$, due to a line load which consists of a unit delta function in time $P(t) = \delta(t)$, for which $\bar{P}(\hat{s}) = 1$, the displacement $u^P(x,t)$ corresponding to the transform (1) associated with any P(t) is then given as the convolution of P(t) with $u_1(2nh,x,t)$ in the form

$$u_1^P(x,t) = \int_0^t u_1(2nh,x,\tau)P(t-\tau)\,d\tau . \tag{9}$$

Accordingly we restrict attention to inverting the transform (1) with $\bar{P}(\hat{s}) = 1$, for which the formal solution is

$$u_1(2nh,x,t) = \frac{1}{4\pi^2 i}\int_{-\infty}^{\infty}\int_{\gamma-i\infty}^{\gamma+i\infty} \frac{m_{22}(k,\hat{s})}{m_{12}(k,\hat{s})}\, e^{\hat{s}t}\, e^{ikx}\, d\hat{s}\, dk \ . \tag{10}$$

The integral with respect to $\hat{s}$ may be evaluated in terms of the residues of the integrand at the zeros of the function $m_{12}(k,\hat{s})$ in the left half plane. The equation

$$m_{12}(k,i\omega) = 0 \tag{11}$$

is the dispersion equation for plane wave propagation in the laminate, corresponding to waves travelling in the direction of the normal to the line load under traction free conditions at the two surfaces of the plate. This equation has an infinite number of pairs of roots, $\omega_j = \pm\omega_j(k)$ (j=1,2,...), each pair corresponding to forward and backward travelling waves associated with one branch of the dispersion curve. In terms of these solutions, equation (10) becomes

$$u_1(2nh,x,t) = \frac{1}{2\pi}\int_{-\infty}^{\infty} dk \sum_{j=1}^{\infty} \left\{\frac{m_{22}(k,\hat{s})}{dm_{12}/d\hat{s}}\, e^{l(kx-l\hat{s}t}\right\}_{\hat{s} = \pm i\omega_j(k).} \tag{12}$$

Both $m_{12}(k,\hat{s})$ and $m_{22}(k,\hat{s})$ are even functions of $\hat{s}$ and equation (12) may be written as

$$u_1(2nh,x,t) = \frac{i}{\pi}\sum_{j=1}^{\infty}\int_{-\infty}^{\infty} R_j(k)\, \sin\omega_j(k)t\; e^{ikx}\, dk \tag{13}$$

where

$$\begin{aligned} R_j(k) &= \left[\frac{m_{22}(k,\hat{s})}{dm_{12}/d\hat{s}}\right]_{\hat{s} = +i\omega_j(k)} \\ &= -\left[\frac{m_{22}(k,\hat{s})}{dm_{12}/d\hat{s}}\right]_{\hat{s} = -i\omega_j(k)} . \end{aligned} \tag{14}$$

It may also be shown that $R_j(k)$ is an even function of k and equation (13) may be further simplified to give

$$u_1(2nh,x,t) = \frac{2i}{\pi}\sum_{j=1}^{\infty}\int_{0}^{\infty} R_j(k)\, \sin\omega_j(k)t\, \cos kx\, dk \tag{15}$$

Equation (4) contains an expression for $V_1^{(n)}$ which is valid provided $p_{44} \neq 0$ and which therefore has the same singularities as $U_1^{(n)}$ for the case $\bar{P}(\hat{s}) = 1$. It may be shown that p_{43}/p_{44} is an odd function of k and we may therefore express the tangential displacement $v_1(2nh,x,t)$ associated with a unit delta function normal line load as

$$v_1(2nh,x,t) = -\frac{2}{\pi}\sum_{j=1}^{\infty}\int_{0}^{\infty} h_j(k)R_j(k)\sin\omega_j(k)t\, \sin kx\, dk\ , \tag{16}$$

where $h_j(k)$ is the value of the ratio p_{43}/p_{44} evaluated at $\hat{s} = i\omega_j(k)$.
The formulae for the transforms of the stress components in equation (4) involve terms of the form $ikU_1^{(n)}$ and $ikV_1^{(n)}$ and these when inverted give $du_1(2nh,x,t)/dx$ and $dv_1(2nh,x,t)/dx$ respectively.

Equations (5) give the transformed normal displacement and normal component of traction at the interface between the top surface layer of material *I* and the rest of the laminate. These have the same singularities as the expression (1) and their inverses yield

$$\begin{aligned} u_1\left[(2n-1)h,x,t\right] &= \frac{2i}{\pi}\sum_{j=1}^{\infty}\int_{0}^{\infty} s_{11}(k)R_j(k)\, \sin\omega_j(k)t\, \cos kx\, dk, \\ t_{11}\left[(2n-1)h,x,t\right] &= -\frac{2}{\pi}\sum_{j=1}^{\infty}\int_{0}^{\infty} s_{12}(k)R_j(k)\, \sin\omega_j(k)t\, \sin kx\, dk, \end{aligned} \tag{17}$$

where we have used the fact that $s_{11}(k)$ is an even function of k and $s_{12}(k)$ an odd function of k. Equations (6), (7) and (8) then yield the remaining stress components on the two sides of the interface in a similar fashion, the resulting integrals being of the forms given in equations (17) but with different factors multiplying $R_j(k)$.

All the results derived in this section relate to the problem of the normal line load acting on the upper surface of the laminate. Results for the effect of the tangential line load may be obtained in a completely analogous way by starting with the solutions given

in equations (2) rather than using the solutions (1). Referring to equations (3), it may be seen that the zeros of the element n_{12}, which determine the singularities of the transforms, occur at the zeros of m_{12} and possibly at the zeros of p_{22}. A detailed examination of the product $p_{22}m_{12}$ shows, however, that this does not vanish at the zeros of p_{22} and therefore the singularities of these transforms occur on the same dispersion curves as for the normal line load problem. Thus all the inversion integrals associated with the tangential line load problem involve the residues $R_j(k)$ multiplied by some appropriate factor. Hence for both the normal and tangential line loads the problem of inverting the transforms reduces to evaluating an infinite sum of infinite integrals of the form

$$\sum_{j=1}^{\infty} \int_0^{\infty} f_j(k) R_j(k) \sin \omega_j(k) t \begin{Bmatrix} \sin kx \\ \cos kx \end{Bmatrix} dk \qquad (18)$$

where $f_j(k)$ is some factor arising from a function of k and $\hat{s}$ which is evaluated on the branch $\hat{s} = i\omega_j(k)$ of the dispersion curve.

The expression (18) consists of a sum of integrals, one along each branch of the dispersion curve. In general both the integration and summation have to be carried out numerically and we must therefore limit the range of integration to some finite interval $(0,\hat{k})$ and restrict the summation to a finite number of branches $j=1,\ldots,P$ of the dispersion curve. We then have to construct a computer programme to solve the dispersion equation

$$m_{12}(k, i\omega_j) = 0 \qquad (19)$$

numerically in order to obtain values of $\omega_j(k)$ along each of the P branches for values of k taken at M intervals $\Delta k = \hat{k}/M$ from $k=0$ to $k=\hat{k}$. It is also necessary to evaluate the residues $R_j(k)$ at each of these values of k for each of the branches $j=1,2,\ldots P$.

4. NUMERICAL METHODS

To carry out the numerical evaluation we choose the values for the material parameters that were previously employed by Green & Baylis [4] and which are derived from measurements carried out by Markham [8] on a carbon fibre/epoxy resin composite. For the inextensible model, these become $c_1^2/c_2^2 = 4.297$ and $c_3^2/c_2^2 = 2.301$. We must also specify the number N, of unit cells forming the laminate and the results reported here relate to the simplest case of N=1 although the computer programmes have been written to cope with the general case of any specified number N of unit cells. In order to obtain the dispersion equation (19) and the expression for the residues given in equation (14), we have made use of the algebraic manipulation programme REDUCE. The outputs from the REDUCE programme consist of a subroutine to evaluate $m_{12}(k,\hat{s})$ and a subroutine for $R(k,\hat{s}) = m_{22}/(dm_{12}/d\hat{s})$ from which to calculate the residues $R_j(k)$ and these subroutines are incorporated into the computer programme which solves the dispersion equation.

The computer programme to produce the solutions $\omega_j(k)$ to the dispersion equation $m_{12}(k,\hat{s}_j(k)) = 0$, where $\hat{s}_j(k) = i\omega_j(k)$, is based on the notion of fixing k, and then, starting from $\omega = 0$, marching up the ω-axis evaluating m_{12} at each step until the required number of zeros of m_{12} have been determined. A zero is indicated by a change of sign of m_{12} at two consecutive values of ω, and by reducing the step length, this zero can be determined to any given degree of accuracy.

Clearly, this method is open to error in that two changes of sign which occur within the same step length will be missed and a change of sign indicates the presence of an odd number of zeros, not necessarily just one. These two possibilities did in fact give rise to problems since adjacent harmonics do, on occasion, run very closely

together. In theory, the answer is simple - the step length has to be chosen sufficiently small! However, since a substantial number of harmonics are required, covering a very large set of values of k, the programme would then become excessively expensive in computer time.

A refinement introduced to save running time is to estimate a value of $\omega_j(k)$ and then proceed to a fine search for a zero in its locality. The programme is initialized by using the value for $\omega_j(0)$, derived by solving the dispersion equation at $k = 0$ analytically. It is then possible to use the history of the j^{th} harmonic to estimate the location of the j^{th} root under inspection. For each new value k_{i+1} of k the root corresponding to the fundamental mode, $j = 1$, is the first to be located and this is estimated by $\omega = \omega_1(k_i) - \epsilon$, where $\epsilon = 5\delta k$, and δk is the step length in k. This allows for the possibility of the dispersion curve having a negative gradient. The step length $h_1(k_{i+1})$ in ω is then taken as the minimum of 0.1ϵ and $0.1\{\omega_2(k_i) - \omega_1(k_i)\}$. Thus, if the previous history indicates that the fundamental mode and first harmonic are very close at k_i, the step length at k_{i+1} is chosen as a tenth of the gap at k_i. Otherwise, experience indicates that an increment of $\epsilon/10$ is sufficiently small.

For each of the remaining roots, $\omega_j(k_{i+1})$ for $j > 1$, the first estimate is based not only on the history of that particular harmonic, but also on the roots already located at k_{i+1} and is given by

$$\omega = \max\{\omega_j(k_1) - \epsilon, \quad \omega_{j-1}(k_{i+1}) + 0.1\, h_{j-1}(k_{i+1})\}. \tag{20}$$

That is, if the root of $\omega_j(k_i)$ is sufficiently far above the previous root at k_{i+1}, $\omega_{j-1}(k_{i+1})$, a substantial amount of computer time can be saved by stepping the first estimate of $\omega_j(k_{i+1})$ over this gap. The step length for locating this root is determined by

$$h_j(k_{i+1}) = \min\left\{\epsilon/10 \;,\; \frac{\omega_{j+1}(k_i)-\omega_j(k_i)}{10} \;,\; \frac{\omega_j(k_i)-\omega_{j-1}(k_i)}{10}\right\}. \tag{21}$$

This allows for the possibility of the j^{th} harmonic at k_i being very close to either the $(j+1)^{th}$ harmonic or the $(j-1)^{th}$ harmonic.

Once the step length h_j and a first estimate ω for $\omega_j(k_{i+1})$ have been established the procedure for locating the root $\omega_j(k_{i+1})$ is as follows: given k_{i+1} and ω, m_{12} can be evaluated. ω is then increased by the step length h_j and m_{12} recalculated with this new value of ω. We continue to increase ω by the step length until a change of sign of m_{12} is observed. The step length is then reduced by a factor of 10, and the process is repeated using the last value of ω before the change of sign occurred as a new estimate of the root. Once a change of sign has been re-established, the step length is reduced by a further factor of ten and the complete procedure repeated, with termination occurring when $\omega_j(k)$ has been determined to the given degree of accuracy.

Having obtained the solutions of the dispersion equation and the associated residues, we are now in a position to perform the numerical integrations and summation involved in inverting the transforms through expressions of the form (18). To do this, we restrict the range of summation from $j = 1$ to P and the interval of integration from $k = 0$ to $\hat{k}$ and rewrite the expression (18) in the approximate form

$$\sum_{j=1}^{P} \int_0^{\hat{k}} f_j(k)R_j(k)\, \sin \omega_j(k)t \begin{Bmatrix}\cos kx \\ \sin kx\end{Bmatrix} dk = \int_0^{\hat{k}} H(k,t) \begin{Bmatrix}\cos kx \\ \sin kx\end{Bmatrix} dk \;, \tag{22}$$

where

$$H(k,t) = \sum_{j=1}^{P} f_j(k)R_j(k)\, \sin \omega_j(k)t. \tag{23}$$

Of the two approximations involved in equation (22), the effect of restricting the summation to a finite number of roots (P) cannot be evaluated without some estimate of the contributions arising from the residues of the excluded branches and in general such an estimate is not available. The effect of restricting the integral to a finite range is to produce a function $\hat{F}(x,t)$ which is defined in terms of the actual signal $F(x,t)$ by

$$\hat{F}(x,t) = \int_{-\infty}^{\infty} F(y,t) \frac{\sin \hat{k}(x-y)}{(x-y)} \, dy, \tag{24}$$

The function $\hat{F}(t)$ defined in equation (24) is the convolution of the true signal $F(x,t)$ with the function $(\sin \hat{k}x)/x$ and exhibits the phenomenon of "windowing". This phenomenon produces a spurious oscillation of wavelength $2\pi/\hat{k}$ and in order to reduce the effect of the oscillation we have made use of the Hamming window function $s(k)$ defined by

$$s(k) = \alpha + (1-\alpha) \cos \left[\frac{k\pi}{\hat{k}} \right] , \tag{25}$$

where α is some parameter satisfying $0 < \alpha < 1$. The procedure is to replace the integrand over the finite range $(0,\hat{k})$ by the product of the integrand with $s(k)$ to give a new approximation $\hat{F}_H(x,t)$ given by

$$\hat{F}_H(x,t) = \alpha \hat{F}(x,t) + \frac{(1-\alpha)}{2} \left\{ \hat{F}(x - \frac{\pi}{\hat{k}}, t) + \hat{F}(x + \frac{\pi}{\hat{k}}, t) \right\} . \tag{26}$$

The convolution terms in the braces are each half a wavelength out of phase with the convolution $\hat{F}(x,t)$ and this serves to dampen out the oscillation. In evaluating our numerical results we have used the value $\alpha = 0.54$ recommended by Hamming [7]. Note that both $\hat{F}(x,t)$ and $\hat{F}_H(x,t)$ tend to the true signal as $\hat{k} \to \infty$. There is one further approximation required in order to perform the integration and this consists of replacing the integral by a finite sum of terms. This has been done using the trapezium rule, with interval length $\hat{k}/M$ and it can be shown that this procedure is equivalent to replacing the convolution integral $\hat{F}(x,t)$ defined by equation (24) by the convolution $\tilde{F}(x,t)$ defined by

$$\tilde{F}(x,t) = \frac{\hat{k}}{2M} \int_{-\infty}^{\infty} F(y,t) \frac{\sin \hat{k}(x-y) \cos \frac{\hat{k}}{2M} (x-y)}{\sin \frac{\hat{k}}{2M} (x-y)} \, dy . \tag{27}$$

The calculated result is then the Hamming function of this convolution and is given by

$$\tilde{F}_H(x,t) = \alpha \tilde{F}(x,t) + \frac{(1-\alpha)}{2} \left\{ \tilde{F}(x - \frac{\pi}{\hat{k}}, t) + \tilde{F}(x + \frac{\pi}{\hat{k}}, t) \right\} . \tag{28}$$

The convolution $\tilde{F}(x,t)$ tends to $\hat{F}(x,t)$ in the limit as M increases to infinity, but for finite values of M the function defined by equation (27) is periodic in x with wavelength $4\pi M/\hat{k}$ and the numerical integration procedure is therefore limited to values of x satisfying $0 \leq x < 4\pi M/\hat{k}$.

In performing the numerical integration we have chosen as unit of length the half thickness h of each ply and as unit of time the quantity h/c_1. For a given value of γ, the dispersion equation has been solved for eighteen modes (P=18) with values of kh ranging from zero to 20 ($\hat{k}$=20/h) in steps of 0.002, corresponding to M = 10,000. This gives rise to 180,000 values of $\omega_j(k)$ and an equal number of values of the residues $R_j(k)$ which form the data matrix for the numerical inversions. The procedure for this is to specify a value of t and to form the sums $H(k,t)$ appropriate to the particular displacement or stress being evaluated. Each sum $H(k,t)$ is multiplied by the corresponding value of the Hamming factor $s(k)$ and the product is stored. Using the

trapezium rule, the integral is then evaluted for a range of values of x from x = 0 to $x = c_1 t$ in steps of $\Delta x = 2\pi/\hat{k}$.

5. RESULTS

In this section we present a set of curves showing the variation of displacements and stresses at the outer surfaces of the plate as functions of the propagation distance x at various times. These results are derived by numerical integration along the dispersion curves and are presented here for propagation at the angle $\gamma = 60^0$ only. Calculation of each of these latter sets of results involves the use of 360,000 stored values for each angle of propagation γ and results for other angles of propagation will appear elsewhere.

The plots display the variation of displacements and stresses as functions of distance from the impact point at different values of the reduced time $T = c_1 t/h$. Figures 1a and 1b show the normal displacement u_1 at the upper and lower surfaces respectively.

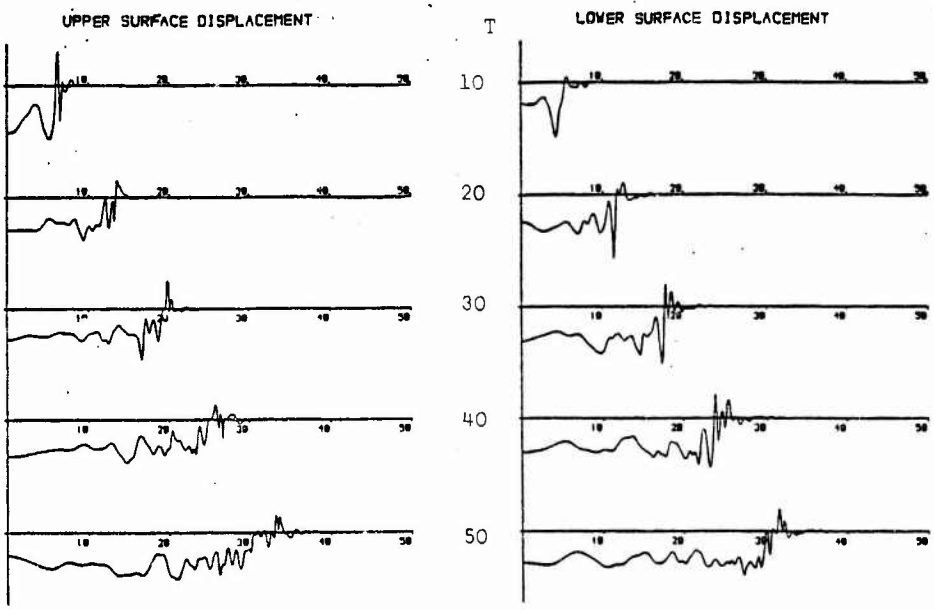

Figure 1a

Figure 1b

Each shows the variation with distance at times T = 10, 20, 30, 40, 50. Figures 2a and 2b show the upper and lower normal surface displacements at considerably larger times, namely T = 100, 200 and 500. The graphs indicate that the normal displacements on the upper and lower surfaces are nearly the same, which implies that the disturbance is mainly flexural. This is not surprising since we are considering an impact on the upper surface, which induces a mainly bending deformation of the plate.

The first arrivals shown in the figures occur at a disturbance of approximately $\frac{2}{3}T$. This corresponds to a wave speed of $\frac{2}{3}c_1$ and is identical with the speed of shear waves in the outer material. This result is consistent with the ghost velocity phenomenon discussed in [6]. Figures 3 – 6 inclusive, display the normal displacement u_1, tangential displacement u_2, the discontinuous shear traction t_{13} along the fibre direction and the in-plane shear stress component t_{23} respectively, all at time T = 40.

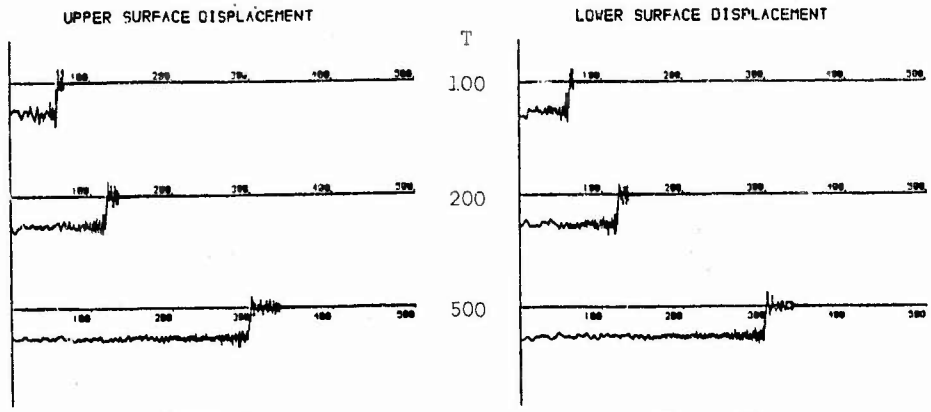

Figure 2a

Figure 2b

Each figure presents results at both the upper and lower surfaces, derived from using the transforms given in equation (4) at the upper surface and their equivalents at the lower surface. It may be seen from equations (4) that the in-plane stress components t_{22} and t_{33} have terms in the transforms which involve $kV_1^{(n)}$ and these terms may be evaluated directly from the stress term t_{23} by an appropriate scaling. The normal displacements, shown in Figure 3 are obtained by inverting the transform given by equation (1) using the

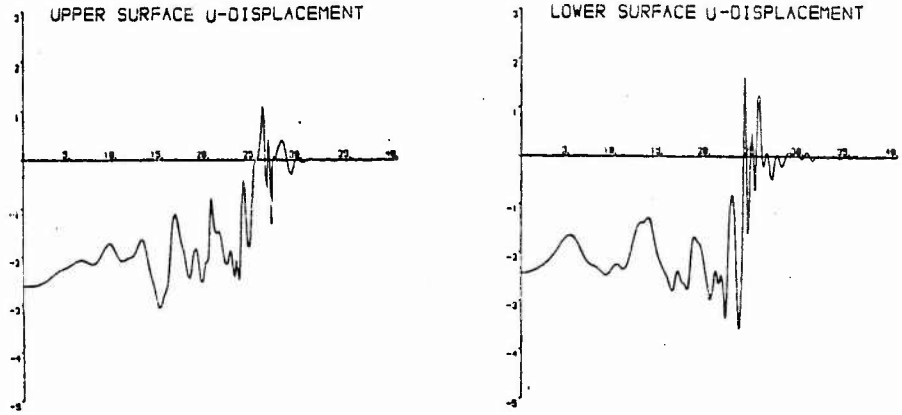

Figure 3

Hamming window. The results show little trace of a spurious oscillation and the windowing appears to be successful. The discontinuous tangential stress t_{13} shown in Figure 5 is in effect derived from this displacement by differentiation with respect to x. This serves to roughen the numerical results and there is now some indication of a superimposed oscillation. The tangential displaeement u_2 is obtained by inverting the first expression in equation (4) which involves multiplying the normal displacement transform by the factor p_{43}/p_{44}. The results shown in Figure 4 exhibit a considerable windowing effect, despite the use of the Hamming technique and this is further accentuated in Figure 6 since the in-plane tangential stress is essentially the x derivative of the tangential displacement.

On comparison of the results obtained on the upper surface with the corresponding results on the lower surface, we find that the disturbance on the upper surface travels approximately two units further than on the lower surface. This is a consequence of the fact that the effect of the impact has to travel through the plate thickness before it can affect the lower surface.

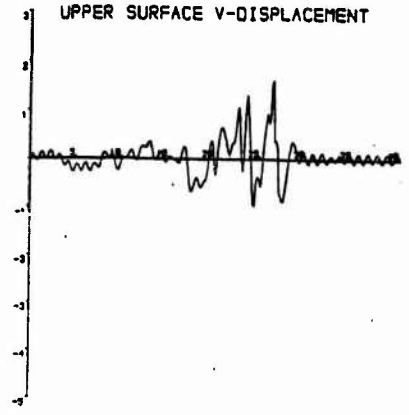

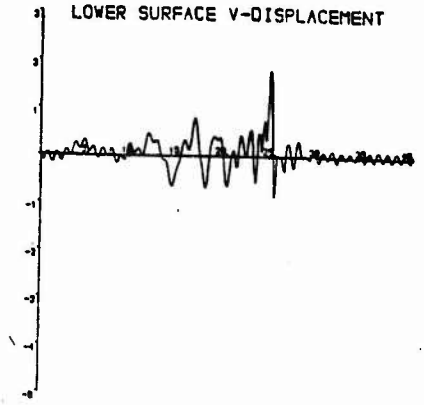

Figure 4

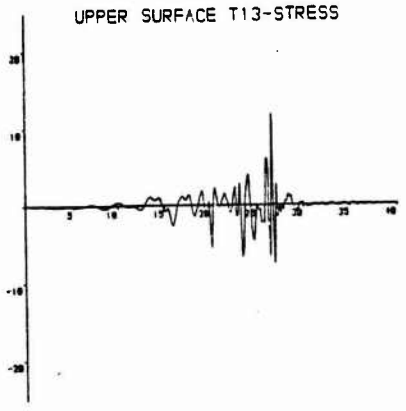

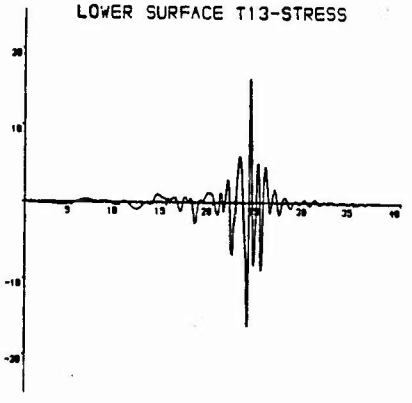

Figure 5

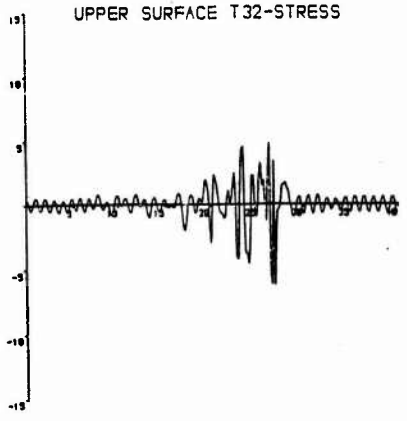

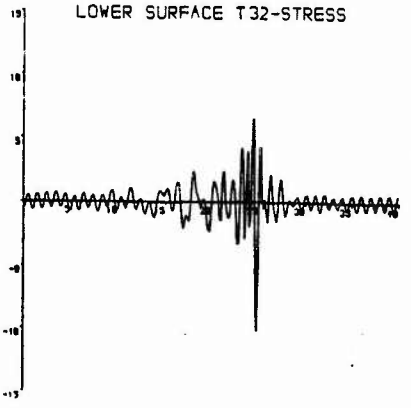

Figure 6

ACKNOWLEDGEMENTS

We take this opportunity to express our gratitude to Lt. Col. J.G.R. Hansen, U.S.A.F., E.O.A.R.D., for his support of this work through the award of grant AFOSR-86-0330. We also express our heartfelt thanks to Mrs. Anne Perkins for her patience and consideration in the typing of this work.

REFERENCES

[1] G. C. EVERSTINE and A. C. PIPKIN, 1971,
Z. Angew. Math. Phys. **22**, 825–834. Stress channelling in transversely isotropic elastic composites.

[2] W. A. GREEN, 1982, Quart. J. Mech. Appl. Math. **35**, 485–507.
Bending waves in strongly anisotropic elastic plates.

[3] W. A. GREEN and D. MILOSAVLJEVIĆ, 1985, Int. J. Solids & Structures, **21**, 343–353.
Extensional waves in strongly anisotropic elastic plates.

[4] E. R. BAYLIS and W. A. GREEN, 1986, J. Sound & Vibr. **110**, 1–26.
Flexural waves in fibre-reinforced laminated plates.

[5] E. R. BAYLIS and W. A. GREEN, 1986, J. Sound & Vibr. **111**, 181–190.
Flexural waves in fibre-reinforced laminated plates. part II.

[6] W. A. GREEN and E. R. BAYLIS, 1988, Proceedings of 3rd International Conference on Recent Adcances in Structural Dynamics. The contributions of high harmonics to transient waves in plates and laminates.

[7] R. W. HAMMING, 1977, Digital Filters, Prentice-Hall, London.

[8] M. F. MARKHAM, 1970, Composites 1, 145–149.
Measurement of the elastic constants of fibre composites by ultrasonics.

THE CONTRIBUTION OF HIGH-HARMONICS TO TRANSIENT WAVES IN PLATES AND LAMINATES

W. A. Green
Department of Theoretical Mechanics,
The University,
Nottingham, NG7 2RD, U.K.

and

E. Rhian Baylis
Department of Engineering
University of Leicester
Leicester LE1 7RH

Research sponsored by the Air Force Office of Scientific Research,
Air Force Systems Command, USAF under Grant Number AFOSR-86-0330.
The U.S. Government is authorised to reproduce and distribute
reprints for governmental purposes.

1. INTRODUCTION

The transmission of impact stress waves in plates and laminates is controlled by the dispersion curves for the propagation of plane harmonic waves subject to traction free conditions on the faces. There exists an infinite number of these dispersion curves, which relate phase velocity to wavelength, corresponding to the harmonics of the dispersion equation. Each of these harmonics will in general contribute to the transient motion but for a single plate the bulk of the disturbance is normally associated with the fundamental mode and the first two or three harmonics, see e.g. Jones [1]. This corresponds to a speed of propagation of the front which is considerably less than the speed of longitudinal waves in an infinite medium whereas it is known that the first arrivals travel with this speed. In order to obtain this result it is necessary to take into account the behaviour of the higher harmonics. The dispersion curves for high harmonics in a single plate of isotropic elastic material exhibit a series of plateaux and step regions (see Redwood [2]) with the phase velocity along the plateaux being slightly above the velocity of longitudinal waves but slowly decreasing with wavelength. This corresponds to a group velocity slighly below that of longitudinal waves. The cumulative effect of a large number of high harmonics can therefore produce an extended range of values of wavelengths travelling with this group velocity and it is these which give rise to the precursor signal.

In this paper we are concerned with the transmission of impact stress waves in a fibre-reinforced laminated plate. The plate is made up of 4n plies, each of depth h, with the reinforcement in each ply consisting of a family of parallel fibres lying in the plane of the ply. The plies are arranged in pairs with the fibre directions in alternate pairs being orthogonal to each other, forming a symmetric lay up of n unit cells, each having a $(0°/90°/90°/0°)$ configuration. We assume each ply to be of the same material and model the mechanical behaviour as that of a homogeneous transversely elastic continuum which is inextensible in the direction of transverse isotropy. This direction is taken to coincide with the fibre direction in each ply and the idealization of inextensibility is a mathematical convenience which is intended to reflect the property that the extensional modulus of the composite along the fibre direction can be up to 100 or more times that in the cross-fibre direction. A discussion of the implications and possible range of validity of both the continuum assumption and the idealization of inextensibility is contained in the paper by Baylis and Green [3] which is included in these proceedings.

We consider in particular a line load impact acting on the upper surface of the plate in such a way as to generate a plane wave disturbance travelling in the laminate with wave fronts parallel to the line load and orthogonal to the plane of the plies. In Section 2 we introduce a double transform of the displacement and stress components in

each of the plies and show that the equations of motion and stress–strain relations then yield a system of ordinary differential equations for the variation of these transformed quantities with depth in the laminate. These equations are solved in each layer using the propagator matrix method of Gilbert and Backus [4] and the solutions in adjacent plies are related to each other through the boundary conditions. This allows the transformed quantities at any point in the plate to be completely determined in terms of the transform of the impact load on the upper surface.

The procedure for inverting the transforms is outlined in Section 3 where it is shown that this entails solving the dispersion equation (relating frequency to wavenumber), associated with the propagation of plane harmonic waves in the laminate under traction free conditions at the surfaces. The complete inversion involves evaluating an infinite integral along each branch of this dispersion curve and summing the result over all the branches, which are infinite in number. In practice both the range of integration and the number of modes are finite and a discussion of the effects of the former is contained in paper [3]. Here we are concerned with the effect of the number of harmonics over which summation takes place and in particular with the contributions of the high harmonics to the disturbance. With this in mind, we include in Section 3 the results of the stationary phase approximation to the inversion integrals. These bring out the significance of the group velocity and its turning points in determining the disturbance at large times.

Finally, Section 4 contains plots of the dispersion curves and their associated group velocity curves, for propagation at an angle of 60^0 to the fibre direction in the outer material of a laminate consisting of a single unit cell. The higher harmonic dispersion curves exhibit plateau and step regions, similar to those of an isotropic plate, corresponding to relatively flat maxima of the group velocity curves. We also show plots of the upper surface displacements as functions of position at a given time, calculated using the first two modes, the first ten modes and the first eighteen modes of the dispersion curves. These bring out the contributions of the higher harmonics to the early arrivals and display the phenomenon of channelling of the disturbance within the core in the short wavelength/high frequency limit.

2. GOVERNING EQUATIONS AND PROPAGATOR SOLUTIONS

We consider a laminated plate composed of layers of the idealized fibre reinforced material which is inextensible in the fibre direction, the fibres being in the plane of the layers and with the fibre directions in adjacent layers being orthogonal to each other. We choose a Cartesian Coordinate system of axes with origin in the middle surface of one of the layers and with Ox_3 parallel to the fibre direction in that layer. Letting Ox_2 be parallel to the fibre direction in the adjacent layers then the normal to the laminate coincides with the x_1–axis. We shall be concerned with plane waves generated by a line load acting on the upper surface of the laminate along a line making an angle $(\pi/2-\gamma)$ with the x_3–axis. The resulting disturbance will generate a displacement vector $\underline{u}(x_1,x_2,x_3,t)$ of the form

$$\underline{u}(x_1,x_2,x_3,t) = \underline{u}(x_1,x,t) \quad , \tag{1}$$

where

$$x = x_3 \cos\gamma + x_2 \sin\gamma \quad , \tag{2}$$

which corresponds to a plane wave whose normal lies in the x_2x_3 plane at an angle $-\gamma$ to the x_3–axis. The components $t_{ij}(x_1,x_2,x_3,t)$ of stress in each layer of the laminate will likewise reduce to functions $t_{ij}(x_1,x,t)$ and these are given in terms of the strain components via the constitutive equations appropriate to each layer (see for example Baylis & Green [5]). Before proceeding further it is convenient to take the Laplace Transform in time and Fourier Transform with respect to the space variable x of both

the displacement components $u_i(x_1,x,t)$ and the stress components $t_{ij}(x_1,x,t)$. Thus we define displacement transforms U,V,W by

$$U(x_1,k,\hat{s}) = \int_{-\infty}^{\infty}\int_0^{\infty} u_1(x_1,x,t)e^{-\hat{s}t}e^{-ikx}\,dt\,dx\,,$$

$$V(x_1,k,\hat{s}) = \int_{-\infty}^{\infty}\int_0^{\infty} u_2(x_1,x,t)e^{-\hat{s}t}e^{-ikx}\,dt\,dx\,, \tag{3}$$

$$W(x_1,k,\hat{s}) = \int_{-\infty}^{\infty}\int_0^{\infty} u_3(x_1,x,t)e^{-\hat{s}t}e^{-ikx}\,dt\,dx,$$

and stress transforms $T_{ij}(x_1,k,\hat{s})$ by

$$T_{ij}(x_1,k,\hat{s}) = \int_{-\infty}^{\infty}\int_0^{\infty} t_{ij}(x_1,x,t)e^{-\hat{s}t}e^{-ikx}\,dt\,dx\,. \tag{4}$$

In a general elastic material the transforms of the constitutive equations and the stress equations of motion then yield a system of six first order ordinary differential equations for $U,V,W,T_{11},T_{12},T_{13}$, as functions of x_1, together with three equations to determine the remaining stress transforms T_{22},T_{23},T_{33} in terms of these six quantities. For the idealized inextensible material, however, the displacement transform in the fibre direction is identically zero and the reaction stress associated with the inextensibility constraint is not determined by the constitutive equations but is obtained from one of the stress equations of motion. Thus the equations reduce to four first order ordinary differential equations together with relations to determine the remaining stress transforms. Using the subscript 1 to denote the layers for which the fibre direction is parallel to the x_3-axis, the appropriate equations may be derived from those given in Baylis & Green [5]. The differential equations then have the form

$$\frac{dU_1}{dx_1} = \frac{c_2^2}{c_1^2}T_1 - \left[1 - \frac{2c_2^2}{c_1^2}\right]iksV_1\,,$$

$$\frac{dV_1}{dx_1} = S_1 - iksU_1\,,$$

$$\frac{dT_1}{dx_1} = \frac{(\hat{s}^2-k^2c^2c_3^2)}{c_2^2}U_1 - iksS_1\,, \tag{5}$$

$$\frac{dS_1}{dx_1} = \left[4k^2s^2\left(1-\frac{c_2^2}{c_1^2}\right) + \frac{k^2c^2c_3^2+\hat{s}^2}{c_1^2}\right]V_1 - iks\left[1-\frac{2c_2^2}{c_1^2}\right]T_1\,,$$

where $T_1 = \frac{T_{11}}{\rho c_2^2}$, $S_1 = \frac{T_{12}}{\rho c_2^2}$, $c = \cos\gamma$ and $s = \sin\gamma$.

The inextensibility constraint becomes

$$W_1 = 0\,, \tag{6}$$

and the stress transforms are given by

$$T_{22} = \rho(c_1^2-2c_2^2)\frac{c_2^2}{c_1^2}T_1 + iks\rho 4c_2^2\left[1-\frac{c_2^2}{c_1^2}\right]V_1 ,$$

$$T_{23} = \rho c_3^2 ikc\, V_1 , \qquad T_{31} = \rho c_3^2 ikc\, U_1 , \tag{7}$$

$$T_{33} = -\rho\frac{c_3^2c_2^2}{c_1^2}(T_1 + 2iks\, V_1) .$$

In equations (5) and (7), ρ is the density of the continuum and c_1^2, c_2^2, c_3^2 are squared wave speeds derived from the elastic constants of the continuum (Green [6]).

The solution of the differential equations (4) may be written in terms of the propagator matrix $\underline{P}(x_1-\bar{x}_1)$ in the form

$$\underline{Y}(x_1) = \underline{P}(x_1-\bar{x}_1)\underline{Y}(\bar{x}_1) , \tag{8}$$

where $\bar{x}_1$ is some fixed value of x_1 within the layer and x_1 is any other value in the same layer, $\underline{Y}(x_1)$ is the vector $(T_1(x_1), S_1(x_1), U_1(x_1), V_1(x_1))^T$ where T denotes the transpose, and the components of the 4×4 matrix $\underline{P}$ are given in Table 1.

$$\underline{P}(h) = \begin{pmatrix} \alpha C_1+(1-\alpha)C_2 & \alpha s\frac{S_1}{p_1}+(1-\alpha)\frac{p_2S_2}{s} & -\frac{2\alpha^2s^2S_1}{(1-\alpha)p_1}+(1-\alpha)2p_2S_2 & 2\alpha s(C_1-C_2) \\ (1-\alpha)\frac{p_1S_1}{s}+\frac{\alpha sS_2}{p_2} & (1-\alpha)C_1+\alpha C_2 & -2\alpha s(C_1-C_2) & 2(1-\alpha)p_1S_1-\frac{2\alpha^2s^2S_2}{(1-\alpha)p_2} \\ -\frac{(1-\alpha)}{2}\left(\frac{p_1S_1}{s^2}-\frac{S_2}{p_2}\right) & -\frac{(1-\alpha)}{2s}(C_1-C_2) & \alpha C_1+(1-\alpha)C_2 & -(1-\alpha)\frac{p_1S_1}{s}-\frac{\alpha sS_2}{p_2} \\ \frac{(1-\alpha)}{2s}(C_1-C_2) & \frac{(1-\alpha)}{2}\left(\frac{S_1}{p_1}-\frac{p_2S_2}{s^2}\right) & -\frac{\alpha sS_1}{p_1}-(1-\alpha)\frac{p_2S_2}{s} & (1-\alpha)C_1+\alpha C_2 \end{pmatrix}$$

TABLE 1 Elements of the propagator matrix P(h).

The terms appearing in the matrix are defined by $s = \sin\gamma$, $c = \cos\gamma$

$S_1 = \sinh p_1kh$, $C_1 = \cosh p_1kh$, $S_2 = \sinh p_2kh$, $C_2 = \cosh p_2kh$.

$$p_1^2 \frac{(c_1^2s^2+c_3^2c^2-v^2)}{c_1^2} , \quad p_2^2 = \frac{(c_2^2s^2+c_3^2c^2-v^2)}{c_2^2} , \quad v^2 = -\frac{\hat{s}^2}{k^2} , \quad \alpha = 1-\frac{2c_2^2s^2}{(v^2-c_3^2c^2)}$$

Using subscript 2 to denote the transformed quantities within a layer of material with the fibre direction parallel to the x_2-axis, the constraint condition gives

$$V_2 = 0 , \tag{9}$$

and the equations equivalent to (5) involve U_2, W_2, T_2 and R_2 where $R_2 = T_{13}/\rho c_2^2$. Letting $\underline{Z}(x_1)$ denote the vector $(T_2,R_2,U_2,W_2)^T$ the solution of these equations is given by

$$\underset{\sim}{Z}(x_1) = \underset{\sim}{Q}(x_1 - \hat{x}_1)\underset{\sim}{Z}(\hat{x}_1) \tag{10}$$

where $\hat{x}_1$ is some fixed value of x_1 within the layer and x_1 is any other value in the same layer. The components of the 4 × 4 propagator matrix $\underset{\sim}{Q}$ may be derived from those of $\underset{\sim}{P}$ by the substitutions given in Table 2.

$p_1 \to q_1$,	$p_2 \to q_2$,	$\alpha \to \hat{\alpha}$,	$s \to c$,	
$S_1 \to \hat{S}_1$,	$C_1 \to \hat{C}_1$,	$S_2 \to \hat{S}_2$,	$C_2 \to \hat{C}_2$,	

TABLE 2 Transformation taking elements p_{ij} into q_{ij}.

The terms appearing in the table are defined by

$$q_1^2 = \frac{(c_1^2c^2 + c_3^2s^2 - v^2)}{c_1^2}, \quad q_2^2 = \frac{(c_2^2c^2 + c_3^2s^2 - v^2)}{c_2^2}, \quad \hat{\alpha} = 1 - \frac{2c_2^2c^2}{(v^2 - c_3^2s^2)},$$

$$\hat{S}_1 = \sinh q_1 kh, \quad \hat{C}_1 = \cosh q_1 kh, \quad \hat{S}_2 = \sinh q_2 kh, \quad \hat{C}_2 = \cosh q_2 kh.$$

Equations (8) and (10) yield the solution of the governing equations in individual layers of material with fibres parallel o the x_3-axis and the x_2-axis respectively. In order to obtain the solution in a multi-layered laminate it is necessary to satisfy the appropriate conditions at the upper and lower surfaces as well as continuity conditions at the interfaces. In general, the conditions at the interface between two dissimilar elastic materials which are bonded together requires continuity of all three displacement components and the three components of traction across the interface. In terms of the transformed quantities these continuity conditions are

$$U_1 = U_2, \quad V_1 = V_2, \quad W_1 = W_2, \quad T_1 = T_2, \quad S_1 = S_2, \quad R_1 = R_2 . \tag{11}$$

For the idealized inextensible material, however, it has been shown by Baylis and Green [5] that there exists the possibility of a discontinuity in the tangential component of stress parallel to the fibre direction across any surface in the material and in particular this allows a discontinuity in S_2 in material *2* at any interface or free boundary in these materials. Thus at an interface between materials *1* and *2* conditions (11) reduce to

$$U_1 = U_2, \quad T_1 = T_2, \quad V_1 = 0, \quad W_2 = 0, \tag{12}$$

the last two conditions being a consequence of the inextensibility constraints applied to the displacement continuity conditions.

We take as our unit cell, a layer of thickness 2h of material *1* sandwiched between two layers each of thickness h of material *2* and we assume that this cell is embedded in a repeating pattern. Imposing the interface constraint condition $V_1 = 0$ at the upper and lower surface of material *1* allows us to express all the displacement and stress transforms inside that material in terms of the components of the vector $\underset{\sim}{X} = (T\ U)^T$ at some fixed surface x_1 = constant. Since the unit cell is embedded in a repeating pattern we can regard each of the outer layers of the unit cell as one half of a layer of thickness 2h of material *2* sandwiched on each side by material *1*. Then the constraint conditions $W_2 = 0$ which must be satisfied at the interfaces again allows us to express the transforms within material *2* in terms of the vector $\underset{\sim}{X}$ at some ed value of x_1 in material *2*. Combining these then leads to a relation between the value $\underset{\sim}{X}^{(B)}$ at the lower surface of the unit cell and the value $X^{(A)}$ at the upper surface in the form

$$\underset{\sim}{X}^{A} = \underset{\sim}{D}\ \underset{\sim}{X}^{(B)} \tag{13}$$

where the components d_{rs} (r,s= 1,2) of the 2 × 2 matrix $\underset{\sim}{D}$ are expressed in terms of the components of the propagators $\underset{\sim}{P}(h)$ and $\underset{\sim}{Q}(h)$ for layers of depth h of materials *1* and *2* respectively. Applying equation (13) to a sequence of (n−1) unit cells then gives

$$\underset{\sim}{X}^{(n-\frac{1}{2})} = \underset{\sim}{D}^{(n-1)}\ \underset{\sim}{X}^{(\frac{1}{2})}$$

$$= \frac{(\lambda_1^{n-1}-\lambda_2^{n-1})\underset{\sim}{D}\ \underset{\sim}{X}^{(\frac{1}{2})} - \lambda_1\lambda_2(\lambda_1^{n-2}-\lambda_2^{n-2})\underset{\sim}{X}^{(\frac{1}{2})}}{(\lambda_1-\lambda_2)}\ , \tag{14}$$

where we have used the Cayley–Hamilton theorem to express $\underset{\sim}{D}^{n-1}$ in terms of $\underset{\sim}{D}$, $\underset{\sim}{I}$ and the eigenvalues λ_1, λ_2 of $\underset{\sim}{D}$. Equation (14) refers to a set of (n−1) unit cells assumed to be embedded in a repeating pattern so that the constraint conditions arising from inextensibility is operative on every layer of thickness 2h of both material *1* and material *2*. In order to consider wave motion in a laminate of finite depth 4nh, it is necessary to encase the (n−1) unit cells in two half cells, each consisting of an inner layer of material *2* and an outer layer of material *1*. Then each of the layers of material *2* is still constrained by the inextensibility condition imposed by the outer layer of material *1* and the expressions previously derived for the transmission through material *2* may again be employed in these layers. Each of the outer layers (of thickness h) of material *1* at the top and bottom of the complete plate must be treated separately. Each is subject to the constraint $V_1 = 0$ at the interface with material *2* and it will be assumed that the tangential component of traction S_1 vanishes at the outer surface. These two conditions allow the transforms within these layers to be expressed in terms of the vectors $\underset{\sim}{X}$, as before, though the expressions differ from those relevant to material *1* when it is embedded in a unit cell. (Details of the relations are given in the paper by Green and Baylis [7].) Applying these gives for the overall laminate

$$\underset{\sim}{X}^{(n)} = \underset{\sim}{M}\ \underset{\sim}{X}^{(0)} \tag{15}$$

where $\underset{\sim}{X}^{(0)}$ and $\underset{\sim}{X}^{(n)}$ denote the value of $\underset{\sim}{X}$ at the bottom surface and the top surface respectively and $\underset{\sim}{M}$ is the overall transmission matrix for the laminate.

If the upper surface of the laminate is subjected to a time dependent normal line load of the form

$$t_{11}(x_2,x_3,t) = P(t)\ \delta(x_3\cos\gamma + x_2\sin\gamma) = P(t)\ \delta(x)$$

where $\delta(x)$ is the Dirac delta function, and the lower surface of the laminate is traction free, then

$$\underset{\sim}{X}^{(n)} = \begin{bmatrix} \bar{P}(\hat{s}) \\ U_1^{(n)} \end{bmatrix}\ , \qquad \underset{\sim}{X}^{(0)} = \begin{bmatrix} 0 \\ U_1^{(0)} \end{bmatrix}\ , \tag{16}$$

where $\bar{P}(\hat{s})$ is the Laplace transform of P(t). Substituting from (16) into (15) then gives the displacement transform $U_1^{(0)}$ at the bottom surface in terms of the stress transform $\bar{P}(\hat{s})$ as

$$U_1^{(0)} = \frac{\bar{P}(\hat{s})}{m_{12}(k,\hat{s})}\ , \tag{17}$$

and the displacement transform $U^{(n)}$ at the upper surface is given by

$$U_1^{(n)} = \frac{m_{22}(k,\hat{s})}{m_{12}(k,\hat{s})}\ \bar{P}(\hat{s})\ . \tag{18}$$

Equations (17) and (18) relate to the normal line load acting on the upper surface

of the plate. We may examine the case of a tangential line load in a similar fashion. Because of the inextensibility constraint in the x_3-direction at the upper surface the component $t_{.3}$ of the tangential stress in the x_3-direction induces a singularity in the stress component t_{33} at the surface but transmits no disturbance into the material. It is only the tangential component t_{12} in the x_2-direction that produces a wave motion in the underlying laminate. To obtain the solution to this problem we proceed as above save that the conditions imposed on each of the outer layers of material *1* are that $V_1 = 0$ at the interface of the layer with material *2* and that $T_1 = 0$ at the outer boundary. Writing $\hat{\underset{\sim}{X}} = (S\ U)^T$ we can then express $\hat{\underset{\sim}{X}}^{(n)}$ at the upper surface of the laminate in terms of $\hat{\underset{\sim}{X}}^{(0)}$ at the lower surface in the form

$$\hat{\underset{\sim}{X}}^{(n)} = \underset{\sim}{N}\ \hat{\underset{\sim}{X}}^{(0)}, \tag{19}$$

where the elements of the matrix $\underset{\sim}{N}$ are known functions of the elements of $\underset{\sim}{P}(h)$ and $\underset{\sim}{Q}(h)$.

For a tangential line load with component t_{12} given by

$$t_{12}(x_2,x_3,t) = Q(t)\ \delta(x_3 \cos\gamma + x_2 \sin\gamma) = Q(t)\ \delta(x)$$

acting on the upper surface of the plate and with the lower surface traction free, equation (19) gives

$$\begin{aligned} U_1^{(0)} &= \frac{\bar{Q}(\hat{s})}{n_{12}(k,\hat{s})} \\ U_1^{(n)} &= \frac{n_{22}(k,\hat{s})\bar{Q}(\hat{s})}{n_{12}(k,\hat{s})} \end{aligned} \tag{20}$$

where $\bar{Q}(\hat{s})$ is the Laplace transform of $Q(t)$ and $U_1^{(0)}$, $U_1^{(n)}$ are the transforms of the normal displacements on the lower and upper surfaces respectively. The components n_{12} and n_{22} of the matrix $\underset{\sim}{N}$ may be expressed in terms of the components of $\underset{\sim}{M}$ and the propagator $\underset{\sim}{P}(h)$ in the form

$$n_{12} = -\frac{p_{22}m_{12}}{p_{12}}, \qquad n_{22} = m_{22} - \frac{p_{32}m_{12}}{p_{12}}. \tag{21}$$

Combining equations (20) linearly with (17) and (18) gives the solution for an arbitrary line load on the upper surface of the plate.

3. INVERSION OF TRANSFORMS

The propagator method developed in Section 2 yields expressions for the transformed displacement and stress components at any position in the laminate and it is necessary to invert these transforms in order to recover the solutions. As an example of the inversion procedure we consider the normal component of displacement $u_1(2nh,x,t)$ at the upper surface $x_1 = 2nh$ as a function of x and t due to a line load $P(t) = \delta(t)$. The transform is then given by equation (18) with $\bar{P} = 1$ and the formal solution is

$$u_1(2nh,x,t) = \frac{1}{4\pi^2 i}\int_{-\infty}^{\infty}\int_{\gamma-i\infty}^{\gamma+i\infty} \frac{m_{22}(k,\hat{s})}{m_{12}(k,\hat{s})}\, e^{\hat{s}t}\, e^{ikx}\, d\hat{s}\, dk. \tag{22}$$

The integral with respect to $\hat{s}$ may be evaluated in terms of the residues of the integrand at the zeros of the function $m_{12}(k,\hat{s})$ in the left half plane. The equation

$$m_{12}(k,i\omega) = 0$$

is the dispersion equation for plane wave propagation in the laminate, corresponding to waves travelling in the direction of the normal to the line load under traction free conditions at the two surfaces of the plate. This equation has an infinite number of pairs of roots, $\omega_j = \pm\omega_j(k)$ (j=1,2,...), each pair corresponding to forward and backward travelling waves associated with one branch of the dispersion curve. In terms of these solutions, equation (22) may be written in the form

$$u_1(2nh,x,t) = \frac{1}{2\pi} \sum_{j=1}^{\infty} \int_{-\infty}^{\infty} R_j(k) \left[e^{i(kx-\omega_j t)} - e^{i(kx+\omega_j t)} \right] dk \qquad (23)$$

where $R_j(k)$ is the residue of m_{22}/m_{12} at $\xi = i\omega_j(k)$. The terms on the right hand side of equation (23) involve integration along each branch of the dispersion curve and a summation over all the branches. A detailed account of the approximate numerical evaluation of this expression is contained in [3]. Here we give a brief derivation of the asymptotic solution at large times, using the method of stationary phase.

Writing the Integrals which appear in equation (23) in the form

$$\int_{-\infty}^{\infty} R_j(k)\, e^{i(kx-\omega_j t)}\, dk = \int_{-\infty}^{\infty} R_j(k)\, e^{-it\theta_j}\, dk \ ,$$

where

$$\theta_j = (\omega_j(k) - k\,x/t),$$

the rapid oscillation produced by the exponential term for small changes in k (and therefore θ_j) at large values of t produces cancellation of the integrands, except for those values of k for which $d\theta_j/dk$ is zero. The major contribution to the integral then comes at those values k_g of k for which θ_j is stationary and which are given by solving the equation

$$C_j(k_g) = x/t \ , \qquad (24)$$

where $C_j(k) = d\omega_j/dk$ is the group velocity on the j^{th} branch of the dispersion curves. For a specified value of t, equation (24) determines one or more values of k_g at any given value of x and the contribution from the integral at that value of x and t is then given approximately by

$$\left[\frac{2\pi i}{t \left(\frac{d^2\omega_j}{dk^2} \right)_g} \right]^{\frac{1}{2}} R_j(k_g)\, e^{i(k_g x-\omega_j(k_g)t)},$$

provided $d^2\omega_j/dk_g^2 \neq 0$. At the stationary points of the group velocity, $dC_j/dk = d^2\omega_j/dk^2 = 0$, this result breaks down and the approximation must be carried to higher order, giving the result

$$2\pi \left[\frac{2}{t \left(\frac{d^3\omega_j}{dk^3} \right)_g} \right]^{\frac{1}{3}} R_j(k_g)\, e^{i(k_g x-\omega_j(k_g)t)} Ai(v), \qquad (25)$$

where Ai(v) is the Airy function and

$$v = [x - C_j(k_g)t] \left[2/t \left(\frac{d^3\omega_j}{dk^3} \right)_g \right]^{\frac{1}{3}} .$$

Thus the stationary phase approximation at ordinary points of the group velocity curve shows that the long time solution decays as $t^{-\frac{1}{2}}$ whereas at maxima and minima of the group velocity the decay goes more slowly as $t^{-1/3}$. These maxima and minima are the points corresponding to the wave fronts and it is these wave front solutions, given by equation (25), which dominate at large times. A detailed discussion of these phenomena for a single plate of isotropic elastic material is given in the paper by Jones [1].

4. RESULTS

The results we present in this section are in the form of graphs and fall into three sets. The first set consists of the dispersion curves, relating the scaled frequency $\omega h/c_2$ to the non-dimensional wave number kh for values of the angle of propagation $\gamma = 90^0$ and $\gamma = 60^0$. The dispersion curves together with their associated residues provide the fundamental information required to invert the transforms, but we have seen in Section 3 that the long time solution is governed by the group velocity curves and in particular that the wave fronts are related to the maxima and minima of the group velocity. Our second set of results displays a selection of group velocity at $\gamma = 60^0$. Finally, we show the variation of the normal component of displacement at the upper surface as a function of x at time $t = 40h/c_1$, calculated for $\gamma = 60^0$, using the 2 fundamental modes, the first 10 modes and the first 18 modes of the dispersion curves.

The laminate with which we are dealing consists of an arrangement of 4 plies which is symmetric about the middle surface. It may be shown that, in consequence, the dispersion equation factorizes into two distinct equations, one associated with the symmetric (longitudinal) motion of the plate and the other with the antisymmetric (flexural) motion. The dispersion curves for the fundamental modes of these two equations have been examined in detail by Baylis [8] and Baylis and Green [5],[9]. They show that the limiting velocity of short waves (large kh) propagating at angle γ is either the velocity of Rayleigh type surface waves at angle γ in the outer material or of shear waves at angle γ in the inner material according as to whether γ is less than or greater than some critical value γ_c, which, for the parameters employed here, is 46.3^0. The limiting short wavelength velocity of all the other harmonics is either the velocity of shear waves at angle γ in the outer material or the velocity of shear waves at an angle γ in the inner material, according as to whether γ is less than or greater than 45^0. These are the speeds $v_{1s} = (c_3^2c^2+c_2^2s^2)^{\frac{1}{2}}$ in the inner material (material *1*) and $v_{2s} = (c_3^2s^2+c_2^2c^2)^{\frac{1}{2}}$ in the outer material (material *2*) at which $p_2 = 0$ and $q_2 = 0$ respectively. We can also associate with each material a dilatational wave speed $v_{1d} = (c_1^2s^2+c_3^2c^2)^{\frac{1}{2}}$ and $v_{2d} = (c_1^2c^2+c_3^2s^2)^{\frac{1}{2}}$ at which $p_1 = 0$ and $q_1 = 0$, respectively. For values of $\gamma < 45^0$ we have that $v_{1d} < v_{2d}$ but $v_{1s} > v_{2s}$ with the inequalities reversed for $\gamma > 45^0$. (Note that $v_{1d} \geq v_{1s}$ and $v_{2d} \geq v_{2s}$ for all γ.) On any branch of a dispersion curve at points where the phase velocity $v = \omega/k$ is greater than the supremum (v_{1d}, v_{2d}) all of p_1, p_2, q_1, q_2 are pure imaginary and the solutions correspond to progressive waves in all regions. As the phase velocity drops below the supremum (v_{1d}, v_{2d}) either p_1 or q_1 becomes real and the associated dilatational wave motion is evanescent. Continued reduction in v makes both p_1 and q_1 real, corresponding to evanescent dilatational disturbances in both materials and as v decreases further with increasing k the supremum (v_{1s}, v_{2s}) is reached making either p_2 or q_2 real and the motion subsequently involves a progressing shear wave in one material with all the other waves being evanescent.

Figure 1 shows a total of 26 branches (13 each of the symmetric and antisymmetric modes) of the dispersion curves for propagation at the angle $\gamma = 90^0$. All modes except the fundamental mode of the antisymmetric motion exhibit a cut-off frequency in the long wavelength limit $kh \to 0$. A striking feature of the graph is the existence of the two clear ghost lines brought about by the osculation of the branches. (These are particularly clear when the graph is viewed at almost grazing incidence). These ghost lines have slopes $\omega/k = c_1$ and $\omega/k = c_2$, which correspond to $v = v_{1d}$ and $v = v_{2d} = v_{2s}$ respectively at $\gamma = 90^0$. As the dispersion curves approach the first ghost line from the left they exhibit the plateau and step phenomenon described by

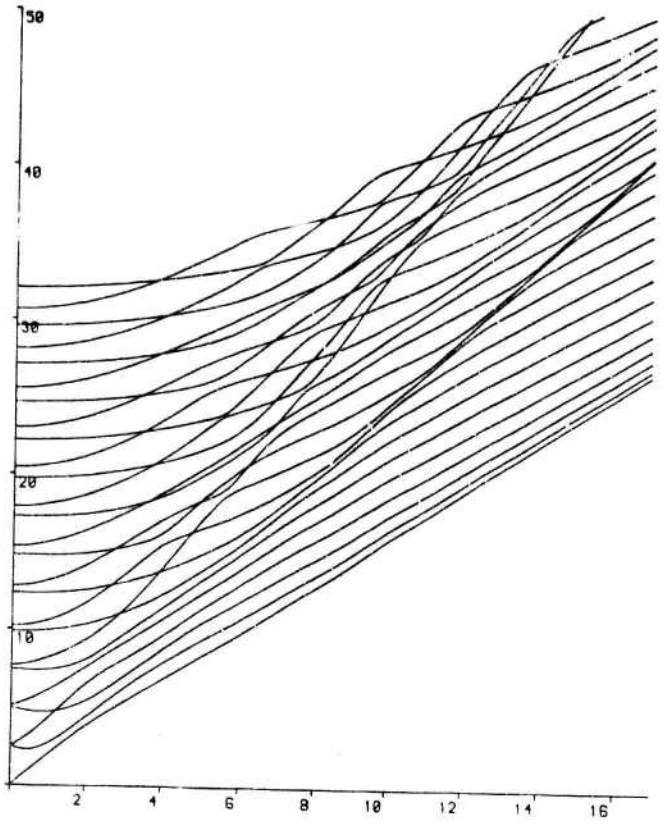

Figure 1

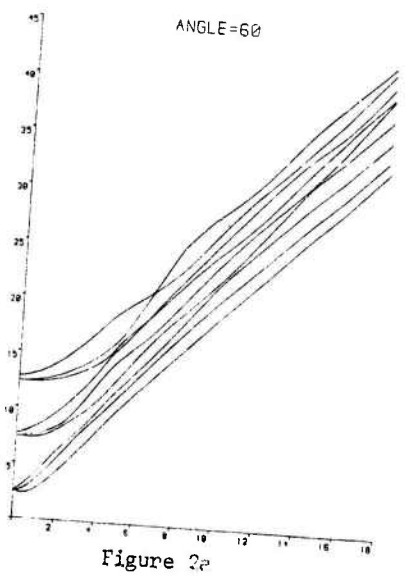

Figure 2a

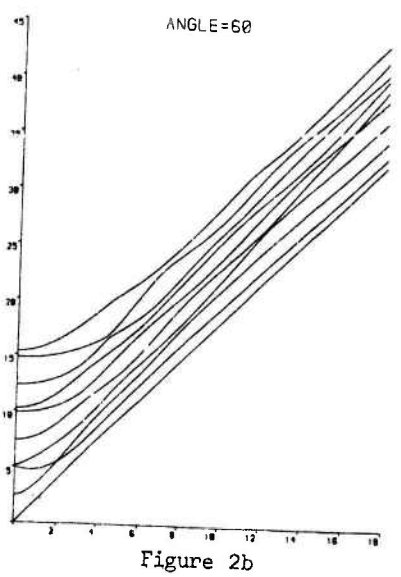

Figure 2b

Redwood [2]. Along the plateaux the curves are almost parallel to the ghost line, with the phase velocity and group velocity virtually constant at the value given by the slope of the ghost line. On the steps the phase velocity exhibits a small but sudden drop, with an associated drop in the group velocity, either ending up on the next plateau, if still to the left of the ghost line, or passing through and moving rapidly towards the second ghost line, where the phenomenon is repeated. On crossing the second ghost line the dispersion curves are virtually parallel, with the slope $\omega/k = c_2$, as they tend to the limiting velocity v_{1s} of shear waves in the inner material as $kh \to \infty$. Figure 2 contains two sets of dispersion curves, set (a) corresponding to symmetric modes and set (b) to antisymmetric modes at angle 60^0. As in Figure 1, all the branches except the fundamental antisymmetric mode (curves (b)), exhibit a cut-off frequency in the long wavelength limit $kh \to 0$. The curves again display the ghost lines through not to such a marked extent as in Figure 1 since the number of curves is now either 9 or 10 in each figure. Despite this, it is still possible to identify three ghost lines in Figure 2 as opposed to two in Figure 1 since at $\gamma = 90$ two of the 4 speeds v_{1d} , v_{2d} , v_{1s} , v_{2s} become equal.

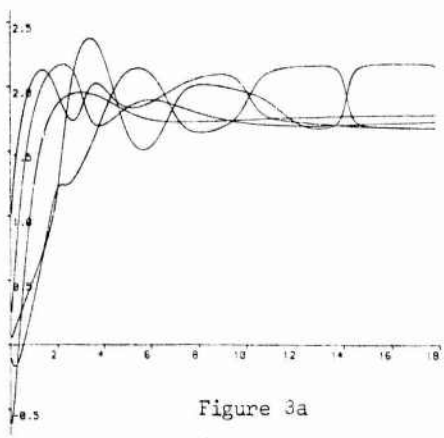

Figure 3a

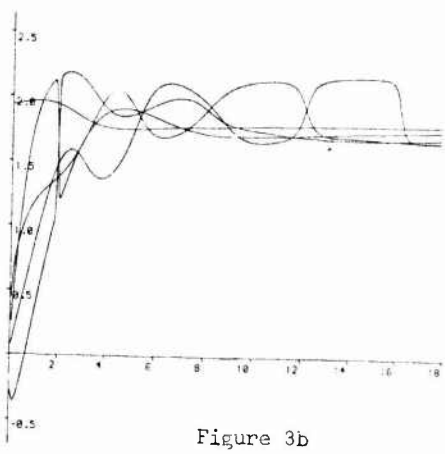

Figure 3b

Figures 3 shows graphs of the group velocity C_g, against kh. These have been obtained by numerical differentiation of the dispersion curves, using a central difference formula. Figure 3a shows the first five harmonics of the symmetric modes at $\gamma = 60^0$ and Figure 3b gives the first five harmonics of the antisymmetric mode for the same angle. At this angle of propagation we have $v_{1d} = 3.06$, $v_{2d} = 2.62$, $v_{2s} = 2.20$ and $v_{1s} = 1.81$. None of our curves approaches the value of v_{1d} which is not surprising since it may be seen from Figure 2 that the first ghost line is associated with harmonics of order greater than five. There is one of the five curves of Figure 3a which has a maximum at $C_g = 2.4$, this being the highest of the five harmonics which may be seen from 2a to have a plateau close to the second ghost line. Both Figures 3a and 3b possess harmonics with maxima close to $C_g = 2.20$, corresponding to the third ghost line associated with this angle of propagation. We have remarked in Section 3 that the local maxima and minima of the group velocity curves correspond to the wavefronts, which are expected to dominate the disturbance at large times. The higher harmonics shown in Figure 3 exhibit long flat maxima at the ghost velocities, which do not appear in the fundamental modes. It is pointed out by Jones [1] for an isotropic plate, that the residues associated with the higher harmonics are small compared with those arising from the lowest modes and our numerical results show this to be the case here also. Nevertheless, the total contribution arising from the succession of plateau regions associated with these high harmonics at the ghost velocities, will give rise to precursor waves which are not exhibited by the solution from the fundamental mode alone nor from approximate plate theories designed to reproduce the fundamental mode.

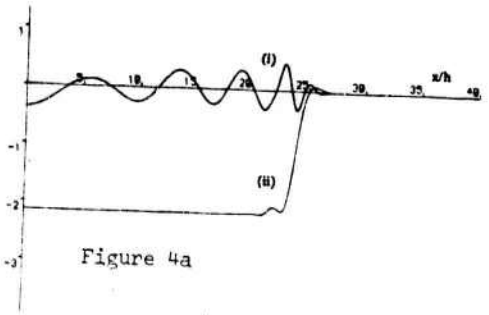

Figure 4a

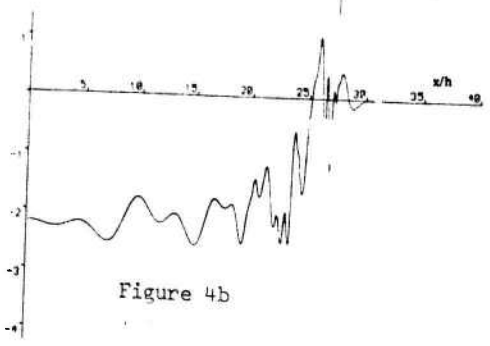

Figure 4b

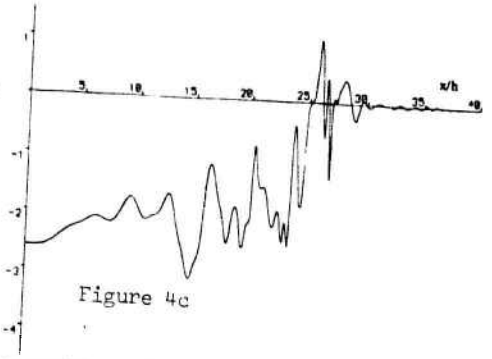

Figure 4c

In order to examine the effects of the harmonics, we have evaluated the contributions to the inversion integral (23) arising from the fundamental modes of the dispersion curves of both the symmetric and antisymmetric motion at $t = 40h/c_1$, as a function of x. These are shown in Figure 4a where the curve intersecting $x = 0$ at a value below -2 corresponds to the antisymmetric (bending) disturbance. The contribution to the component of normal displacement at the upper surface due to these two modes is obtained by subtracting the symmetric mode curve from the anti-symmetric. It may be seen that each curve corresponds to a disturbance which has propagated to $x \approx 27h$ corresponding to a speed of propagation $v \approx 2.19$ in the units which we are employing. These curves may be contrasted with that in Figure 4b which gives the upper surface normal displacement calculated using the first 5 modes of both the symmetric and anti-symmetric dispersion equations. Figure 4b shows the disturbance having travelled to $x \approx 30h$ corresponding to $v \approx 2.44$, which is close to the maximum group velocity to be seen in Figure 2. The curve shown in Figure 4c is calculated using 18 harmonics and shows a disturbance having travelled a distance of the order of $x \approx 36h$, corresponding to $v \approx 2.93$, which is close to the speed of longitudinal waves in the inner material. A feature of this curve which is not to be seen in either of the others is the oscillation (particularly evident between $x = 30h$ and $x = 40h$), which arises due to the "windowing" effect associated with cutting off the numerical integration at $k = 20$. It is evident from Figures 2a and 2b that each of the first five harmonics of the symmetric and antisymmetric motion have crossed the last ghost velocity curve before $k = 20$. The motion corresponding to these branches is therefore confined to a shear disturbance in the core at the cut-off value $k = 20$, so that no "windowing" is evident. For the higher harmonics, which are included in Figure 4c, this is not the case and these would make contributions to the upper surface displacement for values of k beyond the cut-off at $k = 20$, and hence give rise to the "windowing" effect.

ACKNOWLEDGEMENTS

We take this opportunity to express our gratitude to Lt. Col J.G.R. Hansen, U.S.A.F., E.O.A.R.D., for his support of this work through the award of grant AFOSR-86-0330. We also express our heartfelt thanks to Mrs. Anne Perkins for her patience and consideration in the typing of this work.

REFERENCES

[1] R. P. N. JONES, 1964, Quart. J. Mech. Appl. Math. 17, 401–421.
Transverse impact waves in a bar under conditions of plane–strain elasticity.

[2] M. REDWOOD, 1960, Mechanical waveguides, New York, Pergamon Press.

[3] E. R. BAYLIS and W. A. GREEN, 1988, Proceedings of 3rd International Conference on Recent Advances in Structural Dynamics. Impact stress waves in fibre–reinforced laminated plates.

[4] F. GILBERT and G. E. BACKUS, 1966, Geophysics, 31, 326–332.
Propagator matrices in elastic waves and vibration problems.

[5] E. R. BAYLIS and W. A. GREEN, 1986, J. Sound & Vibr. 110, 1–26.
Flexural waves in fibre–reinforced laminated plates.

[6] W. A. GREEN, 1982, Quart. J. Mech. Appl. Math. 35, 485–507.
Bending waves in strongly anisotropic elastic plates.

[7] W. A. GREEN and E. R. BAYLIS, 1986, Archives of Mechanics, 31, 301–317.
Wave propagation in laminated plates of inextensible transversely isotropic elastic material.

[8] E. R. BAYLIS, 1987, Ph.D. Thesis, University of Nottingham.
Wave propagation in fibre–reinforced laminates.

[9] E. R. BAYLIS and W. A. GREEN, 1986, J. Sound & Vibr. 111, 181–190.
Flexural waves in fibre–reinforced laminated plates, part II.

RESPONSE OF LAMINATED PLATES TO NON-STATIONARY RANDOM EXCITATION

by

Gabriel Cederbaum[1], Liviu Librescu[2] and Isaac Elishakoff[3]

1. ABSTRACT

The response of composite laminated plates subjected to non-stationary random excitation is determined. First-order shear deformation theory is used for the analysis of symmetric cross-ply and antisymmetric angle-ply plates, considered in this study. The time-dependent component of the forcing function is taken as a product of a well-defined, slowly varying envelope function, and a noise function, assumed to be white or narrow-band excitation.

2. INTRODUCTION

Some very important and practical dynamic loads are being treated as non-stationary random processes. Among these are earthquake ground motion, wind gusts, the launch phase of missile flight and pyrotechnic firing.

A recent concept for modelling the non-stationary process is Priestley's evolutionary spectra [1], in which it is defined in terms of a stationary process, whose intensity and frequency composition varying deterministically with time. However, the mathematical treatment becomes much easier by assuming uniform modulation of the frequency composition and a deterministic function for the time-dependent description of the intensity. Such a description was given by Shinozuka [2], and is more justified where the excitation is of a very short time interval.

The response of single and multi-degree of freedom systems to non-stationary random excitation is treated in [3-6], and [7-12], respectively, and that of continuous structures in [13-14]. The case of composite laminated plates under stationary random loads was studied in [15-17] and by the authors of this paper in [18-19]. To the best of our knowledge, the present treatment of the non-stationary counterpart of the above is the first of its kind.

The mean-square transverse displacement is obtained herein for symmetric cross-ply and antisymmetric angle-ply, simply-supported, rectangular plates, modelled within the first order shear deformation theory [20-21]. The deterministic function is taken in step, pulse or exponentially decaying terms. The stationary random process is either an ideal white noise or a correlated noise - narrow-band. Some approximate solutions are also presented and discussed.

3. GENERAL CASE

Using the modal analysis technique, the equation of motion for the generalized coordinates, $T_{mn}(t)$, in a decoupled form was obtained as [18-19]

$$\ddot{T}_{mn}(t) + 2\xi_{mn}\omega_{mn}\dot{T}(t) + \omega_{mn}^2 T(t) = \frac{1}{J_{mn}} F_{mn}(t) \tag{1}$$

where J_{mn} stands for the generalized mass (norm), and

$$F_{mn}(t) = \int_0^a\int_0^b P(x,y,t)W_{mn}(x,y,)dydx = P_{mn}P(t) \ . \tag{2}$$

For homogeneous initial conditions, the solution for $T_{mn}(t)$ is

---

[1] Department of Solid Mechanics, Materials and Structures,
Tel-Aviv University, Ramat-Aviv, Israel.

[2] Department of Engineering Science and Mechanics,
Virginia Polytechnic Institute and State University, Blacksburg, Virginia,
on leave from the Tel-Aviv University, Ramat-Aviv, Israel.

[3] Department of Aeronautical Engineering,
Technion - Israel Institute of Technology, Haifa, Israel.

$$T_{mn}(t) = \frac{P_{mn}}{J_{mn}\omega_{d_{mn}}} \int_0^t h_{mn}(t - t_1)P(t_1)dt_1 \tag{3}$$

where

$$\omega_{d_{mn}} = \omega_{mn}\sqrt{1 - \xi_{mn}^2}\ ;\ h_{mn}(t - t_1) = \exp[-\xi_{mn}\omega_{mn}(t - t_1)] \sin[\omega_{d_{mn}}(t - t_1)]\ . \tag{4}$$

The solution function for the transverse displacement is then

$$W(x,y,t) = \sum_{m,n} W_{mn}(x,y)\ \frac{P_{mn}}{\omega_{d_{mn}} J_{mn}} \int_0^t (\exp[-\xi_{mn}\omega_{mn}(t - t_1)] \sin[\omega_{d_{mn}}(t - t_1)]P(t_1))dt_1\ . \tag{5}$$

The non-stationary random excitation is presented as [2]

$$P(t) = g(t)G(t) \tag{6}$$

where $g(t)$ is a deterministic slowly-varying function, and $G(t)$ is a stationary random process with zero mean and autocorrelation function $R(t_2 - t_1)$.

The mean-square transverse displacement at any time instant, t, is then

$$E[W^2(x_1,y_1,t_1;x_2,y_2,t_2)] = \sum_{m,n}\sum_{p,q} W_{mn}(x_1,y_1)W_{pq}(x_2,y_2)\ \frac{P_{mn}P_{pq}}{J_{mn}\omega_{d_{mn}}\omega_{d_{pq}}J_{pq}}$$

$$\times \int_0^t\int_0^t (\exp[-\xi_{mn}\omega_{mn}(t - t_1)]\sin[\omega_{d_{mn}}(t - t_1)]g(t_1)$$

$$\times \exp[-\xi_{pq}\omega_{pq}(t - t_2)]\sin[\omega_{d_{pq}}(t - t_2)]g(t_2)\ R(t_2 - t_1))dt_2dt_1 \equiv R_W\ . \tag{7}$$

Since the natural frequencies of the laminated plates were found to be well separated (see Table 1), and in the case of light damping, only the autocorrelation terms need be taken into account, which enables us to write Eq. (7) in the form

$$R_W = \sum_{m,n} W_{mn}^2\ \frac{P_{mn}^2}{J_{mn}^2\omega_{mn}^2\left[1 - \xi_{mn}^2\right]} \int_0^t\int_0^t (\exp[-\xi_{mn}\omega_{mn}(t - t_1)] \sin[\omega_{d_{mn}}(t - t_1)]g(t_1)$$

$$\times \exp[-\xi_{mn}\omega_{mn}(t - t_2)] \sin[\omega_{d_{mn}}(t - t_2)]g(t_2)R(t_2 - t_1))dt_2dt_1 \equiv \sigma_W^2(t)\ . \tag{8}$$

4. CROSS-PLY LAMINATES

In the following examples we will consider a rectangular cross-ply laminate (0^0,90,90^0,0^0), in which each layer is made of graphite-carbon (Material 1) with the following elastic constants [22]:

$E_1 = 25.1$ MSI $E_2 = 4.8$ MSI

$G_{13} = 1.2$ MSI $G_{23} = 0.47$ MSI $\nu_{12} = 0.31$

and the shear correction factor k is taken to be 5/6.

4.1 WHITE NOISE EXCITATION MODULATED BY A UNIT STEP FUNCTION

For this case

$$g(t) = U(t) = \begin{matrix} 1 & t \geq 0 \\ 0 & t < 0 \end{matrix} \quad ;\ R(t_2 - t_1) = R(\tau) = 2\pi S_0\delta(\tau)\ . \tag{9}$$

Equation (8) is then written as

$$R_W = 2\pi S_0 \sum_{m,n} \frac{P_{mn}^2 W_{mn}^2(x_1,y_1)}{J_{mn}^2\omega_{mn}^2\left[1 - \xi_{mn}^2\right]} \int_0^t (\exp[-2\xi_{mn}\omega_{mn}(t - t_2)]\sin^2[\omega_{d_{mn}}(t - t_2)])dt_2\ , \tag{10}$$

and for the case where the plate is driven by a point load, applied at its centre ($x = a/2$; $y = b/2$), the mean-square transverse displacement at the driven point is

$$R_W = 2\pi S_o \sum_{m,n} \frac{1}{J_{mn}^2 \omega_{mn}^2 \left[1 - \xi_{mn}^2\right]} \int_0^t \left\{\exp[-2\xi_{mn}\omega_{mn}(t - t_2)] \sin^2[\omega_{d_{mn}}(t - t_2)]\right\} dt_2 . \quad (11)$$

Integration leads to

$$R_W = \pi S_o \sum_{m,n} \frac{1}{J_{mn}^2 2\xi_{mn}\left[1 - \xi_{mn}^2\right]\omega_{mn}^3} (1 - \exp[-2\xi_{mn}\omega_{mn} t]$$

$$x \left(1 + \frac{\xi_{mn}\omega_{mn}}{\omega_{d_{mn}}} \sin [2\omega_{d_{mn}} t] + 2 \frac{\xi_{mn}^2 \omega_{mn}^2}{\omega_{d_{mn}}^2} \sin^2 \omega_{d_{mn}} t\right) \quad (12)$$

and setting $\epsilon_{mn} = \dfrac{\xi_{mn}}{\sqrt{1 - \xi_{mn}^2}}$, Eq. (12) becomes

$$R_W = \pi S_o \sum_{m,n} \frac{1}{J_{mn}^2 2\xi_{mn}\left[1 - \xi_{mn}^2\right]\omega_{mn}^3} (1 - \exp[-2\xi_{mn}\omega_{mn} t](1 + \epsilon_{mn} \sin [2\omega_{d_{mn}} t]$$

$$+ 2\epsilon_{mn}^2 \sin^2[\omega_{d_{mn}} t]). \quad (13)$$

In our case $\xi_{mn} << 1$ from which $\epsilon_{mn} << 1$ too, and Eq. (13) can be written as

$$R_W = \pi S_o \sum_{m,n} \frac{1}{J_{mn}^2 2\epsilon_{mn}\omega_{d_{mn}}^3}) (1 - \exp[-2\epsilon_{mn}\omega_{d_{mn}} t]) \quad (14)$$

which is correct within an order of ϵ. A comparison of these two results is shown in Figure 1.

4.2 WHITE NOISE EXCITATION MODULATED BY A RECTANGULAR STEP FUNCTION

For a rectangular step function of duration t_o

$$g(t) = U(t) - U(t - t_o) . \quad (15)$$

Equation (15) enables us to describe the response of the system as a superposition of two step loads

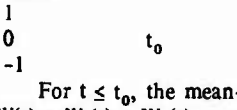

For $t \le t_o$, the mean-square response is as in 4.1. For $t > t_o$ the response is written as

$$W(t) = W_1(t) + W_2(t) \quad (16)$$

where $W_1(t)$, and $W_2(t)$ are the result of $g_1(t)$ and $g_2(t)$, respectively. The mean-square is then

$$E[W(t_1)W(t_2)] = E[(W_1(t_1) + W_2(t_1)][W_1(t_2) + W_2(t_2)]$$

$$= E[W_1(t_1)W_1(t_2)] + E[W_2(t_1)W_2(t_2)] + E[W_1(t_1)W_2(t_2)] + E[W_2(t_1))W_1(t_2)] \quad (17)$$

and for $t_1 = t_2 = t$

$$E[W^2(t)] = E[W_1^2(t)] + E[W_2^2(t)] + 2E[W_1(t)W_2(t)]. \quad (18)$$

If $W_1(t) = Z(t)$ then $W_2(t) = - Z(t - t_o)$ and

$$E[W^2(t)] = E[Z^2(t)] + E[Z^2(t - t_o)] - 2E[Z(t))Z(t - t_o)]. \quad (19)$$

From Eq. (8) it can be seen that (for a point load as in 4.1)

$$E[Z(t)Z(t - t_o)] = - 2\pi S_o \sum_{m,n} \frac{W_{mn}^2 P_{mn}^2(x_1 y_1)}{J_{mn}^2 \omega_{mn}^2 \left[1 - \xi_{mn}^2\right]} \int_0^t \int_0^{t-t_o} (\exp[-\xi_{mn}\omega_{mn}(t - t_1)] \sin[\omega_{d_{mn}}(t - t_1)]$$

$$x \exp[\xi_{mn}\omega_{mn}(t - t_o - t_2)] \sin [\omega_{d_{mn}}(t - t_o - t_2)]\delta(t_2 - t_1))dt_2 dt_1$$

$$= -2\pi S_0 \sum_{m,n} \frac{1}{J_{mn}^2 \omega_{mn}^2 \left[1 - \xi_{mn}^2\right]} \int_0^{t-t_0} (\exp[-2\xi_{mn}\omega_{mn}(t - t_0 - t_2)]$$

$$x \sin[\omega_{d_{mn}}(t - t_0 - t_2)]]dt_2 . \tag{20}$$

Comparison of the above with Eq. (11), Eq. (19) can be rewritten as

$$E[W^2(t)] = E[Z^2(t)] + E[Z^2(t - t_0)] - 2E[Z^2(t - t_0)] = E[Z^2(t)] - E[Z^2(t - t_0)] \tag{21}$$

and using the solution in Eq. (14)

$$\{1 - \exp[-2\epsilon_{mn}\omega_{d_{mn}} t]\} \qquad 0 \le t \le t_0$$

$$R_W = \pi S_0 \sum_{m,n} \frac{1}{J_{mn}^2 2\epsilon_{mn}\omega_{mn}^3}) \; x$$

$$(\exp[-2\epsilon_{mn}\omega_{d_{mn}} t](\exp[2\epsilon_{mn}\omega_{d_{mn}} t_0] - 1)) \qquad t > t_0. \tag{22}$$

The obtained results are shown in Figure 2. This problem was solved in [4] for a single degree of freedom system - SDF.

4.3 WHITE NOISE EXCITATION MODULATED BY EXPONENTIALLY DECAYING FUNCTIONS

For this case

$$g(t) = g[\exp(-\alpha t) - \exp(-\beta t)]U(t) \tag{23}$$

where $\alpha < \beta$ are nonnegative constants, sufficiently small to keep g(t) slowly-varying, and g is a normalization constant, determined from the condition

$$\sup_t |g(t)| = 1 .$$

where sup denotes the least upper bound. Equation (23) is frequently used in earthquake response [2] and in gust analysis [23].

For the same load as in 4.1 Eq. (11) now reads

$$R_W = 2\pi S_0 \sum_{m,n} \frac{1}{J_{mn}^2 \omega_{mn}^2 (1 - \xi^2_{mn})} \int_0^t e^{-2(t-t_2)} g^2 \left[e^{-2\alpha t_2} + e^{-2\beta t_2} - 2e^{-(\alpha+\beta)t_2}\right] dt_2$$

$$= 2\pi S_0 \sum_{m,n} \frac{q^2}{J_{mn}^2 \omega_{mn}^2 (1 - \xi^2_{mn})} \left[\frac{1}{2(1 - \alpha)} (e^{-2\alpha t} - e^{-2t}) \right.$$

$$\left. + \frac{1}{2(1 - \beta)} (e^{-2\beta t} - e^{-2t}) - \frac{2}{2 - \alpha - \beta} (e^{-(\alpha+\beta)t} - e^{-2t})\right] \tag{24}$$

and

$$g = 1/(e^{-\alpha t_0} - e^{-\beta t_0}) \; ; \; t_0 = (\ell n\, \beta - \ell n\, \alpha)/(\beta - \alpha). \tag{25}$$

The results for $\alpha = 0.1$, $\beta = 0.5$ are displayed in Figure 3

A special case of Eq. (23) is for $\alpha = 0$, so that

$$g(t) = g[1 - \exp(-\beta t)]U(t). \tag{26}$$

For $t \to \infty$, $[1 - \exp(-\beta t)] \to 1$, so $g \equiv 1$, and Eq. (24) now reads

$$R_W = 2\pi S_0 \sum_{m,n} \frac{1}{J_{mn}^2 \omega_{mn}^2 (1 - \xi^2_{mn})} \left[\frac{1}{2} (1 - e^{-2t}) \right.$$

$$\left. + \frac{1}{2(1 - \beta)} (e^{-2\beta t} - e^{-2t}) - \frac{2}{2 - \beta} (e^{-\beta t} - e^{-2t})\right] . \tag{27}$$

The results for $\beta = 0.5$ are shown in Figure 4.

4.4 NARROW BAND EXCITATION MODULATED BY A UNIT STEP FUNCTION

For this case

$$g(t) = U(t) = \begin{cases} 1 & t \geq 0 \\ 0 & t < 0 \end{cases} \tag{28}$$

and G(t) is noise correlated as an exponentially decaying harmonic function, for which

$$R(t_2 - t_1) = \sum_{m,n}^{\infty} R \exp[-\alpha_{mn}(t_2 - t_1)] \cos[\Omega_{mn}(t_2 - t_1)] , \tag{29}$$

where Ω_{mn} is the center frequency of the exponentially decaying harmonic function.

Defining α_{mn} in the form

$$\alpha_{mn} = \epsilon_{mn}\, \mu\Omega_{mn} , \tag{30}$$

then if $\epsilon_{mn}\mu$ is sufficiently small, the center frequency of the excitation band lies in the neighbourhood of the damped natural frequency of the mn-th mode. This can be formulated through the relation

$$\lambda_{mn} \equiv \Omega_{mn}/\omega_{d_{mn}} = 1.0 + \epsilon_{mn}\beta \tag{31}$$

where $\beta \simeq 1.0$.

Equation (8) for this case reads

$$R_W \simeq \sum_{m,n} \frac{R}{J_{mn}^2 \omega_{mn}^2 \left(1 - \xi_{mn}^2\right)} \int_0^t \int_0^t \{\exp[-\xi_{mn}\omega_{mn}(t - t_1)] \sin[\omega_{d_{mn}}(t - t_1)]$$

$$\times \exp[-\xi_{mn}\omega_{mn}(t - t_2)] \sin[\omega_{d_{mn}}(t - t_2)] \exp[-\epsilon_{mn}\mu\Omega_{mn}|t_2 - t_1|]\cos[\Omega_{mn}(t_2 - t_1)]\} dt_2 dt_1 . \tag{32}$$

We next define the following parameters

$$\tau_{i_{mn}} = \xi_{mn}\omega_{mn} t_i \quad (i = 1,2)$$

$$\eta_{mn} = \xi_{mn}\omega_{mn} t$$

$$K_{mn} = \frac{R}{\epsilon_{mn}^2 J_{mn}^2 \omega_{mn}^4 \left(1 - \xi_{mn}^2\right)} = \frac{R}{\xi_{mn}^2 J_{mn}^2 \omega_{mn}^4} \tag{33}$$

to obtain

$$R_W \simeq \sum_{m,n} K_{mn} \exp[-2\eta_{mn}] \int_0^{\eta_{mn}} \int_0^{\eta_{mn}} \{\exp[\tau_{2_{mn}} + \tau_{1_{mn}}]$$

$$\times \exp[-\lambda_{mn}|\tau_{2_{mn}} - \tau_{1_{mn}}|] F_{mn}\} d\tau_{2_{mn}} d\tau_{1_{mn}} \tag{34}$$

where

$$F_{mn} = \cos[\beta(\tau_{2_{mn}} - \tau_{1_{mn}})] + \cos[k_1(\tau_{2_{mn}} - \tau_{1_{mn}})]$$

$$- \cos k_2\{\cos[k_1\tau_{2_{mn}} - \beta\tau_{1_{mm}}] + \cos[k_1\tau_{1_{mm}} - \beta\tau_{2_{mm}}]\}$$

$$- \sin k_2\{\cos[k_1\tau_{2_{mn}} - \beta\tau_{1_{mm}}] + \sin[k_1\tau_{1_{mm}} - \beta\tau_{2_{mm}}]\}$$

and

$$k_1 = \frac{2 + \epsilon_{mn}\beta}{\epsilon_{mn}} \quad ; \quad k_2 = \frac{2\eta_{mn}}{\epsilon_{mn}} .$$

Extending the solution of this problem for an SDF system, presented in [5], by implying Riemann's lemma, [24], F_{mn} in Eq. (34) may be written as

$$F_{mn} = \cos[\beta(\tau_{2_{mm}} - \tau_{1_{mm}})],$$

by which Eq. (34) is written as

$$R_W = \sum_{m,n} K_{mn} \left\{ \frac{1 + \mu}{\beta^2 + (1 + \mu)^2} + \frac{(1 - \mu)\exp[-2\eta_{mn}]}{\beta^2 + (1 - \mu)^2} \right.$$

$$- \frac{2\exp[-(1+\mu)\eta_{mn}]}{[\beta^2 + (1+\mu)^2][\beta^2 + (1-\mu)^2]} [(\beta^2 + 1 - \mu^2)\cos\beta\eta_{mn} + 2\mu\beta \sin\eta_{mn}]) . \quad (35)$$

The stationary level of Eq. (36) is obtained by setting $t \to \infty$ ($\eta_{mn} \to \infty$):

$$R_W = \frac{1+\mu}{\beta^2 + (1+\mu)^2} \sum_{m,n} K_{mn} . \quad (36)$$

For $\beta = 0$ ($\Omega_{mn} = \omega_{d_{mn}}$), Eq. (35) now reads

$$R_W = \sum_{m,n} K_{mn} \{ \frac{1}{1+\mu} + \frac{\exp[-2\eta_{mn}]}{1-\mu} - \frac{2\exp[-(1+\mu)\eta_{mn}]}{(1+\mu)(1-\mu)} , \quad (37)$$

and with $\mu = 1$, L'Hospital's rule yields

$$R_W = \sum_{m,n} K_{mn} \frac{1}{2} (1 - (1 + 2\eta_{mn})\exp[-2\eta_{mn}]) . \quad (38)$$

Results, normalized to the stationary level, are shown in Figure 5, for $\mu = 0.1$ and $\beta = 0$, 1 and 5.

5. REMARKS

Remark 1. Consider the solution of Eq. (32) for the case where the center frequency of the excitation band coincide with the damped natural frequency of the mn-th mode, i.e., $\omega_{d_{mn}} = \Omega_{mn}$ (solved in [13-14]). Each term of the correlation function (29) may be rewritten, dropping the subscripts, as

$$R = R_0 e^{-\alpha|\tau|} \cos\Omega\tau \qquad \alpha > 0 \qquad \Omega > 0 \quad (39)$$

and its spectrum function, obtained via the Wiener-Khintchine relationship, is

$$S = \frac{R\alpha}{\pi} \left[\frac{\omega^2 + \alpha^2 + \Omega^2}{\omega^4 + 2\omega^2(\alpha^2 - \Omega^2) + (\alpha^2 + \Omega^2)^2} \right] \quad (40)$$

or

$$S = \frac{R\alpha}{\pi} \left[\frac{2\Omega^2 + \alpha^2}{\Omega^4 + 2\Omega^2\alpha^2 - 2\Omega^4 + \alpha^4 + 2\alpha^2\Omega^2 + \Omega^4} \right] = \frac{R\alpha}{\pi} \left[\frac{2\Omega^2 + \alpha^2}{4\Omega^2\alpha^2 + \alpha^4} \right] . \quad (41)$$

Since $\alpha << \Omega$ ($\epsilon\mu << 1$)

$$S = \frac{R\alpha}{\pi} \left[\frac{2\Omega^2 + \alpha^2}{\alpha^2(4\Omega^2 + \alpha^2)} \right] \simeq \frac{R\alpha}{\pi} \frac{1}{2\alpha^2} = \frac{R}{2\pi\alpha} , \quad (42)$$

which does not depend on Ω, so the system is actually excited by a white noise of the above intensity, so that there is no overshooting of the stationary level.

Remark 2. Although the stationary level is reached at $t \to \infty$, it can be seen from Eq. (35) that the stationary level is also reached (for the same t) as ω_{mn} increases. Since the natural frequencies are far apart and K_{mn} includes ω_{mn}^4 in the denominator, it is justified, for this problem, to take into consideration the first mode only.

Remark 3. Considering a rectangular step function for g(t), in the same manner as in Eq. (19), and within the assumptions of [5], it is seen that $E[Z^2(t)]$ is again as per Eq. (35), and so is $E[Z^2(t - t_0)]$ with $\eta_{mn} \to (\eta_{mn} - \eta_{0_{mn}})$, where $\eta_{0_{mn}} = \xi_{mn}\omega_{mn}t_0$, t_0 being the ending moment of the pulse. The last term $E[Z(t)Z(t - t_0)]$ turns out, in integration, to be

$$R_W = \sum_{m,n} K_{mn} \{ \frac{1}{2} \left[\frac{1+\mu}{\beta^2 + (1+\mu)^2} - \frac{1-\mu}{\beta^2 + (1-\mu)^2} \right] e^{\eta_{0_{mn}}}$$

$$+\frac{\beta^2+1-\mu^2}{[\beta^2+(1-\mu)^2][\beta^2+(1-\mu)^2]}\left[\cos(\beta\eta_{0_{mn}})e^{\eta_{0_{mn}}}\right.$$

$$\left.-\frac{2\mu\beta}{[\beta^2+(1-\mu)^2][\beta^2+(1+\mu)^2]}\sin(\beta\eta_{0_{mn}})e^{\eta_{0_{mn}}}\right]$$

$$-\frac{\beta^2+1-\mu^2}{[\beta^2+(1-\mu)^2][\beta^2+(1-\mu)^2]}\left[\cos(\beta\eta_{mn})e^{-(1+\mu)\eta_{mn}+\eta_{0_{mn}}}\right.$$

$$\left.+\cos\beta(\eta_{mn}-\eta_{0_{mn}})e^{-(1+\mu)\eta_{mn}+\eta_{0_{mn}}}\right]$$

$$-\frac{2\mu\beta}{[\beta^2+(1-\mu)^2][\beta^2+(1-\mu)^2]}\left[\sin(\beta\eta_{mn})e^{-(1+\mu)\eta_{mn}+\eta_{0_{mn}}}\right.$$

$$\left.+\sin\beta(\eta_{mn}-\eta_{0_{mn}})e^{-(1+\mu)\eta_{mn}+\eta_{0_{mn}}}\right]$$

$$+\frac{1+\mu}{\beta^2+(i-\mu)^2}e^{-2\eta_{mn}+\eta_{0_{mn}}}\Big\}. \tag{43}$$

When $t \to \infty$, the total mean-square should tend to zero, so that Eq. (43) is at first glance incorrect, since its time-independent components apparently depend on η_0, and thus do not cancel out their counterparts in the two preceeding terms (the trivial solution $\eta_0 = 0$ is irrelevant). However, it can be shown that within the same order of accuracy, ϵ, these terms do not actually depend on η_0. Setting

$$A = \frac{1}{2}\left[\frac{1+\mu}{\beta^2+(1+\mu)^2}-\frac{1-\mu}{\beta^2+(1-\mu)^2}\right]$$

$$B = \frac{1-\mu^2+\beta^2}{[\beta^2+(1+\mu)^2][\beta^2+(1-\mu)^2]}$$

$$C = -\frac{2\mu\beta}{[\beta^2+(1+\mu)^2][\beta^2+(1-\mu)^2]}, \tag{44}$$

the time-independent terms of Eq. (43) can be written, for each mn, as

$$Ae^{\eta_0}+B\cos(\beta\eta_0)e^{\mu\eta_0}+C\sin(\beta\eta_0)e^{\mu\eta_0}. \tag{45}$$

Expending the trigonometric and the exponential terms in their Taylor series, namely

$$e^{\eta_0}=1+\eta_0+\frac{\eta_0^2}{2}+\frac{\eta_0^3}{6}+\ldots$$

$$e^{\mu\eta_0}=1+\mu\eta_0+\frac{\mu^2\eta_0^2}{2}+\frac{\mu^3\eta_0^3}{5}+\ldots$$

$$\cos\beta\eta_0=1-\frac{\beta^2\eta_0^2}{2!}+\frac{\beta^2\eta_0^4}{4!}-\ldots$$

$$\sin\beta\eta_0=\beta\eta_0-\frac{\beta^3\eta_0^3}{3!}+\frac{\beta^5\eta_0^5}{5!}-\ldots \tag{46}$$

But the terms in which η_0 is at the powers of two or more, ϵ is also at the power of two or more, respectively, so they can be dropped within the order of accuracy, ϵ, and it remained only to verify that

$\eta_0[A+\mu B+\beta C]=0$ or $A+\mu B+\beta C=0$,

which is in fact the case. The conclusion is that since these terms do not depend on η_0, we may set $\eta_0 = 0$ and obtain the asymptotic result (mean-square tends to 0). Yet, right after t_0, the mean-square has negative values which are not of the order of ϵ (see Figure 6). This yields the final conclusion that Riemann's lemma is inapplicable in the case of a rectangular pulse. However, from the engineering point of view, since overshooting occurs before t_0, in order to calculate its amount, one can use this approximation for a rectangular pulse too.

6. ANGLE-PLY LAMINATES

An antisymmetric angle-ply laminated plate, made of the same material (Material 1) is considered next.

By arranging the layers in the sequence (30°,-30°,30°,-30°), and by considering the excitation as in 4.4, we obtain the results shown in Figure 7. It can be seen that the response is similar to that in Figure 4.5 for $\mu = 0.1$ and $\beta = 5$.

The level of overshooting are also investigated, for the same loading case and for different values of the angle θ. Two cases are considered: 1) a plate of two layers $(\theta,-\theta)$ and 2) a plate of four layers $(\theta,-\theta,\theta,-\theta)$. It can be seen from Figure 8 that the plate given superior performance with four layers at $\theta = 15^0$. Addition of another even number of layers may improve the performance to some extent, as it was shown in other context in [25].

7. SUMMARY AND CONCLUSION

The response of simply-supported rectangular plates to non-stationary random excitation is presented. It was found that no overshooting occurs in the case of shaped white noise, while overshooting up to 2.2 times above the stationary level was obtained in the cae of shaped narrow-band excitation, for both the cross-ply and angle-ply variants. In the latter, improved performance was found at $\theta = 15^0$ with four layers or more.

Table 1
NATURAL FREQUENCIES OF CROSS-PLY LAMINATE
$(0^0, 90^0, 90^0, 0^0)$ A = B = 50H

M	N	Natural Frequencies (rad/sec)
1	1	4859.0675
1	3	20788.342
1	5	53872.430
1	7	100584.30
3	1	33884.710
3	3	42018.487
3	5	67897.037
3	7	110903.77

8. REFERENCES

1. M.B. PRIESTLEY 1967 Journal of Sound and Vibration 6, 86-97. Power Spectral Analysis of Nonstationary Random Processes

2. M. SHINOZUKA 1969 Columbia University, Technical Report No. 4. Random Processes with Evolutionary Power.

3. T.K. CAUGHEY and H.J. STUMPF 1961 Journal Applied Mechanics ASME 28, 563-556. Transient Response of a Dynamic System Under Random Excitation.

4. R.L. BARNOUSKI and J.R. MAURER Journal of Applied Mechanics 36, No. 2, Trans. ASME, Vol. 91, Ser. E., 221-227. Mean-Square Response of Simple Mechanical Systems to Nonstationary Random Excitation.

5. L.L. BUCCIARELI, Jr. and C. KUO 1970 Journal of Applied Mechanics 36, No. 2, Trans. ASME, Vol. 91, Ser. E., 221-227. Mean-Square Response of a Second Order System to Nonstationary Random Excitation.

6. R. COROTIS and T.A. MARSHALL 1977 ASCE, Journal Engineering Mechanics Division 103, 501-513. Oscillator Response to Modulated Random Excitation.

7. R. HOLMAN and G.C. HART 1974 Journal Engineering Mechanics Division ASCE, 100, 415-431. Nonstationary Reponse of Structural Systems.

8. S.K. HAMMOND 1968 Journal of Sound and Vibration 7, 393-416. On the Response of Single and Multidegree of Freedom Systems to Nonstationary Random Excitations.

9. MASRI 1978 Journal Applied Mechanics, Trans. ASME 45, 649-656. Response of Multidegree of Freedom System to Nonstationary Random Excitation.

10. C.W.S. TO 1982 Journal of Sound and Vibration 83, 273-291. Nonstationary Random Response to Multi-Degree-of-Freedom System by the Theory of Evolutionary Spectra.

11. D.A. GASPARINI 1979 Journal Engineering Mechanics Division ASCE 105, No. EM1, Proc. Paper 14341, 13-27. Response of MDOF Systems to Nonstationary Random Excitation.

12. R.B. COROTIS and E.H. VENMARCKE 1975 Journal Engineering Mechanics Div. ASCE, 101, 623-637. Time-Dependent Spectral Content of System Response.

13. G. AHMADI and M.A. SATTER 1975 AIAA Journal 13, 1097-1100. Mean-Square Response of Beams to Non-Stationary Random Excitation.

14. G. AHMADI 1978 Nuclear Engineering and Design 50, 327-345. Earthquake Response of Linear Continuous Systems.

15. M. WITT and K. SOBCZYK 1980 Internal Journal of Solids and Structures 16, 231-238. Dynamic Response of Laminated Plates to Random Loading.

16. M. WITT 1987 Refined Dynamical Theories of Beams, Plates and Shells and Their Applications, Elishakoff, I. and Irretier, H., Eds., Springer, Berlin, 274-285. Dynamic Response and Reliability of Laminated Plates to Random Loading.

17. C. MEI and C.B. PRASAD 1987 AIAA Dynamics Specialists Conference, Monteray, CA, April 9-10, 809-826. Effects of Large Deflection and Transverse Shear on Response of Rectangular Symmetric Composite Laminates Subjected to Acoustic Excitation.

18. G. CEDERBAUM, L. LIBRESCU and I. ELISHAKOFF 1987 20th Midwestern Mechanics Conference, West Lafayette, Indiana, Aug. 31-Sept. 2. Dynamic Response of Flat Panels Made of Advanced Composite Materials Subjected to Random Excitation.

19. G. CEDERBAUM, I. ELISHAKOFF and L. LIBRESCU 1987. SES Meeting, Salt Lake City, Utah, Sept. 20-23. Random Vibrations of Laminated Plates.

20. P.C. YANG, C.H. NORRIS and Y. STAVSKY 1965 International Journal of Solids and Structures 2, 665-684. Elastic Wave Propagation in Heterogeneous Plates.

21. J.M. WHITNEY and N.J. PAGANO 1970 Journal of Applied Mechanics Trans. of the ASME 37, 1031-1036. Shear Deformation in Heterogeneous Anisotropic Plates.

22. N.J. PAGANO and S.R. SONI Proceedings of the First Conference on Composite Materials, Dayton, Ohio, Oct. 7-9, 450-471. Strength Analysis of Composite Turbine Blades.

23. L.J. HOWELL and Y.K. LIN 1971 AIAA Journal 9 No. 11, 201-2207. Response of Flight Vehicle to Nonstationary Atmospheric Turbulence.

24. H. JEFFREYS and B.S. JEFFREYS 1956 Cambridge University Press, Methods of Mathematical Physics, 3rd Ed.

25. R.M. JONES 1975 Mechanics of Composite Materials, Scripta Book Company, Washington, D.C.,

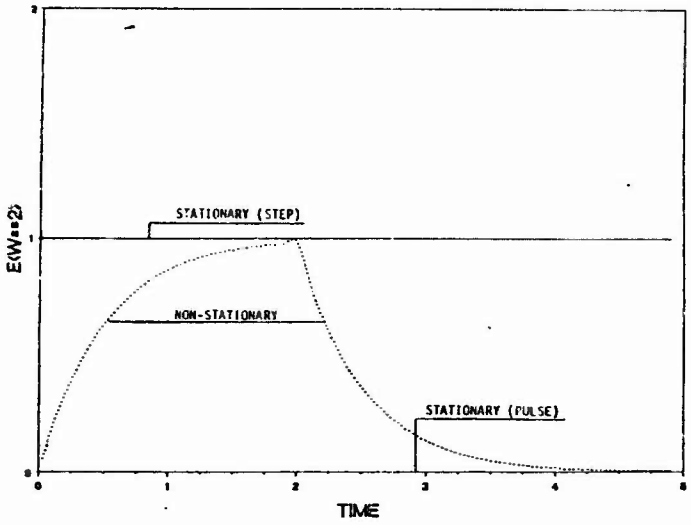

Figure 2: Mean square response - Case 2.

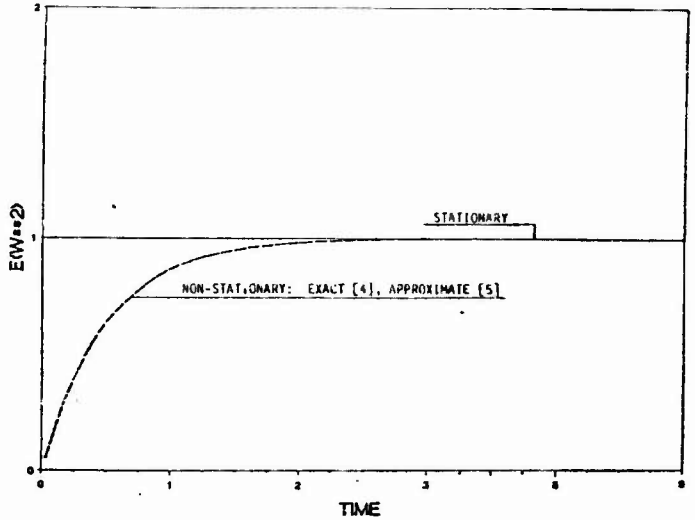

Figure 1: Exact [4] and approximate [5] relative mean-square response - Case 1.

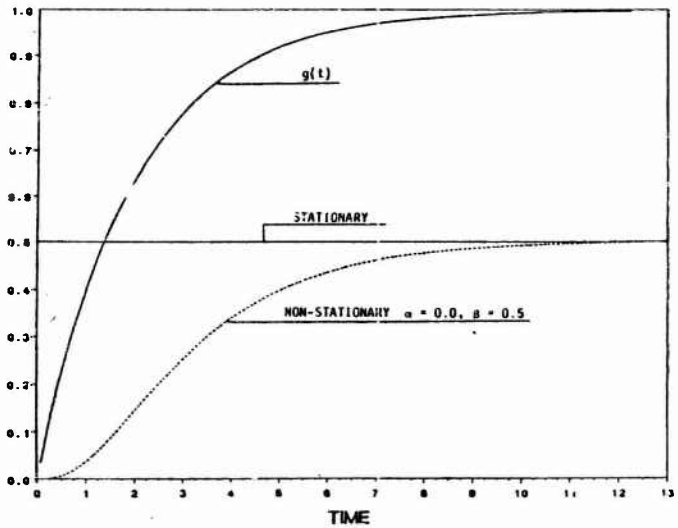

Figure 4: Mean square response - Case 3, $\alpha = 0$, $\beta = 0.5$.

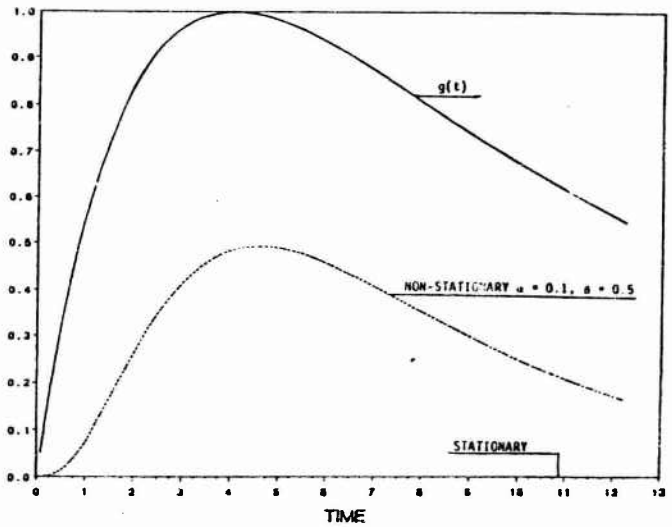

Figure 3: Mean square response - Case 3, $\alpha = 0.1$, $\beta = 0.5$.

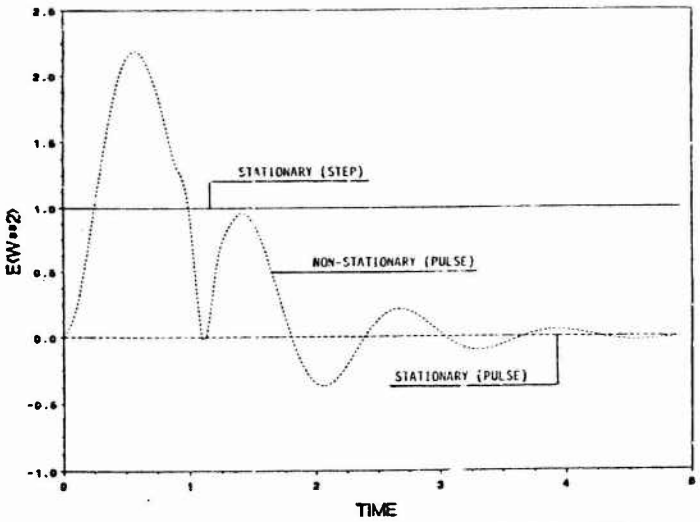

Figure 6: Mean square response - narrow bands modulated by a unit pulse $\mu = 0.1$, $\beta = 5$, $n^o = 1$.

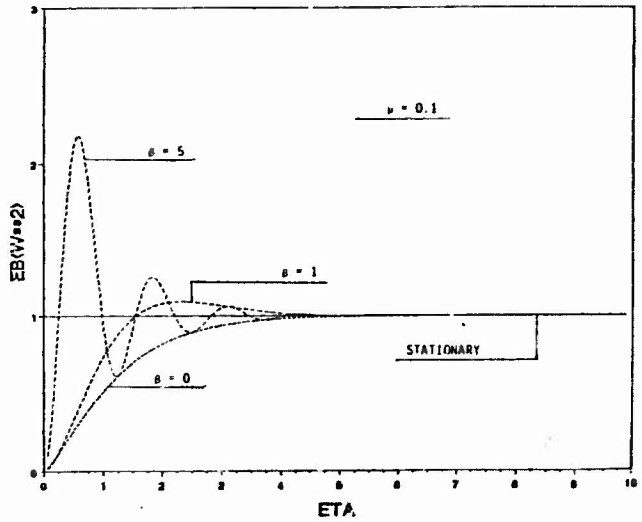

Figure 5: Mean square response - Case 4, $\mu = 0.1$, $\beta = 0, 1, 5$.

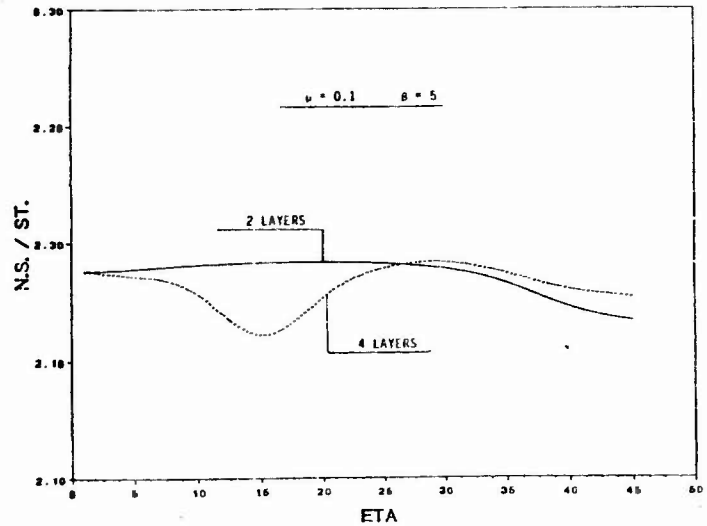

Figure 8: Relative mean square response vs. β - Case 4, $\mu = 0.1$, $\beta = 5$, A.P.

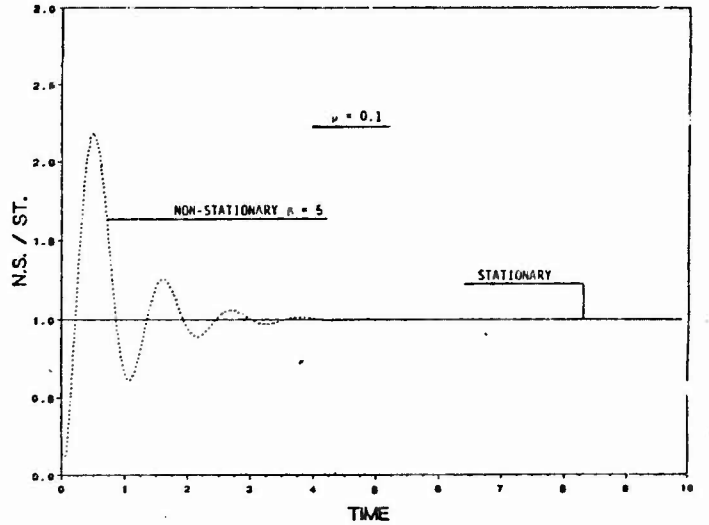

Figure 7: Mean square response - Case 4, $\mu = 0.1$, $\beta = 5$, A.P.

NONLINEAR VIBRATIONS OF ANTISYMMETRIC ANGLE-PLY LAMINATES USING A SIMPLE HIGHER-ORDER THEORY

S.P. Lim
K.H. Lee
N.R. Senthilnathan

Department of Mechanical and Production Engineering
National University of Singapore

1. INTRODUCTION

It was shown in reference [1] that a simple nonlinear shear deformation theory of plates can be obtained from a recently proposed higher-order theory [2] of plates by making the assumption that the inplane rotation tensor does not vary through the thickness. The theory was shown to have one variable less than the Reissner-Mindlin theories and accounted for a parabolic variation of the transverse shear stresses with zero values at the free surfaces. Numerical results for the nonlinear periods obtained from the present theory for thick rectangular isotropic and transversely isotropic plates were found [3] to be in good agreement with those from Reissner-Mindlin theory. It is the purpose of the present study to extend the simple nonlinear shear deformation theory presented in reference to the nonlinear vibration of laminated plates. The solution method developed by Chandra and Basavaraju [4] for the nonlinear vibration of thin laminates is adopted here for the nonlinear vibration of simply-supported thick antisymmetric angle-ply (45°/-45°) laminates. Nonlinear frequencies from the present theory are compared with those from the Reissner-Mindlin theory [5].

2. EQUATIONS OF MOTION

The nonlinear governing equations of the present theory[6] for the free vibration of unsymmetric angle-ply laminates in terms of the transverse displacements and stress function can be written (neglecting inplane rotary inertia) as

$$A_{22}^{*}\psi_{,xxxx} + (2A_{12}^{*} + A_{66}^{*})\psi_{,xxyy} + A_{11}^{*}\psi_{,yyyy}$$

$$- (2B_{26}^{*} - B_{61}^{*})w^{b}_{,xxxy} - (2B_{16}^{*} - B_{62}^{*})w^{b}_{,xyyy}$$

$$- \frac{4}{3h^2}(2E_{26}^{*} - E_{61}^{*})w^{s}_{,xxxy} - \frac{4}{3h^2}(2E_{16}^{*} - E_{61}^{*})w^{s}_{,xyyy} = w^{2}_{,xy} - w_{,xx}w_{,yy} \qquad (1)$$

$$\rho h\ddot{w}^{b} + L_1 w^{b} + L_2 w^{s} + L_4 \psi = F(w,\psi) \qquad (2)$$

$$\rho h\ddot{w}^{s} + L_2 w^{b} + L_3 w^{s} + L_5 \psi = F(w,\psi) \qquad (3)$$

where

$$L_1 = D_{11}^* \frac{\partial^4}{\partial x^4} + 2(D_{12}^* + 2D_{66}^*) \frac{\partial^4}{\partial x^2 \partial y^2} + D_{22}^* \frac{\partial^4}{\partial y^4}$$

$$L_2 = \frac{4}{3h^2} \left[F_{11}^* \frac{\partial^4}{\partial x^4} + 2(F_{12}^* + 2F_{66}^*) \frac{\partial^4}{\partial x^2 \partial y^2} + F_{22}^* \frac{\partial^4}{\partial y^4}\right]$$

$$L_3 = \frac{16}{9h^4} \left[H_{11}^* \frac{\partial^4}{\partial x^4} + 2(H_{12}^* + 2H_{66}^*) \frac{\partial^4}{\partial x^2 \partial y^2} + H_{22}^* \frac{\partial^4}{\partial y^4}\right]$$

$$- \left[\left(A_{55} - \frac{8}{h^2} D_{55} + \frac{16}{h^4} F_{55}\right) \frac{\partial^2}{\partial x^2} + \left(A_{44} - \frac{8}{h^2} D_{44} + \frac{16}{h^4} F_{44}\right) \frac{\partial^2}{\partial y^2}\right]$$

$$L_4 = -\left(2B_{26}^* - B_{61}^*\right) \frac{\partial^4}{\partial x^3 \partial y} - \left(2B_{16}^* - B_{62}^*\right) \frac{\partial^4}{\partial x \partial y^3}$$

$$L_5 = -\frac{4}{3h^2} \left(2E_{26}^* - E_{61}^*\right) \frac{\partial^4}{\partial x^3 \partial y} - \frac{4}{3h^2} \left(2E_{16}^* - E_{62}^*\right) \frac{\partial^4}{\partial x \partial y^3}$$

$$F(w,\psi) = w_{,xx}\, \psi_{,yy} - 2w_{,xy}\psi_{,xy} + w_{,yy}\psi_{,xx}$$

$w = w^b + w^s$, ρ and h are mass density and thickness of the plate respectively. (4)

The unstarred elastic constants A_{ij}, B_{ij}, E_{ij}, D_{ij}, F_{ij} and H_{ij} are defined in the same way as in reference [2] while the starred quantities are related to the unstarred quantities in the following way.

$$[A_{ij}^*] = [A_{ij}]^{-1}, \quad [B_{ij}^* \; E_{ij}^*] = -[A_{ij}^*][B_{ij} \; E_{ij}]$$

$$\begin{bmatrix} D_{ij}^* & F_{ij}^* \\ F_{ij}^* & H_{ij}^* \end{bmatrix} = \begin{bmatrix} D_{ij} & F_{ij} \\ F_{ij} & H_{ij} \end{bmatrix} - \begin{bmatrix} B_{ij} \\ E_{ij} \end{bmatrix} \begin{bmatrix} B_{ij} & E_{ij} \end{bmatrix} \tag{5}$$

In equations (2) and (3) ψ is the Airy stress function which is related to the inplane stress resultants by the following relations

$$N_x = \psi_{,yy}, \; N_y = \psi_{,xx} \quad \text{and} \quad N_{xy} = -\psi_{,xy} \tag{6}$$

3. BOUNDARY CONDITIONS

Let a and b be the lengths of the edges of the rectangular plate along the x and y axes. The transverse boundary conditions for the simply-supported plate are given by

$$w^b = w^s = w^b_{,xx} = w^s_{,xx} = 0 \qquad \text{at } x = 0, a$$

$$w^b = w^s = w^b_{,yy} = w^s_{,yy} = 0 \qquad \text{at } y = 0, b \tag{7}$$

The inplane boundary conditions corresponding to the movable edges (zero average normal and tangential boundary forces) are given by

$$\int_0^b (\psi_{,yy})_{x=0,a}\, dy = 0 \qquad \int_0^b (\psi_{,xy})_{x=0,a}\, dy = 0$$

$$\int_0^a (\psi_{,xx})_{y=0,b}\, dx = 0 \qquad \int_0^a (\psi_{,xy})_{y=0,b}\, dx = 0 \tag{8}$$

The inplane boundary conditions corresponding to the immovable edges (zero average shear force and zero tangential displacement) are given by

$$v_o = 0 \qquad \text{at } x = 0, a$$

$$\int_0^b (\psi_{,xy})_{x=0,a}\, dy = 0$$

$$u_o = 0 \qquad \text{at } y = 0, b$$

$$\int_0^a (\psi_{,xy})_{y=0,b}\, dx = 0 \tag{9}$$

where u_o and v_o are the inplane displacements at the midplane.

4. APPROXIMATE SOLUTION

A one-term Galerkin approximation will be applied to solve the coupled nonlinear governing equations (1), (2) and (3). Present method is an extension of the solution method proposed by Chandra and Raju [4] for the nonlinear analysis of clamped unsymmetric laminates with movable and immovable edges. The notation, however, are those given in reference [7]. The displacement functions that satify the transverse boundary conditions are assumed as

$$w^b = h\zeta^b(t)\left(\sin\frac{\pi x}{a}\sin\frac{\pi y}{b}\right)$$

$$w^s = h\zeta^s(t)\left(\sin\frac{\pi x}{a}\sin\frac{\pi y}{b}\right) \tag{10}$$

Using equations (10) in the equations of motion (1,2,3) and following the procedure outlined in reference [4] it can be obtained that

$$\ddot{\zeta} + \omega_o^2\,\zeta^b + \omega_1^2\,\zeta^s + (\alpha^2 + \gamma_o)\,\zeta^3 = 0$$

$$\ddot{\zeta}^{b} + \omega_1^2 \zeta^{b} + \omega_2^2 \zeta^{s} + (\alpha^2 + \gamma_o)\zeta^3 = 0 \tag{11}$$

However since $\zeta = \zeta^{b} + \zeta^{s}$ equations (11) can be reduced to one equation in terms of ζ given by

$$\ddot{\zeta} + \bar{\omega}_o^2 \zeta + (\alpha^2 + \gamma_o)\zeta^3 = 0 \tag{12}$$

where

$$\omega_o^2 = \pi^4 \left[3d_{11}^* + 2\lambda^2(d_{12}^* + 2d_{66}^*) + 3\lambda^4 d_{22}^* + \frac{H_6^2}{H_3}\right]$$

$$\omega_1^2 = \pi^4 \left\{\frac{4}{3}\left[3f_{11}^* + 2\lambda^2(f_{12}^* + 2f_{66}^*) + 3\lambda^4 f_{22}^*\right] + \frac{H_6 H_7}{H_2}\right\}$$

$$\omega_2^2 = \pi^4 \left\{\frac{16}{9}\left[3h_{11}^* + 2\lambda^2(h_{12}^* + 2h_{66}^*) + 3\lambda^4 h_{22}^*\right] + \frac{H_7^2}{H_3}\right\}$$

$$+ \pi^2 \left(\frac{a}{h}\right)^2\left[\left(A_{55} - \frac{8}{h^2} D_{55} + \frac{16}{h^4} F_{55}\right) + \lambda^2\left(A_{44} - \frac{8}{h^2} D_{44} + \frac{16}{h^4} F_{44}\right)\right]$$

$$\alpha^2 = \frac{\pi^4}{16 d_{11}^*}\left(a_{11}^* + \lambda^4 a_{22}^*\right)$$

$$\gamma_o = \frac{\pi^4}{8 d_{11}^*} \frac{a_{12}^*}{\left(a_{12}^{*2} - a_{11}^* a_{22}^*\right)} \cdot \left(\lambda^4 a_{12}^* a_{22}^* - 2\lambda^2 a_{11}^* a_{22}^* + a_{11}^* a_{12}^*\right)$$

$$\bar{\omega}_o^2 = \frac{\omega_o^2 \omega_3^2 - \omega_4^2 \omega_1^2}{\omega_3^2 - \omega_4^2}$$

$$\omega_3^2 = \omega_2^2 - \omega_1^2 \,, \quad \omega_4^2 = \omega_1^2 - \omega_o^2$$

$$H_7 = \frac{4\lambda}{3}\left(2e_{26}^* - e_{61}^*\right) + \frac{4\lambda^3}{3}\left(2e_{16}^* - e_{62}^*\right)$$

$$\left(E_{16}^*, E_{26}^*, E_{61}^*, E_{62}^*\right) = h^3\left(e_{16}^*, e_{26}^*, e_{61}^*, e_{62}^*\right)$$

$$\left(F_{11}^*, F_{12}^*, F_{22}^*, F_{66}^*\right) = \frac{E_1 h^5}{\mu}\left(f_{11}^*, f_{12}^*, f_{22}^*, f_{66}^*\right)$$

$$\left(H_{11}^*, H_{12}^*, H_{22}^*, H_{66}^*\right) = \frac{E_1 h^7}{\mu}\left(h_{11}^*, h_{12}^*, h_{22}^*, h_{66}^*\right) \tag{13}$$

The starred quantities and other constants are defined in the same way as in reference [7]. $\gamma_o = 0$ for the movable edge condition.

5. NUMERICAL RESULTS AND DISCUSSION

Equation (12) is the well-known Duffing's equation whose solution methods are standard [7].

The nondimensionalised frequency ($\bar{\omega}_o/\omega_o$) - amplitude (w_o/h) response of two-layered antisymmetric angle-ply (45°/-45°) laminates are shown in figures 1 and 2 for movable and immovable edges respectively. The corresponding results from a Reissner-Mindlin theory[5] for movable edges are also included in figure 1. It is observed that the present results for movable edges agree well with those from reference [5] for $w/h < 1$. The large differences in the two values at $w/h > 1$ could be due to the differences in the way the 'movable' edge condition is treated in the two references. Inplane conditions along the edges are satisfied in an average sense in the present analysis, whereas, they are satisfied in absolute terms in reference [5].

6. CONCLUSIONS

A simple higher-order shear-deformation theory of plates developed before by the authors is used to study the nonlinear vibration of simply-supported, thick antisymmetric angle-ply (45°/-45°) laminates. The simplicity of the governing equations allow a direct extension of the solution methods developed before for thin plates to shear-deformable plates. The nonlinear frequencies from the present theory agree well with those from a Reissner-Mindlin type theory.

7. REFERENCES

1. S.P. LIM, K.H. LEE and N.R. SENTHILNATHAN 1987 Proceedings of the International Conference on Computational Engineering Mechanics, Beijing, China, 545-557. Linear and nonlinear bending of shear-deformable plates.

2. J.N. REDDY 1984 Journal of Applied Mechanics 45, 745-752. A simple higher-order theory for laminated composite plates.

3. K.H. LEE, N.R. SENTHILNATHAN, S.P. LIM and S.T. CHOW. Nonlinear vibration of thick rectangular plates using a simple higher-order theory. To be published in the International Journal of Nonlinear Mechanics.

4. R. CHANDRA and B. BASAVARAJU 1975 Journal of Sound and Vibration 40, 393-406. Large deflection vibration of angle-ply laminated plates.

5. K.S. SIVAKUMARAN and C.Y. CHIA 1985 Journal of Applied Mechanics 52, 536-542. Large-amplitude oscillations of unsymmetrically laminated anisotropic rectangular plates including shear, rotatory inertia and transverse normal stress.

6. N.R. SENTHILNATHAN, S.P. LIM, K.H. LEE and S.T. CHOW 1987, AIAA Journal 25, 1268-1271. Buckling of shear deformable plates.

7. C.Y. CHIA 1981 Nonlinear analysis of plates McGraw-Hill company, N.Y.

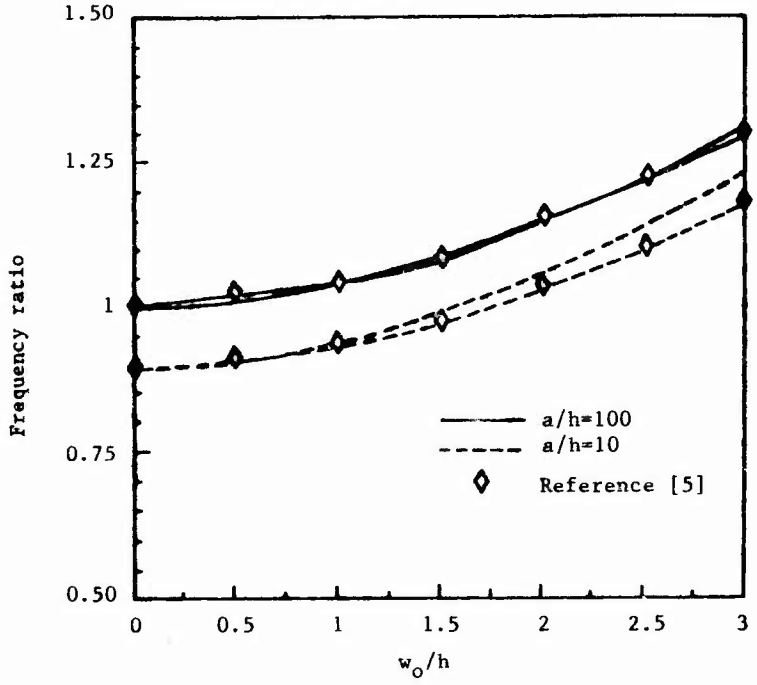

Figure 1. Nonlinear vibrations of square antisymmetric angle-ply plates, movable edges.

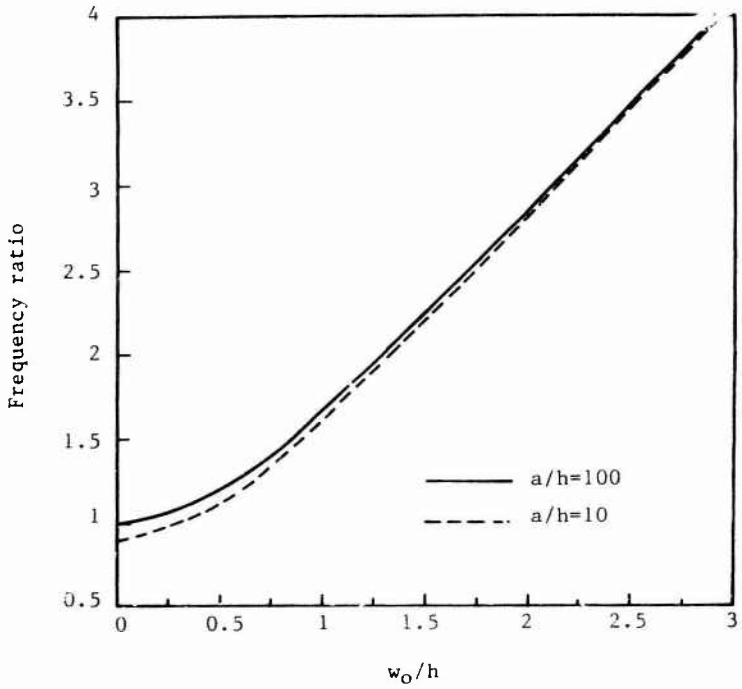

Figure 2. Nonlinear vibrations of square antisymmetric angle-ply plates, immovable edges.

ON TRANSIENT RESPONSE OF LAMINATED COMPOSITE PLATES BASED ON A HIGHER-ORDER THEORY

Mallikarjuna and T. Kant

Department of Civil Engineering
Indian Institute of Technology
Powai, Bombay 400 076, INDIA

1. INTRODUCTION

The transient analyses of laminated plates of finite dimensions have not received adequate consideration in the literature. The following brief review of previous research on transient response of elastic plates provides a background for the present paper.

For the dynamic behaviour of laminated plates, Mindlin's theory for homogeneous isotropic plates has been extended to laminated plates by Yang et al. [1] and by Whitney and Pagano [2]. Moon [3], using Mindlin theory investigated the response of infinite laminated plates subjected to transverse impact loads at the centre of the plate. Chow [4] employed the Laplace transform technique to study the dynamic response of orthotropic laminated plates. Wang et al. [5] applied the method of characteristics to investigate the dynamic response of unsymmetrical orthotropic laminated plates. Sun et al. [6-8] employed the classical method of separation of variables combined with the Mindlin-Goodman [9] procedure for treating time-dependent boundary conditions and/or dynamic external loadings on plates under cylindrical bending. Reddy [10,11] presented closed form solution and finite element results for linear transient analysis of layered composite plates. All of these investigations are based on either the classical (Kirchhoff) plate theory or the first order shear deformable (Mindlin/Reissner) theory.

A higher order shear deformation theory developed by one of the present authors [12] is employed here to investigate the transient response of isotropic and layered anisotropic composite plates. The finite element idealization is adopted and the quadratic nine noded Lagrangian isoparametric plate element is used together with selective integration. Explicit time marching scheme is adopted for integration of the dynamic equilibrium equation and a diagonal 'lumped' mass matrix is employed with a special procedure. Numerical results are presented and compared with results from other sources. A review of the literature indicates that no previous finite-element analyses of higher-order theory for transient response of plates are available.

2. THEORY

The present higher-order shear deformation theory is based on the displacement model

$$u(x,y,z,t) = u_o(x,y,t) + z\theta_x(x,y,t) + z^2 u_o^*(x,y,t) + z^3\theta_x^*(x,y,t)$$

$$v(x,y,z,t) = v_o(x,y,t) + z\theta_y(x,y,t) + z^2 v_o^*(x,y,t) + z^3\theta_y^*(x,y,t)$$

$$w(x,y,z,t) = w_o(x,y,t) \tag{1}$$

where t is the time, u_o, v_o and w_o are the inplane and transverse displacements of a point (x,y) on the mid-plane respectively and θ_x, θ_y are the rotations of normals to mid-plane about y and x axes respectively. The parameters u_o^*, v_o^*, θ_x^*, θ_y^* are the corresponding higher-order deformation terms in the Taylor's series expansion and are also defined at mid-plane.

The strains associated with the displacements in (1) are,

$$\varepsilon_x = \frac{\partial u_o}{\partial x} + z\frac{\partial \theta_x}{\partial x} + z^2\frac{\partial u_o^*}{\partial x} + z^3\frac{\partial \theta_x^*}{\partial x}\ ;\quad \varepsilon_y = \frac{\partial v_o}{\partial y} + z\frac{\partial \theta_y}{\partial y} + z^2\frac{\partial v_o^*}{\partial y} + z^3\frac{\partial \theta_y^*}{\partial y}$$

$$\varepsilon_z = 0\ ;\ \gamma_{xy} = \left(\frac{\partial u_o}{\partial y} + \frac{\partial v_o}{\partial x}\right) + z\left(\frac{\partial \theta_x}{\partial y} + \frac{\partial \theta_y}{\partial x}\right) + z^2\left(\frac{\partial u_o^*}{\partial y} + \frac{\partial v_o^*}{\partial x}\right) + z^3\left(\frac{\partial \theta_x^*}{\partial y} + \frac{\partial \theta_y^*}{\partial x}\right)$$

$$\gamma_{yz} = \theta_y + \frac{\partial w_o}{\partial y} + z(2v_o^*) + z^2(3\theta_y^*)\ ;\quad \gamma_{zx} = \theta_x + \frac{\partial w_o}{\partial x} + z(2u_o^*) + z^3(3\theta_y^*) \tag{2}$$

The stress-strain relations for the L^{th} lamina of the laminate coordinates (x,y,z) are written in a compact form as

$$\underset{\sim}{\sigma} = \underline{Q}\,\underset{\sim}{\varepsilon} \tag{3a}$$

where $\underset{\sim}{\sigma} = \left[\sigma_x, \sigma_y, \tau_{xy}, \tau_{yz}, \tau_{zx}\right]^T$; $\underset{\sim}{\varepsilon} = \left[\varepsilon_x, \varepsilon_y, \gamma_{xy}, \gamma_{yz}, \gamma_{zx}\right]^T$

and $$\underline{Q} = \begin{bmatrix} \underline{Q}_{ij} & 0 \\ 0 & \underline{Q}_{\ell m} \end{bmatrix};\quad \begin{matrix} i,j = 1,2,3 \\ \ell,m = 4,5 \end{matrix} \tag{3b}$$

Integration of (3a) through the plate thickness gives the plate constitutive relations. The following eighteen stress-resultants for the n-layered laminate are thus obtained:

$$\begin{bmatrix} N_x, N_y, N_{xy} \\ N_x^*, N_y^*, N_{xy}^* \end{bmatrix} = \sum_{L=1}^{n} \int_{h_L}^{h_{L+1}} \begin{bmatrix} \sigma_x, \sigma_y, \tau_{xy} \\ z^2\sigma_x, z^2\sigma_y, z^2\tau_{xy} \end{bmatrix} dz\ ;$$

$$\begin{bmatrix} M_x, M_y, M_{xy} \\ M_x^*, M_y^*, M_{xy}^* \end{bmatrix} = \sum_{L=1}^{n} \int_{h_L}^{h_{L+1}} \begin{bmatrix} z\sigma_x, z\sigma_y, z\tau_{xy} \\ z^3\sigma_x, z^3\sigma_y, z^3\tau_{xy} \end{bmatrix} dz$$

$$(Q_x, S_x, Q_x^*) = \sum_{L=1}^{n} \int_{h_L}^{h_{L+1}} \tau_{xz}(1, z, z^2)dz;\quad (Q_y, S_y, Q_y^*) = \sum_{L=1}^{n} \int_{h_L}^{h_{L+1}} \tau_{yz}(1, z, z^2)dz \tag{4}$$

where $N_x^*, N_y^*, N_{xy}^*, M_x^*$ .... etc. are the higher-order stress resultants as defined in (4) above.

After integration, this can be written in the matrix form as

$$\begin{bmatrix} \underset{\sim}{N} \\ \underset{\sim}{N}^* \\ \underset{\sim}{M} \\ \underset{\sim}{M}^* \end{bmatrix} = \sum_{L=1}^{n} \begin{bmatrix} Q_{ij}\theta_1 & Q_{ij}\theta_3 & Q_{ij}\theta_2 & Q_{ij}\theta_4 \\ & Q_{ij}\theta_5 & Q_{ij}\theta_4 & Q_{ij}\theta_6 \\ & & Q_{ij}\theta_3 & Q_{ij}\theta_5 \\ \text{SYMMETRICAL} & & & Q_{ij}\theta_7 \end{bmatrix} \begin{bmatrix} \underset{\sim}{\varepsilon}_o \\ \underset{\sim}{\varepsilon}_o^* \\ \underset{\sim}{k} \\ \underset{\sim}{k}^* \end{bmatrix} ;$$

$$\begin{bmatrix} \underset{\sim}{Q} \\ \underset{\sim}{Q}^* \end{bmatrix} = \sum_{L=1}^{n} \begin{bmatrix} Q_{m\ell}\theta_1 & Q_{m\ell}\theta_2 & Q_{m\ell}\theta_3 \\ & Q_{m\ell}\theta_3 & Q_{m\ell}\theta_4 \\ \text{SYMMETRICAL} & & Q_{m\ell}\theta_5 \end{bmatrix} \begin{bmatrix} \underset{\sim}{\phi} \\ \underset{\sim}{\phi}^* \end{bmatrix} \qquad (5)$$

in which, $\underset{\sim}{\varepsilon}_o = \left[\varepsilon_{xo}, \varepsilon_{yo}, \varepsilon_{xyo}\right]^T$, $\underset{\sim}{\varepsilon}_o^* = \left[\varepsilon_{xo}^*, \varepsilon_{yo}^*, \varepsilon_{xyo}^*\right]^T$

$\underset{\sim}{k} = \left[k_x, k_y, k_{xy}\right]^T$, $\underset{\sim}{k}^* = \left[k_x^*, k_y^*, k_{xy}^*\right]^T$

$\underset{\sim}{\phi} = \left[\phi_x, \phi_y\right]^T$, $\underset{\sim}{\phi}^* = \left[\varepsilon_{xzo}, \varepsilon_{yzo}, \phi_x^*, \phi_y^*\right]^T$

In all the above relations, n is the number of layers and

$$\theta_i = \frac{1}{I}\left(h_{L+1}^i - h_L^i\right) , \quad i = 1,2,3,4,5,6.7 \qquad (6)$$

3. FINITE ELEMENT DISCRETISATION

Whatever is the approximate discretisation scheme in space, the dynamic problem (in the absence of damping) invariably gives rise to a set of ordinary differential equations of the form

$$\underline{M}\, \ddot{\underset{\sim}{a}}(t) + \underline{k}\, \underset{\sim}{a}(t) = \underset{\sim}{P}(t) \qquad (7)$$

in which the dots denote differentiation in time, t, $\underset{\sim}{a}$ is the nodal displacement vector, $\underline{M}$ is the mass matrix and $\underset{\sim}{P}(t)$ is the vector of forces which varies with time, t.

In C^o finite element theory, the continuum displacement vector within the element is discretised such that

$$\underset{\sim}{a}(x,y,t) = \sum_{i=1}^{NN} N_i(x,y)\, \underset{\sim}{a}_i(t) \qquad (8)$$

in which the term $N_i(x,y)$ is the shape function associated with node i,

NN is the number of nodes in the element. The elements of the stiffness matrix can readily be computed using the standard relation,

$$\underline{k}^{e}_{ij} = \int_{-1}^{+1}\int_{-1}^{+1} \underline{B}_i^T \underline{D}\, \underline{B}_j \,|\underline{J}|\, d\xi\, d\eta \tag{9}$$

where $\underline{B}$ is the strain-displacement matrix

$\underline{J}$ is the Jacobian matrix.

The mass matrix $\underline{M}$ in (7) is given by

$$\underline{M} = \int_{\text{Area}} \underline{N}^T \bar{\underline{m}}\, \underline{N}\, dA \tag{10}$$

where $\underline{N} = [\underline{N}_1, \underline{N}_2, \cdots \cdots \underline{N}_{NN}]$

and $$\bar{\underline{m}} = \begin{bmatrix} I_1 & & & & & & & & 0 \\ & I_1 & & & & & & & \\ & & I_1 & & & & & & \\ & & & I_2 & & & & & \\ & & & & I_2 & & & & \\ & & & & & I_3 & & & \\ & & & & & & I_3 & & \\ & & & & & & & I_4 & \\ 0 & & & & & & & & I_4 \end{bmatrix}$$

$$(I_1, I_2, I_3, I_4) = \sum_{L=1}^{n} \int_{h_L}^{h_{L+1}} (1, z^2, z^4, z^6)\, \rho^L\, dz$$

in which (I_1, I_2) and (I_3, I_4) are normal inertia, rotary inertia and higher-order inertias respectively. ρ^L is the material density of the L^{th} layer.

4. TIME STEPPING AND STABILITY

As already mentioned, the integration in time of (7) is performed using the explicit central difference scheme which is given by

$$\underset{\sim}{a}^{n+1} = \underline{M}^{-1}\left[(\Delta t)^2 (-\underline{k}\, \underset{\sim}{a}^{n} + \underset{\sim}{p}^{n}) - \underline{M}\, \underset{\sim}{a}^{n-1} + 2\underline{M}\, \underset{\sim}{a}^{n}\right] \tag{11}$$

where suffices n-1, n, n+1 stand for three successive time intervals and Δt is the time step length. If $\underline{M}$ is diagonal, the computation at every time step is trivial. Unfortunately this is not usually the case and further approximation has been made to bring about the diagonalization using a special lumping procedure (see ref. [13]).

The estimate of the critical time step length of the transient solution of Mindlin plates given by Tsui and Tong [14] is used with minor modification

in the present study. The critical time step length is thus given as

$$\Delta t = \Delta x \left[\frac{\rho (1-\nu^2) E_2 R}{2 + 0.83 (1-\nu) \{ 1 + 1.5 (\Delta x/h)^2 \}} \right]^{1/2} \qquad (12)$$

where $R = E_1/E_2$, Δx is the smallest distance between finite element node points, ν is the Poisson's ratio.

5. NUMERICAL EXAMPLES AND DISCUSSION

In all of the numerical examples presented herein, zero initial conditions were assumed. All of the computations were carried in single precision on CYBER 180/840 Computer. Due to biaxial symmetry of the problems discussed, only one quadrant of the plate was analysed except for angle-ply plates which are analysed by discretising full plates with 4 x 4 mesh.

The following two sets of data and boundary conditions were used:

DATA 1 : Square plate, $a = b = 25$ cm, $h = 5$ cm, $q_o = 10$ N/cm^2
$\rho = 8 \times 10^{-6}$ N-sec^2/cm^4, $\nu = 0.25$, $E_2 = 2.1 \times 10^6$ N/cm^2

DATA 2 : Plate with $a = \sqrt{2}$ and $b = 1$, $h = 0.2$, $\rho = 1$, $q = 1$
$\nu = 0.3$, $E_2 = 1.0$ (non-dimensional)

BOUNDARY CONDITIONS:

Simply supported plate:
$$x = 0,a \; ; \quad v_o = v_o^* = w_o = \theta_y = \theta_y^* = 0$$
$$y = 0,b \; ; \quad u_o = u_o^* = w_o = \theta_x = \theta_x^* = 0$$

Clamped plate :
$$x = 0,a; \; u_o = v_o = u_o^* = v_o^* = w_o = \theta_x = \theta_y = \theta_x^* = \theta_y^* = 0$$
$$y = 0,b; \; u_o = v_o = u_o^* = v_o^* = w_o = \theta_x = \theta_y = \theta_x^* = \theta_y^* = 0$$

When an orthotropic or layered composite plate was analysed, the ratio of E_1 to E_2 was taken to be 25, and $G_{12} = G_{23} = G_{13} = 0.5\, E_2$.

In order to investigate the numerical convergence and accuracy of the transient behaviour of the element, a simply-supported, generally orthotropic ($0^\circ/90^\circ/0^\circ/90^\circ$) plate with suddenly applied uniform pulse loading was analysed using DATA 1. Table 1 shows centre deflection and normal stress for different meshes and time steps. From this table it is found that the safe estimate of the critical time step length given by (12) is valid for transient analysis of fibre reinforced composite thick plates.

The second example is taken from Reismann and Lee [15], who presented an analytical solution to the problem (see Fig. 1). The problem consists of a simply-supported rectangular plate subjected to a uniform pulse loading on a square (side = 0.2b) area at the centre of the plate. The present finite element solution for the centre deflection is in excellent agreement with the

thick plate solution. Since the bending moment in the present study was calculated at the Gauss points, it is not expected to match exactly with that at the centre of the plate.

Table 2 presents centre deflection, centre normal stress, corner in-plane shear stress, and transverse shear stress at the midside for two layer cross-ply, simply-supported square plate (DATA 1), subjected to suddenly applied sinusoidal loading. The present solutions with the closed form solutions (Mindlin's theory) [10] are compared. It is found that the Mindlin's theory predicts slightly lower values of period and stresses. To show the effect of the coupling between the inplane displacements (u_o, v_o, u_o^*, v_o^*) and bending displacements (w , $\theta_x, \theta_y, \theta_x^*, \theta_y^*$), and boundary conditions on the centre transverse deflection and stresses, a two-layer, angle-ply ($45^o/-45^o$) plate (DATA 1) subjected to suddenly applied uniform pulse loading, was analysed for two different boundary conditions: simply supported and clamped. The results are shown in Fig. 2. It is seen that the coupling has a noticeable influence on the response of the plate.

The last example is concerned with transient response of a four-layer ($30^o/45^o/90^o/0^o$), clamped square plate (DATA 1) under impulsive loading: $q = q_o\, \theta(t - t_o)$, t_o = 10 μ-sec, $\theta(t)$ denotes the heavy side step function. Fig. 3 shows plots of the centre deflection and normal stress with respect to time. Since no damping or internal friction is included in the present model the solutions do not decay with time.

6. CONCLUSIONS

Numerical results of the linear dynamic analysis of isotropic, orthotropic, and layered composite plates are presented. The present higher-order shear deformable theory does not require the usual shear correction coefficients generally associated with the Mindlin-Reissner type of theories. The present finite element results agree very well with the exact solutions available in the literature for isotropic plates. New results are presented and compared wherever possible for the transient response of composite plates.

ACKNOWLEDGEMENT

Partial support of this research by the Aeronautics Research and Development Board, Ministry of Defence, Government of India, through its Grant No. Aero/RD-134/100/84-85/362 is gratefully acknowledged.

REFERENCES

1. P.C. YANG, C.H. NORRIS and Y. STAVSKY 1966 International Journal of Solids and Structures 2, 665-684. Elastic wave propagation in heterogeneous plates.

2. J.M. WHITNEY and N.J. PAGANO 1970 Journal of Applied Mechanics 37, 1031-1036. Shear deformation in heterogeneous anisotropic plates.

3. F.C. MOON 1973 Journal of Applied Mechanics 40 , 485-490. One dimensional transient waves in anisotropic plates.

4. T.S. CHOW 1971 Journal of Composite Materials 5, 306-319. On the propagation of flexural waves in an orthotropic laminated plate and its response to an impulsive load.

5. A.S.D. WANG, P.C. CHOW and J.L. ROSE 1972 American Institute of Aeronautics and Astronautics Journal 1088-1090. Strongly coupled stress waves in heterogeneous plates.

6. C.T. SUN and J.M. WHITNEY 1974 Journal of the Acoustical Society of America 55(5), 1003-1008. Forced vibrations of laminated composite plates in cylindrical bending.

7. C.T. SUN and J.M. WHITNEY 1975 American Institute of Aeronautics and Astronautics Journal 13(10), 1259-1260. Dynamic response of laminated composite plates.

8. J.M. WHITNEY and C.T. SUN 1977 Journal of the Acoustical Society of America 61(1), 101-104. Transient response of laminated composite plates subjected to transverse dynamic loading.

9. R.D. MINDLIN and L.F. GOODMAN 1950 Journal of Applied Mechanics 17, 377-380. Beam vibrations with time-dependent boundary conditions.

10. J.N. REDDY 1982 Journal of Applied Mechanics 49, 403-408. On the solutions to forced motions of rectangular composite plates.

11. J.N. REDDY 1983 International Journal for Numerical Methods in Engineering 19, 237-255. Dynamic (transient) analysis of layered anisotropic composite-material plates.

12. B.N. PANDYA and T. KANT 1987 Composite Science and Technology (in press, 1988). Finite element analysis of laminated composite plates using a higher-order displacement model.

13. R.D. COOK 1981 Concepts and Applications of Finite Element Analysis. New York: John Wiley and Sons.

14. T.Y. TSUI and P. TONG 1971 American Institute of Aeronautics and Astronautics Journal 9, 2062-2063. Stability of transient solution of moderately thick plates by finite difference method

15. H. REISMAN and Y. LEE 1969 Development in Theoretical and Applied Mechanics 4, 3-18, (Ed. D. Frederick), Pergamon Press, New York. Forced motions of rectangular plates.

16. MALLIKARJUNA and T. KANT 1988 American Institute of Aeronautics and Astronautics Journal (under review). Finite element formulation of a high-order theory for dynamic response of laminated composite plates.

17. MALLIKARJUNA and T. KANT 1988 ASME, Journal of Applied Mechanics (communicated). Finited element transient response of composite and sandwich plates with a refined higher-order theory.

Table 1. Convergence of centre deflection and stress for different time steps, (DATA 1) 4 layer ($0^\circ/90^\circ/0^\circ/90^\circ$) square plate

Time μ-sec	$W_o \times 10^3$ / σ_x top	Δt = 0.25 μ-sec			Δt = 0.5 μ-sec			Δt = 0.74 μ-sec
		2x2	3x3	4x4	2x2	3x3	4x4	2x2
40	W_o	0.23878	0.23878	0.23911	0.23880	0.23875		0.23867
	σ	193.157	189.934	189.071	193.230	189.929		193.033
80	W_o	0.47768	0.47692	0.47685	0.47767	0.47690		0.47768
	σ	391.481	385.588	387.391	391.078	385.182	UNSTABLE	390.592
120	W_o	0.23701	0.23371	0.23185	0.23698	0.23361		0.23738
	σ	196.270	190.045	186.166	196.282	190.340		197.333
160	W_o	-0.00092	-0.00371	-0.00113	-0.00091	-0.00566		-0.00094
	σ	-2.0816	-11.367	-2.863	-1.32508	-11.389		-1.1805
200	W_o	0.24325	0.24566		0.24328	0.24573		0.24261
	σ	193.219	195.437		193.123	196.001		192.712

Table 2. Comparison of transverse deflection and stresses obtained in the present study with Mindlin plate closed form solution 10 for two layer cross-ply ($0^\circ/90^\circ$) square plate (DATA 1) under suddenly applied sinusoidal load

Time μ-sec	Centre deflection $W_o \times 10^3$		Normal stress σ_x		Inplane shear stress τ_{xy}		Transverse shear stress τ_{xz}	
	Present	CFS	Present	CFS	Present	CFS	Present	CFS
20	0.0468	0.0365	38.95	28.48	2.527	1.611	2.190	3.450
40	0.1660	0.1472	125.5	113.6	10.41	8.506	5.730	6.699
60	0.3136	0.2922	239.8	227.2	19.26	16.47	12.00	14.04
80	0.4290	0.4116	324.0	319.1	26.96	23.85	15.89	17.34
100	0.4697	0.4604	357.2	357.8	29.11	26.27	18.40	20.13
120	0.4174	0.4173	315.2	323.1	26.13	24.12	16.19	17.09
140	0.2945	0.3010	224.9	233.0	18.21	17.05	12.21	12.89
160	0.1477	0.1562	112.7	119.6	9.079	8.848	6.327	6.501
180	0.0354	0.0414	28.48	30.40	2.016	2.029	2.155	2.264
200	0.0013	0.0013	3.324	0.742	0.159	0.248	0.548	0.937

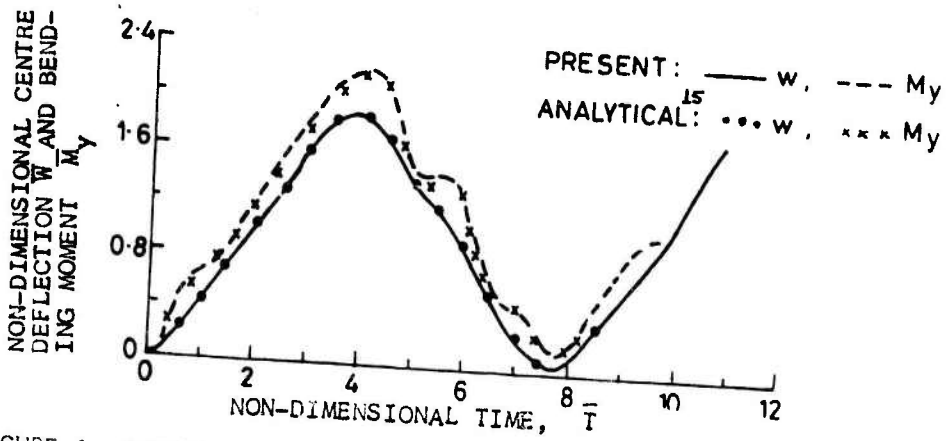

FIGURE 1. NON-DIMENSIONALIZED CENTRE DEFLECTION AND BENDING MOMENT VERSUS TIME FOR SIMPLY-SUPPORTED, RECTANGULAR, ISOTROPIC PLATE UNDER SUDDENLY APPLIED LOADING (DATA 2, 4x4, ΔT = .02, $\bar{w} = wEah/qb^3$, $\bar{T} = t/b\sqrt{E/\rho}$ $\bar{M}_y = 12\ a\ M_y/qb^2h^2$)

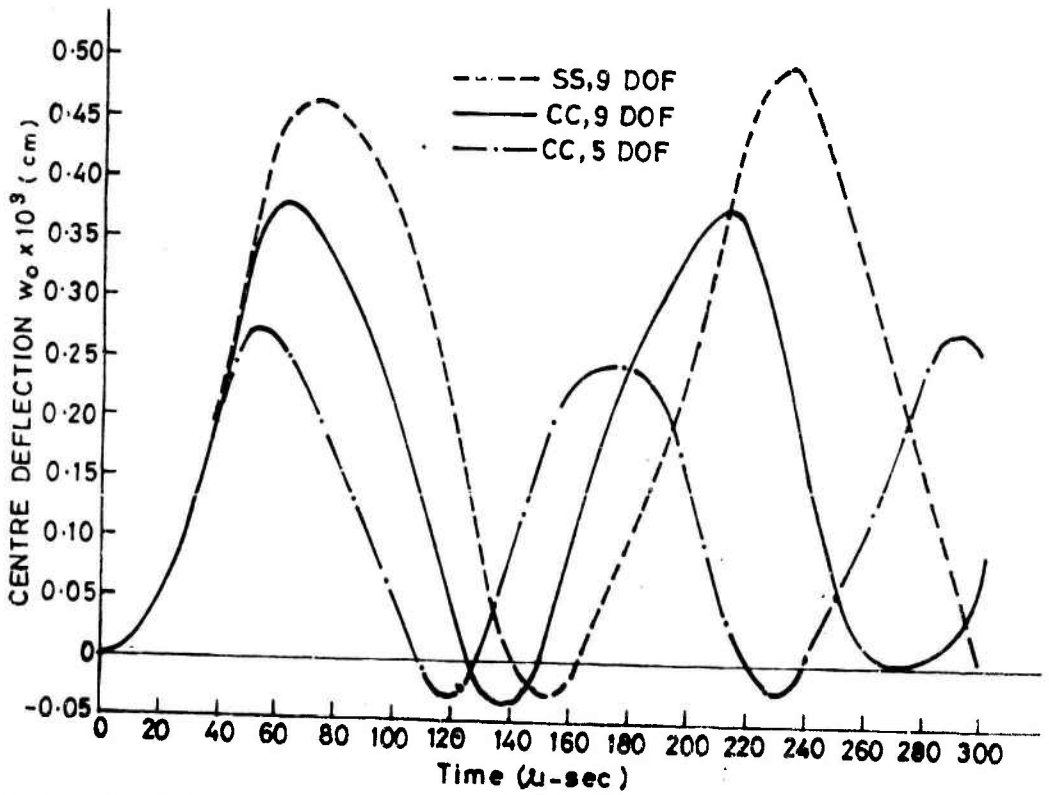

FIGURE 2 (a). CENTRE DEFLECTION OF ANGLE-PLY (45°/-45°) PLATES UNDER PULSE LOADING (DOF = DEGREES OF FREEDOM, SS = SIMPLY SUPPORTED, CC = CLAMPED, DATA 1, 4X4 MESH)

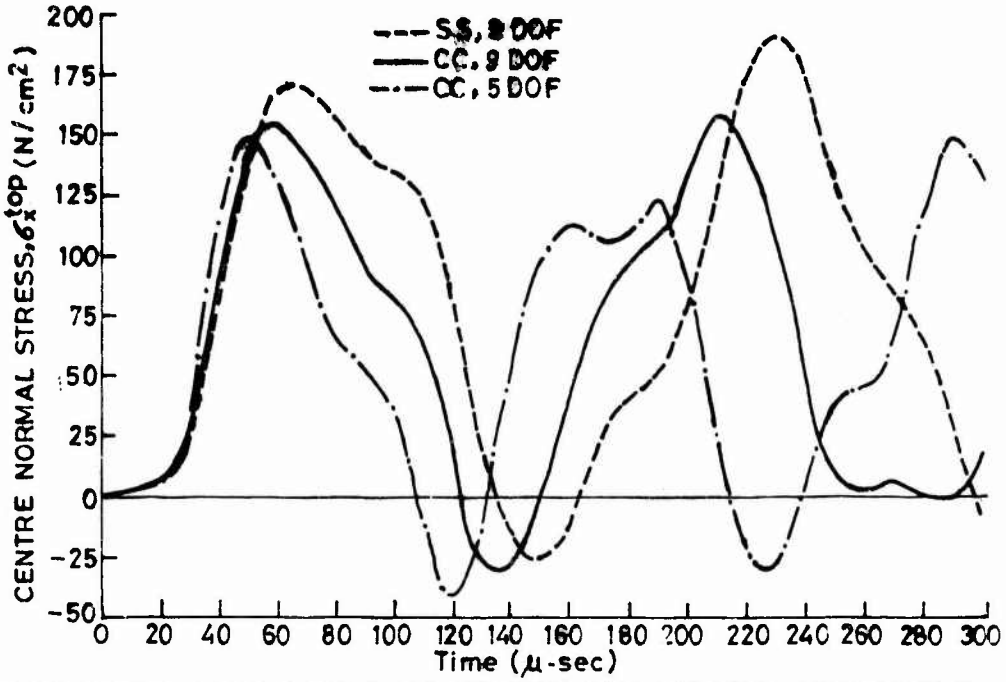

FIGURE 2 (b) - CENTRE NORMAL STRESS VERSUS TIME FOR ANGLE-PLY (45°/45°) PLATES UNDER PULSE LOADING, (DATA-1)

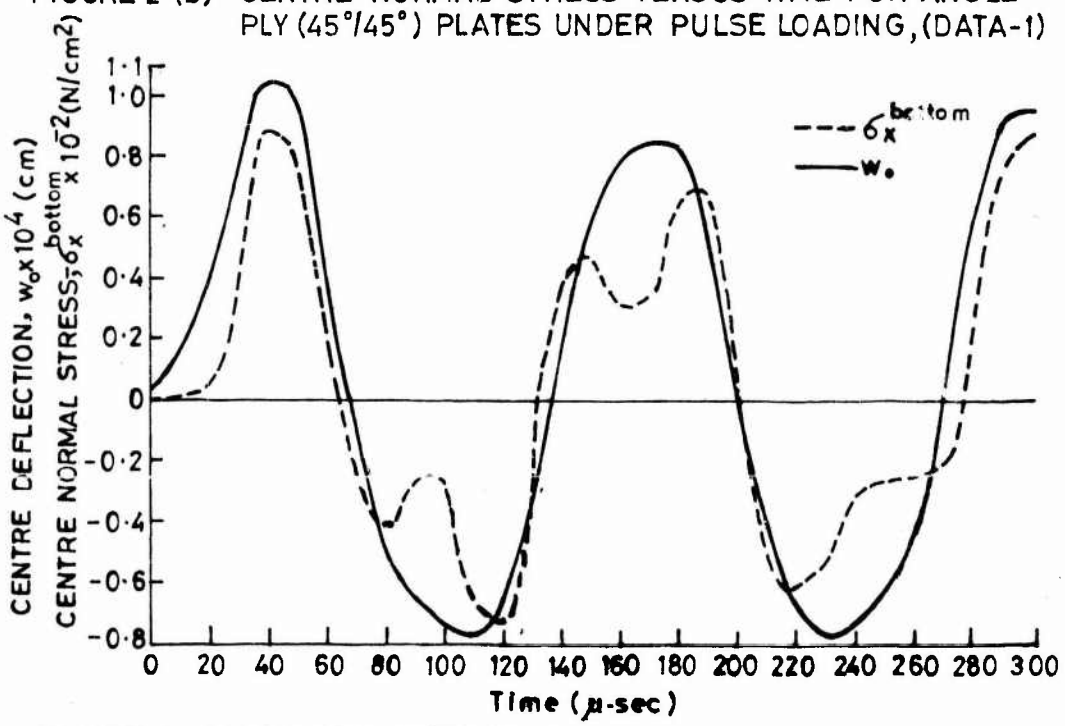

FIGURE 3 - CENTRE DEFLECTION AND NORMAL STRESS FOR FOUR-LAYER (30°/45°/90°/0°) CLAMPED PLATE UNDER IMPULSIVE LOADING, $q = q_o H(t - t_o)$, t_o = 10 μ-sec, DATA-1, q_o = 10 N/cm^2

FREE VIBRATION AND BUCKLING OF CROSS-PLY LAMINATED SHEAR-DEFORMABLE SHALLOW SHELL-TYPE PANELS

by

L. Librescu, A. A. Khdeir, and D. Frederick
Department of Engineering Science and Mechanics
Virginia Polytechnic Institute and State University
Blacksburg, Virginia 24061 USA

1. INTRODUCTION

A tremendous interest in the analysis of laminated composite plate and shell-like structures has emerged in recent years. This interest is due to the advent and increased use of high modulus, high strength, low weight composite materials in the various fields of modern technology. It is further fueled by the fact that the classical theory (based on Love-Kirchhoff (LK) assumptions) fails to predict accurately the static and dynamic response, when the structures in question are rather thick and/or when they exhibit high anisotropy ratios.

In such cases more refined theories are needed. They are to incorporate the effects of transverse shear deformation, transverse normal stress as well as other higher order effects. Pertinent analyses devoted to the substantiation of single layered or laminated composite shell theories are presented in the literature, e.g., in [1] in which the reader could also find extensive pertinent references.

The goal of this paper is two fold: i) to develop a simple shear-deformable theory for doubly-curved shallow cross-ply composite shells and ii) to apply a powerful solution technique, based on the state-space concept to evaluate the (static and dynamic) response of such shells for a variety of boundary conditions.

The theory developed in this paper is aimed at preserving all the advantages of the first order transverse shear deformation theory (FSDT), both with regard to the number of involved unknowns and the order of the associated governing equations. However, in contrast to FSDT the present theory is based on: i) an accurate representation of transverse shear stress components across the shell thickness (thus eliminating the need for a shear correction factor), and ii) the elimination of the contradictory assumption involving the simultaneous consideration of zero transverse normal stress σ^{33} and zero transverse normal strain e_{33}. Furthermore, the results obtained will be compared with their counterparts obtained within the framework of FSDT and classical theory (CST), for which their response characteristics will be determined by the same state-space technique.

2. PRELIMINARIES

Let us consider the case of a shallow composite panel constituted of a finite number, N, of homogeneous layers. We will consider that the material of each constituent layer is linearly elastic and anisotropic and that all layers are perfectly bonded.

All points in the 3D space of the composite shell are referred to a set of curvilinear orthogonal coordinates x^1, while the reference surface S) σ of the composite shell defined by $x^3 = 0$, is selected as the mid-

surface of the laminate, so that the external boundary surfaces of the panel are defined by $x^3 = \pm h/2$ where h denotes the total uniform thickness of the laminated shell.

3. BASIC ASSUMPTIONS AND GEOMETRICAL RELATIONS

In order to reduce the 3D problem to an equivalent 2D one we shall use the equations connecting the covariant derivatives of space tensors with their surface counterparts. Such relationships, useful in the forthcoming developments, are:

$$T_{\alpha\|\beta} = \mu_\alpha^\nu(\bar{T}_{\nu|\beta} - b_{\nu\beta}\bar{T}_3) \; ; \; T_{\alpha\|3} = \mu_\alpha^\nu \bar{T}_{\nu,3}$$

$$T_{3\|\alpha} = \bar{T}_{3,\alpha} + b_\alpha^\nu \bar{T}_3 \; ; \; T_{3\|3} = \bar{T}_{3,3} \tag{1}$$

Here, partial differentiation is denoted by a comma $(\,)_{,i} \equiv \partial/\partial x_i$, while $(\,)\|_i$ and $(\,)|_\alpha$ stand for the covariant differentiations with respect to the space and surface metrics, respectively, while the shifted components are identified by an upper bar. In the above relationships (as well as in the following developments) the Einsteinian summation convention applies to repeated indices where Latin indices range from 1 to 3 while the Greek indices range from 1 to 2. The conditions of shallowness of a shell, are discussed e.g. in [1]. Let Z denote the amount of deviation of the shell reference surface from a plane Π (measured normal to the plane). This quantity is assumed to be small when compared with a maximum length of an edge of the shell or with a minimum radius of curvature of the RS. For this case assuming properly that

$$\max Z_{,\alpha} \ll 1 \tag{2}$$

gives rise to the result that the metric tensors associated with the system of coordinates on σ and with its projection on the plane Π are the same and in addition that the curvature tensor of the reference surface behaves as a constant in the differentiation operation.

These are important conclusions allowing one to infer that if the projected coordinate curves on Π constitute a Cartesian orthogonal net, then the original ones on σ are to be, on the basis of (2), also a Cartesian orthogonal net. Due to the equivalence of the two metrics, we may also conclude that the surface covariant differentiations may be done with respect to the plane Π and thus it is possible to change the order of the covariant differentiations (since the Riemann-Christoffel tensor associated with the plane vanishes).

For the shallow shell theory (SST) we may appropriately consider that

$$\mu_\beta^\alpha \; (\equiv \delta_\rho^\alpha - x^3 b_\beta^\alpha) + \delta_\beta^\alpha \tag{3}$$

where μ_β^α referred to as the shell tensor plays the role of a shifter in the space of normal coordinates ([1]). From (3) we may also conclude that in this case

$$\mu \equiv |\mu_\beta^\alpha| = (g/a)^{1/2} \to 1 \tag{4}$$

where $g \equiv \det(g_{ij})$ and $a \equiv \det(a_{\alpha\beta})$. Here δ^{α}_{β} and b^{α}_{ρ} denote the Kronecker delta and the mixed curvature tensor, respectively, while g_{ij} and $a_{\alpha\beta}$ denote the metric tensors of the space and surface σ, respectively.

It is worth mentioning that the equations which will be obtained in this framework are not only applicable to the theory of shells which are geometrically shallow, but also to other kinds of shells (i.e., to closed cylindrical shells or in general to ones of zero Gaussian curvature), whose state of stress and strain exhibit a high degree of variability. In this connection it should be noted that the well-known Donnell-Mushtari Vlasov shell-theory corresponds entirely to such an approximate theory (see e.g. [1]).

4. DISPLACEMENT REPRESENTATION AND STRAIN MEASURES

In order to model the theory of laminated shells there are, roughly speaking, two main approaches: i) to start with some statical assumptions concerning, e.g., the variation of transverse shear stresses across the laminate thickness or ii) to start with a certain representation of the displacement field through the entire laminate (or through each layer separately, by preserving however its continuity between the contiguous layers). Although the first approach was used in several papers the second one appears more promising.

While the stress field exhibits jumps, the displacement field is to be assumed continuous through the laminate thickness. That is why, in the following, the latter option will be adopted. In this sense, the shifted displacements will be represented as:

$$\overline{V}_{\alpha}(x^{\omega},x^{3};t) = \overset{(0)}{V}_{\alpha} + x^{3}\overset{(1)}{V}_{\alpha} + (x^{3})^{2}\overset{(2)}{V}_{\alpha} + (x^{3})^{3}\overset{(3)}{V}_{\alpha} \; ; \; \overline{V}_{3}(x^{\omega},x^{3};t) = \overset{(0)}{V}_{3} \tag{5}$$

where

$$\overset{(m)}{V}_{i} \equiv \overset{(m)}{V}_{i}(x^{\omega};t).$$

The form of the representation given in Eq. (5) has as a goal the exact fulfillment of tangential static conditions on the boundary surfaces $x^3 = \pm h/2$, i.e., of

$$[\sigma^{\alpha 3}]^{h/2}_{-h/2} = p^{\alpha}_{(0)} \quad \text{and} \quad [\sigma^{\alpha 3}x^{3}]^{h/2}_{-h/2} = p^{\alpha}_{(1)} \tag{6}$$

where $\sigma^{\alpha 3}$ are the transverse shearing components of the stress tensor σ^{ij}, while $p^{\alpha}_{(0)}$ and $p^{\alpha}_{(1)}$ denote the tangential load and load couple components, respectively (measured per unit area of the reference surface).

The constitutive equation employed is the one associated with an elastic anisotropic body

$$\sigma^{\alpha 3} = 2E^{\alpha 3\omega 3}e_{\omega 3} \tag{7}$$

where $e_{\omega 3}$ denote the transverse shear components of the strain tensor e_{ij} expressible in terms of the displacement components as

$$2e_{ij} = V_{i\|j} + V_{j\|i} \tag{8}$$

In the case of cross-ply laminated shells, (the axes of orthotropy coinciding in each point with the geometrical ones), employment in (6) of (7) and (8) yields:

$$V_\lambda^{(2)} = \frac{2}{h} p^\alpha_{(0)} F^{<+>}_{\alpha 3 \lambda 3} \; ; \; V_\lambda^{(3)} = -\frac{4}{3h^2}\left(-\frac{4}{h} p^\alpha_{(1)} F^{<+>}_{\alpha 3 \lambda 3} + V^{(0)}_{3,\lambda} + V^{(1)}_\lambda + b^\gamma_\lambda V^{(0)}_\lambda\right) \quad (9)$$

In (7) and (9) E^{ijmn} and F_{ijmn} denote the tensors of elastic moduli and of elastic compliances, respectively, while the plus sign in the brackets <> signifies that the respective quantity affected by this sign belongs to the top layer. In the remaining developments, the affiliation of a quantity to a certain layer k will be identified by including the letter k in the brackets <>, (e.g., $E^{\alpha\beta\rho\omega}_{<k>}$). By virtue of (9), upon fulfilling the static tangential conditions (6), the total number of nine unknown functions, (i.e., $V^{(0)}_3$ and $V^{(m)}_\alpha$, $m = \overline{0,3}$) may be reduced to five (i.e., $V^{(0)}_3$, $V^{(0)}_\alpha$ and $V^{(1)}_\alpha$), i.e., to the same unknowns as in the case of FSDT.

In the following, for purposes of simplification, we shall consider that $p^\alpha_{(0)} = p^\alpha_{(1)} = 0$. By virtue of (5), (9) and (8), the expressions for the nonvanishing components of the strain tensor are obtained and given in [1]. It is shown in [1] that when

$$V^{(1)}_\alpha = -\left(V^{(0)}_{3,\alpha} + b^\rho_\alpha V^{(0)}_\rho\right) \quad (10)$$

and when the terms of order x^3/R are neglected with respect to unity, the strain measures reduce to the ones associated with CST of shallow shells. In the case of FSDT, the displacement field across the laminate thickness is represented as

$$V_\alpha(x^\omega, x^3; t) = V^{(0)}_\alpha + x^3 V^{(1)}_\alpha \; ; \; V_3(x^\omega, x^3; t) = V^{(0)}_3 \quad (11)$$

while the associated strain measures are obtained and defined in [1].

5. CONSTITUTIVE EQUATIONS

The 3D constitutive equations associated with an elastic anisotropic body may be expressed as

$$\sigma^{\alpha\beta} = \tilde{E}^{\alpha\beta\omega\rho} e_{\omega\rho} + \delta_A \frac{E^{\alpha\beta 33}}{E^{3333}} \sigma^{33} \; ; \; \sigma^{\alpha 3} = 2E^{\alpha 3 \omega 3} e_{\omega 3}. \quad (12)$$

Here

$$\tilde{E}^{\alpha\beta\omega\rho} = E^{\alpha\beta\omega\rho} - \frac{E^{\alpha\beta 33} E^{33\omega\rho}}{E^{3333}}$$

where δ_A is a tracer identifying the contribution of σ^{33} in the constitutive equations (and later in the governing equations).

In order to express σ^{33} in terms of the basic unknowns, we will use the third 3D equation of motion, in which the covariant space differentiation is to be converted into surface differentiation. This conversion yields:

$$\sigma^{3\beta}{}_{|\beta} + \sigma^{33}_{,3} + b_{\gamma\beta}\sigma^{\beta\gamma} = \rho \overset{\cdot\cdot}{V}{}^{(0)}_{3} \tag{13}$$

where the dots denote time derivatives and ρ denotes the mass density. Integration of (13) over the segment $[0,x^3)$ and consideration of the assumptions pertinent to SST yields its expression displayed in [1]. The expressions for the stress resultants $L^{\alpha\beta}_{(0)}$, $L^{\alpha 3}_{(0)}$ and stress couples $L^{\alpha\beta}_{(1)}$ are expressed as

$$\{L^{\alpha\beta}_{(0)},\ L^{\alpha\beta}_{(1)}\} = \sum_{k=1}^{N} \int_{h_{\langle k-1\rangle}}^{h_{\langle k\rangle}} \sigma^{\alpha\beta}_{\langle k\rangle}(1,x^3)\,dx^3\ ;\ L^{\alpha 3}_{(0)} = \sum_{K=1}^{N} \int_{h_{\langle k-1\rangle}}^{h_{\langle k\rangle}} \sigma^{\alpha 3}_{\langle k\rangle}\,dx^3 \tag{14}$$

Considered in conjunction with strain-displacement equation (see [1]) the latter equations yield the constitutive equations expressed in terms of the displacements, where $h_{\langle k\rangle}$ and $h_{\langle k-1\rangle}$ denote the distances from the reference surface to the top and bottom surfaces of the k^{th} laye., respectively.

They may be expressed as

$$\begin{aligned}
L^{\alpha\beta}_{(0)} &= \tfrac{1}{2} F^{\alpha\beta\omega\rho}\big(V^{(0)}_{\omega|\beta} + V^{(0)}_{\rho|\omega} - 2b_{\omega\rho}V^{(0)}_{3}\big) + \big(G^{\alpha\beta\omega\rho} - \tfrac{4}{3h^2} I^{\alpha\beta\omega\rho}\big)\big(V^{(1)}_{\omega|\rho} + V^{(1)}_{\rho|\omega}\big) \\
&\quad - \tfrac{4}{3h^2} I^{\alpha\beta\omega\rho} V^{(0)}_{3,\omega\rho} - \delta_A\big(J^{\alpha\beta\rho\omega} - \tfrac{4}{3h^2} L^{\alpha\beta\rho\omega}\big)\big(V^{(0)}_{3,\omega\rho} + V^{(1)}_{\omega|\rho} + b^{\gamma}_{\omega}V^{(0)}_{\gamma|\rho}\big) \\
&\quad - \delta_A X^{\alpha\beta\omega\rho}\big(V^{(0)}_{\omega|\rho} + V^{(0)}_{\rho|\omega} - 2b_{\omega\rho}V^{(0)}_{3}\big) + \delta_A\delta_B \Lambda^{\alpha\beta 33}\overset{\cdot\cdot}{V}{}^{(0)}_{3} \\
L^{\alpha\beta}_{(1)} &= \tfrac{1}{2} G^{\alpha\beta\omega\rho}\big(V^{(0)}_{\omega|\beta} + V^{(0)}_{\rho|\omega} - 2b_{\omega\rho}V^{(0)}_{3}\big) \\
&\quad + \tfrac{1}{2}\big(H^{\alpha\beta\omega\rho} - \tfrac{4}{3h^2} S^{\alpha\beta\omega\rho}\big)\big(V^{(1)}_{\omega|\beta} + V^{(1)}_{\rho|\omega}\big) - \tfrac{4}{3h^2} S^{\alpha\beta\omega\rho} V^{(0)}_{3,\omega\rho} - \delta_A\big(K^{\alpha\beta\omega\rho} \\
&\quad - \tfrac{4}{3h^2} R^{\alpha\beta\omega\rho}\big)\big(V^{(0)}_{3,\omega\rho} + V^{(1)}_{\omega|\rho} + b^{\gamma}_{\omega}V^{(0)}_{\gamma|\rho}\big) - \delta_A Y^{\alpha\beta\omega\rho}\big(V^{(0)}_{\omega|\rho} \\
&\quad + V^{(0)}_{\rho|\omega} - 2b_{\omega\rho}V^{(0)}_{3}\big) + \delta_A\delta_B \Omega^{\alpha\beta 33}\overset{\cdot\cdot}{V}{}^{(0)}_{3} \\
L^{\alpha 3}_{(0)} &= \big(M^{\alpha 3\omega 3} - \tfrac{4}{h^2} P^{\alpha 3\omega 3}\big)\big(V^{(1)}_{\omega} + V^{(0)}_{3,\omega} + b^{\gamma}_{\omega}V^{(0)}_{\gamma}\big).
\end{aligned} \tag{15}$$

Here $F^{\alpha\beta\omega\rho}...Y^{\alpha\beta\omega\rho}$ denote the various rigidity quantities defined in [1], while the tracer δ_B identifies the contribution brought by the inertia terms in σ^{33}. As it may be seen, the constitutive equations (15) exhibit a coupling between the stretching and bending identified by the presence in $L^{\alpha\beta}_{(0)}$ of the bending quantities (i.e., $V_{2\,(0)}^{(1)}$ and $V_3^{(0)}$) and in $L^{\alpha\beta}_{(1)}$ and $L^{\alpha 3}_{(0)}$ of stretching quantities (i.e., of V_α). This physical coupling (occuring in the constitutive equations) becomes immaterial when the laminated composite is considered to be a symmetric layup.

6. THE GOVERNING EQUATIONS

The governing equations expressed in terms of the displacement quantities are obtained by replacing the stress-resultants and stress-couples (also expressed in terms of displacements) in the equations of motion of a shell element.

The macroscopic equations of motion (in number equal with the number of unknowns) are obtained adequately by taking the moments of order zero and one of the 3D elastokinetic equations (see e.g. [1]).

The equations of motion are:

$$L^{\alpha\beta}_{(0)}\big|_\alpha + p^\beta_{(0)} - f^\beta_{(0)} = 0 \;;\; b_{\alpha\beta}L^{\alpha\beta}_{(0)} + L^{\alpha 3}_{(0)}\big|_\alpha + p^3_{(0)} - f^3_{(0)} = 0 \qquad (16)$$

$$L^{\alpha\beta}_{(1)}\big|_\alpha - L^{\beta 3}_{(0)} + p^\beta_{(1)} - f^\beta_{(1)} = 0$$

Here the stress resultants and stress couples are to be considered in the sense of (14) while $p^\alpha_{(0)}$ and $p^\alpha_{(1)}$, according to the previous convention are to be considered as zero quantities. Also, $f^\beta_{(0)}$, $f^3_{(0)}$ and $f^\beta_{(1)}$ denote the inertia terms given by

$$f^\alpha_{(0)} = (m_{(1)}\ddot{V}^{(0)}_\lambda + m_{(2)}\ddot{V}^{(1)}_\lambda + m_{(4)}\ddot{V}^{(3)}_\lambda)a^{\alpha\lambda} \;;\; f^3_{(0)} = m_{(1)}\ddot{V}^{(0)}_3 \qquad (17)$$

$$f^\alpha_{(1)} = (m_{(2)}\ddot{V}^{(0)}_\lambda + m_{(3)}\ddot{V}^{(1)}_\lambda + m_{(5)}\ddot{V}^{(3)}_\lambda)a^{\alpha\lambda}$$

where $m_{(i)}$ $(i = \overline{1,5})$ denote the reduced mass terms defined by

$$m_{(i)} = \frac{1}{i}\sum_{k=1}^{N}\rho_{\langle k\rangle}(h^i_{\langle k\rangle} - h^i_{\langle k-1\rangle}) \qquad (18)$$

For computational purposes, we consider the case of a shallow panel whose reference surface projects on Π as a rectangle.

We will refer the points of σ to a system of coordinates coinciding with the lines of curvature, these being assumed parallel to the axes of

orthotropy of individual layers and to the projection on Π of the panel edges. In such a coordinate system (in which framework the distinction between contravariant, covariant and mixed tensors is immaterial and covariant differentiation reduces to partial differentiation), the governing equations may be compactly expressed as:

$$L_{ij}v_j + F_j = 0 \quad (i,j\ \overline{1,5}) \tag{19}$$

where the displacement and the force vectors are:

$$[v_j]^T = [v_1 \equiv {}^{(0)}V_1\ ,\ v_2 \equiv {}^{(0)}V_2\ ,\ v_3 \equiv {}^{(0)}V_3\ ,\ v_4 \equiv {}^{(1)}V_1\ ,\ v_5 \equiv {}^{(1)}V_2]$$

$$[F_j]^T = [0,\ 0,\ 0,\ 0,\ p^3_{(0)}] \tag{20}$$

while the operators L_{ij} are presented in [1].

7. FIRST ORDER TRANSVERSE SHEAR DEFORMATION AND CLASSICAL THEORIES OF SHALLOW COMPOSITE SHELLS

In order to compare the numerical results with the ones derived within the framework of FSDT and CST, several results pertaining to these theories will be recorded here. Consistent with the assumptions implied by FSDT, the associated constitutive equations are:

$$L^{\alpha\beta}_{(0)} = F^{\alpha\beta\omega\rho}{}^{(0)}e_{\omega\rho} + G^{\alpha\beta\omega\rho}{}^{(1)}e_{\omega\rho}\ ;\ L^{\alpha\beta}_{(1)} = G^{\alpha\beta\omega\rho}{}^{(0)}e_{\omega\rho} + H^{\alpha\beta\omega\rho}{}^{(1)}e_{\omega\rho} \tag{21}$$

$$L^{\alpha 3}_{(0)} = K^2_{(\omega)}E^{\alpha 3\omega 3}({}^{(1)}V_\omega + {}^{(0)}V_{3,\omega} + b^\gamma_\omega\, {}^{(0)}V_\gamma)$$

where $K^2_{(1)}$ and $K^2_{(2)}$ denote the shear correction factors.

As in the previous case, the governing equations in terms of displacements may be obtained in a straightforward manner. In the special case of the rectangular projection of the panel contour on Π, the governing equations may be formally represented as in Eqs. (19). The operators L_{ij} associated with this case are displayed in [1]. For CST, the constitutive equations may be expressed as

$$L^{\alpha\beta}_{(0)} = F^{\alpha\beta\omega\rho}{}^{(0)}e_{\omega\rho} + G^{\alpha\beta\omega\rho}{}^{(1)}e_{\omega\rho}\ ;\ L^{\alpha\beta}_{(1)} = G^{\alpha\beta\omega\rho}{}^{(0)}e_{\omega\rho} + H^{\alpha\beta\omega\rho}{}^{(1)}e_{\omega\rho} \tag{22}$$

where the strain measures are defined in [1]. Within the framework of CST, the transverse shear stress resultants have a static character only (in the sense that they intervene in the equation of motion only and not in the constitutive equations). Elimination of $L^{\alpha 3}_{(0)}$ in $(16)_{2,3}$ yields the equations of motion in an appropiate form as:

$$L^{\alpha\beta}_{(0)}\big|_\alpha = f^\beta_{(0)}\ ;\ b_{\alpha\beta}L^{\alpha\beta}_{(0)} + L^{\alpha\beta}_{(1)}\big|_{\alpha\beta} + p^3_{(0)} - f^3_{(0)} - f^\beta_{(1)\beta} = 0, \tag{23}$$

wherefrom the governing equations in terms of the displacements may easily be obtained. For the case of doubly-curved panels of rectangular projection on Π, they may be expressed as

$$L_{ij}v_j + F_i = 0 \quad (i,j = \overline{1,3}) \tag{24}$$

where

$$[v_j]^T = [\overset{(0)}{V_1}, \overset{(0)}{V_2}, \overset{(0)}{V_3}] \tag{25}$$

$$[F_i]^T = [0, 0, p^3_{(0)}]$$

while the operators L_{ij} are displayed in [1].

8. SOLUTION PROCEDURE

A generalized Lévy type solution considered in conjunction with the state space concept is used in order to analyze the free-vibration and buckling problems of composite shallow panels exhibiting a rectangular ($\ell_1 \times \ell_2$) projection on the plane Π.

The edges $x_2 = 0, \ell_2$ are considered invariably simply supported, while the remaining ones ($x_1 = \pm \ell_1/2$) may have arbitrary combinations of edge conditions. We will follow Levy's procedure, and will represent the unknown quantities so as to satisfy identically the boundary conditions (BC) at $x_2 = 0, \ell_2$ (i.e. $\overset{(0)}{V_3} = \overset{(0)}{V_1} = \overset{(1)}{V_1} = L^{22}_{(0)} = L^{22}_{(1)} = 0$ for HSDT and FSDT and $\overset{(0)}{V_3} = \overset{(0)}{V_1} = L^{22}_{(0)} = L^{22}_{(1)} = 0$ for CST). For the free vibration problem we are to drop the load term $p^3_{(0)}$ in the governing equations (19), (24), and represent the displacement quantities as:

$$\begin{Bmatrix} \overset{(0)}{V_1}(x_1,x_2;t) \\ \overset{(0)}{V_2}(x_1,x_2;t) \\ \overset{(0)}{V_3}(x_1,x_2;t) \\ \overset{(1)}{V_1}(x_1,x_2;t) \\ \overset{(1)}{V_2}(x_1,x_2;t) \end{Bmatrix} = \begin{Bmatrix} U_m(x_1)\sin \alpha_2 x_2 \\ V_m(x_1)\cos \alpha_2 x_2 \\ W_m(x_1)\sin \alpha_2 x_2 \\ X_m(x_1)\sin \alpha_2 x_2 \\ Y_m(x_1)\cos \alpha_2 x_2 \end{Bmatrix} e^{j\omega_m t} \tag{26}$$

where $j = \sqrt{-1}$, $\alpha_2 \equiv m\pi/\ell_2$ and ω_m denotes the eigenfrequency associated with the m^{th} eigenmode. The representation (26) is available both for FSDT and HSDT. For CST, in which framework only $\overset{(0)}{V_1}$, $\overset{(0)}{V_2}$ and $\overset{(0)}{V_3}$ intervene, their representation given by $(26)_{1,2,3}$ holds valid as well. For the static compressive buckling problem, the inertia terms are to be dropped from the governing equations and in addition $p^3_{(0)}$ is to be given by

$$p^{3}_{(0)} \to - T_{11} V^{(0)}_{3,11} - T_{22} V^{(0)}_{3,22} \tag{27}$$

where T_{11} and T_{22} denote the compressive uniform loads acting on the panel edges. The representation (26) of the displacement quantities subsists in this case, too, where however, due to the non-oscillatory character of the problem, $\omega_m \to 0$. Substitution of (26) into Eqs. (19) and their FSDT counterparts results in five differential equations in the x_1-coordinate, which may be presented, for both HSDT and FSDT in a similar way as:

$$\underset{\sim}{Z}' = A\underset{\sim}{Z} \tag{28}$$

where the matrix A is defined in [1] for both HSDT (and FSDT) as a 10 x 10 matrix and for CST as a 8 x 8 matrix.

A formal solution to the equation (28) is given by

$$\underset{\sim}{Z}(x_1) = e^{Ax_1}\underset{\sim}{K} \tag{29}$$

Here $\underset{\sim}{K}$ is a constant column vector associated with the boundary conditions while e^{Ax_1} is defined in [1]. Substitution of (29) into the boundary conditions associated with the remaining two opposite edges $x_1 = \pm \ell_1/2$ results in a homogeneous system of equations given by:

$$M_{ij}K_1 = 0 \ , \tag{30}$$

where ($i,j = \overline{1,10}$ for HSDT and FSDT) and ($i,j = \overline{1,8}$ for CST). The condition of nontriviality applied to (30) yields the determinantal equation

$$|M_{ij}| = 0 \tag{31}$$

wherefrom, the eigenfrequencies or the buckling loads (associated with the considered BC at $x_1 = \pm \ell_1/2$) may be determined.

9. NUMERICAL RESULTS AND CONCLUSIONS

A number of cases allowing one to obtain the trend of variation of eigenfrequencies and of buckling loads with the variation of geometrical parameters and/or the boundary conditions have been considered in [1]. It was assumed that the thickness and the material for all the laminae are the same, having the following characteristics. For the eigenvibration analysis:

$$E_1 = 25E_2, \ E_2 = E_3; \ G_{12} = G_{13} = 0.5 \ E_2;$$

$$G_{23} = 0.2 \ E_2; \ \nu_{12} = \nu_{13} = 0.25; \ \nu_{23} = 0.49,$$

while for the buckling analysis:

$$E_1 = 40 \ E_2; \ E_2 = E_3, \ G_{12} = G_{13} = 0.6 \ E_2$$

$$G_{23} = 0.5 \ E_2, \ \nu_{12} = \nu_{13} = 0.25; \ \nu_{23} = 0.49$$

The numerical results displayed in [1] allow one to infer the following. a) In the case of non-thin panels or in the case of panels whose materials exhibit high orthotropy ratios, the effect of transverse shear deformation is always to be incorporated into the analysis. This is equivalent to saying that in these cases CST fails to predict adequately the panel response characteristics (in the sense that both the eigenfrequencies and the buckling loads are overpredicted, b) The fundamental frequencies obtained as per HSDT and FSDT, appear underpredicted within FSDT when an antisymmetric laminate is considered and overpredicted when an symmetric laminate is analyzed (throughout the present numerical analyses $K^2_{(1)} = K^2_{(2)} = 5/6$). c) The buckling loads predicted by FSDT are more conservative when compared with their HSDT counterparts. The same conclusion emerges within every considered lamination scheme (i.e. symmetric or antisymmetric). d) The buckling loads experienced by the symmetrical laminates are higher than the ones arising in an antisymmetric laminate. In addition as it may be inferred this increase in the buckling loads is much higher within CPT than within FSDT and HSDT. For other numerical results and conclusions concerning this problem as well as for the effects of various edge conditions the reader is referred to the following Tables as well as to [1]. The boundary conditions on the edges $x_1 = \pm \ell_1/2$ are simply supported-simply supported (SS), simply supported-clamped (SC), clamped-clamped (CC), free-free (FF), free-simply supported (FS), and free-clamped (FC).

10. REFERENCES

1. D. FREDERICK, L. LIBRESCU and A. A. KHDEIR, "A Shear Deformable Theory of Laminated Composite Shallow Elastic Shells and Their Response Analysis, Part I. Free Vibration and Buckling," (submitted for publication).

Acknowledgement The partial support of this work by NASA Langley Research Center through Grant NAG-1-749 is gratefully acknowledged by L. Librescu.

Table 1: Nondimensionalized fundamental frequencies ($\bar{\omega} = (\omega t_1^2/h)\sqrt{\rho/E_2}$) of cross-ply spherical panels for various boundary conditions, ($t_1/t_2 = 1$; $t_1/h = 10$).

Lamination	R/t_1	Theory	SS	SC	CC	FF	FS	FC
0°/90°	5	HSDT	9.292	11.057	14.157	5.811	6.130	6.533
		FSDT	9.247	11.004	14.081	5.787	6.105	6.511
		CST	9.903	12.465	16.820	6.162	6.510	6.971
	20	HSDT	8.966	10.691	12.772	5.790	6.116	6.557
		FSDT	8.922	10.640	12.713	5.768	6.093	6.535
		CST	9.588	12.165	15.822	6.132	6.493	7.002
	plate	HSDT	8.944	10.662	12.673	5.796	6.123	6.566
		FSDT	8.900	10.612	12.622	5.774	6.100	6.544
		CST	9.566	12.145	15.771	6.136	6.500	7.014
0°/90°/0°	5	HSDT	12.200	14.084	17.387	3.894	4.403	6.116
		FSDT	12.394	14.499	17.959	3.891	4.397	6.163
		CST	15.290	22.640	32.785	4.009	4.562	6.861
	20	HSDT	11.973	13.832	15.848	3.797	4.329	6.097
		FSDT	12.178	14.264	16.487	3.794	4.325	6.146
		CST	15.116	22.562	32.136	3.909	4.490	6.863
	plate	HSDT	11.958	13.815	15.739	3.790	4.324	6.095
		FSDT	12.163	14.248	16.383	3.788	4.320	6.144
		CST	15.104	22.557	32.093	3.902	4.485	6.863

Table 2: Nondimensionalized fundamental frequencies ($\bar{\omega} = (\omega a_1^2/h)\sqrt{\rho/E_2}$) of cross-ply cylindrical panels for various boundary conditions. ($R_1 = \infty$, $R_2 = R$, $a_1/a_2 = 1$, $a_1/h = 10$).

Lamination	R/a_1	Theory	SS	SC	CC	FF	FS	FC
0°/90°	5	HSDT	8.959	10.685	12.705	5.740	6.054	6.547
		FSDT	8.931	10.647	12.663	5.716	6.030	6.524
		CST	9.598	12.154	15.747	6.096	6.444	7.014
	20	HSDT	8.934	10.656	12.672	5.786	6.110	6.557
		FSDT	8.894	10.609	12.623	5.763	6.087	6.535
		CST	9.560	12.136	15.757	6.128	6.489	7.008
	plate	HSDT	8.944	10.662	12.673	5.796	6.123	6.566
		FSDT	8.900	10.612	12.622	5.774	6.100	6.544
		CST	9.566	12.145	15.771	6.136	6.500	7.014
0°/90°/0°	5	HSDT	12.009	13.854	15.768	3.776	4.306	6.127
		FSDT	12.212	14.284	16.408	3.773	4.301	6.176
		CST	15.136	22.560	32.062	3.894	4.472	6.901
	20	HSDT	11.961	13.817	15.741	3.789	4.323	6.097
		FSDT	12.166	14.250	16.385	3.787	4.318	6.146
		CST	15.106	22.557	32.091	3.902	4.484	6.866
	plate	HSDT	11.958	13.815	15.739	3.790	4.324	6.095
		FSDT	12.163	14.248	16.383	3.788	4.320	6.144
		CST	15.104	22.557	32.093	3.902	4.485	6.863

Table 3: Nondimensionalized critical buckling loads ($\bar{T}_{22} = T_{22}a_2^2/E_2h^3$, $T_{11} = 0$) of cross-ply spherical panels for various boundary conditions, ($a_1/a_2 = 1$, $a_1/h = 10$).

Lamination	R/a_1	Theory	SS	SC	CC	FF	FS	FC
0°/90°	5	HSDT	12.431	17.995	22.376	5.003	5.520	6.290
		FSDT	12.214	17.685	21.511	4.936	5.447	6.216
		CST	13.877	22.341	32.632	5.552	6.132	7.028
	20	HSDT	11.610	16.812	20.935	4.916	5.424	6.240
		FSDT	11.406	16.526	20.131	4.852	5.355	6.170
		CST	13.015	21.193	31.333	5.432	6.010	6.972
	plate	HSDT	11.555	16.720	20.859	4.916	5.421	6.237
		FSDT	11.353	16.437	20.067	4.851	5.351	6.166
		CST	12.957	21.116	31.280	5.425	6.003	6.968
0°/90°/0°	5	HSDT	13.154	15.209	18.522	2.045	2.582	5.563
		FSDT	13.072	15.157	18.427	2.044	2.579	5.574
		CST	18.726	29.888	40.100	2.139	2.724	6.972
	20	HSDT	12.844	14.624	16.789	1.932	2.479	5.490
		FSDT	12.773	14.589	16.799	1.933	2.478	5.502
		CST	18.402	29.527	39.274	2.020	2.618	6.931
	plate	HSDT	12.824	14.585	16.649	1.925	2.472	5.485
		FSDT	12.753	14.551	16.662	1.925	2.471	5.497
		CST	18.380	29.503	39.219	2.012	2.611	6.928

Table 4: Nondimensionalized critical buckling loads ($\bar{T}_{22} = T_{22}a_2^2/E_2h^3$, $T_{11} = 0$) of cross-ply cylindrical panels for various boundary conditions, ($R_1 = \infty$, $R_2 = R$, $a_1/a_2 = 1$, $a_1/h = 10$)

Lamination	R/a_1	Theory	SS	SC	CC	FF	FS	FC
0°/90°	5	HSDT	11.688	16.927	20.790	4.878	5.381	6.267
		FSDT	11.532	16.686	20.026	4.811	5.310	6.191
		CST	13.187	21.385	31.298	5.425	6.001	7.051
	20	HSDT	11.549	16.730	20.841	4.909	5.414	6.233
		FSDT	11.359	16.458	20.057	4.844	5.344	6.162
		CST	12.972	21.134	31.281	5.425	6.002	6.974
	plate	HSDT	11.555	16.720	20.859	4.916	5.421	6.237
		FSDT	11.353	16.437	20.057	4.851	5.351	6.166
		CST	12.957	21.116	31.280	5.425	6.003	6.968
0°/90°/0°	5	HSDT	12.831	14.593	16.657	1.918	2.464	5.553
		FSDT	12.759	14.557	16.669	1.917	2.462	5.564
		CST	18.394	29.506	38.223	2.012	2.609	7.018
	20	HSDT	12.824	14.586	16.649	1.924	2.472	5.490
		FSDT	12.753	14.551	16.662	1.925	2.470	5.501
		CST	18.381	29.503	39.219	2.012	2.611	6.933
	plate	HSDT	12.824	14.585	16.649	1.925	2.472	5.485
		FSDT	12.753	14.551	16.662	1.925	2.471	5.497
		CST	18.380	29.503	39.219	2.012	2.611	6.928

ON THE FREE VIBRATIONS OF LAMINATED CONICAL SHELLS OF VARIABLE THICKNESS

N.Sankaranarayanan, K.Chandrasekaran and G.Ramaiyan
Anna University,Madras, India.

1. INTRODUCTION

Conical shells of constant and variable thickness find widespread applications as structural elements in missiles, nose-cones and off-shore structures. Because of their better specific and directional properties,laminated constructions of these elements are increasingly preferred. Recently the use of such structural elements as dynamic absorbers, in controlling machinery vibrations, has been suggested [1]. The study of their free vibrational characteristics for evaluating their dynamical behaviour is important. A simple and straight forward procedure, based on the Rayleigh-Ritz technique, for the free vibrational analysis of laminated conical shells of variable thickness, has been given by the authors [2,3]. The present paper deals with the experimental determination of the natural frequencies and the corresponding mode-shapes of two models and their comparison with the theoretical values.

2. OUTLINE OF THE THEORY

The detailed theoretical formulation and the solution procedure have been given in reference [3]. Love's theory, as extended to the analysis of laminated thin shells, forms the basis of the formulation. A general lamination sequence, with layers of specially orthotropic materials, is considered. A linear variation in thickness, with the thickness increasing proportional to the meridional distance from the vertex, is assumed. To facilitate easy computations a transformation of the meridional coordinate is effected as given by,

$$y = (x - x_1)/(x_2 - x_1) \quad ; \quad o \leq y \leq 1 \qquad (1)$$

A separable solution for the displacements is assumed as,

$$\begin{aligned} u(y,\theta,t) &= U(y) \cos n\theta \, e^{i\omega t} \\ v(y,\theta,t) &= V(y) \sin n\theta \, e^{i\omega t} \\ w(y,\theta,t) &= W(y) \cos n\theta \, e^{i\omega t} \end{aligned} \qquad (2)$$

where, u,v and w are the displacements at point on the reference surface along the three coordinate axes, as shown in Figure 1. A standard Rayleigh-Ritz procedure is adopted for the formulation of the free vibration problem using assumed displacement functions which completely satisfy the geometric boundary conditions. The displacements are assumed in the following f .n :

$$U(y) = \sum_{i=0}^{M} a_i \, f(i,y); \; V(y) = \sum_{i=0}^{M} b_i \, g(i,y) \text{ and } W(y) = \sum_{i=0}^{M} c_i \, p(i,y) \qquad (3)$$

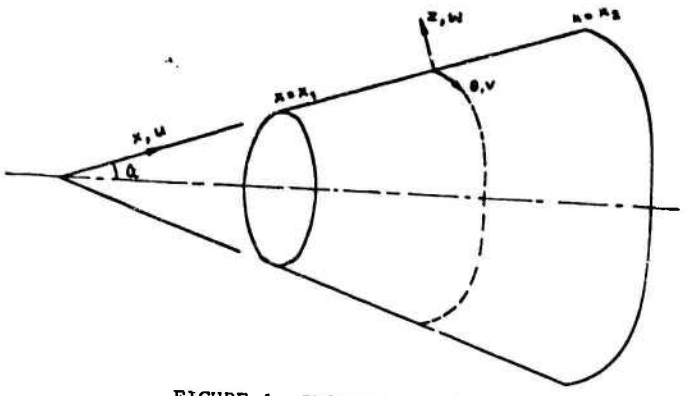

FIGURE 1 GEOMETRY OF SHELL

In equation (3) a_i, b_i and c_i are undetermined constants. The functions f, g and p, satisfying different geometric boundary conditions are given explicitly, in Table 1. On minimising the total potential with respect to the undetermined constants, a generalised algebraic eigenvalue problem results. A simultaneous iteration technique is used to obtain the dominant eigenvalues and eigenvectors and hence the natural frequencies and mode shapes.

TABLE 1

DISPLACEMENT FUNCTIONS

End conditions Small End - Large End	Geometric Boundary conditions		Assumed displacement functions	
	Small End y = 0	Large End y = 1	f(i,y) g(i,y)	p(i,y)
Fixed-Fixed	U = 0 V = 0 W = 0 dW/dy = 0	U = 0 V = 0 W = 0 dW/dy = 0	$(1-y)y^{i+1}$	$(1-y)^2y^{i+2}$
Hinged-Hinged	U = 0 V = 0 W = 0	U = 0 V = 0 W = 0	$(1-y)y^{i+1}$	$(1-y)y^{i+1}$
Fixed-Free	U = 0 V = 0 W = 0 dW/dy = 0	--	y^{i+1}	y^{i+2}
Free-Fixed	--	U = 0 V = 0 W = 0 dW/dy = 0	$(1-y)y^{i}$	$(1-y)^2y^{i}$

3. EXPERIMENTAL INVESTIGATIONS

Inorder to check the validity of the analysis procedure, experiments were carried out on two shell models. A sweep test, using an electro-dynamic exciter and other related instrumentation, was conducted on the first model. A modal analysis test, using a FFT analyser and an instrumented hammer, was carried out on the other model. These two tests are described below.

3.1 Sweep Test

3.1.1 Fabrication Of The Model

A conical shell model, made of aluminium, was fabricated at the workshop, out of a plate cut out to the required development and then rolled to shape. The two edges were welded together by TIG welding, to form the meridional seam. A thick end flange was welded on to the smaller end of the shell, for the purposes of machining and mounting. The shell was then mounted on a specially designed turning fixture and machined to provide the required variation in thickness.

3.1.2 Experimental Procedure

The test model was mounted, with its axis horizontal, using fixtures. Two very heavy and sturdy channels provided the support for a thick plate on which the flanged end of the shell was rigidly bolted. The entire set-up was then mounted on an isolation bed, to eliminate external influences. The schematic diagram of the entire test set-up is shown in Figure 2a. The photograph of the same is also provided. The electrodynamic exciter was located at a point very near the free end of the shell. An audio-frequency oscillator was used to vary the frequency of the excitation. The response was picked up using a piezo-electric accelerometer. The signal from the accelerometer, amplified by a charge amplifier, after passing through a band-pass filter, was fed to one of the traces of a dual-trace oscilloscope. The test procedure consisted of varying the frequency of excitation and observing the response to locate the natural frequencies. Several test runs were made to eliminate spurious frequencies and to provide reproducible results. After the natural frequencies were identified, at each of these frequencies, the pick-up was mounted at several grid points marked on the surface of the shell, to identify the mode shapes. By observing the variation of the signal along the meridians and along the circumference at several points on the meridians, the modal parameters for the particular frequency were determined.

3.1.3 Experiment On The Laminated Model

The aluminium shell model, used in the previous test, was laid up on the inner surface, with a composite consisting of chopped strand glass mat reinforcement and a polyester resin matrix. A number of layers were laid to provide the required thickness. The laminated shell was once again mounted on the turning fixture on a lathe and machined to give the required variation in thickness. Simultaneously, a seperate plate was laid up of the same composite, from which

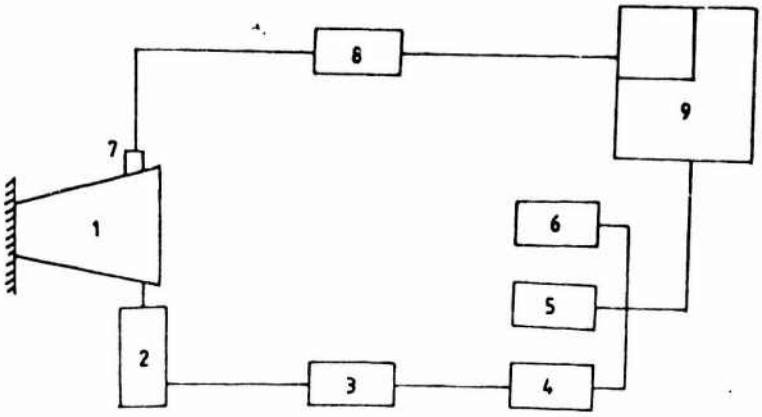

1 SHELL MODEL
2 EXCITER
3 AMMETER
4 POWER AMPLIFIER
5 OSCILATOR
6 FREQUENCY COUNTER
7 ACCELEROMETER PICKUP
8 CHARGE AMPLIFIER
9 OSCILLOSCPE

(a) SWEEP TEST

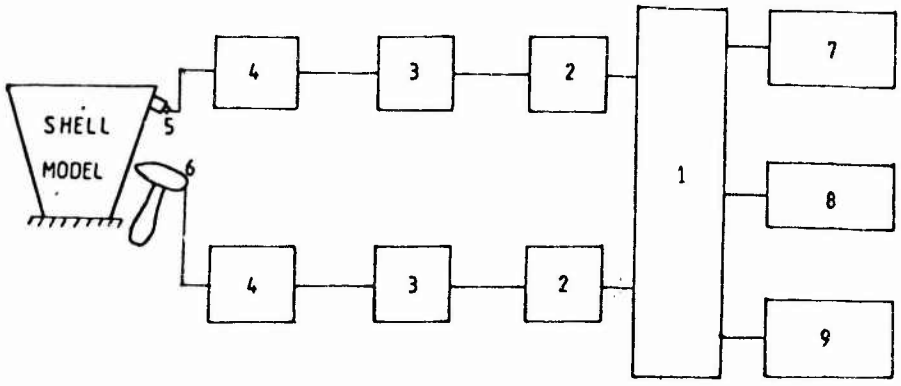

1. Fast Fourier analyser
2. A to D Converter
3. Antialiasing Filter
4. Power Unit
5. Piezoelectric accelerometer
6. Instrumented Impulse Hammer
7. Graphic Printer
8. Graphics Plotter
9. Graphics Terminal

(b) MODAL ANALYSIS

FIGURE 2 SCHEMATIC DIAGRAM OF THE EXPERIMENTAL SETUP AND THE RELATED INSTRUMENTATION

standard specimen were cut out in differenct directions, for tensile tests. These were tested in an UTM, to determine the Young's modulus for the composite. By standard immersion tests, the density of the composite was also determined. The values of the elastic modulus determined from the various specimen varied only marginally, indicating that the behaviour resembled that of an isotropic material. The avarage of all these values was taken as the modulus of the composite. The material properties are specified in Table 2. The sweep test on the laminated model was then conducted in the same manner as described earlier.

TABLE 2

MATERIAL PROPERTIES OF THE EXPERIMENTAL SHELL LAYERS

Material	Density ρ	Young's modulus E_{xx}	Young's modulus E_{00}	Shear modulus G	Poison's Ratio μ
	$x10^4 N.S^2/m^4$	$x10^{10}$ N/m^2	$x10^{10}$ N/m^2	$x10^{10}$ N/m^2	
Aluminium	0.2793	6.750	6.750	2.5960	0.30
GFRP	0.1380	0.416	0.416	0.1664	0.25

3.2. Modal Analysis Using FFT Analyser

3.2.1. Experimental model

One difficulty, encountered in the previous test, was that the shell possessed a high stiffness and consequently the natural frequencies were considerably higher. This resulted in difficulties of identifying the mode shapes corresponding to higher meridional modes and for higher circumferantial wave numbers. Hence it was decided to go in for another model, much thinner than the previous one, so that more frequencies could be identified. The second model was fabricated in the same manner as the first one. However, because of the difficulties encountered in machining the model to provide the variation in thickness, it was not possible to considerably reduce the thickness. This resulted in the same difficultues faced with respect to the higher modes. To enhance the credibility, however, it was decided to go in for a modal analysis test this time.

3.2.2. Test procedure

A schematic diagram of the test set-up is shown in Figure 2b. A photograph of the same is also provided. The heart of the set-up is the FFT analyser interfaced to a micro-computer. A modal analysis

software provides the results of the analysis. This software consists of four segments, viz., the set-up step, the mode identification step, the print step and the display step. In the first step, the parameters that describe the particular test, like the number of transfer functions, the transducer sensitivities, the storage locations, the block size, etc., are specified to provide a caliberation in engineering units. After measurements are made, in the second step, the modal parameters are identified. The last two steps are for providing the results of these measurements by way of natural frequencies, the mode-shapes, the damping ratios, etc. Animated displays of mode-shapes are also possible.

For the purpose of the test, 48 grid points on the shell were marked, to serve as points of excitation. The excitation was provided by an instrumented hammer. Impulses were given at all the 48 points, by striking with the hammer. The response was picked up by an accelerometer from a selected fixed point and fed to the FFT analyser. To ensure reasonable statistical accuracy, 10 recordings were taken for each point of excitation. For all frequencies below 2000 Hz, the natural frequencies and the corresponding mode-shapes were obtained.

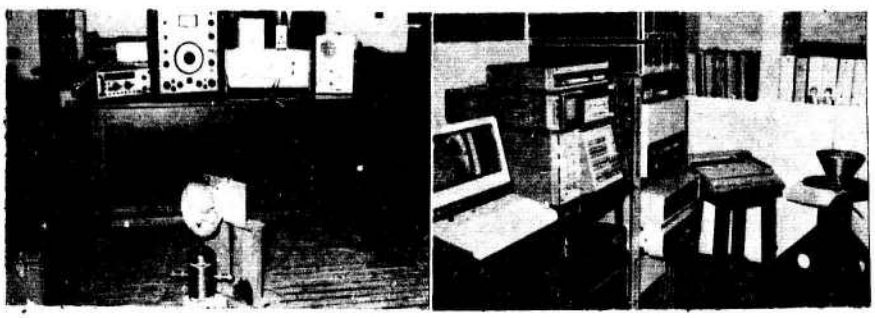

PHOTOGRAPHS SHOWING THE TEST SETUP, SWEEP TEST (LEFT) AND MODAL ANALYSIS (RIGHT)

4. RESULTS AND DISCUSSIONS

4.1 Results of the Sweep test

Figure 3 shows the comparison between the theoretically evaluated natural frequencies for the first meridional mode, for the homogeneous shell, and the experimentally determined ones. A similar comparison is provided for the laminated model in Figure 4. In both these figures, the trend is the same. For lower values of the circumferantial wave number, viz., n=1 and n=2, there is considerable difference between the two frequencies. For the higher values of n, these two move closer to each other. The very low values of the measured frequencies, corresponding to n=1 and n=2, could be due to the reason that these are the inextensional ones. Seide [4] has reported that for lower circumferantial wave numbers, the condition of restraint on circumferantial and meridional

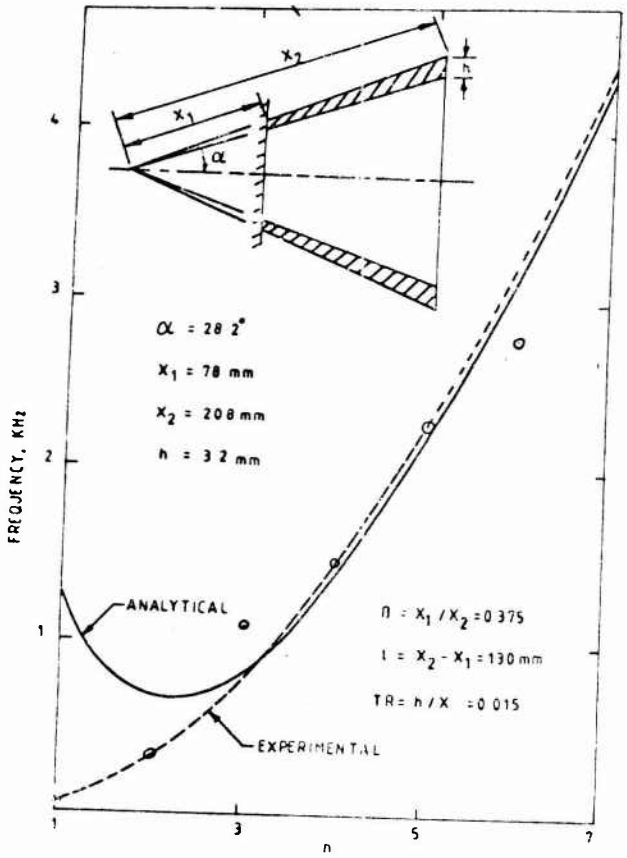

FIGURE 3 COMPARISON OF EXPERIMENTAL RESULTS WITH THEORETICAL PREDICTIONS FOR A HOMOGENEOUS SHELL - SWEEP TEST

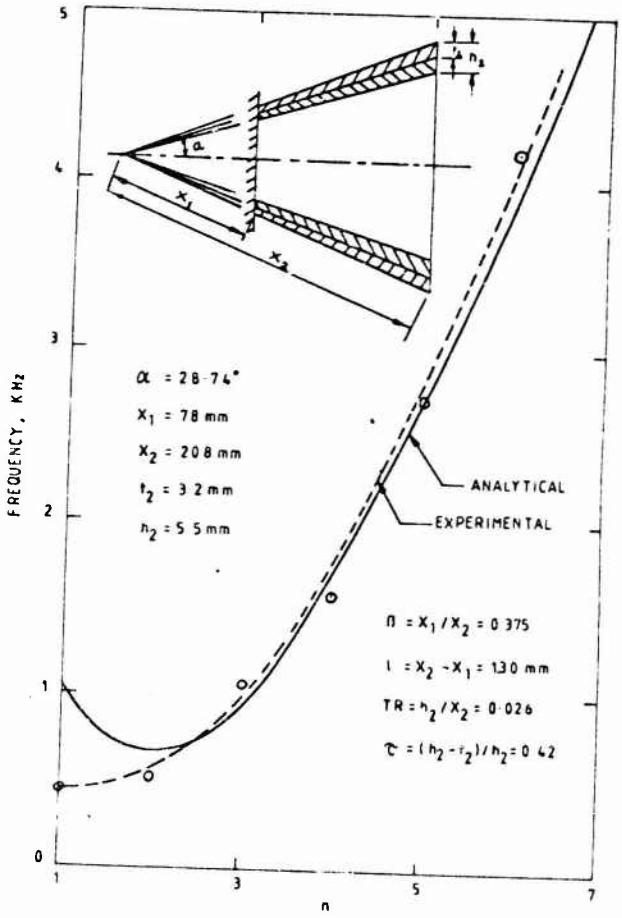

FIGURE 4 COMPARISON OF EXPERIMENTAL RESULTS WITH THEORETICAL PREDICTIONS FOR A LAYERED SHELL - SWEEP TEST

displacements of the edges significantly affects the frequencies. The frequency of a shell with zero circumferantial shear force is considerably lower than that for a shell with zero circumferantial displacement. Arnold and Warburton [5] have also commented on this aspect, in the case of cylindrical shells. For cylindrical shells with circumferantially restrained edges, the energy associated with stretching of the middle surface is predominant, for low values of n. But the edge condition of zero circumferantial shear force inhibits the building up of a membrane stretching force and the vibration mode tends to be predominantly inextensional. This accounts for the lower frequencies. For larger values of 'n' , bending predominates, and edge effects die out, resulting in higher frequencies. Hence it is to be concluded that, in the present case, there might have been some circumferantial slipping of the edge at the support, and only partial restraint was provided. Similar experiences have been reported by Weingarten and Gelman [6], Chandrasekaran and Ramamurti [7]and by Wilkins et al. [8]. The difficulties in identifying the mode-shapes for higher frequencies have also been experienced by Seide [4]. Considering all these aspects, it is observed that satisfactory comparison between theory and experiment has been obtained.

4.2 Results of the modal analysis test

Table 3 provides the comparison between theoretical and experimental results for the second model. The modal parameters were obtained from the displayed mode-shapes. Figure 5 shows the comparison by way of a graph. Once again, it is observed that for lower values of n, the measured frequencies are much lower than the predicted ones. For higher values of n, the comparison is better. Similar arguments as made earlier, could be advanced regarding the results. On the whole, there is reasonable agreement between the results. One more point to be noted is the versatality and the ease of the modal analysis procedure compared to the sweep test procedure. The vast difference between the two methods has to be experienced to be understood.

TABLE 3.

COMPARISON OF EXPERIMENTAL AND THEORETICAL FREQUENCIES MODAL ANALYSIS.

m	n	Theoretical Frequencies Hz	Experimental Frequencies Hz	Damping factor (Experimental)
1	1	841	--	--
1	2	429	457.5	0.4453
1	3	525	545.8	1.3800
1	4	903	838.4	1.4386
1	5	1419	1252.3	1.8809

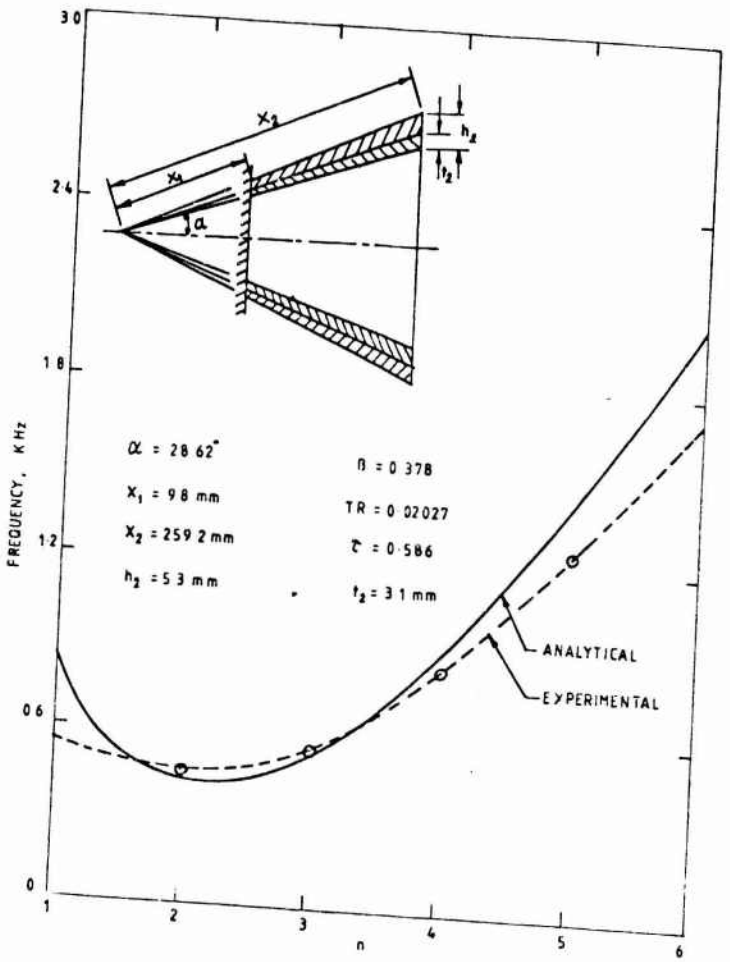

FIGURE 5 COMPARISON OF EXPERIMENTAL RESULTS WITH THEORETICAL PREDICTIONS - MODAL ANALYSIS

5. ACKNOWLEDGEMENT

The facilities provided by the Machine Dynamics Division of the Indian Institute of Technology, Madras and the Structures Division of the National Aeronautical Laboratory, Bangalore, for carrying out the tests, are greatfully acknowledged.

REFERENCES

1. VON.D. BASCHORR and H. ALBERT OTTOBRUNN 1979 Sonderdruck Aus VDI-Z 121, 253-261 (In German). Vibration absorbers for reducing the machine noise.

2. N. SANKARANARAYANAN et al. 1987 Journal of Sound and Vibration 118. Axisymmetric vibrations of laminated conical shells of variable thickness.

3. N. SANKARANARAYANAN et al. 1988 Journal of Sound and Vibration 123. Free vibrations of laminated conical shells of variable thickness (Scheduled for publication).

4. P. SEIDE 1965 Israel Journal of Technology 3, 50-61. On the free vibrations of simply supported truncated conical shells.

5. R.N. ARNOLD and G.B. WARBURTON 1953 Proceedings of The Institution of Mechanical Engineers (London) Series A 16, 62-80. The flexural vibrations of thin cylinders.

6. V.I. WEINGARTEN and A.P. GELMAN 1967 Proceedings of the ASCE Journal of Engineering Mechanics Division 93, 127-138. Free vibrations of cantilever conical shells.

7. K. CHANDRASEKARAN and V. RAMAMURTI 1982 Transactions of the ASME Journal of Mechanical Design 104, 453-462. Asymmetric free vibrations of layered conical shells.

8. D.J. WILKINS et al. 1970 Journal of Sound and Vibration 13, 211-228. Free vibrations of orthotropic sandwich conical shells with various boundary conditions.

4. TESTING TECHNIQUES AND CORRELATION

FUTURE TRENDS IN MODAL ANALYSIS

Bob Rost, Ph.D. Dave Brown, Ph.D.

Department of Mechanical and Industrial Engineering
University Of Cincinnati
Cincinnati, Ohio 45221

1. ABSTRACT

Since 1980, the technical developments in the area of modal analysis has been accelerating. This period of development has been characterized by the influx of new researchers and international interest in the area. It has been the emergences of multiple-input/multiple-output measurement techniques and parameter identification methods based on the redundant information between multiple rows/columns of the frequency response function matrix. Much of the work has been driven by the need for better computer models to predict hardware changes for improved design. The development of improved measurement and data analysis equipment has triggered many of the newer developments. This paper will examine some of the current and future development trends in the area of modal analysis.

2. INTRODUCTION

Over the past ten years, there has been a significant increase in the technology associated with modal analysis. [1-5] These developments have been primarily in the areas of parameter identification. The majority of this effort has been documented in the proceeding of the International Modal Analysis Conference (IMAC). These developments have triggered more recent efforts in the measurement and signal processing areas. New techniques for measuring frequency response functions for multiple-inputs and multiple-outputs have been developed. Also, new algorithms to compute the "best" frequency response function in the presence of noise on both the input and the output have been written.

In this paper, work in progress at the University of Cincinnati and other research institutions as well as future trends that are just starting to be investigated will be discussed for the following areas:

- Measurement and Signal Processing
- Parameter Estimation
- Modeling
- Non-linearities

In the measurement and parameter estimations areas, the problem areas are broken into the following sub categories:

- Trouble Shooting
- Finite Element Verification and Perturbation
- Modal Model Generation

A brief review of the current technology and future trends will be given for each category with a more detailed discussion of those technologies currently under development at the University of Cincinnati.

3. HISTORY

Modal testing during the mid 1960's was based upon sine testing methods. [6,7] Forced normal mode testing with multiple transducers for the affluent users and roving transducers for the ordinary user was the most common experimental method to determine the structures damped natural frequency, damping, and mode shapes. During this period of time, the transducer and signal conditioning for a single channel was between 1500 and 3000 dollars which limited the multiple transducer testing to large companies and/or government agencies. It was not uncommon for a large scale modal test to require months of data collection and data reduction.

Tracking filters and Co-Quad Analyzers were a step improvement in the technology for the roving transducer testing but mode shapes were measured by roving a transducer over the test object one eigenvalue (natural frequency) at time to determine quadrature mode shapes. Testing was very slow and quadrature mode shapes were insufficient to separate closely coupled modes. In general, the forced normal mode or force appropriation methods which could separate the closely coupled modes were not practical with roving transducers.

In, the late sixties and early seventies frequency response parameter estimation methods were developed to separate closely coupled modes for the roving transducer testing methods. These methods required hundreds of frequency response functions to be estimated which was not practical to with swept sine testing methods. With the advent of the Fourier analyzers systems which were developed in the late sixties and perfected during the early seventies it became practical to measure many more degrees of freedom and therefore improve the system parameters estimated from a modal test. The Fourier analyzer also reduced the time required to make the necessary measurements to a much more reasonable time frame.

During, the mid seventies the primary developments were single-input parameter estimation, broadband excitation and signal processing for these broadband methods. [8,9,10] For example:

- Parameter Estimation Techniques
  - i. Single Degree of Freedom
  - ii. Circle Fits
  - iii. Least Squares Complex Exponential

- Excitation Techniques
  - i. Impact Testing
    - a. Impact Hammers
    - b. Force Windows
    - c. Exponential Windows
  - ii. Random
    - a. Pure
    - b. Pseudo
    - c. Periodic
    - d. Transient or Burst
  - iii. Chirps
    - a. Fast Sweeps
    - b. Periodic

These methods, coupled with animated displays, were adequate for general trouble-shooting and were used with success during the mid-seventies.

During the late seventies, greater emphasis was placed upon Finite Element Model Verification and Modal Modeling. Initially, it was felt that single input testing techniques and parameter estimation would separate closely coupled modes and could be used for these applications. As single input methods were perfected, it became evident that for regions of high modal density and coupling, these methods were inadequate.

Because of these limitations, it became obvious that multiple measurements (multiple-inputs/multiple-outputs) should be used to estimate global modal parameters. This technology guarantees consistent estimates of frequency and damping for measurements that are acquired simultaneously. [1-5] Therefore, in the late seventies, modal testing reached the same point that it had reached in the mid sixties with normal mode testing, measuring possibly hundreds of channels simultaneously.

Fortunately, in the late seventies and the early eighties with advances in electronics and computer technology, it was practical to consider developing a system with a low cost per channel, making it possible to make hundreds of simultaneous measurements. The problem was to initiate commercial development of such a system. It was chicken and egg problem, a commercial vendor had to be guaranteed of a sufficient market and the market could not be developed until the cost per channel was low enough.

In order to convince vendors, it was necessary to develop the other parts of a modal testing system, the signal processing and the parameter estimation. Multi-input broadband testing methods were developed in the late seventies and the early eighties. During the eighties a large number of multi-input parameter estimation algorithms were developed. It was the development of the time domain polyreference algorithm which triggered the parameter estimation developments. Currently, there are a large number of time, frequency and spatial domain methods which can be used to estimate modal parameters for multiple-input frequency response functions. In fact, most of the methods can be unified and derived from a common origin. [4] A much better understanding of the linear parameter estimation problem now exists.

During the mid-eighties, prototype transducer systems were developed to demonstrate the feasibility of producing low cost per channel measuring systems.[11] These system were designed so that the calibration, cabling and connectivity could be automated.

4. FUTURE TRENDS IN MODAL ANALYSIS

In this section a short description of future trends will be developed according to the categories and sub categories given in the introduction.

4.1 Measurement and Signal Processing

- Transducers and Signal Conditioning

The current trend in transducer design for modal analysis has been to build small light weight but sensitive transducers. These transducers, in general, have built-in electronics either charge or voltage with the resulting low output impedance. The low output impedance means unshielded and inexpensive cabling can often be used. The noise floor in the newer built-in electronics has improved drastically in the last several years making the newer transducers competitive against the transducers with external charge amplifiers.

The cost has dropped from the $1500 - $3000 per channel price range of the 1960's to $120 - $400 for the transducer/signal conditioning today.

The cost of the filtering and digital signal processing has also been dropping drastically in the last several years with the development of new integrated circuits for both analog and digital filtering. The top of the line systems which includes high sampling rates and processing speed, anti-aliasing in the 100 db per octave range and build-in zoom per channel cost in the $2000-3000 per channel range. In the future for the high channel count systems, the sampling rate and signal processing can be compromised to reduce the cost. This will be covered in more detail later in the paper.

The types of data acquisition depends upon the application, therefore a brief summary of the trends for the primary modal applications are given below:

- Trouble Shooting

With the exception of the aerospace industry, trouble shooting vibration and acoustic problems has historically been the primary application of modal analysis. These modal analysis applications are characterized by quick look capability on operating system very often located in the field. The success of trouble shooting has played a significant role in expanding the field of modal analysis.

- Number of Channels

In the trouble shooting area, the emphasis on data acquisition hardware will be on portability and flexibility. The system will be 2 to 8 high cost channels in a small package. Several special signal conditioning channels will also be included for tachometer signals, since operating data is important in the trouble shooting applications.

- Transducers and Signal Conditioning

The transducers in the trouble shooting area will be a conventional transducers (accelerometers, load cells, microphones, strain gages, etc) that will operate in a variety of environmental conditions. The frequency range,

sensitivity, and size will be depend upon the application.

- Signal Processing

  A full array of signal processing tools will be available including Fast Fourier Transforms, statistical functions, window functions for many types of data, octave band analysis, waterfall displays,etc.

- Testing Configuration

  Very often, the operating configuration is tested in the trouble shooting applications. Of course, laboratory test are performed and the testing configuration can be free-free, fixed or a simulated operating constraint. Therefore, research in the area of correlating results from lab modal tests and operating tests is an ongoing and important area. Completing this step would be a major improvement in the entire modal analysis area. It would allow for a much better understanding of the entire problem.

- Excitation

  For trouble shooting applications, impact testing or operating inputs is often used. In these cases, a quick look at natural frequencies and sometimes reduced mode shapes is obtained. For laboratory testing, electro-mechanical or hydraulic exciters are used with random or some other broadband excitation method.

  In the future, improved testing methods with operating inputs are likely to be developed. This may include the application of known inputs on rotating components to compute operating frequency response functions.

4.2 Finite Element Verification and Perturbation

In the finite element verification area, it is important that the modal analysis perform an excellent job of extracting the modal parameters. Therefore, finite element verification requires the highest levels of technology both from a measurement standpoint and data analysis. Therefore, the most advanced parameter estimation algorithms will be used and these algorithms will require the most consistent measurements. Therefore, simultaneous measurements should be made if possible. In general, poorer quality simultaneous measurements are better than excellent independent measurements.

- Number of Channels

  Large numbers of simultaneous response channels (256-1024) with a number of simultaneous input channels is very important for this application. This obvious will depend upon the size of the test article but for aircraft, spacecraft, automobiles, machine tools, etc. the channels count should be high in order to make the best possible measurements.

- Transducers and Signal Conditioning

  In order measure hundreds of channels of data, the channel cost has to be low. Therefore, the frequency range and environmental package can be compromised. The accelerometers are generally very low mass but very high sensitivity. They should be

permanently mounted to the test object so that retests will be as consistent as possible.

For large measurement arrays, automatic calibration and transducer identification (point number, direction, serial number, etc.) methods will be developed to handle the cabling and connectivity problems.

Optical techniques will be developed to supplement and/or replace conventional accelerometers especially for very small or very large structures. With optical measurements spatial domain parameter estimation will work well.

- Signal Processing

Presently, signal processing for hundreds of simultaneous broadband channels would be prohibitively expensive for most users. One solution will be to use sine testing, this will be the least expensive solution. Currently, at the University of Cincinnati the development of a spatial sine testing system is high priority. This system promises to be very inexpensive per channel and has a number of advantages from a data signal processing standpoint and also from a data analysis standpoint. [29-31]

The second method and one that is currently used will be to multiplex banks of transducers into a multi-channel front end. This has the disadvantage that data is not taken completely simultaneous which is desirable. However, this can be minimized if the all the transducers are premounted on the structure to minimize frequency shifts.

In the more distant future broadband systems capable of sampling hundreds of channels will be developed at reasonable cost.

- Testing Configurations

For finite element modeling, the current testing procedures is to test the structure either in a free-free or a fixed configuration. The free-free testing configuration is in general the easiest configuration for laboratory modal testing. Unfortunately, it doesn't allow measurement of many of the constraint modes which can be very important in many modeling circumstances.

In the future, mass loaded or perturbed configurations may be tested. A number of perturbed configurations including the free-free and fixed cases may used to confirm a single finite element model. This becomes possible if all the transducers are premounted, in this case the amount of time to test a given configuration is determined primarily by the data acquisition time.

- Excitation

Almost all finite element verification tests are conducted in a laboratory test. For this testing, electro-mechanical or hydraulic exciter systems are used. Historically, this has been primarily with broadband excitation signal but may include more sine testing in the near future. For very large structures initial conditions or operating inputs may be used.

4.3 Modal Model Generation

In the future, there will be a greater use of modal models generated directly from test data. For this case, even more stringent requirements are placed upon the modal testing procedures. However, the comments which were applied to the finite element verification are applicable to this case.

4.4 Parameter Estimation

Currently, there is a great deal literature in the multi-input parameter estimation area. Most of this literature can be found in the proceedings of the International Modal Analysis Conference (IMAC). It was the development of the time domain polyreference algorithm in the early 1980's which has trigger much of the recent development. The polyreference method changed the major concepts on parameter estimation from curve fitting to linear system analysis.

The linear system analysis has unified many of the existing techniques.

A list of the most popular current techniques are given below:

Time Domain

- Complex Exponential
- ITD (Ibrahim Time Domain)
- Polyreference
- ERA
- Direct Parameter Estimation

- Frequency Domain
  - Orthogonal Polynomial
  - Polyreference
  - Direct Parameter Estimation

- Spatial Domain
  - Little-MAC
  - Multi-MAC
  - Complex Mode Indicator Function (CMIF)

A summary of the characteristics of the above techniques is given in Table 1.

Modal Parameter Estimation Characteristics							
	Time, Frequency, or Spatial Domain	Single or Multiple Degrees-of-Freedom	Global Modal Frequencies and Damping Factors	Repeated Modal Frequencies and Damping Factors	Global Modal Vectors	Global Modal Participation Factors	Residuals
Quadrature Amplitude	Frequency	SDOF	No	No	No	No	No
Kennedy-Pancu Circle Fit	Frequency	SDOF	No	No	No	No	Yes
SDOF Polynomial	Frequency	SDOF	Yes/No	No	No	No	No
Non-Linear Frequency Domain	Frequency	MDOF	No	No	No	No	Yes
Complex Exponential	Time	MDOF	No	No	No	No	No
Least Squares Complex Exponential (LSCE)	Time	MDOF	Yes	No	No	No	No
Ibrahim Time Domain (ITD)	Time	MDOF	Yes	No	Yes	No	No
Multi-reference Ibrahim Time Domain (MITD)	Time	MDOF	Yes	Yes	Yes/No	No/Yes	No
Eigensystem Realization Algorithm (ERA)	Time	MDOF	Yes	Yes	Yes	Yes	No
Orthogonal Polynomial	Frequency	MDOF	Yes	No	No	No	Yes
Multi-reference Orthogonal Polynomial	Frequency	MDOF	Yes	Yes	Yes	Yes	Yes
Polyreference Time Domain	Time	MDOF	Yes	Yes	No	Yes	No
Polyreference Frequency Domain	Frequency	MDOF	Yes	Yes	Yes	Yes	Yes
Time Domain Direct Parameter Identification	Time	MDOF	Yes	Yes	Yes	Yes	No
Frequency Domain Direct Parameter Identification	Frequency	MDOF	Yes	Yes	Yes	Yes	Yes
Multi-MAC	Spatial	SDOF	No	Yes	Yes	No	No
Multi-MAC / CMIF / Enhanced FRF	Spatial	MDOF	Yes	Yes	Yes	Yes	No

TABLE 1. Summary of Parameter Estimation Algorithms

One of the newer concepts in parameter estimation is the concept of a characteristic space.[29-31] This space is defined as a volume (three-dimensional frequency response or unit impulse matrix) with the three axis corresponding to two spatial and one temporal. The two spatial axis corresponds to the input locations and output locations, and the temporal axis is either time or frequency. This concept coupled with linear system analysis allows the derivation from a common origin of most of the methods listed above.

The future trends in the parameter estimation area appears to be more of the same. Using perhaps more spatial and perturbated configuration information in the estimation process. Perturbated configuration information refers to the process of testing, a system in a number of constrained testing configurations (from free-free, mass loaded to fixed) and using all of this information in the estimation process.

Future parameter estimation procedure will make better use of the finite element models as weighting matrices. Also the finite model will be used more directly to choose the input and output points for the modal test.

Non-linear estimation procedures are in the initial phases of development and will be pursued more heavily in the future.

4.5 Non-linearities

Non-linearities have always been a source of measurement errors in modal testing. New methods are being evaluated which help to identify and document nonlinear system parameters. Some of these techniques are based on Hilbert Transforms [23-28] while others are based on higher order frequency response function algorithms. [23-28] Figure 1 is a summary of system non-linearities.

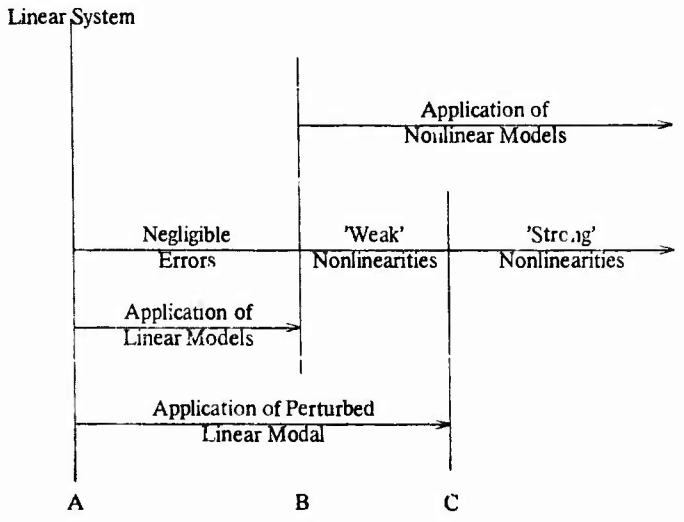

Figure 1. Evaluation of Linear and Nonlinear Systems

A great deal of work will be performed in the future on understanding non-linearities.

5. SUMMARY

This paper is brief survey on present state-of-the-art and future trends in the area of modal analysis. The main concentration has been in the area of measurements, signal processing and parameter estimation.

REFERENCES

[1] Allemang, R. J., "Investigation of Some Multiple Input/Output Frequency Response Function Experimental Modal Analysis Techniques," Doctor of Philosophy Dissertation, University of Cincinnati, Mechanical Engineering Department, 1980, 358 pp.

[2] Rost, R.W. "Investigation of Multiple Input Frequency Response Function Estimation Techniques for Modal Analysis," Doctor of Philosophy Dissertation University of Cincinnati Mechanical Engineering Department 1985, 219 pp.

[3] Leuridan, J. M., Brown, D. L. and Allemang, R. J., *Time Domain Parameter Identification Methods for Linear Modal Analysis: A Unifying Approach,* Journal of Vibration, Acoustic, Stress, and Reliability in Design Paper Number 85-DET-90, 8 pp.

[4] Leuridan, J.M. "Some Direct Parameter Model Identification Methods Applicable for Multiple Input Modal Analysis," Doctoral Dissertation, University of Cincinnati, Mechanical Engineering Department, 1984, 384 pp.

[5] Allemang, R.J., Brown, D.L. *Experimental Modal Analysis and Dynamic Component Synthesis,* Final Report USAF AFWAL-TR-87-3069, Six Volumes, 1988.

[6] Bishop, R. E. D. and Gladwell, G. M. L., *An Investigation Into The Theory of Resonance Testing,* Philosophical Transactions, Royal Society of London Series A, Vol. 255, Number A1055, 1963, pp. 241-280.

[7] Kennedy, C. C. and Pancu, C. D. P., *Use of Vectors in Vibration Measurement and Analysis,* Journal of Aeronautical Sciences, Vol. 14, Number 11, 1947, pp. 603-625.

[8] Brown, D. L., Allemang, R. J., Zimmerman, R. and Mergeay, M., *Parameter Estimation Techniques for Modal Analysis,* SAE Paper# 790221, 1979.

[9] Brown, D.L., Carbon, G.D., Ramsey, K.. "Survey of Excitation Techniques Applicable to the Testing of Automotive Structures," SAE Paper Number 770029, 1977

[10] Halvorsen, W.G., Brown, D.L., "Impulse Technique for Structural Frequency Response Testing," Sound and Vibration, November. 1977, pp. 8-21

[11] Poland, J. "An Evaluation of a Low-Cost Accelerometer Array System, Advantages and Disadvantages," Master of Science Thesis, Department of Mechanical Engineering, University of Cincinnati, 1986, 81 pp.

[12] Lecture Notes, Experimental Modal Analysis Short Course, Structural Dynamics Research Laboratory, Department of Mechanical and Industrial Engineering, University of Cincinnati, Cincinnati, OH., 1977-1984.

[13] Allemang, R.J., Rost, R.W., Brown, D.L., "Multiple Input Estimation of Frequency Response Functions: Excitation Considerations," ASME Paper Number 83-DET-73, 1983, 11 pp.

[14] Olsen,N., "A Comparison of Excitation Techniques for Modal Analysis," Proceedings, International Modal Analysis Conference, 1982, pp. 200-210.

[15] Allemang, R.J., Rost, R.W., Brown, D.L., "Dual Input Estimation of Frequency Response Functions for Experimental Modal Analysis of Aircraft Structures," Proceedings, International Modal Analysis Conference, pp.333-340, 1982.

[16] Carbon, G.D., Brown, D.L., Allemang, R.J., "Application of Dual Input Excitation Techniques to the Modal Testing of Commercial Aircraft," Proceedings, International Modal Analysis Conference, pp.559-565, 1982.

[17] Allemang, R.J., Brown, D.L., Rost, R.W., "Dual Input Estimation of Frequency Response Functions for Experimental Modal Analysis of Automotive Structures," SAE Paper Number 820193.

[18] Allemang, R.J., Brown, D.L., Rost, R.R., "Multiple Input Estimation of Frequency Response Functions for Experimental Modal Analysis," U.S. Air Force Report Number AFATL-TR-84-15, 1984, 185 pp.

[19] Mitchell, L. "Improved Methods for Fast Fourier Transform (FFT) Calculation of Frequency Response Functiors," ASME Journal of Mechanical Design, Vol. 104/2, pp.277-279.

[20] Vold, H., Crowley, J., Rocklin, G. "A Comparison of H_1,H_2,H_v, Frequency Response Functions," Proceedings of the 3rd International Modal Analysis, 1985, pp.272-278. 1977, pp. 427-434

[21] Rost, R.W., Leuridan, J., "A Comparison of Least Squares and Total Least Squares for Multiple Input Estimation of Frequency Response Functions," ASME Paper Number 85-DET-105, 1985.

[22] Wicks, A., Vold, H., "The H_s Frequency Response Estimator," Proceedings, International Modal Analysis Conference, 1986, pp. xxx-yyy.

[23] Tomlinson, G.R.; Ahmed, I., "Frequency and Damping Estimates from a Non-linear Structure - Causalisation and Random Excitation," Proceedings of the Tenth International Seminar on Modal Analysis, K.U. Leuven, Belgium, Part IV, 1985.

[24] Tomlinson, G.R.; Hilbert, J.H., "Identification of the Dynamic Characteristics of a Structure with Coulomb Friction," Journal of Sound and Vibration, 64 (2), 1979, pp. 233-242.

[25] Rades, M., "Identification of the Dynamic Characteristics of a Simple System with Quadratic Damping," Serie de Mecanique Appliquee, 28 (4), 1983, pp. 439-446.

[26] Tomlinson, G.R., "Detection, Identification, and Quantification of Nonlinearity in Modal Analysis - A Review," Proceedings of the Fourth International Modal Analysis Conference, 1986, pp. 837-843.

[27] Vinh, T.; Haoui, A.; Chevalier, Y., "Extension of Modal Analysis to Nonlinear Structures by Using the Hilbert Transform," Proceedings of the Second International Modal Analysis Conference, 1984, pp. 852-857.

[28] Hopton, G.W., "Detecting Nonlinearities Utilizing Multiple Input Frequency Response Function Estimation Theory," Master of Science Thesis, Department of Mechanical Engineering, University of Cincinnati, 1987, 107 pp.

[29] Rost, R.W., Brown, D.L., "Overview of Mulit-Input Frequency Domain Modal Testing Methods with an Emphasis on Sine Testing," Shock and Vibration Conference, October 1987.

[30] Severyn, A., Lally, M., Rost, R., Brown, D., "Hardware Considerations for Spatial Domain Sine Testing," presented at the 12th International Conference on Modal Analysis, Leuven, Belgium, 1987.

[31] Deblauwe, F., Shih, C., Rost, R., Brown, D., "Survey of Parameter Estimation Algorithms Applicable to Spatial Domain Sine Testing," presented at the 12th International Conference on Modal Analysis, Leuven, Belgium, 1987.

IMPULSE TESTING TECHNIQUES APPLIED TO LARGE VIBRATION ISOLATORS

G. R. Tomlinson and P. Milas

Heriot-Watt University
Department of Mechanical Engineering
James Nasmyth Building
Riccarton
Edinburgh
EH14 4AS

1. INTRODUCTION

The low and high frequency vibration isolation and transmissibility properties of resilient mounts have been widely described by many authors [1→4].

The existence of shear and compressional waves in vibration isolators is not usually a problem in the majority of applications but in some cases the high frequency signatures can play an important role in relation to the structure borne sound paths.

Situations where knowledge of these are necessary usually relate to military requirements although components which are subjected to a wide range of excitation frequencies can suffer fatigue due to efficient wave transmission paths at high frequencies. In the case of large vibration isolators (i.e. those capable of supporting masses in excess of say 1000kg) the shear and compressional waves can occur at relatively low frequencies, certainly below 150 Hz. In order to measure the transmission characteristics of such mounts, procedures involving sophisticated and expensive equipment are often employed. Figure 1 shows a diagrammatic sketch of such a test used to measure the transmissibility characteristics of a large vibration isolator. The need for such an arrangement stems from the requirement of the large pre-load. However in many cases the pre-load will not cause a significant change in the material properties [5] which in turn implies that the wave effects will also not change significantly.

This paper describes a very simple procedure for identifying the wave effects in large mounts using the well known impulse testing method. It is based upon the fact that a pre-load is not necessary to characterise the principal compressional and shear wave frequencies. It is considered that the procedure could be gainfully employed in assessing the relative performance of vibration isolators.

2. BASIS OF THE PROCEDURE

The basic idea is very simple. If one considers the input/output relations for a mass and spring (modelled as a complex stiffness) as shown in Figure 2a,b the resulting equations for harmonic excitation are,

$$T = \left|\frac{x_o}{x_i}\right| = \frac{(1 + \delta^2)^{1/2}}{[(1 - n^2)^2 + \delta^2]^{1/2}} \quad ; \; n^2 = \omega^2/\omega_n^2 \qquad (1)$$

$$G(\omega) = \left|\frac{x_o}{Fin/_k}\right| = \frac{1}{[(1 - n^2)^2 + \delta^2]^{1/2}} \qquad (2)$$

If $\delta < 1.0$; $(1 + \delta^2)^{1/2} \rightarrow 1.0$ and equations (1) and (2) become the same. By locating the vibration mount on a base with a very high dynamic impedance characteristic (compared to the mount) and applying an impulsive force as the input, the resulting transient response can be used to obtain the frequency response function $G(\omega)$ of the mount, which to a first approximation, resembles equation (2) .Thus one can identify the resonance condition.

2.1 Compressional Wave Characteristion

The type of vibration isolator in question is shown in Figure 1. Some of these may be prismatic, whilst others may be quite complex in shape. For purposes of analytical and experimental comparison the isolators considered in this paper resemble a rectangular parallelpiped. The material properties of the mount obtained from a series of static compression and shear tests are shown in Table 1. These properties were used in the following analysis for calculating the wave frequencies.

The compressional wave characteristics are calculated by applying the Love Theory [6]. This assumes that under deformation plane sections remain plane and that the longitudinal stresses are uniformly distributed across the section. Radial inertia effects are included with this theory, this being important since the aspect ratio (width/height) of the isolator is close to unity. The inertance of the system can be shown to be [4]

$$IN = \left|\frac{\ddot{x}_1}{F_1}\right|_{x_2 = 0} = \frac{-\omega^2 \sin(N^* L)}{\Lambda^* [\cos(N^* L) - \gamma(N^* L)\sin(N^* L)]} \qquad (3)$$

$$= \frac{-\omega^2 \sin(N^* L)}{\Lambda^* \varepsilon^*} \qquad (4)$$

$$\text{where } (N^*)^2 = \frac{\omega^2 \rho / E}{1 - \frac{\omega^2 \rho \nu^2 k^2}{E}} \qquad \Lambda^* = \frac{A \omega^2 \rho}{N^*} \qquad (5)$$

ρ is the mass density, γ the ratio of the supported mass to the mass of the isolator, k is the polar radius of gyration of the isolator, A is the cross-sectional area, L is the length, E, ν the Youngs Modulus and Poisson's ratio. The transmissibility function corresponding to equation (1) is [4],

$$T = \frac{1}{\cos(N^* L) - \gamma (N^* L) \sin(N^* L)} = \frac{1}{\varepsilon^*} \qquad (6)$$

Equations (3) and (6) show that the conditions in terms of the resonance frequencies are the same, i.e. $\varepsilon \to 0$.

Equations (3) and (6) are shown plotted in Figure 3 for a simulated isolator where it can be seen that the same resonant conditions are identified from both curves.

Thus by utilising the inertance function obtained from an impulse test, the compressional wave frequencies should be identifiable.

2.2 Application to a Large Industrial Isolator

The isolator shown in Figure 1 was employed to study the usefulness of the impulse procedure. The basic equipment employed for the tests is shown in Figure 4(a), Figure 4(b) shows a typical set of experimental results. The first peak at 80 Hz corresponds to the mass-spring resonance of the mass of the top-plate on the mount compressional stiffness. The other major peaks at 275, 342 and 409 Hz represent the waves frequencies. The last peak at 805 Hz was shown to correspond to the first natural frequency of the top-plate considered as a beam on an elastic foundation [7] using the expressions

$$f = \left[f_1^2 + f_F^2 \right]^{1/2} \qquad (7)$$

$$f = \frac{4.73^2}{2\pi L^2} \left(\frac{EI}{M} \right)^{1/2}, \qquad (8)$$

$$f_F = \frac{K_F / A_F}{4\pi^2 \rho_F} \quad ; \quad K_F = \frac{E_F A_F}{L_F} \qquad (9)$$

where the subscript F represents the foundations, in this case the resilient material of the isolator. Using the values for the material properties given in Table 1 in equations (7) to (9) the calculated value of the first bending mode frequency of the top plate is 805 Hz. Confirmation of this characteristic was obtained by a simple modal analysis which revealed the mode shapes shown in Figure 5. Also shown in Figure 5 are the normalised theoretical first mode shape and the measured mode shape showing the similarity between the results.

The theoretical predictions for the compressional wave characteristics based upon the estimated values of Youngs' Modulus and Poisson's are shown on Figure 6. It can be seen that the theoretical values of the resonance frequencies compare closely for the first three resonances. However the overall amplitude characteristics differ from the theoretical model since the theoretical model treats the top plate as a mass whereas the experimental results display the top-plate flexural resonance. (In practise this top-plate flexural resonance would normally be suppressed due to the local fixing conditions). As a further check on the effectiveness of the impulse testing procedure, the isolator was excited at the same excitation point as the impulse method using a large vibration exciter. The harmonic input force was measured using a force transducer and the inertance function measured over the frequency range 0 → 100 Hz.

The results are shown in Figure 7 where it can be seen that almost identical characteristics are obtained with those of Figure 4b from the impulse testing method.

Thus in summary, one can state that the impulse testing procedure can be effectively used to detect the compressional wave effects in large vibration isolators.

3. TRANSVERSE WAVE EFFECTS

In practise, vibration isolators are frequently employed in configurations where they are subjected to excitations which will induce compressional and transverse waves. The impulse procedure can also be employed to investigate the transverse wave characteristics. Figure 8 shows the results obtained from subjecting the top plate of the mount to a transverse impulsive force and measuring the inertance frequency response characteristics.

Transverse waves appear to be present at 160, 296 and 448 Hz ; the 32 Hz peak corresponding to the mass-spring characteristic in the transverse plane. Tests repeated orthogonally to this direction revealed very similar results. Again, confirmation of these results was obtained by connecting two mounts together (back to back) and subjecting these to harmonic forced excitation. Figure (9) shows the results which are in good agreement with the impulse tests.

3.1 Theoretical Predictions

By considering the isolator as an element subjected to pure shear, the resulting equations governing the inertance function can be shown to be [8]

$$IN = \frac{-\omega^2 \sin(n_s^* L)}{\lambda_s^* \left[\cos(n_s^* L) - \gamma n_s^* L \sin(n_s^* L)\right]} \qquad (10)$$

$$= \frac{\text{mass of end-plate}}{\text{mass of resilient element}}$$

$$n_s^* = \left[\frac{2\rho\omega^2 (1+\nu)}{E}\right]^{1/2}$$

$$\lambda_s^* = K G A n_s^*$$

$$K = \frac{10(1+\nu)}{12 + 11\nu} \text{ (for a rectangle [7])}$$

A = cross sectional area of mount

G = shear modulus

Using the material and geometrical properties given in Table 1, the theoretical inertance characteristics for shear waves are shown in Figure 10. In this case, the comparison between the experimental and theoretical results is not as close as the compressional wave case. The reason for this is due to the fact that the flexure characteristics of the mount have an influence on the behaviour. Treating the isolator as a shear beam, the natural frequencies are found from the equations [7]

$$f_{s_i} = \frac{\lambda i}{2\pi L}\left[\frac{KG}{\mu}\right]^{1/2} \qquad (11)$$

$$\cot \lambda_i = \left[\frac{M}{\mu A L}\right]\lambda_i \qquad (12)$$

Using the parameters of Table 1 the fundamental natural frequency has a value of 46 Hz which compares with the theoretical value of 44 Hz from equation (10). However, by combining the effects of flexure and shear using the well known Southwell-Dunkerlay approximation,

$$f^2 = \frac{f_{f_1}^2 f_{s_1}^2}{f_{f_1}^2 + f_{s_1}^2} \qquad (13)$$

where f is the fundamental frequency of a uniform beam with an end mass in flexure and f is the fundamental frequency of a shear beam from equation (11), the resulting fundamental frequency for the isolator is calculated as 35 Hz, which is very close to the experimental result shown in Figure 8, 9. In summary, the transverse characteristics of such isolators need to be analysed using combined flexure and shear deformation properties by utilising for example, the Bresse-Timoshenko theory [6].

3.2 Effect of Pre-load on the Wave Characteristics

In practise, the isolators are subjected to considerable pre-loads resulting in up to 10% strain in the compressional direction. In order to estimate the effect pre-load would have on the wave properties, the wave velocity through the resilient material was measured in the compressional direction as a function of pre-load. The velocity in the compressional direction was measured using an ultrasonic transducer which generated pulses at a frequency of 20kHz. The pulses were detected on the opposite face of the isolator using another ultrasonic receiver. The time delay between the pulses was measured for several pre-load ranges in the transverse and longitudinal directions which provided an estimate of the wave velocity through the mount. Typical results are shown plotted in Figure 11. The wave velocity in the longitudinal direction is proportional to the elastic modulus which in turn controls the wave frequencies. The variation in these properties is not significant over the range of pre-loads seen by the isolators in practise (from Figure 11 the change is less than 10% for the normal operating pre-loads) thus the effect of the pre-load on the wave frequencies will be small.

Consequently, for large vibration isolators it would appear that a rapid assessment of the dynamic properties is obtainable using simple impulse testing procedures. However, it should be stressed that with more complex geometries the effect of the pre-load may result in significant distortion of the isolator geometry which may well lead to changes in the wave characteristics. Further, the effect of temperature and pre-load on the resilient material properties may also play an important role in the overall dynamic performance of an isolator. Work into the characterisation of these properties is currently being undertaken.

CONCLUSIONS

Impulse testing procedures can be gainfully employed to determine the compressional and transverse wave characteristics of large vibration isolators. For the types of isolator tested it has been shown that the wave frequencies are nominally invariant with the pre-load over their in-service operating range. As a result, the testing procedure can be considerably simplified.

Theoretical predictions of the compressional wave frequencies can be successfully carried out for prismatic isolators using the Love Theory. Accurate prediction of the transverse wave characteristics requires the application of the Bresse-Timoshenko theory which accounts for combined shear and flexure in the system.

REFERENCES

1. I.I. Klyukin 1979 Vibration attenuation of resilient mounts and dampers underneath actively vibrating machines.

2. M. Harrison, A.O. Sykes and M. Martin 1952 Journal of Acoustical Society of America, Vol 24 (1), 62-71. Wave effects in Isolation Mounts.

3. E.E. Ungar 1963 Journal of Engineering for Industry, Trans. Asme 243-246 Wave effects in viscoelastic leaf and compression spring mounts.

4. J.C. Snowdon 1968 Vibration and Shak in Damped Mechanical Systems. John Wiley and Sons Inc. New York.

5. R.W. Fillers and N.W. Tschoegh 1977 Transactions of the Society of Rheology Vol 21 (1), 51-100. The effect of pressure on the mechanical properties of polymers.

6. S.O. Oyadiji 1983 Ph.D Thesis, University of Manchester. Vibration transmissibility characteristics of reinforced flexible pipes.

7. R.D Blevins 1979 Formulas for natural frequencies and mode shapes. Van Nostrand Rheinhold Co, N. York.

8. P. Milas 1987 Internal Report, Heriot-Watt University, Department of Mechancial Engineering. Characterisation of the dynamic behaviour of resilient mounts using impulse methods.

TABLE 1:	MATERIAL PROPERTIES OF VIBRATION ISOLATOR (AT 21°C)
Mean Youngs Modulus (in compression)	7.9 E6 N/m^2
Mean Shear Modulus	2.2 E6 N/m^2
Mass Density	1010 Kg/m^3
Top Plate Mass	5.5 Kg
Loss Factor	0.1
Poissons Ratio	0.4

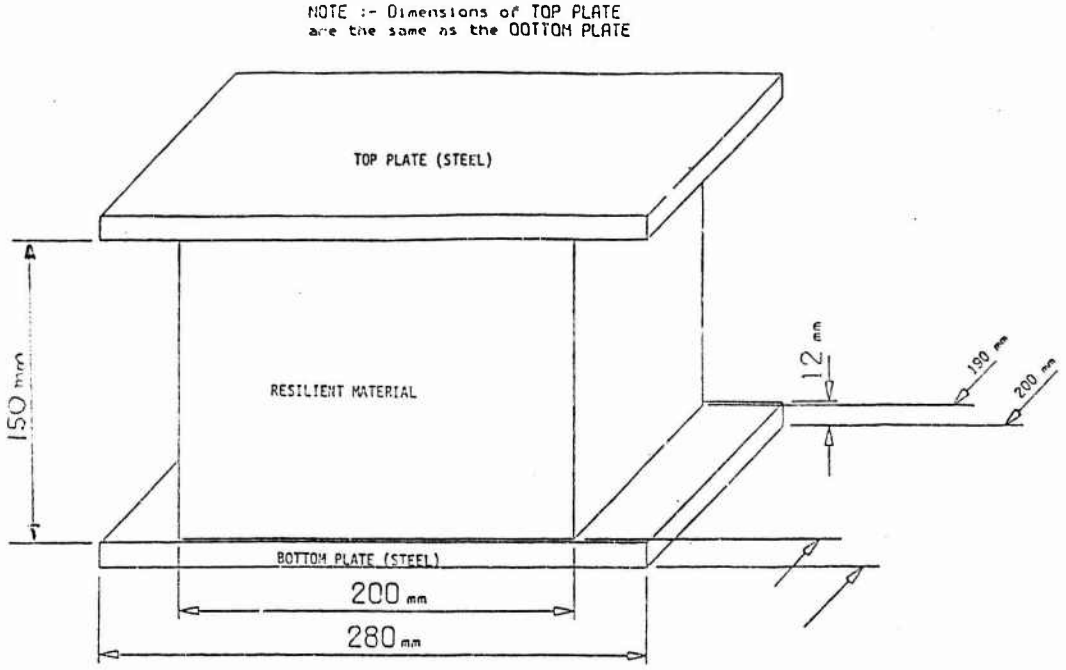

DETAILS OF MOUNT USED IN THE TESTS

Fig 1.

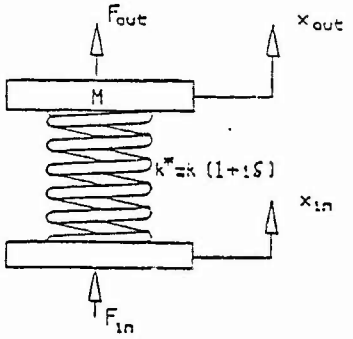

Fig. 2a

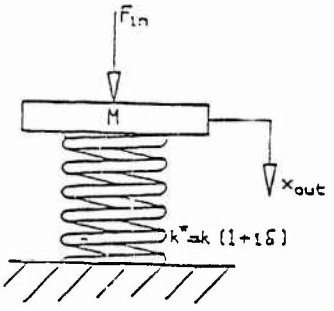

Fig. 2b

FIG 2: SIMPLE COMPLEX-SPRING MODELS

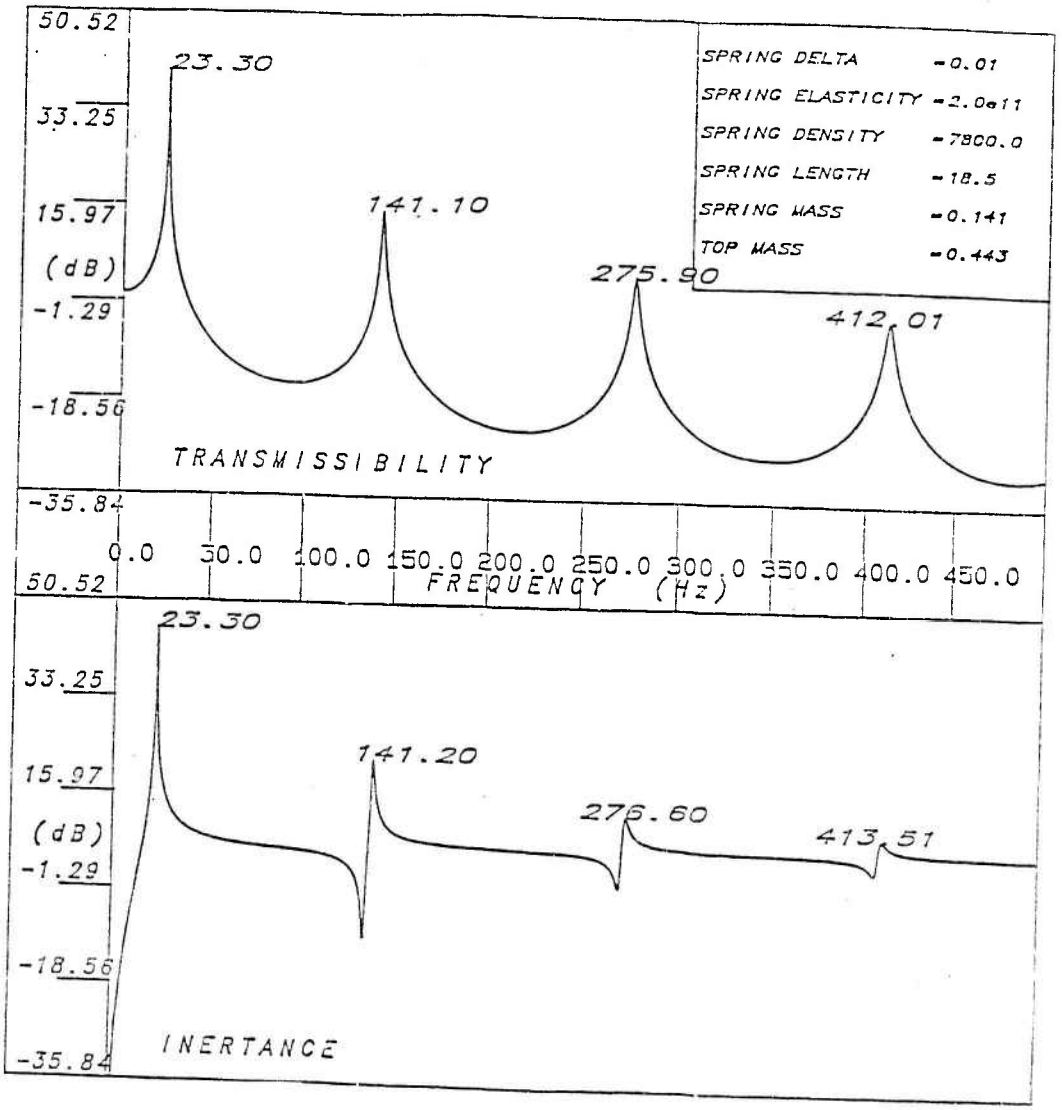

FIG 3: THEORETICAL RESULTS OBTAINED FOR TRANSMISSIBILITY AND INERTANCE OF A COMPLEX MASS/SPRING

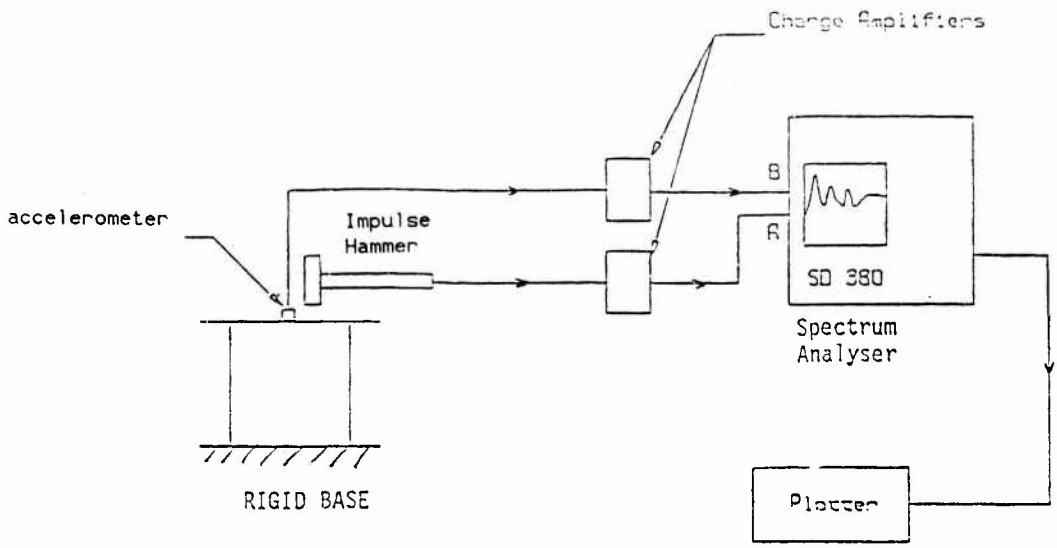

FIG. 4(a)

Experimental set-up for measuring the longitudinal inertance of the mount.

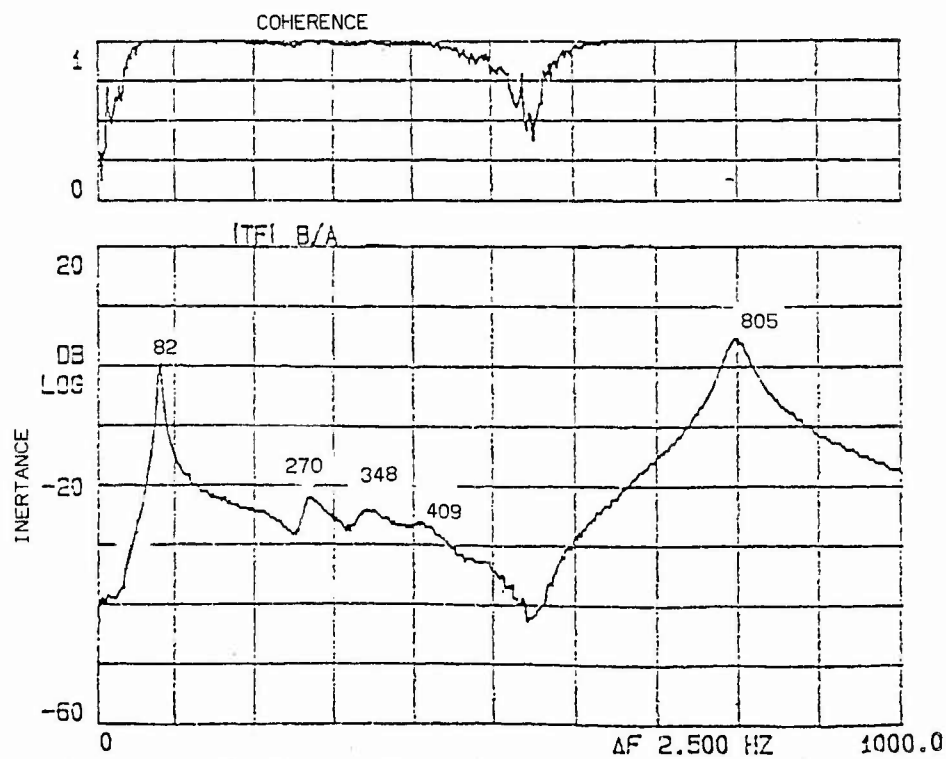

FIG 4(b) TYPICAL EXPERIMENTAL RESULTS FROM IMPACT TESTS

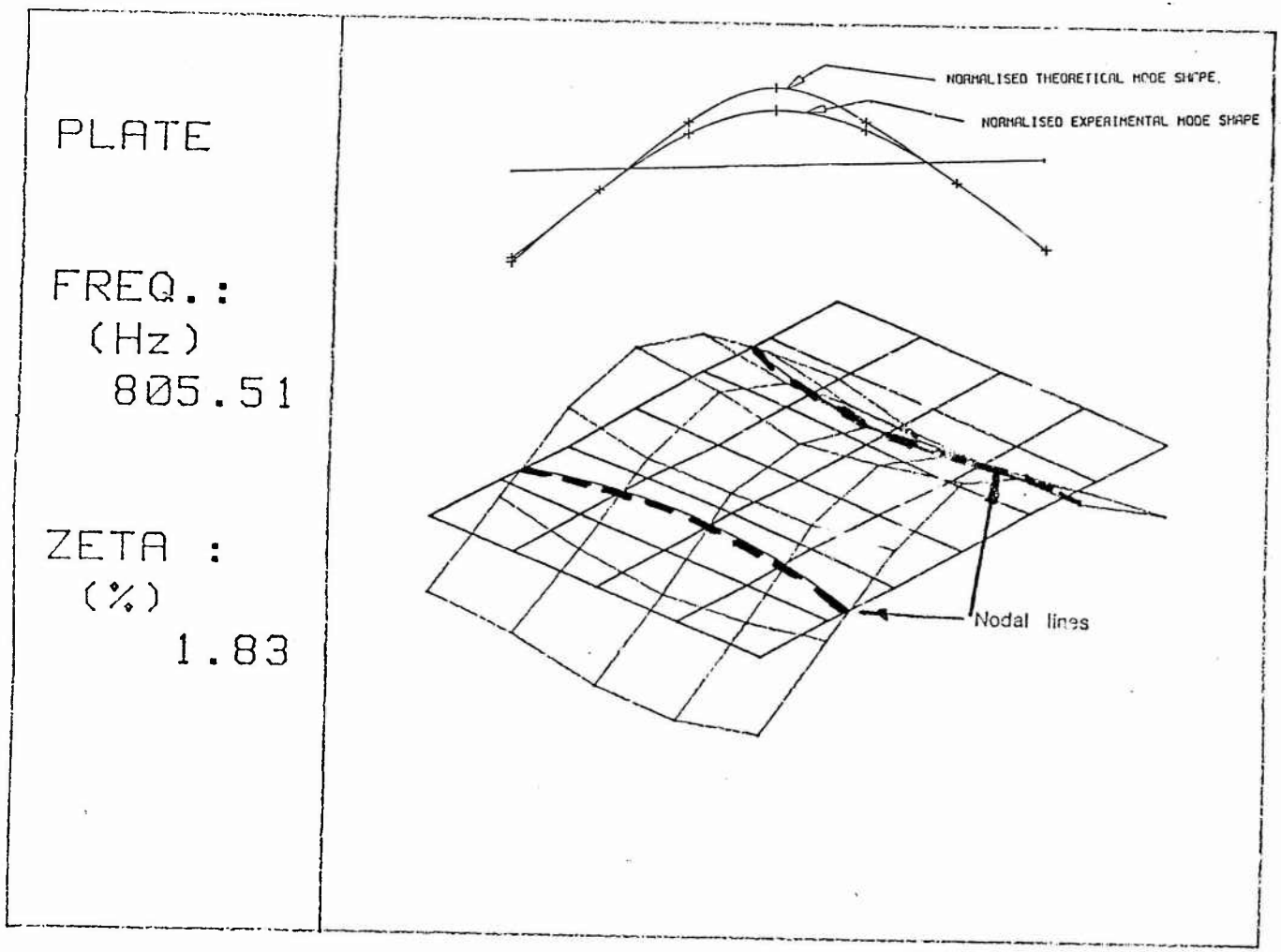

FIGURE 5. RESULTS OF MODAL ANALYSIS OF TOP-PLATE OF VIBRATION ISOLATOR

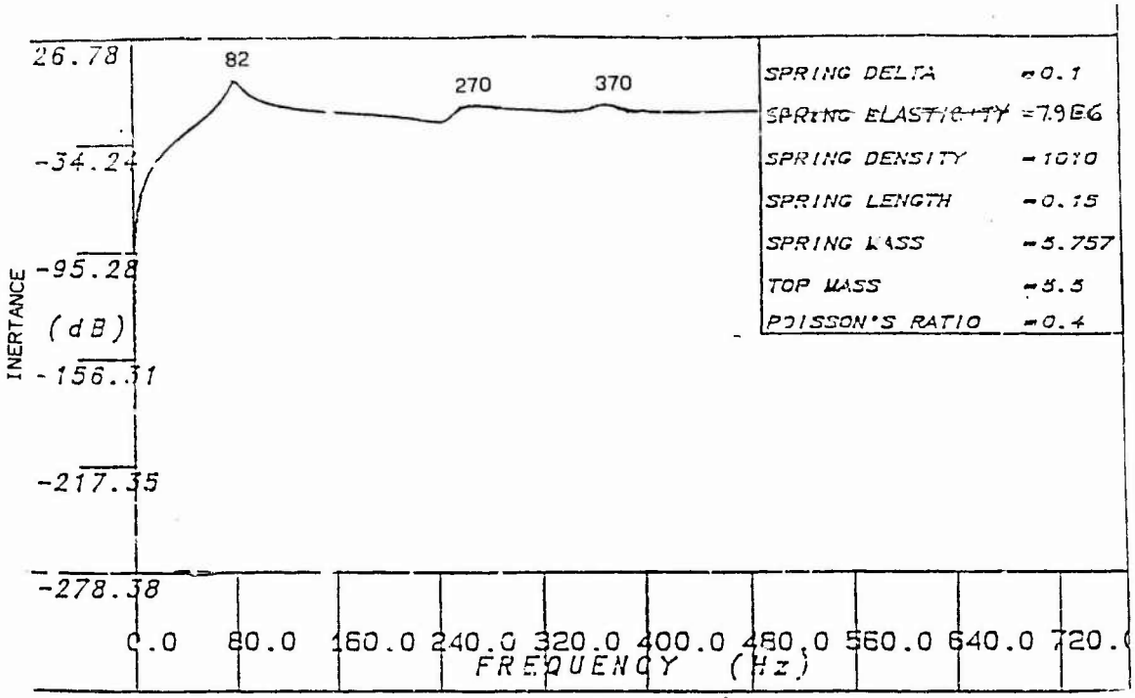

FIG 6: THEORETICAL PREDICTIONS OF THE COMPRESSIONAL WAVE CHARACTERISTICS FOR THE ISOLATOR

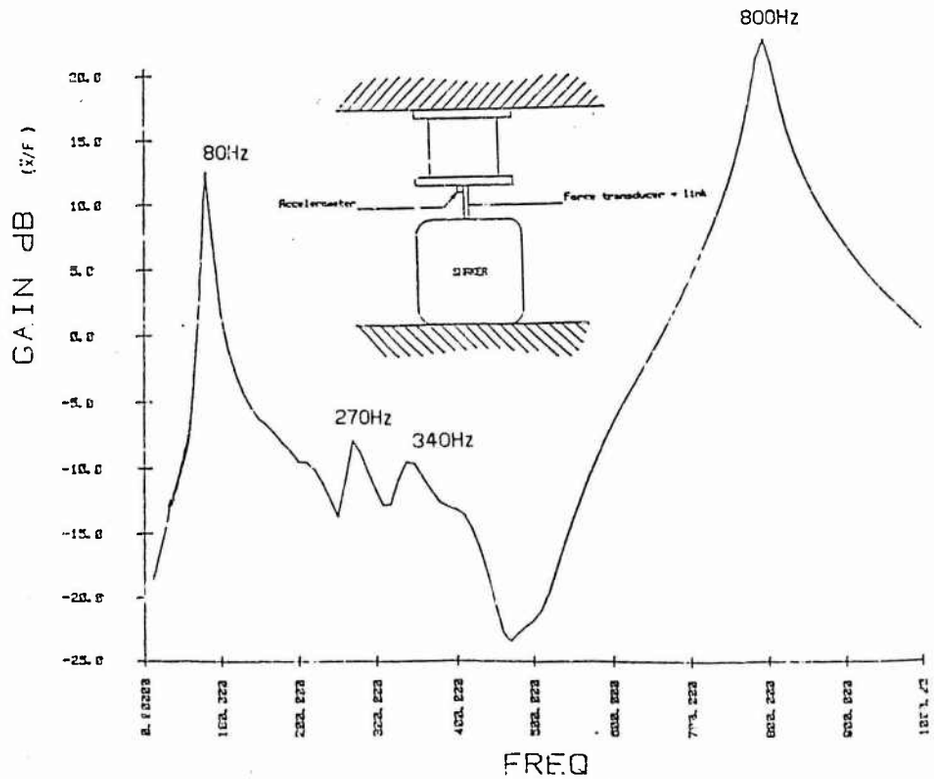

FIG 7: FREQUENCY RESPONSE FUNCTION IN COMPRESSIONAL DIRECTION USING SINUSOIDAL EXCITATION

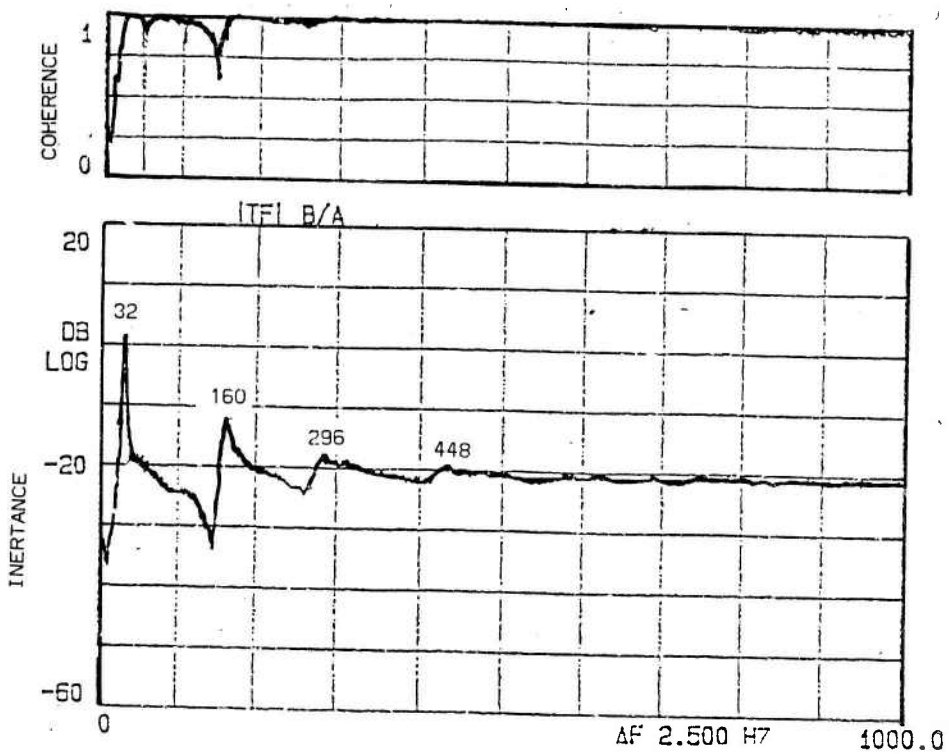

FIG 8: TRANSVERSE WAVE EFFECTS USING IMPACT EXCITATION

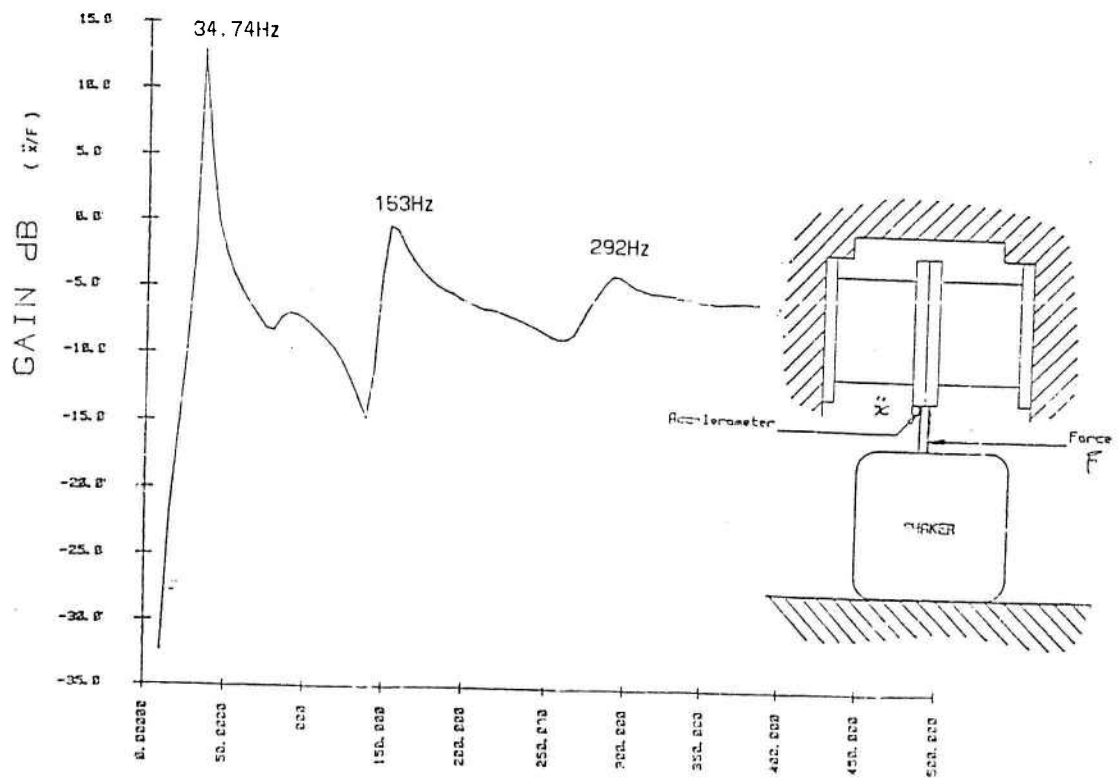

FIG 9: FREQUENCY RESPONSE FRUNCTION IN SHEAR DIRECTION FROM SINUSOIDAL EXCITATION

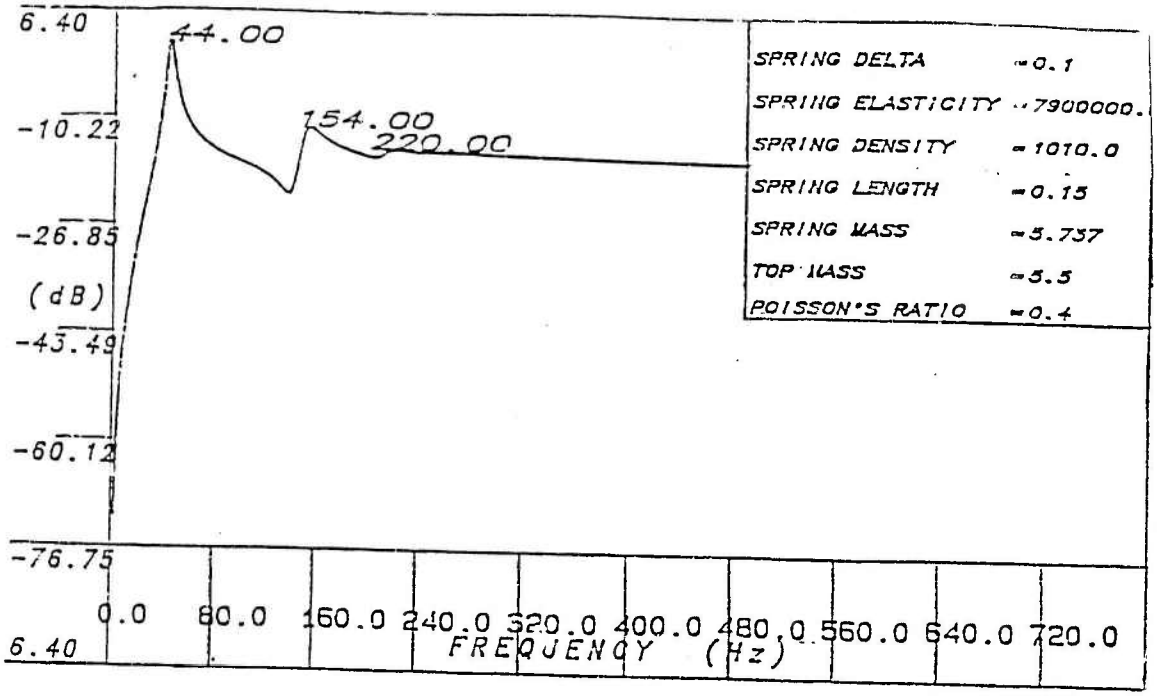

FIG 10 THEORETICAL SHEAR WAVE CHARACTERISTICS FOR THE ISOLATOR

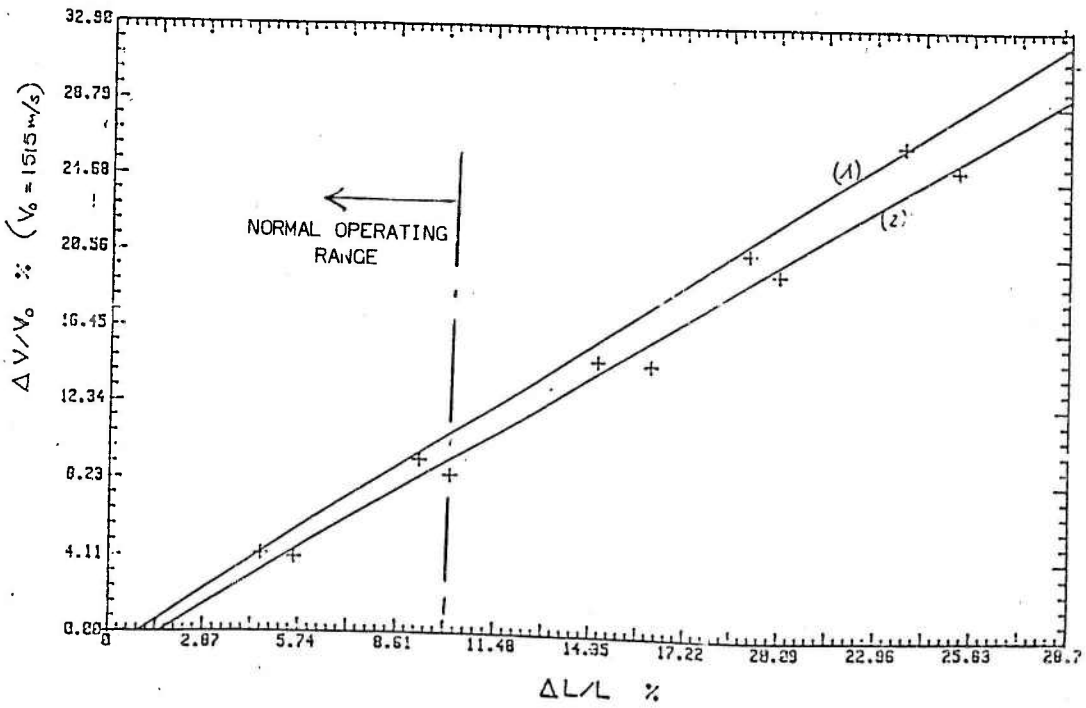

FIG. 11

EFFECT OF PRE-LOAD ON THE LONGITUDINAL WAVE VELOCITY AT TWO DIFFERENT POINTS
(1) CENTRE OF MOUNT, (2) EDGE OF MOUNT

THREE METHODS FOR DETERMINING NATURAL FREQUENCIES AND DAMPING RATIOS FROM VIBRATION SPECTRA

H G D Goyder - Harwell Laboratory

1. INTRODUCTION

A common objective in experimental studies is to determine the natural frequencies and damping ratios of a structure. In this paper, three new methods for achieving this objective are described. The approach taken is to develop a general theoretical model which describes vibration spectra and then see how the parameters of the model may be determined from measured spectra. An important part of this approach is to see how noise corrupts measurements since this controls the accuracy with which natural frequencies and damping ratios may be determined. Attention is also paid to the form the model takes. As will be shown, some simple recasting of the model often considerably simplifies the process of extracting the model parameters.

The three methods described below for determining the natural frequencies and damping ratios have been developed for different types of vibration measurements. The first method is appropriate where only a response spectrum has been measured and it is assumed that the excitation is white. The other methods are applicable to the results of a modal test where a complex frequency response function (FRF) (ie both magnitude and phase) has been measured. In each case, a frequency domain, rather than time domain approach has been taken. The frequency domain approach has the advantage of separating resonances which have similar frequencies. In the time domain, similar natural frequencies cause beating phenomena which makes interpretation of the time histories difficult.

2. MODELS FOR VIBRATION SPECTRA

The basis of a vibration spectra is the FRF of the structure. The FRF is most easily defined for a sinusoidal force and is the ratio of the response amplitude to the force. This ratio is defined as a complex number so that both modulus and phase is represented. The vibration spectrum for a structure may be calculated from its FRF and the excitation spectrum.

The general differential equation describing a linear structure is

$$a_n \frac{d^n y}{dt^n} + a_{n-1} \frac{d^{n-1} y}{dt^{n-1}} \cdots + a_o y =$$

$$= b_m \frac{d^m x}{dt^m} + b_{m-1} \frac{d^{m-1}}{dt^{m-1}} \cdots + b_o x \qquad (1)$$

Here, $y = y(t)$ is the response while $x = x(t)$ is the excitation force. a_n and b_m are coefficients in the equation. This equation may be deduced from the general matrix equation for linear systems, by eliminating all the displacements except for the displacement where the structure is to be observed.

Taking the Fourier transform of the above equation and writing $Y(i\omega)$ and $X(i\omega)$ for the Fourier transform of y and x, respectively, gives

$$\frac{Y(i\omega)}{X(i\omega)} = H(i\omega) = \frac{b_m(i\omega)^m + b_{m-1}(i\omega)^{m-1} \ldots b_o}{a_n(i\omega)^n + a_{n-1}(i\omega)^{n-1} \ldots a_o} \qquad (2)$$

where $H(i\omega)$ is the FRF. In general the order of the differential equation may be infinite so that both n and m are infinite. Equation (2) represents one model for the FRF. However this model is rarely used in vibration work because of the large number of coefficients (a_n and b_m) involved. By factorising the polynomials in equation (2) the FRF may be written

$$H(i\omega) = G \frac{(i\omega - c_1)(i\omega - c_2) \ldots (i\omega - c_m)}{(i\omega - d_1)(i\omega - d_2) \ldots (i\omega - d_n)} \qquad (3)$$

Here G is a constant and c_m and d_n are the roots of the polynomials. c_m and d_n are known as poles and zeros respectively. Both c_m and d_n may be complex. Because the a_n's and b_m's are real, the roots of the polynomials are either real or occur in complex conjugate pairs. By combining complex conjugate pairs, $H(i\omega)$ may also be written

$$H(i\omega) = G \frac{(r_1 + i\omega s_1 - \omega^2)(r_2 + i\omega s_2 - \omega^2) \ldots}{(p_1 + i\omega q_1 - \omega^2)(p_2 + i\omega s_2 - \omega^2) \ldots} \qquad (4)$$

Here, all the r's, s's, p's and q's are real. A further more familiar form for the FRF may be found by expressing equation (4) in partial fractions. If the quadratic form of the denominators is retained, then $H(i\omega)$ becomes

$$H(i\omega) = \sum_{j=1}^{N} \frac{u_j + i\omega v_j}{p_j + i\omega q_j - \omega^2} \qquad (5)$$

Here, $N = n/2$. A more conventional notation for this equation is

$$H(i\omega) = \sum_{j=1}^{N} \frac{u_j + i\omega v_j}{\omega_j - \omega^2 + 2i\zeta_j\omega_j\omega} \qquad (6)$$

where ω_j is the natural frequency while ζ_j is the damping ratio. As can be seen, the formulation above has led naturally to a definition of damping in terms of a viscous damping ratio. Hysteretic damping could also be modelled. However the use of hysteretic damping seems inappropriate since the objective is to identify damping associated with each resonance rather than modelling damping as a single structural property. Also it should be noted that hysteretic damping is a valid model for only a limited frequency band [1]. It is not therefore as general a model for damping as the viscous damping ratio.

The coefficients p, q and d may be identified by comparing equations 6, 5 and 3. This gives

$$\omega^2_j = p_j \qquad 2\zeta_j\omega_j = q_j \qquad (7), (8)$$

$$\text{Im}\{d_n\} = \omega_j\sqrt{1-\zeta^2} \qquad \text{Re}\{d_n\} = \zeta\,\omega_n \qquad (9), (10)$$

Equation 6 can be used for data fitting directly (see for example [2]), however the factorised polynomial ratio (equation 3) will be used in preference.

3. NOISE MODELS

In order to fit a theoretical model to measure data, it is necessary to have a model for the likely noise in the data. This is important because if the structure of the noise is ignored, then undue emphasis may be placed on fitting to regions where the noise is exceptionally large. Similarly, not enough emphasis may be placed on regions where the noise contents is small. Clearly some technique for weighting measured data according to its noise content is needed. In this section the noise structure for three different measurement configurations is investigated. This noise structure is then used in each of the three fitting procedures developed below.

3.1 Response Spectrum only

If the excitation is unknown and unmeasured then it is necessary to make deductions from the response spectrum. This circumstance is often found where a structure is in operation and is excited by the operational environment. If the excitation is random and the spectrum is flat, at least within the bandwidth of the oscillator, then it is possible to deduce a natural frequency and damping ratio. If the (unknown) excitation spectrum is $S_{xx}(\omega)$ and the response spectrum is $S_{yy}(\omega)$ then

$$S_{yy}(\omega) = |H(\omega)|^2 \, S_{xx}(\omega) \tag{11}$$

The measured spectrum $S_{yy}(\omega)$ is thus proportional to the modulus squared of the FRF if $S_{xx}(\omega)$ is assumed to be white. Because the excitation is random, the spectrum $S_{yy}(\omega)$ cannot be measured exactly and only an estimate may be obtained. This estimate contains noise due to the random nature of the excitation. By using a large number of averages in the calculation of $S_{yy}(\omega)$ the noise may be made small but it is generally not insignificant. With the assumption that the excitation is white, the noise content of $S_{yy}(\omega)$ is Gaussian (as long as enough averages have been taken, in theory the noise is χ^2 distributed [3]). The important point however is that the noise is weighted by the FRF and is proportional to its magnitude squared. Thus the noise model appropriate to this circumstance is

$$\bar{S}_{yy}(\omega) = |H(\omega)|^2 \, [1 + W(\omega)] \tag{12}$$

Here the overbar indicates that the spectrum is a measured spectra and includes noise. $W(\omega)$ represents a random variable which is Gaussian with zero mean and with the same variance for each frequency. It can be seen that the variance of the noise on $\bar{S}_{YY}(\omega)$ will be largest where $|H(\omega)|$ is largest, namely at resonance. Equation (13) will be used in section 4, when considering the extraction of natural frequencies and damping ratios from response spectra.

3.2 Transient Excitation

Here it is assumed that a modal test is being performed and measurements of both the excitation force and the response are being taken. In a transient test the force is applied for a brief duration and the FRF calculated from a ratio of the Fourier transform of the response to the Fourier transform of the force. Two methods for applying the transient excitation are commonly used, namely, an impulse (eg hammer excitation) [4] or an electrodynamic shaker [5].

The principle cause of noise in this circumstance is extraneous excitation which causes vibration in addition to the applied excitation. Thus the equation describing each test is

$$\bar{Y}(i\omega) = H(\omega)\ \bar{X}(\omega) + H(\omega)\ Z(\omega) \tag{13}$$

Here $\bar{Y}(\omega)$ and $\bar{X}(\omega)$ are the Fourier transforms of the measured response and force respectively. $Z(\omega)$ is the unwanted excitation from the environment. $H(\omega)$ is usually calculated from

$$\bar{H}(i\omega) = \bar{Y}(i\omega)/\bar{X}(i\omega) \tag{14}$$

where $\bar{H}(i\omega)$ is the calculated FRF. It can be seen that $\bar{H}(\omega)$ is given by

$$\bar{H}(i\omega) = H(i\omega)\ [1 + Z(i\omega)/\bar{X}(i\omega)] \tag{15}$$

If both the environmental excitation $Z(i\omega)$ and the applied excitation $\bar{X}(i\omega)$ are independent of frequency (ie a flat spectrum) then the noise is once again proportional to the FRF and the noise model is

$$\bar{H}(i\omega) = H(i\omega)\ [1 + W(i\omega)] \tag{16}$$

However, in some circumstances $\bar{X}(i\omega)$ is not flat. This specially occurs when an electrodynamic shaker is used, since this tends to couple with the structure [6]. The problem with a electrodynamic shaker is that excitation at the resonance frequencies is limited due to the inertia of the coil and the back e.m.f. s generated within the coil. It can be shown that in this case the force spectrum is inversely proportional to the FRF. Thus $\bar{X}(i\omega)$ may be modelled as

$$\bar{X}(i\omega) = P(i\omega)/H(i\omega) \tag{17}$$

where $P(i\omega)$ is the Fourier transform of the signal used to drive the power amplifier which excites the shaker. The resulting noise model for this case is thus

$$\bar{H}(i\omega) = H(i\omega)[1 + H(i\omega)\ Z(i\omega)/P(i\omega)] \tag{18}$$

or

$$\bar{H}(i\omega) = H(i\omega)[1 + H(i\omega)\ W(i\omega)] \tag{19}$$

if both $Z(i\omega)$ and $P(i\omega)$ are flat spectra. Thus the noise in the measured FRF is proportional to the square of the FRF. This noise may cause considerable distortion to the peaks of the measured FRF

3.3 Random Excitation

Random excitation may also be used for modal testing. In this type of test, the random excitation is generally applied by means of an electrodynamic shaker and measurements are made of the excitation force and the response. Spurious excitation of the structure is generally the main source of the noise. The equation describing this measurement method is

$$\bar{S}_{yx}(i\omega) = H(i\omega)\ \bar{S}_{xx}(i\omega) + H(i\omega)\ S_{zx}(i\omega) \tag{20}$$

where $\bar{S}_{yx}(i\omega)$ is the cross-spectral density function between the response and force, $\bar{S}_{xx}(i\omega)$ is the auto-spectral density function of the force, and $S_{zx}(i\omega)$ is the cross-spectral density function between the applied excitation and the spurious excitation. The FRF is generally calculated from

$$\bar{H}(i\omega) = \bar{S}_{yx}(i\omega)/\bar{S}_{xx}(i\omega) \qquad (21)$$

It can be seen that the calculated FRF is given by

$$\bar{H}(i\omega) = H(i\omega)\,[1 + \bar{S}_{zx}(i\omega)/\bar{S}_{xx}(i\omega)] \qquad (22)$$

If it is assumed that the environmental noise is uncorrelated with the applied excitation and the cross spectral density function $S_{zx}(i\omega)$ will be zero. However, because of the random nature of the excitation and noise, $S_{zx}(i\omega)$ will only approach zero as the number of averages becomes large. Consequently, this term will be the main contribution to the noise. If both the excitation and environmental noise are white, the model for the noise in the measured FRF will be

$$\bar{H}(i\omega) = H(i\omega)\,[1 + W(i\omega)] \qquad (23)$$

Thus once again the noise is proportional to the FRF. If however, the shaker exhibits the feedback effect mentioned previously, then a more complex noise source will be created. This problem has been analysed and is presented in [6]. For this case, the noise cannot be simply modelled and detailed analysis of the interaction between the shaker and the structure is needed. This is beyond the scope of this paper.

4. METHOD 1: RESPONSE SPECTRUM ONLY

If a structure is being excited by a random force and if the excitation is assumed to be white, then the measured response spectrum is given by equation (12). This equation may be recast to give

$$W(\omega) = \bar{S}_{yy}(\omega)/|H(\omega)|^2 - 1 \qquad (24)$$

If the correct values for natural frequencies and damping ratios are inserted into the model FRF, $H(i\omega)$, then values for the noise may be calculated using the above equation. If the noise model is correct, then these calculated values of $W(\omega)$ would be distributed as a Gaussian random variable. This condition may be inverted in order to obtain a criterion for selecting the parameters of the FRF. This criterion is the basis of the "least squares" fitting process [3]. Thus the mean square error associated with a set of frequency values may be written

$$K\varepsilon^2 = \sum_{k=1}^{K} [\bar{S}_{yy}(\omega_k)/|H(\omega_k)|^2 - 1]^2 \qquad (25)$$

where ε is the r.m.s. error. The unknown parameters in the FRF may now be chosen so that they minimise the value of ε. An appropriate model for $H(i\omega)$ is given by equation (3). If the summation is performed only in the region of a resonance, then this model may be simplified so that only one pole is significant. This simplification results in the model for $H(i\omega)$ being

$$|H(i\omega)|^2 = G/|i\omega - d_j|^2 = G/(\omega^2 - 2\omega\omega_j\sqrt{1-\zeta_j^2} + \omega_j^2) \qquad (26)$$

where values for d_j have been substituted from equations (9) and (10). All the poles and zeros, other than the pole of interest have been included in G, which is assumed to be a constant over the frequency range of the summation. Equation (25) may now be written

$$K G\varepsilon^2 = \sum_{k=1}^{K} \left[\bar{S}_{yy}(\omega_k)(\omega_k^2 - \omega_k D_2 + D_1) - G\right]^2 \qquad (27)$$

where $D_1 = \omega_j^2$ and $D_2 = 2\omega_j\sqrt{(1-\zeta)^2}$. Values of D_1, D_2 and G may be found by calculating the derivative of $G\varepsilon^2$ and equating to zero. It should be noted that since equation (27) is quadratic in D_1, D_2 and G, a set of linear equations is found and thus each of D_1, D_2 and G may be found directly without iteration and approximation. The point of interest is that despite the noise source being complicated by being proportional to the FRF, the model fitting problem has ultimately led to a simple linear formulation. It is also interesting that the polynomial in the fitting equation is of second order which is the smallest order polynomial for three unknowns. A very simple and effective algorithm may therefore be constructed using this procedure. Figure (1) shows a resonant peak of a measured response spectrum. By using the above procedure, the natural frequency, damping ratio and value of G were calculated. These values were then used to regenerate the response function. This regenerated function is also shown in figure 1.

5.0 METHOD 2: COMPLEX FREQUENCY RESPONSE FUNCTION

If a complex FRF is available, then a complex model must be fitted to the data. Complex data provides twice as much information as real data, consequently more accuracy in determining natural frequencies and damping ratios is possible. For the case where the noise is proportional to the FRF, a similar analysis to that conducted in the previous section may be undertaken. The only difference is that a complex formulation is required. Thus from equations (16) or (23) the complex noise may be written

$$W(i\omega) = \frac{\bar{H}(i\omega)}{H(i\omega)} - 1 \qquad (28)$$

$H(i\omega)$ may be modelled following equation (3) as

$$H(i\omega) = \frac{G}{i\omega - d_j} \qquad (29)$$

where G is a complex constant and models all the zeros and poles other than the pole of interest. An error expression for the data interval being fitted may now be formulated. This error expression may be written

$$K G\bar{G}\varepsilon^2 = \sum_{k=1}^{K} \left[H(i\omega_k)(i\omega_k - d_j) - G\right]\left[\bar{H}(i\omega_k)(-i\omega_k - \bar{d}_j) - \bar{G}\right] \qquad (30)$$

Here the second term in brackets is the complex conjugate of the first, (the (-) indicates conjugation) thus enabling a real error to be constructed. There are now two complex unknowns, d_j and G which may also be expressed as four real unknowns. These unknowns may be found by taking the derivative of the above expression with respect to each unknown equating to zero, and obtaining a set of simultaneous equations. Because equation (30) is quadratic, the four resulting equations are linear and thus the unknown parameters may be found in one step. Thus a straightforward one step method has been presented which takes into account the noise structure of the complex FRF.

6. METHOD 3: AN EXACT PROCEDURE

The above analysis will be satisfactory as long as the noise is proportional to the FRF and it is reasonable to assumed that G is a con-

stant. It has already been pointed out that the noise can be more complicated than that assumed above. Also, it is not uncommon to find zeros close to poles, or poles and zeros close to poles. (this is the difficult case of close natural frequencies). In this case assuming G to be constant can be dubious. Although the above analysis is entirely satisfactory, within its restrictions, a more exact method is worth considering.

An exact method may be developed by considering the reciprocal of the FRF. The favourable properties of the reciprocal FRF was first noted by Goyder [7]. Thus writing

$$R(i\omega) = 1/H(i\omega) \tag{31}$$

defines a new FRF, $R(i\omega)$ which is the reciprocal of the usual FRF. The relationship between the measured and model reciprocal FRF functions may thus be written

$$\bar{R}(i\omega) = R(i\omega)/\{1 + W(i\omega)\} \tag{32}$$

where the overbar indicates the measured reciprocal FRF function. Using equation (3), the model for $R(i\omega)$ may be simplified to

$$R(i\omega) = (i\omega - d_j)\, G(i\omega) \tag{33}$$

Here, the pole of interest has now come to the numerator and is written explicitly. The remaining zeros and poles are expressed by $G(i\omega)$. Note that G is no longer considered a constant but is now regarded as a complex function of frequency. Also G has been moved from the denominator to the numerator for convenience. Substituting this model into equation (32) gives

$$\bar{R}(i\omega) = (i\omega - d_j)\, G(i\omega)/\{1 + W(i\omega)\} \tag{34}$$

In this formulation the objective is to find the zero of the measured reciprocal FRF. If the noise function is well behaved then this is the classical problem of finding the zero of a function. The usual method for doing this is to employ Newton's method. In order to employ Newton's method, the following notation will be used. In equation (34), d_j is the j'th pole of the FRF. The subscript j will now be dropped and be supplanted by the subscript k. d_k will be the k'th approximation to the pole of the FRF. Using Newton's method, an improved estimate d_{k+1} to the pole may be found by calculating

$$d_{k+1} = d_k - \bar{R}(i\omega_k)/\bar{R}'(i\omega_k) \tag{35}$$

where $\bar{R}'(i\omega)$ is the derivative of the measured reciprocal frequency response function evaluated at the frequency ω_k. Thus by calculating the slope of the measured reciprocal FRF and using Newton's method, a value for the pole may be found as exactly as numerical conditions allow. A number of points are worth noting. First, equation (34) is a complex formulation of Newton's methods. The ordinary real method carries over to the complex method exactly, with some advantages. Because of the analytic nature of the function being investigated, it is not necessary to determine the derivative in any particular direction. Thus the derivative may be obtained by calculating $\bar{R}'(i\omega_k)$ from

$$\bar{R}'(i\omega_k) = \frac{d}{d\omega}\,\mathrm{Re}\,\{\bar{R}(i\omega_k)\} + i\,\frac{d}{d\omega}\,\mathrm{Im}\,\{\bar{R}(i\omega_k)\} \tag{36}$$

Thus the complex slope is obtained by measuring separately the slope of the real part and imaginary part of the reciprocal FRF. This is

generally a straightforward procedure because as may be seen from equation (33) the reciprocal FRF approximates to a straight line close to the root. In fact it is only the influence of noise and neighbouring poles and zeros that make this function deviate from a straight line.

In the usual application of Newton's method, the derivative is recalculated at the location of the current root estimate in order to obtain an estimate for the improved root. This is not possible here, since values of $\bar{R}(i\omega)$ are only available for real frequencies. However, it is possible to recalculate the derivative at the point $\omega_k = Im\{d_k\}$ which is close to the actual location of the root. The only problem in calculating the slope is that the noise may introduce errors. In order to examine the influence of noise, equation 32 may be rewritten

$$\bar{R}(i\omega) = R(i\omega)\{1 - W(i\omega) \ldots\} \qquad (37)$$

where the noise term has been brought to the numerator by using the binomial expansion. It may be seen that the influence of the noise is a minimum at the resonance because at this location $R(i\omega)$ has a zero. This is a further advantage of using reciprocal FRFs. Because of the influence of the noise, it is generally necessary to introduce some smoothing when calculating the slope of the reciprocal FRF.

It should be noted that there is a category difference between finding the natural frequencies and damping ratios using Newton's method and by the curve fitting method described previously. In the curve fitting case, errors in the model (eg assuming no influence of neighbouring poles and zeros or noise) are reflected by errors in the values obtained for the natural frequencies and damping ratios. In the use of Newton's method, no assumptions are made about the disposition of neighbouring poles and zeros and the structure of the noise. The Newton's method can therefore be thought of as an exact method. Thus by using Newton's methods, natural frequencies and damping ratios may be found for very complicated FRFs with an unknown noise structure.

The following technique has been developed in order to apply this method. First, the complex reciprocal of the measured FRF is calculated. This new function is then smoothed. The smoothing is achieved by fitting a straight line through a small number of points Thus for each frequency of interest, the value of $\bar{R}(i\omega_k)$ is replaced by $\bar{R}_s(i\omega_k)$ where the smoothed FRF is composed of a complex straight line formed from 3, 7 or 9 points. The straight lines used are overlapping so that over the interval containing the resonance, the function $\bar{R}(i\omega_k)$ has the same number of points as the function $R_s(i\omega_k)$. Since the calculation of the straight line used for smoothing involves calculating the slope of the reciprocal FRF, equation (36) may be calculated for each frequency value. Thus from each point on the FRF, a value for the natural frequency and damping ratio is obtained. This procedure is illustrated in figures (2) to (5). Figure 2 shows one resonance of a measured FRF. Figure 3 shows the reciprocal FRF. The natural frequencies and damping ratios calculated from each point are shown in figures (5) and (6) on much expanded scales. Three points were used for smoothing. By analysing the spread of results it may be seen that the frequency has been determining to an accuracy of better than ± 0.025% while the damping ratio has been determined to an accuracy better than ± 1%.

7. CONCLUSIONS

Three methods for determining natural frequencies and damping ratios from measured spectra have been presented. In order to characterise the FRF of the structure being investigated, an unusual model has been used. This model takes the form of a polynomial ratio in which the polynomials are factorised. In order to facilitate the fitting of models to measured data, an analysis of noise has been undertaken. In general, the noise on a spectra has been shown to be proportional to the FRF. The first method for determining natural frequencies and damping ratios is applicable where only a response spectrum is available. A novel curve fitting procedure has been developed which turns out to be a surprisingly simple one-step method involving the solution of three simultaneous equations. The second method extends this model fitting procedure to the case where a complex FRF has been measured. The third method is appropriate where there are close natural frequencies and a complicated noise spectrum. For this case, an exact method has been developed based on Newton's method for finding the roots of an equation. The method has been demonstrated with measured data.

8. REFERENCES

1. R.E.D. BISHOP and W.G. PRICE 1986 A note on hysteretic damping of transient motions. Random Vibration - Status and Recent Developments, Elishakoff and Lyon, Elsevier.

2. H.G.D. GOYDER 1980 Method and application of structural modelling from measured structural frequency response data. J.Sound and Vib. 68 (2) 209 - 230.

3. J.M. JENKINS and D. WATTS 1968 Spectral analysis and its applications. Holden Day.

4. D. EWINS 1984 Modal Testing: Theory and Practice. John Wiley.

5. R.G. WHITE and R.J. PINNINGTON 1982 Practical application of the rapid frequency sweep technique for structural frequency response measurements. The Aeronautical Journal of the Royal Aeronautical Society.

6. H.G.D. GOYDER and A.P. LINCOLN 1988 An experimental technique for investigating nonlinear structures. Recent Advances in Structural Dynamics.

7. H.G.D. GOYDER 1984 Foolproof methods for frequency response measurements. Recent Advances in Structural Dynamics.

9. ACKNOWLEDGEMENTS

The work described in this paper was undertaken as part of the underlying research programme of the UKAEA.

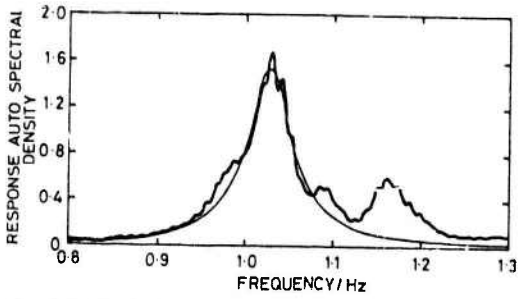

FIGURE 1. MEASURED RESPONSE AUTO SPECTRAL DENSITY AND REGENERATED SPECTRAL DENSITY FOLLOWING CURVE FITTING USING EQUATION 27.

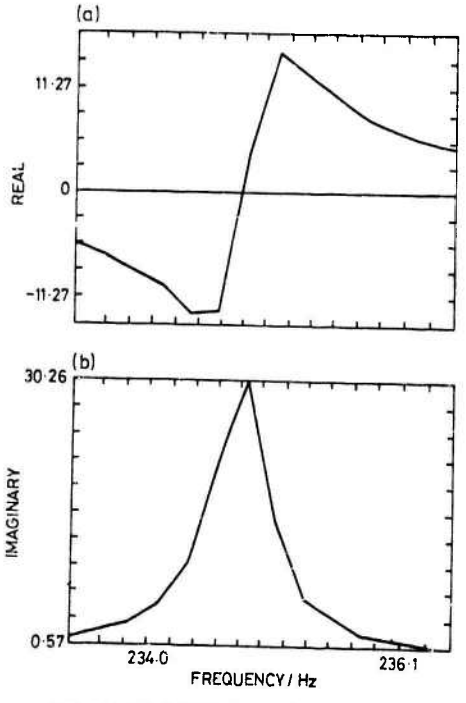

FIGURE 2. (a) REAL PART (b) IMAGINARY PART OF MEASURED FRF

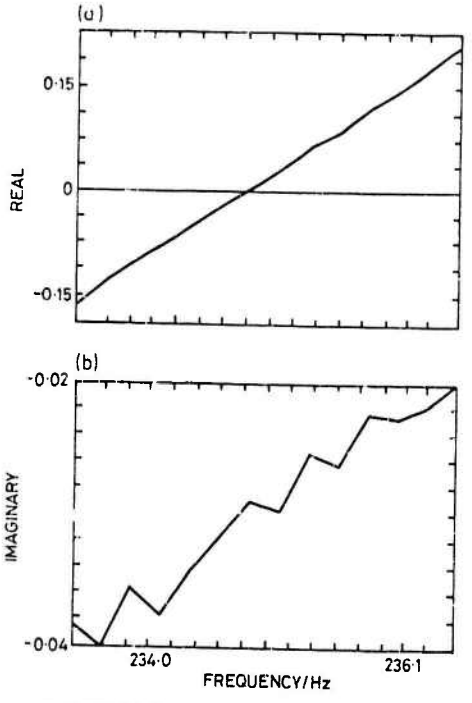

FIGURE 3 (a) REAL PART (b) IMAGINARY PART OF MEASURED RECIPROCAL FRF

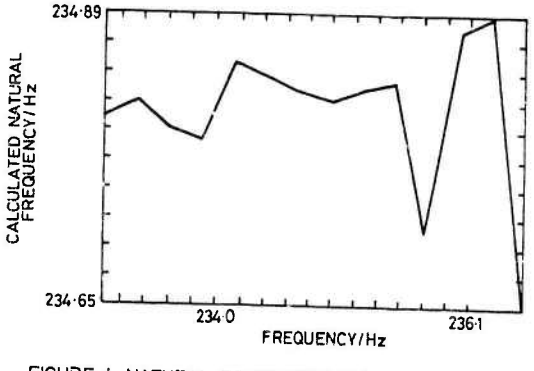

FIGURE 4. NATURAL FREQUENCY VALUES CALCULATED FROM EACH MEASURED VALUE OF THE FRF

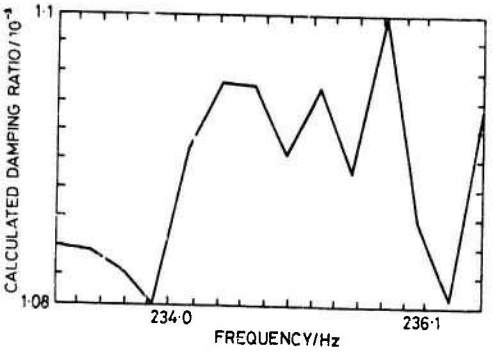

FIGURE 5. DAMPING RATIO VALVES CALCULATED FROM EACH MEASURED VALUE OF THE FRF

APPLICATION OF FILTERING TECHNIQUES FOR SYSTEM IDENTIFICATION OF VIBRATING STRUCTURES

by

T. K. Tee,

J. E. Mottershead

R. Stanway

and

D. J. Brookfield

Department of Mechanical Engineering,
The University of Liverpool,
Liverpool L69 3BX, U.K.

SUMMARY

This paper describes the application of sequential frequency domain filtering to the estimation of physical parameters in linear models of vibrating structures. Preliminary experimental results from a portal frame rig are included to demonstrate the application of the technique. Model order, scaling and choice of frequency response function are shown to be important factors to be considered by the user.

1. INTRODUCTION

This paper is concerned with the estimation of mass, stiffness and damping properties of structures using measured vibration data without the use of a modal decomposition. The system identification technique applied in the paper is a least-squares filter. Least-squares methods are usually categorised, as either 'batch' or 'sequential'.

In the batch processing case the computation is carried out on the complete set of data as a whole. This remains the most common method of data processing and it has given rise to various algorithms such as Gauss-Newton and Quasilinearisation both of which are treated in the book by Kalaba and Spingarn [1]. Stanway and Mottershead [2] have demonstrated a disadvantage of the batch processing method, namely that it depends on a preselected set of data which may be insufficient to allow parameter estimation with sufficient accuracy. This latter problem can be misleading to the novice user because it can lead to convergence of the estimates to erroneous values. Thus it is necessary to check the estimates by re-running the algorithm over an expanded set of measured data.

In the sequential processing method parameter estimates are updated continuously while working serially through the data. The non-linear, time domain filter of Detchmendy and Sridhar [3] is typical of this approach. The method of Detchmendy and Sridhar is operated in the continuous time domain and the algorithm equations involve integration which introduces a beneficial 'smoothing' effect in the presence of measurement noise. A further advantage of operating in continuous time is that the parameters

extracted are the physical parameters of a differential equation. In a discrete time filter such as Unbehauen [4] the estimated parameters are those of a difference equation.

The user should be aware of the assumptions and approximations involved in the chosen approach to system identification. For instance, if it is necessary to obtain values for the physical parameters of a linear system using a discrete time approach then it will be necessary to perform a logarithmic transformation. In order to avoid the significant errors which may be introduced by the log. transformation a continuous time approach may be preferred. However unless an analogue computer is used there will be approximations due to the process of numerical integration.

In system identification of linear, large-scale vibrating structures involving many degrees of freedom it is helpful to reformulate the filter in the continuous frequency domain. Whereas the state vector of the time domain filter includes both the displacement and velocity states at each degree of freedom and the unknown parameter states, the state vector of the frequency domain filter comprises the unknown parameter states alone. Thus frequency domain filters involve smaller order matrix equations than do time domain filters for the estimation of the same number of unknown parameters. Various filter formulations have been implemented in the continuous frequency domain. An output error filter [5] resulting in a non-linear algorithm was found to converge slowly and despite the advantages of frequency domain formulation mentioned above it involved a complex matrix manipulation in an inner loop of the computer program which resulted in large CPU times. To overcome this latter problem a linear, equation error algorithm [6] was developed which converged extremely rapidly (about 1000 times faster than the output error filter) but was prone to bias in the presence of measurement noise. Recently an instrumental variables (I.V.) filter [7] has been presented which results in swift convergence of asymptotically unbiased parameter estimates.

In system identification generally a major problem is that of non-uniqueness of the estimated model. This problem can be attacked by ensuring that any a priori information is made available to the algorithm. In the specific case of estimating physical parameters in vibrating structures the mass matrix is usually positive definite. Mottershead, Tee and Lees [8] have shown that when the filter algorithm is constrained to ensure positive definiteness of the mass matrix then convergence is accelerated and the algorithm is more tolerant of measurement noise.

In this paper the authors describe some preliminary experimental results obtained from a portal frame rig. Scaling of the model parameters is discussed and the implementation of an automatic scaling method in a FORTRAN program is explained. The use of displacement/force and acceleration/force frequency response functions is discussed and the paper demonstrates how models can be built covering discrete frequency bands.

2. STRUCTURAL MODEL

A multi-degree-of-freedom vibrating system can be modelled as follows,

$$\underline{q}(\omega) = \underline{B}(\omega)\{\underline{z}(\omega) - \underline{\xi}\} \qquad (1)$$

where $\underline{q}(\omega)$ is a vector of known forces,
$\underline{z}(\omega)$ is a vector of measured displacement responses,
$\underline{\xi}$ is a measurement noise vector

and $\underline{B}^{-1}$ is the matrix of frequency response functions.

Typically $\underline{B}(\omega)$ will have the form,

$$\underline{B}(\omega) = -\omega^2\underline{M} + j\omega\underline{C} + \underline{K} \tag{2}$$

where $\underline{M}$ is the system mass matrix
$\underline{K}$ is the stiffness matrix
and $\underline{C}$ is a matrix of viscous damping coefficients.

Equation (2) can easily be altered to accommodate other forms of damping.

Rewriting equations (1) and (2) in state space, then

State equation:
$$\frac{d\underline{x}}{d\omega} = \{0\} \tag{3}$$

where the state vector $\underline{x}$ contains the unknown mass, stiffness and damping parameters which are independent of frequency.

Measurement equation (given in complex form to indicate the difference in phase between the excitations and responses):

$$\begin{aligned} \mathrm{Re}\underline{q}(\omega) &= \mathrm{Re}\big(\underline{B}(\underline{x},\omega)\ \underline{z}(\omega)\big) - \mathrm{Re}\big(\underline{B}(\underline{x},\omega)\underline{\xi}\big) \\ \mathrm{Im}\underline{q}(\omega) &= \mathrm{Im}\big(\underline{B}(\underline{x},\omega)\ \underline{z}(\omega)\big) - \mathrm{Im}\big(\underline{B}(\underline{x},\omega)\underline{\xi}\big) \end{aligned} \tag{4}$$

The problem at hand is to estimate the unknown parameters $\underline{x}$ using measured responses $\underline{z}(\omega)$ and known excitations $\underline{q}(\omega)$.

3. FILTER EQUATIONS

A linear frequency domain filter can be formulated by minimising the cost functional,

$$J = \int_0^{\Omega} \underline{\varepsilon}^T\ \underline{Q}\ \underline{\varepsilon}\ d\omega \tag{5}$$

where $\underline{Q}$ is a weighting matrix and $\underline{\varepsilon}$ represents the equation error given by,

$$\underline{\varepsilon} = \underline{q}(\omega) - B(\hat{\underline{x}},\omega)z(\omega) \tag{6}$$

$\hat{\underline{x}}$ is an estimate of the unknown parameters and a matrix $\underline{H}$ is given by,

$$\underline{H}(\omega) = \frac{\partial}{\partial\hat{\underline{x}}}\ (\underline{B}(\hat{\underline{x}},\omega)\underline{z}(\omega))^T \tag{7}$$

The filter equations have been presented [6] in complex form. Estimates can be extracted from the real component of the equation error as follows:

$$\begin{aligned} \frac{d\hat{\underline{x}}}{d\Omega} &= 2\ \underline{P}'\Omega)\mathrm{Re}(\underline{H}(\Omega))\underline{Q}\ \mathrm{Re}(\underline{q}(\Omega) - \underline{B}(\hat{\underline{x}},\Omega)z(\Omega)) \\ \frac{d\underline{P}}{d\Omega} &= -2\ \underline{P}(\Omega)\mathrm{Re}(\underline{H}(\Omega))\underline{Q}\ \mathrm{Re}(\underline{H}^T(\Omega))\underline{P}(\Omega) \end{aligned} \tag{8}$$

Two further equations of identical structure can be formed to enable estimates to be extracted from the imaginary component of the equation error.

Equations (8) are based on known excitations and measured displacements. They can be modified to allow for alternative response measurements. For instance if it is required to process measured accelerations then forming the accelerations in $\underline{z}(\omega)$ the array $\underline{B}$ must be redefined such that,

$$\underline{B} = \left(\underline{M} + \frac{\underline{C}}{j\omega} - \frac{\underline{K}}{\omega^2}\right).$$

In both cases the array $\underline{P}$ is a weighting array the elements of which converge to small values indicating accurate convergence of the parameter estimates $\underline{\xi}$. It is a feature of linear filters (derived from linear state and measurement equations) that the array $\underline{P}$ can be computed independently of $\underline{\xi}$.

4. SCALING OF THE STRUCTURAL MODEL

It has been reported previously [5,6] that scaling of the structural model can be beneficial to the conditioning of the filter equations and convergence of the estimates. In [5] Mottershead and Stanway suggest scaling of the model as follows,

$$\left(\underline{A}\,\underline{K} + j\left(\frac{\omega}{\alpha}\right)\alpha\,\underline{A}\,\underline{C} - \left(\frac{\omega}{\alpha}\right)^2 \alpha^2\,\underline{A}\,\underline{M}\right)\frac{1}{e}\left(\underline{z} - \underline{\xi}\right) = \frac{1}{e}\,\underline{A}\,\underline{q} \qquad (9)$$

If $\underline{A}$ has the units of flexibility (stiffness^{-1}), $\sim$ has the units of time^{-1} and e has the units of displacement, then $\underline{A}\,\underline{K}$ is a scaled, non-dimensional stiffness matrix, $\alpha\,\underline{A}\,\underline{C}$ is a non-dimensional damping matrix and $\alpha^2\underline{A}\,\underline{M}$ is a non-dimensional mass matrix, $\frac{1}{e}(\underline{z} - \underline{\xi})$ is a non-dimensional displacement vector, $\frac{1}{e}\,\underline{A}\,\underline{q}$ is a vector of non-dimensional forces and $\left(\frac{\omega}{\alpha}\right)$ represents non-dimensional frequency. It should be noted that in the case of the linear filter when a common scaling factor ($\underline{A}$) is applied to both the applied forces and the parameter states then $\underline{H}(\Omega)$ is unaltered and the convergence of $\underline{P}$ and the scaled parameters $\underline{\xi}$ remains unchanged.

The frequency scaling factor α can be used to adjust the parameter values so that in the scaled form the numerical values of mass, stiffness and damping are of the same order. Unless scaling of this type is applied, the filter tends to give convergence of parameters with the largest numerical values first and small parameters tend to converge much more slowly. The factor α can be set once before processing begins and need not be adjusted again.

It can be seen from equations (8) that if the vector of residuals ($\underline{q} - \underline{B}\,\underline{z}$) is small then convergence of the filter results will be sluggish. This problem can be remedied by applying a large scaling factor $^1/e$. Because the measured frequency response functions may have vastly differing amplitudes particularly around resonances it is necessary to alter the factor $^1/e$ during processing. Changing $^1/e$ interactively can be very time consuming and tedious so a method has been developed to automate the task.

The automatic scaling technique relies on increasing $^1/e$ until an overflow or underflow error is generated by the program when computing the derivatives $\frac{d\underline{\hat{x}}}{d\Omega}$ and $\frac{d\underline{P}}{d\Omega}$. The factor $^1/e$ is then reduced slightly to a large value which is just capable of avoiding the underflow/overflow error. In this particular implementation the process is achieved by using the ERRSET library routine which is available on the University's IBM 3083 computer. The only other reason for reducing $^1/e$ is when undesirable trends are detected in the convergence of the $\underline{P}$ matrix. In particular if $\underline{P}$ tends to increase instead of reduce or if $\underline{P}$ becomes negative (often an indicator of numerical instability) then $^1/e$ will be reduced even though an underflow/overflow error has not been generated.

5. FREQUENCY RESPONSE FUNCTIONS

The experimental results presented in the sequel use frequency response functions as the measured responses $\underline{z}$. This has the useful effect of combining in one quantity the noise picked up in measuring both forces and responses. It also means that the elements of $\underline{q}$ are known to be either unity (at stations where excitation is applied) or zero.

Convergence of the estimates is strongest at resonance where the amplitude of the frequency responses is greatest. It is usually the case in structures that displacement/force frequency response functions display the greatest peaks at the low frequency modes. Conversely the greatest peaks of acceleration/force frequency response functions are at higher frequencies. Thus frequency response data in many forms may be exploited by the perceptive user in the modelling of vibrating structures using the filtering technique.

6. PORTAL FRAME RIG

A portal frame rig was built in order that the frequency domain filter could be applied to physically realistic data. In particular the rig displayed features such as light damping and closely spaced modes which are common in the dynamics of larger structures. The rig is shown in Figure 1 and its first three mode shapes are shown in Figure 2.

7. EXPERIMENTATION

An experiment was performed using the portal frame rig. Accelerometers were mounted at the two ends of the top beam and at the mid-points of the supporting legs. Stations 2 and 3 (see Figure 1) correspond to the accelerometer positions on the top of the beam and stations 1 and 4 denote accelerometer locations on the two legs. Persistent multi-frequency excitation was applied to the structure at station 1. Station 1 is a suitable location for the exciter since it is likely to stimulate all three modes. The frequency band of the excitation was 0-200 Hz, the highest natural frequency being at around 100 Hz and the fourth natural frequency being at around 390 Hz.

Estimates of mass, stiffness and damping were computed using the frequency domain filter. An initial estimate $\underline{\hat{x}}(0)$ was provided using a reduced finite element model. A plot of the measured acceleration/force frequency response function at station 1 with the finite element simulated frequency response function superimposed is shown in Figure 3. It can be seen that the finite element model is significantly in error. The initial

values of the elements of $\underline{P}$ were set as follows,

$$P_{ij}(0) = 3.0 \quad (i=j)$$
$$P_{ij}(0) = 1.0 \quad (i \neq j)$$

which are sufficiently large to promote rapid convergence of $\underline{\theta}$ without inducing numerical instability.

The mass, stiffness and damping parameters were estimated in turn. Firstly the data was processed keeping the stiffnesses and damping constant whilst the masses were estimated. Then stiffness was estimated keeping mass and damping steady and finally the damping was computed. This strategy of selectively estimating the parameters was pursued on the basis that the filter results were likely to converge most rapidly when the number of unknowns was kept reasonably small. The filter was applied in regions close to the three natural frequencies of the rig and data was obtained using zoom techniques which are generally available on modern multi-channel spectrum analysers.

8. RESULTS

The results of the experiment are presented as reconstructed frequency responses (based on the estimated parameters) which are superimposed on the measured frequency response functions. Results were obtained corresponding to models of order 3 or 4.

8.1 3-Degree-of-Freedom Model

Figure 4 shows measured and reconstructed acceleration/force frequency response functions at station 1. In the region of the second and third modes there is almost perfect agreement both in amplitude and phase. Processing was confined to the band of frequencies 80-110 Hz in order to obtain these results. The natural frequency at around 10 Hz does not appear on the reconstructed frequency response.

In order to model the fundamental mode data was processed separately in the 10 Hz region. For example, Figure 5 shows the measured and reconstructed displacement/force frequency response at station 2. The model developed in the 10 Hz region is different from that developed in the 80-110 Hz band. Such models are thus band limited.

8.2 4-Degree-of-Freedom Model

Figure 6 again shows measured and reconstructed acceleration/force frequency response functions at station 1. The results were obtained by processing locally around the two higher modes (80-110 Hz) and the 1st mode is not represented in the reconstructed data. Generally the results are in good agreement though not quite as good as the results from the 3-degree-of-freedom model. Two computational modes were found in the reconstructed data at frequencies in excess of 1000 Hz.

9. CONCLUSIONS

The continuous frequency domain filter has been applied to measured data gathered from a portal frame rig. The method is capable of providing models in terms of physical parameters (mass, stiffness and damping) in specific frequency bands around prominent natural frequency peaks. The method does not rely upon a modal decomposition and it is tolerant of

significant errors in the original (finite element) model.

ACKNOWLEDGEMENT

T. K. Tee is supported by an S.E.R.C. (C.A.S.E.) award in collaboration with the Central Electricity Generating Board.

REFERENCES

1. R. KALABA and K. SPINGARN 1982 Control, Identification and Input Optimisation. New York: Plenum Press.

2. R. STANWAY and J. E. MOTTERSHEAD 1986 Transactions of the Institute of Measurement and Control 8, 1, 9-16. Identification of Combined Viscous and Coulomb Friction: A Numerical Comparison of Least Squares Algorithms.

3. D. M. DETCHMENDY and R. SRIDHAR 1966 Transactions of the American Society of Mechanical Engineers, Journal of Basic Engineering 88D, 362-268. Sequential Estimation of States and Parameters in Noisy Non-Linear Dynamical Systems.

4. H. UNBEHAUEN 1982 Identification of Vibrating Structures (contribution to H. G. Natke) 53-120. Introduction to System Identification Using Parameter Estimation Methods.

5. J. E. MOTTERSHEAD and R. STANWAY 1986 Journal of Sound and Vibration, 109, 3, 495-506. Identification of Structural Vibration Parameters by Using a Frequency Domain Filter.

6. J. E. MOTTERSHEAD, A. W. LEES and R. STANWAY 1987 Transactions of the American Society of Mechanical Engineers, Journal of Vibrations, Acoustics, Stress and Reliability in Design, 109, 262-269. A Linear, Frequency Domain Filter for Parameter Identification of Vibrating Structures.

7. J. E. MOTTERSHEAD In press. Transactions of the American Society of Mechanical Engineers, Journal of Vibrations, Acoustics, Stress and Reliability in Design. A Unified Theory of Recursive Frequency Domain Filters with Application to Structural Dynamics.

8. J. E. MOTTERSHEAD, T. K. TEE and A. W. LEES 1988 Transactions of the American Society of Mechanical Engineers, Journal of Vibrations, Acoustics, Stress and Reliability in Design, 110, 49-52. Identification of a Positive Definite Mass Matrix.

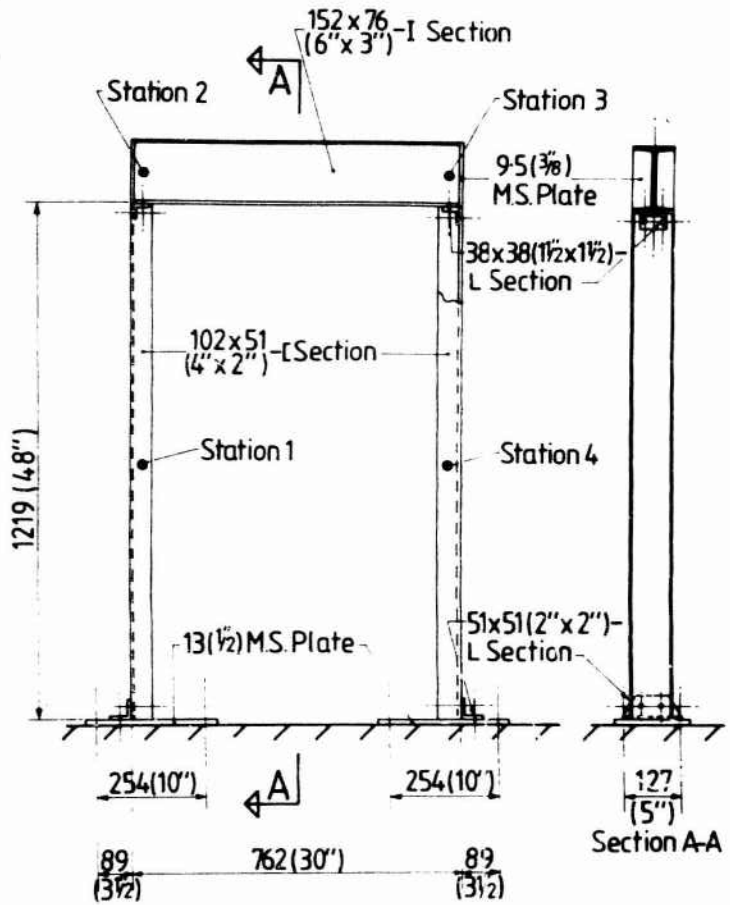

FIG. 1 Portal frame rig.

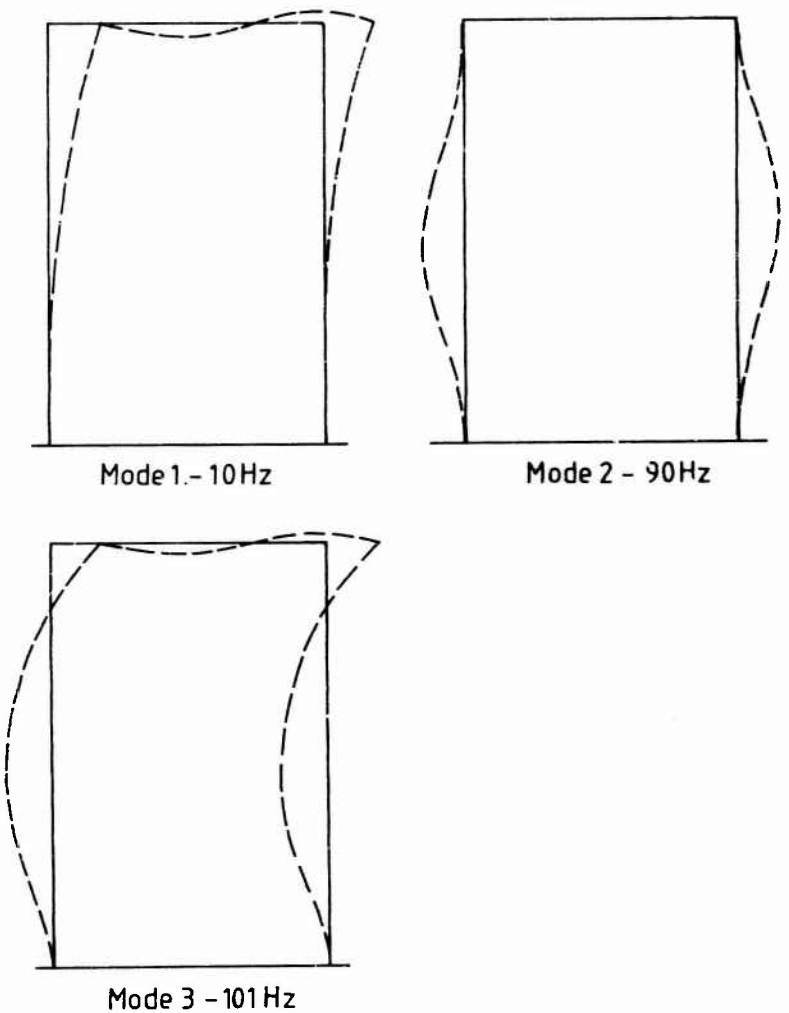

FIG. 2 Mode shapes of portal frame rig

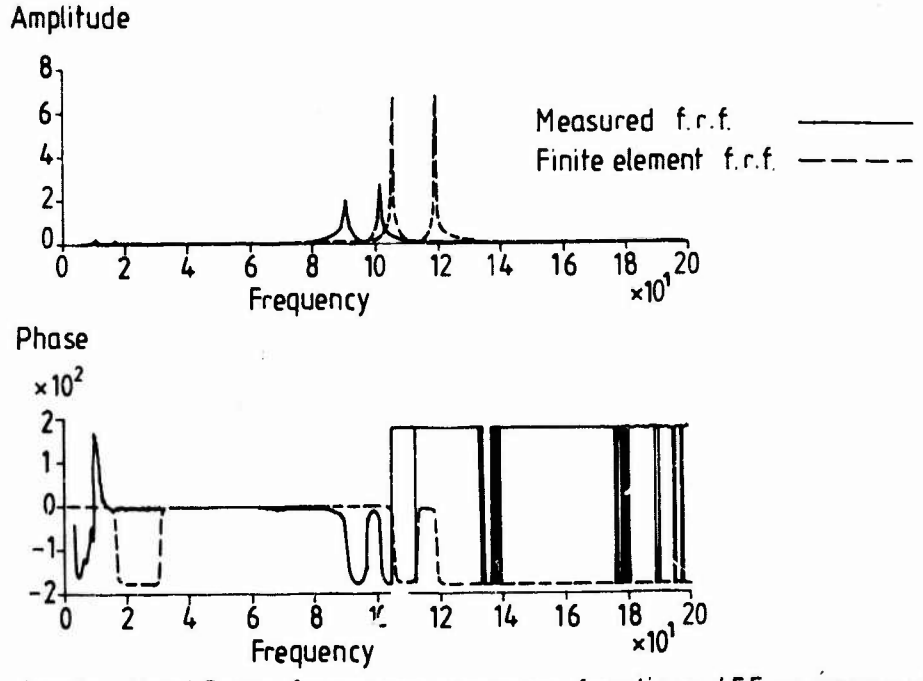

FIG. 3 Acceleration/ Force frequency response functions (F.E. vs measured) Station 1.

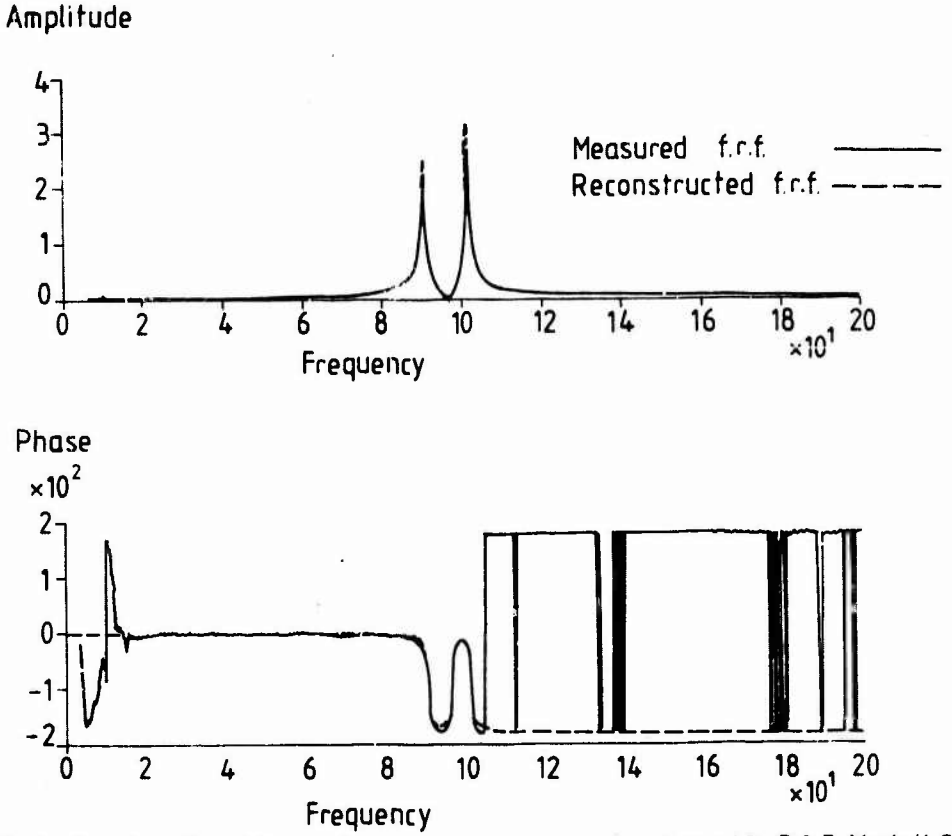

FIG. 4 Acceleration / Force frequency response functions (3-D.O.F. Model) Station 1

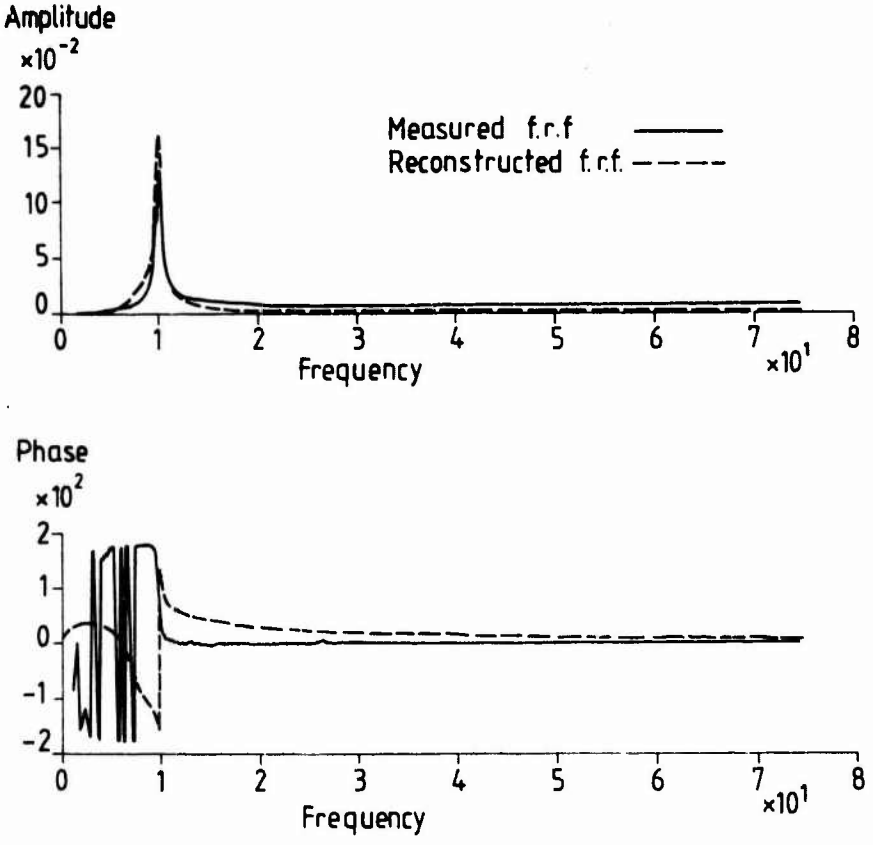

FIG.5. Displacement/ Force frequency response functions - Station 2

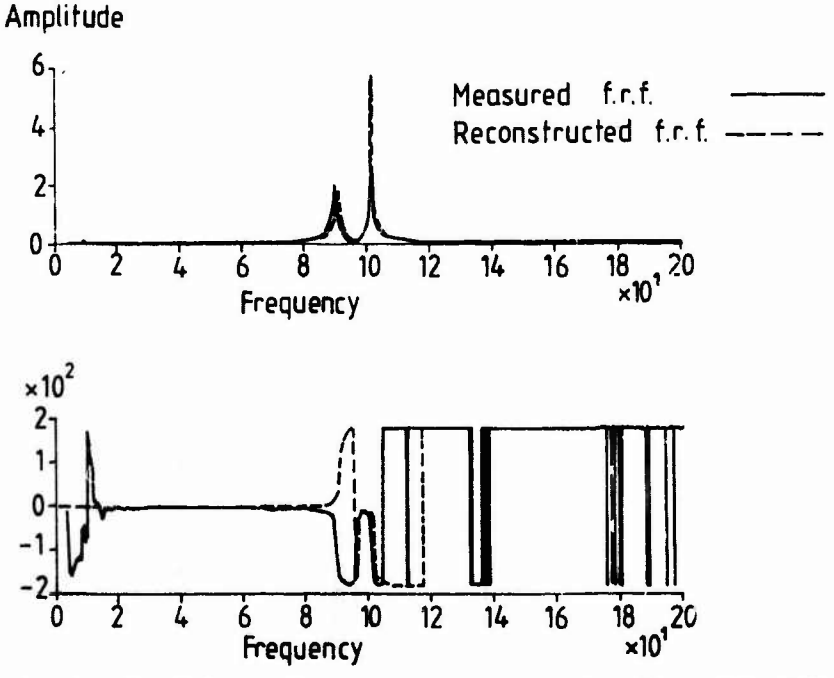

FIG. 6 Acceleration/ Force frequency response functions (4. D.O.F. model) Station 1.

IDENTIFICATION OF LINEAR/NONLINEAR RESTORING FORCE SURFACES IN SINGLE - AND MULTI-MODE SYSTEMS

K. Worden, G.R. Tomlinson

Heriot-Watt University
Department of Mechanical Engineering
James Nasmyth Building
Riccarton
Edinburgh
EH14 4AS

ABSTRACT.

An implementation of the Masri/Caughey Identification procedure is considered. Using an improved interpolation scheme the procedure is shown to accurately identify both SDOF and MDOF systems. It is demonstrated that a slightly modified version of the procedure can identify systems even if the modal matrix is estimated incorrectly.

1. INTRODUCTION.

The aim of this paper is to describe the nonparametric identification procedure devised by Masri and Caughey [1,2,3]. It is hoped that the procedure can be used to identify the types of nonlinear dynamical systems which are of interest to modal analysts.

The dynamical system

$$m\ddot{y} + f(y,\dot{y}) = x(t) \tag{1}$$

where $x(t)$ is a time dependent input force and y is the system displacement, is identified by representing the possibly nonlinear restoring force $f(y,\dot{y})$ by a surface over the phase-plane (the $(y,\dot{y})$ plane). This surface is in turn represented by a series expansion of the form

$$f(y,\dot{y}) = \sum_{i=o}^{m} \sum_{j=o}^{n} C_{ij}\, T_i(y)\, T_j(\dot{y}) \tag{2}$$

where the T_i, T_j are Chebyshev polynomials. Orthogonal polynomials are used because the coefficients are independent of the a priori model order. Chebyshev polynomials are chosen because the integrals required for the evaluation of the C_{ij} are quite straightforward. Also, Chebyshev polynomials provide almost the best polynomial approximation to a given function.

Recently, Hammond et.al. [4] have provided an alternate means of obtaining the force surfaces using ideas from optimal control theory. In addition, O'Donnell and Crawley [5] have independently developed a variant of the Masri/Caughey procedure which they have used to study nonlinear joints in space structures.

2. SDOF SYSTEMS.

One begins with equation (1). The mass m and the time histories of $y, \dot{y}, \ddot{y}$ and x are assumed known. In general it is impractical to measure $\dot{y}$ $\ddot{y}$ and y simultaneously. As numerical differentiation is notoriously difficult, one should measure the acceleration $\ddot{y}$ and integrate to find y and $\dot{y}$. In simulations and experimental studies a simple trapezium rule algorythm has proved adequate. Only simulated data is considered below. In this case data was produced by integrating equation (1) $y, \dot{y}$, and $\ddot{y}$ were obtained directly from the simulation.

Data is recorded with a constant sampling interval Δ. The kth sampling instant being $t_k = (k - 1)\,\Delta$. The sampled accelerations etc. are denoted by $\ddot{y}_k = \ddot{y}(t_k)$, $\dot{y}_k = \dot{y}(t_k)$ etc. Given the quantities $\ddot{y}$ and x at a sampling instant ti, the restoring force can be calculated using (1).

$$f_i = f(y_i, \dot{y}_i) = x_i - m\ddot{y}_i \tag{3}$$

This procedure generates a sequence of triplets $(y_i, \dot{y}_i, f_i)$ such that for each point in the phase plane corresponding to a sampling instant, one knows the height of the restoring force surface above the point.

The Chebyshev polynomials are defined by [6]

$$T_n(x) = \begin{cases} \cos\,(n\cos^{-1}x) & |x| \le 1 \\ \cosh\,(n\cosh^{-1}x) & |x| \ge 1 \end{cases} \tag{4}$$

and are orthogonal on the interval [-1, 1] as follows:

$$\int_{-1}^{+1} dx\; T_i(x)\; T_j(x)\; \omega(x) \quad = \frac{\pi}{2}\,(\delta_{nm} + \delta_{on}\delta_{om}) \tag{5}$$

where δ_{ij} is the Kronecker delta, and $\omega(x) = (1 - x^2)^{-1/2}$ is the weighting factor required for orthogonality, because evaluation of the C_{ij} in equation (2) uses the orthogonality relations. The data (y,y) is mapped into the rectangle [-1,1] x [-1,1] in the phase plane. The mapping being given by

$$\bar{y}_i = \zeta(y_i) = \frac{y_i - 1/2(y_{max} + y_{min})}{1/2\,(y_{max} - y_{min})}$$

$$\bar{\dot{y}}_i = \dot{\zeta}(\dot{y}_i) = \frac{\dot{y}_i - 1/2(\dot{y}_{max} + \dot{y}_{min})}{1/2\,(\dot{y}_{max} - \dot{y}_{min})} \tag{6}$$

In this case $\dot{\zeta}$ does not mean $d\zeta/dt$. One now requires the expansion

$$f(y,\dot{y}) = \bar{f}(\bar{y},\bar{\dot{y}}) \cong \sum_{i=o}^{m} \sum_{j=o}^{n} C^{\zeta}_{ij}\, T_i\,[\zeta(y)]\; T_j[\dot{\zeta}(\dot{y})] \tag{7}$$

and the C^{ζ} clearly depend on the sample of data chosen. The orthogonality relation (5) allows one to evaluate the coefficients as follows:

$$C^{\zeta}_{ij} = X(i)X(j) \int\int_{-1}^{+1} dxdy\ \omega(x)\omega(y)\ \bar{f}(x,y)\ Ti(x)Tj(y) \qquad (8)$$

where $X(i) = (1 + \delta_{oi})/\pi$. In the angular coordinates (θ,χ), where $\theta = \cos^{-1} x$ and $\chi = \cos^{-1} y$. The integral (8) becomes

$$C^{\zeta}_{ij} = X(i)X(j) \int\int_{o}^{\pi} d\theta d\chi\ \bar{f}(\cos\theta,\cos\chi)\ \cos\ (i\theta)\cos(j\chi)$$

If the θ-range is divided into n_θ intervals of length π/n_θ , and the χ range into n_χ intervals of length π/n_χ . The integral can be approximated by the summation

$$C^{\zeta}_{ij} = X(i)X(j) \sum_{m=1}^{n_\theta} \sum_{n=1}^{n_\chi} \Delta\theta\Delta\chi\ \bar{f}\ (\cos[(m-1)\Delta\theta], \cos\ [(n-1)\Delta\chi])$$

$$\times \quad \cos[i\Delta\theta(m-1)]\ \cos[j\Delta\chi(n-1)]$$

It is evident that the C^{ζ} can now be evaluated if some interpolation scheme can evaluate f at the points $(\cos[(m-1)\Delta\theta], \cos\ [(n-1)\Delta\chi])$.

3. THE INTERPOLATION PROCEDURE.

The software package TILE4 [7] was used to interpolate a continuous surface from the irregularly spaced data. The package, using Sibson's natural neighbour method, can produce C^0 and C^1 surfaces and is based on the construction of a Delaunay triangulation. For the sake of completeness the construction is outlined here. A more detailed discussion can be found in [8].

Consider a set of N points in the plane $\{Pi,\ i = 1,N\}$. One defines the tile Ti of a point Pi as the set of all points in the plane which have Pi as their nearest neighbour from the set $\{Pi\}$. The set of tiles covers the plane, the subdivision they provide is called a Dirichlet tessellation. If two tiles have a section of boundary in common, even if only a point, they are termed contiguous. Joining all contiguous pairs of points with a line segment provides a triangulation of the plane called the Delaunay triangulation. The construction can now be refined. One defines the subtile Tij of Ti as the subset of Ti containing those points which have Pj as their second nearest neighbour from $\{Pi\}$. These constructions are shown for the simplest non-trivial case of N = 4 in figure 1.

One now denotes the areas of Ti and Tij by Ai and Aij respectively and introduces the normalised subtile area λij, where

$$\lambda ij = Aij/Ai$$

If one now adds a point P_{N+1} with coordinates $\underline{x}$ one must refine the tesselation accordingly T_{n+1} the tile of P_{N+1} is defined. A_{N+1}, is the area of T_{N+1} and $A_{N+1,i}$ is the area of Pi subtile. If one then forms

$$\lambda i(\underline{x}) = A_{N+1,i}/A_{N+1}$$

It can be shown, that the λi's provide a barycentric coordinate system for the neighbourhood of P_{N+1}. This in turn implies that

$$f(\underline{x}) = \sum_{i} \lambda i(\underline{x})\ fi$$

is a C^0 interpolant for f over the point P_{N+1}, if fi is the value of a function over the plane at Pi. It is also possible to determine approximate gradients for f at each Pi and to use them to construct a C^1 interpolation.

This is only an effective interpolation method over an area of the plane well-covered by data, i.e. it cannot extrapolate. In general, after scaling the data will not cover the region $[-1,1] \times [-1,1]$. Figure 2 shows the distribution of 10000 points of data from a simulated Van der Pol oscillator, the data clearly does not cover the region. One circumnavigates this problem by performing another transformation of the type (6) to map a rectangle well-covered by data onto $[-1,1] \times [-1,1]$. This step requires care as too restrictive a transformation will linearise the data. In the case of the Van der Pol data, the region inside the dashed rectangle shown was singled out.

Another problem which may occur is lack of smoothness in the true force surface. It may not be differentiable as in the piecewise linear system (fig.3) or even continuous as in the system with Coulomb friction in figure 4. In this case the C^1 interpolation may be badly behaved near singularities where the gradients are ill-defined. A way of obtaining a good surface is to transplant areas of C^0 surface (the neighbourhoods of singularities) into an overall C^1 interpolation. The surface in figure 4 was produced in this way.

4. MDOF SYSTEMS.

For a Multi-degree-of-freedom system, Newton's second law (1) becomes

$$[m]\ddot{\underline{y}} + f(\underline{y},\dot{\underline{y}}) = \underline{x}(t) \qquad (9)$$

where [m] is the n x n mass matrix and underlines denote n-vectors. If the system were linear one would have

$$\underline{f} = \underline{f}_l = [c]\dot{\underline{y}} + [k]\underline{y} \qquad (10)$$

where [c] is the damping matrix and [k] is the stiffness matrix. For a general nonlinear system the restoring force will approximately take the form (10) at low excitation levels. If one estimates the modal matrix for this approximately

linear system $[\psi]_l$ and changes to 'normal' coordinates $\underline{u} = [\psi]_l^T \underline{y}$, one expects simplications as follows: if the system were linear the transformed equations would become (assuming proportional damping)

$$[m]\ddot{\underline{u}} + [c]\dot{\underline{u}} + [k]\underline{u} = [\psi]_l^T \underline{x} = \underline{q}$$

where $[m] = [\psi]_\ell^T [m] [\psi]_\ell$, $[c]$ and $[k]$ are diagonal. The system is clearly decoupled into n SDOF systems.

$$m_i\ddot{u}_i + c_i\dot{u}_i + k_iu_i = q_i$$

where m_i, c_i and k_i are the diagonal entries of $[m]$, $[c]$ and $[k]$. If the system is nonlinear this decoupling does not occur, however the underlying linear system is decoupled so one expects some simplification to follow the change to 'normal' coordinates. Equation (9) becomes

$$[m]\ddot{\underline{u}} + \underline{h}(\underline{u},\dot{\underline{u}}) = q(t) \qquad (11)$$

here $\underline{h} = [\psi]_\ell^T \underline{f}$

As before, one assumes that $[\psi]_\ell$, $[m]$, $y, \dot{y}, \ddot{y}$ and $\underline{x}$ are obtainable so that the restoring force can be calculated from

$$\underline{h} = \underline{q} - [m]\ddot{\underline{u}} = [\psi]_\ell^T (\underline{x} - [m]\ddot{\underline{y}})$$

and the i^{th} component of $\underline{h}$ is given by

$$h_i = q_i - m_i\ddot{u}_i$$

and h_i is not simply a function of u_i and $\dot{u}_i$. As a first estimate one assumes that the main dependence of h_i is on u_i and $\dot{u}_i$. One forms

$$h_i^{(1)}(u_i,\dot{u}_i) = \sum_m \sum_n C1^{(i)}_{mn} T_m(u_i) T_n(\dot{u}_i)$$

which contains all terms of the form $(u_i)^\alpha(\dot{u}_i)^\beta$. To include effects from still coupled modes one needs terms like $(u_i)^\alpha.(u_j)^\beta$ and $(u_i)^\alpha.(u_j)^\beta$ where $i \neq j$. In order to do this, one forms the first residual term

$$r_i^{(1)}(\underline{u},\dot{\underline{u}}) = h_i(\underline{u},\dot{\underline{u}}) - h_i^{(1)}(u_i, \dot{u}_i)$$

and then forms the expansion

$$h_i^{(2)}(\underline{u},\dot{\underline{u}}) = \sum_j \sum_m \sum_n C2^{(i)(j)}_{mn} T_m(u_i)\, T_n(u_j) = r_i^{(1)}(\underline{u},\dot{\underline{u}})$$

including only those modes which interact with the i^{th} mode. Displacement - velocity cross-coupling is accounted for in a similar manner. One forms

$$r_i^{(2)}(\underline{u},\dot{\underline{u}}) = r_i^{(1)}(\underline{u},\dot{\underline{u}}) - h_i^{(2)}(\underline{u},\dot{\underline{u}})$$

and

$$h_i^{(3)}(\underline{u},\dot{\underline{u}}) = \sum_j \sum_m \sum_n C3^{(i)(j)}_{mn} T_m(u_i) T_n(\dot{u}_j) \cong r_i^{(2)}(\underline{u},\dot{\underline{u}})$$

So the final restoring force model has the form

$$h_i(\underline{u},\dot{\underline{u}}) = h_i^{(1)}(u_i,\dot{u}_i) + h_i^{(2)}(\underline{u},\dot{\underline{u}}) + h_i^{(3)}(\underline{u},\dot{\underline{u}})$$

Because the procedure can account for modal coupling we can remove the proportionality restriction on the damping.

Example 1: The System

$$\begin{bmatrix}\ddot{y}_1\\ \ddot{y}_2\end{bmatrix} + 20\begin{bmatrix}\dot{y}_1\\ \dot{y}_2\end{bmatrix} + 10^4\begin{bmatrix}2 & -1\\ -1 & 2\end{bmatrix}\begin{bmatrix}y_1\\ y_2\end{bmatrix} + 5\times 10^9\begin{bmatrix}y_1^3\\ 0\end{bmatrix} = \begin{bmatrix}x\\ 0\end{bmatrix}$$

was simulated where x was a Gaussian white noise sequence of RMS = 200. The force surfaces identified are shown in figures 5 -8. To check the accuracy of the surfaces, time data predicted using the model was compared with the true data. The result is shown in figure 9. An example of a Chebyshev fit to an interpolated surface is shown in figure 10.

In general, if one carries out the procedure for a MDOF system a problem arises if the estimated modal matrix $[\psi]_\iota$ is not accurate. The procedure effectively identifies the wrong system. Consider the linear system

$$[m]\underline{\ddot{y}} + [c]\underline{\dot{y}} + [k]\underline{y} = \underline{x} \qquad (12)$$

The Masri/Caughey procedure actually identifies the system

$$[\psi]_\iota^T[m][\psi]_\iota[\psi]_\iota^T\underline{\ddot{y}} + [\psi]_\iota^T[c][\psi]_\iota[\psi]_\iota^T\underline{\dot{y}} + [\psi]_\iota^T[k][\psi]_\iota[\psi]_\iota^T\underline{y} = [\psi]_\iota^T\underline{x} \qquad (13)$$

Usually, if $[\psi]_\iota$ is incorrectly estimated it will not be orthogonal, i.e. $[\psi]_\iota[\psi]_\iota^T \neq 1$ in which case system (13) is not physically equivalent to system (12) i.e. they are not related by a change of coordinates. The remedy is simple. If $[\psi]_\iota^{-1}$ is used throughout instead of $[\psi]_\iota^T$ the two systems are equivalent, the change of coordinates being simply $[\psi]_\iota^{-1}.\ y = \underline{u}$. There is nothing to be lost by adopting this modification as $[\psi]_\iota^{-1} = [\psi]_\iota^T$, if the estimate is accurate and the equations decouple as required. The results of modifying the procedure are shown below.

Example 2: The system

$$\begin{bmatrix}\ddot{y}_1\\ \ddot{y}_2\end{bmatrix} + 20\begin{bmatrix}\dot{y}_1\\ \dot{y}_2\end{bmatrix} + 10^4\begin{bmatrix}2 & -1\\ -1 & 2\end{bmatrix}\begin{bmatrix}y_1\\ y_2\end{bmatrix} = \begin{bmatrix}x\\ 0\end{bmatrix}$$

was simulated with x as before. The true modal matrix for the system is $[\psi]_\iota = \begin{bmatrix}1 & 1\\ 1 & 1\end{bmatrix}$, using the incorrect $[\psi]_\iota = \begin{bmatrix}1 & 1\\ 0.5 & -0.5\end{bmatrix}$, the system was identified, first using the $[\psi]_\iota^T$ version and then using the $[\psi]_\iota^{-1}$ version. The results are shown in figures 11 and 12. The modified procedure gave significantly better results. The mean-square-error between the estimated and true time data is normalised so that using the mean level of the data as a model results in a mse of 100.

Some of the force surfaces obtained appear very noisy. There is a simple explanation. Consider the linear system in example 2 with the estimated modal matrix

$$[\psi]_l = \begin{bmatrix} 1 & 1 \\ 0.5 & -1 \end{bmatrix}$$

In normal coordinates, $\underline{u} = [\psi]_l^T \underline{y}$ the equations of motion become

$$\ddot{u}_1 + 20\dot{u}_1 + 12.6\,\dot{u}_2 + 13416u_1 + 37800u_2 = q.$$

$$\ddot{u}_2 + 12.6\dot{u}_1 + 20\,\dot{u}_2 + 37800u_1 + 30000u_2 = 0$$

the restoring forces being

$$h_1 = 20\dot{u}_1 + 12\,6\dot{u}_2 + 13416u_1 + 37800u_2 \qquad (14)$$

$$h_2 = 12.6\dot{u}_1 + 20\dot{u}_2 + 37800u_1 + 30000u_2$$

If the surface $h_1\ (u_1\ ,\ \dot{u}_1\ )$ is formed, because all information about time is discarded when the data is assembled in the phase plane the most one can say about the variables u_1 and $\dot{u}_1$ at a particular point is that they have probability distributions. $P(x,y)$ is the joint probability density function of two variables x an y and $P_x\ (y)$ is the p.d.f for the variable y with x constant. It is clear from (14) that the value of the restoring force h_1 above the point $(u_1\ ,\ \dot{u}_1)$ will be

$$h_1(u_1\ ,\dot{u}_1\ ) = 20\dot{u}_1 + 12.6\ X_1 + 13416u_1 + 37800X_2$$

where X_1 is a random variable with p.d.f $Pu_1(\dot{u}_2\ )$ and X_2 is also a random variable with p.d.f. $Pu_1(u_2)$. This means that the interpolation procedure sees the deterministic $u_1\ ,\ \dot{u}_1$ dependent part of h_1 with a random $u_2\ ,\ \dot{u}_2$ dependent part superimposed. One can see this effect clearly in figures 5 and 7. If the surface is then modelled by a $h_1\ (u_2\ ,\ \dot{u}_2)$ expansion as above, the residual surface formed.

$$R_1^{(1)}(u_2,\ \dot{u}_2\ ) = 12.6\dot{u}_2 + 37800u_2$$

will be much smoother, as in figures 6 and 8.

Because of this effect, one no longer has the option of forming C^1 interpolations. This unpredictability in the restoring force data means tht one could have two data points arbitrarily close in the phase plane with different force values above them. this would make the estimated gradients excessively large and the interpolated surface would have large spikes in it. This effect has been observed. In this paper C^0 interpolations were used for the MDOF system and C^1 interpoiations for the SDOF systems.

Conclusion

The results presented here indicate that a practical implementation of the Masri/Caughey procedure is possible. Merits are (i) an easily interpreted picture of the nonlinearity is produced (ii) computer storage and timing requirements are modest, and (iii) there is no restriction on the type of excitation which can be used as long as it excites the nonlinearities. Possible disadvantages are (i) an estimate on [m] is required, the procedure does not seem sensitive to the [ψ] estimate. (ii). It is not clear how to deal with systems with memory, for this reason hysteretic systems are excluded from this study. The procedure can not be considered as a replacement for other identification methods i.e. the Hilbert transform, NARMAX modelling and the Volterra/Wiener series as it produces different information. It should rather be regarded as a useful adjunct.

Acknowledgments to Dr S Billings, Prof. J.C. Eilbeck, S.J. Gifford and particularly N.J. Barton for a number of useful discussions and also to S.J. Gifford for providing most of the Graphics routines used. This work has been carried out under SERC Grant no GR/D75809. In collaboration with Dr S. Billings of Sheffield University, England.

REFERENCES

1) S. Masri & T. Caughey. "A non-parametric Identification Technique for nonlinear dynamic problems." J.Appl. Mech. 46 p 433 (79).

2) S. Masri, M.Sassi & T. Caughey. "Non-parametric Identification of nonlinear systems". UCLA preprint.

3) K. Worden, Nonlinear Vibrations Short Course notes. Heriot-Watt. Dept. Mech. Eng September (1987).

4) J.K. Hammond, M.R. Lo, J. Seager Smith, "Identification of Nonlinearities in vibrating systems using optimal control techniques". Proc. IMAC./1987.

5) K.J. O'Connell & E.F. Crawley "Identification of nonlinear system parameters or space structure joints using the force state mapping technique". MIT space systems lab. preprint SSL # 16-85.

6) L. Fox & I. Parker "Chebyshev Polynomials in numerical analysis" O.U.P (1968)

7) Tile 4 Interpolation Package - R. Sibson. University of Bath + Manual.

8) R.Sibson. "A Brief description of Natural Neighbour Interpolation". In "Interpreting Multivariate data." ed. V. Barnett. John Wiley and sons. (1981).

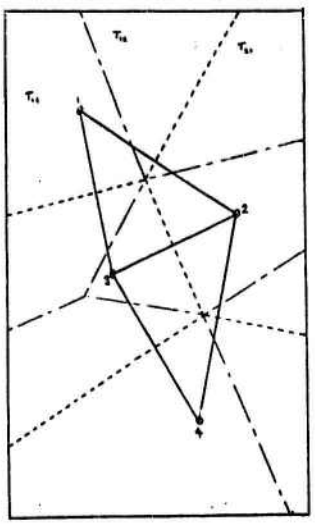

Fig 1. Tessellation and Triangulation for four points

----- Tile boundery

- — - Subtile boundery

——— Triangulation

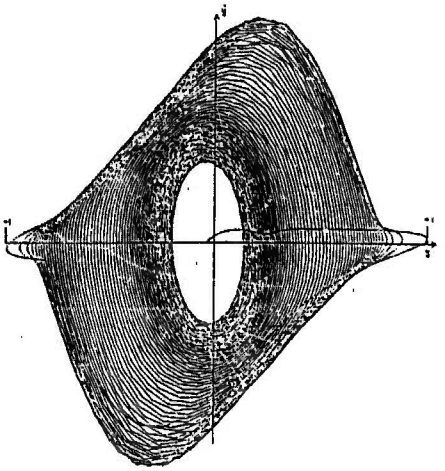

Fig 2. 10000 points of Van dar Pol date

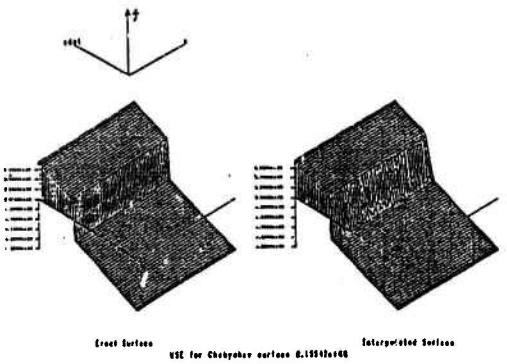

Fig 3. Coulomb friction Surface

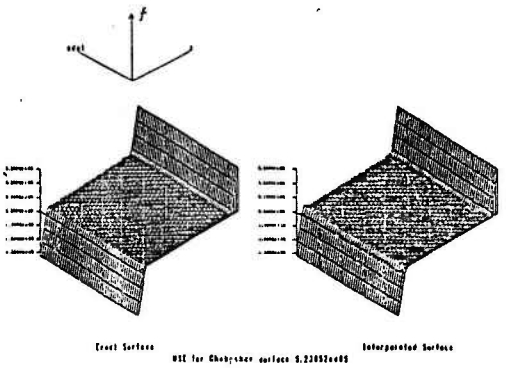

Fig 4. Piecewise linear surface

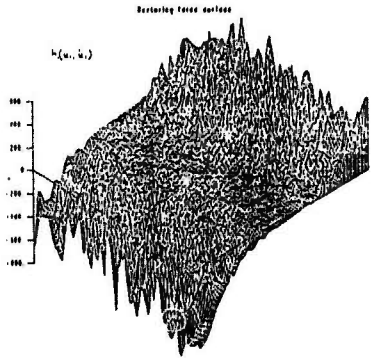

Fig 5. Force surface 2DOF System in exemple 1 dof 1 first expension $h^{(1)}$

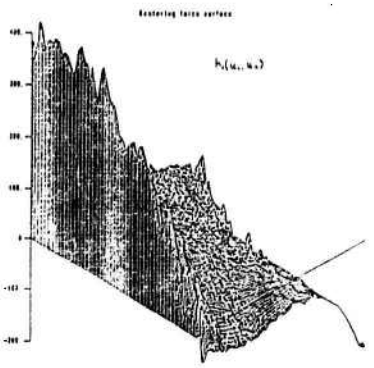

Fig 6. Dof 1 second expansion $h^{(1)(2)}$

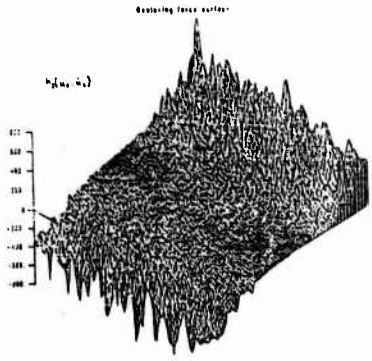

Fig 7. Dof 2 first expansion $h^{(2)}$

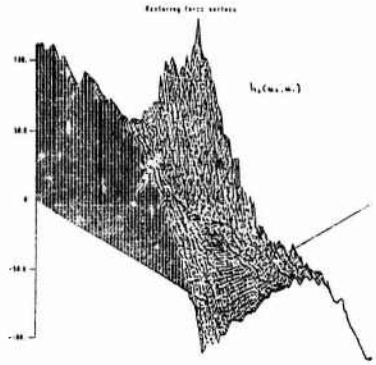

Fig 8. Dof 2 second expansion $h^{(2)(1)}$

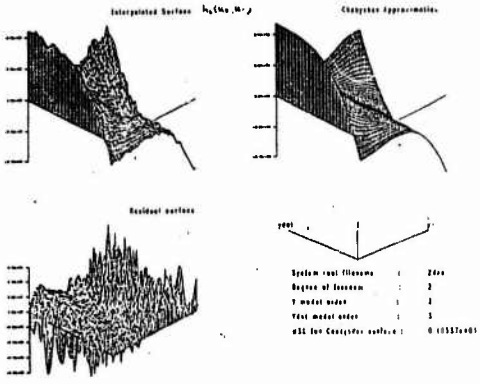

Fig 9 Chebyshev surface corresponding to $h^{(2)(1)}$

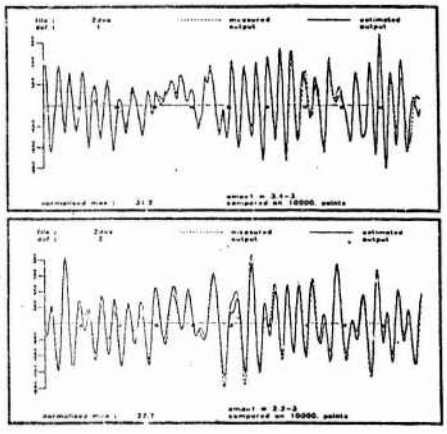

Fig 10 Comparison of predicted time data for system (1) with actual data

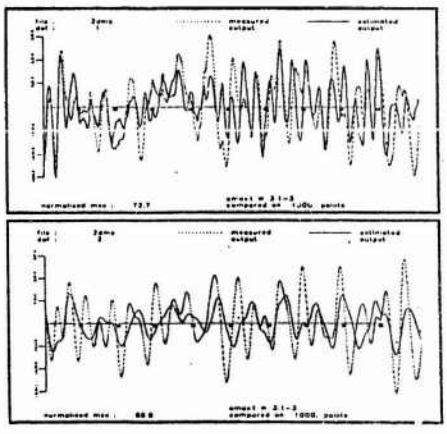

Fig 11 Comparison of time data for system (2) - Identification using $[\psi]^T$

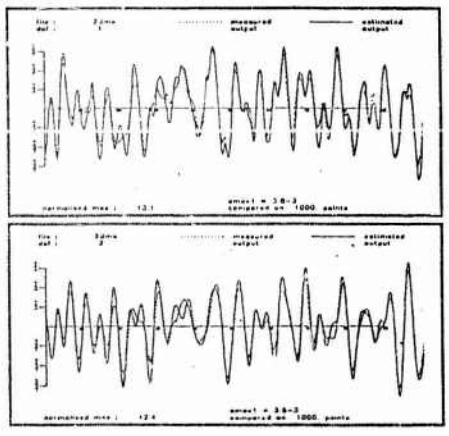

Fig 12 Comparison of time data for system (2) - Identification using $[\psi]^{-1}$

ON IDENTIFICATION OF LINEAR AND NONLINEAR STRUCTURAL SYSTEMS

F. Benedettini, D. Capecchi, F. Vestroni

Dipartimento di Ingegneria delle Strutture, delle Acque e del Terreno
Università dell'Aquila, 67040 Monteluco di Roio (AQ), Italy

1. INTRODUCTION

System Identification has received considerable attention in the field of structural engineering over the last decade. This is due to the increased interest in building mathematical models able to predict correctly the response of structures to various external loadings, mainly those of a time-dependent nature. Many are the aims of structural identification and as a consequence many techniques and models have been employed to meet the particular case.

When the behaviour of the structure can be assumed to be linear, system identification comes down to a question of parametric estimation in which more or less a-priori information is used in the analytical model. For many mechanical and civil structures the measured data are incomplete, however a meaningful mathematical model exists, so it is possible to apply parameter adjustment techniques selecting parameters in such a way as to reduce differences between measured and calculated quantities. In the work presented here a Bayesian identification approach is followed; nonlinear estimators are obtained also for linear elasto-mechanical systems because the relationships between response quantities - like modal quantities - and structural parameters are nonlinear. To provide an analytical approximation of this relationship, two different techniques are adopted, one based on an interpolation method and the other on an asymptotic expansion. The techniques are particularly useful in the numerical procedures involved in the identification problem. Their validity and aspects concerning identifiability and proper selection of parameters and observed values are discussed through the solution of the identification of stiffness characteristics of a finite element model of spatial frame structure using pseudo-experimental data.

Where the nonlinear response of structures is concerned, the mathematical models of the system are not so well established and structured compared with the elastic case. Nonparametric identification methods thus become attractive, since they are flexible and furnish a functional representation of the system. A nonparametric model described by polynomials is used for identification of the response of an elasto-plastic and a hysteretic degrading one-dimensional system.

2. IDENTIFICATION OF LINEAR STRUCTURES

2.1. Bayesian estimation approach

Available measured data of the response of structural systems under known loadings are often very limited since the response in all the principal degrees-of-freedom cannot be recorded. It is then convenient to adopt a physical interpretative model, such as a finite element model, in a system identification procedure which allows use to be made of all a priori information on system behaviour derived from the theory of structures and the knowledge of the constitutive mechanical relationships [1 - 4]. Uncertainties regarding some assumptions in system modeling are limited solely to the values of a certain number of physical parameters, which are determined in such a way as to minimize the difference between measured and predicted response quantities according to a selected criterium.

Let $h(x)$ be the function which relates the vector x of parameters with the observed response $\bar{z}$. The following relation between $\bar{z}$ and x is assumed:

$$\bar{z} = h(x) + n \qquad (1)$$

where n is stochastic vector noise, independent of x. Errors are present both in the mathematical model and in the experimental data; so there is little sense in forcing the model to match the data. It is more correct in this context to follow a Bayesian approach according to which the best estimate $\hat{x}$ of parameters x is that which maximizes the probability of occurrence of x given measured quantities $\bar{z}$. The value of $\hat{x}$, assuming normal distribution for x and n, is furnished [3] by the minimum of the function:

$$l(x) = [\bar{z}-h(x)]^T \Sigma_n^{-1} [\bar{z}-h(x)] + (x-x_0)^T \Sigma_x^{-1} (x-x_0) \qquad (2)$$

which plays the role of the objective function in the problem. It is made up of two terms, the first takes into account the difference between measured $\bar{z}$ and predicted h(x) quantities, the second the distance of x from the initial estimated values of parameters x_0, weighted by the inverse of the covariance matrices of the noise Σ^{-1}_n and of the parameters Σ^{-1}_x. Since the response quantities depend nonlinearly on the parameters, the minimization of l(x) is sought by a numerical iterative procedure. For large structures this is not a simple task, because at every iteration step the direct problem has to be solved.

2.2. Parameters and observed quantities

The behaviour of a physical - finite element - model depends on a large number of parameters and furnishes a detailed description of the response by means of many quantities. In principle the algorithm h(.) in eq. (1) establishes a relationship between all the p observable quantities and all the q governing parameters; actually only $m < p$ components of $\bar{z}$ are observed in the real structure and only $n < q$ parameters x of the model are considered. The need is felt for an optimal selection criterium of a limited number of z and x components The choice has to be made with the aim of obtaining a correct parameter estimation and a good fit for measured data, as the two requirements are not equivalent. Indeed fitting capability of the model always improves with an increase in the ratio n/m, while the parameter estimation can deteriorate; consequently the forecasting property of the model may become unsatisfactory. As far as fitting is concerned, little can be done before the experimental values are known, so this aspect can offer no contribution to the selection problem. It is, however, possible to achieve a-priori accuracy of parameter estimation by adopting a statistical identification approach. Parameter covariance can be evaluated on the basis of statistical properties of the measured quantities [5, 6]. As the number of measurements is often fixed for practical reasons, the problem is that of choosing those parameters with the most satisfactory covariance and those observable quantities which furnish minimum covariance for the set of selected parameters.

In the Bayesian approach, assuming normal distribution for the experimental and analytical errors, the covariance matrix of the parameters is approximately given [5] by:

$$\Sigma_{(m)} = (H^T_{(m)} \Sigma^{-1}_{n(m)} H_{(m)} + \Sigma_x^{-1})^{-1} \qquad (3)$$

where $H = \left.\frac{\partial h}{\partial x}\right|_{x = x_0}$

is the sensitivity matrix of the problem and the sub-index (m) specifies that the quantity refers to a set of m measures among p candidates.

When the variance of the i-th parameter, represented by the diagonal element σ_{ii} of $\Sigma_{(m)}$, is too high for various sets of m measures, this parameter is eliminated from the model. After having chosen the parameters, the set of m quantities to be observed can be selected in such a way that a suitable norm of $\Sigma_{(m)}$ is minimized; the trace is assumed as a norm:

$$\| \Sigma_{(m)} \| = \frac{1}{\mathrm{tr}\,[\Sigma^{-1}_{(m)}]} \qquad (4)$$

The point made earlier still remains valid if a deterministic context is involved. In this case Σ_n is only a weighting matrix, Σ_x vanishes and Σ is simply the Hessian matrix of l(x). In any case, the selection based on the minimization of the $\|\Sigma_{(m)}\|$ results in better conditioning

of the numerical identification algorithm.

2.3. Approximate models

To reduce the amount of computational effort, two different techniques have been developed to obtain an approximate relationship of $h(x)$ in the neighbourhood of the reference solution corresponding to the base value x^0 of the parameters. In both techniques reference is made to a finite element model of the structure and to natural frequencies and modal shapes as observed quantities.

2.3.1 Asymptotic approximation

The first technique which gives an analytical approximation of $h(x)$ is an asymptotic expansion of response quantities in terms of the characteristics parameters which makes use of local properties of the reference solution $h(x^0)$ and of a perturbational procedure to determine the coefficients of the series up to the second order [7]. Attention is focused on the relationship between tne eigenvalues and eigenvectors of the free oscillations of the structure, λ_i and u_i respectively, and the parameters x.

Let the mass matrix be considered costant and the stiffness matrix be a regular function of x:

$$K = K_0 + \Sigma_h K_h \varepsilon_h + \Sigma_h \Sigma_l K_{hl} \varepsilon_h \varepsilon_l + 0(\varepsilon^3) \tag{5}$$

where ε_h is the variation of the h-th component of x and matrices K_h, K_{hl} are directly defined by eq. (5). Under these assumptions the response $h(x)$ (which stands for λ or u) is also a regular function of x:

$$h(x) = h(x^0) + \Sigma_h h_h \varepsilon_h + \Sigma_h \Sigma_l h_{hl} \varepsilon_h \varepsilon_l + 0(\varepsilon^3) \tag{6}$$

where the unknowns coefficients h_h and h_{hl} are to be determined. By introducing the previous expansion in the equations of the eigenvalue problem and by equating the coefficients of the same monomials ε_h, ε_{hl} a series of successive linear equations is obtained at different orders:

$$\begin{aligned}
\varepsilon^0 \quad & (K_0 - \lambda_0 M)\, u_0 = 0 \\
& u_0^T M\, u_0 = 1 \\
\varepsilon^1 \quad & (K_0 - \lambda_0 M)\, u_h = -(K_h - \lambda_h M)\, u_0 \\
& u_0^T M\, u_h = 0 \\
\varepsilon^2 \quad & (K_0 - \lambda_0 M)\, u_{hl} = -(K_h - \lambda_h M)\, u_l - (K_l - \lambda_l M)\, u_h - (K_{hl} - \lambda_{hl} M)\, u_o \\
& u_0^T M\, u_{hl} = 0
\end{aligned} \tag{7}$$

Since the left hand side operator is singular, the compatibility conditions at each order furnish the coefficients of the eigenvalues expansions:

$$\begin{aligned}
\lambda_h &= u_0^T K_h\, u_0 \\
\lambda_{hl} &= u_o^T K_h\, u_l + u_o^T K_l\, u_h + u_o^T K_{hl}\, u_o
\end{aligned} \tag{8}$$

The solution of the system (7) thus determines u_h and u_{hl}.

An example has been developed to show the accuracy of the proposed technique; a symmetrical three span, ten-storey plane frame is considered (fig. 1-a) for which the stiffness (EI) of the first and second interstorey cclumns and the first storey beams are considered as three variable parameters, x_1, x_2 and x_3 respectively. Exact and approximate results for the first three modes are compared for percentage variations of parameters along trisetting lines of parameter space x_1 x_2 x_3. The results obtained for 24 sets of parameters (± 40%, ± 60% and ±

Table 1. Approximation errors (%) in modal values for different directions of parameter variations.

Δx %	Modal Value	Direction 1	2	3	4	5	6	7	8	Mean
40	λ_1	0.55	0.22	0.01	0.28	0.25	0.68	0.71	1 26	0.50
60		1.58	0.49	0.80	1.79	1.85	3.56	3.91	6.62	2.58
40	u_1	0.30	0.55	0.10	0.16	0.21	0.36	0.39	0.62	0.28
60		0.91	0.29	0.56	0.90	1.22	1.72	1.91	2.78	1.29
40	λ_2	0.47	0.25	0.10	0.19	0.48	0.52	0.77	0.94	0.47
60		1.41	0.59	1.22	1.42	2.90	2.61	3.87	4.18	2.28
40	u_2	0.49	0.26	0.30	0.29	0.63	0.57	0.71	0.86	0.51
60		1.49	0.66	1.50	1.42	3.23	2.59	3.29	3.60	2.22
40	λ_3	0.18	0.19	0.21	0.08	0.57	0.07	0.46	0.25	0.25
60		0.58	0.50	1.25	0.11	2.88	0.46	2.08	0.93	1.10
40	u_3	0.50	0.35	0.48	0.40	1.01	0.62	0.85	0.76	0.62
60		1.54	1.00	2.21	1.49	4.74	2.59	3.77	2.95	2.54

80% parameter variation on the 4 trisetting lines) are very encouraging; some of the reaults are reported in Table 1 in the form of approximation errors defined by:

$$e_\lambda = \frac{|\bar{\lambda} - \lambda|}{\bar{\lambda}} \qquad e_u = \frac{\|\bar{u} - u\|}{\|\bar{u}\|}$$

for eigenvalues and eigenvectors rispectively, where $\bar{\lambda}$, $\bar{u}$ are the true values and λ, u the approximate ones, while $\|\ .\ \|$ means euclidean norm. For modifications of parameters up to 60% a response variation of the order of 10 + 15% is obtained compared with the basic solution, the maximum error between exact and approximate solution being 3%. For higher modifications the errors grow, as is evident from fig. 1-b.

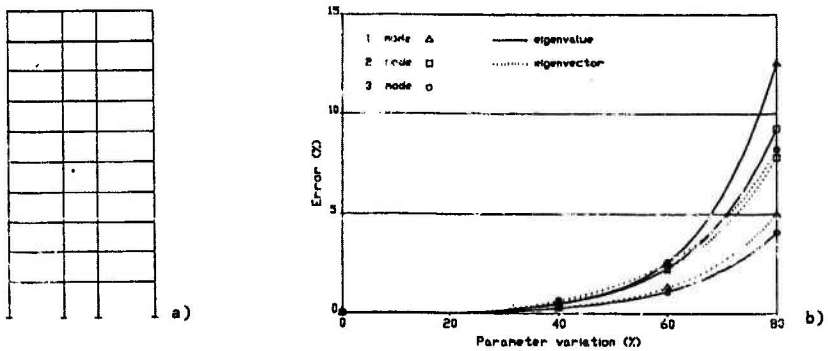

Fig. 1 - Plane frame considered (a) and errors in eigenvalues and eigenvectors (b).

2.3.2. Quadratic polynomial interpolation

In this second technique each component $h_i(x)$ of the modal responae is approximated by the interpolation formula:

$$\tilde{h}_i(x) = h_i(x^0) + \sum_1^n{}_k\ a_{ik}\ (x_k - x_k^0) + b_{ik}\ (x_k - x_k^0)^2 \qquad i = 1,\ 2,\ \ldots\ m \tag{9}$$

where n is the number of parameters and m that of observed measures [9, 10]. The coefficients a_{ik}, b_{ik} are determined by imposing passage through three points, namely the solutions furnished

by the model for three sets of parameters - the base x^0, upper x^u and lower x^l values - therefore (2n + 1) modal analyses have to be solved. As there are no mixed terms in the interpolation formula (9), by a suitable choice of x^u and x^l, a block-diagonal system of equations is obtained and each couple of values of the unknown coefficients a_{ik}, b_{ik} can be determined separately from the others [10].

The capability of the technique to provide a satisfactory representation of the relationship between response quantities and parameters in the neighbourhood of the base solution may be illustrated by means of an example concerning the modal response of a four-storey spatial frame described by a finite element model, the plan of which is shown in fig. 2. Some simplifying modelling assumptions have been made, e.g. the horizontal diaphrams are considered infinitely rigid in-plane, the soil-structure interaction is taken into account through a rigid mat and lumped springs, while the stiffness of infilling walls is represented by truss elements.

Ten parameters are considered in this application: the soil shear modulus x_1, the nominal radius x_2 of the foundation, the storey stiffness x_3, x_5, x_7, x_9 of exterior walls and the storey stiffness x_4, x_6, x_8, x_{10} of the lift core. All parameters are dimensionless since they are normalized to their base value. The approximated model has been determined by adopting as the upper and lower values 1.5 and 0.5 times the base value, with the exception of x^u_2, x^l_2 for which 1.2 and 0.8 have been considered. The shape of the first ten modes, for the base parameter configuration, is shown in fig. 3.

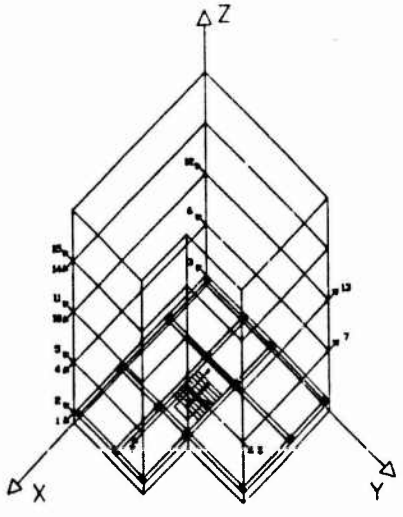

Fig. 2 - Geometry of F.E. model and definition of observed values.

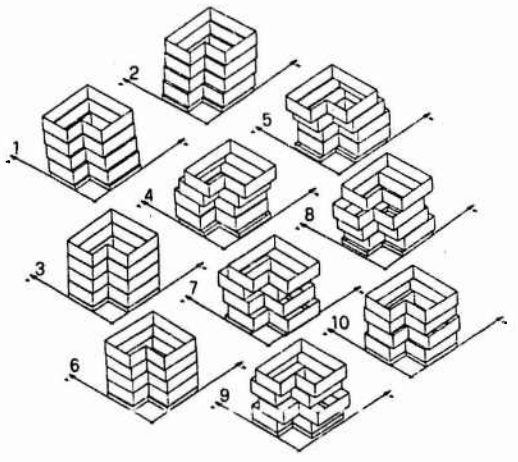

Fig. 3 - First ten mode shapes for parameter base values.

The errors in frequencies calculated with approximated model are reported in Table 2 for different cases obtained by varying ten parameters one at a time and finally all together; for the last case the euclidean norm of the error in a reduced set of eigenvector components is reported as well. The value of each varied parameter is collected in the vector:

$$x_s^T = \{0.80,\ 1.12,\ 0.80,\ 1.15,\ 0.75,\ 1.20,\ 1.15,\ 1.20,\ 0.75,\ 0.80\}$$

In the range of parameters considered the maximum error for the frequencies is found to be in the order of 1% and for the first six eigenvectors in the order of 3%. Higher modes exhibit more complex dependence on the parameters and greater differences arise between exact and approximated results.

Table 2. Approximation errors (%) in modal values.

Varied Param.	Mode 1	2	3	4	5	6	7	8	9	10
x_1	0.34	0.40	0.25	0.38	0.41	0.71	0.84	0.84	0.05	0.06
x_2	0.09	0.10	0.09	0.02	0.19	0.31	0.04	0.08	0.05	0.06
x_3	0.01	0.01	0.01	0.00	0.10	0.00	0.00	0.00	0.00	0.01
x_4	0.00	0.00	0.00	0.00	0.07	0.00	0.00	0.00	0.00	0.01
x_5	0.01	0.01	0.02	0.00	0.16	0.00	0.00	0.00	0.02	0.02
x_6	0.00	0.00	0.00	0.00	0.16	0.00	0.00	0.00	0.00	0.01
x_7	0.00	0.00	0.02	0.00	0.17	0.01	0.00	0.00	0.00	0.01
x_8	0.00	0.00	0.00	0.00	0.17	0.00	0.00	0.00	0.00	0.01
x_9	0.24	0.00	0.01	0.01	0.15	0.07	0.00	0.00	0.03	0.06
x_{10}	0.00	0.00	0.00	0.00	0.16	0.00	0.00	0.00	0.00	0.01
x_1+x_{10}	0.50	0.71	0.43	0.52	0.61	1.03	1.12	1.40	0.51	1.80
	0.40	0.53	0.72	1.70	2.10	3.25	6.51	7.10	22.70	19.23

2.4. Structural identification

The structure illustrated in fig. 2 and previously described is referred to in the solution of a problem of structural identification. Within this ambit the 'exact' finite element model is not used but the relationship between response quantities and structural parameters has been represented by an approximate model as per the Par. 2.3.2. technique. The aim of this study is to examine some aspects of identifiability conditions and the trend of errors in the estimation of parameters and in the prediction capability as a consequence of adopting the estimation of parameters and in the prediction capability as a consequence of adopting the simplified model and also of the numerical errors in the minimization algorithm.

The ten parameter introduced in Par. 2.3.2. are here referred to. As the choice of observed measures concerns, 15 degrees of freedom are selected between 70 candidates, following the minimum parameter convariance matrix criterium. Their position and direction are indicated by arrows in fig. 2. The first 10 frequencies and the selected components of the corresponding eigenvectors obtained by means of the finite element model for a given values of parameters:

$$x_s^T = (0.80,\ 1.12,\ 0.80,\ 1.15,\ 0.75,\ 1.20,\ 1.15,\ 1.20,\ 0.75,\ 0.80)$$

are assumed as pseudo-experimental data. The analysis is performed in a deterministic context according to which Σ^{-1}_x disappears from the objective function given by eq. (2) and Σ^{-1}_n has a diagonal form and is only a weighting matrix. Its coefficients are chosen in such a way that all observed values are uniformly scaled. Because of the fact that the expression of $l(x)$ is polinomial in x, its minimum can be efficiently found using a gradient algorithm type. Given the quite regular shape of $l(x)$, the Newmark method has been chosen owing its good convergence rate.

The experimental information used for identification purpose varies from the total set of observed modal quantities (10 frequencies and 150 eigenvector components) up to 2 frequencies. Moreover three cases of different sets of parameters are considered, ten ($x_1 + x_{10}$), six (x_1, x_3, x_5, x_7, x_9, x_{10}) and two (x_1, x_2) parameters are assumed. Identification results are checked for accuracy by means of the indices:

$$e_x = \frac{\| \hat{x} - x_s \|}{\| x_s \|} \qquad e_z = \sqrt{\frac{l(\hat{x})}{m}}$$

where x is the estimated parameter vector and m is the number of measurements considered. Table 3 gives e_x and e_z values for the various cases taken into account, where the observed values are indicated in the form of the number of frequencies plus the number of eigenvectors. As can be seen, when only the frequencies are used as observed values and their number equals that

of the parameters, identification results in a badly conditioned problem as is evidenced by the condition number κ, i.e. the ratio of the maximum and minimum eigenvalues of the Hessian matrix, in the order of 10^7, so the problem becomes very sensitive to numerical errors. The two parameter case provides the best estimate, for which κ is lower and equal to 10^3.

Tab. 3. Identification errors (%) in parameters and in observed values.

Observed values	Ten parameters		Six parameters		Two parameters	
	e_x	e_z	e_x	e_z	e_x	e_z
2 + 0	–	–	–	–	13.7	0.0
6 + 0	–	–	100.	0.0	7.6	0.1
10 + 0	200.	0.0	14.1	0.1	4.9	0.2
10 + 1	6.3	0.1	6.5	0.1	4.8	0.2
10 + 5	3.2	0.2	4.4	0.1	6.0	0.2
10 + 10	30.3	2.7	17.6	2.7	12.8	4.3

When more measurements than parameters are considered the errors e_x and e_z remain within satisfactory bounds, except for the 10 eigenvector case, where the bad results are due principally to the reduced approximation capacity of the model for higher modes already outlined and evidenced in Table 2.

3. IDENTIFICATION OF NONLINEAR STRUCTURES

3.1. Parametric and nonparametric models

Identification of non linear response of structures is a more complex process than that involved in the linear case. On the one hand the solution of dynamic problems, usually made in the time domain context, is a very lengthy task, on the other hand the description of the dynamic behaviour is more difficult and calls for the study of very complex models.

When a good knowledge of the structure is available, use can be made of parametric models whose behaviour is defined by a limited number of parameters and rules. Where complex systems are concerned, for which there is insufficient information on geometry and materials and a detailed description cannot be made, the use of parametric models may not be realistic; in such cases nonparametric models become attractive [11-13]. These models consider the structure like a black-box and are extremely flexible, thus making a good fit of the structural response feasible whatever shape it assumes.

The nonparametric models considered in this paper are particularly suitable for the analysis of nonlinear elastic behaviour, however they can be used for hysteretic models too, though with a lower degree of accuracy. In the following discussion the nonparametric approach is used in the study of a single degree of freedom system with two different hysteretic force-displacement laws.

3.2. Choice criterium

The response z of the s.d.o.f. structural observed system, under excitation q, satisfies the equation:

$$m\ddot{z} + \bar{f} = \bar{q} \tag{10}$$

where m is the mass and f the restoring force. Assuming m to be known, and $\ddot{z}$, $\bar{q}$ to be measured, $\bar{f}$ is consequently obtained.

If z is the response of the assumed analytical model, characterized by a restoring force f, to obtained an approximation of $\bar{f}$, the following two functional expressions of f to be minimized can be considered:

$$1(f) = \int_0^T [z(t) - \bar{z}(t)]^2 \, dt \tag{11-a}$$

$$1'(f) = \int_0^T [m \ddot{\bar{z}}(t) + f(t) - \bar{q}(t)]^2 \, dt = \int_0^T [f(t) - \bar{f}(t)]^2 \, dt \tag{11-b}$$

Expression (11-a) is related to the response errora and expression (11-b) to equation errors which are equal to restoring force errors. It should be observed that f(t) values are obtained by examination of $\bar{z}(t)$, $\dot{\bar{z}}(t)$, while $\bar{f}(t)$ is given by $\bar{q}(t) - m \ddot{\bar{z}}(t)$.

The first functional expression permita a lesa biaaed estimate of f and does not require knowledge of $\dot{\bar{z}}(t)$ and $\ddot{\bar{z}}(t)$; however, it does need aolution of differential equation (10) for each assumed model f of $\bar{f}$. The second expression needs all the quantities $\bar{z}(t)$, $\dot{\bar{z}}(t)$, $\ddot{\bar{z}}(t)$ but only requires the computation of f(t) each time. Following a parametric approach, the two functional expreasions become ordinary objective functions 1(.) of the parameter vector λ the minimum for which can usually be obtained by direct aearch techniquea. In the nonparametric case, the preceeding aituation is again obtained when f is expressed in an approximate parametric form; otherwise a general function approximation technique has to be used.

3.3. Polynomial nonparametric models

The function $\bar{f}(t) = \bar{q}(t) - m \ddot{\bar{z}}(t)$ is seen aa a function $f(\bar{z}, \dot{\bar{z}})$ of the two atate variables $\bar{z}$, $\dot{\bar{z}}$, assuming for each f(t) value the corresponding $\bar{z}(t)$, $\dot{\bar{z}}(t)$ couple. Actually, where hysteretic oscillators are concerned, f(z, ż) is not a unique value function; the asaumption made when a nonparametric model is adopted is that this fact is not so relevant and that an ordinary function f(z, ż) exists such that the surface defined by f, in the space f, z, ż, contains the curve $\bar{f}(t)$. $\bar{z}(t)$, $\dot{\bar{z}}(t)$ with a good degree of approximation. The choice criterium (11-b) can then be written as:

$$1(f) = \sum_1^N{}_k \, [f(\bar{z}_k, \dot{\bar{z}}_k) - \bar{f}(\bar{z}_k, \dot{\bar{z}}_k)]^2 \tag{11-c}$$

where the summation over N time steps t_k substitutes the integral and $\bar{z}_k$, $\dot{\bar{z}}_k$ means $\bar{z}(t_k)$, $\dot{\bar{z}}(t_k)$.

Assuming regularity of f, the following series expansion can be considered:

$$f(z, \dot{z}) = \sum_0^{\infty}{}_j \sum_0^{\infty}{}_i \, a_{ij} \, g_i(z) \, h_j(\dot{z}) \tag{12}$$

provided that $g_i(z)$ $h_j(z)$ possesaes the necessary completness requirements. Such requirements are satisfied when monomial z^i, $\dot{z}^j$ or order i, j Chebyshev polynomials are considered for g_i, h_j functiona. By considering the coefficient a_{ij} up to order n an approximate parametric expresaion is obtained for f. The a_{ij} values can be calculated by aubstituting the expression for f in (11-c), which leads to the following objective function:

$$1(a_{ij}) = \sum_1^N{}_k \, [\bar{f}(\bar{z}_k, \dot{\bar{z}}_k) - \sum_0^n{}_i \sum_0^n{}_j \, a_{ij} \, g_i(\bar{z}_k) \, h_j(\dot{\bar{z}}_k)]^2 \tag{13}$$

An ordinary least squarea method is used for the minimization of $1(a_{ij})$; this requires the aolution of a linear system of (n+1)x(n+1) equations. When Chebyshev polynomials are considered, owing to the fact that they are orthogonal, a direct expreasion for each a_{ij} coefficient is possible, without requiring any explicit parametrization. This approach haa been followed in ref. [11].

3.4. Identification example

The fitting capacity of nonparametric models has been teated aasuming two different hysteretic modela. In the first case, concerning an elastoplaatic oscillator, the non parametric

model in question is obtained using mononials like z^1 z^2 up to an order of n = 3. Sinusoidal external force in the form $q = q_0 e^{-dt} \sin\omega t$ is considered. The expression of the oscillator response is approximately similar, so the form of the hysteretic loops obtained is regular and symmetrical. Fig. 4 shows the identified force-displacement and force-velocity laws in a nondimensional plane.

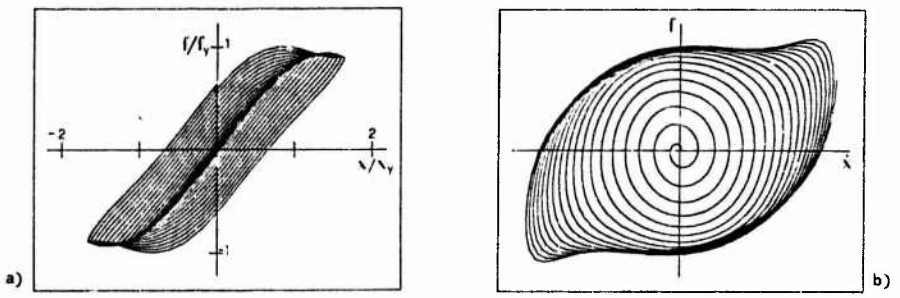

Fig. 4 - Identified force-displacement (a) and force-velocity cycles (b) for elastoplastic oscillator.

The second case considered concerns a degrading hysteretic model which reproduces the behaviour of reinforced concrete columns. It is a layered model which has been described in ref. [14] having a natural period T = 0.5 sec. The nonparametric model considers Chebyschev polynomials up to an order n = 3. The external action consists of Taft 21.07.52 N69W earthquake accelerogram scaled in such a way that the maximum displacement normalized with respect to the displacement at yielding is about four. Fig. 5 shows layered model loops and the identified ones.

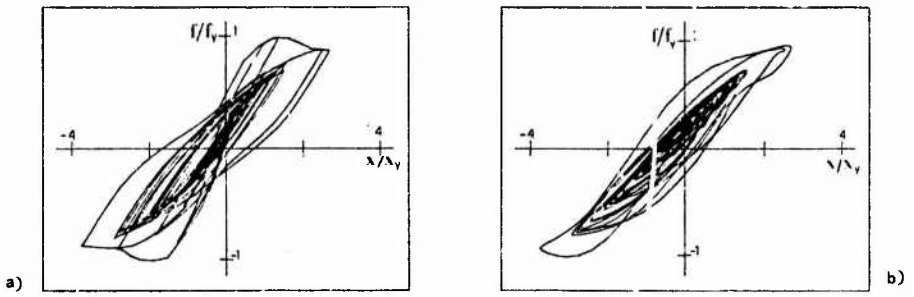

Fig. 5 - Histeretic cycles for degrading oscillator under Taft accelerogram excitation (a) and identifiad cycles (b).

As it can be seen, agreement is not as good as in the preceding case. It is felt that further efforts shoulds be made to shed more light on the behaviour of these nonparametric models and studies are now being carried on in this regard

CONCLUSIONS

During the last decade structural identification has received great attention also in the field of civil engineering. For large complex structures the availability of experimental results could not be quite wide: therefore it is convenient to use all prior information in the modelling of the structure and to adopt physical models in the identification of linear dynamic behaviour.

A finite element model of the structure is referred to in which some physical quantities are uncertain. Their values are determined on the base of a comparison between measured and

predicted modal quantaties within a Bayesian framework. An approximated technique is illustrated to represent the relation between response quantities and structural parameters; it is shown that this technique is very effective in the numerical procedure of parameter estimation and the sensitivity analysis. An example of structural identification of a building has been developed; the general aspects of the optimal choice of measured quantities, of identifiability and of numerical errors are discussed.

For the identification of nonlinear structures, mainly when sparsely instrumented, nonparametric models can be attractive. A series expansion of the force-deformation relationship through ordinary and Chebyshev polynomials has referred to in the identification of the response of two different hysteretic oscillators subjected to a strong earthquake. The results are encouraging but further research is needed to enlight the effectiveness of nonparametric models.

ACKNOWLEDGEMENT

This paper is supported in part by Ministery of Education, 60% funds, 1986.

REFERENCES

1. J.D. Collins, G.C. Hart, T.K. Hasselman and B. Kennedy 1974, AIAA Journal, Vol. 12 No. 2, 185-190. Statistical identification of structures.

2. H.G. Natke 1982 Identification of Vibrating Structures. CISM Courses and Lectures, No. 272, Springer-Verlag.

3. Natke, H.G. and Cottin, N. 1985 Aachen. Proceedings Int. Symp. on Aeroelasticity. Updating mathematical models on the basis of vibration and modal test results. A review of experience.

4. D. Capecchi and F. Vestroni 1986 University of L'Aquila, Inst. of Scienza delle Costruzioni Pubbl. N. 96. Problems on parametric identification of structures (in Italian).

5. J.K. Sprandel 1979 Ph.D. Thesis, Purdue University. Structural parameter identification of member characteristics in a finite-element model.

6. P.C. Shah and F.E. Udwadia 1978 ASME Journal of Applied Mechanics, Vol. 45, 188-196. A methodology for optimal sensor locations for identification of dynamic systems.

7. F. Benedettini and D. Capecchi 1987 Meccanica (in press). A perturbation technique in sensitivity analisys of elastic structures.

8. G.C. Hart and J.P.T. Yao 1977 Journal of the Engineering Mechanics Division, ASCE, Vol. 103, No. EM6, 1089-1104. "System identification in structural dynamics.

9. S.F. Masri and S.D. Werner 1985 Earthquake Engineering and Structural Dynamics, Vol. 13, 635-649. An evaluation of a class of practical optimization techniques for structural dynamics applications.

10. F. Vestroni and D. Capecchi 1986 Venice. First AIOM Congress, 337-345. Problems related to identification of a pipeline in dynamic analysis (in Italian).

11. S.F. Masri and T.K. Caughey 1979 ASME Journal of Applied Mechanics, Vol. 6, 433-447. A nonparametric identification technique for nonlinear dynamic problems.

12. E.F. Crawley and K.J. O'Donnel 1987 AIAA Journal, Vol. 25 No. 7, 1003-1010. Force-state mapping identification of nonlinear joint.

13. S. Toussi and J.T.P. Yao 1983 Journal of the Engineering Mechanics Division, ASCE Vol. 109 No. 5, 1189-1202. Hysteresis identification of existing structures.

14. D. Capecchi and F. Vestroni 1984 2nd Italian Conf. on Earthquake Engineering, Rapallo, 7.175-7.186. Cyclic behaviour and seismic response of a model with decay for reinforced concrete members (in Italian).

ON THE USE OF OVERSIZED MODELS FOR MODAL IDENTIFICATION IN STRUCTURAL DYNAMICS

John Brandon

Department of Manufacturing and Manufacturing Systems Engineering
University of Wales Institute of Science and Technology
Cardiff
WALES

1 INTRODUCTION

In multi-mode curve fitting algorithms, beneficial results are widely observed when the number of modes to be identified is set significantly greater than prior knowledge of the structure would suggest. The resulting additional modes are called mathematical or "ghost modes". Perhaps the latter description is more suitable, since the extra data do not represent genuine structural properties but are constructed from system noise. The most extreme case of this practice is the class of free time domain methods such as Ibrahim's method where the data space is completed with "noise modes" (ie the number of identified modes is equal to the number of measurement stations) [1,2,3].

The author knows of no current literature which explains adequately why the addition of ghost modes improves the confidence of the analyst in the genuine structural modes. Thus the current peper sets out to explain this phenomenon in a heuristic fashion using analysis based on the concept of the bounding properties of Gerschgorin discs. The intention here is to present plausible explanations, founded on established numerical theory, rather than rigorous analytical results.

This paper develops a number of previous works by the author. Rank estimation was considered previously in ref[4] and the analysis presented here will use as a case study Ibrahim's method which has been considered elsewhere in refs [5,6]. The current paper should be seen as part of a series which sets out to examine the fundamental characteristics of identification algorithms. It is gradually becoming understood that the underlying numerical procedures are common to a number of competing methods in structural dynamics identification, (this was recently observed by Brown [7]). A taxonomic study, in the same style as that in the control literature by Eykhoff [8], is currently in progress. It is interesting to note that many of the strategies currently vying for favour in modal analysis, eg maximum liklihood, extended least squares, generalised least squares etc, are part of Eykhoff's amorphous "bag of tricks" which was the subject of his classification.

2 STRUCTURE OF THE IDENTIFICATION PROBLEM

The identification problem of interest may be defined as follows:

> Given a series of observations of an array of sensors sampled simultaneously, to identify natural frequencies (in complex form) and corresponding mode shapes.

Factors which corrupt the data, for example due to the instrumentation and signal processing, are important in the theory of modal analysis (for example see Ewins[9]), but will not be addressed in this paper. The objective of the current work is to assess the consequences of the errors rather than their origin. Neither is it intended in the current work to form any judgement of the suitability of different response measures (receptance/ mobility/inertance). It is assumed that the data can be represented in discretised (ie matrix) format and that each of the measurements is independently subject to error. Two formulations will be discussed. In the first case, the measurements are assumed to be expressed in the form of the receptance matrix, with the identification being carried out in the frequency domain. The second case will use the initial transformation involved in the Ibrahim time domain algorithm.

2.1 Receptance identification

The output from the majority of current signal processing hardware can be programmed so that it comprises a sequence of estimates of the receptances of a vector of measurement points as referred to the driving point. These in the majority of cases are measured at fixed frequency intervals, although the spacing may be varied eg logarithmically. Denoting this matrix of measurements as $\underline{\mathbf{Q}}$, then, assuming the data to be free of error, there exists a factorisation of $\underline{\mathbf{Q}}$:

$$\underline{\mathbf{Q}} = \underline{\mathbf{E}} \quad \underline{\mathbf{W}} \quad \underline{\mathbf{F}} \qquad (1)$$

Where $\underline{\mathbf{E}}$ is a matrix whose columns are the modal vectors of the structure (normalised in the least squares norm ie $\underline{\mathbf{q}}_i^t \, \underline{\mathbf{q}}_i = 1$), $\underline{\mathbf{W}}$ is the diagonal matrix of the weights of the modes in the observed data and the rows of $\underline{\mathbf{F}}$ comprise the dynamic magnification factors of each mode at the excitation frequencies.

The identification is often achieved iteratively:

(i) estimates are made of natural frequencies;
(ii) the estimate to $\underline{\mathbf{F}}$ is constructed;
(iii) each side of equation (1) is post -multiplied by the inverse of $\underline{\mathbf{F}}$ (or the Moore-Penrose generalised inverse or pseudo-inverse if $\underline{\mathbf{F}}$ is not square or is square but singular (see Chen and Fuh [10] and Brandon [11,12]);

2.2 Time domain methods

In the time domain methods, for example free decay methods, the data is again capable of representation in matrix factor form (see Brandon(6))

$$\underline{P} = \underline{E} \quad \underline{W} \quad \underline{D} \qquad (2)$$

where, as before, $\underline{E}$ contains normalised modes, $\underline{W}$ comprises the modal weights, but $\underline{D}$ is now constructed from the transient time behaviour corresponding to each of the system modes.

2.3 Canonical forms

Although the analysis is not presented here, it would appear that a factorisation into the three matrices as shown above is common to a large class of identification methods and as such forms the basis of a canonical form of the identification problem, ie a standard form on which error analysis can be based.

As will be seen, the numerical properties of this factorisation are far from ideal but represent a suitable first step.

2.4 Segregation of the errors

Consider the structure of equation (1) as defined: the matrix $\underline{E}$ comprises only structural properties (the mode shapes); similarly $\underline{F}$ contains corresponding frequency and damping properties. Under the usual linearity assumptions prevailing in modal analysis these system properties are fixed and unambigous. The experimental indeterminancy can be isolated to the weighting matrix $\underline{W}$ which represents the test configuration and excitation conditions.

Experimental errors can thus be considered to cause errors only in the weighting matrix which should be re-defined:

$$\underline{W} = \underline{W}_s + \underline{W}_e \qquad (3)$$

where $\underline{W}_s$ is the (diagonal) matrix corresponding to the genuine data (signal) and $\underline{W}_e$ is the (generally full) matrix of experimental errors (noise).

2.5 Rank uncertainty

In experimental conditions it is usually not possible to make an a priori decision concerning the number of modes which will be identified in a structure. Even where a theoretically derived model is available, eg a finite element study, it is not unusual to detect resonant phenomena unpredicted by the model or to fail to measure predicted

modes. Examination of test results (eg Lembregts et al[13]) shows considerable uncertainties as to the rank of the data matrix and equivalently the number of identifiable modes (for further related commentary see Brandon[4]).

The rank of the data matrix affects the order of the matrices in equation (1). Assuming m measurement stations, f frequencies and k genuine modes, $\underline{Q}$ is mxf, $\underline{E}$ should be mxk, $\underline{W}$ kxk and $\underline{F}$ is kxn (typically f>m>n). However the number of modes is in general unknown a priori and the analyst uses a model containing p predicted modes making $\underline{E}$ mxp, $\underline{W}$ pxp and $\underline{F}$ pxf. The additional columns of $\underline{E}$ and rows of $\underline{F}$ (similarly scaled) must be chosen so that the matrices are of full rank, ie the rows/columns comprise a set of p linearly independent vectors. The remainder of the current paper will assess particularly the possible consequences of the common practice of choosing p>k (the oversized model) but also the effect of underestimates of the rank.

3 NUMERICAL CONCEPTS

Error analysis for the identification problem depends on the separation of the components of $\underline{W}_s$ and $\underline{W}_e$ of the modal weighting matrix $\underline{W}$. This is not however the whole story since the errors themselves may be affected by the scaling of product matrices $\underline{E}$ and $\underline{F}$. In this case the advantageous computational properties of more well known factorisations, for example the Singular Value Decomposition (SVD), do not necessarily apply to this problem. The power of the SVD stems from the property that the left and right factor matrices are unitary matrices, (see for example Noble and Daniel [14]) which consequently have a numerically neutral effect. In this case, however, whilst the columns of $\underline{E}$ and the rows of $\underline{F}$ respectively are normalised with respect to themselves, they are not orthogonal with respect to each other. This is a consequence of the fact that in structural dynamics the generalised eigenvalue problem is solved rather than the standard one.

3.1 Gerschgorin disc's- a suitable basis for error analysis

Much of the theoretical basis for error analysis is based on the properties of the eigensystem of the coefficient matrices. In matrix inversion, for example, the condition number, the key measure of the quality of the system matrix, is usually defined as the ratio of its largest to smallest eigenvalue. In the solution of eigenproblems the appropriate condition numbers depend on the closeness of pairs of adjacent eigenvalues (see Wilkinson [15]). From a heuristic point of view therefore, there is considerable merit in examining the behaviour of the weighting matrix, when subject to error, in terms of the bounds of its eigenvalues. This is particularly attractive in this case, since $\underline{W}$ is nominally diagonal, ie the diagonal entries are the eigenvalues of $\underline{W}$.

In this respect the Gerschgorin theorems provide an ideal analytical model. These are analysed in considerable detail by Wilkinson[15]. Their use in structural dynamics was probably first proposed by Lancaster[16]. Both of these texts are however deeply analytical and may be inaccessible to the general reader. The text by Meirovitch[17] contains an accessible and concise description of the theorems.

The Gershgorin discs provide bounds for each of the eigenvalues of a matrix by comparing the diagonal and off-diagonal terms. Specifically every eigenvalue σ of $\underline{W}$ lies within at least one of the discs

$$| \sigma - w_{mm} | = \sum_{\substack{i=1 \\ i \neq m}}^{n} | a_{mi} | \quad (4)$$

It should be noted that there are two discs associated with each diagonal element ie based on rows (as defined above) and columns (transposing the indices in (4)). The smaller disc naturally provides the stronger estimate. The Gerschgorin discs therefore allow the estimation of possible errors in the diagonal entries of $\underline{W}$ in terms ofits off diagonal entries.

example

The Gerschgorin discs for the matrix

$$\begin{bmatrix} 1+i & 0.4 & 0.1 \\ 0.3 & 2.0 & 0.1 \\ 0.4 & 0.7 & 3.0 \end{bmatrix}$$

are as shown in Fig 1, where C_i and R_i are the discs corresponding to the ith column respectively. It can be seen from this example that reliance on only either the set of row or of column discs gives an unsatisfactory result,in this application, since overlapping discs imply failure to resolve modes.

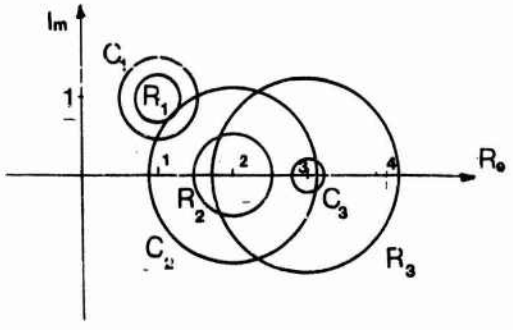

Fig 1 Row and column Gerschgorin discs

It should be noted that the Gerschgorin discs, as defined above, give rather weak bounds on the eigenvalues. Methods are described by Wilkinson[15] for weighting the rows/ columns to achieve considerably sharper error bounds.

3.2 Diagonal dominance- a related concept

A related concept to Gerschgorin discs is that of diagonal dominance. This again compares the diagonal entry with the absolute row/column sum of the off diagonal entries. In this case if

$$| w_{mm} | > \sum_{\substack{j=1^{n} \\ j \neq m}} | w_{jm} |$$

for all m, then the matrix is diagonally dominant . The consequence of diagonal dominance is that the matrix is guaranteed to be nonsingular (see for example Noble and Daniel[14]). Strongly diagonally dominant matrices (ie replacing > with » above) have attractive numerical properties, giving in general well conditioned inversion. It has rarely been remarked in the literature that diagonal dominance is equivalent to the condition that none of the Gerschgorin discs encloses the origin and that strong diagonal dominance often leads to disjointness in the discs (although this is implicit in Gerschgorin's second theorem (see Meirovitch[17])).

3.3 Measuring the errors- various matrix norms

The definitions of Gerschgorin discs and diagonal dominance naturally use the absolute row sum and absolute column sum norms, the $\|.\|_{\infty}$ and $\|.\|_{1}$ norms respectively. The natural norm for eigenvalue problems is the $\|.\|_{2}$ or least squares norm, which underlies the theory of the pseudo-inverse which is in increasing use in identification problems[12]. The norm most easy to compute in identification problems is variously termed the Frobenius/ Euclidean/ Schur norm $\|.\|_{E}$. It is not intended to discuss in any detail the respective merits of these norms since their properties are all extensively recorded in standard texts (for example [14]). It should be realised however that the availability of any norm allows the computation of bounds for all the others.

4 THE IDENTIFICATION PROCESS

Although not a complete description of the process, the estimation of a modal weighting matrix (implicitly or explicitly) is a central feature of many practical identification algorithms. As has been suggested the Gerschgorin discs indicate whether a mode can be identified, although they do not necessarily provide a practical method of doing so. It has been shown that the separation of the Gerschgorin discs is dependent on the ratio of the diagonal

term to the absolute row/column sum of the corresponding off-diagonal terms. In practical terms the quality of the identification is judged in terms of a residual which quantifies the discrepancy between the experimental data and the identified structural properties. In general an a posteriori estimate of the residual is formed by subtracting the effects of the identified modal properties from the data matrix.

4.1 Significance of the residual

Taking for example the frequency response case, in the formulation defined in equations (1) and (3), the structural properties are represented by the product $\underline{E}\,\underline{W}_s\,\underline{F}$ and the residual by the product $\underline{E}\,\underline{W}_e\,\underline{F}$. These contributions may be characterised by the Euclidean norm, where

$$\| \underline{A} \|_E = \sqrt{\sum |a_{ij}|^2}.$$

As the assumed rank increases the Euclidean norm of the modal weighting matrix $\underline{W}_s$ increases monotonically (since this is a diagonal matrix to which significant terms are replacing zeroes in the diagonal as the assumed rank increments), whilst the norm of the noise weighting matrix $\underline{W}_e$ correspondingly decreases monotonically. As has already been stated, the availability of any norm allows bound to be set on all other norms. Particularly the monotonic decreasing of the Euclidean norm of the error weighting matrix implies a consequent monotone reduction of the $\|.\|_1$ and $\|.\|_\infty$ norms and hence the radii of the Gerschgorin discs.

4.2 Consequences of the error bounds for overdetermined systems.

As has been described above, an increment in the assumed rank of the system causes a reduction in the Euclidean norm of the error matrix, measured usually in terms of the magnitude of the residual. (Wilkinson[15] presents similar analysis for the Jordan canonical form of a general matrix.) By the bounding properties of the norms, the Gershgorin discs enclosing the diagonal terms in the matrix of identified modal weights $\underline{W}_s$ contract to increase the confidence of the analyst in the identified modes. It follows that when the system is overdetermined, ie the rank of the system is chosen greater than the number of identifiable modes, the radii of the Gershgorin discs will continue to contract, (and consequently the confidence of the analyst will continue to increase), as the assumed rank is incremented. An unfortunate consequence of the above analysis, however, is that the discs of previously identified "ghost" modes will also contract, making them increasingly likely to be identified as genuine structural modes. It has been shown previously[5] that the effects of random noise cannot be completely eliminated from the identified modes. Conversely, the noise cannot be

isolated to or from the ghost modes.

There have been relatively few studies of identification algorithms tested on systems which have a simple known spectrum. Goyder reported the use of an incremental multi-degree of freedom algorithm on a simple cantilever structure [18]. Although on theoretical grounds there should have been five modes, the algorithm identified fourteen modes within the frequency range studied (see also[19]).

5 CONCLUSIONS

Error analysis of a number of identification algorithms can be based on the canonical form developed in the paper.

Error bounds for identified modal properties depend on the radii of Gerschgorin discs for the modal weighting matrix.

The discs contract as the assumed rank is incremented, leading to increased confidence in the identified modes.

The contracting Gershgorin discs can increase confidence indiscriminately for both genuine and ghost modes. Thus the increased confidence in the identified data may lead to spurious conclusions.

6 REFERENCES

1. S R IBRAHIM and E C MIKULCIK, 1976, Shock and Vibration Bulletin, 46, 187-196, The experimental determination of vibration parameters from time responses.
2. R S PAPPA AND S R IBRAHIM, 1981, Shock and Vibration Bulletin, 51,43-72, A parametric study of the Ibrahim time domain modal identification algorithm.
3. S R IBRAHIM and R S PAPPA, 1982, Jnl Spacecraft and Rockets, 19 459-462, Large modal survey testing using the Ibrahim time domain identification technique.
4.J A BRANDON, The significance and practice of rank estimation in structural dynamics identification algorithms, in Numerical Techniques for Engineering Analysis and Design, Vol I, Eds Pande and Middleton, Martinus Nijhoff, 1987, section S5 pp1-8.
5. J A BRANDON, 1985, AIAA Jnl., 23, 815-6, On the theoretical justification of Ibrahim's method.
6. J A BRANDON, 1987, 5th Intl. Modal Analysis Conference, Imperial College London, 2, pp857-861, Subspace behaviour in Ibrahim's time domain algorithm.
7. F DEBLAWE, D L BROWN and R J ALLEMANG,1987, 5th International Modal Analysis Conference, London, 2, 832-845, The polyreference time domain technique.
8 P EYKHOFF, 1982, IFAC Symp on Identification and System Parameter Identification, Washington, 31-42, On the coherence among the multitude of system identification methods.

9 D J EWINS, 1984, Modal Testing: Theory and Practice, Chichester, Research Studies Press.
10 S Y CHEN and J S FUH, 1984, AIAA Journal, 22 , 1827-8, Application of the generalised inverse in structural system identification.
11 J A BRANDON, 1985, AIAA Journal, 23 , 1839-40, Comment on "Application of the Generalised inverse in structural system identification".
12 J A BRANDON, 1988, 6th Intl Modal Analysis Conf, Orlando, Fa, On the robustness of algorithms for the computation of the pseudo inverse for modal analysis.
13 F LEMBREGTS, R SNOEYS AND J LEURIDAN, 1987, 5th Intl Modal Analysis Conf, London, 2, 966-978, Application and evaluation of multiple input modal parameter estimation.
14 B NOBLE AND J W DANIEL, 1977, Applied Linear Algebra, Englewood Cliffs, NJ, Prentice-Hall.
15 J H WILKINSON, 1965, The algebraic eigenvalue problem, Oxford UP. 16 P LANCASTER, 1966,Lambda matrices and vibrating systems, Pergamon.
17 L MEIROVITCH, 1980,Computational methods in structural dynamics, Sijthoff and Noordhoff.
18 H G D GOYDER, 1976,Institute of Sound and Vibration Research, Southampton U, Report ISVR87, Structural modelling by the curve fitting of frequency response data.
19 H G D GOYDER, 1980, J Sound and Vibration, 68, pp209-230, Methods and application of structural modelling from measured frequency response data.

AN EXPERIMENTAL TECHNIQUE FOR INVESTIGATING NONLINEAR STRUCTURES

H G D Goyder - Harwell Laboratory
A P Lincoln - Prosig Computer Consultants

1. INTRODUCTION

Experimental techniques for investigating vibration are now widely used and there is a considerable literature. This approach to vibration is generally called experimental modal analysis and the book by Ewins [1] summarises the methods used in its application. Essentially a modal analysis is conducted by applying a force to a structure and measuring the time history of this force and the resultant motion. From these measurements, a transfer function is calculated which relates the response to the applied force. For linear structures, this transfer function completely characterises the structure, and by analysing the transfer function, basic parameters such as natural frequencies, damping ratios and mode shapes may be deduced.

Most of the experimental methods developed for modal analyses rely upon the structure being linear. The purpose of this paper is to extend the theoretical and experimental techniques of modal analysis so that nonlinear structures may be tested. Problems arise with nonlinear structures because the effects of any nonlinear components depend on the amplitude and velocity of the structure. Thus when a modal analysis is performed, the resulting transfer function depends on the degree to which the nonlinear component is excited. Thus, for example, if an impulse is used to excite a nonlinear structure, a different transfer function will be obtained for each different impulse magnitude. If the structure is linear, every transfer function is identical.

If a nonlinear structure is to be characterised by a transfer function, it is necessary to arrange for the non-linear components to be excited in an appropriate fashion. It is therefore necessary to choose a suitable excitation force. A good choice is to use the force which replicates the excitation that the structure will experience when it is in operation. An excitation of this form ensures that the nonlinear components will be excited in a realistic manner. An excitation which is chosen arbitrarily will not in general be suitable. Thus one of the objectives of this study was to develop a method for exciting a structure in a realistic manner.

A further consideration is the choice of excitation function. Typical functions used for modal analysis are sine waves, impulses, spectrally shaped transients and stationary random signals. Goyder [2] has compared the use of the these functions for nonlinear structures and has demonstrated that the use of stationary random signals has several advantages. These advantages may be summarised as follows.

(i) The transfer function is continuous.
(ii) The transfer function obtained may be interpreted in the same way as that of a linear structure, ie as a summation of resonances.
(iii) The transfer function correctly models damping in the sense that all the energy dissipated within a nonlinear structure is properly accounted for.
(iv) The transfer function is optimum in the sense that there is no better linear model (in the least squares sense) which describes the non-linear system.

Because of these favourable properties, it was decided that random excitation would be used for the modal analysis.

This paper describes (i) the experimental techniques which were developed in order to apply realistic excitation forces to nonlinear structures and (ii) the method by which transfer functions may be deduced from the measurements.

2. THE PRINCIPLE DIFFICULTIES

A number of problems must be overcome before a nonlinear structure can be satisfactorily tested. These problems are illustrated in figures 1 to 3. Figure 1 shows the spectrum of a stationary random signal which was applied to a electrodynamic shaker. This spectrum is the voltage applied to the power amplifier which excites the shaker. The voltage has been arranged to have a band pass spectrum which is flat between 75 Hz and 350 Hz. Figure 2 shows the spectrum of the force actually applied to the structure. Although the band pass nature of the spectrum is still apparent, it is clear that there are several peaks and troughs. These peaks and troughs are a combination of characteristics from the shaker and structure. The modulus of the transfer function for the structure (inertance) is shown in figure 3. The structure, which was non-linear, consisted of a 3.36m tube with a 0.0175m outside diameter. The tube was loosely supported at its ends, by plates with clearance holes. Additional vibration constraints were also applied by means of five friction restraints. The tube was allowed to slide against these restraints, thus allowing friction to oppose the motion (this experimental configuration models tubes within heat exchangers). The transfer function was measured by a technique which will be described below. It can be seen that the troughs in the force spectrum correspond to the resonances of the structure. The peaks in the force spectrum correspond to combined resonances of the shaker and tube. It can thus be seen that there is a strong feedback between the motion of the structure the force applied to the structure.

One objective of the study was to determine how a force could be applied to a structure so that this force was representative of the forces likely to be found when the structure was in operation. The approach developed to over come the difficulties shown in figures 1 to 3 was to weight the signal applied to the shaker so that the distortions introduced by the shaker were accounted for. For a linear structure, this procedure involves weighting the signal applied to the shaker by a transfer function which is the inverse of the transfer function between the force and the applied signal. However, because the structure is nonlinear, this weighting cannot be performed directly and an iterative method must be used.

A further difficulty arises in the calculation of the transfer function of the structure. The transfer function of the structure is found from the ratio of the spectrum of the response to the spectrum of the force (the details will be given below). When calculating this transfer function, it is desirable to use a method which rejects noise. This is particularly important for nonlinear structures because the nonlinearities produce an additional response which is similar to noise. It is clear that both the force signal and the response signal are contaminated by noise and that a method must be developed for rejecting noise from both of these signals. This is clear from figure 2 where the force signal is seen to be dependent on the motion of the structure and thus also dependent on the noise in the structure. The method for determining the transfer function given below rejects noise from both the force and the response signals.

Thus the principal difficulties to be overcome are due to the force applied to the structure being dependent on the motion of the structure. The way that this difficulty has been overcome is given in the subsequent sections.

3. CONTROL OF THE EXCITATION FORCE

The method for achieving control of the excitation force is described in this section. In order to simplify this discussion, the following nomenclature will be used. The auto-spectral density function (power spectrum) of the force will be called the force-spectrum. The auto-spectral density function of the signal applied to the power amplifier which excites the shaker will be called the drive spectrum (it should be noted that the actual signal to the shaker is dependent on the motion of the structure due to the back emf generated in the shaker coil. For this reason it is inappropriate to use the signal applied to the shaker in any control circuit. However the power amplifier used to excite the shaker acts as a buffer and the effect of the back emf is not apparent at the input to the power amplifier). Finally, the desired force spectrum will be called the target spectrum, thus the objective is to adjust the drive spectrum so that the force spectrum becomes the target spectrum.

The control of the force spectrum has been achieved by means of a computer. The control strategy operates as follows. First the target spectrum is input to the computer. The target spectrum is chosen so that it represents the likely environment of the structure. A drive signal is then constructed. The drive spectrum may be adjusted to take any appropriate form. The drive signal is converted to an analogue signal and applied to the power amplifier which energises the shaker. The actual force which is applied to the structure is measured and is fed back to the computer where it is digitised. Finally, the force spectrum is calculated and compared with the target spectrum. From the discrepancies between the force spectrum and the target spectrum, a new drive spectrum may be deduced.

The process of measuring the force spectrum and updating the drive spectrum cannot be performed in real time. This is because of the long record length required in order to obtain an accurate spectra for the force. An iterative approach has therefore been adopted. During one iteration, the drive signal is maintained with the same spectrum and the force spectrum is measured. This situation is maintained until the measured force spectrum has reached a specified accuracy. The drive signal is then halted and a new (improved) drive spectrum calculated. The next iteration may now begin with an improved spectrum. Because of this iterative process any changes in the force spectrum due to nonlinear effects may be taken into account in the adjusting process.

This algorithm has been successfully implemented and the results are shown in figures 4 and 5. Here, figure 1 has been used as the target spectrum. Figure 4 is the drive spectrum and figure 5 is the force spectrum. It can be seen that a much improved force spectrum, compared to figure 2, has been achieved.

4. THE ALGORITHM FOR FORCE CONTROL

Details of the algorithm for force control are as follows. At the end of the nth iteration, let the drive auto-spectral density be $D_n(\omega)$, and the measured force auto-spectral density be $F_n(\omega)$. The target spectrum is $S(\omega)$. The new drive spectrum for the n+1 th iteration is calculated from

$$D_{n+1}(\omega) = g_1 D_n(\omega)\, S(\omega)/g_2\, F_n(\omega) \qquad (1)$$

Here g_1 and g_2 are gains which are applied to the drive spectrum and measured force spectrum respectively (it is necessary to control the gains in order to achieve good quantisation through the analogue to digital and digital to analogue converters.) The drive signal is calculated as follows. In the frequency domain, a signal is calculated which has random phase but has a modulus spectrum equal to the square root of $D_n(\omega)$. This signal is then converted back to the time domain by means of an inverse Fourier transform and then output as the drive signal. Attention has to be paid to the windowing of the spectrum since it is necessary to output a sequence of drive time histories which must be independent and yet join together smoothly. By using this technique, record lengths of indefinite duration may be generated.

It is important to show that the use of equation (1) will be successful and that by its implementation the force spectrum will converge to the target spectrum. In order to show this, it is necessary to model the transfer function between the drive signal and force signal. If this transfer function is written $H(\omega)$ then the relationship between $F_n(\omega)$ and $D_n(\omega)$ is

$$F_n(\omega) = |H(\omega)|^2\, D_n(\omega) + R(\omega) \qquad (2)$$

Here, $R(\omega)$ models the effects of noise and non-linearities. Thus all the non-linear effects are given by $R(\omega)$ while $H(\omega)$ models all the linear effects. This type of division may always be made [3]. Substituting equation (2) into equation (1) to eliminate $F_n(\omega)$ gives

$$D_{n+1}(\omega) = g_1 D_n(\omega)\, S(\omega)/g_2 \left(|H(\omega)|^2 D_n(\omega) + R(\omega)\right) \qquad (3)$$

This is a non-linear difference equation. The analysis of difference equations is similar to that of differential equations [4]. First we determine the fixed points (fixed points are where $D_{n+1}(\omega) = D_n(\omega)$). Thus selecting $D_{n+1}(\omega) = D_n(\omega)$ gives fixed points (denoted by $D_1(\omega)$ and $D_2(\omega)$) of

$$D_1(\omega) = 0 \qquad (4)$$

and

$$g_2|H(\omega)|^2\, D_2(\omega) + g_2 R(\omega) = g_1\, S(\omega) \qquad (5)$$

or

$$D_2(\omega) = g_1 S(\omega) - g_2 R(\omega)/g_2\, |H(\omega)|^2 \qquad (6)$$

The resulting force spectrum corresponding to the fixed points may now be found by substituting $D_1(\omega)$ and $D_2(\omega)$ into equation (2). This gives

$$F_1(\omega) = R(\omega) \qquad (7)$$

for the first fixed point and

$$F_2(\omega) = g_1 S(\omega)/g_2 \qquad (8)$$

for the second fixed point. Clearly convergence to the first fixed point is undesirable, while convergence to the second fixed point yields a perfect result.

By performing a stability calculation it is possible to see if the algorithm will converge onto the desired fixed point. It is only necessary to perform a stability calculation in the neighbourhood of the fixed point and consequently a linearised analysis may be conducted. The basis for the stability analysis is as follows. Equation (3) may be written as

$$D_{n+1}(\omega) = f(D_n(\omega)) \tag{9}$$

where $f(\cdot)$ is the function on the right hand side of equation (3). A Taylor series expansion about the fixed points yields

$$D_{n+1}(\omega) = f(D_j(\omega)) + (D_n(\omega) - D_j(\omega))\, f'(D_j(\omega)) \ldots \tag{10}$$

where $D_j(\omega)$ is the fixed point $D_1(\omega)$ or $D_2(\omega)$ and f' is the derivative of f at $D_j(\omega)$. This equation may be written as

$$D_{n+1}(\omega) - D_j(\omega) = (D_n(\omega) - D_j(\omega))\, f'(D_j(\omega)) \ldots \tag{11}$$

If only first order terms are considered, then this equation has the solution

$$D_n(\omega) - D_j(\omega) = A(f'(D_j(\omega)))^n \tag{12}$$

where A is the starting condition for $n = 0$. This equation is convergent as long as

$$f'(D_j(\omega)) < 0 \tag{13}$$

For equation (3), the first fixed point yields

$$f'(D_1(\omega)) = g_1\, S(\omega)/g_2\, R(\omega) \tag{14}$$

while the second fixed point yields

$$f'(D_2(\omega)) = g_2\, R(\omega)/g_1\, S(\omega) \tag{15}$$

Consequently the algorithm will converge to the desired fixed point if

$$g_2\, R(\omega)/g_1\, S(\omega) < 1 \tag{16}$$

Thus for the algorithm to be stable, the noise contributed to the measured force must be less than the target spectrum. If this conditions is not met, then the desired fixed point ($D_2(\omega)$) is unstable and the force spectrum converts to the first fixed point. It should be noted that each spectral line is independent and that the above analysis applies to each line independently. Thus it is possible for the spectrum to converge at some frequencies and diverge at others.

The algorithm has thus been shown to be effective because it converges to the desired targets spectrum unless it is overwhelmed by the presence of noise and nonlinearities.

5. LIMITATIONS OF THE SHAKER CONTROL ALGORITHM

There are computational and experimental difficulties which limit the overall effectiveness of the method. Firstly the drive and force signal have to pass through digital to analogue and analogue to digital converters respectively. This introduces a quantisation error. This error is severe because the signals have a Gaussian probability density function. The difficulty is that if the tails of the Gaussian distribution are to be digitised then the bulk of the signal will be limited to relatively few quantisation levels. The approach used here is to optimise the digitisation so that a compromise is made between adequately quantising the bulk of the signal while allowing some sampling of the extreme values. In order to quantify this compromise, it is useful to define a crest factor. This factor relates the r.m.s. value of the

signal to the maximum level that will be realised (voltage values larger than the maximum are clipped). Thus the crest factor is defined as

$$C = \text{Maximum Voltage/r.m.s. Voltage} \tag{17}$$

A suitable value for the crest factor is about 3.

A second difficulty is the dynamic range of the measurements. The principle restriction to the dynamic range is due to the quantisation of the time domain signals. This effect is to some extent diminished if, as in this case, a spectral approach is adopted. The averaging used when calculating the spectra reduces this quantisation noise. The ratio of the maximum peak level in an auto-spectral density function to the noise floor expresses the dynamic range (in our case with 2048 levels of quantisation, this gave a dynamic range of 30 dB). The most arduous case is where the shaker introduces a trough in the force spectrum (this occurs at a structural resonance). To compensate for the trough, the drive spectrum must have a corresponding peak. The noise floor is thus controlled by the height of this peak. If the peak is large, much of the dynamic range may be used in defining the peak and great accuracy in achieving a target spectrum is not possible. However, in most cases, a dynamic range of 30 dB appears adequate.

Finally, experimental errors may cause difficulties. It sometimes happens that the link between the shaker and the structure does not transmit a straightforward force. Sometimes a bending force is transmitted or the structure is constrained by the link. In these cases, the forces being applied to the structure are not measured and are not fed back to the computer. This leads to a false excitation of the structure. Attention should thus be paid to the details of the link between the shaker and structure.

6. MEASUREMENTS OF THE TRANSFER FUNCTION

Figure 2 demonstrates that the force applied to the structure is a combination of the drive signal and the response. This combination is shown in figure 6 where the shaker and structure are described in terms of input/output control systems. The problem is that any noise or nonlinearities are fed back to the force. This is represented in figure 6 by an element with transfer function $B(\omega)$. The shaker is considered as having transfer function $A(\omega)$. The equations, in the frequency domain, which describe this coupled system are as follows

$$Q(\omega) = H(\omega)\ P(\omega) + W(\omega) \tag{18}$$

$$P(\omega) = A(\omega)\ Z(\omega) + B(\omega)Q(\omega) \tag{19}$$

Here $P(\omega)$ is the force applied to the structure, $Q(\omega)$ the response of the structure and $H(\omega)$ the linear transfer function. Effects of noise and and nonlinearity are described by $W(\omega)$. The force $P(\omega)$ is composed of the drive signal $Z(\omega)$ acting through the shaker transfer function $A(\omega)$. The effect of feedback is described by the transfer function $B(\omega)$.

The objective is to calculate the transfer function for the structure from measurements of the force, response and drive signals. One conventional method is to calculate the cross-spectral density function between the response and force $(S_{QP}(\omega))$ and divide by the auto-spectral density function of the force $(S_{PP}(\omega))$. This gives the transfer function $H_1(\omega)$ thus

$$H_1(\omega) = S_{QP}(\omega)/S_{PP}(\omega) \tag{20}$$

This calculation method is effective if $P(\omega)$ is uncorrelated with $W(\omega)$ in which case $H(\omega) = H_1(\omega)$. However, in our case, $P(\omega)$ is correlated with $W(\omega)$ as shown by equation (19). This means that the above expression gives

$$H_1(\omega) = H(\omega)\left(|A(\omega)|^2 S_{ZZ}(\omega) + \bar{B}\, S_{WW}(\omega)\right)/\left(|A(\omega)|^2 + |B(\omega)|^2 S_{WW}(\omega)\right) \tag{21}$$

Thus, unless the noise is zero $(S_{WW}(\omega) = 0)$ the calculated transfer function $H_1(\omega)$ is contaminated by noise.

The procedure developed to overcome this problem is to use the drive spectrum $Z(\omega)$ and to calculate the transfer function $H_3(\omega)$ according to

$$H_3(\omega) = S_{QZ}(\omega)/S_{PZ}(\omega) \tag{22}$$

from equation 18 it may be seen that

$$S_{QZ}(\omega) = H(\omega)\, S_{PZ}(\omega) \tag{23}$$

Consequently $H_3(\omega) = H(\omega)$. The beauty of this estimation method is that $Z(w)$ is available within the computer and is thus completely uncontaminated by noise. Consequently this method rejects noise from both the force and response spectra, thus leading to a very accurate estimation of the structural transfer function.

The noise analysis presented above throws doubt on the usefulness of the standard definition of coherence. The coherence of a system is the relationship between the total response of the system and the response that is modelled by the transfer function. Thus for noise, which is uncorrelated with the force, the coherence is given by

$$\gamma^2(\omega) = |H_1(\omega)|^2\, S_{PP}(\omega)/S_{QQ}(\omega) \tag{24}$$

or

$$\gamma^2(\omega) = |S_{QP}(\omega)|^2/S_{QQ}(\omega)S_{PP}(\omega) \tag{25}$$

However, the noise is correlated with the force and thus the above equations are not applicable. The equivalent definition for our configuration is

$$\gamma^2(\omega) = |H_3(\omega)|^2\, S_{PP}(\omega)/S_{QQ}(\omega) \tag{26}$$

An example of coherency calculated using this equation is shown in figure 7. This coherency corresponds to the transfer function shown in figure 3. The coherency calculated in this fashion indicates not only the degree of noise in the structure but also the extent of the nonlinearities. This is because nonlinearities and noise are being modelled as similar effects.

7. CONCLUSIONS

Some techniques have been presented for experimentally investigating a nonlinear structure. First, a method was presented for controlling the excitation force applied to the structure. This is important because a nonlinear structure will exhibit different characteristics depending on the level to which the nonlinear elements are excited. The

method presented enables the spectral content of the force to be specified. A suitable specification being the spectra that the structure will experience in its operating environment. The method also enables unwanted effects introduced by the use of electrodynamic shakers to be removed. The method for generating the specified spectrum is applicable to a fully non-linear structure and is achieved by means of an iterative algorithm. The algorithm has been shown to be stable and convergent. The second technique to be developed is a new method for calculating a transfer function. This method is designed to reject noise which may contaminate both the force and response signals. It has been shown that the conventional method for calculating the transfer function is inappropriate. This new technique is particularly useful for nonlinear structures where the nonlinear effects appear like additional noise.

Finally a fresh definition of coherency has been employed. Once again, this is necessary because the conventional definition fails to take into account noise sources which affect both the response and the applied force.

These new experimental techniques enable modal surveys of nonlinear structures to be undertaken with confidence.

8. REFERENCES

1. D. EWINS. 1984 Modal Testing: Theory and Practise. John Wiley

2. H.G.D. GOYDER 1984 Proc.2nd Int.Conf. on Recent Advances in Structural Dynamics, University of Southampton. Foolproof methods for frequency response measurements.

3. G.M. JENKINS and D.G. WATTS 1968 Spectral analysis and its applications. Holden Day, p 154.

4. J. GUCHKENHEIMER and P. HOLMES 1983 Non-linear oscillations, dynamics systems, and bifurcations of vector fields. Springer-Verlag, p 16.

9. ACKNOWLEDGEMENTS

The work described in this paper was undertaken as part of the Underlying Research Programme of the UKAEA. The authors also acknowledge the assistance of Prosig Computer Consultants Ltd.

APPENDIX

This appendix lists the relevant details of the computer system used to implement the procedures outlined above. Host Processor PDP 11/23; Array Processor (floating point) SKYMNK-Q; maximum sample rate 4096 samples per second; A to D and D to A Converters 12 bit ± 10V parallel sample and hold; all spectra calculated with 2000 spectral lines and Hanning windows.

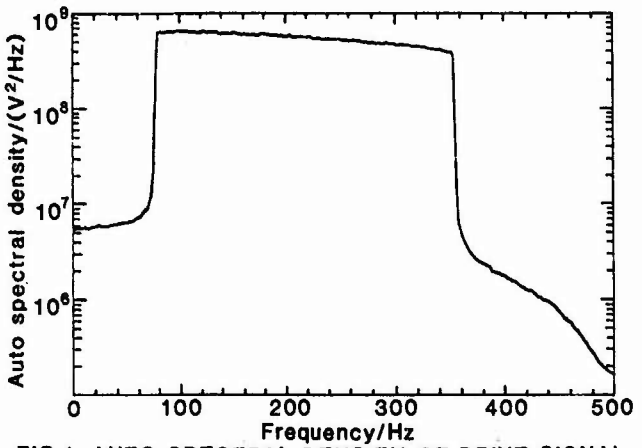

FIG.1. AUTO SPECTRAL DENSITY OF DRIVE SIGNAL TO SHAKER

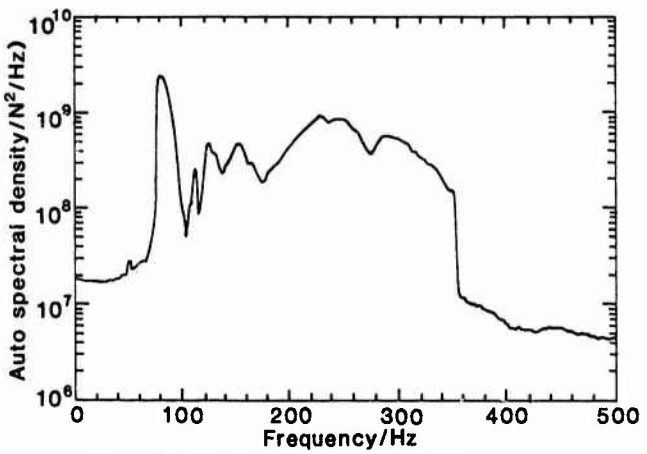

FIG.2. AUTO SPECTRAL DENSITY OF FORCE EXCITING THE STRUCTURE

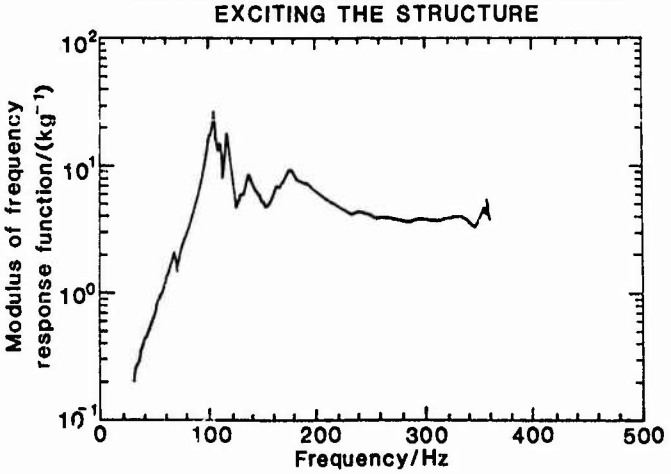

FIG.3. MODULUS OF FREQUENCY RESPONSE FUNCTION OF THE STRUCTURE

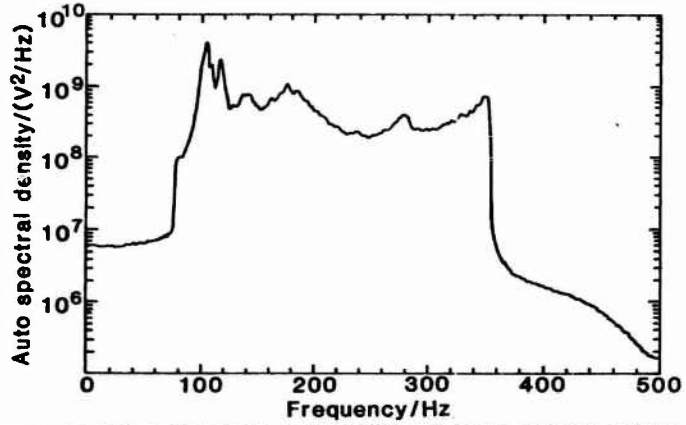

FIG.4. AUTO SPECTRAL DENSITY OF THE DRIVE SIGNAL TO THE SHAKER, WEIGHTED TO COMPENSATE FOR EFFECTS CAUSED BY THE SHAKER

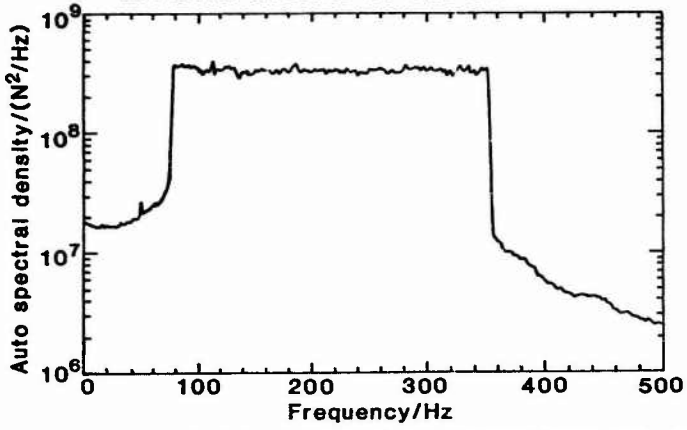

FIG.5. AUTO SPECTRAL DENSITY OF FORCE APPLIED TO THE STRUCTURE, USING A WEIGHTED DRIVE SIGNAL

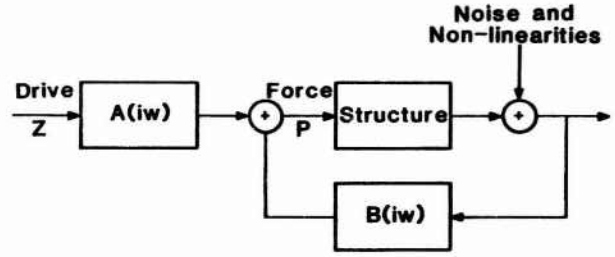

FIG.6. INTERACTIONS BETWEEN A SHAKER AND A STRUCTURE

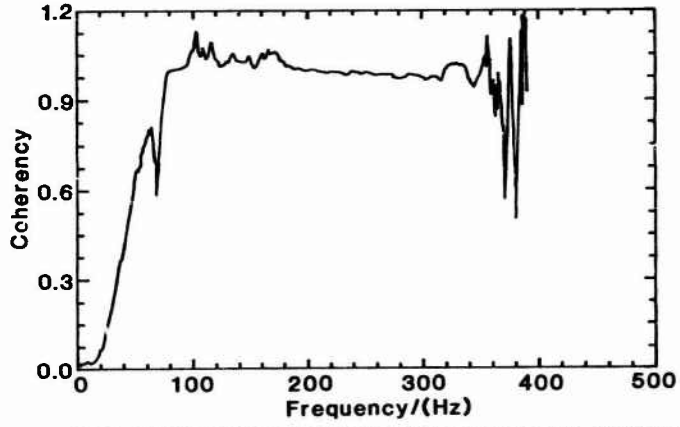

FIG.7. COHERENCY BETWEEN EXCITATION FORCE AND STRUCTURAL RESPONSE

Nonlinear System Identification Using the Surface of Nonlinearity Form: Discussion on Parameter Estimation and Some Related Problems

H.R.Lo and J.K.Hammond

ISVR, The University, Southampton, England.

1. INTRODUCTION

Nonlinear system identification usually involves the detection of the existence of nonlinearity in the system behavior, the identification of the form of nonlinearity from the restoring force (including both damping which determines the energy dissipation characteristic and the stiffness which affects the response level characteristic), and the parameter estimation of the nonlinear system model.

There are many approaches aiming at resolving the nonlinear system identification problems, which include nonparametric methods such as the Volterra series[1], parametric methods by Billings et al [2][3][4], and procedures for the classification of nonlinearities using Hilbert transform[5]. Extensions to frequency domain methods[6] have been proposed to identify the nonlinearity by analysing the distortion of the frequency response function for several typical nonlinearities.

A method of representing the nonlinearity form as a surface in an appropriately selected space(subset of the state vector written as SSV) has been developed [7]. This is as proposed by Masri [8] and discussed in [9]. The basic procedures involve

(1) Estimating the restoring force or the nonlinear portion of the restoring force (depending upon the prior knowledge) time history.

(2) Choosing an appropriate SSV so that the state-vector dependent restoring force defines a single valued surface.

(3) Transforming the restoring force time history into the SSV to create the surface.

This method was applied to several types of nonlinear systems including both nonhysteretic and hysteretic systems, which are simulated on the computer. And also it has been applied to the identification and modelling of a cable type vibration isolator[9]. In this paper, we will discuss parameter estimation and some related problems.

2. CONSIDERATION OF THE EXCITATION SIGNAL.

A system can be excited by various types of signals, e.g. sine wave, swept sine wave, random signals are very commonly used in tests. The responses of a system correspond to these different excitation signals are different in many aspects. One aspect is that their patterns in the SSV are different. For many systems, the SSV is the state space itself, i.e. for a second order system the plane formed by displacement and velocity (sometimes called the phase plane). For example, for the system with the mixed type of nonlinearities of cubic stiffness and quadratic damping, its orbit in the phase plane with sine wave excitation is a fixed closed curve, one example of which is plotted in fig.1; and its orbit with a swept sine excitation is a group of similar curves with regular change in their size and shape, the curves for the same system are plotted in fig.2; while its orbit with random excitation is irregular in both size and shape and

covers an area of the phase plane, the curves of which are plotted in fig.3. From this fact, it is apparant that tests using periodic signals such as sine waves provide limited information about the nonlinear force which is state dependent because the states accessed are very limited, and the tests using signals such as swept sine or random can give more information about the state dependent nonlinear force because the states accessed are much larger. The deterministic signals like swept sine usually will give a deterministic pattern in a clearly defined region of SSV (we are excluding systems exhibiting 'chaos' from this discussion), while random signal will give a random pattern in an area of SSV. Hence, to get the surface representing the nonlinearity of a system, the excitation signal should be chosen as those with wide frequency band or with random nature.

3. RELIABILITY OF THE SURFACE

Because of the way in which the surface of nonlinearity form is produced, the quality of the surface depends on the density of the points on the SSV plane. Hence, the density of the 'point of state' in SSV can be used as a reference for judging the relative quality of the surface.

The density of points can be increased either by increasing the data length of the signals i.e.increasing the sampling rate or the time length, or by limiting the accessible area of the SSV, e.g.using swept sine siganl in appropriate frequency range may achieve better density than the random signal for the same data length in some area.

But in practice, the data length is always limited, hence the surface can not be completely accurate. Basically, the surface suffers from two sources of error: the bias error and the random error. The bias error is due to the feature that a state point is determined in a square at a point at the middle and the value on the surface which corresponds to this square is computed by averaging the restoring force values whose corresponding state-vector are in this square. The bias error depends on the square size and the surface shape (e.g.the gradiant and the curvature). The random error is induced from the random distribution of the points in the specified square, but usually this random error is relatively small in the sense that the general shape will not be blurred by it. When the signals are contaminated by random noise, the random error in the surface may be large. The random error can be reduced by increasing the square size.

4. PARAMETER ESTIMATION OF HYSTERETIC SYSTEMS WITH A PARTICULAR MODEL FROM THE SURFACE

The previously discussed surface is a representation of the form of nonlinearity of the system. It can also be used to estimate the parameters in a mathematical model of the system. Parameter estimation will be demonstrated on the single degree of freedom hysteresis systems which conform to Wen's model[10], i.e. a system described by

$$\ddot{x} + C\dot{x} + z = f(t) \qquad (1)$$

where the nonlinearity is described by

$$\dot{z} = A\dot{x} - \alpha|\dot{x}|\,z\,|z|^{(n-1)} - \beta\dot{x}\,|z|^{n} \qquad (2)$$

where α, β, A and n are constant parameters of the system, z is the hysteretic force, $\ddot{x}$ and $\dot{x}$ are the acceleration and velocity.

Simulations of this model show that z displays a hysteretic form, i.e.z is a multi-valued function of x and z vs. x at any time depends on its history. So, obviously on the SSV composed of x and dx/dt, z will <u>not</u> form a single valued surface. From equation(1), on the SSV formed by z and $\dot{x}$, $\dot{z}$ will be a single-valued surface. So the form of nonlinearity for this

system will be represented by the surface formed by $\dot{z}$ vs. z, $\dot{x}$. (In a practical system identification exercise where the form of model may not be known a priori, different possibilities for the SSV composition should be tried to find the most appropriate one).

The hysteresis model in equation(1) and equation(2) is simulated for both n=1 and n=2 cases.

Other parameters are selected as

$A=35530.6,\ \alpha=3.0,\ \beta=-3.0$

Swept sine signal and Gaussian random signal are used as excitations.

For the cases of n=1, the state vector(z, $\dot{x}$) end point orbit curves are plotted in fig.4 and fig.5 for swept sine and random excitations respectively. In these two simulations, the data lengths are the same. From the graphes, it can be seen that for the swept sine excitation, the points are limited in a ring-shaped area(denoted by R), while for random excitation, the points are distributed in an area(denoted by C). Generally, the density of points in R is larger than the density of points in C.

The surfaces are plotted using simulation data in the square region defined by $\dot{x}_{min}=-78$, $\dot{x}_{max}=78$, and $z_{min}=-.25E5$, $z_{max}=.25E5$ and are shown in fig.6 and fig.7. The surface is designed so that in the area with no points, the surface values are set to zero. According to the state vector end point orbit curves in fig.4, the $\dot{z}$ vs.z at $\dot{x}$ = 54.6 and $\dot{z}$ vs.$\dot{x}$ at z=0.1755E5 have relatively large densities of points, hence they should give better quality of surface.

When n=1, equation(2) becomes

$$\dot{z} = A\dot{x} - \alpha|\dot{x}|z - \beta\dot{x}|z| \qquad (3)$$

Using the parameters given above, the theoretical $\dot{z}$ vs.z with $\dot{x}$ = 54.6 is created and plotted in fig.8 together with the corresponding surface curves for comparison. **(see end)

From equation(3) and the curve in fig.8, it can be seen that $\dot{z}$ vs.z is a linear relationship, and the slope has a switch at z=0, i.e.

$$\dot{z} = A\dot{x} + [-\alpha|\dot{x}| - \beta\dot{x}\,\mathrm{sign}(z)]z$$

i.e.

$$\dot{z} = A\dot{x} + [-\alpha|\dot{x}| + \beta\dot{x}]z \quad \text{for } z<0$$

$$= A\dot{x} + [-\alpha|\dot{x}| - \beta\dot{x}]z \quad \text{for } z>0$$

Now, for $\dot{x}$ = 54.6

$$\dot{z} = 54.6A + 54.6(-\alpha+\beta)z \quad \text{for } z<0$$

$$= 54.6A + 54.6(-\alpha-\beta)z \quad \text{for } z>0$$

So, a standard least-square curve fitting program using polynomial curve fitting with the form of

$$\dot{z} = a_0 + a_1 z + a_2 z^2 + \ldots + a_n z^n$$

was applied.

It was found that both in swept sine excitation case and when parameter estimation with random excitation is carried out within an area with high density of points, the dominance of the 0th and 1st orders took place, while if the parameter estimation with random excitation is carried out in an area in which the density of points is not high, the dominance of 0th and 1st orders will not take place. The parameter estimation results are shown in table 1. In the estimation of α and β, the coefficients a_0 and a_1 are used. A, α and β are calculated according to the formula

$$A^* = (a_0^- + a_0^+)/(2*54.6)$$

$$\alpha^* = -(a_1^- + a_1^+)/(2*54.6)$$

$$\beta^* = (a_1^- - a_1^+)/(2*54.6)$$

Similarly, for the case of n=2, the state vector($z, \dot{x}$) end point orbit curves for swept sine excitation and Gaussian random excitation are plotted in fig.9 and fig.10. The surfaces are produced in the region defined by $\dot{x}_{min}$=-0.9, $\dot{x}_{max}$=0.9 and z_{min}=-230, z_{max}=230 for swept sine and random excitations and are plotted in fig.11 and fig.12. The theoretical relations of $\dot{z}$ vs.z at $\dot{x}$=-0.54 is plotted in fig.13 and the parameter estimation results are listed in the Table 2.

In this case, equation(2) becomes

$$\dot{z} = A\dot{x} - \alpha|\dot{x}|\,z|z| - \beta\dot{x}|z|^2 \qquad (4)$$

This equation shows that $\dot{z}$ vs.$\dot{x}$ is still a linear relationship, while $\dot{z}$ vs.z is a quadratic relationship. As in the previous case, for swept sine excitation and random excitation with small area (i.e.the area with relatively high density of points), the dominance of the 0th and the 2nd orders still took place, but in this case, for random excitation with large area (i.e.the area with relatively low density of points), the dominance of the 0th and the 2nd orders also took place. Assuming that the polynomial in curve fitting has the form

$$\dot{z} = b_0 + b_1 z + b_2 z^2 + \ldots + b_n z^n$$

and the estimated b_0 and b_2 are used for calculating A^*, α^* and β^* according to the formula

$$A^* = -(b_0^- + b_0^+)/(2*0.54)$$

$$\alpha^* = (b_2^- - b_2^+)/(2*0.54)$$

$$\beta^* = (b_2^- + b_2^+)/(2*0.54)$$

From the above estimation results, it can be seen that :

(1)For swept sine excitation, the area with high density of point in SSV is quite clearly defined and is quite limited. Within this area, parameter estimation gives good results.

(2)For random excitation, the state vector end points spread over a larger area. The curve fitting on this large area suffers form random error significantly (in the sense that the dominance of the expected terms may or may not take place, and the parameter estimation may be poor).

But if only the area with large density of points is used for parameter estimation, the estimation can be reasonably good.

5. THE MODELLING OF A CABLE TYPE VIBRATION ISOLATOR

The method of system identification using the nonlinearity form surface has been applied to the modelling of a cable type vibration isolator which has some difference in the hysteresis characteristics from the systems from Wen's model.

The isolator under test is an Aeroflex series C3-H-610, which is made up of stranded wires. The dry friction between the strands and the changing stiffness of the cable make the restoring force and the displacement display a hysteretic relationship. One typical hysteresis loop from the measured signals of test 322 in compression mode, which was excited by swept sine signal, is plotted in fig.14.

According to the working mechanism of cable type structures which has been discussed with detail in [9], the SSV is selected as z^*, $\dot{x}$, in which

$$z^* = (z + \text{sign}(\dot{x})\, z_0)/|z_m + \text{sign}(\dot{x})\, z_0|.$$

The state vector end point orbit curve is plotted in fig.15. The surface of $\dot{z}$ vs. z^*, $\dot{x}$ is plotted in fig.16. It should be noted that only in the area with large density of points, the surface is useful.

According to the surface and with reference of Wen's hysteresis model, the hysteresis model for cable type structure is proposed as

$$\dot{z} = -G\,\text{sign}(\dot{x}) + [A\,\text{sign}(\dot{x}) - \alpha\, z\, |z^*|^{(q-1)} - \beta\,\text{sign}(\dot{x})\, |z^*|^q]\, |\dot{x}|^p \qquad (5)$$

where z^* is as defined above.

And the curve fitting of the 'good quality' portion gives the parameters as:

G=1050
A=16115
α=0.55173E5
β=-0.53790E5
p=0.48
q=1.9

The simulation of model in equation(5) with these parameters gives reasonably good prediction of the measured response and restoring force time histories. The measured and predicted accelerations and restoring forces are plotted.in fig.17 and fig.18.

6. CONCLUSION.

It has been shown that the quality of the surface representing the nonlinear form depends on the density of 'points of state' in SSV. The surface usually suffers from the errors of bias and random nature. In the areas of high density of points, the surface can be used for parameter estimation.

Although for many nonhysteretic systems the SSV are the same as their phase planes, for more complicated nonlinear systems like hysteretic system, some synthesized state vectors may

have to be used so that a single valued surface can be produced. In this case, the selection of appropriate SSV usually needs some prior knowledge. For hysteretic systems from Wen's hysteresis model, the SSV can be chosen as z and $\dot{x}$, while for cable type hysteretic systems, the SSV should be z* and $\dot{x}$.

According to the surface generated from the test on a cable type vibration isolator and with reference to Wen's hysteresis model, a hysteresis model is proposed for the cable type structures with hysteresis.

** The $\dot{z}$ vs. $\dot{x}$ relation is always linear for Wen's hysteresis model. To save space of this paper, the estimation sample results for $\dot{z}$ vs. $\dot{x}$ relations are omitted.

References:

[1] M. SHETZEN 1980 The Volterra and Wiener Theories of Nonlinear systems. Wiley.

[2] I.J. LEONTARITIS AND S.A. BILLINGS 1985 Int. J. Control 41(2), 303-328 Input-output Parametric Models for Non-linear Systems, Part I: Deterministic Non-linear Systems.

[3] I.J. LEONTARITIS AND S.A. BILLINGS 1985 Int. J. Control 41(2), 329-344 Input-output Parametric Models for Non-linear Systems, Part II: Stochastic Non-linear Systems.

[4] S.A. BILLINGS AND W.S.F. VOON 1986 Int. J. Control 44(3), 803-822 Stepwise-regression/prediction Error Estimation for Non-linear Systems.

[5] Vibration Ayalysis and Identification of Non-linear Structures. Short Course Notes. 26th-28th, Sept.1984. University of Manchester.

[6] J. HE and D.J. EWINS 1987 Proc. of the 5th IMAC, London, England. A Simple Method of Interpretation for the Modal Analysis of Nonlinear Systems.

[7] J.K. HAMMOND, H.R. LO and J. SEAGER SMITH 1987 Proc. of the 5th IMAC, London, England. Identification of Nonlinearities in Vibrating Systems Using Optimal Control Techniques

[8] S.F. MASRI, R.K. MILLER, H. SASSI and T.K. CAUGHEY 1984 Proc. of the Second International Conference on RECENT ADVANCES IN STRUCTURA DYNAMICS 511-520. Time Domain Analysis of Nonlinear Vibration Data.

[9] H.R. LO, J.K. HAMMOND and M.G. SAINSBURY 1988 Proc. of the 6th IMAC, U.S.A. Nonlinear System Identification and Modelling with Application to an Isolator with Hysteresis.

[10] Y.K. WEN 1976 J. Eng. Mech. Div., Proc. of ASCE, Vol.102, No.EM2 Method for Random Vibration of Hysteretic System

Table 1: Parameter Estimation of Wen's Model with n=1

True parameters: A=35530.6 α=3.0 β=-3.0

	SWEPT SINE	Err %	RANDOM (L.D.P)	Err %	RANDOM (H.D.P)	Err %
A	35452.4	0.22	38051.3	7.1	36240.8	2.0
α	2.967	1.1	2.436	18	2.943	1.9
β	-2.967	1.1	-2.354	22	-2.962	1.3

Table 2: Parameter Estimation of Wen's Model with n=2

True parameters: A=35530.6 α=3.0 β=-3.0

	SWEPT SINE	Err %	RANDOM (L.D.P)	Err %	RANDOM (H.D.P)	Err %
A	35490.7	0.11	35351.9	0.50	35379.6	0.42
α	2.921	2.6	2.907	3.1	2.930	2.3
β	-2.939	2.0	-2.939	2.0	-2.961	1.3

Note: L.D.P. represents Low Density of Point;
H.D.P. represents High Density of Point.

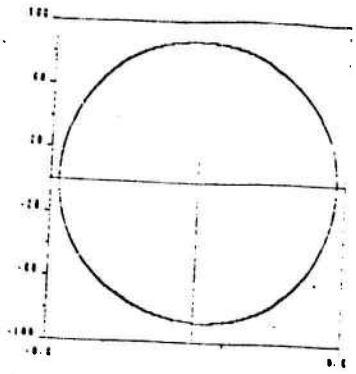

Fig.1 State vector end point obit with sine input of a nonlinear system.

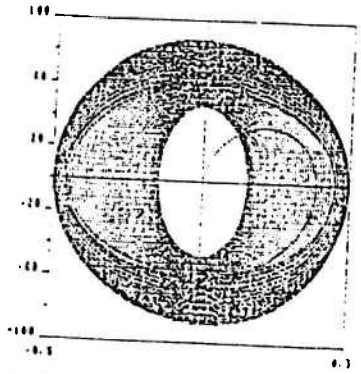

Fig.2 State vector end point obit with swept sine input of a nonlinear system.

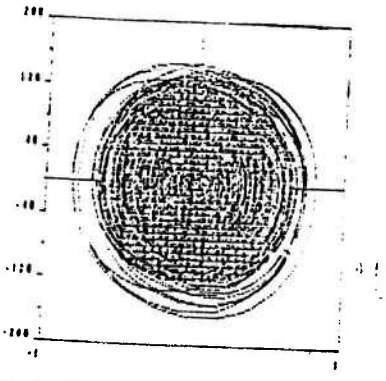

Fig.3 State vector end point obit with random input of a nonlinear system.

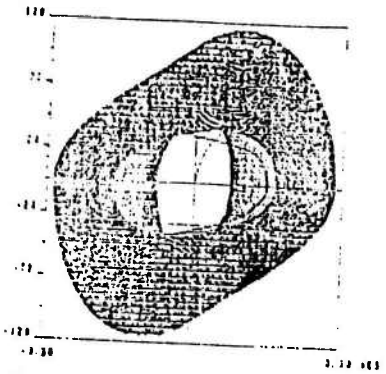

Fig.4 $(z, \dot{x})$ obit curve of a Wen's hysteretic model (n=1) with swept sine input.

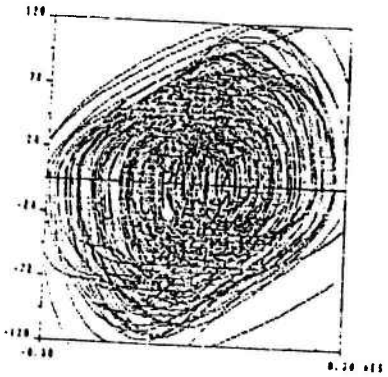

Fig.5 $(z, \dot{x})$ obit curve of a Wen's hysteretic model (n=1) with random input.

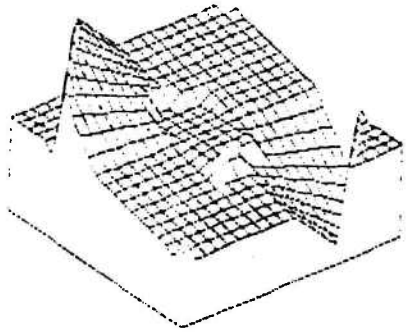

Fig.6 $\dot{z}$ vs z, $\dot{x}$ surface of a Wen's hysteretic model (n=1) with swept sine input.

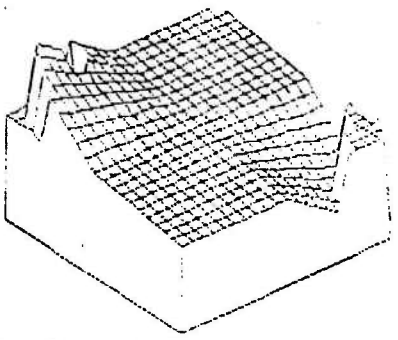

Fig.7 $\dot{z}$ vs z, $\dot{x}$ surface of a Wen's hystereic model (n=1) with random input.

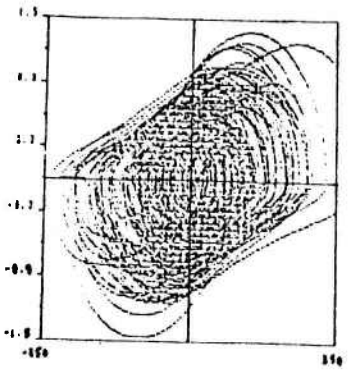

Fig.10 (z, $\dot{x}$) obit curve of a Wen's hysteretic model (n=2) with random input.

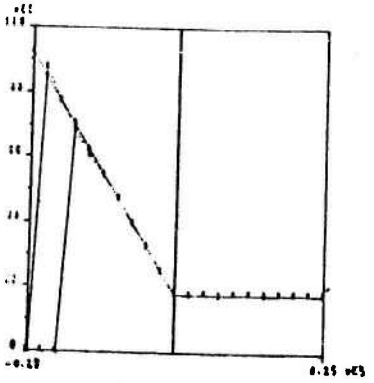

Fig.8 $\dot{z}$ vs z relation of a Wen's hysteretic model (n=1). Comparison of theoretical curve, curve from swept sine input and curve from random input.

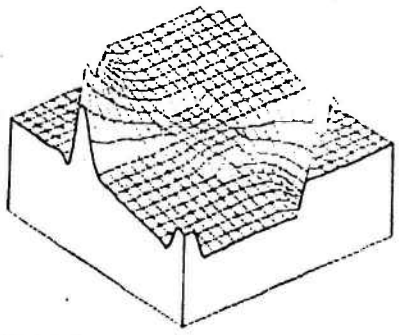

Fig.11 $\dot{z}$ vs z, $\dot{x}$ surface of a Wen's hysteretic model (n=2) with swept sine input.

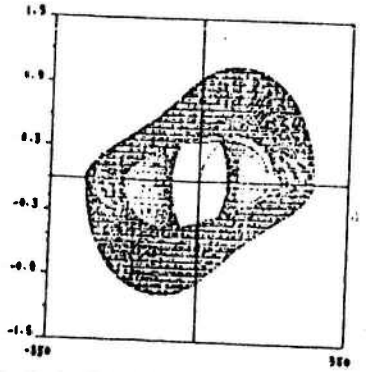

Fig.9 (z, $\dot{x}$) obit curve of a Wen's hysteretic model (n=2) with swept sine input.

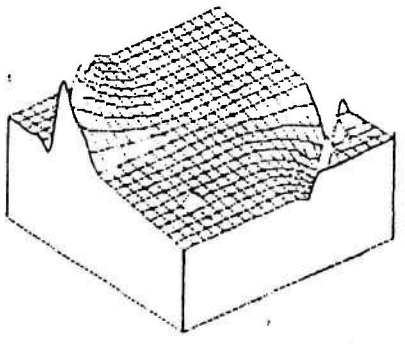

Fig.12 $\dot{z}$ vs z, $\dot{x}$ surface of a Wen's hysteretic model (n=2) with random input

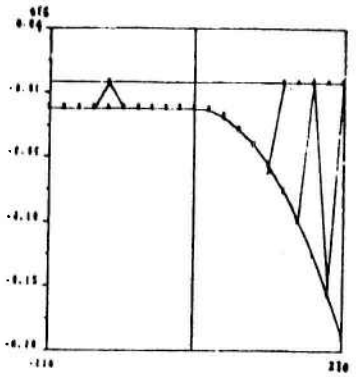

Fig.13 $\dot{z}$ vs z relation of a Wen's hysteretic model (n=2). Comparison of theoretical curve, curve from swept sine input and curve from random input.

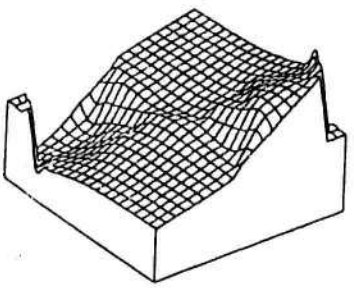

Fig.16 $\dot{z}$ vs z^*, $\dot{x}$ surface of the isolator.

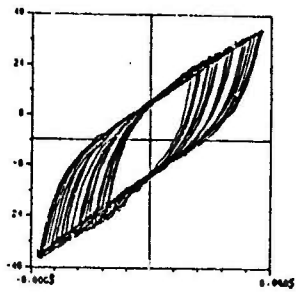

Fig.14 Hysteresis loops of an isolator with swept sine input.

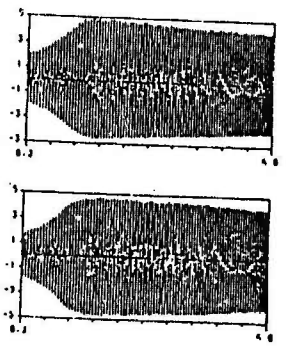

Fig.17 Comparison of the measured and the predicted accelerations of the isolator.

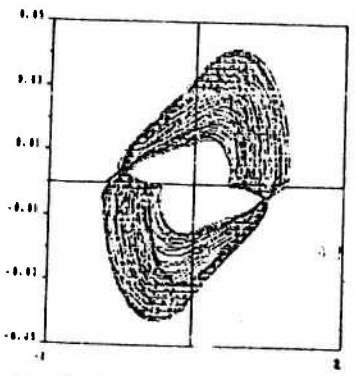

Fig.15 (z^*, $\dot{x}$) obit curve of the isolator vibration.

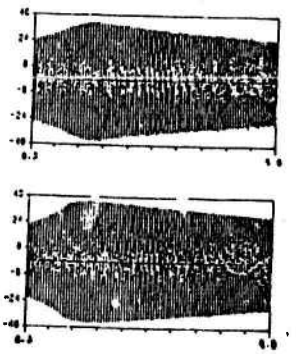

Fig.18 Comparison of the measured and the predicted hysteretic forces of the isolator.

MULTILEVEL SUBSTRUCTURING AND MODE SUPERPOSITION FOR COMPLEX STRUCTURES

L. Gazdag
Tungsram Laser Technology Inc.
Budapest, Hungary

G.T. Endrőczi
Hungarian Academy of Sciences
Central Research Institute of Physics
Budapest, Hungary

1. INTRODUCTION

During the past decades many substructure mode synthesis techniques have been proposed for the dynamic analysis of complex structures. The fundamental idea of modal synthesis method is to treat the structure as an assembly of connected substructures. The vibration modes for each component are determined separately and then synthesized into the system modes. In general, three kinds of basic modal synthesis method can be distinguishable depending on whether the substructure modes are obtained by specifying the interface as fixed [1-3], free [4-6] or loaded [7-9]. Some other hybrid variants [10-11] may also be generated by different substructure interface identification.

The substructuring and the mode superposition [12-14] are significant problems in the study of the modal synthesis techniques. The substructuring requires a realistic analytical modal of the system while from the computational point of view, it is desirable, that the mode superposition must be easy to handling large matrices and large number of generalized coordinates. Thus, the balance of the dynamic modeling and the solving method is a very important question of the dynamic analysis.

The purpose of this paper is to show the idea and applications of the multilevel substructuring. The multilevel substructuring offers greater accuracy in the dynamic modeling and reduced storage and cost of computations in the mode superposition. Practically all structures can be divided into a set of similar substructures having the same modal parameters. The primary substructures are subdivided into basic elements where it is necessary. Hereby the structural modification and the assembling are simplified and the multilevel substructuring is utilized both experimentally and theoretically.

As an illustration of the method described a structural design is presented for an airborne telescope structure. The geometrical boundary conditions are determined by the allowable relative displacement and angular deflection of the mirrors.

2. GENERAL MODAL SYNTHESIS

There are two common ideas behind all modal synthesis methods: they all regard a structure as an assembly of connected substructures and the motion of each substructure is represented by a linear combination of the substructure modes. The modal synthesis methods are essentially a Rayleigh-Ritz type discretization procedures.

The selecting of substructure modes has an assumptation that these modes can satisfy an exact eigenvalue problem. If there were an exact eigenvalue solution at the substructure level, the synthesis would be unnecessary. Unfortunately, there is no exact mathematical description for the effects of adjacent substructures. This is the reason for the broad variety of methods proposed [15-18].

In the modal interpretation the dynamical equilibrium equation can be written as follows:

$$\underline{\underline{M}}\,\ddot{\underline{q}} + \underline{\underline{K}}\,\underline{o} = \underline{0} \qquad (1)$$

The damping and the external forces are ignored for simplification reasons. The system is of order m, the number of modes taken into account.

According to (1) the uncoupled assembly of A and B substructures is given by

$$\begin{bmatrix} M^A & 0 \\ 0 & M^B \end{bmatrix} \begin{bmatrix} \ddot{q}^A \\ \ddot{q}^B \end{bmatrix} + \begin{bmatrix} K^A & 0 \\ 0 & K^B \end{bmatrix} \begin{bmatrix} q^A \\ q^B \end{bmatrix} = \begin{bmatrix} 0 \\ 0 \end{bmatrix} \tag{2}$$

The modal analysis of substructures produces modal expansion

$$\begin{bmatrix} x_a^A \\ x_c^A \\ \hline x_c^B \\ x_b^B \end{bmatrix} = \left[\begin{array}{cc|cc} \phi_{aa}^A & \phi_{ac}^A & 0 & 0 \\ \phi_{ca}^A & \phi_{cc}^A & 0 & 0 \\ \hline 0 & 0 & \phi_{cc}^B & \phi_{cb}^B \\ 0 & 0 & \phi_{bc}^B & \phi_{bb}^B \end{array}\right] \begin{bmatrix} q_a^A \\ q_c^A \\ \hline q_c^B \\ q_b^B \end{bmatrix} \tag{3}$$

where the partition of modal coordinates into interior /a,b/ and interface /c/ components has no physical meaning. The modal expansion is truncated, as dim $q <$ dim x. The interior components tend to the static condensation while the interface one towards the identity.

$$\underline{x} = \underline{\underline{\Phi}}\, \underline{q} \tag{4}$$

The synthesis of substructural modes corresponds to the assembly of substructural mass and stiffness matrices.

$$\operatorname{diag} \underline{\underline{M}}^* = \underline{\underline{\Phi}}^T \underline{\underline{M}}\, \underline{\underline{\Phi}} \tag{5}$$

$$\operatorname{diag} \underline{\underline{K}}^* = \underline{\underline{\Phi}}^T \underline{\underline{K}}\, \underline{\underline{\Phi}}$$

The required compatibility equation is reducible by a new simplified modal interface coordinate, utilizing

$$x_c^A = x_c^B \tag{6}$$

$$\bar{q}_c = \frac{1}{2}\left[\phi_{cc}^A \, q_c^A + \phi_{cc}^B \, q_c^B\right] \tag{7}$$

or generally

$$\underline{q} = \underline{\underline{T}} \, \underline{\bar{q}} \tag{8}$$

See Figure 1 for the illustration of the whole procedure, the modal transformation from physical to modal coordinates (4) and the modal assembly transformation from modal to condensed coordinates (8).

3. MULTILEVEL SUBSTRUCTURING

The substructuring determines the possible ways of the mode superposition, therefore, the first step of the optimisation is the choice of a suitable model. Generally, the main problems in the computation of dynamic response for structures are the following:

- large number of degrees of freedom
- nonlinear deformations
- difficult boundary conditions

These properties appear often together in a complex structure. However, some advantageous characteristics may also be identified on the structures, like symmetrical or periodical parts, similar substructures having similar boundary conditions and same modal parameters. Hereby the dynamical modeling offers special simplifications without any source of error.

Let us now consider a complex structural system having s substructures. The non-periodic substructures have different mode shapes and interface junctions, while the periodic substructures have the same modal parameters. Denoting the

periodic /p/ and non-periodic /r/ substructures

$$s = \sum_i p_i + r \tag{9}$$

where the sum p_i refers to the different type periodic substructures. The common mode shape matrix is $\underline{\underline{\Psi}}_s$, which has periodic and non-periodic parts in the diagonalized form, Ψ_p and $\Psi_{1\ldots r}$ respectively.

$$\underline{\underline{\Psi}}_s = \left[\begin{array}{ccccc|c} \Psi_1 & & & & 0 & 0 \\ & \ddots & & & \vdots & \vdots \\ & & \ddots & & \vdots & \vdots \\ & & & \ddots & \vdots & \vdots \\ 0 & \cdots & \cdots & \cdots & \Psi_r & 0 \\ \hline 0 & \cdots & \cdots & \cdots & 0 & \Psi_p \end{array}\right] \tag{10}$$

The Ψ_p represents the periodic substructures, it must be generated only once, notwithstanding that the modal matrix includes it p times beside the non-periodic parts. The elementary computations are reduced to the number of type of the periodic substructures. If the periodic substructures have the same modal parameters and interface junctions, the experimental and analytical modal analysis have expanded convergence.

Local nonlinearities can be separated with this kind of substructuring, which is very useful for inhomogeneous systems. The multilevel substructuring is shown in Figure 2.

4. MODE SUPERPOSITION

The mode superposition is time consuming on the largest digital computers, even for simple structural systems. This fact is due to the change of the stiffness matrix with the deformation, whereby the stiffness matrix must be recomputed at each step.

The governing eigenvalue problem using conventional mode superposition leads to the following form:

$$\underline{\underline{K}}\ \underline{\underline{Z}} = \underline{\underline{M}}\ \underline{\underline{Z}}\ \underline{\underline{\Lambda}} \tag{11}$$

where $\underline{\underline{Z}}$ is the matrix of eigenvectors and $\underline{\underline{\Lambda}}$ is the matrix of eigenvalues. It is of particular importance that both matrices $\underline{\underline{K}}$ and $\underline{\underline{M}}$ are diagonals.

If $\underline{\underline{M}}$ is positive definite, then $\underline{\underline{M}} = \underline{\underline{S}}\ \underline{\underline{S}}^T$ for any nonsingular matrix $\underline{\underline{S}}$, the problem of equation (11) is equivalent to the solution of the standard eigenvalue problem.

$$\tilde{\underline{\underline{K}}}\ \tilde{\underline{\underline{Z}}} = \underline{\underline{\Lambda}}\ \tilde{\underline{\underline{Z}}} \tag{12}$$

where $\tilde{\underline{\underline{K}}} = \underline{\underline{S}}^{-1}\ \underline{\underline{K}}\ \underline{\underline{S}}$ and $\tilde{\underline{\underline{Z}}} = \underline{\underline{S}}^T\ \underline{\underline{Z}}$.

Another transformation matrix $\underline{\underline{S}} = \underline{\underline{R}}\ \underline{\underline{D}}$ is obtained using the spectral decomposition of $\underline{\underline{M}}$

$$\underline{\underline{M}} = \underline{\underline{R}}\ \underline{\underline{D}}^2\ \underline{\underline{R}}^T \tag{13}$$

where the columns in $\underline{\underline{R}}$ are the eigenvectors and $\underline{\underline{D}}^2$ is a diagonal matrix with the eigenvalues of $\underline{\underline{M}}$.

In lumped mass analysis, where $\underline{\underline{M}}$ have zero elements on the diagonal, it is necessary to use static condensation. Rewriting the equation (11) as

$$\begin{bmatrix} K_{11} & K_{12} \\ K_{21} & K_{22} \end{bmatrix} \begin{bmatrix} z_1 \\ z_2 \end{bmatrix} = \lambda \begin{bmatrix} M_{11} & 0 \\ 0 & 0 \end{bmatrix} \begin{bmatrix} z_1 \\ z_2 \end{bmatrix} \tag{14}$$

where the notation is obvious. The condensed eigenvalue problem is

$$K_1\ z_1 = \lambda\ M_1\ z_1 \tag{15}$$

where $K_1 = K_{11} - K_{12}K_{22}^{-1}K_{21}$ and $M_1 = M_{11}$.

The multilevel substructuring allows the using of the general mode superposition methods (12) - (14). This subject is detailed in [9], [15-17].

5. APPLICATIONS

The structural design of an airborne Cassegrain telescope is presented using the multilevel substructuring. The successful structural design requires the analysis of internal loads when the structure is placed in its operating enviroment. The dynamical boundary conditions are measured on the platform, see Figure 3.

The mechanical structural design is combined with the optical quality parameters. The geometrical boundary conditions determine the relative displacement and the angular deflection of the mirrors. Due to the optical consideration the maximum relative displacement and the maximum angular deflection are

$$\begin{aligned} d_{max} &= 10^{-5}\,m \\ \alpha_{max} &= 2.5\times10^{-4}\,rad \end{aligned} \qquad (16)$$

The telescope must be a lightweight structure and it has to endure the maximum loads by radial and axial direction separately. The radial loads causes disturbances in the torsion of the mirror mountings and the whole structure, the axial load changes the focal length.

So, the basic conception of this telescope structure is that it should be a rod-like system with cross braces. This structure can afford the necessary flexibility maintaining the dynamic stability. If the components will be rods and rings the problem can be drawn up as follows: considering the geometrical and dynamical boundary conditions we have to find the optimal

numbers, sizes, coupling points, material properties of rods and rings [18].

Figure 4-6 present the vibration test results of the best combination. The structural system has 40 substructures, $p_1 = 8$, $p_2 = 16$, $p_3 = 16$, thus each is periodic.

The efficiency of computations at substructure level is

$$\eta_{sub} = \frac{s}{s - \sum(p_i - 1)} = 13.3 \qquad (17)$$

The percentage errors of natural frequencies, namely the measured / calculated ratio is under 0.6%.

6. CONCLUSIONS

The main achievement of this study is the presentation of the idea and application of the multilevel substructuring. The division of primary substructures into elementary substructures result in a lot of loaded interface junctions. The loaded - loaded combination constitutes the best overall compromise with a very accurate low frequencies. The consistent interface load as well as a symmetric interface modal parameter are proposed as optimum, outlined by Reference [19], comparing the fixed, free and loaded interface variant of modal synthesis techniques.

The multilevel substructuring has no additional source of error. Problem oriented interactive synthesis procedure is required, utilizing the periodic, symmetrical or modular parts in the substructuring. Some advantageous properties are proved as follows:

- significant decrease in the number of operations
- reduced storage
- isolation of local non-linearities
- flexible data handling
- interface compatibility

REFERENCES

[1] W.C. HURTY 1965 AIAA Journal 3/4/, 678-685. Dynamic Analysis of Structural Systems Using Component Modes.

[2] R.R. CRAIG JR. and M.C.C. BAMPTON 1968 AIAA Journal 6/7/, 1313-1319. Coupling of Substructures for Dynamic Analyses.

[3] W.C. HURTY, J.D. COLLINS and G.C. HART 1971 Computers and Structures 1, 535-563. Dynamic Analysis of Large Structures by Modal Synthesis Techniques.

[4] R.L. GOLDMAN 1969 AIAA Journal 7/6/, 1152-1154. Vibration Analysis by Dynamic Partitioning.

[5] S. HOU 1969 The Shock and Vibration Bulletin 40, 25-39. Review of Modal Synthesis Techniques and a New Approach.

[6] S. RUBIN 1975 AIAA Journal 13/8/, 995-1006. Improved Component-Mode Representation for Structural Dynamic Analysis.

[7] G.M.L. GLADWELL 1964 Journal of Sound and Vibration 1, 41-59. Branch Mode Analysis of Vibrating Systems.

[8] W.A. BENFIELD and R.F. HRUDA 1971 AIAA Journal 9/7/, 1255-1261. Vibration Analysis of Structures by Component Mode Substitution.

[9] L. MEIROVITCH 1980 Computational Methods in Structural Dynamics. Alphen aan den Rijn, Sijthoff - Noordhoff.

[10] R.H. MACNEAL 1971 Computers and Structures 1, 581-601. A Hybrid Method of Component Mode Synthesis.

[11] R.M. HINTZ 1975 AIAA Journal 13/8/, 1007-1016. Analytical Methods in Component Modal Synthesis.

[12] N.F. MORRIS 1977 Computers and Structures 7, 65-72. The Use of Modal Superposition in Nonlinear Dynamics.

[13] K.J. BATHE and S. GRACEWSKI 1981 Computers and Structures 13, 699-707. On Nonlinear Dynamic Analysis Using Substructuring and Mode Superposition.

[14] D.E. NEWLAND 1987 Journal of Sound and Vibration 112/1/, 69-96. On the Modal Analysis of Non-conservative Linear Systems.

[15] K.J. BATHE and E.L. WILSON 1973 International Journal for Numerical Methods in Engineering 6, 213-226. Solution Methods for Eigenvalue Problems in Structural Mechanics.

[16] R.D. HENSHELL and J.H. ONG 1975 Earthquake Engineering and Structural Dynamics 3, 375-383. Automatic Masters for Eigenvalue Economization.

[17] A.K. NOOR 1981 Computers and Structures 13, 31-44. Recent Advances in Reduction Methods for Nonlinear Problems.

[18] L. GAZDAG 1986 37th Congress of the International Astronautical Federation, Innsbruck, Austria, October 4-11. Dynamic Analysis of Periodic Structures by an Improved Modal Synthesis Technique.

[19] A. CURNIER 1983 Journal of Sound and Vibration 90/4/, 527-540. On three Modal Synthesis Variants.

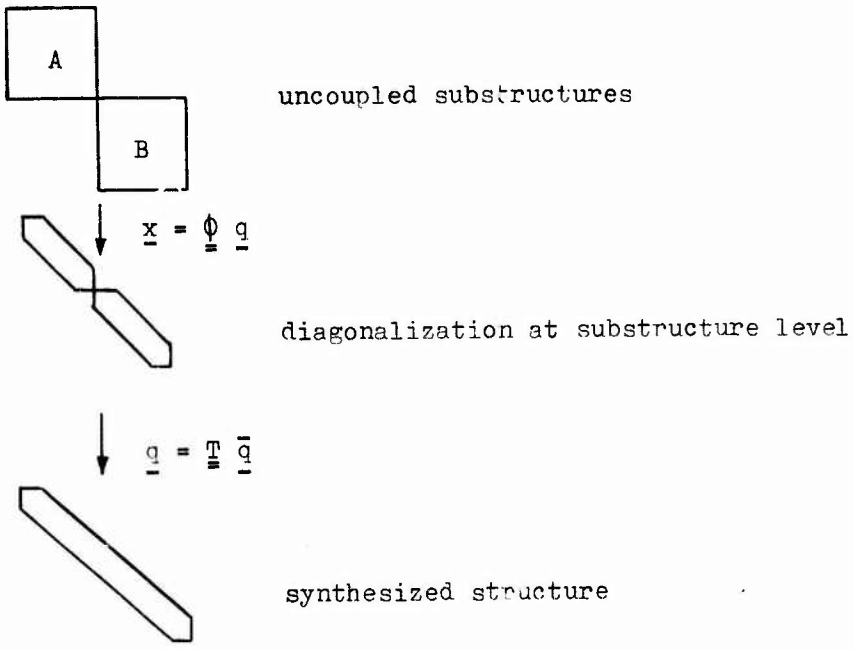

Figure 1. Illustration of modal synthesis.

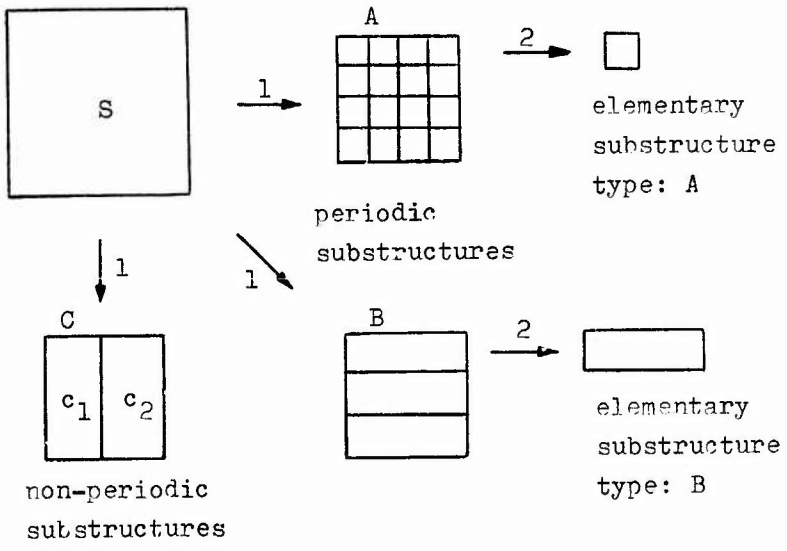

Figure 2. Illustration of multilevel substructuring.

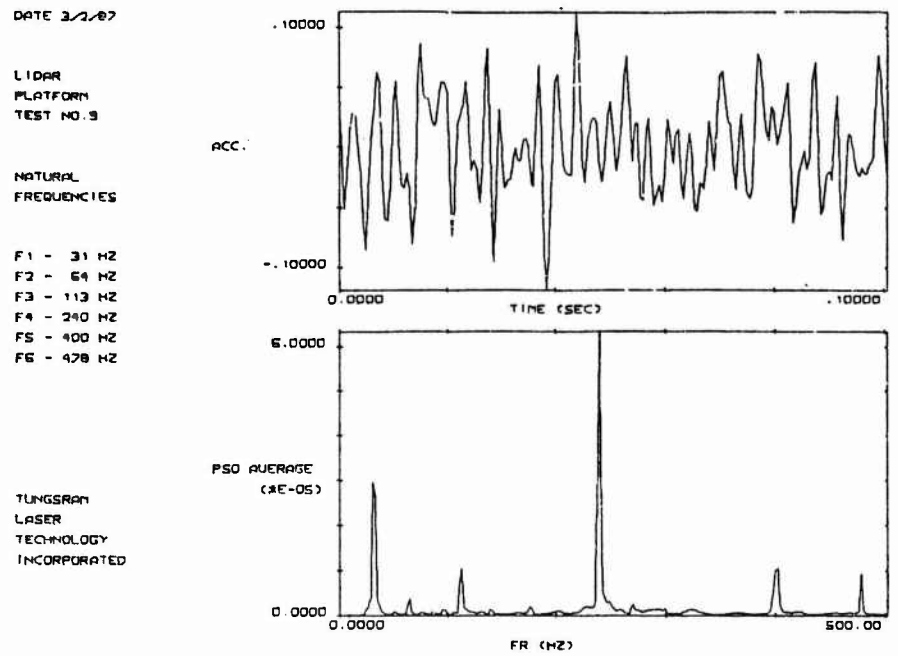

Figure 3. Platform test results.

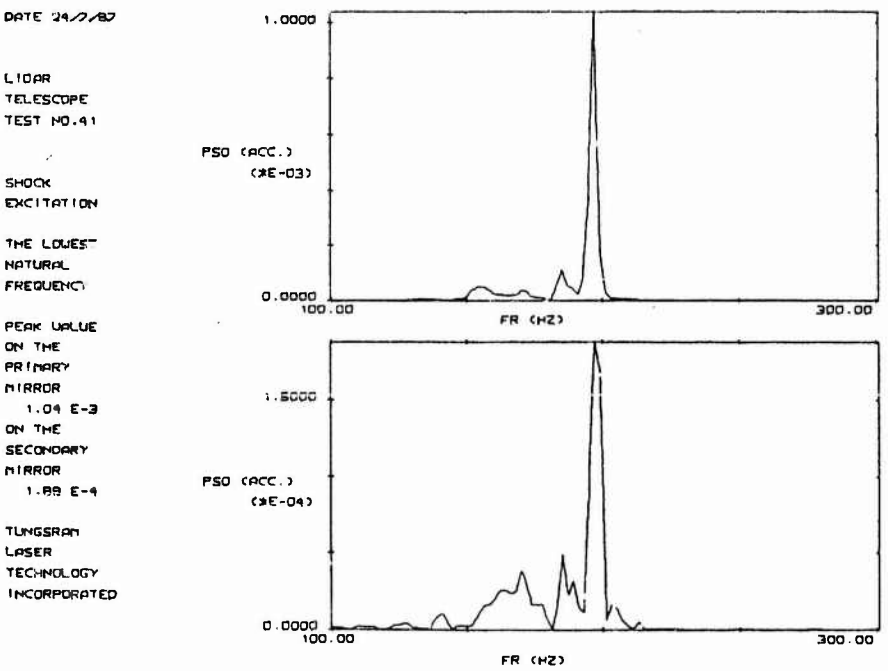

Figure 4. The lowest natural frequency of the telescope structure.

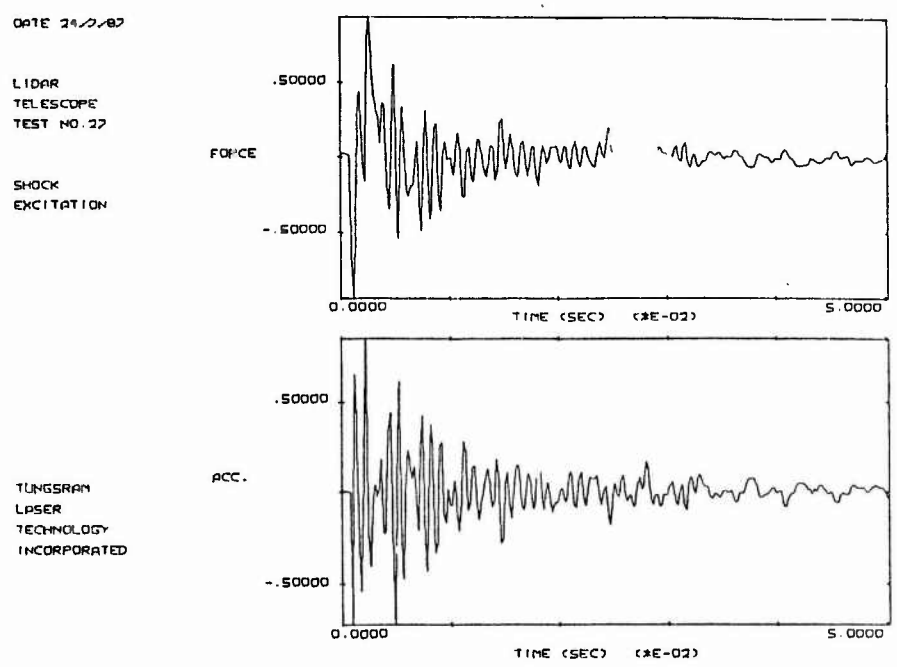

Figure 5. Shock excitation.

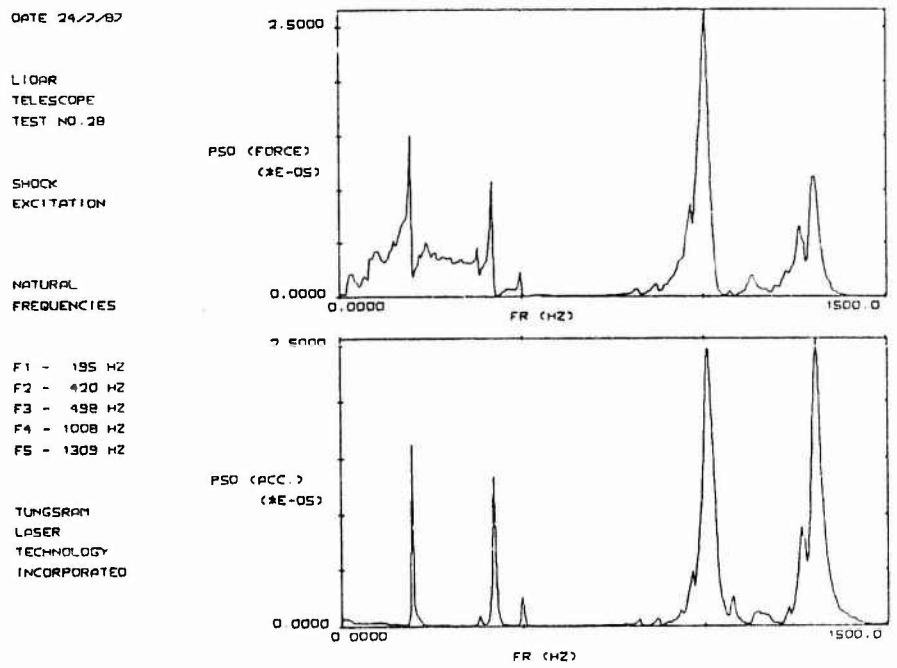

Figure 6. Frequency analysis of the telescope structure.

METHODS USING FREQUENCY-RESPONSE FUNCTIONS FOR THE ANALYSIS OF ASSEMBLED STRUCTURES

P.O. Larsson

ASEA BROWN BOVERI Corporate Research
5405 Baden-Dättwil, Switzerland

ABSTRACT

Substructuring is an effective tool for the analysis of assembled mechanical structures. A critical evaluation was made of the special class of substructuring methods making use of frequency-response functions that can be determined by theoretical methods or by measurements. The use of experimental data is of great advantage when dealing with structures of which the dynamic behaviour is influenced by phenomena that are difficult to describe theoretically. The possibilities and limitation when using two different formulations that have been suggested for this type of analysis were considered. Further, a study of the sensitivity to errors in the input was attempted in a more quantitative way than in previous works. Finally some further examples on what performance can be expected from these methods in practice are added to those already found in the literature.

1. INTRODUCTION

The dynamic properties of an assembled system can be predicted on the basis of theoretical and experimental analysis of its sub-systems using different techniques of substructuring. In the many different applications of substructuring various aspects are of importance. In most cases the advantages are direct consequences of the inherent modularity. The substructuring methods in the present approach are one step towards an optimal use of experiments and theoretical modelling in a fruitful combination to determine reliably the dynamic properties of a structure and to obtain good descriptions that can be used for analysis and prediction of its dynamic behavior. This is especially useful when dealing with structures whose dynamic behavior is influenced by phenomena that are difficult to model theoretically, for instance assembled, non-homogeneous structures with bolted, riveted, glued or welded joints. The damping of a structure is a quantity that must almost always be determined from measurements on the complete structure or on sections of it. Almost exclusively the methods for substructuring are limited to linear structures. After the coupling the substructures are forced to move together by the introduction of coupling constraints. Thus, mathematically, coupling systems together is nothing other than the determination of various properties of constrained linear systems. A manifold of methods, or of versions of the same methods, has been suggested for calculating properties of an assembled structure knowing those of its components.

In this work important characteristics of the methods that primarilly deal with the determination of the response properties were studied. The response properties are most often in the form of transfer functions or frequency response functions, and these methods are here referred to as COUPLING USING RESPONSE FUNCTIONS. The goal with this work was to assess the possibilities to use these methods as practical tools and to identify weaknesses and to suggest improvements. Because of the availibility of many

earlier studies and good review papers in this field, the present paper is concentrated on some selected problems.

A short overview is given in the next section in which a few comments on other alternative methods are included. A detailed treatment of the possibilities and limitations when using some different formulations is given. An attempt has been made to find a useful measure for the errors in the frequency-response functions of the coupled structure resulting from errors in the data from the components. Finally some experience and results gained from applications to a laboratory-structure are presented.

2. OVERVIEW AND BACKGROUND

Most of the methods that have been suggested for substructuring can be sorted into one of two categories depending on whether free-vibration properties or response properties are primarily being used to characterise the substructures. The difference is not always clear since, for linear systems, the response properties and free-vibration properties are closely related. With the present objectives of a combined theoretical and experimental approach it is essentially a question of sorting out and studying those methods that work well in combination with a set of properties that has been derived mainly from measurements.

The first category of methods is characterised by the use of the free-vibration properties or the modal properties to describe the behavior of the structures. This is referred to as MODAL COUPLING and is essentially an application of methods belonging to the large class of methods of component-mode synthesis or CMS, using measured modal parameters. Common to these methods is the use of the coefficients in a sum of mode-shapes as generalised coordinates [1]. Most of these methods essentially mean formulating a constrained eigenvalue problem from which the free-vibration properties of the coupled system can be found. A rigorous treatment and a good summary of the use of CMS methods in conjunction with measured modal parameters has been presented by Craigh [2]. An application, similar to this presented within this work, was presented in [3].

In this work those methods belonging to the second category have been studied. COUPLING USING RESPONSE FUNCTIONS essentially means calculating the frequency-response functions (FRFs) of an assembled structure knowing those of the substructures. In some versions the dynamic stiffness, or equivalently mechanical impedance, plays a central role and correspondingly in those cases these methods are then referred to as stiffness- or impedance coupling.

The FRFs can either be derived from a theoretical model or be measured [4]. In the latter case it can either be used directly, as measured, or after a curve-fit and following regeneration from a set of modal parameters using the equation

$$I_{ij}(\omega) = R_{lf,ij} + \sum_r \frac{-\omega^2 \cdot {}^r\Phi_i \cdot {}^r\Phi_j}{\omega^2 - \omega_r^2 - i \cdot \eta_r \cdot \omega_r^2} + R_{hf,ij} \qquad (1)$$

for an FRF of inertance type. ${}^r\Phi$ is the mode-shape vector, ω_r the natural frequencies and η_r, the modal damping factors. The $R_{lf,ij}$ and $R_{hf,ij}$ are the low- and high-frequency residual terms representing those modes not included as individual terms in the sum. If the structure is free to move like a rigid body its inertial properties must be included in a good model.

This can either be done by including the corresponding rigid-body modes or representing them with the low-frequency residual terms [5]. A real advantage over the modal coupling have the present methods in situations where the required modal parameters are not so readily available. This is the case for structures having very close natural frequencies or high damping. The FRFs are still well defined as long as the structure can be described as linear. However in this case it is not so easy to recognise the contribution from each individual mode and thus to determine the modal properties.

The basic ideas of impedance coupling were presented long ago by Bishop and Johnson [6]. Ewins and co-workers, among others, have investigated the usefulness of these methods as engineering tools [7]. Goyder studied the propagation of errors in the case when only two FRFs were coupled together and found that the largest errors would occur at the natural frequencies of the coupled structure [8]. A comprehensive review of the possibilities and problems using these methods is presented in [9]. It was pointed out how problems with occurrence of erroneous peaks and a high error sensitivity, which tend to spoil the results when damping is low and modes well separated, are much less pronounced when damping is high and modes closely spaced. This is of interest because it is in those cases that the use of modal coupling becomes less attractive. A situation where at least one or a few components are included for which the modal properties are undeterminable is very common in practice. One example is when a structure is mounted to a foundation with less pronounced modal behavior than the structure itself. This motivates a general interest in coupling methods using response functions even in cases where modal coupling might be an alternative.

Another problem often discussed is that of defining a useful set of coordinates. During measurements these corresponds to the points and directions in which measurements are made. For beam-type or slender structures proper coupling constraints are most easily formulated using rotations as coordinates. It is well known that these are difficult to handle when making measurements [10]. It is quite obvious and has also been shown that it is not satisfactory just to leave the rotational coordinates out without making sure that compatibility is being properly enforced when formulating the constraints between only the translational coordinates. Strictly speaking, this is not a problem only when coupling using response functions, but always when formulating coupling constraints when the deformation of the substructures is expressed using a limited set of coordinates.

In [11] a comparison was made between modal coupling and the present methods. It was suggested that these methods should be seen as a complement to the modal methods rather than a substitute. These authors used a set of equations which is different from those normally used in stiffness coupling and which accepts very general forms of coupling constraints. The advantages of using different formulations are treated in the following.

3. COUPLING EQUATIONS

STIFFNESS COUPLING or IMPEDANCE COUPLING has been well described by Ewins[4]. This method can be easily understood by looking at the inverse of the receptance matrix, $\alpha^{-1}(\omega)$, as a dynamic stiffness matrix, $Z(\omega)$, for each substructure, a and b.

$$Z_a(\omega) = (\alpha_a)^{-1} \qquad Z_b(\omega) = (\alpha_b)^{-1} \qquad (2)$$

After having introduced the concept of dynamic-stiffness matrix it is clear that the dynamic stiffness matrices of coupled systems can be found by a normal matrix assemblage as it is often used in structural dynamics, for instance when assembling the system stiffness matrix from the stiffness matrices of the elements in a finite element model. The constraints in this formulation are introduced by setting the interface coordinates on both structures equal. The final formula for the frequency response matrix of the coupled system includes three matrix inversions and is of the form

$$\alpha_c = \begin{bmatrix} Z_a^{ss} & Z_a^{si} & 0 \\ Z_a^{is} & Z_a^{ii} + Z_b^{ii} & Z_b^{is} \\ 0 & Z_b^{si} & Z_b^{ss} \end{bmatrix}^{-1} \tag{3}$$

Superscript i refers to the interface coordinates and s to the rest. Another approach will result in equations with which very general forms of constraints can be handled. Therefore, this method will be referred to as THE METHOD OF GENERAL CONSTRAINTS. It was presented and also used for this type of coupling by Crowley and Vold etc. [12] who presented a slightly heuristic derivation only for the case in which the response properties are expressed as transfer functions in the Laplace domain. Here any set of constraints that can be expressed as a system of linear equations of the form

$$C^T \cdot X = 0 \tag{4}$$

can be used. Where C^T is the $N_c x (N_a+N_b)$ linear constraint matrix expressing the N_c geometric constraints introduced through the coupling. X is the vector of complex response amplitudes including all $(N_a + N_b)$ coordinates of both sub-structures, a and b.

$$X = \begin{Bmatrix} X_a \\ X_b \end{Bmatrix} \tag{5}$$

The equations of motion of the linear system under action of a set of linear constraints can be written down using the Lagrange's equations of motion and taking the constraints into consideration using the Lagrange multiplier technique [13]. By specialising to sinusoidal motion and introducing complex notation a useful expression for the FRF of the coupled structure can easily be found. It can be shown that the FRF-matrix of the coupled system can be written as

$$\alpha_c = \left(1 - \alpha \cdot C \cdot (C^T \cdot \alpha \cdot C)^{-1} \cdot C^T \right) \cdot \alpha \tag{6}$$

where α is the frequency-response matrix of the total system before coupling partitioned in accordance with (5),

$$\alpha = \begin{bmatrix} \alpha_a & 0 \\ 0 & \alpha_b \end{bmatrix} \tag{7}$$

It should be noted that the order of the matrix α_c is the same as the order of the FRF-matrix before coupling, α. Thus if two coordinates are set equal by the coupling constraints both will exist as separate coordinates in α_c after the coupling. However the corresponding columns and rows will then be equal.

Both equations (3) and (6) are valid if the receptances, α_{ij}, are replaced by the corresponding mobilities or inertances. That is, the ratio between the velocities or accelerations respectively, and forces. Both of the equations can also easily be generalised to include the cases where more than two substructures are involved without having to perform the coupling in many steps, although this might be useful in some cases.

3.1 Applicability

In many applications both suggested equations are equivalent and either can be used to give the same result. In certain cases the differences are important. For proper use it is important to know the limitation of the equations. Both suggested equations are useful as long as the included matrix inversions are well defined. Thus using equation (3) the FRF-matrices of all substructures and of the coupled structure must exist and must not be singular. Thereby many practically interesting cases are excluded. Equation (6) is useful as long as the expression $(C^T\alpha\ C)$ is invertable. This expression contains only those coordinates included in the coupling constraints. In the special case of coupling where interface coordinates on both structures are simply set equal, the elements of the coupling matrix C will be 1, -1 or zero, and the expression $(C^T\alpha\ C)$ equals the sum of the partitions corresponding to the interface coordinates of each FRF-matrix.

When investigating the nature of these matrix expressions, whether they are invertable or not, a distinction should be made between the true FRF-matrix of a structure and an eventual estimate for it. It may very well be the case that an estimate for the FRF-matrix, or a part of it, that has been generated from a limited set of modal data using the formula (1), is singular although this is not the case for the real structure.When using equation (1) to generate a FRF-matrix or a part of it, but neglecting the influence from residual terms and including eventual freedom to move like a rigid body in terms of rigid-body modes. a criterion for the resulting matrix not to be singular is that the number of linearly independent mode-shape vectors included equals the number of coordinates. This is not always the case after leaving higher modes out [4]. Refinement of the models by inclusion of more modes or residual terms will often remove the singularity.

A situation where this is not the case is when many coordinates have been defined on a structure or on a part of it that is practically rigid. Then a dependence of some of the coordinates resulting from the rigidity will prevent the mode-shapes from being linearly independent. If it is plausible to describe the structure as rigid, then the dependence of the coordinates must be accepted rather than be disguised by the inclusion of some small and approximate residual terms.

Thus in situations where the respective matrices in equations (3) or (6) are singular this is either a result of a too coarse approximation or corresponding to a physical fact. Considering the matrix inversion included in each algorithm it is clear that equation (6) is less restrictive in its

applicability than equation (3). The few remaining situations where equation (6) is not applicable correspond to situations where the number of coordinates included in the coupling constraints is unneccessarily high in order to prescribe compatibility properly.

3.2 Enforcement of compatibility

Selecting an improper set of coordinates can lead to break-down of the used algoritm. However, the choice of coordinates is often dictated by the need to assure continuity of the displacement field of the coupled structure. This is often achieved by setting translations and rotations equal. Since rotations are difficult to measure directly they are often expressed in terms of translations. Whenever a rotation can be expressed as a linear combination of translations the method of general constraints in equation (6) is ideally suited. Thereby the need to determine the FRFs for rotational coordinates explicitly in a first step is eliminated. Only the proper rotational compatibility must be assured by finding the coupling constraints between a set of translational coordinates.

Several expressions are given in the literature for calculation of rotations from a set of translations. In the simplest case an inclination is calculated from the translations of two points, which is exact if the structure is locally rigid and always in the limiting case when the two points are infinitely close [4,14]. More sophisticated methods to determine rotations have been suggested that assume rigid-body motion of a group of points on a part of a structure [15,16].

Another possible approach is based on the interpolation of the displacement field between the points of translational coordinates in order to find expressions for the rotations [13]. Then the distance between the points of translational coordinates can be choosen larger without introducing systematic errors. The risk of poor accuracy resulting from cancellation of terms is thereby reduced. This means loss in relative accuracy when subtracting two almost equal quantities from each other that are represented with a limited accuracy. Also in this case the resulting constraints are linear and can thus conveniently be treated when using equation (6).

4. PROPAGATION OF ERRORS

At certain frequencies very small changes in the response levels of the substructures will result in big changes in the FRFs of the coupled structure. This is an inherent feature of the calculations. Intuitively this can be understood by realising that sharp peaks in the FRF of the coupled structure will frequently occur at frequencies where the response levels of the substructures are changing smoothly. In practice this will lead to a high error sensitivity. Errors in the individual FRFs of a substructure will result in a set of FRFs that do not correspond to a unique set of modal parameters according to the equation (1). Such a set is said not to be self-consistent. This will not only result in lower accuracy of the FRFs of the coupled structure but to FRFs that are difficult to interpret because of the occurrence of erroneous peaks or so called 'ghost-peaks'.

These phenomena will now be tackled quantitatively, and a measure of error will be sought that could be useful in practice. An exact error analysis for both equations (3) or (6) is difficult. Three matrix inversions are included in equation (3). Therefore the propagation of

errors during matrix inversion were believed to be of interest, although not immediately giving information about the error sensitivity of the whole sequence of operations. How an error in a matrix A influences the accuracy of the solution x to the linear equation system A x = b can be studied using the methods in [17]. The maximum-norm of a vector x and the corresponding matrix-norm of the matrix A are defined as

$$\|x\| = \underset{i=1,N}{MAX}\{\,|x_i|\,\} \tag{8}$$

$$\|A\| = \underset{j=1,N}{MAX}\left\{\,\sum_{i=1,N}|A_{ij}|\,\right\} \tag{9}$$

Using a procedure similar to those in [17], an upper limit for the error δx in the solution x can be expressed in terms of the errors δA in the matrix A as

$$\frac{\|\delta x\|}{\|x\|} \le \kappa(A+\delta A)\cdot\frac{\|\delta A\|}{\|A+\delta A\|} \tag{10}$$

$\kappa(A)$ is the condition number of a matrix A with respect to the given norm, defined as $\kappa(A)=\|A\|\cdot\|A^{-1}\|$. This can be used to find an upper limit for the errors in the inverse of matrix A, $\delta(A^{-1})$, by realising that the inversion of a matrix can be looked upon as the simultaneous solution of a set of linear equation written as

$$A\cdot A^{-1}=I \tag{11}$$

Each column of the inverse A^{-1} is the solution to a linear system of equations with the righthand side equal to $(0...1..0)^T$. The inequality (10) is now used with x replaced by the j:th column of A^{-1}. Using that

$$\|(j\text{ th col. of }A^{-1})\| \le \underset{i,j=1,N}{MAX}\left\{\,\left|(A^{-1})_{ij}\right|\,\right\} \qquad (j=1,N) \tag{12}$$

$$\underset{j=1,N}{MAX}\{\,\|(j\text{ th col. of }\delta(A^{-1}))\|\,\} = \underset{i,j=1,N}{MAX}\left\{\,\left|\delta(A^{-1})_{ij}\right|\,\right\} \tag{13}$$

an upper limit of the error in the inverse of the matrix A can be formulated as

$$\frac{\underset{i,j=1,N}{MAX}\left\{\left|\delta(A^{-1})_{ij}\right|\right\}}{\underset{i,j=1,N}{MAX}\left\{\left|A^{-1}{}_{ij}\right|\right\}} \le \kappa(A+\delta A)\cdot\frac{\|\delta A\|}{\|A+\delta A\|} \tag{14}$$

In a numerical experiment the FRFs for two structures were generated theoretically. These were used in coupling calculations before and after polluting them with random noise. The generated FRFs are not shown but the condition number of the FRF-matrices for each of the two components and the

coupled system are shown in figures 1a,b and c. The natural frequencies in each case are indicated with arrows. At each natural frequency the condition number is very large. The erroneous peaks in the FRFs of the coupled system that resulted when using polluted data is marked with a circle in figure 2. Each of them can be identified with a peak in some of the curves showing the condition number. Also when the condition number is a relatively coarse measure for the errors during matrix inversions and the three condition numbers do not directly give information about the error sensitivity of the complete expression (3), the result is in perfect correspondence with earlier assumptions of an error sensitivity that varies strongly with the frequency and is very high in the vicinity of the natural frequencies of any of the involved structures.

5. APPLICATION TO A REAL STRUCTURE

The test structure can be seen in figure 3. It consists of three steel tubes of the same lengths that can be mounted very tightly together thanks to the relatively thick flanges with holes for bolts. Various configurations were assigned short names to make reference quick and convenient. Thus 'A' is a single tube-section mounted on the plate, 'B' is one free section, 'AB' means two sections on top of each other on the base-plate and 'BB' means two or three sections mounted together but otherwise free. The analysis was made in one plane. In the range 0 to 3.2 kHz the tubes, either free or fixed to the base plate, have well separated modes. THe modal data of components A and B are shown in table 1. The four modes of B within this range can be seen in figures 4 a and b. For A and B the whole upper half of the FRF matrix in the defined frequency range 0 to 3.2 kHz was measured. For the built-up configurations AB and BB a limited set of FRFs were measured and analysed for later comparison with corresponding calculated FRFs. Several estimates of the modal parameters and the residual terms were found by curve-fitting using the program MODENT [18]. The low-frequency residual terms could be checked against estimates resulting from calculation of the inertial properties knowing the mass distribution. In most cases the various estimates for a quantity were very similar. Having measured and analysed all FRFs required for configurations A and B calculation of the properties of various assembled configurations was attempted and the solution was compared to the results from measurements. Here any of the equations (3) and (5) could be used.

The coordinates used when studying the structure AB are shown in figure 5. At the coupling three of these from each component were included in the constraints. Coupling analysis was here made using the regenerated FRFs. Two calculated FRFs of the coupled system can be seen in the figures 6 a and b together with their measured counterparts for comparison. Both calculated and measured FRFs could be analysed and a comparison of the resulting natural frequencies and damping factors is shown in table 2.

Similarly in figure 7, a measured FRF for the configuration BB is shown together with the corresponding FRF when calculated using FRFs for the substructures that were regenerated from modal data. In figure 8 a FRF is shown that has been calculated using FRFs for one component directly as it was measured. The natural frequencies for the substructures(S) and for the coupled structure(C) are indicated with arrows. The well known difficulties with high error sensitivity and the occurrence of spurious peaks were recognised. The condition number for the FRF-matrix of the substructures is shown in figure 9. Calculating the condition number from the measured FRFs or using those regenerated from modal data resulted in only minor differences. Also here a correlation between peaks in the condition number and the occurrence of large errors was found.

6. CONCLUSIONS

The methods for analysis of coupled structures that are dealing with the determination of response properties were studied. Since the general principles and problems are known, the attention was concentrated on a few special problems after a very short review.

It is always important to know the limits of the equations that are being used. Using a special formulation, here referred to as THE METHOD OF GENERAL CONSTRAINTS, all well formulated problems can be treated uniformly. At the same time there are various ways in which the coupling constraints can be introduced. This offers many possibilities to enforce proper rotational compatibility when dealing with slender structures.

The main problem using these methods is the high accuracy of the input data that is required. Errors in the input data will not only reduce the accuracy but make the result hard to interpret. Ideas for finding a useful quantitative measure for the error sensitivity were tried out. It resulted in a fairly coarse measure because of the complicated algebra involved. Still a clear correlation between the suggested error measures and the errors in the result was found which can be interpreted as a verification of earlier assumptions about a strongly varying error sensitivity. The experience from this and earlier works shows that these methods can reall deliver useful results if care is taken in their application.

REFERENCES

1. R.R. CRAIGH, Jr. 1981, Structural Dynamics, - An Introduction to Computer Methods, New York: John Wiley & Sons.
2. R.R. CRAIGH, Jr June 1985, Proc.: Combined Experimental/Analytical Modeling of Dynamic Structural Systems, ASCE/ASME Mechanics Conference, Albuquerque, New Mexico, p.1-30, A review of the time-domain and frequency-domain component mode synthesis methods.
3. D. MARTINEZ, T.CARNE, D.GREGORY, K.MILLER April 1984, Report, Sandia National Laboratories, Albuquerque, New Mexico, Combined experimental/analytical modeling using component mode synthesis.
4. D.J. EWINS 1984, Modal Testing: Theory and Practice, Hertfordshire, U.K: Research Studies Press Ltd.
5. M.L. LAMONTIA February 1984, Proc.: 2nd IMAC (Int. Modal Analysis Conf.), Florida, On the determination and use of residual flexibilities, inertia restraints and rigid body modes.
6. BISHOP JOHNSON 1960, The Mechanics of Vibration, Cambridge, U.K: Cambridge University Press.
7. D.J. EWINS, J.M.M. SILVA, G. MALECI 1980, Shock and Vibration Bulletin, Vol.50, No.2, Vibration Anlysis of a helicopter plus an externally-attached structure.
8. H.G.D. GOYDER 1980, Journal of sound and vibration, 86(2), Methods and application of structural modelling from measured structural frequency response data.
9. D.J. EWINS June 1985, Proc: Combined Experimental/Analytical Modeling of Dynamic Structural Systems, ASCE/ASME Mechanics Conference, Albuquerque, New Mexico, p.31-48, Modal test requirements for coupled structure analysis using experimentally-derived component models.

10. D.J. EWINS, P.T. GLEESON 1975, Shock and Vibration Bulletin, Vol.45, No.5, Experimental determination of multidirectional mobility data for beams.

11. J.R. CROWLEY, S.M. CROWLEY, G.T. ROCKLIN, T.E. GORMAN 1985 Proc.: 3rd IMAC (Int. Modal Analysis Conf.), Florida. A comparison of SMURF and modal modeling.

12. J.R. CROWLEY, G.T. ROCKLIN, A.L. KLOSTERMAN, H.VOID February 1984, Proc.: 2nd IMAC (Int. Modal Analysis Conf.), Florida, Direct structural modification using frequency response functions.

13. P.O. LARSSON January 1988, Research Report, ASEA Brown Boveri Corporate Research, CH-5405 Baden/Dättwil, Switzerland, Methods using frequency-response functions for the analysis of assembled mechanical structures.

14. W.-H.CHEN, J.-S. CHERNG 1985, Journal of sound and vibration, 103(1), Modal synthesis via combined experimental and finite element techniques with consideration of rotational effects.

15. M.FURUSAWA,T.TOMINAGA February 1986, Proc.: 4th IMAC (Int. Modal Analysis Conf.), Los Angeles, Rigid body mode enhancement and rotational of estimation for experimental modal analysis.

16. J.CROWLEY,D.J.BROWN, T.ROCKLIN February 1986, Proc.: 4th IMAC (Int. Modal Analysis Conf.), Los Angeles, Uses of rigid body calculations in test.

17. G.DAHLQUIST, A. BJÖRK 1974, Numerical Methods, Eaglewood Cliffs, USA: Prentice Hall Inc.

18. D.A. ROBB 1986, Program Manual, Imperial College (Mech.Eng.Dpt.), London,UK, User's Guide to Program MODENT 5.1.

TABLES AND FIGURES

MODAL DATA			
COMPONENT 'A'		COMPONENT 'B'	
FREQUENCY Hz	DAMPING Loss factor, η	FREQUENCY Hz	DAMPING Loss factor, η
62.1	0.005	402.5	0.003
543.0	0.002	1245	0.009
1097	0.012	2323	0.005
1545	0.002	2650	0.005
1692	0.001		
2847	0.002		

Table 1. Measured modal parameters of component A and B.

MODAL DATA OF STRUCTURE 'AB'			
Estimated from CALCULATED FRFs		Estimated from MEASURED FRFs	
FREQUENCY Hz	DAMPING Loss factor, η	FREQUENCY Hz	DAMPING Loss factor, η
26	?	27	?
119.4	0.014	98.1	?
394.4	0.020	406.2	0.015
766.2	0.014	725.0	0.011
1306	0.005	1294	0.005
1856	0.003	1819	0.004
2494	0.003	2482	0.005
> 3200	-	3145	0.003

Table 2. Comparison between modal parameters of structure AB that have been derived from calculated and measured FRFs respectively

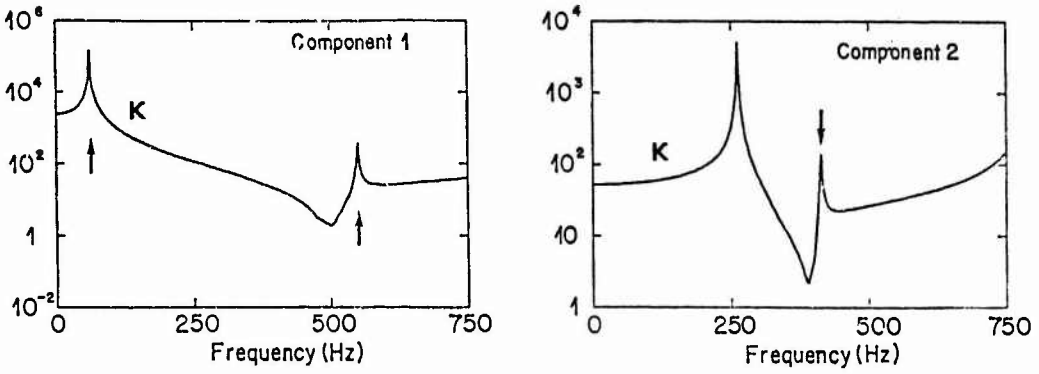

Figure 1a,b. Condition number of FRF-matrices that have been generated from a set of modal parameters. The natural frequencies of each component are indicated with arrows.

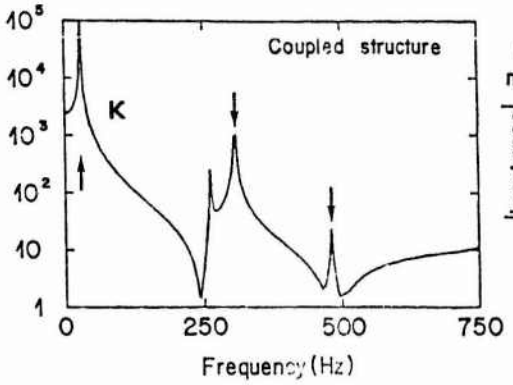

Figure 1c. Condition number of the FRF-matrix of the coupled structure. The natural frequencies of the coupled structures are indicated with arrows.

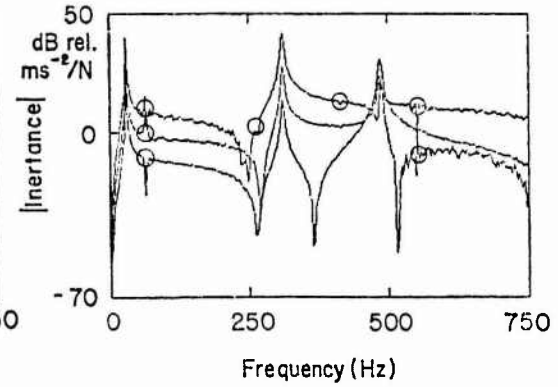

Figure 2. Sample FRFs of the coupled structure. The circles indicate the occurence of erroneous peaks.

Figure 3. Photo of the test structure. Two tube sections mounted on the base plate.

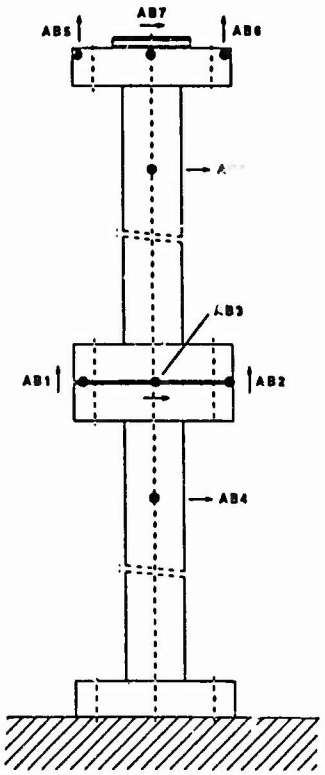

Figure 5. Definition of coordinates of structure AB.

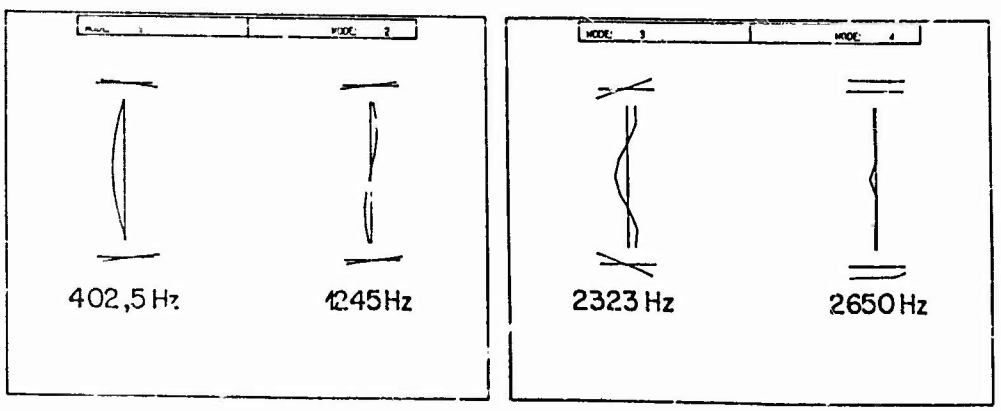

Figure 4ab. The four lowest modes of component B. Three bending modes and one longitudinal mode.

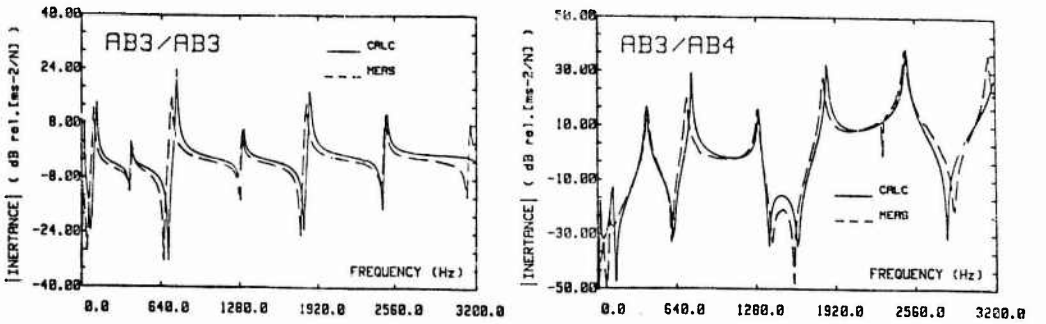

Figure 6ab. Calculated and measured FRFs of structure AB.

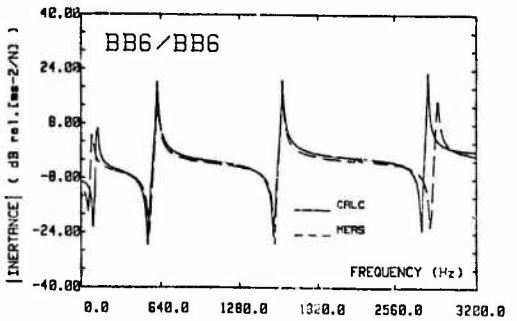

Figure 7. Calculated and measured FRFs of structure BB.

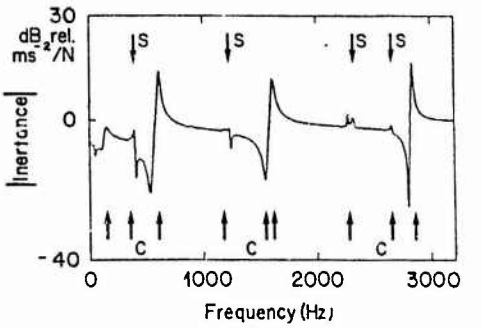

Figure 8. FRF of structure BB. Calculated using measured FRFs for one of the substructures and FRFs generated from a set of modal data for the other.

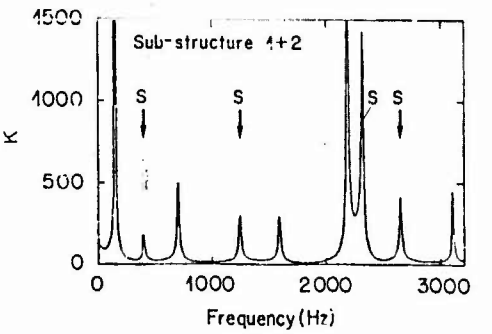

Figure 9. Condition number of the FRF-matrices of the substructures. Calculated using measured FRFs.

The arrows marked S and C indicate the natural frequencies of the substructures and of the coupled structure respectively.

LMS-LINK CORRELATING AND VALIDATING FINITE ELEMENTS ANALYSIS FOR DYNAMIC STRUCTURE BEHAVIOUR WITH EXPERIMENTAL MODAL ANALYSIS.

Johann Zeischka, Marc Brughmans, Olivier Storrer

1. INTRODUCTION

The study of the dynamic behaviour of the structures can be divided into two classes namely analytical-numerical and experimental methods. The most widely used method for analytical-numerical analysis is the finite element method. Modal analysis is the preferred method for the experimental oriented analyst.

For complex real-life structures the application of the finite element method requires usually a simplification of reality to obtain a manageable FE model. In addition to this fact a number of design parameters of a FE analysis are not under direct control of the FE analyst. As design parameters one can regard boundary conditions, variations of plate thickness and so on.

The unknown quality of FE-results demand a verification by experimental analysis. Recent developments in hardware and especially in software for experimental analysis resulted in more accurate and faster modal analysis [1]. One can expect that experimental modal analysis reflects the true dynamic behaviour of structures.

The scope of LMS-LINK is to combine and evaluate data of finite element analysis and experimental analysis. The principal functional modules of LMS-LINK are shown in fig.1 and will be described hereunder.

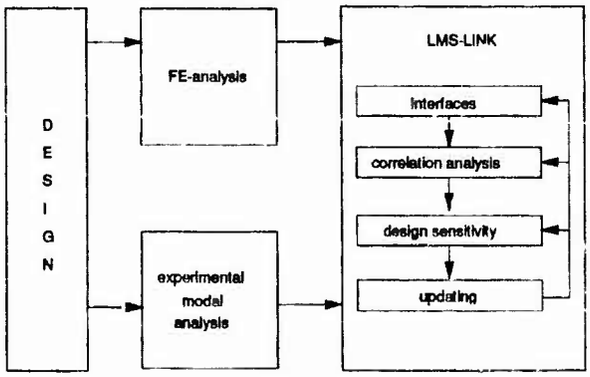

Fig. 1 : Principal functional modules of LMS-LINK.

2. INTERFACES

A neutral file interface based on Esprit CAD*I project nr.322 guarantees an easy interfacing of different finite element programs to LMS-LINK. The CAD*I neutral file also facilitates data transfer between different hardware installations. A common database of finite element and experimental data ensures data consistency.

3. CORRELATION ANALYSIS.

In a real-world finite element analysis a huge number of variations of design parameters should have to be evaluated in searching a state as close as possible to the reference state; in the following the experimental data will be referred to as reference state. It is obvious that an updating process without limitation of the design parameters will yield to unacceptable requirements in computer resources. Therefore a proper correlation analysis is the essential tool in selecting the design variables. Mode shape correlation analysis can be divided in qualitative and quantitative correlation.

3.1. Geometrical correlation.

The first step in the correlation analysis is the determination of the geometrical correspondence between finite element nodes and measurement points. A semi-automatic procedure will assist the user in establishing a common wire frame model. Local coordinate systems are supported. See fig. 2 for the FE model of the supporting bridge of the ORA experiment (Occultation radiation anemometer) and the equivalent wire frame model for correlation analysis. The ORA experiment will be mounted on the European retrievable carrier (EURECA).

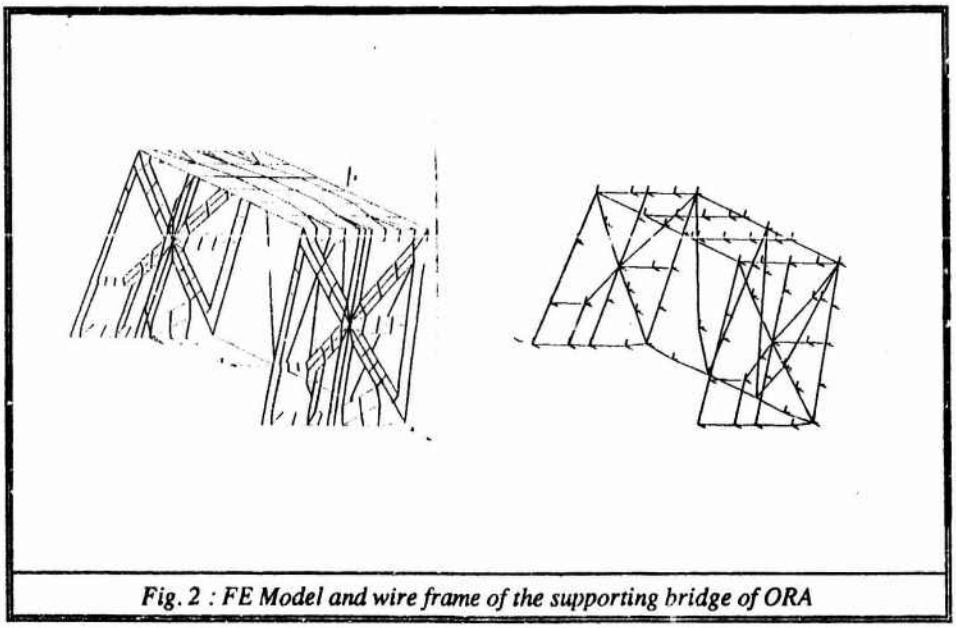

Fig. 2 : FE Model and wire frame of the supporting bridge of ORA

3.2. Mode shape correlation by animation.

A qualitative correlation can be gained from extensive real time animation features. Multiple windows help to evaluate different mode shapes. Mode shapes can be manipulated such as substracted from each other to visualize differences between two mode shapes. As an example of mode shape animation we refer to fig. 3 where the first experimental and analytical mode shapes are depicted.

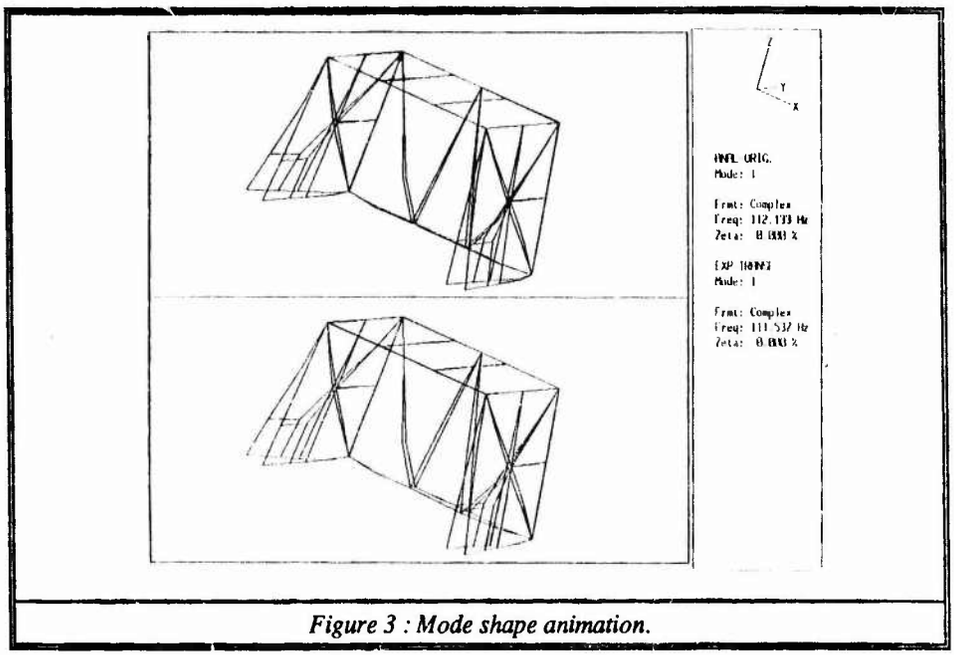

Figure 3 : Mode shape animation.

3.3. Mode shape correlation by Modal Assurance Criterion.

The modal assurance criterion (MAC) between two eigenvectors Φ_i and Φ_j is defined by

(1)
$$MAC_{ij} = \frac{(\Phi_i^T \Phi_j)}{(\Phi_i^T \Phi_i)(\Phi_j^T \Phi_j)}$$

The MAC is an averaged value for the correlation of mode shapes. The value of the MAC lies in the range between zero and one, close to one implies a good correlation. An example of correlation by MAC value is given in table 1 and 2 for the bridge of ORA (Occultation radiation anemometer) spacecraft structure. Smoothing will be discussed later.

	Hz	01 112.133	02 132.857	03 182.836	04 338.811	05 437.817
1	111.537	.844	.000	.026	.010	.000
2	132.932	.000	.761	.003	.028	.150
3	140.771	.011	.026	.858	.004	.000
4	319.496	.005	.015	.064	.710	.000
5	331.874	.008	.000	.130	.393	.039

Table 1 : Modal Assurance Criterion : MAC
rows : exp. - transformed columns : anal.-original

	Hz	01 112.133	02 132.857	03 182.836	04 338.811	05 437.817
1	111.537	.916	.000	.028	.011	.000
2	132.932	.000	.877	.004	.033	.173
3	140.771	.012	.028	.926	.004	.000
4	319.496	.006	.018	.079	.873	.000
5	331.874	.008	.000	.130	.393	.039

Table 2 : Modal Assurance Criterion : MAC with smoothed experimental eigenvectors
rows : exp. - transformed columns : anal.-original

3.4. Statistical mode shape correlation.

In contrast to the MAC a basic statistical procedure allows a more subtle evaluation of the finite element results compared to experimental data. A statistical evaluation can be based for example on the error e_i^k between experimental and analytical mode shapes $\Phi_{exp,i}$ and $\Phi_{FE,i}$ for component K and mode i. Φ_{min} is the minimum amplitude to be assumed as reliable. For example Φ_{min} can be expressed in percent of the maximum amplitude.

(2)

$$e_i^k = \frac{\Phi_{exp,i}^k - \Phi_{FE,i}^k}{\Phi_{exp,i}^k} \; for \; \forall i where \; \mathrm{abs}(\Phi_{exp,i}^k) > \Phi_{min}$$

with a mean value for n degrees of freedom for component k

(3)

$$\overline{e_i^k} = \frac{1}{n} \sum_{m=1}^{n} e_i^k$$

and a standard deviation of

(4)

$$\sigma_i^2 = \frac{1}{n-1} \sum_{m=1}^{n} (e_i^k - \overline{e_i^k})$$

An evaluation of the results of (2) helps to identify alignment errors by minimisation of the errors. Further evaluation allows identification of significant differences between FE and experimental analysis ; such differences for example can be caused by local modes not adequatlcy present in the FE analysis. After deletion or modification of components calculations (2) (3) and (4) can be repeated for a new set of comparable components of the eigenvectors. A scaling of the eigenvectors (5) (6) can be based on the modal scale factor (MSF).

(5)
$$MSF_i = \frac{\Phi^T_{\exp,i}\Phi_{FE,i}}{\Phi^T_{\exp,i}\Phi_{\exp,i}}$$

(6)
$$\Phi'_{FE,i} = \frac{1}{MSF_i}\Phi_{FE,i}$$

or the average error $\bar{e}$. The average error $\bar{e}$ can be selected as mean value for all components or $\bar{e}$ can be" the mean value $\bar{e}_i$ for the most participating component.

(7)
$$\Phi'_i = \frac{1}{1-\bar{e}}\Phi_i$$

Table 3 and 4 show the results of a statistical evaluation of the components for the first four modes of the ORA bridge.

mode	component-X	component-Y	component-Z
1	-6.9	-11.3	-29.7
2	26.2	-18.9	-12.5
3	-15.1	11.4	-17.2
4	-33.3	-6.8	-24.2

Table 3 : average error $\bar{e}_i$ in percent of FE analysis for ORA bridge with respect to experimental analysis for ORA bridge.

mode	component-X	component-Y	component-Z
1	-3.1	-0.7	-12.3
2	13.5	-12.9	24.7
3	-23.0	8.6	-34.3
4	-16.3	-3.7	-22.1

Table 4 : average error $\bar{e}_i$ in percent of FE analysis with respect to smoothed experimental analysis for ORA bridge.

For interpretation of table 3 and 4 one has to know that the components in Z-direction are substantially smaller than those in the other directions. It is beyond the scope of this paper to explain details of tables 3 and 4 ; the reader should review tables 1 and 2. In general only a careful qualitative and quantitative correlation will yield to valuable conclusions concerning the discrepancy between FE analysis and experimental data.

3.5. Mode shapes expansion.

One inherent difference between finite element analysis and experiment modal analysis is the number of degrees of freedom involved. In an experimental analysis this number usually does not exceed a practical limit of a few hundred measurement points, where a finite element analysis might show more than 10.000 degrees of freedom.

Several schemes for expansion of the set of measurement points are available such as static (8) and dynamic expansion (9). The subscript a indicates the set of measurement points and the subscript o to the remaining degrees of freedom of the finite element analysis.

An alternative to (8) and (9) is the expansion based on an orthogonal projection of the experimental modes on modes of a FE analysis (10, 11), where T is a transformation matrix determined by equation (10).

(8) $$\Phi_i = K_{OO}^{-1} K_{OA} \Phi_a$$

(9) $$\Phi_i = -(K_{OO} - \omega^2 M_{OO})^{-1} (K_{OA} - \omega^2 M_{OA}) \Phi_a$$

(10) $$\Phi_{\exp,a} = \Phi_{FE,a} T$$

(11) $$\Phi_{\exp,o} = \Phi_{FE,o} T$$

In [2] it has been shown that expansion and smoothing by orthogonal projection removes random unbiased noise of the experimental mode shape. See for example table 2 of the MAC values after smoothing which have to be compared to table 1.

4. SENSITIVITY ANALYSIS.

The simplifications incorporated in a finite element analysis will require an updating of the stiffness and mass matrices by changes of parameters {p} about {dp}. From the equation of free motion first order sensitivities can be derived for the frequency and the eigenvectors. [3] see equations (12) and (13) for unit modal mass scaled eigenvectors.

(12)
$$\frac{\delta f_i}{\delta p} = \frac{1}{8\pi^2 f_i}\{\Phi_i\}^T \frac{\delta[K]}{\delta_p}\{\Phi_i\} - \frac{f_i}{2}\{\Phi_i\}^T \frac{\delta[M]}{\delta p}\{\Phi_i\}$$

(13)
$$\frac{\delta\{\Phi_i\}}{\delta p} = \sum_{\substack{j=1 \\ j\neq i}}^{m} \left[\frac{\{\Phi_j\}^T \frac{\delta[K]}{\delta p}\{\Phi_i\}}{\left((2\pi f_i)^2 - (2\pi f_j)^2 \right)} \right] \{\Phi_j\}$$

$$-\frac{1}{2}\left[\{\Phi_i\}^T \frac{\delta[M]}{\delta p}\{\Phi_i\}\right]\{\Phi_i\}$$

$$-\sum_{\substack{j=1 \\ j\neq i}} \left[\frac{(2\pi f_i)^2 \left[\{\Phi_j\}^T \frac{\delta[M]}{\delta_p}\{\Phi_i\} \right]}{\left((2\pi f_i)^2 - (2\pi f_j)^2 \right)} \right] \{\pi_j\}$$

In LMS-LINK tools are incorporated to group and select elements for design sensitivity analysis. The changes of the stiffness and mass matrices are based on proportional updating of element matrices [4]. This procedure combines good computational efficiency with reliable results. Graphical presentation of the results with colour permits visual recognition of most sensitive regions.

5. UPDATING

The theory in progress of implementation in LMS-LINK is based on [5] and will be briefly outlined hereafter.

The stiffness and mass matrices (K,M) are assumed to depend on some set of parameters {p}. The eigenvectors determined by means of the finite element model fulfill the well known orthogonality conditions. The orthogonality conditions are given in (14) and (15) for eigenvectors scaled to unity of modal mass.

(14)
$$\Phi_{FE,i}^T K \Phi_{FE,j} = \omega_{FE,i}^2 \delta_{ii} = k_{ij}$$

(15)
$$\Phi_{FE,i}^T M \Phi_{FE,j} = \delta_{mij}$$

The finite element solution based on the current state of the parameters should lead by appropriate changes about {dp} to the reference state, hence

(16)
$$\omega_{EXP,j}\delta ij^2 = k_{ij} + \sum\left(\Phi^T_{exp,i}\frac{\delta K}{\delta p}\Phi_{EXP,j}\right)dp$$

(17)
$$\delta_{ij} = m_{ij} + \sum\left(\Phi^T_{EXP,i}\frac{\delta M}{\delta p}\Phi_{EXP,j}\right)dp$$

(18)
$$\omega_{EXP,i} = \omega_{FE,i} + \sum\left(\frac{\delta\omega_i}{\delta p}\right)dp$$

Equations (16) to (18) are ordinary sensitivity equations of the form

(19)
$$\{q\} = \{q_s\} + [S]\{dp\}$$

where q_s indicates the state variable for current parameter values and q presents the desired state. The equation of type 19 is solved by a Bayesian least square fit (20), where w_e and w_s are some weighting functions, which allow to express the confidence of the analyst.

(20)
$$\| \lceil w_e \rfloor [\{qs\} + [S]\{dp\} - \{q\}] \|_2 + \| \lceil wsuba \rfloor \{ps\} + \{dp\} - \{po\} \|_2 = 0$$

This method has been successfully applied for the simulation of detection of structural damage of a steel offshore platform jacket (see fig 5) [6]. First the finite element model was reduced to the measurement points and then updated to reflect the undamaged states. After formation of a structural failure the monitoring will show changes in the modal parameters. See table 4 for a comparison of the first three eigenfrequencies for the different states of the structure.

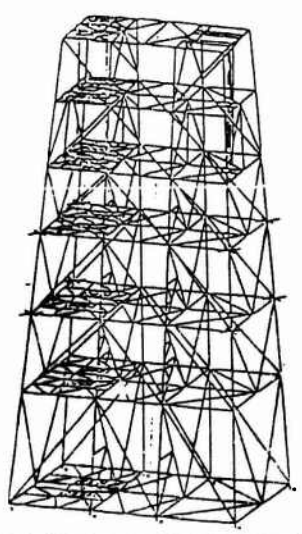

Figure 5 : Offshore platform jacket.

Mode (Hz)	Undamaged			Damaged	
	reference set	condensed FE model	update condensed FE model	reference set	updated FE model
1	.6441	.7795	.6440	.6265	.6271
2	.7265	.8556	.7265	.7265	.7252
3	.8497	1.1946	.8950	.8843	.8843

Table 5 : Comparison of first three eigenfrequencies (Hz) for different states

Application of the above outlined theory indicated following relative stiffness matrix changes (see table 6 for following relative stiffness matrix changes). These stiffness changes correspond with the simulated failure in a diagonal (dofs 16 and 18) with high accuracy.

.	.	.
.	.	.
.	.	.
(7,7) : 0.	(8,8) : 0.	(9,9) : 0.
(10,10) : 0.0007	(11,11) : 0.	(12,12) : 0.0022
(13,13 : -0.0016	(14,14) : 0.0020	(13,13) :-0.1243
(16,16) : -0.8619	(17,17) : -0.1197	(18,18) :-0.8289
(19,19) : -0.0023	(20,20) : -0.0080	(21,21) : 0.
(22,22) : -0.0002	(23,23) : 0.	(24,24) :-0.003

Table 6 : Relative stiffness matrix changes.

6. CONCLUSION

Efficient correlation analysis will play a key factor in the determination of discrepancies between FE analysis and experimental analysis and in reducing the number of design variables to a minimum. A proper correlation analysis will also eliminate artificial reference states.

A tight connection between finite element department and the experimental department will result in a faster and more reliable design methodology.

REFERENCES

1. U. VANDEURZEN, J. LEURIDAN, M. MERGEAY, D. ROESSEMS 1985, Versatile computer workstation for multiple input/output structural testing and analysis. 18 th Int. Symposium on Automotive Technology and Automation, Florence, Italy, 1988 (to be published).

2. J.LIPKENS and U. VANDEURZEN 1987, The Use of Smoothing Techniques for Structural Modification Applications. Proceedings of 12th International Seminar on Modal Analysis, Leuven, Belgium.

3. T. JANTER, P. SAS, R. SNOEYS 1987, Sensitivity of Physical model parameters. Proceedings of 12th International Seminar on Modal Analysis, Leuven, Belgium.

4. O.STORRER, J.ZEISCHKA, J.LEURIDAN, U.VANDEURZEN 1987, Proportional Sensitivity Analysis using FEA Element Matrices. Proceedings of 12th International Seminar on Modal Analysis, Leuven, Belgium.

5. W. HEYLEN 1982, Optimization of Modal Analysis by means of Experimental Obtained Dynamic Data. Proceedings of the first International Modal Analysis Conference, pp. 32-38, Orlando, Florida, USA.

6. J. LEURIDAN, A. DE LANDSHEER, M. BRUGHMANS 1987, the "Link" Program for Dynamic Model Optimization in Structure Design Analysis and Monitoring. Proceedings of the fifth International Modal Analysis Conference, London, UK

VIBRATIONAL POWER TRANSMISSION THROUGH DISCONTINUITIES

J.L. Horner and R.G. White

Institute of Sound and Vibration Research
University of Southampton

1. INTRODUCTION

When attempting to control the vibration levels transmitted from a machine through the structure upon which it is mounted, it is desirable to be able to identify and quantify the vibration paths in the structure. By absorbing the mechanical energy along the propagation paths in some convenient manner, it should be possible to reduce the sound radiated from the structure. One method of obtaining path information is to use the concept of vibrational power transmission.

In any vibrating system there are a variety of mechanisms by which the vibration is transmitted through the substructure. The concept of power flow allows the various transmission paths to be compared. Simple measurements of vibration amplitude at various points in the structure are not sufficient to identify the vibration paths. If stationary waves are present in the structure, large vibration amplitudes will be measured while little power is being transmitted through the structure. Thus, it is necessary to measure the structural wave intensity which indicates the distribution of vibrational power.

By using the concepts developed by Pavic [1] and implemented by Redman-White [2], it is possible to measure time-averaged power flow in a beam or a plate to within half a wavelength of a discontinuity. The work presented in this paper is concerned with the effect of discontinuities on power transmission in uniform beams. Methods for predicting the effect of various types of discontinuities on the power transmission in a beam have been developed and the power flow in the far and near field of beam discontinuities has been measured.

Previous work in this field has been concerned with measuring power in a beam away from the effects of discontinuities. Apart from the time-domain methods developed by Noiseux [3] and Pavic [1], frequency domain methods for measuring power flow have been developed by Verheij [4] and Meyer [5]. Before it is possible to predict power transmission, it is necessary to know the effect the discontinuity has on a wave which impinges upon it. Doyle and Kamle [6] predicted the reflection and transmission coefficients for a beam with change of material or area. Experiment confirmed the predicted coefficients. Work on beams with bends or branch joints was carried out by Lee and Kolsky [7], Desmond [8], Rosenhouse, Ertel and Mechel [9] and Doyle and Kamle [10]. By using the reflection and transmission coefficients for different types of discontinuity, it is possible to predict the vibrational power associated with flexural and longitudinal waves on either side of the discontinuity.

2. THEORY

2.1 Input Power to a Structure

Assume a harmonic force input, $|F|\sin\omega t$, to a structure with point inertance, $|I_{ii}|e^{i\phi}$. The time averaged input power $\langle P\rangle_{in}$ can be found [11] from

$$\langle P\rangle_{in} = \frac{1}{T}\int_0^T |F|\ |V|\sin\omega t\ \sin(\omega t + \Phi)dt$$

$$\therefore \quad \langle P\rangle_{in} = \frac{1}{2}\ |F|^2\ \mathrm{Im}\left\{\frac{I_{ii}}{\omega}\right\} \qquad (1)$$

2.2 Transmitted Flexural Power in a Uniform Beam

Consider a section of a uniform beam with a flexural wave propagating through the beam (figure 1). Two loads act on this beam element; the shear force and the bending moment. Assuming the flexural wave can be described using Euler-Bernoulli beam theory, by

$$W = A_4\sin(\omega t - k_f x)$$

Shear force on section $S = EI\frac{\partial^3 W}{\partial x^3}$; Bending moment on section $M = EI\frac{\partial^2 W}{\partial x^2}$

Instantaneous rate of working in cross section X,

$$X = S\frac{\partial W}{\partial t} - M\frac{\partial^2 W}{\partial x \partial t}$$

$$X = EI\frac{\partial^3 W}{\partial x^3}\cdot\frac{\partial W}{\partial t} - EI\frac{\partial^2 W}{\partial x^2}\cdot\frac{\partial^2 W}{\partial x \partial t} \qquad (2)$$

$$X = EIk_f^3\,\omega A_4^2$$

$$\text{Time Averaged Power } \langle P\rangle_t = \frac{1}{T}\int_0^T X dt = EIk_f^3\omega A_4^2 \qquad (3)$$

$$\langle P\rangle_t = \frac{1}{T}\int_0^T X dt$$

2.3 Power Flow through Two Changes in Cross-Section or Material in a Collinear Beam

In a substructure it is likely to encounter a discontinuity consisting of two changes of cross-section or material, i.e. change in section due to a weld or a lap joint. It is a complicated wave problem as multiple reflections can occur within the joint. Figure 2 shows such a joint at four different time intervals.

It was assumed that the joint was of such dimensions that near field waves decayed before reaching the other discontinuity. It was also assumed that a travelling wave which was the product of a second reflection would have insufficient energy to produce any effect on its third impingement.

Thus, the wave motion at 1, the left hand side of the joint at 'a' would be,

$$W_1(x,t) = \left\{A_4 e^{-ik_1 x} + (A_3 + F_3)e^{ik_1 x} + (A_1 + F_1)e^{k_1 x}\right\}e^{i\omega t}$$

For 2, the right hand side of the joint at 'b',

$$W_2(x,t) = \left\{D_4 e^{-ik_1 x} + D_2 e^{-k_1 x}\right\}e^{i\omega t}$$

For J1, the right hand side of the joint at 'a',

$$W_{J1}(x,t) = \left\{(B_4 + E_4)e^{-ik_2x} + C_3e^{ik_2x} + (B_2 + E_2)e^{-k_2x}\right\}e^{i\omega t}$$

and for J2, the left hand side of the joint at 'b',

$$W_{J2}(x,t) = \left\{B_4e^{-ik_2x} + C_3e^{ik_2x} + C_1e^{k_2x}\right\}e^{i\omega t}$$

The power flow expressions on either side of the joint can be determined in the same manner as section 2.2.

If $A_3 = r_{3A}\,A_4$, $F_3 = r_{3F}\,A_4$, $A_1 = r_{3A}\,A_4$ and $F_1 = r_{1F}\,A_4$ then the power in the near field of beam 1 is,

$$\langle P\rangle_t = EI\omega k_1^3 A_4^2 \left\{(1 - (r_{3A} + r_{3F})^2) + \frac{(r_{1A} + r_{1F})e^{k_1x}}{4\pi^2}\right.$$

$$[(r_{3A} + r_{3F})(\mathrm{Cos}(2\omega T + k_1x) + \mathrm{Sin}(2\omega T + k_1x) - \mathrm{Cos}k_1x$$

$$- \mathrm{Sin}k_1x) + (\mathrm{Cos}(2\omega T - k_1x) - \mathrm{Sin}(2\omega T - k_1x) + \mathrm{Cos}k_1x$$

$$\left. - \mathrm{Sin}k_1x)\right\} \qquad (4)$$

In the far field, this reduces to

$$\langle P\rangle_t = EI\omega k_1^3 A_4^2 (1 - (r_{3A} + r_{3F})^2) \qquad (5)$$

The power in the near field of beam 2, if $D_4 = t_4A_4$ and $D_2 = t_2A_2$, is,

$$\langle P\rangle_t = EI\omega k_1^3 A_4^2 [t_4^2 - \frac{t_2t_4e^{-k_1x}}{2\pi} \mathrm{Cos}k_1x] \qquad (6)$$

In the far field, the above becomes,

$$\langle P\rangle_t = EI\omega k_1^3 A_4^2 t_4^2 \qquad (7)$$

To obtain the reflection and transmission coefficients for the joint; if subscript, a, denotes the joint end at a and subscript, b, denotes it at b, then using eqns. (9) - (12).

$$r_{3A} = r_{a3} \qquad r_{3F} = t_{b4}\, r_{b3}\, t_{a4}$$
$$r_{1A} = r_{a1} \qquad r_{1F} = t_{b2}\, r_{b3}\, t_{a4}$$
$$t_2 = t_{a4}\, t_{b2} \qquad t_4 = t_a\ \ t_{b4}$$

where, from reference [6], the following expressions are given for the near and far field reflection coefficients,

$$R = 4\sqrt{\frac{E_BI_B}{E_AI_A}} \qquad Q = 4\sqrt{\frac{n_Ae_A}{n_Be_B}}$$

$$D = 2RQ(R^2 + Q^2) + (1 + R^2Q^2)$$
$$r_1 = \frac{(1 - R^4Q^4)(1 - i)}{D}$$

$$r_3 = \frac{2RQ(R^2 - Q^2) - i(1 - R^2Q^2)^2}{D}$$

$$t_2 = \frac{-2(1 - R^2Q^2)(R + iQ)}{DQ}$$

$$t_4 = \frac{2 + (1 + R^2Q^2)(R + Q)}{DQ} \qquad (12)$$

As expected, analysis of the above equations shows that a joint in a beam reduces the power transmitted through the beam. If a beam of area 3×10^{-4} m^2 has a joint in it of 9.6×10^{-4} m^2, the power transmitted by the joint is 50% of the power impinging on the joint.

2.4 Power Flow through Non-Collinear Beam

Assume a beam is bent through an angle Φ (figure 4). A flexural wave impinges on the bend, causing longitudinal and flexural waves to be transmitted and reflected.

On the incident side of the junction,

$$W_-(x,t) = \left\{A_4 e^{-ik_f x} + A_3 e^{ik_f x} + A_1 e^{k_f x}\right\} e^{i\omega t}$$

$$V_-(x,t) = A_{L1} e^{ik_L x}\, e^{i\omega t}$$

Consider an element of the beam (figure 4) and the loads acting upon it. Thus, instantaneous rate of working X,

$$X = S\frac{\partial W}{\partial t} - M\frac{\partial^2 W}{\partial x \partial t} - EA\frac{\partial u}{\partial x}\frac{\partial u}{\partial t}$$

$$X = -EI\omega k_f^3 \left[A_1 A_3 e^{k_f x}\,(\mathrm{Sin}(2\omega t + k_f x) - \mathrm{Cos}(2\omega t + k_f x)\right.$$

$$+ A_1 A_4 e^{kx}\,(\mathrm{Sin}(2\omega t - k_f x) + \mathrm{Cos}(2\omega t - k_f x)) + A_3^2$$

$$\left. - A_4^2\right] - EAk_L A_{L1}^2 \omega \mathrm{Sin}^2(\omega t + k_L x)$$

If $A_3 = r_3 A_4$, $A_1 = r_1 A_4$ and $A_{L1} = r_L A_4$, then the power in the near field is

$$\langle P\rangle_t = EI\omega k_f^3 A_4^2 \left\{[1 - r_3^2] + \frac{r_1 e^{k_f x}}{2\pi}\,\mathrm{Cos}kx\right\} - A_4^2\left[\frac{EAk_L r_L^2}{2}\right] \qquad (8)$$

Similarly, for the angled arm of the beam, if $\Psi = x\mathrm{Cos}\Phi$,

$$W_+(\Psi,t) = [B_2 e^{-k_f \Psi} + B_4 e^{-ik_f \Psi}]\, e^{i\omega t}$$

$$U_+(\Psi,t) = B_{L2} e^{-ik_L \Psi}\, e^{i\omega t}$$

Then,

$$X = EI\omega k_f^3 \left[B_4^2 + B_2 B_4 e^{-k_B x}\,(\mathrm{Sin}(2\omega t - k_f x) - \mathrm{Cos}(2\omega t - k_f x))\right]$$

$$+ EAk_L\omega B_{L2}^2 \sin^2(\omega t - k_1 x)$$

and if $B_2 = t_2 A_4$, $B_4 = t_4 A_4$ and $B_{L2} = t_L A_4$,

$$\langle P \rangle_t = EI\omega k_f^3 A_4^2 \left[t_4^2 - \frac{t_2 t_4 e^{-k_f x}}{2\pi} \cos k_f x\right] + \frac{EAk_L t_1^2 A_4^2}{2} \qquad (9)$$

To obtain the reflection and transmission coefficients, the conditions of equilibrium and continuity at the discontinuity must be considered. There are six conditions and these are:

$$W_-(o) = U_+(o)\sin\theta + W_+(o)\cos\theta,$$

$$U_-(o) = U_+(o)\cos\theta - W_+(o)\sin\theta,$$

$$\frac{\partial W_-(o)}{\partial x} = \frac{\partial W_+(o)}{\partial \varphi^2},$$

$$\frac{\partial^2 W_-(o)}{\partial x^2} = \frac{\partial^2 W_+(o)}{\partial \varphi^2}$$

$$EA\frac{\partial u_-(o)}{\partial x} = EA\frac{\partial u_+(o)}{\partial \varphi}\cos\theta - EI\frac{\partial^3 W_+(o)}{\partial \varphi^3}\sin\theta$$

$$EI\frac{\partial^3 W_-(o)}{\partial x^3} = EA\frac{\partial u_+(o)}{\partial \varphi}\sin\theta + EI\frac{\partial^3 W_+(o)}{\partial \varphi^3}\cos\theta$$

By substituting the correct wave equations into the above, expressions can be obtained for the reflection and transmission coefficients for the discontinuity.

3. MEASUREMENT OF VIBRATIONAL POWER IN A BEAM

3.1 Measurement in the Far Field of a Discontinuity

From eqn. (2), it can be found that, in the far field of a discontinuity, the power due to the shear force equals the power due to the bending moment. Thus,

$$\text{Total Power Flow} = \langle P_t \rangle = 2\langle P_s \rangle = 2\langle P_m \rangle$$

where $$\langle P_s \rangle = EI\frac{\partial^3 W}{\partial x^3} \cdot \frac{\partial W}{\partial t}$$

and $$\langle P_m \rangle = -EI\frac{\partial^2 W}{\partial x^2} \cdot \frac{\partial^2 W}{\partial x \partial t}$$

Now the shear force component is

$$P_s = EI\omega k^3 A_4^2 \cos^2(\omega t - k_f x)$$

The output of a linear accelerometer attached to the beam would be

$$\frac{\partial^2 W}{\partial t^2} = -\omega^2 A_4 \sin(\omega t - k_f x)$$

and the output of a rotational accelerometer attached to the beam would be

$$\frac{\partial^3 W}{\partial x \partial t^2} = k\omega^2 A_4 \cos(\omega t - k_f x)$$

Applying a $-\pi/2$ phase shift to the output of the linear accelerometer would give

$$\frac{\partial^2 W(q)}{\partial t^2} = \omega^2 A_4 \cos(\omega t - k_f x)$$

Thus, $$P_s = \frac{EIk^2}{\omega^3} \frac{\partial^3 W}{\partial x \partial t^2} \cdot \frac{\partial^2 W}{\partial t^2} \quad \text{and as} \quad k_f^4 = \frac{\omega^2 m_0}{EI}$$

Then, $$\langle P \rangle_t = \frac{2\sqrt{m_0 EI}}{\omega^2} \left\langle \frac{\partial^3 W}{\partial x \partial t} \frac{\partial^2 W}{\partial t^2}(q) \right\rangle \tag{10}$$

Using finite difference methods to evaluate the spatial and temporal derivatives [1].

$$\left.\frac{\partial^2 W}{\partial t^2}\right|_{x=0} \approx \frac{1}{2}\left[\left.\frac{\partial^2 W}{\partial t^2}\right|_{x=\frac{\Delta}{2}} + \left.\frac{\partial^2 W}{\partial t^2}\right|_{x=-\frac{\Delta}{2}} \right]$$

$$\left.\frac{\partial^3 W}{\partial x \partial t^2}\right|_{x=0} \approx \left[\left.\frac{\partial^2 W}{\partial t^2}\right|_{x=\frac{\Delta}{2}} - \left.\frac{\partial^2 W}{\partial t^2}\right|_{x=-\frac{\Delta}{2}} \right]$$

and letting $\left.\frac{\partial^2 W}{\partial t^2}\right|_{x=-\frac{\Delta}{2}} = a_1$ and $\left.\frac{\partial^2 W}{\partial t^2}\right|_{x=\frac{\Delta}{2}} = a_2$

Thus eqn. (10) becomes,

$$\langle P \rangle_t \approx \frac{\sqrt{m_0 EI}}{\Delta\omega^2} \langle (a_2 - a_1)(a_2(q) + a_1(q)) \rangle \tag{11}$$

$$\langle P \rangle_t \approx \frac{2\sqrt{m_0 EI}}{\Delta\omega^2} \langle a_2 a_1(q) \rangle \tag{12}$$

The above two equations can be used to measure power flow in the far field of a beam discontinuity. To account for the errors introduced by using finite difference techniques, a correction factor must be used on the measured result.

$$\langle P \rangle_t = \langle P \rangle_{\text{measured}} \frac{k\Delta}{\sin(k\Delta)}$$

3.2 Measurement in the Near Field of a Discontinuity

In the near field of a discontinuity, the flexural wave equation is of the form,

$$W = \text{Re}\left\{A_1 e^{kx} + A_3 e^{ikx} + A_4 e^{-ikx}\right\} e^{i\omega t}$$

Thus, in this region, the instantaneous rate of working is equal to,

$$X = -EI\omega k^3 \left[A_1 A_3 e^{kx} (\sin(2\omega t + kx) - \cos(2\omega t + kx))\right.$$

$$+ A_1A_4e^{jkx}\,(\mathrm{Sin}(2\omega t - kx) + \mathrm{Cos}(2\omega t - kx)) + A_3^2 - A_4^2]$$

It can be found that the above is approximately equal to,

$$\left[\frac{\partial^2 W}{\partial t^2}\cdot\frac{\partial^3 W(q)}{\partial x\partial t^2} - \frac{\partial^2 W(q)}{\partial t^2}\cdot\frac{\partial^3 W}{\partial x\partial t^2}\right]_{\text{NEAR FIELD}}$$

$$- 2\left[\frac{\partial^2 W}{\partial t^2}\cdot\frac{\partial^3 W(q)}{\partial x\partial t^2}\right]_{\text{FAR FIELD}}$$

Thus, in the near field,

$$\langle P\rangle \approx \frac{4EIk^2}{\Delta\omega^3}\left[\langle a_1a_2(q)\rangle_{\text{NEAR FIELD}} - \langle a_1a_2(q)\rangle_{\text{FAR FIELD}}\right] \qquad (13)$$

The above equation allows near field power to be measured using two accelerometers in the far field of the discontinuity and two accelerometers in the near field. This allows great access to the near field of a joint than previous techniques, i.e. Pavic [1] used four accelerometers in the near field and physical transducer size was a great limitation.

3.3 Comparison of Theoretical and Measured Power Flow in the Region of a Beam Discontinuity

A 6 mm x 50 mm x 6 m mild steel beam was suspended at four points by wires. The ends of the beam were embedded in sand boxes to reduce end reflections. The beam contained a butt weld at a position 900 mm from the mid point. The butt weld was of dimension 7.5 mm x 51 mm x 8 mm. The beam was excited at its mid point using a 30 lb electrodynamic shaker. Input power was measured using digitally acquired signals captured from a force transducer and an accelerometer at the point of excitation. Transmitted power was measured using two accelerometers connected via charge amplifiers to the Power Flow Meter developed by Redman-White [2]. This meter implements equation (11).

Initially, power was measured in the far field of the beam discontinuity. Figure 5 shows the comparison of measured and predicted far field power. The far field power was predicted using equations (5) and (7). From figure 5 it can be seen that the predicted far field power on the "reflecting" side of the joint is slightly greater than that measured. This is due to the prediction being based on the amplitude of the wave in the section of the beam without any discontinuities. This wave amplitude would be slightly different than the amplitude of the impinging wave on the weld because the impinging wave contains an extra component due to the reflection of the reflected impinging wave on the source. The difference between predicted and measured transmitted power is due to energy losses in the joint which are not included in the model. The joint was modelled as an energy conserving system. Also, the quality of the joint is unknown. Any dislocations in the weld would reduce the transmission of power through the joint.

Power was also measured in the near field of the discontinuity, where the forward travelling wave impinged on the weld. Figure 6 shows the comparison of measured and predicted near field power. Near field power was measured using equation (13) and predicted using equation (4). The discrepancies between measured and predicted values were due to the approximation in the near field measurements. The predicted values were based on measured far field results.

4. CONCLUSIONS

It is possible to measure the flexural wave power transmitted along a uniform beam. By considering the loads acting on an element of beam, it is possible to predict the power in the near and far fields of discontinuities in the beam. Using the prediction equations, it should be possible to design joints which minimise the transmission of power through them. The techniques used to measure power on either side of a weld in a collinear beam, could equally be applied to each arm of a branch joint. To measure the longitudinal wave power component, strain gauges would have to be attached to the beam.

ACKNOWLEDGEMENT

This work has been carried out with the support of the Procurement Executive, Ministry of Defence.

REFERENCES

1. G. PAVIC 1976 PhD Thesis, University of Southampton. Techniques for the determination of vibration transmission mechanisms in structures.

2. W. REDMAN-WHITE 1984 PhD Thesis, University of Southampton. The measurement of structural wave intensity.

3. D.U. NOISEUX 1970 Journal of the Acoustical Society of America, Vol. 47, 238-247. Measurement of power flow in uniform beams and plates.

4. J.W. VERHEIJ 1980 Journal of Sound and Vibration, Vol. 70, 133-139. Cross spectral density methods for measuring structure-borne power flow in beams and pipes.

5. B. MEYER 1987 Electricité de France. Structural intensity: what to measure and how?

6. J.F. DOYLE and S. KAMLE 1985 ASME Journal of Applied Mechanics, Vol. 52, 669-673. An experimental study of the reflection and transmission of flexural waves at discontinuities.

7. J.P. LEE and H. KOLSKY 1972 ASME Journal of Applied Mechanics, Vol. 39, 809-813. The generation of stress pulse at the junction of two non-collinear rods.

8. T.P. DESMOND 1981 ASME Journal of Applied Mechanics, Vol. 48, 148-154. Theoretical and experimental investigation of stress waves at a junction of three bars.

9. G. ROSENHOUSE, H. ERTEL and F.P. MECHEL 1981 Journal of the Acoustical Society of America, Vol. 70, 492-499. Theoretical and experimental investigations of structure-borne sound transmission through a T-joint in a finite system.

10. J.F. DOYLE and S. KAMLE 1987 ASME Journal of Applied Mechanics, Vol. 54, 136-140. An experimental study of the reflection and transmission of flexural waves at an arbitrary T-joint.

11. E.E. UNGAR, N. KORONAIOS and J.E. MANNING 1967 Bolt, Beranek & Newman Inc., Report No. 1491. Application of statistical energy analysis to vibrations of multi-panel structures.

APPENDIX: NOTATION

A = area
A_1 = amplitude of reflected exponentially decaying wave
A_3 = amplitude of reflected flexural wave
A_4 = amplitude of forward travelling flexural wave
B_2 = amplitude of transmitted exponentially decaying wave
B_4 = amplitude of transmitted travelling flexural wave
C_1 = amplitude of reflected exponentially decaying wave
C_3 = amplitude of reflected travelling flexural wave
D = material constant
D_2 = amplitude of transmitted exponentially decaying wave
D_4 = amplitude of transmitted travelling flexural wave
E = Young's modulus of elasticity
E_2 = amplitude of reflected exponentially decaying wave
E_4 = amplitude of reflected travelling flexural wave
F = force
F_1 = amplitude of transmitted exponentially decaying wave
F_3 = amplitude of transmitted travelling flexural wave
I = moment of inertia
I_{11} = point inertance of a structure
k_f = flexural wave number
k_A = flexural wave number in Section A
k_B = flexural wave number in Section B
M = bending moment force
$\langle P \rangle$ = time averaged power
Q = material constant
R = material constant
r_1 = reflection coefficient for exponentially decaying waves
r_3 = reflection coefficient for travelling waves
S = shear force
T = time interval, averaging period
t = time
t_2 = transmission coefficient for exponentially decaying waves
t_4 = transmission coefficient for travelling waves
v = velocity amplitude
W = displacement
X = instantaneous rate of working in cross-section
x = distance along beam
Θ = angle of bend in beam
Φ = phase angle
ω = frequency in radians
Δ = accelerometer spacing
λ = wavelength

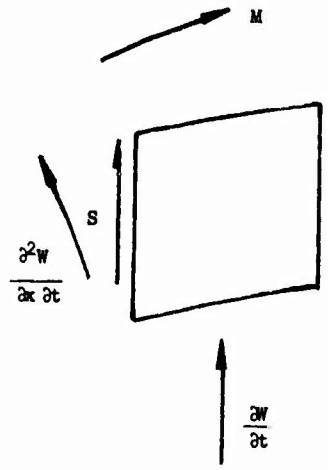

FIGURE 1

SECTION OF UNIFORM BEAM EXPERIENCING FLEXURAL WAVE MOTION

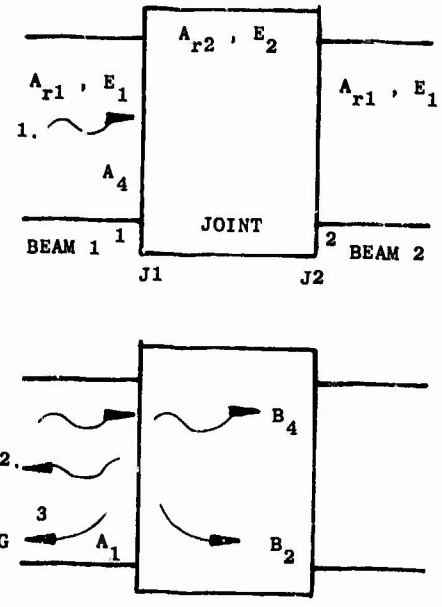

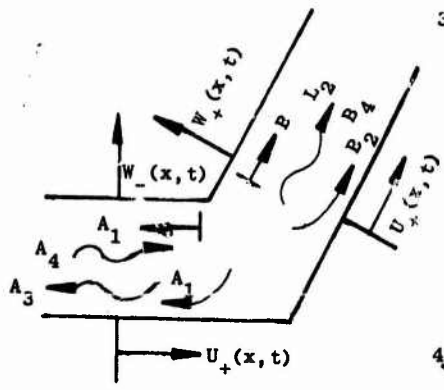

FIGURE 3

WAVE MOTION IN NON-COLLINEAR BEAM

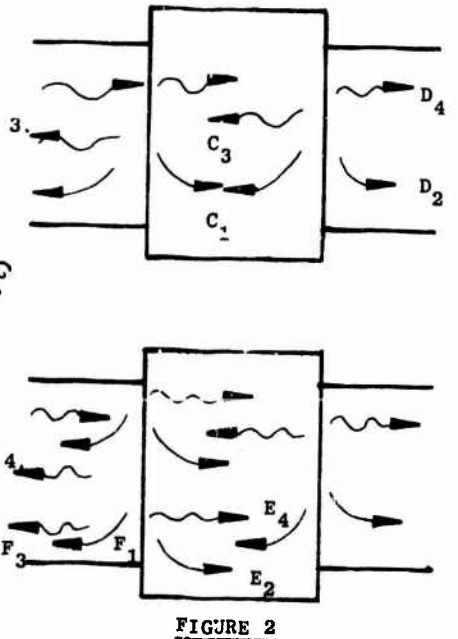

FIGURE 2

WAVE MOTION AT FOUR TIME INTERVALS DUE TO TWO DISCONTINUITIES IN A UNIFORM BEAM

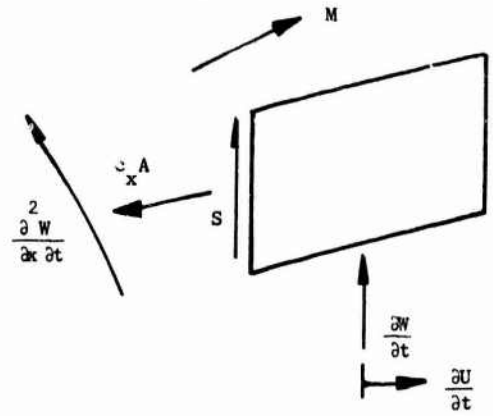

FIGURE 4

ELEMENT OF BEAM EXPERIENCING FLEXURAL AND LONGITUDINAL WAVE MOTION

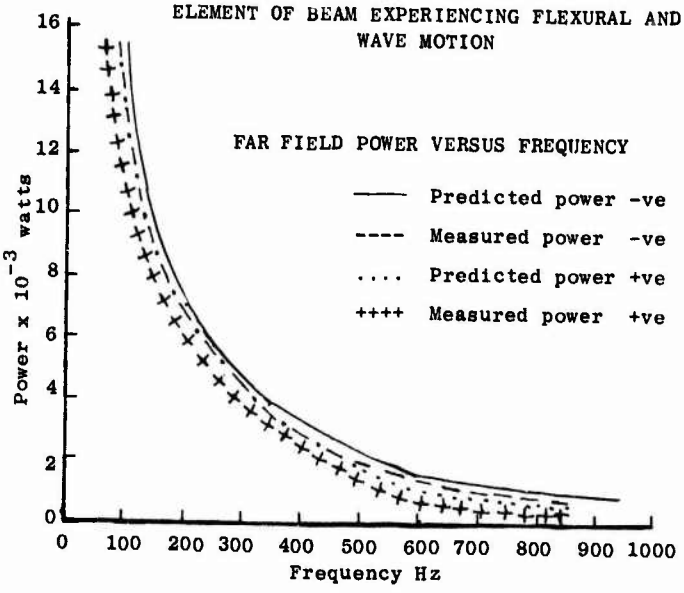

FIGURE 5

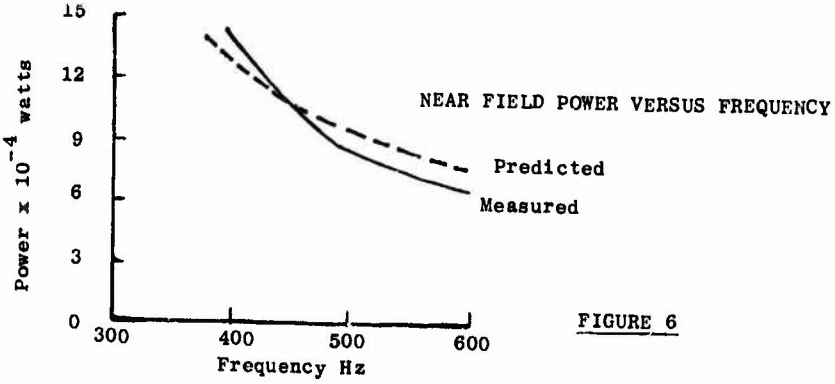

FIGURE 6

GIANT MAGNETOSTRICTIVE DEVICES IN STRUCTURAL ACOUSTICS

B.A.T. Petersson

Department of Engineering Acoustics
Lund Institute of Technology

1. INTRODUCTION

In several branches of structural acoustics rather specific and demanding requirements are put on the experimental equipment. Hereby a manifold of devices and principles is needed. Moreover, often the experimentalist desires to tailor fit a device or a technique to the situation.

The magnetostriction phenomenon, in principle, realises another possibility to register the dynamic behaviour of or excite structural systems. The exploitation of this material property however has been hampered by its "weakness". Recently, alloys posessing huge magnetostrictive features have been developed leading to significant figures of merit. The alloys have been termed giant magnetostrictive. Summarising the advantages and disadvantages it is found that a high output may be gained from a small size sample but this is counterbalanced by a relatively high cost and design difficulties.

Principally the alloys can be applicable in a variety of situations but to mention a few relevant, vibration excitation, active vibration control and motion registration may be put forward.

The intention of this paper is to give an overview of the application of the alloys in vibration excitation and more specifically in moment excitation where advantage is taken of the small physical size [1]. Hereby hopefully some light will be thrown indirectly on the application in other situations.

2. MAGNETOSTRICTION

Since the mid of the last century transition metals such as nickel have been recognised to be magnetostrictive. Their usefulness in applications with respect to magnetostriction however is rather limited since the exhibited magnetic moments are small.

The extraordinary magnetostrictive characteristics of rare earth metals have been known for more than 20 years [2]. The hindrance in this case has been the low ordering temperature below which the magnetostriction dominates the thermal expansion. In the beginning of the 1970's the research on magnetostriction was focussed on obtaining RFe_2-alloys (R denotes rare earth metal) with ordering temperature above room temperature [2]. The magnetostriction realised for such alloys is of the order of $2 \cdot 10^{-3}$ which is to be compared with that of nickel, $3 \cdot 10^{-5}$. Thus the exploitation of the magnetostrictive transduction phenomenon become feasible.

Briefly, the magnetostriction originates from the fact that the magnetic anisotropy energy depends upon the strain. In order for the crystal to

minimise its energy th' crystel deforms when presented to e megnetic field. Conversely, a change in the interior magnetic charecteristics is encountered if the crystel is deformed.

It is noteable thet no linear megnetostriction will result if the magnetic enisotropy is independent of the strain but thet, at the same time, the anisotropy cen be a hindrence to obtain a large magnetostriction. This means that grain orientation by some directional solidification becomes necessary to achieve e useful performance of a polycrystalline sample if a low excitation field is desired.

Among the elloys exhibiting the giant magnetostrictive feature, the composition $Tb_{0.27}Dy_{0.73}Fe_2$ may be argued to be the most advanced and has been given the name Terfernol-D.

Apart from the large magneto-elastic coupling for the RFe_2 alloys, also, the static and dynamic material properties can be strongly influenced. As an example, a variation of up to 60% in the Young's modulus is possible which, in turn, affects the speed of sound for the material [2].

A very useful feature of RFe_2 alloys is the possibility to tailor make their characteristics to suit a certain application. Some examples of such tailor made characteristics are:

- $TbDyFe_2$ compounds show step wise change in the thermal expansion above a certain temperature where the break temperature can be adjusted by means of the magnetic field.
- RFe_2 alloys in bi-metal configurations eq. $TbFe_2$ (positive magnetostriction) and $SmFe_2$ (negative magnetostriction) reveals a large bending motion

Table 1 below shows the magneto-elastic forces and energies which can be produced by RFe_2 alloys. The quantity $E\lambda_s$ can be interpreted as the pressure a blocked rod with a cross-sectional area of 1 m^2 can give whereas $E\lambda_s^2/2$ refers to the amount of magnetic energy per unit volume which can be transformed into elastic energy. As seen from the table the possible energy transformation is about 10^3 times bigger for $TbFe_2$ than for a classical magnetostrictive material as Ni.

Table 1. Elastic and magneto-elastic properties a), [2].

	$TbFe_3$	$ErFe_2$	YFe_2	$TbFe_2$	Ni
v_l(m/sec)	3940	4120	4340	4230	-
v_s(m/sec)	1980	2180	2720	2320	-
ρ(g/cm^3)	9.1	9.7	6.7	9.4	-
$E \times 10^{-10}$ (newton/m^2)	9.4	12.1	12.7	13.1	21[b]
$\lambda, \times 10^6$	1750	-229	-	693	-31[c]
$E\lambda, \times 10^{-7}$ (newton/m^2)	17	2.8	-	9	0.7
$E\lambda_s^2/2 \times 10^{-3}$ (joule/m^3)	145	3.2	-	32	0.1

[a] Clark et al. (1973b).
[b] "Nickel", The International Nickel Co., Inc., (1951).
[c] Went (1951).

As stated earlier, the giant magnetostriction of RFe_2 alloys makes them very useful as high-power elements in transducers. One of the most prominent parameters with respect to such transducers is the so-called magneto-mechanical coupling factor which expresses the fraction of magnetic energy which is converted into elastic energy or vice versa. The diagram in Figure 1 shows the coupling factor, k_{33}, as function of the field applied. As is seen the coupling factor has a maximum between 100 and 500 Oe (8 - 40 kA/m).

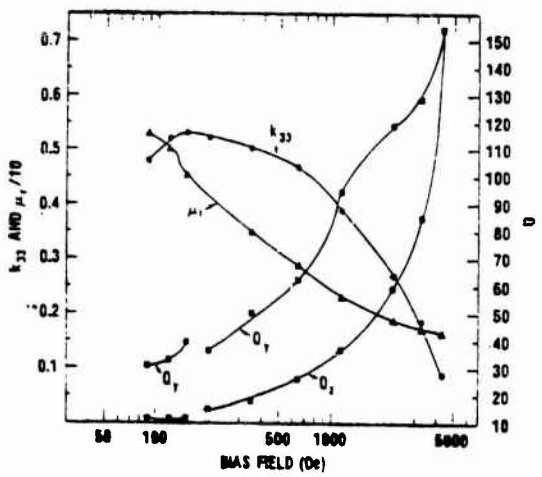

Figure 1. Coupling factor k_{33}, Q factor and relative permeability μ_r of $Tb_{0.3}Dy_{0.7}Fe_2$ as a function of bias field. Q_Z, the quality factor at constant current drive includes both mechanical and electrical losses whereas Q_Y, the quality factor at constant voltage drive, includes only mechanical losses, (taken from Savage et al. 1975), [2].

In this diagram also the permeability, μ_r, should be considered. As is seen, the permeability is low which in certain applications must be considered as beneficial since the inductance in the driving coil then will be small and its performance at high frequencies is improved.

Finally, some operational curves for Terfenol-D are given in Figure 2.

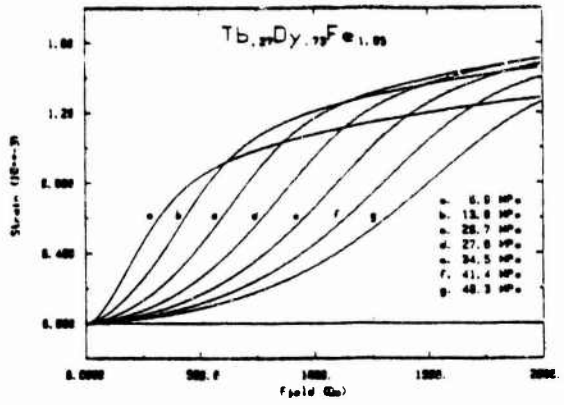

Figure 2. Magneto-elastic strain as a function of applied field at various static stresses for $Tb_{0.27}Dy_{0.73}Fe_{1.95}$, [4].

The prestress is varied up to 48 MPa but this value should not be considered as an upper limit [3]. A prestress is advantageous and necessary in most applications and can be achieved mechanically, co-linear with the operational direction. Alternatively, the prestress can be obtained by means of a secondary magnetic field perpendicular to the exciting field so that tne lattice is end-positioned [4].

A related branch worth mentioning in this context is amorphous magnetic alloy called Metglas [2], [5]. This material is featured by an extremely large magneto-mechanical coupling. Thereby high sensitivity transducers for the registration of stress, strains and the like can be made. The sensitivity can be compared with the sensitivity of ordinary strain gauges and is found to be of the order 10^3 better. Metglas is made as film-like ribbons but can also be sputtered on a specific base plate.

Accordingly there are several reasons to further investigate the possibilities opened by the giant magnetostrictive materials with respect to applications in structural acoustics.

3. MOMENT EXCITATION

A survey of the pertinent literature reveals four main types of problems in experimentally obtaining moment mobilities, [1]:

a) The physical size of the excitaiton arrangement,
b) the fastening of the excitation arrangement,
c) registration of the excitation,
d) numerical procedure for deriving the moment mobility from measured, raw data.

These types of difficulties all are more or less intimately related to the way of excitation. Moreover, the literature survey points at the circumstance that a direct measurement technique has not been paid as much interest as variations on indirect techniques. Hereby, it seems concludable that in order to minimise the numerical problems a direct technique is desirable.

The fact that new materials have opened alternative means for excitation whereby, at the same time, the physical dimensions may be reduced also has made the direct technique more feasible. Therefore the experimental work carried out has been focussed on direct techniques.

The first attempt in the direction of a moment exciter is sketched in Figure 3, [6].

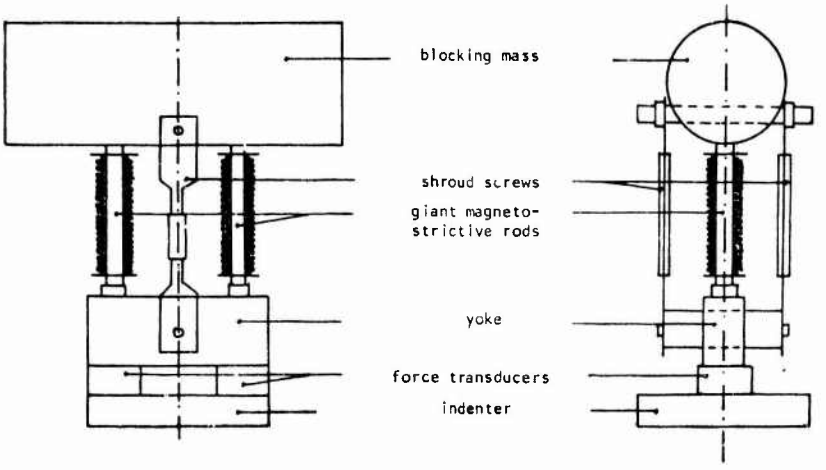

Figure 3. Sketch of prototype to a moment exciter.

In this exciter two Terfenol-D rods of length 50 mm were used. The coils were made up of 500 turns, 1 mm copper wire. An aligned precompression was established by means of shroud screw-like arrangements.

To obtain a modulated magnetic field for the magnetostrictive rods, a dc-current was added to an amplified ac-current in the secondary coil of the amplifier. Both the current and the voltage were controlled so that the strain was nominally equal for both the rods. Two ordinary force transducers registered the forces acting on the measurement object via a circular indenter and two miniature accelerometers registered the motion.

Both the signals quantifying the force couple and the accelerations were fed to summation/subtraction-devices leaving two signals, one proportional to the moment and the other proportional to the angular acceleration. In turn, the transfer function was derived by means of a two-channel FFT-analyzer.

The experience gained from this prototype pointed at problems in reaching the correct operational point. Furthermore, some mechanical deficiances were recognised.

A serious drawback of using a dc-current to establish the necessary magnetic bias field is the heating of the coils. The improvements of the prototype therefore included permanent magnets and a common prestress arrangement cf. Figure 4.

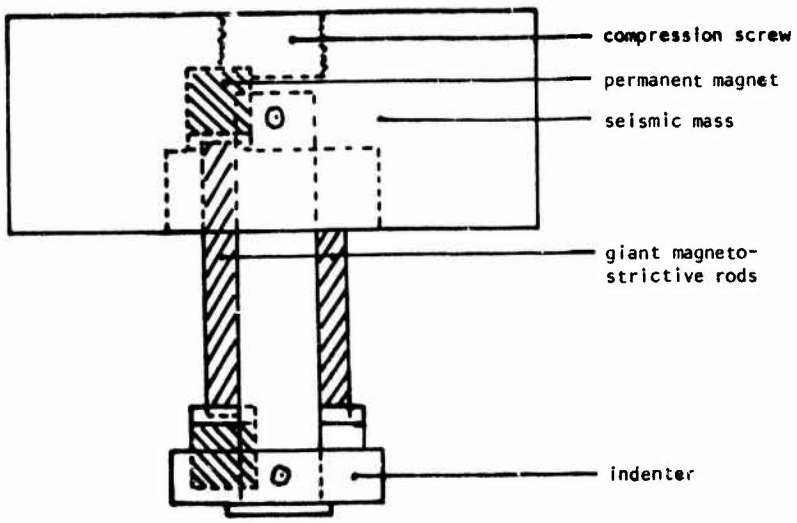

Figure 4. Revised version of prototype to a moment exciter.

Another difference between the second and the first version is the exclusion of the force transducer. This introduced the necessity of 4-channel measurement, cf. [1].

A few results from the test with the second version of the moment exciter are shown in Figures 5 through 8.

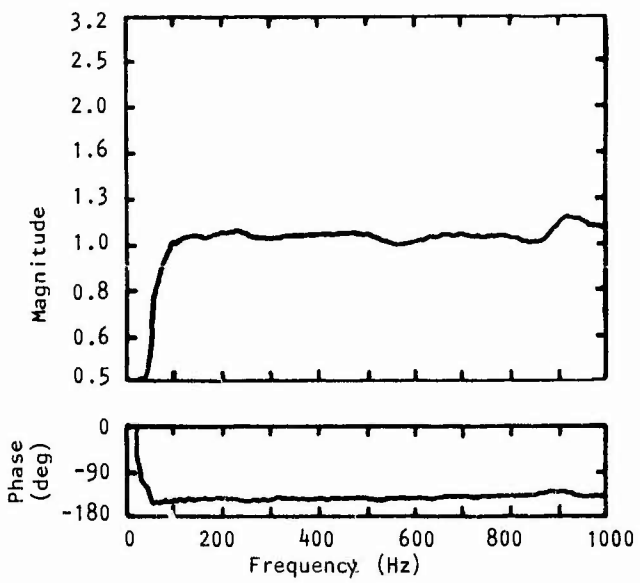

Figure 5. Magnitude and phase of the complex ratio of the accelerations at the unloaded indenter for the two positions opposite to the magnetostrictive rods.

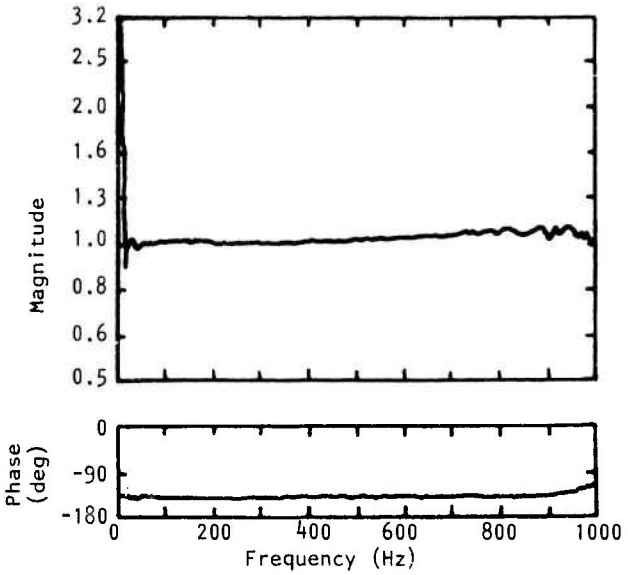

Figure 6. Magnitude and phase of the complex ratio of the accelerations at the loaded indenter, for the two positions opposite to the magnetostrictive rods.

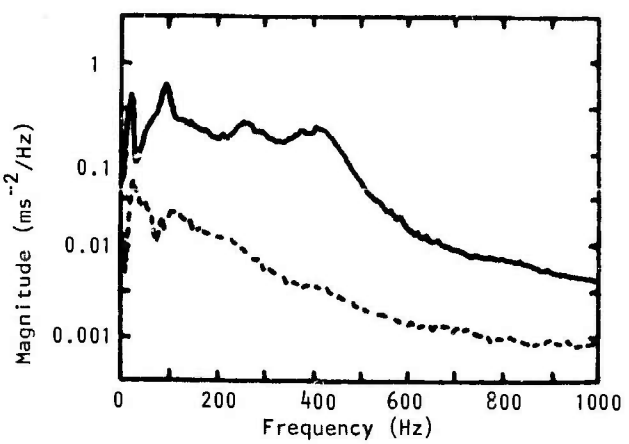

Figure 7. Comparison of the sum (——) and difference (---) of the two acceleration levels. Measurements made with the indenter loaded.

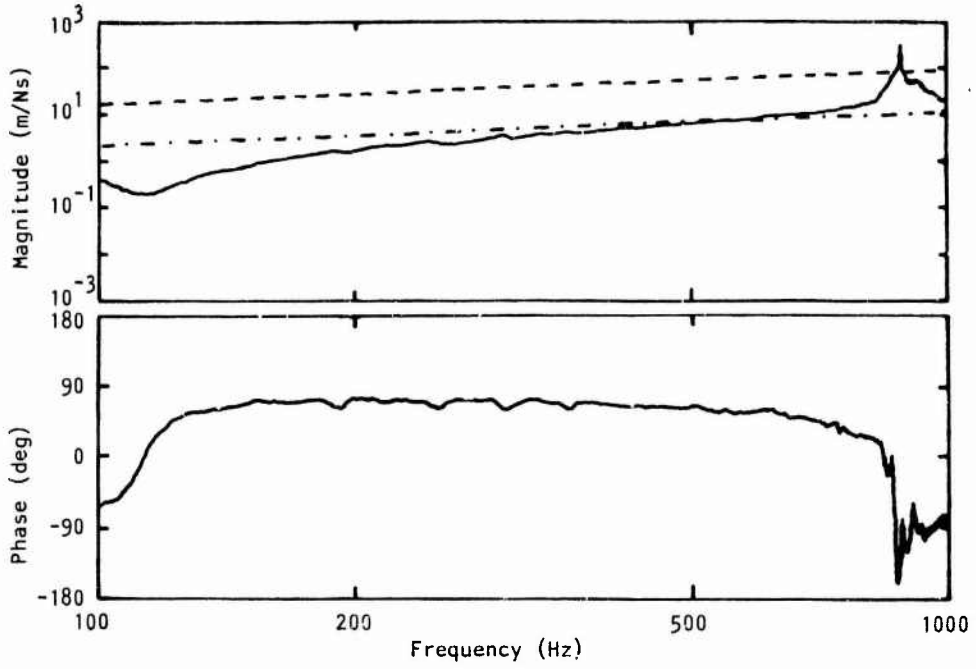

Figure 8. Moment mobility for an aluminium plate (1 mm thickness) embedded in sand. Measured (——) and calculated with ideal moment (---) and rotatory (-·-·-) excitation.

A comparison of the results in Figures 5 and 6 reveals a small difference in the performance between the loaded and the unloaded exciter. Hence the stability is not satisfactory. From Figure 7 it is seen that despite a manual tuning of the exciter, the suppression of the translatory component is not sufficient. It therefore seems appropriate to include magnetostrictive strain gauges on the Terfenol rods to monitor their operational conditions. Such an inclusion also make a feedback control feasible.

Finally, the measured moment mobility in Figure 8 refers to a thin aluminium plate embedded in sand. The results exhibit the, essentially stiffness governed, behaviour of a moment excited plate. The application of the excitation at the plate surface introduces an ambiguity with respect to the actual excitation condition. This is also reflected in the results whereby these are to be compared with the theoretical results for ideal moment and rotational excitations. Such a comparison moreover points at the necessity of a minimum lever.

4. CONCLUDING REMARKS

This study indicates that giant magnetostrictive devices may be useful in experimental structural acoustics. Their limited physical size combined with the comparatively large mechanical output make them attractive for experimental work. For the specific case of direct moment excitation these features are essential if the desirable range of Helmholtz numbers is wide. The inherent non-linearity in the operational characteristics of a giant magnetostrictive sample introduces disadvantages with respect to the manageability. Hereby the control of the mechanical and magnetic parameters is of vital importance if a decoupling of excitation components is to be achieved. The results obtained must be judged promising and further development of the device for moment excitation seems appropriate. It can be concluded that the control of the actual strain of the rods is desirable whereby an inclusion of Metglas ribbons, fastened on the rods realises a suitable means. In such a way a complete feed-back control can be established. The very high degree of similarity of the magnetostrictive rods substantially improves the possibility to achieve a satisfactory performance of multi-rod arrangements.

Finally, the influence of the excitation condition with respect to moment mobility should be emphasized.

5. ACKNOWLEDGEMENT

The financial support received from the Swedish Council for Building Research and the Swedish National Board for Technical Development is gratefully acknowledge.

6. REFERENCES

[1] Petersson, B. 1986. Department of Engineering Acoustics, Lund Institute of Technology, Report TVBA-3035. On the experimental techniques for measuring moment mobility.

[2] Clark, A.E. 1980. North-Holland Publishing Company, New York. Ferromagnetic Materials, I, Chr 7, (Ed. Wohlfarth, E.P.).

[3] Clark, A.E. 1986. Proc. of the 1:st Int. Conf. on giant magnetostrictive alloys and their impact on actuation and sensor technology, Marbella. Magnetostrictive properties of Iron-Lantheanidez alloys.

[4] Clark, A.E., Spano, M.L. and Savage, H.T. 1983. IEEE Transactions on magnetics, 19, 1964-1966. Effect of stress on the magnetostriction and magnetization of rare earth - $Fe_{1.95}$ alloys.

[5] Savage, H.T. and Spano, M.L. 1982. Journal of Applied Physics, 53, 8092-8097. Theory and application of highly magnetoelastic Metglas 2605SC.

[6] Petersson, B. 1986. Journal of Sound and Vibration, 116, 191-194. On the use of giant magnetostrictive devices for moment excitation.

5. VIBRATION CONTROL AND DAMPING

RECENT ADVANCES IN STRUCTURAL DAMPING

David I.G. Jones
Materials Laboratory, AFWAL/MLLN
Wright-Patterson AFB, Ohio 45433

INTRODUCTION

It is quite impossible to describe the current state-of-the-art in structural damping in a few short pages. Of necessity, therefore, this will be a brief, selective, even biased, survey of those developments which seem of most significance in the near future, both with respect to technical questions and potential applications. Current work in the damping area spans a very wide variety of activities, ranging from very abtruse, scientific, questions which nevertheless impact all other activities, to the very complex issues involveo in the application of the technology for noise and vibration control, which takes one into economic, management, national policy, production and other arenas. The scientific questions which continue to abound may often be addressed by individuals and small research groups with the expenditure of modest resources, but the application questions will involve large programs, large organizations, government/industry cooperation etc. Both types of activity, however, are equally important in their respective ways, and each affects the other quite strongly. This paper will review the state-of-the-art in each of these areas, including damping of built-up structures, friction damping, behavior of viscoelastic damping materials, and applications in the automotive, aerospace and engine areas.

2. STATUS OF THE TECHNOLOGY BASE

2.1. Damping in Built-Up Structures

Twentieth century technology continues to depend on the construction of a wide variety of structural systems for specific purposes, and the general changes which have taken place in the technology during the past fifty years are fewer than might be expected. For example, aircraft are still made using skin-stringer-frame types of structure, automobile engines and transmissions have not changed in basic concept for even longer, and future space structures will use truss-like elements not unlike those used for well over a century in bridges and towers. What has changed, in many instances, is the requirements set upon these structures. Aircraft and automotive structures must serve, more than ever before, to separate passengers from noise sources, for example. The stabilization, vibration control and specific weight requirements which may be placed on some space-truss structures would have horrified the Nineteenth Century bridge builders. So we might ask, what developments have taken place with respect to our understanding of damping of built-up structures? The answer seems, surprisingly, or perhaps not, very little! Structures may have changed in some aspects of detail design, materials may have changed, as have requirements, but it would be difficult to find any recent studies which have advanced our ability to predict joint damping better than Ungar [1,2] did or to predict the response of built-up jointed structures better than was achieved by Mead [3,4], Lin [5] and others, in the 1960's. The only major change has been in computer power, software including finite element codes, test instrumentation and electronic analyzers. The difficulty remains in the modelling of the damping, and in the variability of manufactured structures, even when the process is automated.

2.1.1. Damping of Space and Aircraft Structures

Graphic illustration of the still remaining variability of structural damping in spacecraft structures can be found in the current literature. Figure 1 summarizes the results of several investigations [6-8], in the form of plots of modal loss factor versus frequency. The data represents measured modal loss factors for low order modes on several space and aircraft structures, at low stress levels in air. Scatter is seen to be very large, and is quite reminiscent of scatter reported in earlier years for similar structures. The graph does not illustrate the effects of vacuum or of higher order modes, and should therefore be used with caution. Without doubt, the increasing use of composite materials will lead to changes of damping levels, but it does not seem likely that modal loss factors will be any more predictable and we may have to live with this unpredictability for a long time to come. Deliberate efforts to increase the damping by use of additive polymeric damping materials, or by deliberately introducing damping into some composite members by increasing material damping of matrix or fibers, may reduce the variability to some degree, as well as provide higher baseline levels. Figure 2 shows the results of some analytical and experimental investigations of the effect of composite ply orientation on stiffness and damping of specimens representative to some degree of a single truss member [9]. It is seen that it is difficult to achieve the highest levels of stiffness and damping at the same orientation, at least for the case where the major damping contribution is from the matrix. Other investigators have drawn similar conclusions [10]. In the final analysis, it is probably reasonable to conclude that adequate damping will exist, in projected space structures, to meet baseline active control needs in the low order modes, but that higher order modes must be provided with additional passive damping in order to reduce excessive demands on the active control systems, especially with respect to minimization of post maneuver/disturbance stabilization times and to reduce the number of sensors/actuators needed.

2.1.2. Friction damping

Another type of damping which has found some applications, for example in jet engine turbine blades, is sliding friction damping. Some improvement in understanding this type of highly nonlinear damping mechanism have taken place in the past decade or so [11-20]. In simplified systems, in particular, where one or two-degree of freedom models have been used, as in Fig 3, analysis and test data have correlated fairly well, as illustrated in Figure 4 [19,20], for example. In these investigations, simple Coulomb friction laws were used, for which the friction force is independent of velocity except with respect to direction and depends only on a "coefficient of friction" and an overall normal load, corresponding to a "macroslip" model. While this "law" is only of limited validity, little data on more realistic laws is available, and this limits the value of more precise analytical techniques, such as finite element methods, which have been used in efforts to develop "microslip" models as opposed to the "macroslip" models [15]. Approaches which have been used in analysis of friction damping include:

(i) Simple one degree of freedom model [12,13]
(ii) Two degree of freedom model [13,14]
(iii) Receptance/Impedance methods [20]
(iv) Component mode synthesis [18]
(v) Finite element approaches [15]

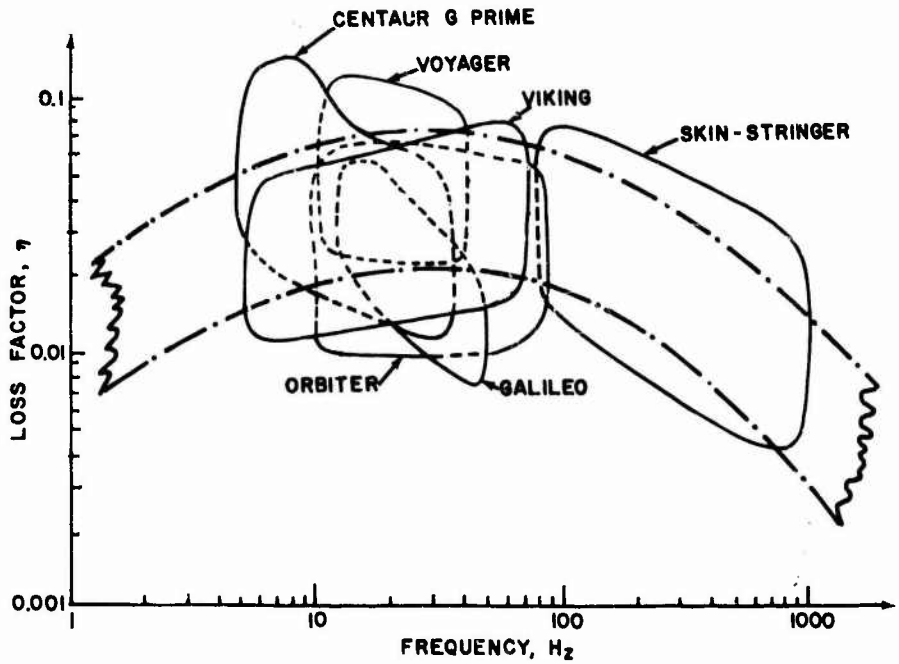

Fig. 1. Modal loss factors versus frequency for spacecraft structures [6-8]

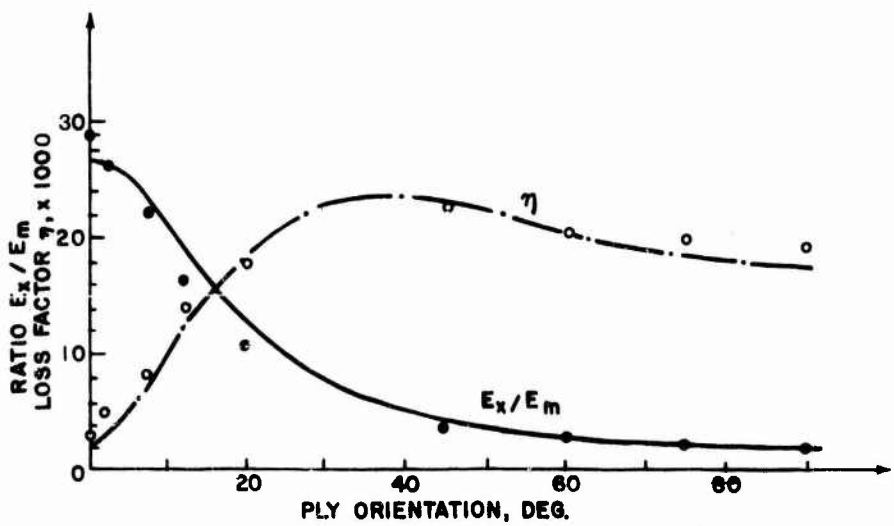

Fig. 2. Damping and stiffness versus fiber direction for composite specimens (E_x = longitudinal modulus, E_m = matrix modulus, η^x = loss factor, [9])

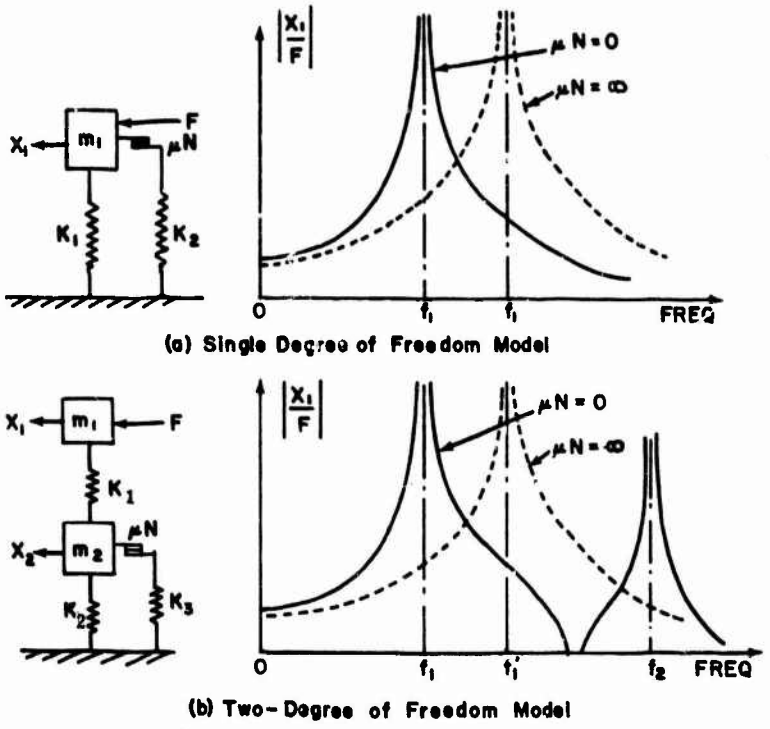

Fig. 3. Simple friction damping models [12-14]

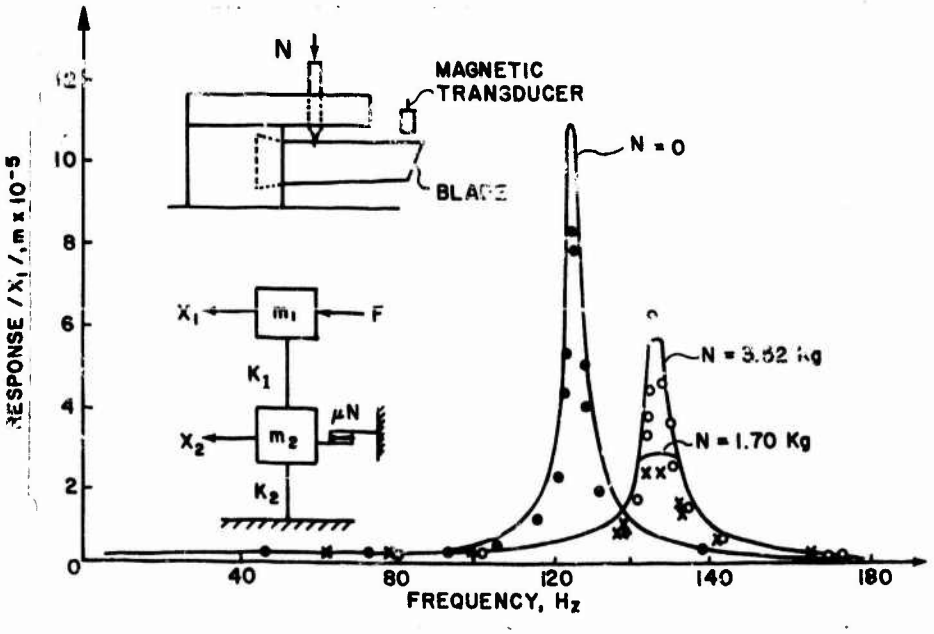

Fig. 4. Comparison of measured and predicted response for a compressor blade with friction damping (N = normal load, μ = friction coefficient, [19])

These approaches have been used for investigation of response behavior of single structural elements, such as turbine blades, and for larger, coupled, systems such as multiple blade-disk structures. While much work remains to be done, a good qualitative understanding of "macroslip" features of frictional damping behavior of quite complicated structures seems to have been achieved, along with some progress toward understanding "microslip" behavior.

2.2 Material Damping

A number of interesting developments have taken place in the area of polymeric viscoelastic damping materials, which in turn have facilitated major applications. The advances were generally evolutionary, building on work going back as far as the 1950's, rather than revolutionary, but they took place nevertheless. Important basic advances include (a) an increased variety of commercial sources [21-37, for example], (b) a wider variety of commercially available test systems [38-41, for example], (c) improved approaches for characterizing the complex modulus properties as a function of frequency and temperature [42-44], (d) increased availability of complex modulus data [45-48] and (e) improved understanding of viscoelastic material dynamic behavior, including impulse response [49]. On the other hand, many questions raised in the past have not yet been fully clarified, including: (a) determination of the variation of Poisson's ratio with frequency and temperature, and whether it is a real or a complex number, (b) how does the relationship between the imaginary and real parts of the complex modulus relate to our understanding of material characteristics, as opposed to a limited current use for identifying erroneous data, (c) how best to determine shift factors in temperature-frequency superposition.

2.2.1. Characterization of Polymeric Material Damping Behavior

The complex modulus model of viscoelastic material damping behavior has gained increased acceptance in recent years. It has become more widely accepted that, while the model is formulated in the frequency domain, nevertheless time domain problems can be addressed by inverse Fourier Transforms provided that the variation of properties with frequency are allowed for over a sufficiently wide range, usually not less than four or five decades [42,49]. The literature on complex modulus behavior of polymeric materials, ranging in style from abstruse scientific studies of carefully characterized pure polymers to engineering evaluations of commercial polymeric damping materials, has continued to grow over the past decades and shows no sign of abating. The frequency or time-temperature superposition approach is still widely accepted [42,50], and used for complex modulus behavior data analysis, though some authors have raised questions regarding its full validity [51]. For engineering purposes, the errors involved do not seem to be very important in view of the usual scatter of measured data, and only under rather exceptional conditions are the discrepancies sufficiently great to be even of scientific importance.

Figure 5 illustrates a plot of shear modulus and loss factor versus reduced frequency for a typical polymeric material [48]. The data was obtained by several measurement methods, including the resonant beam, impedance and stress relaxation techniques. While the agreement of the various methods is generally good, and the scatter is apparently quite low, it is seen that the dynamic range of the modulus values, in particular, is enormous, being about five decades (100 db). This means that differences in the values of the extremal moduli, at very high frequencies and at very low frequencies, even as large as 50 percent, are barely perceptible. The

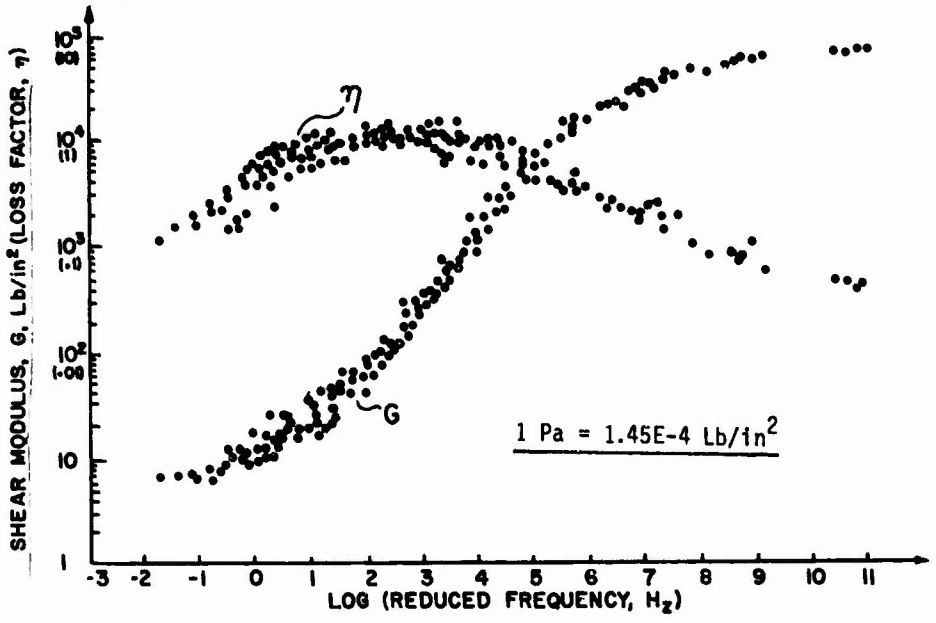

Fig. 5. Plot of shear modulus (G) versus reduced frequency for typical acrylic adhesive (3M-966, [48])

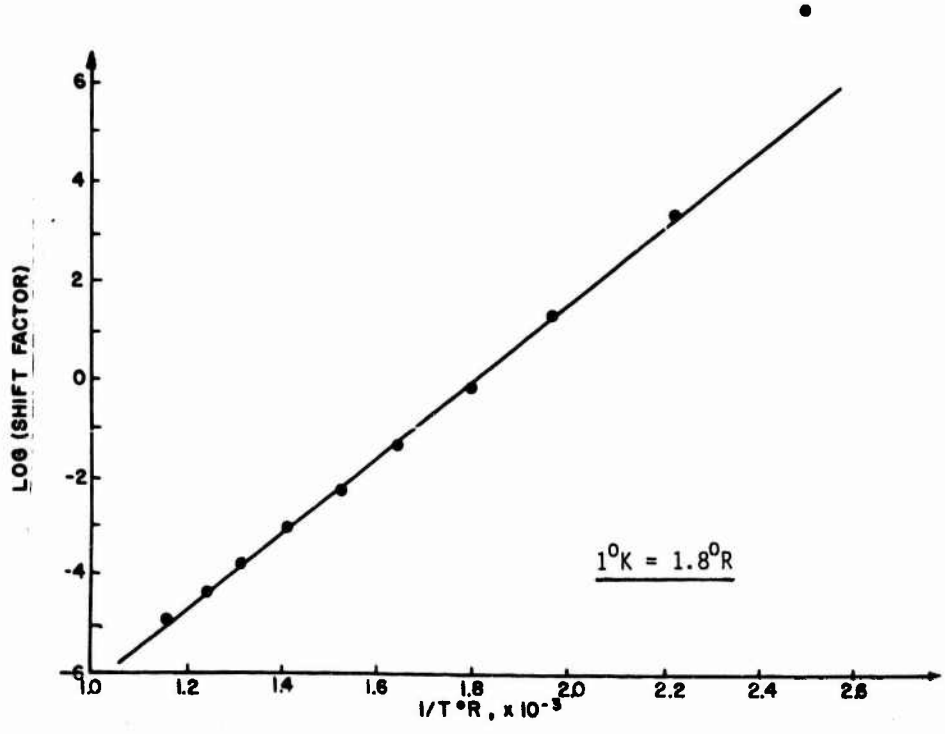

Fig. 6. Plot of log (shift factor) versus inverse absolute temperature (1/T) for typical acrylic adhesive (3M-966)

corresponding shift factors, illustrated in Figure 6 versus 1/T, are equally susceptible to scatter and cannot usually be estimated to within better than about half a decade (about 10 db) overall. This too means that selection of appropriate analytical functions to represent the shift factor versus temperature relationship are subject to much uncertainty. Again, the scatter is often greater than the systematic differences being sought. While claims are made from time to time that better accuracy (lower scatter) can be achieved by particular equipment and methods, any efforts to conduct repeated tests on duplicate specimens, even from the same batch of material, tend to bring back the scatter. This plot represents a fundamental relationship between loss factor and modulus for any given polymer, and scatter is indicative of errors. Another question which has not been resolved with complete success is the measurement of Poisson's ratio over a wide range of frequencies and temperatures. Figure 8, for example, shows a plot of shear modulus, Young's modulus and loss factor versus reduced frequency for the same typical acrylic polymer, again based on several measurement techniques. Poisson's ratio can be determined from the relationship:

$$\nu = E^*/2G^* - 1 \qquad (1)$$

where E^* is the complex Young's modulus and G^* is the complex Shear modulus. Figure 7 seems to indicate that ν is a real number and varies from about 0.35 at the high frequency extemity to 0.50 at the low frequency extremity, but the scatter makes it difficult to establish this with any degree of confidence.

Figures 9 and 10 show two types of nomogram designed to graphically display engineering damping properties. The first (Reduced Temperature Nomogram) is a plot of modulus and loss factor versus reduced frequency with additional scales for frequency and temperature superimposed, and is the current approach being considered for US National standards and International Standards [50,52]. The second is a plot of loss factor versus modulus, with frequency and temperature scales added, and with the reduced frequency eliminated [53]. Both plots have advantages and disadvantages, and are not equally useful for all purposes. The Reduced Temperature Nomogram is often used, currently, for displaying engineering damping data for a wide variety of commercial damping materials, allowing users to quickly and easily scan a variety of materials in search of particular requirements.

2.2.2 Response of Viscoelastically Damped Systems

For prediction of structural response in the frequency domain, analytical techniques for elastic systems may be translated into those for viscoelastic systems by using the Correspondence principle i.e. replacing real elastic moduli by the corresponding complex moduli whenever viscoelastic materials are modelled, not forgetting to allow for the variation of the moduli and loss factors with frequency and temperature. This means that functions of complex variables replace functions of real variables, and in particular real matrix equations are replaced by those having some complex terms. This increases the order of many problems, but is of course a necessary step. One simplification which may be used to minimize this problem is the modal strain energy approach [54], in which the problems are initially solved for the elastic system, strain energies in each mode of the corresponding normal mode solution are computed and the

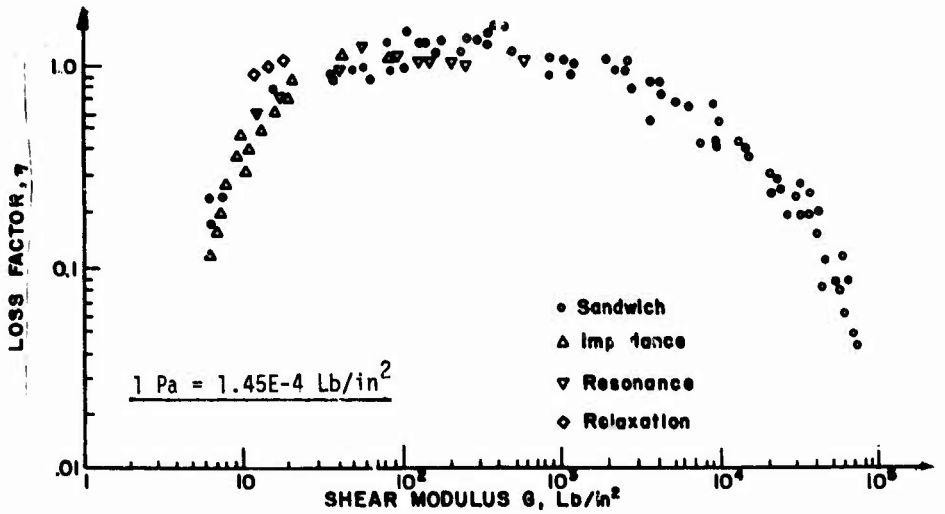

Fig. 7. Plot of log (loss factor) versus log (shear modulus) for typical acrylic adhesive (3M-966)

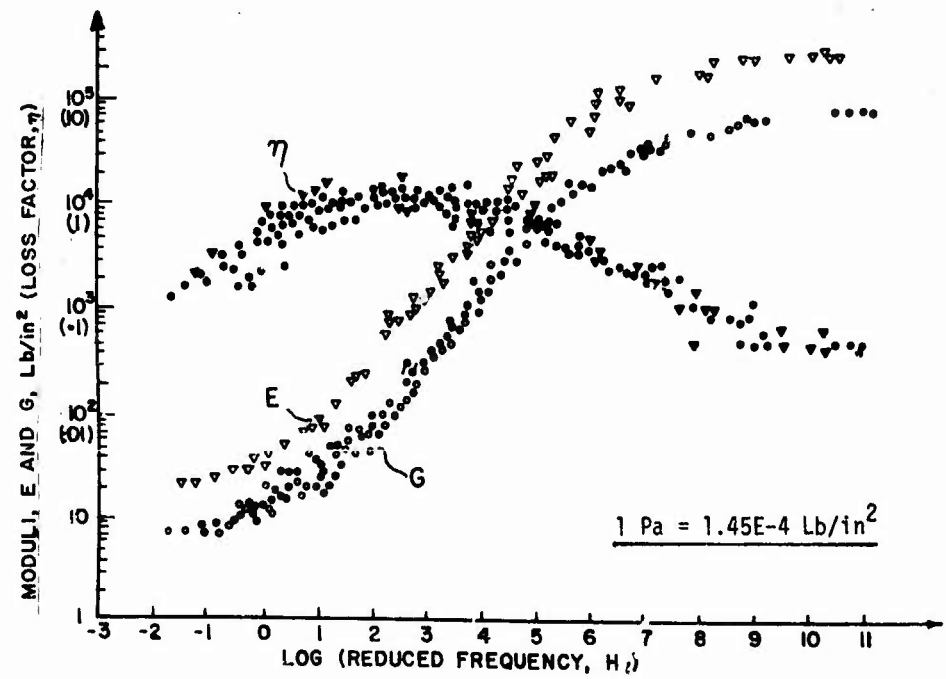

Fig. 8. Plot of log (Young's modulus, E), log (shear modulus, G) and log (loss factor) versus log (reduced frequency) for typical acrylic adhesive (3M-966)

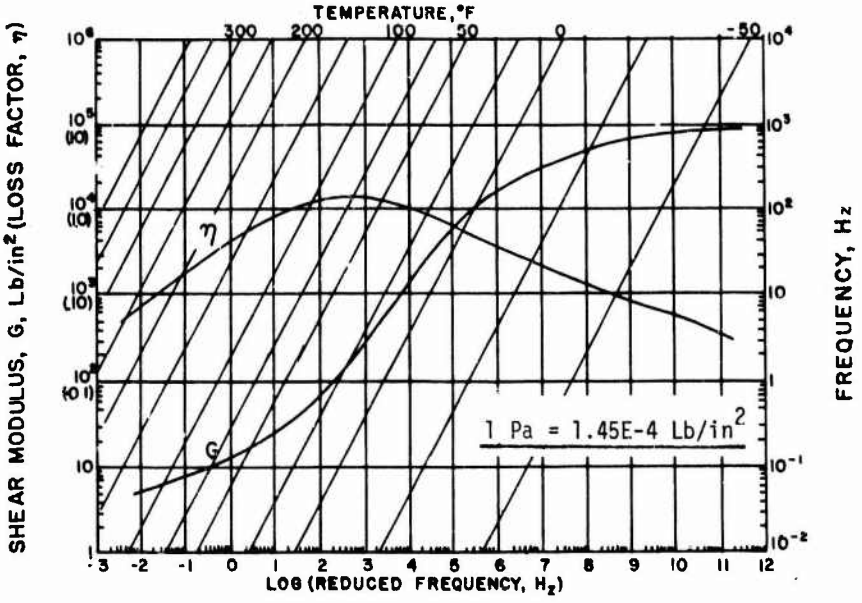

Fig. 9. Nomogram for display of complex modulus data (Reduced temperature nomogram, 3M-966, [42])

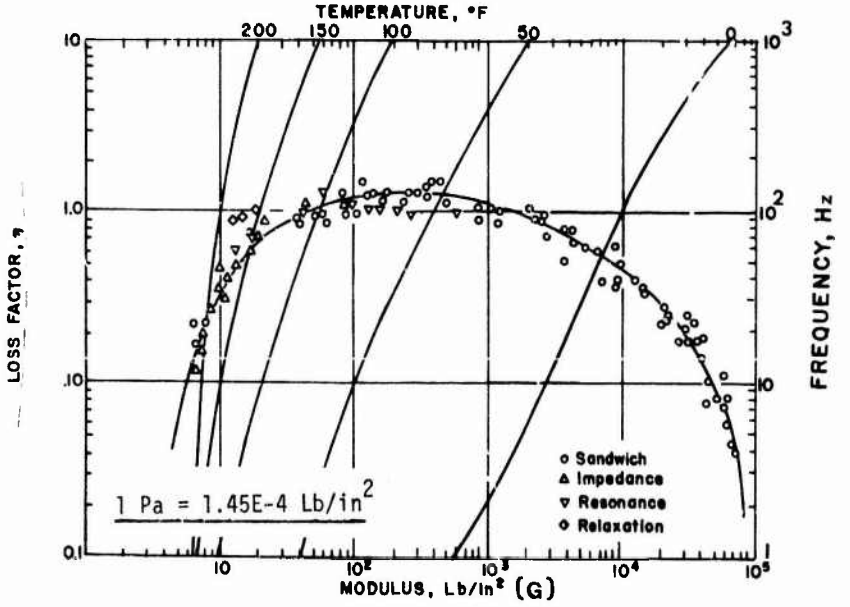

Fig. 10. Nomogram for display of complex modulus data (alternate format, 3M-966, [53])

modal loss factors of the damped system are determined by the simple relationship:

$$\eta_n = \sum_i \eta_{ni} U_{ni} \Big/ \sum_i U_{ni} \qquad (2)$$

where η_{ni} is the loss factor of the ith viscoelastic element (in a finite element analysis), U_{ni} is the strain energy in that element, and η_n is the modal loss factor in the nth mode. This relationship is valid only when the damping does not materially alter the mode shapes, which is often the case in engineering problems.

In transient response situations, the problem may be solved by working first in the frequency domain, then using the Fourier Transform to return to the time domain. This usally has to be accomplished numerically, and the frequency dependence of the viscoelastic materials must be allowed for over a very wide frequency range, usually five decades or more in magnitude. The old nemesis of viscoelastic damping, namely the widely held belief that the complex modulus model is invalid because of non-casuality, arose because such non-casuality does indeed occur for "hysteretic" damping for which modulus and loss factor are constant [49, 55]. As soon as the real material variation with frequency is allowed for, however, the problem vanishes, as illustrated in Figures 11 and 12 [49]. The problem has led to searches for alternate approaches, however, and has been a healthy stimulant for further research. One outcome of such research has been the fractional derivative model, which seeks to develop a relationship between stress and strain in the time domain through series of fractional derivatives of stress and strain [56]. This allows Laplace transforms to be used for time domain problems.

While finite element codes have now been developed to the point where prediction of the effect of selected damping treatments on dynamic response is not, in principle, a difficult problem, the analyses conducted many years ago for very idealized problems have not been lost, but have evolved into useful, simple, approaches for making initial, "back of the envelope", estimates of damping in complicated structures, as a prelude to more exact analysis. For example, the analysis of Ross, Kerwin and Ungar [57] for a constrained layer treatment on a pinned-pinned beam now forms the basis for simple computer codes to determine initial estimates of the effectiveness of layered damping treatments on complicated structures and for usually sufficiently accurate determinations of damping material complex modulus properties from tests on sandwich cantilever beams [42].

2.3 Damping/Dynamic Response Issues

Damping is a measure of the energy dissipation characteristics of polymeric material behavior. It is also a measure of the linear parameter controlling the peak amplitude of each component of the modal response of structures having a unique relationship between the damping, stiffness and mass matrices, known as proportional damping. However, in many complicated structures, the mechanisms of energy dissipation may not be distributed in such a mathematically convenient manner, but may be located at arbitrary areas so that at resonance all points of the structure do not move perfectly in or out of phase i.e. the normal modes become complex. This behavior is now well recognized as a consequence of non-proportional damping and is no more difficult to analyze, at least in principle, than proportional damping in finite element analysis [58]. In most aerospace structures, where the

damping sources are well distributed, obscure in mechanism, and not unduly great, very little advantage is gained by treating the damping as being non-proportional. Therefore, finite element analyses or experimental investigations often treat the damping as a number to be defined arbitrarily, or by measurement, for each term of the modal expansion. Where damping is deliberately introduced by viscoelastic material configurations in properly selected areas, this approach is still profitable, and forms the basis of the well known Modal Strain Energy Method [54].

In the area of experimental modal analysis, compliance measurements conducted by a wide variety of commercial test systems, using various excitation methods, including impact, random, digital sine -sweep etc., and a wide variety of methods for identifying the modal parameters have been developed and used [59]. These identifications are very useful for providing insight into the contribution of each mode, complex or real, in the response of the structure, and may provide an experienced mechanical engineer with useful insight for developing structural modifications to reduce the severity of specific vibrational problems encountered in real engineering systems.

The problem of identifying useful structural modifications which change modal characteristics in a user selectable manner, or of identifying the physical characteristics of specific parts of a system from dynamic response measurements is not so readily addressable. This is because models have to be conceived and the parameters adjusted until the predicted and measured responses agree, and this may require many iterations before success is achieved. The use of identified finite modal expansions, for which modes, frequencies, modal masses and loss factors have been determined during modal analysis, to create compliance matrices of order equal to the number of modes may be more fruitful in the future. The inversion of the compliance matrices to create dynamic stiffness (impedance type) matrices can then lead to rational discrete models of the measured system which may or may not correlate well with actual physical characteristics. Dynamic stiffness models which correlate well with the corresponding physical system have been achieved for rotor-bearing systems, and have led to measurements of rotor and bearing parameters which were extremely difficult to measure in any other way [60]. The dynamic stiffness approach also provides an effective method for identifying system modifications necessary to achieve specific, user selected, changes in modal characteristics of a complicated structure [61].

3. APPLICATIONS OF DAMPING

Many significant applications of damping technology have been engineered in the past ten years or so, and many more are being planned for the future. It is in this area, in fact, that by far the most has been accomplished; indeed the point has been reached where a design guide [45], a major conference proceedings [62] and a textbook [42] have recently been published, representing a summary of the state of the art with respect to design of damping treatments.

3.1 Aerospace Applications

Applications of damping for control of vibrations in printed circuit boards have been developed [63], and in the future we can expect the damping to be incorporated much more integrally into the manufacturing process. Damping has also been evaluated and applied for cabin noise control in many aircraft [64, 65]. The gains to be made in this area in the future will

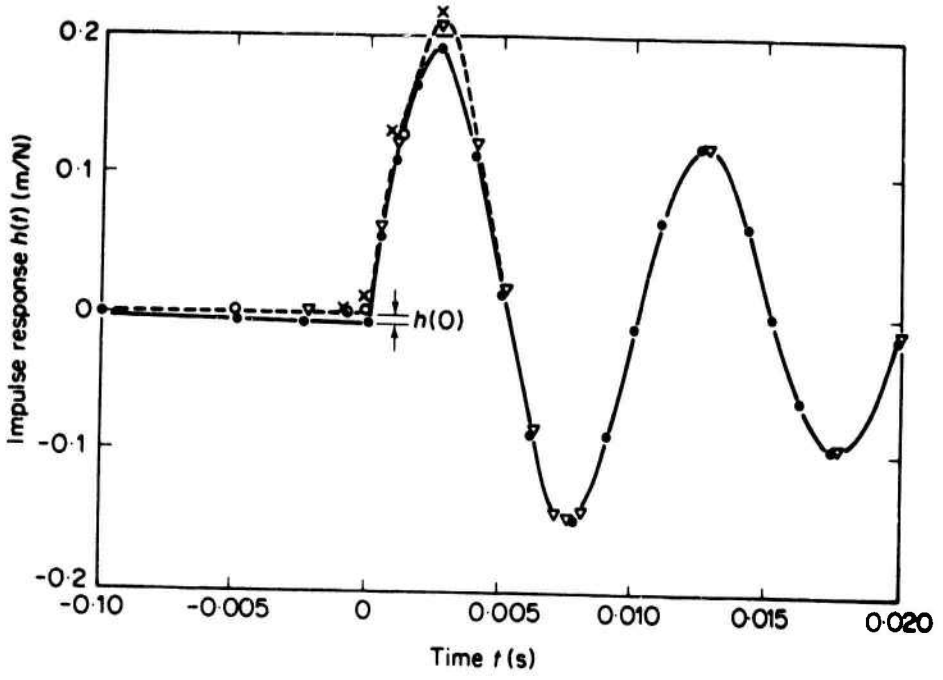

Fig. 11. Impulse response functions for single degree of freedom system with low damping material (BTR; ×∇, complex modulus models; o, viscous model; ● hysteretic model, [49])

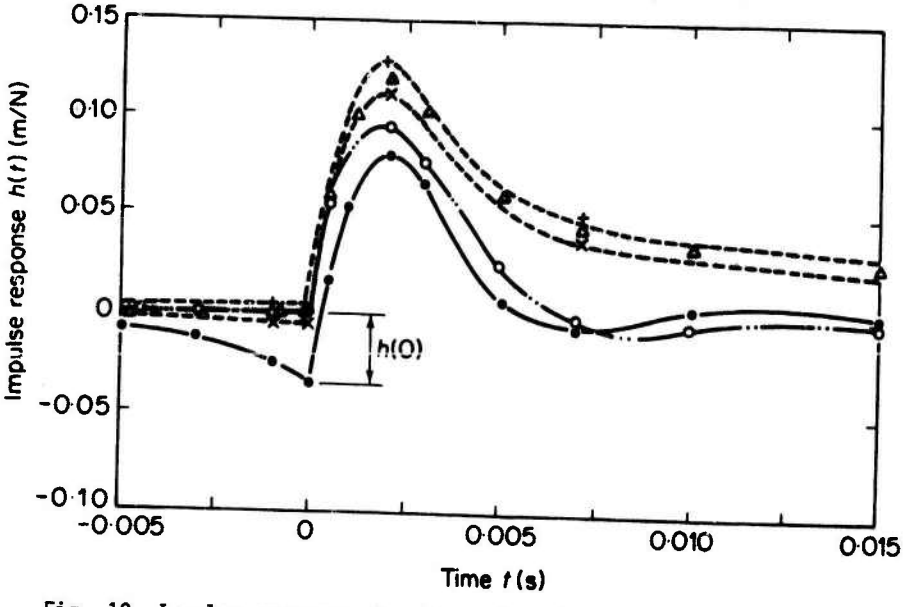

Fig. 12. Impulse response functions for single degree of freedom system with high damping material (3M-466; ×∇+, complex modulus model; o viscous model; ● hysteretic model [49])

depend critically on how well damping can be integrated into the design process, since the use of damping in an additive sense is very inefficient without also controlling the mass and stiffness characteristics of the system.

3.2 Space Applications

The PACOSS [66] and RELSAT [67] programs have initiated the process of designing and space-qualifying viscoelastic damping systems for vibration control in major space structures. This technology will be particularly necessary for control of jitter in SDI systems and in optical inter-satellite communications systems.

Some experiments and analyses have already begun to quantify the requirements. Figure 13, for example, illustrates the distortion requirements for a large mirror system, while Figure 14 shows the effect on transfer functions and response time history of a change of modal loss factors from 0.02 to 0.20 [68]. Figure 15 illustrates the effectiveness of passive damping in easing the requirements on an active control system [69]. Several other important studies have paved the way for design of effective space-qualified damping systems [6,7,70-73]. Much work remains to be done. For example, the viscoelastic materials used will have to remain in space for several years, so outgassing behavior in vacuum will need to be understood and quantified better than at present.

3.3 Gas Turbine Engines

Several applications in Gas Turbine engines have been developed in the past several years [42,74-76]. These have been ad-hoc, additive, treatments developed in response to specific problems which have arisen during the life of particular engines in the US Air Force inventory. The treatments have often been expensive to develop and apply, since they had to work without modifying the components suffering the vibrational problems. Nevertheless, the cost savings achieved by eliminating these problems have been impressive. In most cases, the 'bottom line' has been the driver, but flight safety has gained in the process.

3.4 Automotive

Possibly the greatest advances have been made in this area, because the damping has had to be applied sparingly, for control of internal and external engine noise, at extremely low cost, in order to be accepted even to a degree. Applications in valve covers have been effective, particularly when combined with isolation [77-81]. Steel laminates are being produced, and pressed into a number of body parts [82-84].

CONCLUSIONS

In the short time and few pages available, the author has attempted to give a brief, selective and not unbiased summary of the current state of the art in Structural Damping. Clearly this represents only a sampling, and many times the number of references could easily have been added given the space. What we see, in essence, is a very significant maturing of the area, both with respect to the manner in which old questions have been answered, solved or by-passed, and with respect to the widespread efforts now being made to apply damping for the solution of relevant engineering problems and the critical, yet positive, "can-do", approach being adopted in a large

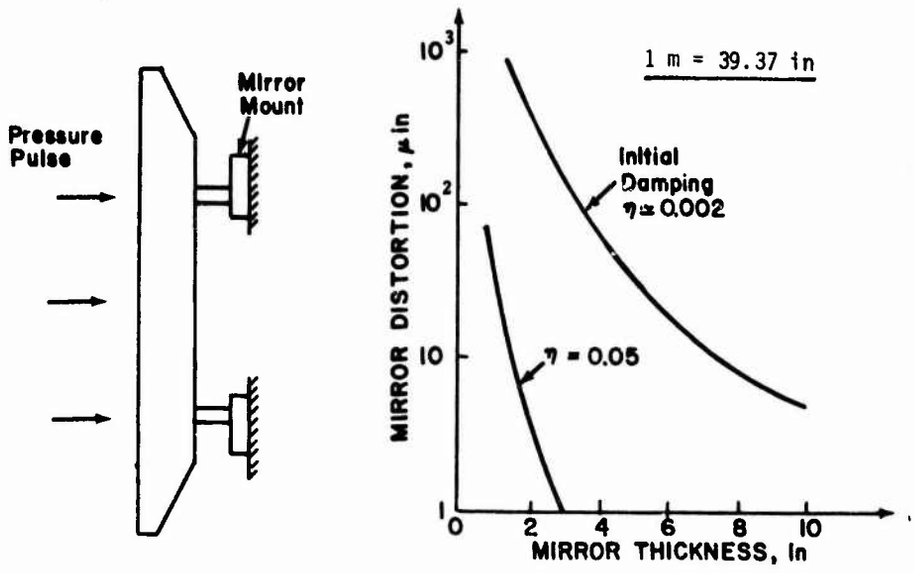

Fig. 13. Distortion requirements for large space mirror [68]

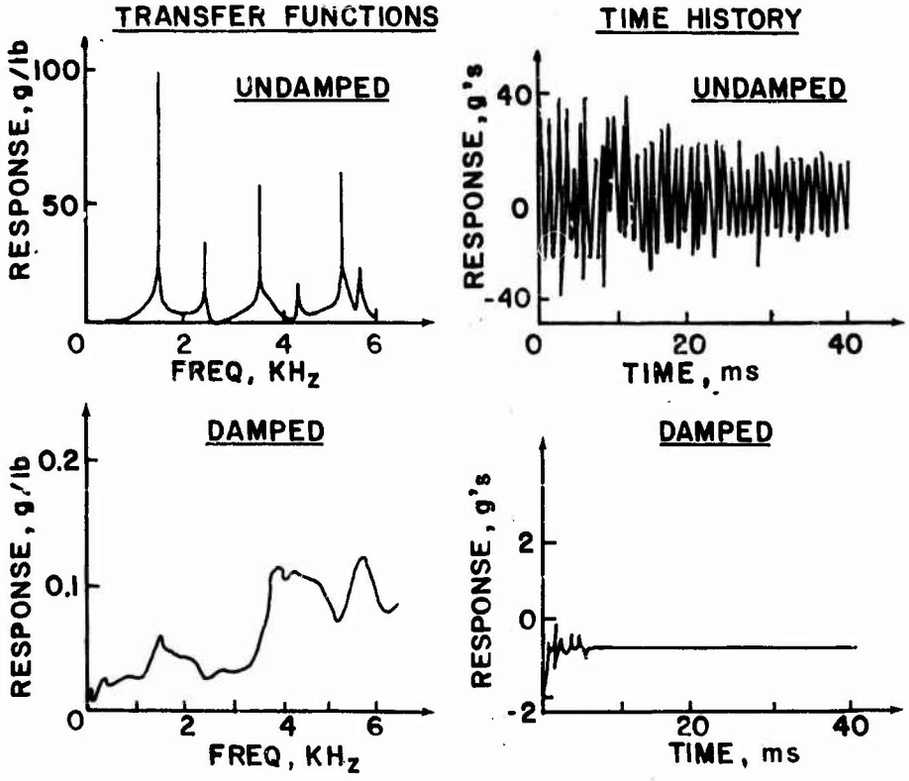

Fig. 14. Effects of passive damping on mirror response [68]

number of these efforts. This is a major change from the situation even ten years ago, when the response one might have received to a suggestion that damping be used to solve a relevant engineering problem would often be a statement such as "damping was tried in 1964 and it didn't work" or "I won't put any of that stuff in my system". Now we see greater understanding of the behavior of damping materials, careful balancing of the pro's and con's for each application, and a healthy concern for cost-benefit ratios. Hopefully, this will be the tone for the future, and if that remains the case, it might well be said that Damping has come of age at last.

ACKNOWLEDGMENTS

Thanks are due to Debbie Brown and Lisa Farmer, AFWAL/MLLN, for typing the manuscript and to Larry Jenkins (AFWAL/ISS) for preparing the figures.

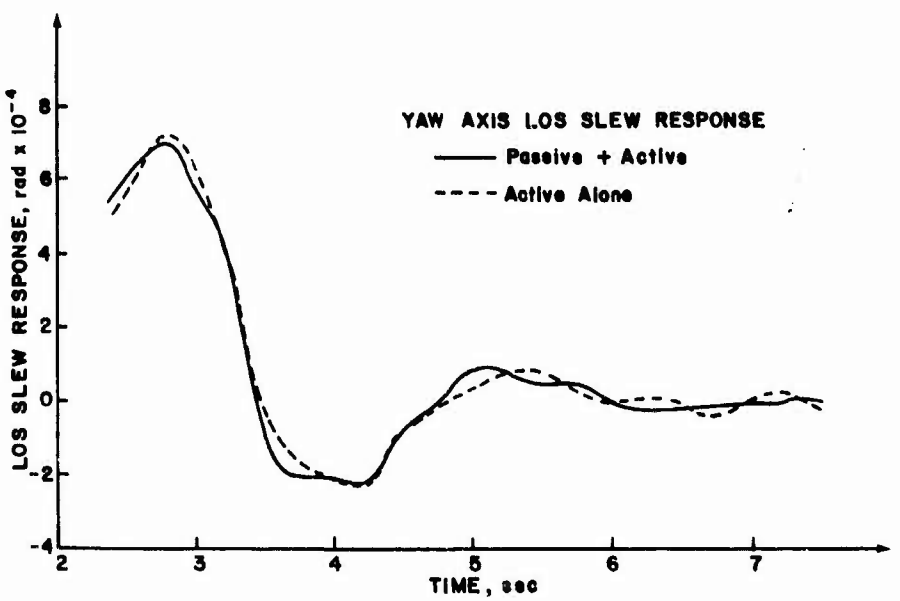

Fig. 15. Effect of active and passive damping on line-of-sight (LOS) response of a space structure [69]

REFERENCES

1. E.E. UNGAR 1964 Shock Vib. Assoc. Environments, Bulletin 33, Part IV, pp 189-199. Vibration Energy Losses at Joints in Metal Structures.

2. E.E. UNGAR 1964 Flight Dynamics Laboratory, Report FDL-TR-64-98. Energy Dissipation at Structural Joints; Mechanisms and Magnitudes.

3. D.J. MEAD 1965 Air Force Materials Lab, Report AFML-TR-65-284. The Effect of Certain Damping Treatments on the Response Of Idealized Aeroplane Structures Excited by Noise.

4. E.J. RICHARDS and D.J. MEAD (eds) 1968 Wiley, London. Noise and Acoustic Fatigue in Aeronautics.

5. Y.K. LIN 1960 J. Appl. Mech, 27(4), pp 669-676. Free Vibrations of Continuous Skin-Stringer Panels.

6. B.K. WADA 1986 Damping 86 Proceedings (ed: L.C. Rogers), AFWAL-TR-86-3059, Vol 2, pp DE-1 to DE-15. Prediction of Spacecraft Damping.

7. H. ASHLEY D.L. and EDBURG 1986 Damping 86 Proceedings (Ed: L.C. Rogers), AFWAL-TR-86-3059, Vol 1, pp DA-1 to DA-17. On the Virtues and Prospects for Passive Damping in Large Space Structures.

8. J. SOOVERE 1986 Damping 86 Proceedings (Ed: L.C. Rogers), AFWAL-TR-86-3059, Vol 1, pp CD-1 to CD-28. Method of Predicting the Damping in Stiffened Structures.

9. S.A. SUAREZ, et al 1986 Damping 86 Proceedings (Ed: L.C. Rogers), AFWAL-TR-86-3059, Vol 2, pp FF1-FF28. The Influence of Fiber Length and Fiber Orientation on Damping and Stiffness of Polymer Composite Materials.

10. R.D. ADAMS 1986 Damping 86 Proceedings (Ed: L.C. Rogers), AFWAL-TR-86-3059, Vol 2, pp FG-1 to FG-22. A Review of the Damping Mechanisms in Advanced Fibre-Reinforced Composites.

11. S.W.E. EARLES 1966 J. Mech. Eng. Sci., 8(2), pp 207-214. Theoretical Estimation of the Frictional Energy Dissipation in a Simple Lap Joint.

12. A.V. SRINIVASAN and D.G. CUTTS 1983 J. Engineering for Power, pp 332-341. Dry Friction Damping Mechanisms in Engine Blades.

13. C. PIERRE, A.A. FERRI and E.H. DOWELL 1985 J. Appl. Mech., Vol 52, pp 958-964. Multi-Harmonic Analysis of Dry Friction Damped Systems Using an Incremental Harmonic Balance Method.

14. R.J. DOMINIC 1984 ASME Paper 84-GT-109. Parametric Study of Turbine Blade Friction Damping Using the Lumped Parameter Analysis.

15. C.H. MENQ and J.H. GRIFFIN 1984 J. Vib. Acoust. Stress and Reliability in Design, ASME Paper 83-DET-24. A Comparison of Transient and Steady State Finite Element Analyses of the Forced Response of a Frictionally Damped Beam.

16. J.H. GRIFFIN and A. SINHA 1984 J. Eng. for Power, ASME Paper 84-GT-139. The Interaction Between Mistuning and Friction in the Forced Response of Bladed Disk Assemblies.

17. C.F. BEARDS 1983 J. Vib. Acoustics, Stress and Reliability, pp 369-373. The Damping of Structural Vibration by Controlled Interfacial Slip in Joints.

18. E.H. DOWELL and E.H. SCHWARTZ 1983 J. Sound Vib. 91(2), pp 255-267 (Part 1) and pp 269-291 (Part 2). Forced Response of a Cantilever Beam with a Dry Friction Damper Attached.

19. A. MUSZYNSKA and D.I.G. JONES 1983 J. Sound Vib. 86(1), pp 107-128. On Tuned Bladed Disk Dynamics: Some Aspects of Friction Related Mistuning.

20. A. MUSZYNSKA, D.I.G. JONES, T. LAGNESE and L. WHITFORD 1981 Shock and Vibration Bulletin 51, pp 89-110. On Nonlinear Response of Multiple Blade Systems.

21. J.P. STEVENS AND CO., Company Literature, Northampton MA. High Performance Urethane Film.

22. ANTIPHON INC., Company Literature, Newark DE. Noise Abatement Materials

23. LORD ACOUSTICAL PRODUCTS, Company Literature, Erie PA. Soundscreen Noise Control Products.

24. SOC. NAT. DES POUDRES ET EXPLOSIFS (SNPE), Technical Literature, Paris FR. Damping Materials

25. SOUNDCOAT INC., Company Literature, Brooklyn NY. Noise Control Materials for Industry.

26. MYSTIC TAPE, Company Literature, Northfield IL. Industrial Pressure Sensitive Tapes.

27. B.F. GOODRICH, Company Literature, Cleveland OH. Elastomer Properties; Nitrile, EPDM, Epichlorohydrin, SBR.

28. 3M COMPANY, Company Literature, St. Paul MN. Product Information; Viscoelastic Polymers.

29. EAR CORPORATION, Company Literature, Westwood MA. The Reduction of High Frequency Vibration and Noise by Using E-A-R Isodamp Isolation Materials

30. PRE FINISH METALS INC., Company Literature, Elk Grove Village IL. Introducing Polycore Composites.

31. VIBRACHOC USA, Company Literature, Phoenix AZ. Vibration and Shock Control.

32. SHELL CHEMICAL COMPANY, Company Literature, Chicago IL. Kraton Thermoplastic Rubber.

33. VIBRATION MOUNTINGS & CONTROLS, INC., Company Literature, Butler NJ. Quiet-Kote.

34. FERRO COMPOSITES CORP., Company Literature, Norwalk CT. Noise Control Systems.

35. ETHYL CORPORATION, Company Literature, Baton Rouge LA. Eypel-F Performance Elastomers.

36. GENERAL ELECTRIC CO., Company Literature, Philadelphia PA. SMRD, a GE Developed Flight Proven Damping Compound.

37. SPECIALTY COMPOSITES CORP., Company Literature, Newark DE. "Tufcote Noise Control Products.

38. IMASS INC, Product Bulletin, Accord MA. Dynastat, A Complete Transient and Dynamic Viscoelastic Analyzer.

39. POLYMER LABORATORIES INC., Product Bulletin, Amherst MA. Dynamic Mechanical Thermal Analyzer.

40. METRAVIB, Product Bulletin, Ecully FR. Viscoanalyzer.

41. DU PONT INSTRUMENTS, Product Bulletin, Wilmington DE. Dynamic Mechanical Analysis.

42. A.D. NASHIF, D.I.G. JONES and J.P. HENDERSON 1985 Wiley, New York. Vibration Damping.

43. D.I.G. JONES 1978 Shock and Vibration Bulletin, 48(2), pp 13-22. A Reduced-Temperature Nomogram for Characterization of Damping Material Behavior.

44. D.I.G. JONES 1979 Aircraft Engineering, pp 9-14. Two Decades of Progress in Damping Technology.

45. J. SOOVERE and M.L. DRAKE 1985 Air Force Wright Aero. Labs. AFWAL-TR-84-3089, Vols, 1-3. Aerospace Structures Technology Damping Design Guide.

46. M. RUDDELL, et al 1982 Air Force Wright Aero. Labs., AFWAL-TR-82-4167. Damping Materials, Finite Elements and Special Projects.

47. M.L. DRAKE and G.E. TERBORG 1980 Air Force Wright Aero Labs., AFWAL-TR-79-4093. Polymeric Materials Testing Procedures to Determine Damping Properties and the Results of Selected Commercial Material.

48. M.L. PARIN 1986 Damping 86 Proceedings, AFWAL-TR-3059, Vol. 1, pp AD-1 to AD-80. PACOSS and RELSAT Damping Material Measurements.

49. D.I.G. JONES 1986 J. Sound Vib., 106(2), pp 353-356. The Impulse Response Functions of a Damped Single Degree of Freedom System.

50. L.C. ROGERS et al 1986 Damping 86 Proceedings, AFWAL-TR-86-3059, Vol. 1, pp AA-1 to AA-B11. Standard Graphical Presentation of Complex Modulus and Data Processing Methodology.

51. J.Y. CAVAILLE, C. JOURDAN and J. PEREZ 1987 J. Polymer Science, 25, pp 1235-1251. Time-Temperature Superposition and Dynamic Mechanical Behavior of Atactic Polystyrene.

52. L.C. ROGERS 1987 Proposed International Standard, ISO TC-108. Graphical Presentation of Damping Material Complex Modulus.

53. D.I.G. JONES and D.K. RAO 1987 ASME Publ., DE-Vol 5, the Role of Damping in Vibration and Noise Control, ed: L.C. Rogers and J.C. Simonis. A New Method for Representing Damping Material Properties.

54. C.D. JOHNSON and D.A. KIENHOLZ 1982 AIAA Journal, 20(9), pp 1284-1290. Finite Element Prediction of Damping in Structures with Constrained Viscoelastic Layers.

55. R.H. SCANLAN 1970 J. Sound Vib., 13(4). Linear Damping Models and Causality in Vibrations.

56. R.L. BAGLEY and P.J. TORVIK 1986 J. Rheology, 30(1), pp 133-155. On the Fractional Calculus Model of Viscoelastic Behavior.

57. D. Ross E.E. UNGAR and E.M. KERWIN 1959 Structural Damping, ASME, pp 49-88. Damping of Plate Flexural Vibrations by means of Viscoelastic Laminae.

58. R.L. ADKINS 1975 Materials Laboratory, AFML-TR-75-2. Modal Analysis of Linear Non-Conservative Systems.

59. R.J. ALLEMANG 1982 Proc. 1st IMAC Conference, Union College, pp 714-726. Experimental Modal Analysis Bibliography.

60. A. MUSZYNSKA 1986 International J. Experimental and Analytical Modal Analysis. Modal Testing of Rotor/Bearing Systems.

61. D.I.G. JONES and A. MUSZYNSKA 1988, J. Vib. Stress and Reliability, ASME. Structural Modification of Advanced Turbomachine Blading by Dynamic Stiffness Matrix Operations.

62. L.C. ROGERS (ed) 1986, AFWAL-TR-86-3059, Vols. I and II. Damping 86 Proceedings.

63. C.V. STAHLE, J.A. STALEY and J.C. STRAI 1986 Damping 86 Proc., AFWAL-TR-86-3059, Vol. 2, pp HE-1 to HE-3. Design and Experimental Verification of Damped Spacecraft Equipment Panels.

64. L.D. POPE et al 1982 J. Sound and Vib., 82(4). Development and Validation of Preliminary Analytical Models for Aircraft Interior Noise Prediction.

65. B.J. HOGAN 1985 Design News. Damped Secondary Aircraft Structure Resists Vibro-Acoustically Induced Damage.

66. D.R. MORGENTHALER 1986 Damping 86 Proceedings, AFWAL-TR-3059, Vol. 2, pp DG-1 to DG-31. Design and Analysis of the PACOSS Representative System.

67. R. IKEGAMI and D.W. JOHNSON 1986 Damping 86 Proceedings, AFWAL-TR-86-3059, Vol. 2, pp HB-1 to HB-20. The Design of Viscoelastic Passive Damping Treatments for Satellite Equipment Support Structures.

68. M.J. LAUCHLIN 1986 Damping 86 Proceedings, AFWAL-TR-86-3059, Vol. 1, pp CA-1 to CA-13. Damped Optics Design.

69. R.N. GEHLING 1986 Damping 86 Proceedings, AFWAL-TR-86-3059, Vol. 2, pp EB-1 to EB-18. Active Augmentation of a Passively Damped Representative Large Space System.

70. E.D. PINSON 1986 Damping 86 Proceedings, AFWAL-TR-86-3059, Vol. 2, pp DC-1 to DC-26. Damping Characteristics of the Solar Array Experiment.

71. R.K. YEDVALLI 1986 Damping 86 Proceedings, AFWAL-TR-86-3059, Vol. 2, pp EA-1 to EA-8. Robust Control Design for Vibration Suppression of Large Space Structures.

72. P.J. LYNCH and S.S. BANDA 1986 Damping 86 Proceedings, AFWAL-TR-86-3059, pp EC-1 to EC-27. Active Control for Vibration Damping.

73. D.F. GOLLA and P.C. HUGHES 1985 J. Appl. Mech., 52, pp 897-906. Dynamics of Viscoelastic Structures-a Time-Domain Finite Elemen Formulation.

74. J.P. HENDERSON 1979 ASME Paper 79-GT-163. Engine Evaluation of a Vibration Damping Treatment for Inlet Guide Vanes.

75. J.P. HENDERSON 1980 ASME Publications AMD-Vol 38, Damping Applications for Vibration Control, ed: P.J. Torvik, pp 145-158. Damping Applications in Aero-Propulsion System.

76. L.C. ROGERS and M.L. PARIN 1978 Wright-Patterson AFB, AFFDL-TM-78-78-FBA, pp 277-284. A Thoroughly Engineered Application of Damping Technology to Jet Engine Inlet Guide Vanes.

77. A.D. NASHIF 1983 Sound & Vib., pp 28-36. Control of Noise and Vibration with Damping Materials.

78. A.D. NASHIF 1980 ASME Publ. AMD-Vol. 38, pp 133-143. Application of Damping for Noise Control.

79. ANON, Nov 1987 Diesel Progress/North American, p 20. Environmental Considerations: Key Engine Design.

80. W.G. HALVORSEN and R.G. SMILEY 1979 Proc. Noise-Con 79, Purdue University. Isolation of Engine Components.

81. J. YAMAGUCHI 1985 Automotive Engineering, 93(2), p 107. Toyota Presents Overview on New Materials.

82. E.J. VYDRA 1987 SAE Paper 870178, SAE Meeting Proc. Multilayer Composite Materials Manufactured by Continuous Coil Coating/Laminating Process.

83. ANON, Mar 1986 Metal Progress News, pp 18-20. Japanese Steelmaker Details Produce Development Efforts.

84. J. YAMAGUCHI 1986 Automotive Engineering, 94(7), p 65. Twin-Streak Injector Lowers Diesel Noise Level.

DAMPING OF CONTINUOUS STRUCTURES BY THE USE OF ELASTIC POROUS MATERIALS

C.U. Bruer * and J.S. Bolton **

*** Anatrol Corporation, 10895 Indeco Drive, Cincinnati OH 45241 U.S.A.**

****Ray W. Herrick Laboratories, School of Mechanical Engineering, Purdue University, West Lafayette IN 47907 U.S.A.**

ABSTRACT

Described in this paper is an investigation of the vibration damping behavior of polyurethane foams of the type normally used to control airborne sound. From measurements initially performed to determine the foam's Young's and shear modulus, it was found that when the foam was applied in deep layers to one side of a metal beam or used as the core between two adjacent metal beams high damping can be produced over extended frequency ranges. This effect appears to result from the finite depth of the foam layer and thus is not accounted for by most existing theories which require the depth of the damping layer to be thin compared with the flexural wavelength of the structure. It is known that in general two wave types (longitudinal and transverse) propagate simultaneously in damping media. Conventional "thin layer" theories generally assume that only one wave type exists depending on the nature of the beam construction. To account for the observed damping effect a theory has been developed which is applicable to beams with damping layers of unrestricted depth and allows for the existence of both longitudinal and transverse wave types simultaneously. This theory models the damping layer as a two-dimensional duct-like acoustical field. Calculations made with this approach have indicated that layers of elastic porous materials may be used in two roles: to control structural vibrations while simultaneously reducing airborne noise.

1. INTRODUCTION AND EXPERIMENTAL PROCEDURE

The demand for lightweight damping materials such as noise control foam has resulted in the use of layer thicknesses from 0.006m to more than 0.025m to produce efficient damping [1]. In a previous paper [2] the dynamic properties of this elastic porous material were determined by means of measurements in conjunction with laminated thin beam theories as derived by Oberst [3,4] and Ross, Kerwin and Ungar [5]. From experiments performed using both beams with a one-sided foam layer and sandwich configurations it has been found that the vibrational behavior and damping effect of these attached layers are quite different from those observed for conventional damping treatments (see Figures 1 and 2, illustrating the transfer functions of a free-free 2.0m long beam (0.0017m thick and 0.038m wide) with a 0.025m deep foam layer attached to one side of it and that of a free-free 2.0m sandwich beam with a 0.006m deep foam core held between identical steel beams (as above), respectively). In a broad frequency range a substantial reduction in vibration amplitudes is observed and the foam's damping effect may be considered as equivalent to the damping effect caused by ordinary, relatively heavy, damping coatings such as polyvinyl chloride materials [2].

However, none of the above-mentioned theories [3-5] can be appropriately used to predict the observed vibrational behavior of these beam structures with foam treatments, since they require the laminated beam to behave like a homogeneous structure. The experimental investigation of the flexural motion of the two external steel beams in the sandwich configuration has shown that they experience relative transverse motion over the highly damped frequency ranges and consequently the composite beam cannot be treated as a homogeneous beam when this feature is observed. In Figure 3 are shown the transfer functions of the 2.0m sandwich beam with 0.006m foam core; these measurements were made using an end-mounted transverse point excitation force (shaker) mounted to one side of the sandwich (the front) and an accelerometer mounted alternately on the front and back beams of the sandwich. Figure 4 shows the ratio of the magnitudes of these transfer functions. It is clear that at frequencies above 600 Hz the degree of relative motion between the constraining beams begins to increase thus confirming that the composite beam is not behaving like a homogeneous beam.

The experiments performed on the sandwich beams have further indicated that the damping process due to the foam core involves more complicated actions than previously assumed. The phenomena observed (i.e., conventional resonant behavior in the lower and higher frequency range, while anomalously high damping occurs between 500 Hz and 1000 Hz (Figure 2)) and the need for a theory which allows the depth of the attached damping layer to be unrestricted have led to the derivations of a "deep layer theory" which will be described in the following sections.

2. DEEP LAYER THEORY

2.1 Background

The damping performance of the foam layer attached to a metal beam is quantified by predicting the point and transfer accelerances of the composite structure. The steel base beam is assumed to conform to the Euler-Bernoulli model: i.e., the equation governing transverse displacement is fourth order and rotary inertia effects are neglected. The foam damping layer is modeled as a two-dimensional duct-like acoustical wave field which is coupled to the base beam *via* distributed stress forcing terms and velocity continuity conditions. The presence of two different wave types (longitudinal and transverse) propagating simultaneously in the foam damping medium is accounted for. Based on the expansion theorem for continuous functions (similar to a Fourier series expansion) the beam's eigenfunctions, obtained from a modal solution approach, are used to expand the acoustical field parameters as necessary to apply boundary conditions. The application of boundary conditions at the beam's free ends, and continuity conditions at the interfaces, results in an infinite set of equations which can be solved for the displacement coefficients of the base beam on a mode by mode basis by making use of the eigenfunctions' orthogonality.

The theory is developed by deriving an "acoustical" model first, which accounts for longitudinal waves traveling in the damping layer only. The damping material is assumed to possess no significant shear stiffness and thus exhibits the properties of an ideal gas or liquid. Calculations made with this model will show that it is feasible to model the unconstrained, deep foam layer, as an acoustical medium in the lower frequency range. Then the general model in which in addition to the longitudinal waves transverse wave propagation is allowed will be described briefly. In this approach the damping layer is modeled as a linear elastic compressible solid medium.

2.2 Acoustical Model

As the damping layer in this model is treated as an ideal two-dimensional duct-like acoustical medium, no tangential stresses exist and the traveling waves are purely longitudinal. All field variables are assumed constant across the width of the beam, an assumption which is valid so long as the width of the beam is very much less than its length. The governing equation which describes the two-dimensional acoustical field may be expressed in the form of the linearized wave equation in terms of the acoustic pressure, p: i.e.,

$$\nabla^2 p + k_l^2 p = 0, \tag{1}$$

where ∇ is the gradient operator and k_l is the longitudinal wave number. For pure longitudinal waves traveling in the acoustical field the propagation speed, c_l, is related to the material properties (bulk modulus, B_o, and mass density, ρ) by $c_l = (B_o/\rho)^{1/2} = \omega/k_l$, with ω being the circular frequency. The classical approach to the solution of equation (1) is in terms of a scalar velocity potential, Φ, from which the pressure, p, and the particle velocity, $\vec{v}_l$, are obtained as:

$$p = \rho \frac{\partial \Phi}{\partial t} = j\omega\rho\, \Phi \tag{2}$$

$$\vec{v}_l = -\nabla \Phi. \tag{3}$$

An appropriate solution for Φ is:

$$\Phi = (A\, e^{-jk_{lx}x} + B\, e^{jk_{lx}x})\, e^{-jk_{ly}y} + (C\, e^{-jk_{lx}x} + D\, e^{jk_{lx}x})\, e^{jk_{ly}y}, \tag{4}$$

where k_{lx} and k_{ly} are the components of the wave number, k_l: i.e., $k_l = \sqrt{k_{lx}^2 + k_{ly}^2}$. The constants A, B, C and D are determined by the boundary conditions. As the beam structure is assumed to be free at both ends, pressure release boundary conditions apply at x=0 and x=l (l being the length of the beam): i.e.,

$$p(x,y) = j\omega\rho\, \Phi(x,y) = 0 \quad \text{at } x=0 \text{ and } x=l. \tag{5}$$

Note that this assumption implies that sound radiation from the core material is neglected. After substitution of (4) into (5) one obtains the characteristic equation

$$\sin(k_{lx} l) = 0, \tag{6}$$

yielding, $k_{lxm} = m\pi/l$ with m = 1,2,3... Consequently there are an infinite number of longitudinal wave numbers, $k_l = [(m\pi/l)^2 + k_{lym}^2]^{1/2}$, and the velocity potential, Φ, may be expressed in terms of an infinite sum over all contributing acoustical eigenfunctions: i.e.,

$$\Phi = -2j \sum_{m=1}^{\infty} \sin(k_{lxm}x)(A_m e^{-jk_{lym}y} + C_m e^{jk_{lym}y}). \tag{7}$$

In the case of a sandwich beam the two further boundary conditions necessary to determine A_m and C_m are found from the force coupling conditions and velocity continuity requirements at the interfaces, y=0 and $y=h_2$ (with h_2 being the thickness of the damping layer). For the unconstrained damping layer, a further pressure release condition at the free surface ($y=h_2$) and a normal velocity continuity condition at the interface with the base beam (y=0) are required. They are, respectively:

$$p(x,y=h_2) = j\omega\rho\,\Phi(y=h_2) = 0 \tag{8}$$

$$j\,\omega\,w(x) = v_{ly}(x,y=0). \tag{9}$$

Here, w(x) denotes the transverse displacement of the beam, while v_{ly} is the normal component of the acoustic velocity defined in equation (3): i.e., $v_{ly} = -\partial\Phi/\partial y$. The damping medium is coupled to the beam's flexure by a distributed normal forcing term. This function, due to the pressure in the acoustical medium, q(x) (see Figure 5), is obtained by multiplying the pressure, p, by the beam's width, b: i.e.,

$$q(x) = p\,b = j\omega\rho\,b\,\Phi. \tag{10}$$

The differential equation which describes the vibrational response of the laminated beam is then derived from the fourth order Euler-Bernoulli beam equation resulting in:

$$\frac{\partial^2}{\partial x^2}\left(EI\,\frac{\partial^2 w(x)}{\partial x^2}\right) + \rho_b A\,\frac{\partial^2 w(x)}{\partial t^2} = f(x) - q(x). \tag{11}$$

Here E is the Young's modulus, I is the moment of inertia, ρ_b is the mass density of the beam material and A is its cross-sectional area. Here f(x) represents the point excitation force: i.e., $f(x) = F_o\delta(x-x_o)$. To solve this equation on a mode by mode basis all displacement and forcing functions are expanded in terms of the beam's eigenfunctions, $\Gamma_n(x)$, restricting the number of vibration modes to N: i.e.,

$$w(x) = \sum_{n=1}^{N} W_n\,\Gamma_n(x), \tag{12}$$

$$f(x) = \sum_{n=1}^{N} F_n\,\Gamma_n(x) \quad \text{with} \quad F_n = \int_0^1 f(x)\Gamma_n(x)\,dx, \tag{13}$$

$$q(x) = \sum_{n=1}^{N} Q_n\,\Gamma_n(x) \quad \text{with} \quad Q_n = \int_0^1 q(x)\Gamma_n(x)\,dx. \tag{14}$$

Thus, equation (11) may be written as:

$$\sum_{n=1}^{N} (EI\lambda_n^4 - \rho_b A\omega^2)\,W_n\Gamma_n(x) = \sum_{n=1}^{N} F_n\Gamma_n(x) - \sum_{n=1}^{N} Q_n\Gamma_n(x). \tag{15}$$

Here λ_n is the n^{th} eigenvalue of the free-free beam found from a modal solution approach; ω is again the circular frequency. In a similar manner equation (9) becomes:

$$j\omega \sum_{n=1}^{N} W_n\Gamma_n(x) = \sum_{n=1}^{N} V_{ly}\Gamma_n(x) \tag{16}$$

where:

$$V_{ly} = \int_0^1 v_{ly}\Gamma_n(x)dx = \int_0^1 \left(-\frac{\partial\Phi}{\partial y}\right)\Gamma_n(x)dx\,. \tag{17}$$

After substitution of the corresponding expression for Φ, and requiring that the number of acoustical eigenfunctions (equation 7) and modes of vibrations, N, be the same, equations (15) and (16) may be written in form of a square matrix from which the displacement

coefficients of the base beam, W_n, may be obtained and the transfer function of the composite structure can be predicted. Note that when a constrained damping layer is treated in this way the pressure release boundary condition at $y=h_2$, equation (8) must be replaced by velocity continuity and force coupling terms. The displacement of the constraining metal beam is also described by a fourth order partial differential equation similar to equation (11), and thus the order of the matrix equation to be solved doubles.

Equations (15) and (16) were programmed on a VAX 11/780. Calculations made with this model yielded an improved agreement with experimental results when compared with predictions of the Oberst theory. The transfer function of a 1.0m long beam with a 0.025m deep foam layer was predicted using the foam's material properties determined as described in reference [2]: i.e., a Young's modulus of $E_2 = 8.5 \times 10^5\ Nm^{-2}$, a loss factor of 0.16 and a mass density of 27 kgm^{-3}. As the foam is known to possess some shear stiffness the bulk modulus, B_o, in the expression for c_l was replaced by the longitudinal stiffness, D: i.e, $c_l = (D/\rho)^{1/2} = [B_o(1-\mu)/(1-2\mu)(1+\mu)]^{1/2}$ with $\mu = 0.3$ being the foam's Poisson's ratio [6]. Figure 6 shows the predicted transfer function which agrees well in characteristic with the corresponding experimental data in the frequency range below 800 Hz (Figure 7): i.e., it accurately predicts that the presence of a foam layer causes the beam eigenfrequencies to be shifted to lower frequencies. In contrast, Figure 8 demonstrates that the approach based on the conventional Euler-Bernoulli beam equation in conjunction with the modified bending stiffness expression (to account for the individual layer properties as derived by Oberst [3,4]) fails to predict the observed shift in eigenfrequencies correctly. The lack of agreement between the modeled results and the experimental observations in the higher frequency range and for transfer functions of sandwich configurations (data not shown here) is not unexpected as any shear actions and thus transverse wave propagation are not accounted for in the acoustical model.

2.3 General Model

The approach described here has been extended to a general model in which the damping layer is allowed to support longitudinal and transverse wave propagation simultaneously. However, its development has not been completed at the present time and therefore calculations with this model have not yet been performed.

The damping layer in this approach is modeled as a two-dimensional elastic compressible solid field and is described by the general field equation in terms of a displacement vector, $\vec{s}$, [6]: i.e.,

$$G\,(\nabla^2\vec{s} + \frac{1}{1-2\mu}\,\nabla\,\mathrm{div}\,\vec{s}) = \rho\,\frac{\partial^2\vec{s}}{\partial t^2} \qquad (18)$$

Here, G is the medium's shear modulus, μ its Poisson's ratio, ρ its mass density and ∇ and div are the gradient and the divergence operators, respectively. This field comprises an irrotational and a divergence-free component and can therefore be described by two velocity potentials, Φ and $\vec{\Psi}$, assumed to be of a form similar to equation (4). As $\vec{\Psi}$ accounts for the sourceless velocity in the field, i.e., $\vec{v}_t = \nabla x \vec{\Psi}$ and $\mathrm{div}\,\vec{\Psi} = 0$, its coefficients and wave numbers refer to the transverse waves traveling in the medium. The total particle velocity is then obtained by superimposing the velocities of the the longitudinal and the transverse waves. To-date the characteristic equation of the damping medium has been derived by applying the corresponding boundary conditions at the free beam's ends and requiring that the normal and shear stresses be zero. The damping layer is coupled to the beam's flexure

by forcing terms and velocity continuity in both normal and tangential directions. These conditions are also expressed in terms of the potentials, Φ and $\vec{\Psi}$, and thus require the exact determination of the longitudinal and transverse wave number components. As in the derivations of the acoustical model the governing equations are expressed in matrix form to obtain a solution for the beam's displacement on a mode by mode basis. A fuller description of this approach may be found in reference [7].

3. SUMMARY AND CONCLUSIONS

A theory related to the damping of vibrating systems by relatively deep layers of acoustical noise control foam has been presented. Experiments with unconstrained and constrained foam layers attached to the beams have motivated the development of a "deep layer" model which allows for the interaction of longitudinal and transverse wave propagation in the damping medium at the same time. The theory has been derived by extending an acoustical model (in which the damping layer is treated as a duct-like acoustical medium) to the general model in which the damping layer is modeled as an elastic compressible solid medium. Calculations with the acoustical model have proven that it is feasible to predict correctly the low-frequency behavior of structures with foam damping layers of unrestricted depth.

4. REFERENCES

1. Anon., 1987 *dBriefs, EAR Division, Cabot Corporation* **1**(2). EAR technology on board new McDonnell Douglas MD-80/UHB jet.
2. C.U. Bruer and J.S. Bolton 1987 *AIAA Paper 87-1907*, 11th Aeroacoustics Conference, October 14-17, Palo Alto, California. Vibro-Acoustic Damping of Extended Vibrating Systems.
3. H. Oberst 1952 *Acustica* Akustische Beihaefte **1-2**(4), AB181-AB195. Ueber die Daempfung der Biegeschwingungen duenner Bleche durch fest haftende Belaege I.
4. H. Oberst and W. Becker 1952 *Acustica* **4**, 434-444. Ueber die Daempfung der Biegeschwingungen duenner Bleche durch fest haftende Belaege II.
5. D. Ross, E.M. Kerwin and E.E. Ungar 1959 *Structural Damping* Papers presented at ASME-Colloquium, Atlantic City New Jersey, edited by Jerome E. Ruzicka, Section III, 50-87. Damping of Plate Flexural Vibrations by Means of Viscoelastic Laminae.
6. L. Cremer, M. Heckl and E.E. Ungar 1973 *Structure-Borne Sound*, 103-152. New York: Springer Verlag.
7. C.U. Bruer 1987 *MSME Thesis, School of Mechanical Engineering, Purdue University*. Measurements and prediction of the effect of damping layers on the dynamic response of beams.

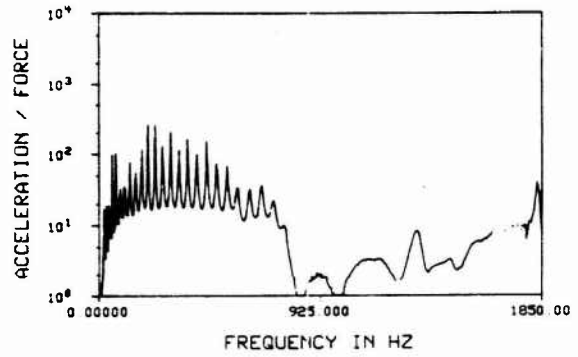

Figure 1. Damping effect of an unconstrained 0.025 m deep foam layer when attached to a 2 m long steel beam.

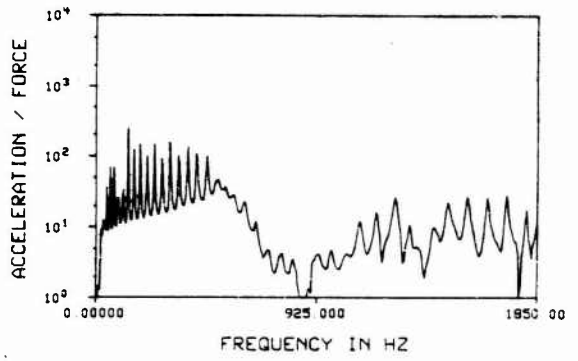

Figure 2. Damping effect of a 0.006 m deep foam core when used in a 2 m sandwich beam.

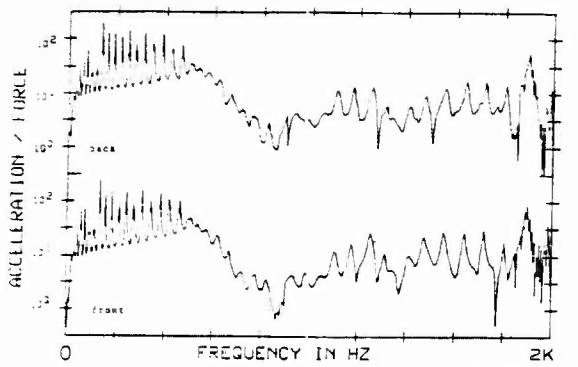

Figure 3. Vibrational response of the constraining beams in the case of a 2 m sandwich beam with 0.006 m foam core.

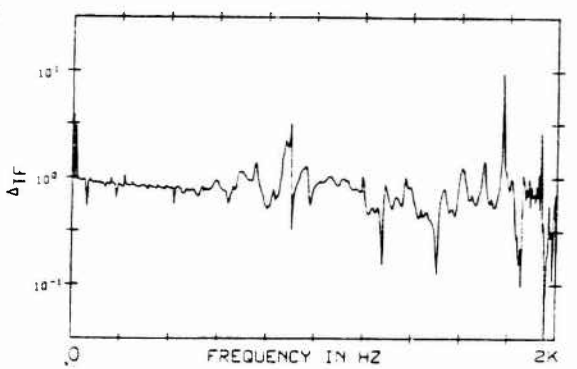

Figure 4. Magnitude of the ratio of the "front" and "back" transfer functions of the sandwich beam.

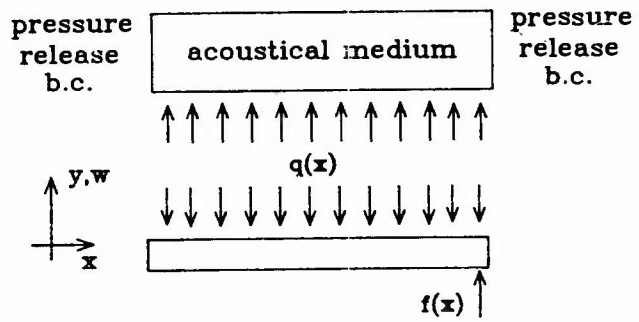

Figure 5. Beam with an acoustical load.

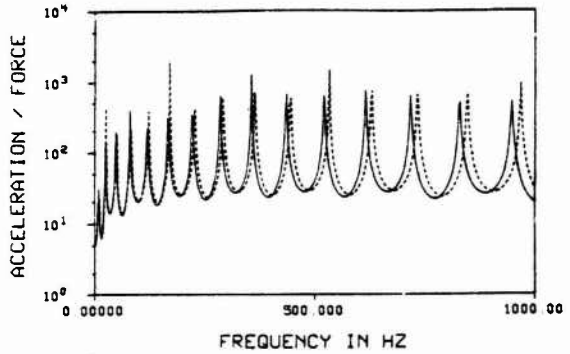

Figure 6. Predicted transfer function of a beam with an unconstrained 0.006 m deep foam layer calculated using Acoustical Model. - - - - - - -, 1 m steel beam; ————, 1 m steel beam plus foam layer.

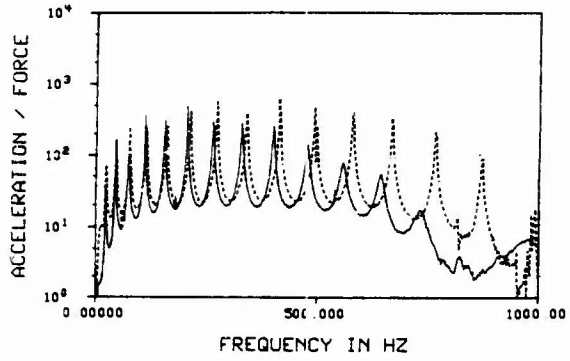

Figure 7. Measured transfer function of a beam with an unconstrained 0.006 m deep foam layer. - - - - - - -, 1 m steel beam; ————, 1 m steel beam plus foam layer.

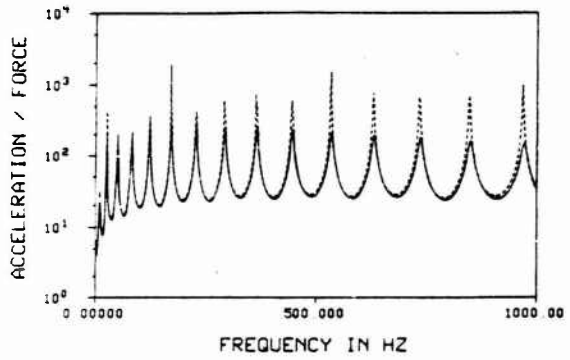

Figure 8. Predicted transfer function of a beam with an unconstrained 0.006 m deep foam layer calculated using Oberst Theory. - - - - - - -, 1 m steel beam; ————, 1 m steel beam plus foam layer.

ASSESSMENT OF FRICTIONAL DAMPING IN TANGENTIALLY LOADED METALLIC INTERFACES

S.N.SHOUKRY

Prod. Eng. Dept., Helwan University, Egypt.

1. ABSTRACT

This paper presents a derived mathematical expression for the energy dissipated per cycle, which occurs, at the metallic interfaces of plane surfaces when subjected to oscillating tangential loads that do not exceed the limiting friction forces. The mechanism of damping has been clarified and its value was quantified in terms of the fundamental information known about the interface; that is, the surface topography, the material properties and the coefficient of friction. It has been found that our mathematical expression gives theoretical results which exactly fit the experimental results measured by Rogers et al (1975) for different metallic interfaces.

As a result of the present work it should be now possible for the machine designer and its builder to make a reasonable assessment of the expected damping at various machine connections.

2. INTRODUCTION

The first systematic treatment for the mechanism of frictional damping was made by Mindlin [1] in 1949. His work was concerned with the relative elastic displacements which occur under the action of a tangential force acting in the plane of the Hertizian contact between two spheres. The treatment was based on the assumption that slip between adjacent points in the contact region will take place whenever the tangential stress at these points has exceeded the product of the normal pressure times the coefficient of friction of the contacting materials. In other words, Mindlin assumed that Amonton's law of friction was applicable to indefinitely small contact spots within the Hertizian area of contact. Mindlin's assumption came during an era where researchers widely believed that the contact spots within the true area of contact between elastic bodies were the result of plastically deformed roughness asperities, and that the force of friction arose from shearing such spots of contact (see Bowden [2]), thus Amonton's law could not hold indefinitely and hence Mindlin's work applies only to perfectly smooth contacting spheres. Inspite of such an argument, Mindlin showed that the experimental results agree with his theory [3, 4] and further expanded his work to the case of an oscillating tangential force acting in the plane of elastic contact between spheres. Further experimental varification of the validity of Mindlin's work has been

reported by Johnson [5] and Goodman [6].

Earls and Philpot [7] considered Mindlin's work too sophisticated to be applicable to plane contacting surfaces since the theory was founded on an elastic mode of deformation whilst roughness asperities deform plastically. They went on to build a mathematical model in which roughness asperities deformed plastically and concluded an expression for the energy dissipated by friction based on the work of Panovko et al [8] on friction damping occuring between the leaves of composit cantilevered beams. It is, firstly, rather striking to find that Panovoko's work was founded on Mindlin's analysis . Secondly, the experimental results of Earls & Philpot showed that the coefficient of friction between metallic surfaces remained fairly constant during the course of repeated cyclic tangential loading (two millions cycles) as long as the displacement amplitude was small. For high amplitudes (near to gross sliding), the coefficient of friction increased towards the limits. Thus Earls and Philpot concluded that for practical application where it is sufficient to estimate the frictional damping within ±30%, the coefficient of friction could be considered constant which again confirms one of Mindlin's fundamental assumptions.

Courtney Pratt and Eisner [9], found that the relative displacement between two bodies in contact consisted of a component of elastic deformation and a component of relative slip with negligible or no plastic deformation. The same was also observed in the work of Johnson and O'Conner [10].

The experiments carried out by Masuko et al [11] on bolted joints subjected to slowly varying tangential oscillating loads revealed that the tangential stiffness and the micro-slip were influenced by the normal load, surface roughness and the direction of machining lays (perpendicular or parallel). Tsutsumi and Ito [12] further investigated the problem and found that the energy loss per cycle could be estimated from the knowledge of the tangential stiffness at zero tangential load, the coefficient of friction, the normal load and the peak tangential displacement amplitude. The stiffness at zero tangential load used in their work was introduced as a term which contains the condition of surface topography of the interface, this stiffness parameter had to be experimentally measured.

Rogers and Boothroyd [13] carried out experiments on the frictional damping in tangentially loaded metallic interfaces, they found that no visible change in the force-displacement hysteresis curve was exhibited in the frequency range 5 to 200 HZ. They also observed the dependance of the amount of the energy dissipated per cycle on the topography of the joint which was, again, related to the experimentally measured joint stiffness at zero tangential load.

In the work so far sited, there has been considerable

agreement between the experimental results obtained by different researchers. This applies to both the general pattern of the tangential load-tangential displacement relation shown in Fig. 1 and the influence of various parameters which affect such relation. However, the semi-imperical formulae suggested by various investigators [for example see references 12 and 13] for either the tangential displacement (or micro-sliding) or the energy dissipated per cycle, failed to include and hence quantify the influence of various parameters and in particular the surface topography. Thus such equations were only of a discriptive nature and could not be employed for the assessment of the machine behaviour during the design stage.

3. THE MICRO-SLIDING CHARACTERISTICS

The author [14] studied the problem with the aim of building a mathematical model for the behaviour of the interface. His concept was; firstly, since the problem involves contact between rough machined surfaces, the stiffness of the interface should be obtained from knowing the surface roughness and the material properties. Secondly, since in most practical applications the surface area of the interface is large compared to the roughness scale, the flatness of the mating surfaces cannot be ignored. We went on to consider that the statistical distribution of the flatness heights over the surface is a full representation of the height distribution of spherical roughness peaks which were assumed to deform elastically upon contact. It was then possible to calculate the true area of contact and the deformation of the interface as a result of the application of any load which is normal to the interface. Referring back to Mindlin's work on the microsliding characteristics within the Hertizian contact region, the author [15] concluded the following set of formulae which fully describe the microsliding characteristics of metallic interfaces which are loaded normal to the interface and subjected to a tangential load (acting in the plane of the interface) which does not exceed the limiting friction force.

During the first application of a monotonically increasing tangential load, the micro-sliding increases along the path OA in Fig. 1 according to the relation

$$S = -\sigma/\delta \ln(1 - T/\mu N) \qquad (1)$$

The above expression shows that when the tangential force approaches the limiting friction force, the displacement tends to infinity which means that gross sliding takes place. The above expression could be expressed in the form

$$T = \mu N [1 - EXP(-\delta S/\sigma)] \qquad (2)$$

After the initial application of a tangential load, and upon its reduction from any limit T', the tangential

displacement follows the path AB in Fig. 1, this path is given by the relation

$$S = S' + 2\sigma/\delta \ln[1 - \{(T'-T)/2\mu N\}] \quad (3)$$

$$T = T' - 2\mu N [1 - EXP\{-\delta(S'-S)/2\sigma\}] \quad (4)$$

If the reduction in the tangential load was stopped at any level $T'' > -T'$ and then the load was increased, the tangential displacement follows the path BA in Fig. 1 and the load-displacement relation along that path is given by

$$S = S'' + 2\sigma/\delta \ln[1 - \{(T-T'')/2\mu N\}] \quad (5)$$

$$T = T'' - 2\mu N [1 - EXP\{-\delta(S-S'')/2\sigma\}] \quad (6)$$

The next step was to validate that the above set of formulae is in quantitative agreement with the experimentally measured tangential deformation. This was achieved by using equations (1) to (6) to calculate the tangential displacement for some of the interfaces for which their tangential load-displacement relation has been experimentally measured and reported in the literature. Namely, the experimental results obtained by Burdekin et al [16] were plotted together with our theoretical results as shown in Fig. 2. One can see that close agreement between the theory and the experimental results has been obtained. Detailed derivation of the theory and the method of comparison has been reported by the author in [15]. The slight deviation between the theory and the experiment was attributed to the accuracy of the transducer used by Burdekin et al [16] in measuring the displacement, as well as the inaccuracy in determining the value of the parameter σ from the values of the CLA measurements needed for our equations. However, the deviation between Burdekin's measurements and our theory did not exceed 39% in case of curve C (smallest displacement), whilst for the rest of the experimental points shown in Fig. 2, the deviation did not exceed 25%.

4. MATHEMATICAL EXPRESSION FOR THE ENERGY DISSIPATION

Turning our attention to the assessment of the energy dissipated per cycle; equations (4) and (6) represent the oscillation of the tangential load between the limits T' and T'' which results in the hysteresis loop responsible for the energy dissipation. In order to calculate the area enclosed by the loop, we will translate the coordinates as shown in Fig. 3 to the point T'', S'', the new coordinates W, X are given by

$$W = T - T'' \quad \& \quad X = S - S''$$

We will also define T_o and S_o to be the peak to peak amplitudes of the tangential load and the associated tangential deformation respectively. Substituting in equations (4) and (6) for the new coordinates we obtain

$$W_d = T_o - 2\mu N\,[1 - \mathrm{Exp}(-\delta(S_o - X)/2\sigma)] \quad (7)$$

$$W_i = 2\mu N\,[1 - \mathrm{Exp}(-\delta X/2\sigma)] \quad (8)$$

Where the suffixes, d and i are for the decrease and increase of loading respectively. The energy dissipated per cycle is obtained from

$$E = \oint W dx = \int_0^{S_o} W_d\, dx - \int_0^{S_o} W_i\, dx$$

Substituting with the values of W_d, W_i and performing the integration we obtain

$$E = 4\mu N\, S_o - T_o S_o - 4\mu N\,(2\sigma/\delta)\,[1 - \mathrm{Exp}(-\delta S_o/2\sigma)] \quad (9)$$

But from either sets of equations (3,4) or (5,6), the relation between the peak to peak force amplitude and the resulting peak to peak displacement is given by

$$T_o = 2\mu N\,[1 - \mathrm{Exp}(-\delta S_o/2\sigma)] \quad (10)$$

OR

$$S_o = 2\sigma/\delta\ \ln(1 - T_o/2\mu N) \quad (11)$$

Substituting from (10) in (9), then

$$E = 4\mu N\,\sigma/\delta\,[\delta S_o/\sigma - (\delta S_o/2\sigma + 2)\,\{1 - \mathrm{Exp}(-\delta S_o/2\sigma)\}] \quad (12)$$

Or substituting from (11) in (9), then

$$E = 4\mu N\,\sigma/\delta\,[(T_o/2\mu N - 2)\ln(1 - T_o/2\mu N) - T_o/\mu N] \quad (13)$$

Either equations (12) or (13) could be used to estimate the energy dissipated per cycle, depending on whether we are controlling the force amplitude or the displacement amplitude.

The above relations show that the energy dissipated per cycle is dependant on the material properties which is represented by the parameter δ, the flatness of the interface, the friction coefficient and the normal load applied to the joint interface.

5. EXPERIMENTAL VARIFICATION

The machine designer could use either equations (12) or (13) in order to predict the damping in joints, provided that such relations are experimentally supported. Perhaps the most comprehensive set (available in the literature) of experimental measurements for the energy dissipation at different metallic interfaces are those measured by Rogers and Boothroyd [17]. Their experiments were carried out for

nominally flat interfaces subjected to dynamic tangential loads in the frequency range 5 to 200 HZ; they reported no frequency dependance of the hysteresis loop. Their measurements were carried out for steel, cast iron, brass and aluminium interfaces. They presented their results in dimensionless form, the dimensionless energy loss EK/N^2 (where K was defined as the experimentally measured stiffness of the interface at zero tangential displacement) was plotted against the dimensionless tangential force $T_o/2N$.

In order to perform a comparison between our theoretical results and Rogers's experiments, equation (13) should be transformed into a compatible none dimensional form. The theoretical tangential stiffness is obtained from (1) by differentiation and setting the tangential displacement S at zero, thus

$$dT/dS)_{S=0} = K = \mu N \, \delta/\sigma \qquad (14)$$

Now substituting in equation (13) with the value of the tangential stiffness obtained from (14)

$$E\gamma/N^2 = 4\mu \, [(H-2\mu) \ln(1-H/\mu) - 2H] \qquad (15)$$

Where $H = T_o/2N$

Equation (15) relates the dimensionless energy loss to the dimensionless tangential force, as obtained from our theory, and this was plotted together with the experimental results of Rogers and Boothroyd [17] in Fig 4. It can be seen that our theory is in perfect agreement with the experimental results. Furthermore, equations (12), (13) and (14) show that the energy loss is independant of the apparent area of contact, and this is further confirmed experimentally in the work of Rogers and Boothroyd.

In metallic interfaces subjected to known normal and tangential forces, the energy loss per cycle can be predicted by knowing the material properties, the friction coefficient and the flatness deviation of the interface. In order to choose the parameters which maximise the energy loss for a particular application we should first decide on the practical requirement of the structure. In machine tool structures it is important to limit the displacements of the interface to a minimum value. Thus one cannot rely on the fact that the damping of the interface will increase with increasing amplitude, that is, working with an H ratio as close as possible to μ as was suggested by Boothroyd [17]. Such an absolute statement according to equation (11) could mean allowing for a relatively large dispalcement at the interface which is in turn directly opposite to the other requirements in machine tool structures. On the other hand the requirement of stiffness of the interface implies that the flatness deviations should be as small as possible whilst the normal load should be as large as possible. An increase in the normal load will increase the energy loss as shown by both equations (12) and (13). However, such an increase in

the normal load should be accompanied by an increase in the tangential force amplitude in order to preserve the value of the ratio H, which in turn leads us to larger displacement amplitudes.

Confusing as it may seem to be, the solution for the problem of optimising the dissipation of energy starts from the examination of equation (11) which relates the tangential displacement to the ratio H. Substituting for δ in equation (11) we can rewrite the expression in the form

$$S_o = -2\mu\sigma/\delta' \ln(1 - Q) \qquad (16)$$

where $Q = H/\mu$

$$\delta' = 2(1 - \nu)/(2 - \nu)$$

$$= 4G'/E'$$

Equation (16) has been used to produce Fig. 5 in which the amplitude of the tangential displacement was plotted against the product of the friction coefficient and the standard deviation of flatness for values of Q ranging from 0.001 to 0.9. It is beleived that Fig. 5 covers most of the practical applications for the interfaces made of similar materials and have poisson's ratio 0.29. From Fig. 5 it is easily seen that if we limit the allowable tangential displacement of the interface at say 0.003 mm peak to peak then such amplitude will be associated with any value of $T_o/2\mu N$ depending on the product of $\mu\sigma$ for the interface. For lower values of $\mu\sigma$, the value of H approaches μ thus the energy dissipated per cycle increases as given by equation (13). Reduction of the product $\mu\sigma$ could be achieved by lubricating the interface, thus, reducing μ and/or by specifying closer tolerences on the flatness deviation of the interface.

6. CONCLUSIONS

It has been shown in this paper that an exact assessment of the damping of the metallic interface could be carried out in terms of the basic data known about the interface. Equations (12) and (13) appear to be in perfect agreement with the experimentally measured results. It is posssible then to predict the joint's frictional damping during the design stage, moreover, the tolerances on both roughness and flatness of the joint could now be functionally laid down in terms of the required stiffness and damping of the joint.

7. NOTATION

E The energy dissipated per cycle.
E' Effective modulus of elasticity.
G Modulus of rigidity.
G' Effective modulus of rigidity.

H None dimensional tangential load (peak value).
K Tangential stiffness of the joint.
N Normal load applied to the joint.
S Tangential displacement of the interface.
S´ Minimum tangential displacement.
S" Maximum tangential displacement.
S_o Peak to peak tangential displacement amplitude.
T Tangential load applied to the joint.
T´ Minimum tangential load.
T" Maximum tangential load.
T_o Peak to peak tangential load amplitude.
δ Material properties parameter.
$\delta = 2(1-\nu)/\mu(2-\nu)$ For similar materials.
$\delta = 4G´/\mu E´$ For different materials.
ν Poisson´s ratio.
μ Coefficient of friction.
σ RMS flatness of the interface.

8. REFERENCES

1. MINDLIN, R.D. 1949. Compliance of elastic bodies in contact. Proc. ASME, J. App. Mech. 71:259-268.

2. BOWDEN, F.P. & D.TABOR 1954. Friction and lubrication of solids. Oxford Univ. Press.

3. MINDLIN, R.D.,W.P.MASON, T.F.OSMER and H.DERESIEWICZ 1951. Effects of an oscillating tangential force on the contact surfaces of elastic spheres. Proc. 1st Nat. Cong Appl. Mech. 1:203-208.

4. MINDLIN, R.D. and H.DERESIEWICZ 1953. Elastic spheres in contact Under varying oblique forces. J. App. Mech. 75:327-344.

5. JOHNSON, K.L. 1955. Surface interaction between elastically loaded bodies under tangential forces. Proc. Roy. Soc. A,203:531-548.

6. GOODMAN, L.E. and C.B.BROWN 1962. Tangential forces between metals. Paper No. 61-WA-29.

7. EARLES, W.E. and M.G.PHILPOT 1976. Energy dissipation at plane surfaces in contact. J. Mech. Eng. Sc. 9:86-97.

8. PANOVKO, Y.G., D.I.GOL´TSEV and G.M.STRAKHOV 1958. Elementary problems of structural hysteresis, (In Russian, Summary from reference 7,page 96-97).

9. COURTNY-PRATT & E.EISNER 1957. The effect of a tangential force on the contact of metallic bodies. Proc. Roy. Soc., A.238:529-550.

10. O´CONNER, J. and K.L. JOHNSON 1963. The role of surface asperities in transmitting tangential forces between

metals. Wear, 6:118-139.

11. MASUKO, M., Y.ITO & T.KOIZUMI 1974. Horizontal stiffness and micro-slip on a bolted joint subjected to repeated tangential static loads. Bul. JSMA, 17:1494-1501.

12. TSUTSUMI, M. and Y.ITO 1979. De[illegible] mechanism of a bolted joint in machine tools. Int. MTDR Conf., 20:443-448.

13. ROGERS, P.F. and G.BOOTHROYD 1975. Damping at metallic interfaces subjected to oscillating tangential loads. J. Eng. Ind. August:1087-1093.

14. SHOUKRY, S.N. & R.H.THORNLEY 1981. Theoretical expressions for the normal and tangential stiffness of machine tool joints. Int. MTDR Conf., 22:131-138.

15. SHOUKRY, S.N. 1985. A mathematical model for the stiffness of fixed joints between machine parts. Proc. Int. NUMETA Conf. Swansea, U.K., 1:851-858

16. BURDEKIN, M., N.BACK & A.COWLEY 1978. Experimental study of normal and shear characteristics of machined surfaces in contact. J. Mech. Eng. Sc. 20:129-132.

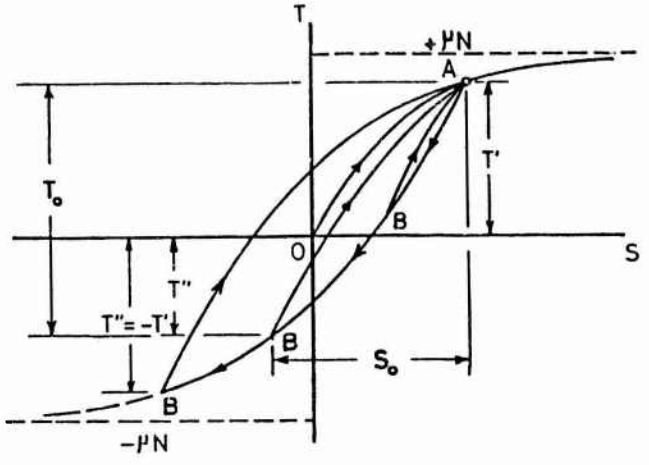

FIG. 1 TANGENTIAL LOAD DISPLACEMENT RELATION.

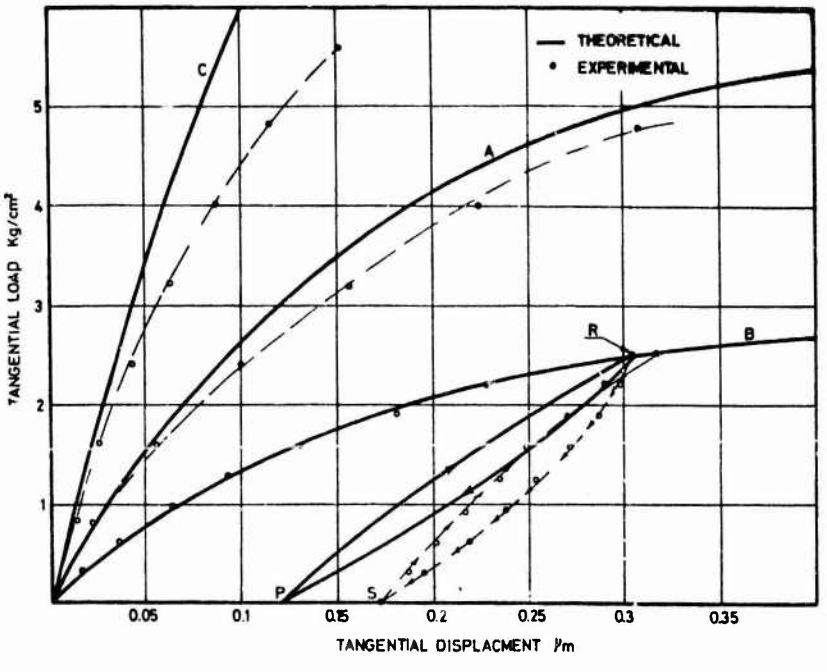

FIG. 2 COMPARISON BETWEEN THE EXPERIMENTAL RESULTS (16) AND OUR THEORETICALLY CALCULATED DISPLACEMENTS USING EQUATIONS (1), (3) AND (5).

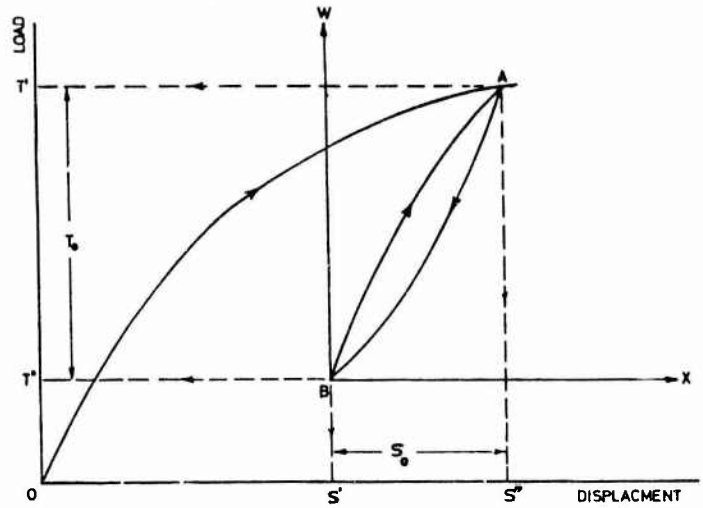

FIG. 3 THE COORDINATES OF THE HYSTERESIS LOOP.

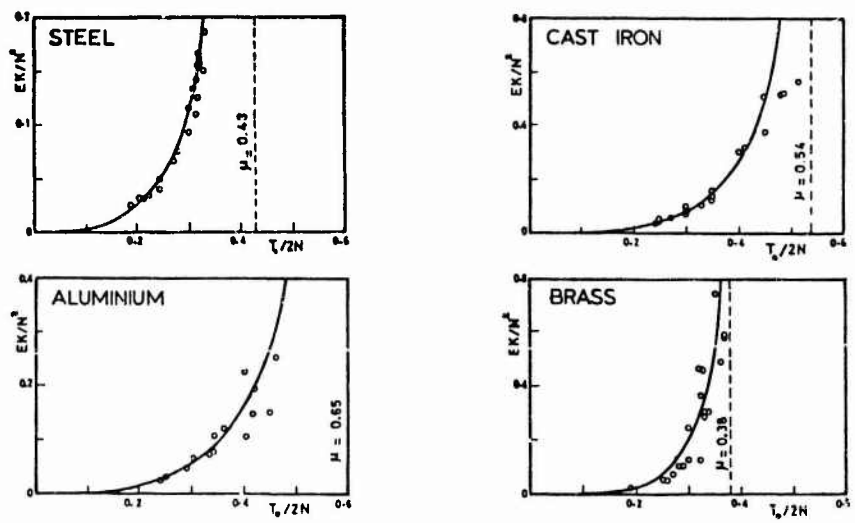

FIG. 4 COMPARISON BETWEEN THE EXPERIMENTAL MEASUREMENTS OF THE ENERGY DISSIPATED PER CYCLE BY ROGERS [13] AND OUR THEORETICALLY CALCULATED CURVES USING EQU. (15).

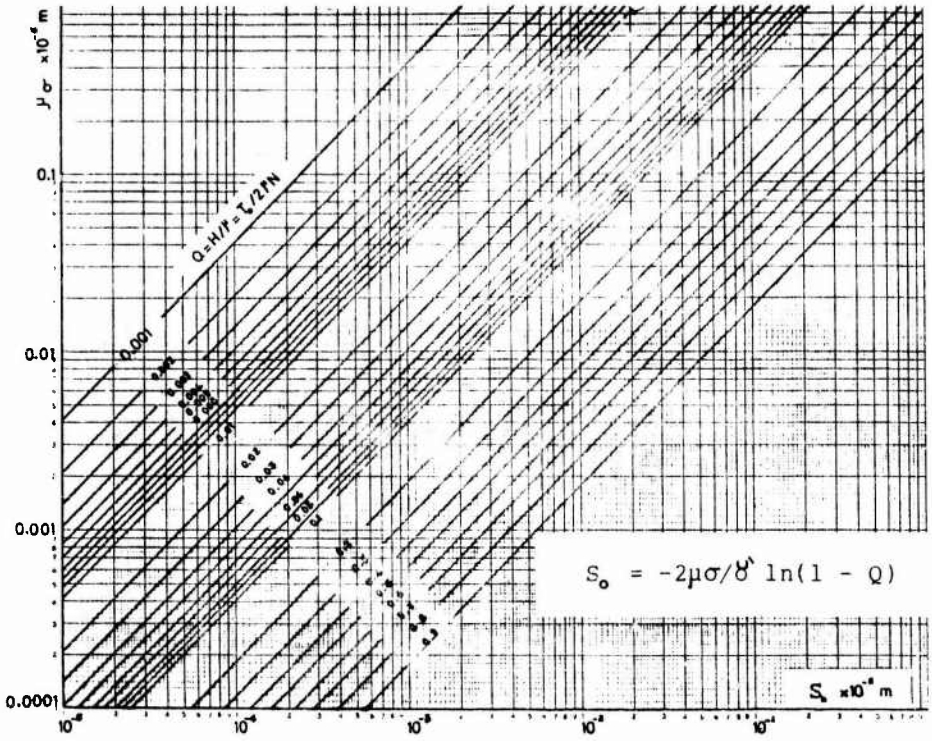

FIG. 5 GRAPHICAL REPRESENTATION OF EQUATION (11).

FRICTION DAMPING DUE TO INTERFACIAL SLIP

J.M. Cuschieri

Center for Acoustics and Vibrations, Department of Ocean Engineering
Florida Atlantic University

V.R. Desai*

WYLE Laboratories, Arlington, Virginia
(*Work done while at Florida Atlantic University)

1. INTRODUCTION

Damping is the only mechanism available in vibration control that dissipates rather than reflects the vibrational energy. Damping mechanisms, especially those associated with the application of viscoelastic materials have been extensively studied. However in controlling vibrations of heavy structures such as machine structures, the use of viscoelastic material damping can be limited.

If the structural damping of a bolted structure is measured and, compared to the damping of its components, the former is considerably higher. This additional damping is attributed to the presence of the joints between the structure components. The joints represent regions of contact between the mating surfaces and energy dissipation can occur when the two surfaces slide relative to each other. Energy can also be dissipated due to air pumping between the adjoining surfaces but this is a completely different mechanism which is beyond the scope of this paper. From previous studies on friction damping [1,2,3,4] it has been found that interfacial slip depends on the coefficient of friction, the applied normal force per unit area and the frequency of the excitation. With the optimization of some of these parameters friction damping can result in very high rates of vibrational energy dissipation without the disadvantages that can be associated with viscoelastic damping.

The mechanism of friction damping can be qualitatively described as follows. The surface of a structure is never perfectly flat but it has tiny asperities. When two such surfaces are brought in contact and the surfaces kept together under pressure, the tips of these asperities touch forming small local contact areas. That means the actual contact area is much smaller than the area of the surfaces and thus high local stresses are formed at the tips of the asperities. Perhaps the most accepted theory for interface friction losses is the one suggested by Ito and Masuko [5]. They postulated that the exact mechanisms by which energy is dissipated are different for low and high interface pressures. At low interface pressure, energy is dissipated due to gross or "macro sliding". The level of energy dissipation thus increases with increasing interface pressure. However, as the interface pressure increases a point is reached at which the asperities start to get mutually embedded. Above this limiting pressure macro sliding stops and only micro slip is allowed. At higher interface pressures energy dissipation is due to the cyclic plastic deformation at the contact spots. Plastic deformation occurs at the tips of the asperities which increases the contact area reducing the tangential stresses at the contact spots with a consequent reduction in energy dissipation. The main limitations of this theory is that it is based on what Schofield [6] pointed out to be rather

low interface pressures compared to the interface pressures in bolted structures. However the quelitetive explanation is still believed to be relevant.

On reviewing past work in the erea of friction demping, the work hes generally been limited to simple butt joints and there is significant disagreement between the results from the different studies. The divergence of the results can to some extent be ettributed to the highly different experimental setups, especially such critical parameters as surface finish and interface pressures. The coefficients of friction selected in these anelysis vary from one study to another which contribute to the different results. Furthermore, in generel, the interface pressures that were considered are lower then whet would be expected in bolted joints.

The earliest work to be found on interface friction damping is the work by Goodman and Klumpp [1]. Their work was mainly exploretory, comparing theorotical results to analytical expressions obtained using classical stress theory with the assumption of coulomb friction et the interface. An important result of this work was that the coefficient of friction approached a mean value, somewhere between the static and dynemic coefficients of friction after a few vibration cycles. The importence of the coefficient of friction was further enalyzed in later work by Goodman and Brown [7] and it was established that increases in the coefficient of friction resulted in the lowering of the rate of dissipation of energy, and hence lower structural loss factors. This result wes disagreed upon in the work by Ungar and Carbonell [2], where it was shown that the loss factor is independent of the coefficient of friction. In later work by Kedrov [8], it was determined that the larger the coefficient of friction the higher is the level of energy dissipetion and thus the higher is the structural loss factor. In other experimental enalyses of friction damping, such es [2, 3 and 9] low interface pressures as compered to those generally present in bolted joints have been considered. In the work by Earles end Williams [3], the analysis is performed for systems with a friction damper at one end of the structure. This is different from the interface friction losses along the entire length of the structure and therefore the applicetion of such studies and their contribution to the understanding of surfece friction damping mechanisms is rather limited.

Wissbrok [10] used a numerical technique to analyze the parameters controlling interface friction damping. A finite element method is developed for a long "double leaf" cantilever beam which is examined for its response to hermonic excitation at the free end. The technique used and the capabilities of the numerical finite element model developed gave promising results. However no further work could be found in the open literature where this technique was further developed to deel with complex structural shapes and to determine the influence of the various parameters on the damping loss fector.

Although a reasonable amount of work has been done in this area of structural damping, the results differ significantly which precludes the optimizetion of friction damping for a perticular application. Furthermore, a detailed quantitative analysis that satisfactorily explains this rather complex phenomena is lacking. Most of the analyses describsd above make assumptions that meny would disagree with or have limitations in the scope of their application. To start to enswer some of the questions regarding the influence of the various parameters on friction damping, a theoretical (numericel) and experimental study has been undertaken based on a double

leaf cantilever. Although this study is not complete, only one specimen is considered, it's a first in a quantitetive explanetion of interface friction damping.

2. FINITE ELEMENT ANALYSIS

The theoretical epproach adopted for this study is a numerical analysis using a general purpose finite element (FE) package. This FE package has a friction gap element, end the algorithm has a "feedback" mechanism such that after the joint forces at each time increment are calculated, if these forces exceed the value required for "no slip" condition, the increment is recycled and the forces recalculated, together with the frictional forces and the net slip at each friction element. This "feedback" mechanism is very similer to the one incorporated in [10].

The FE model consists of plane stress quadrilateral elements modeling the two beams. The elements are connected et ten positions by friction gap elements. The reason for the selection of the quadrilateral elements is that the friction gap element is a rether subtle element, fairly difficult to use and without the right combination of elements, the results were unpredictable and/or erroneous. The input mesh is shown in figure 1. The thickness of the two beams were taken to be variables that can be changed in the input data file to ellow analysis of the influence of the relative thicknesses of the main beam and the auxiliery beam.

The plane stress quadrilateral is a 4-node element with two degrees of freedom (DOF), the displacements in the x and y directions. A uniform pressure can be specified on any of the faces of the element (interfece pressure). The friction gap element is also a 4-node element. The first and last nodes specify the connecting nodes to the two interfaces. The second node, which has one DOF, represents the normal force carried across the gap, while the third node with two DOF represents the frictional force being carried across the gap and the frictional slip. Another input to the friction gap element is the gap closure distence. This is the relative displacement in the direction of the gap, which cannot be exceeded. In the study by Ito et al [5], this distance was determined to be of the order of 0.1 micrometers. This is the value that was used in this analysis.

FE analysis were performed to determine the influence of the interface pressure, the coefficient of friction and different thickness ratios of the main end auxiliary beam. The following conditions were analyzed:

(a) Three different values of interface pressures: 0.1 KN/m^2, 1.0 KN/m^2 and 10.0 KN/m^2
(b) Four coefficient of friction values: 0.15, 0.3, 0.45 and 0.6.
(c) Two different values of thickness ratios: 1.0 and .33. Main beam thickness wes 9.17 cm and the auxiliery beam thicknesses were 9.12 cm end 3.17 cm.

The cantilever was excited by e harmonic force applied at node 42. The forcing function lasted two complete cycles at the frequency of excitation, after which the beam was allowed to decay freely through three complete cycles. The selection of the number of cycles was based on some triel and error where the objective wes to obtein eccurate results with minimum computer run time. The loss factor was calculated from the logarithmic decrement.

A modal enalysis was also carried out and a fundemental frequency of

53.8 Hz was obtained. Thus, in the time decay analysis the frequency of the harmonic force was set at 55 Hz. For frequencies higher than the fundamental frequency, no slip was observed and this was attributed to the use of a coarse mesh FE model. The natural frequencies from the FE modal analysis did not agree with the experimentally measured natural frequencies for an identical cantilever (see section 4). However, the mode shapes were identical and the ratios of the resonant frequencies to the fundamental were also the same. This disagreement is attributed to ineccuracies in the calculated natural frequencies. In fact, in the documentation of the FE package, it's steted that modal analysis should not be used for structures with friction gap elements.

3. EXPERIMENTAL ANALYSIS

For the experimental analysis, (srt up shown in figure 2), two mild steel beams were bolted together with one end of the main beam clamped between two heavy aluminium blocks, and the other end was attached to an uncoupled electromagnetic shaker. The interface pressure was changed by adjusting the tightening torque of the clamping bolts. Experiments were carried out for different interface pressures, surface roughness and beam thickness retios. The main beam was 1.01 m long by 7.6 cm wide and the auxiliary beam wes 0.91 m long and 7.6 cm wide. The reason that the auxiliary beam was shorter than the main beam is that the main beam had approximately 10 cm of its length clamped. The beams were attached by 12 evenly spaced bolts, diemeter 6 mm. For all experiments, excluding those to investigate the effect of the coefficient of friction, the mating surfaces of the two beams were ground to within 0.00254 cm (1/1000 inch).

The first tests were to measure the natural frequencies of the combined centilever beam. Damping loss fector measurements were then performed et the resonant frequencies of the combined system. Because of the setup, modes 2 to 6 were selected for the unequal thickness beams setup and modes 2 to 8 were selected for the equel thickness beems setup. The damping loss factors were measured using the decay (logarithmic decrement) method. To ensure thet a steady state condition was achieved before any measurements were taken, the beams were allowed to vibrate for a few minutes. Different amplitudes of excitation were also investigeted. The interface pressures, which in the results will be given in terms of bolt torques, were selected such that for the lowest bolt torque the two beams were just in contact and the highest bolt torque was the maximum allowed for the type of bolts used.

4. RESULTS

4.1. Experimental Results - Unequal Thickness Beams

The first set of results is for a thickness ratio of 0.33 (3.2 mm thick beam attached to a 9.5 mm thick main beam). The natural frequencies, increased with increesing bolt torque, approaching those for a single cantilever beam of thickness 12.7 mm.

The results for the measured damping loss factor (figure 3) show that the loss factor decreased with increasing bolt torque. However the decrease in loss factor with increasing bolt torque levels off, and for high bolt torques the loss factor is independent of the bolt torque. This is in agreement with the results by Ito et al [5] which show thet for small values of the thickness ratio the energy dissipetion due to friction is

more or less independent of the interface pressure above some pressure level. Another observation (figure 3) is that even at maximum bolt torque the measured loss factors were still higher than for bare steel. This implies that even at high interface pressures there are mechanisms by which energy can be dissipated [9]. From figure 3 it can be observed that while for modes 2 to 4 there is no optimum interface pressure for which the loss factor reaches a maximum, for modes 5 and 6 an optimum interface pressure exists at a bolt torque of approximately 6 kg-cm. This result implies that an optimum interface pressure is frequency dependent.

Comparing the measured loss factors for a particular bolt torque, for different frequencies, the general trend is that the loss factor increases as a function of frequency. Finally, from all results, there is no variation in loss factor with different amplitude of vibration. This is contrary to the findings by Beard [9], but agrees with those found in [4].

4.1.2. Experimental Results - Equal Thickness Beams

The second set of results are for a thickness ratio of unity (both beams of thickness 9.5 mm). The natural frequencies also varied with bolt torque, and as the bolt torque was increased the natural frequencies increased, approaching those for a cantilever beam of thickness 1.9 cm. The results for the measured damping loss factor are shown in figure 4. In this case there is a distinct dependence of the loss factor on the interface pressure, especially for the lower modes, and in general an optimum interface pressure exists. The only exception is mode 2 which exhibits a very high loss factor at low interface pressures which was attributed to other dissipation phenomena. This result of an optimum interface pressure agrees with that found in [1], [2] and [9] which also deal with equal thickness beams.

These results for the equal thickness beams are different from those of unequal thickness beams, that is an optimum interface pressure exists for all modes. Equal thickness beams will in general execute the same spatial motion at a particular frequency, while unequal thickness beams because of their different natural frequencies, each beam will try to behave in a manner characteristic of its own thickness. However, because of the bolts, the motion of each beam is influenced by the motion of the other beam. Thus each beam will experience some form of forced motion and the influence of the interface pressure will be different from that of the equal thickness beams. The resultant motion and the region of slip can therefore be quite complex and the existence of an optimum pressure would be expected to be frequency dependent.

Also, in the case of equal thickness beams, the measured loss factors do show some dependency on the vibration amplitude especially at low bolt torques (excluding mode 7). For the variation of loss factor with frequency at fixed bolt torques, no common trend is observed except for low frequencies and low bolt torques.

The influence of the coefficient of friction was investigated by changing the surface finish of one of the beams. This was done by rubbing the surface with either a 120 Grit sandpaper or with a 60 Grit sandpaper. The results for the measured loss factor are shown in figure 5 and it can be observed that there is an increase in the damping loss factor with increase in surface roughness (coefficient of friction). The measured increase in the loss factor is rather small. However, it was not possible

to measure the change in the coefficient of friction due to the application of the sandpaper, and therefore no relationship can be established for the changes in loss factor with coefficient of friction except that if one increases the other will also increase.

4.2. Finite Element Results

The results from the finite element analysis for the first mode of vibration are shown in Tables I and II. The "*" indicates that that particular set up did not successfully complete due to either excessive computation time or non convergence. From the results it can be observed that for both cases the loss factor decreased with increasing interface pressure, as in the experimental results for the low order modes. Also, as in the for experimental results, the variation of loss factor with the coefficient of friction is rather small. However there is no general trend for the variation of loss factor with coefficient of friction.

5. CONCLUSION

From the results obtained thus far in this study, although not complete, the following conclusions can be made. First, the interface pressure affects the loss factor only for high order modes, and an optimum interface pressure was found for equal thickness structures, whereas for the unequal thickness structures this was observed only at high frequencies. Second, for a given interface pressure the damping loss factor is not highly dependent on frequency except for the higher order modes. Third, increases in the coefficient of friction will only slightly affect the loss factor with no general direction in the expected changes in loss factor. Finally, with regards to the thickness ratio, the main difference was in the existence of an optimum interface pressure.

As a final comment, there are two other phenomena associated with friction damping which would need to be addressed before this damping mechanism can be implemented in practice. (a) As the surfaces rub against each other the asperities slowly wear off, resulting in the removal of material from the structure surfece. This phenomena is what is generally known as "fretting corrosion" and can result in serious structural damage. If the structure is exposed to a corrosive environment, the damage due to fretting corrosion can be significantly accelerated and can quickly lead to mechanical failure. Fretting corrosion can to some extent be reduced by special surface treetments such as shot-peening, nitriding and other surface hardening techniques. (b) To allow for the interfacial slip the bolt stiffness is reduced leading to an overall reduction of the structure stiffness. However this can be compensated for in the design.

REFERENCES

1. L.E. Goodman, J.H. Klumpp, 1956, ASME Journal of Applied Mechanics, 23(3), 421-429. Analysis of Slip Damping with Reference to Turbine Blade Vibration.

2. E.E. Ungar, J.R. Carbonell, 1966, American Institute of Aeronautics and Astronautics Journal, 4, 1385-1390. On Panel Vibration Damping due to Structural Joints.

3. S.W.E. Earls, E.J. Williams, 1972, Journal of Sound and Vibration, 24, 445-458. A Linearized Analysis for Frictionally Damped Systems.

4. C.F. Beards, 1981, ASME Journal of Mechanical design, paper 81-DET-86. Damping of Structural Vibrations of Controlled Interfacial Slip in Joints.

5. Y. Ito, M. Masuko, 1971, Proceedings 12th International Machine Tool Design and Research Conference. Experimental Study of the Optimum Interface Pressure on a Bolted Joint Considering the Damping Capacity.

6. R.E. Schofield, 1973, Proceedings 13th International Machine Tool Design and Research Conference. The damping Effects of Joints Formed From Machined Surfaces - State of the Art.

7. L.E. Goodman, C.B. Brown, 1962, Journal Of Applied Mechanics, 29, 17-22. Energy Dissipation in Contact Friction, Constant Normal and Cyclic Tangential Loading.

8. S.S. Kedrov, 1967, Russian Engineering Journal, 46(9). Establishing Damping Factors in the Joints of Machine Components.

9. C.F. Beards, I.M.A. Imam, 1978, International Journal of Machine Tool Design Research, 18, 131-137. The Damping of Plate Vibration by Interfacial Slip between Layers.

10. H. Wissbrok, 1984, Proceedings Second International Conferen e on Recent Advances in Structural Dynamics. Damped Vibrations of a Jointed Cantilever Beam.

TABLE I

Loss Factor Results From Finite Element Analysis
For Beams With Thickness Ratio 0.33

Pressure KN/m^2	Coefficient of Friction .15	.30	.45	.60
0.1	0.009	*	0.016	0.010
1.0	0.009	0.013	0.008	0.014
10.0	0.004	0.008	0.002	0.001

TABLE II

Loss Factor Results From Finite Element Analysis
For Beams With Thickness Ratio 1.0

Pressure KN/m^2	Coefficient of Friction .15	.30	.45	.60
0.1	*	0.013	0.015	*
1.0	0.035	0.010	0.009	0.014
10.0	0.002	0.008	0.001	0.004

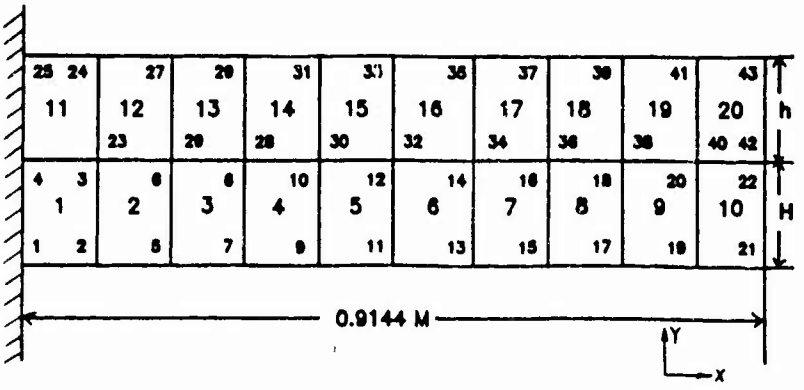

Figure 1 . Input ... sh for MARC Finite Element Analysis

1,2 : B&K 2635 Charge Amplifiers ; 3 : HP 3314A Function Generator ; 4 : HP 5423A Structural Dynamics Analyzer

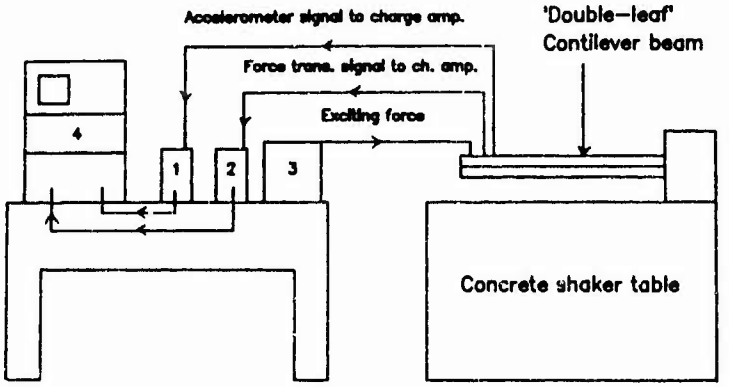

Figure 2 . Schematic diagram of experimental setup used for friction damping tests

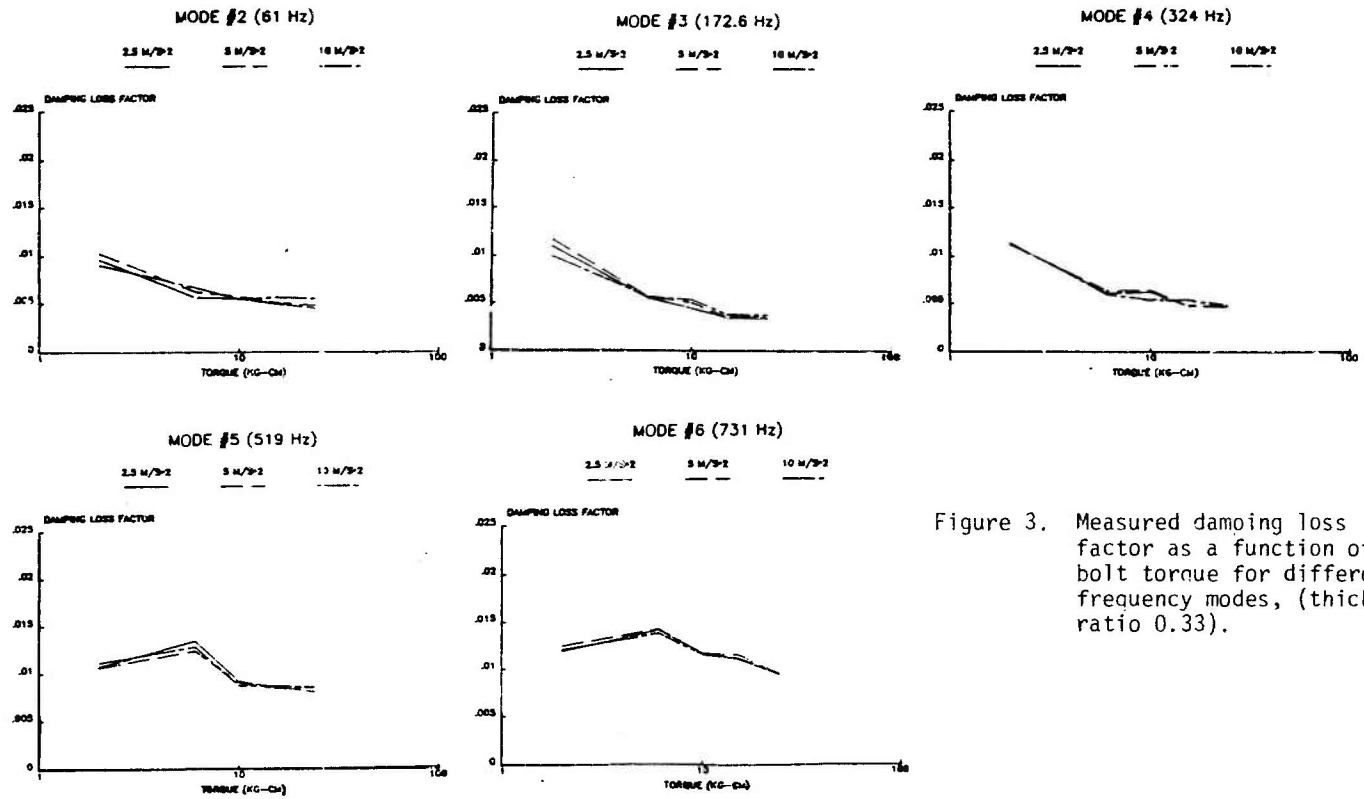

Figure 3. Measured damping loss factor as a function of bolt torque for different frequency modes, (thickness ratio 0.33).

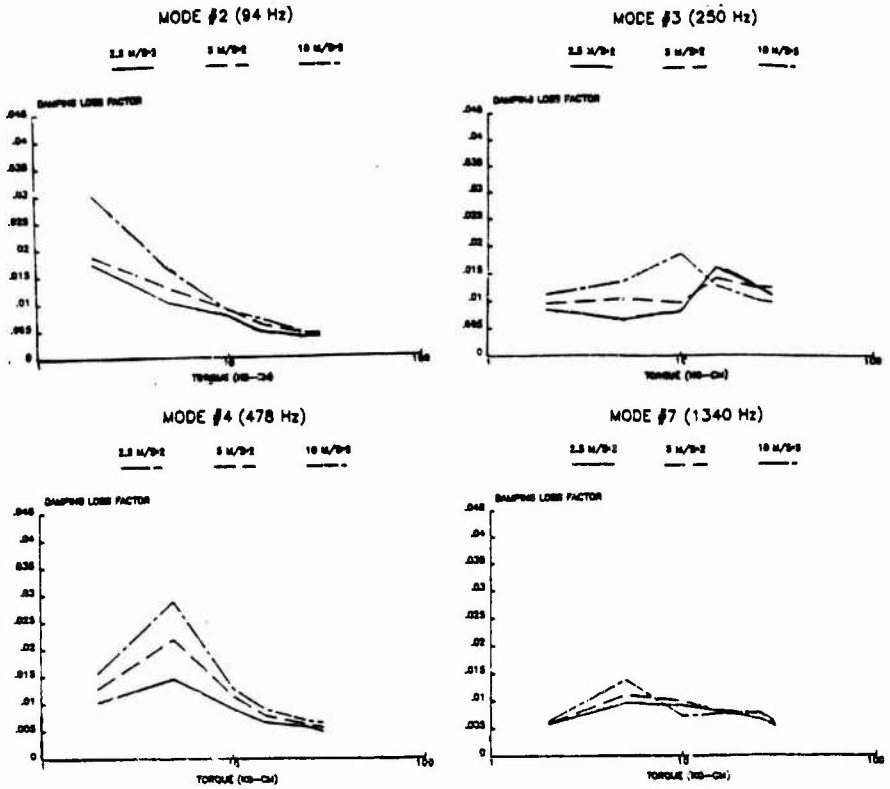

Figure 4. Measured damping loss factor as a function of bolt torque for different frequency modes, (thickness ratio 1.0).

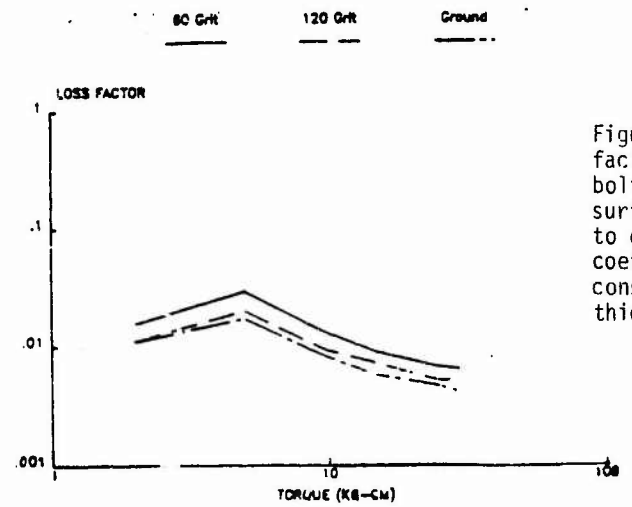

Figure5. Measured loss factor as a function of bolt torque for different surface finishes, equivalent to changes in friction coefficient, (mode 4, constant excitation level, thickness ratio 1.0).

THE BEAN BAG IMPACT DAMPER

E. Semercigil and N. Popplewell

Department of Mechanical Engineering
University of Manitoba
Winnipeg, Canada R3T 2N2

1. INTRODUCTION

A conventional vibroimpact damper is essentially a rigid weight which moves freely between collisions with an excessively vibrating primary system. Attenuation of the primary system's motion will occur possibly by elasto-plastic contact deformations and certainly by momentum transfer if the collisions are repeated and movements just before each collision are in opposite directions. This behaviour is ensured, at least over a limited range of frequencies, by selecting an appropriate clearance between the damper and the primary system. Indeed, the basic principle and limited frequency range of applicability are quite similar to those observed for the better known tuned vibration neutralizer. However, Masri [1] has shown theoretically that a rigid impact damper's performance is superior, for a given weight, to that of the vibration neutralizer. On the other hand, speed discontinuities at a collision make the rigid damper more difficult to analyze. In addition, its collisions produce detrimentally high contact stresses and noise levels. Well documented [2] design charts largely overcome the first objection so that the rigid impact damper's relative unpopularity is presumably due to the latter disadvantages.

The concept of a resilient rather than a rigid impact damper was introduced several years ago[3]. Resilience was derived from a flexible plastic bag which contained 2mm diameter spherical lead shot to maximize the weight to volume ratio. Indeed, the term "bean bag" was coined because of the obvious similarities with a pouffe. Not only was the bean bag much more successful than the rigid damper in delaying the chatter of boring bars but its operation was significantly quieter. This result is no different from that of the classical noise control strategy of reducing the peak contact force at the cost of elongating the contact duration (so that the overall impulse remains approximately constant).

Although clearly superior in practice, the dynamic effect of a bean bag will be shown to be difficult, yet not impossible, to predict. Additional difficulties arise because a bean bag has collision properties which are not constant like those of the rigid impact damper. Experiments to measure these important changes will be described. Then three models of the bean bag will be postulated. Comparisons of the predictions with the experimental data will isolate the important dynamic features of the bean bag.

2. MEASUREMENT OF DYNAMIC BEHAVIOUR

An examination of a bean bag's impact behaviour by suspending it as a simple pendulum to ensure collisions with a stationary wall is tempting because the motion of bean bag need only be considered. Measurement requirements a mplified even further if a conventional coefficient of estitution approach is taken. Then the bean bag's speed just before and after a single collision has merely to be observed. These two values can be calculated straightforwardly by using the bean bag's horizontal distance from the wall at its release position and the greatest such distance after the collision. The wall, of course, should be fixed and have the same geometry and material properties as the primary system. However, a closer examination of the collision would demand at least a cursory inspection of the history of the contact force because this force describes the interplay of the two colliding objects. Furth more, the contact force will be the sole parameter of the collision which influences the subsequent motion.

A special primary system was constructed to avoid unnecessary geometric and material inconsistencies between the bean bag acting as a pendulum or as an impact damper. One side of this primary system consisted exclusively of a Bruel and Kjaer impedance head. The other side was a screw adjusted block having one flat steel face to closely match the contact surface of the impedance head. Both sides were fixed to a fairly substantial steel base such that an intermediary (adjustable) space was left for the bean bag. The bean bag was supported from a sturdy frame by using two long threads to ensure an essentially horizontal, frictionless motion. The impedance head could be removed and fixed to a large steel block for the otherwise identical pendulum set-up. Results from the pendulum and the in-situ impact damping tests are presented in Figure 1 for various relative approach speeds just before a collision, v_{rel-}. Setups for the in-situ and the pendulum measurements are illustrated schematically in Figure 4(a) and 4(b), respectively.

The v_{rel-} and the corresponding relative speed immediately after the collision, v_{rel+}, cannot be found in-situ by using the simple horizontal distance measurements of the pendulum tests. Both v_{rel-} and v_{rel+} had then to be determined indirectly by utilizing availible non-contact displacement transducers. Consequently, more than the single collision of each pendulum test had to be permitted to achieve a steady state condition in order to reasonably approximate the speeds. Of course, the situation of major interest is when the external force, $F_o \sin wt$ in the schematic of Figure 4(a), coincides with the fundamental natural frequency of the primary system. The steady displacement of the primary system has a constant amplitude and, despite the collisions, a single frequency corresponding to w. Hence, the primary system's steady state speed is virtually w times its displacement. The corresponding calculation of the bean bag's speed is somewhat more involved because its displacement could not be measured absolutely without interference but could be only observed relative to the primary system. Details of this calculation and the experimental procedure are given next.

The primary system's displacement, x_1+, was measured by employing a Wayne Kerr capacitive displacement transducer. A typical history of x_1 from a completely at rest initial state is proportional to that presented in Figure 2(a). Arrows in this figure indicate the start of the steady state phase during which the slope of the envelope is invariably horizontal. The figure also suggests that the steady state condition can be quite easily discerned visually. The bean bag's displacement, x_2, was found relative to x_1 by using the non-contacting optical system detailed in reference 3. Instants of, and times between, collisions were observed visually from the contact force history obtained from the impedance head and, after amplification, displayed on a storage oscilloscope. By knowing the instants of collisions, as well as the steady state x_1 and (x_2-x_1), it was possible to determire the total movement of the bean bag between consecutive collisions, d. Now the speed of the bean bag is almost constant between these collisions because the small clearances normally used afford little opportunity for appreciable decelerations. Hence, the bean bag's absolute speed can be computed simply by dividing d by the corresponding time interval between consecutive collisions. The relative speed just before and after a collision may be found straightforwardly from the separate absolute speeds. Different approach speeds were obtained by simply changing the external force's amplitude, F_o.

Representative steady state speeds were checked by using expensive high-speed photography and agreement was within 5%. Remaining parameters like the maximum force, F_c, and the duration, T_c, of a collision were measured directly from records of the contact force history and, hence, should be as least as accurate.

Figure 1 shows that the bean bag generally gives larger F_c, with consistently smaller T_c, for a particular $v_{rel}-$ when it acts as an impact damper rather than as a pendulum. However, the initially different $v_{rel}+/v_{rel}-$ converge with increasing $v_{rel}-$. These trends are consistent with the intuitive idea that the bean bag becomes stiffer with repeated contacts and at greater $v_{rel}-$ or, from Figure 1(d), higher excitation levels. The question remains, however, as to how precisely this phonomenon needs to be modelled to reasonably forecast its consequences on the primary system.

3. MODELLING

The classical approach [2] of describing a collision would be to assume the bean bag as rigid and to use a coefficient of restitution, e, and the conservation of linear momentum. However, only a purely plastic, e=0 collision can produce a finite contact duration like that noted experimentally. A more sophisticated (and recently more popular) equivalent linearization procedure could be employed to relax the rigidity constraint and produce collisions with finite contact durations. Both approaches will be

---

+ A small letter will invariably indicate a time-varying quantity whose amplitude is given by the corresponding capitol letter.

examined and shown to be seriously deficient. Then a semi-empirical procedure which, unlike the previous models, does not assume or directly evaluate the bean bag's deformation behaviour will be reviewed. It will be shown to be capable of giving more accurate predictions of the displacement reductions of the primary system.

The overall strategy used to derive and solve the equations of motion is similar to that adopted in the classical approach. Classically, the contacts and the impact damper's "free flights" are distinguished to more easily define the (rigid) damper's abrupt change in direction caused by a collision. A damper, whether rigid or flexible, has no effect when it is in free flight so that the equations and their solution are then the same regardless. Indeed, the primary system then corresponds to a simple linear oscillator and the frictionless damper merely moves at a constant speed. Hence, both the motion of the primary system and the damper can be easily found analytically [2] if the conditions at the start of the free flight are known.

A collision happens when the relative distance between the primary system and the damper becomes zero. What happens subsequently depends upon the nature of the impact damper and, in turn, upon the realism of the simplifying assumptions associated with the different models. For example if perfectly plastic collisions are assumed, the idealized impact damper will adhere to the primary mass after a contact until its inertial force reverses direction to oppose that of the primary system's velocity. The linearization procedure, on the other hand, leads to a viscously damped oscillator representation of the impact damper whose spring force diminishes to zero at the breaking of contact. In the semi-empirical procedure, a simplification of the experimentally determined contact force history is stipulated, like any given external force, on the primary system immediately after a contact is established. Detachment is imposed after the corresponding experimentally measured contact period. Hence, both the pendulum and the in-situ impact damper data presented in Figure 1 was employed. The simplest reasonable piecewise linear history which satisfied the contact force's greatest experimental value, F_c, and duration, T_c, for a given relative approach speed, v_{rel-}, was used to represent its temporal variation.

During a collision, the adhering plastic damper idealization simply increases somewhat the mass of the primary system. As a consequence, the single degree-of-freedom representation of the non-contacting primary system is still appropriate but it will have a slightly higher natural period than before. Moreover, the analytical solution during the collision will be identical in form to that in the free flight. Of course, a particular contact solution is determined by the need to match conditions at the juxtaposition of the contact and just previous free flight. The displacement of the primary system is always continuous but the then discontinuous speeds must be found from linear momentum conservation and the definition of e. Imposition of the displacement constraint and the speed results leads to the solution during the subsequent contact period. The next free flight solution can be found straightforwardly by

imposing, at its start, the displacements and speeds at the end of the contact. Hence, the complete response history can be developed in a piecewise fashion. The equivalent linearization and semi-empirical approaches only differ somewhat from that described because speeds are no longer discontinuous at the collision of a resilient damper. Imposition of the displacement and speed continuities at the start of a collision in these models supplies the conditions needed to determine that contact's solution again. (It should be noted, however, that the primary system's mass is now always the same whether or not contacts are happening.) Solutions were computed most conveniently by using complex modal superposition for the linearization procedure and numerical integration of the convolution integral in the semi-empirical approach.

Dynamic properties of the primary system are detailed in reference 4. The primary system was driven by an external force of 0.045N at the fundamental natural frequency of 19.85 Hz. Its mass was invariably 35.7 times that of the bean bag. The bean bag's linear oscillator model had a (variable) viscous damping ratio of $-\ln(v_{rel+}/v_{rel-})/n$ after a collision to preserve the ratio of v_{rel+}/v_{rel-} for that collision [5]. The corresponding stiffness was written in the form $k_o(v_{rel-})^{2/3}$ to ensure that the experimental F_c variation in Figure 1(a) was satisfied. The constant k_o was found iteratively for a particular collision as the value which gave the experimentally observed F_c.

4. RESULTS

Experimental data is compared in Figure 2 and 3 with predictions from the impact damper models. The displacement history of the primary system interacting with the bean bag, x_1, is presented after division by the analogous peak value without the bag, X0. Of course, a value of $|x_1/X0|$ less than one implies that the bean bag is attenuating the primary system's original displacement. Figure 2 indicates this to be the case. It also gives an overview of both the initial transient as well as the primary system's ultimate steady state behaviour after the arrows. Column (ii) and (iii) in this figure, on the other hand, present an expansion of just one period of the the steady state $x_1/X0$ with the corresponding contact force history, f_c/Fo. (Fo is merely the amplitude of the external force.) The one extra computed history was derived by using the semi-empirical model and a contact force idealized from the pendulum rather than the in-situ measurements. Typical contact force measurements are presented in column (iii) alongside their respective idealizations in column (ii). It can be seen, by comparing (iiie) and (iiif), that the contact force measured in-situ is larger, more peaked and irregular than that observed in the pendulum tests. Hence, one more line is needed in the representation of (iia) relative to (iib). Although both these idealizations are somewhat arbitrary, they each appear to reasonably reflect the overall trends of the individual contact forces. Indeed, they preserve the different F_c and T_c noted in the in-situ and pendulum measurements for identical v_{rel-}. Of course, the F_c and T_c for a particular computation will alter to reflect the experimantal variations in Figure 1 when v_{rel-} changes during the

transient phase.

Figure 2 shows, not surprisingly, that more accurate predictions of $x_1/X0$ are generally produced when contact force histories become more precise. Clearly, the idealized use of the actual contact force rather than one generated by the pendulum in the semi-empirical model leads to a more realistic prediction. It is also more accurate than either the rigid or equivalent oscillator models of the bean bag. Indeed, a comparison of (iic) and (iid) with (iiie) in Figure 2 indicates that the last two models yield markedly different contact forces from the actual one. However, the plastic model better preserves the quite sharp rise-fall and the impulse of the experimental in-situ contact force so that, of the two models, it gives a superior $x_1/X0$. On the other hand, the impulse is less exact than that in the semi-empirical model with the pendulum data and yet the plastic model still provides a more accurate $x_1/X0$. Consequently, the rise and fall of the contact force history seems to influence the primary system more than its net impulse.

Figure 3 extends the best experimentally correlating case of case (iia) in Figure 2 to comparable situations which involve a simple change in d. Again, d is the distance travelled by the bean bag between two consecutive collisions in the steady state phase. The results of the semi-empirical model presented in (iia) of Figure 2 coincide with point A in Figure 3(a). The ordinate $X1/X0$ in Figure 3(a) is simply the magnitude of the ratio $x_1/X0$ in the steady state as illustrated in Figure 3(c) and 3(e). These last figures, and their steady state counterparts in Figure 3(b) and 3(d), correspond to point B in Figure 3(a). It can be seen from Figure 3(a) that the agreement between the experimental data and the semi-empirical model is noticeably worse at point B compared with point A. This discrepancy is a product of the deterioration in the representation of the contact force at point B by an invariant form. Indeed, in comparison with case (iiie) of Figure 2, the force history in Figure 3(d), shows a much sharper drop after its peak which is not idealized well in Figure 3(b). Another point of interest is that the smaller clearance at point B produces a lower experimental F_c in Figure 3(d) which leads to a greater transient period in Figure 3(e) relative to case (ia) of Figure 2. These observations support the contention that reduced contact forces take longer to compact the lead shot in the bean bag which can noticeably adjust the final character of the contact force. This adjustment alters quite appreciably the primary system's response which, in turn, will presumably modify the contact force. Thus, there appears to be a feedback mechanism which cannot be truely represented by an invariably constant parameter modelling of the bean bag.

5. DISCUSSION AND CONCLUSIONS

The deformation of the bean bag created by a collision has been shown to be so important that it is tempting to speculate on its fundamental mechanics. The very first collision of the bean bag, of course, must generate a rounded contact force history like that observed in the pendulum test. Subsequent collisions must transpose this history towards the peaked character noted in

the in-situ steady state measurements. It has been seen theoretically that such a peakiness is reminiscent of a rigid impact damper. Consequently, it seems that the bean bag does not recover completely from previous collisions so that the lead shot is increasingly compacted and the bean bag eventually becomes more rigid (or stiffer) in time. Furthermore, the compaction of the shot at a given collision can be expected to decrease progressively as the deformation of the bean bag increases. Hence, a hardening rather than the linear spring of the linearization procedure is more appropriate at a collision. The flexibility of the plastic bag ensures some recovery of the shot after its initial compaction. This recovery will be fairly quick at first (with a corresponding drop in the magnitude of the contact force) as the shot fills the void created at the collision interface by the compaction process. Then there will be a greater resistance to further movement of the shot so that the contact force's magnitude will decrease more slowly. All these four deformation stages, particularly the sudden rise and fall of the contact force, have been shown to be significant. Hence, they must be represented more realistically than afforded by the simplest theoretical models. Furthermore, it is important to use data from in-situ rather than pendulum tests.

6. REFERENCES

1. S.F.MASRI 1971 The American Society of Mechanical Engineers, Applied Mechanics Western Conference, Los Angeles, Calif. Paper No. 71-APMW-14. Theory of the Dynamic Vibration Neutralizer with Motion Limiting Stops.

2. C.N.BAPAT and S.SANKAR 1985 Journal of Sound and Vibration 99(1), 85-94. Single Unit Impact Damper in Free and Forced Vibration.

3. N.POPPLEWELL et al. 1983 The 11th International Conference on Acoustics (ICA), Paris, (54-1)-(54-6). Quiet and Effective Vibroimpact Attenuation of Boring Bar Vibrations.

4. C.N.BAPAT 1982 Ph.D. Thesis, University of Manitoba. A Study of Vibroimpact Systems.

5. D.T.NGUYEN et al. 1986 Journal of Sound and Vibration 109(2),293-307. Impact Behaviour of an Oscillator with Limiting Stops-Part I: A Parametric Study.

7. ACKNOWLEDGEMENT

Financial support from the Natural Sciences and Engineering Research Council of Canada is acknowledged gratefully.

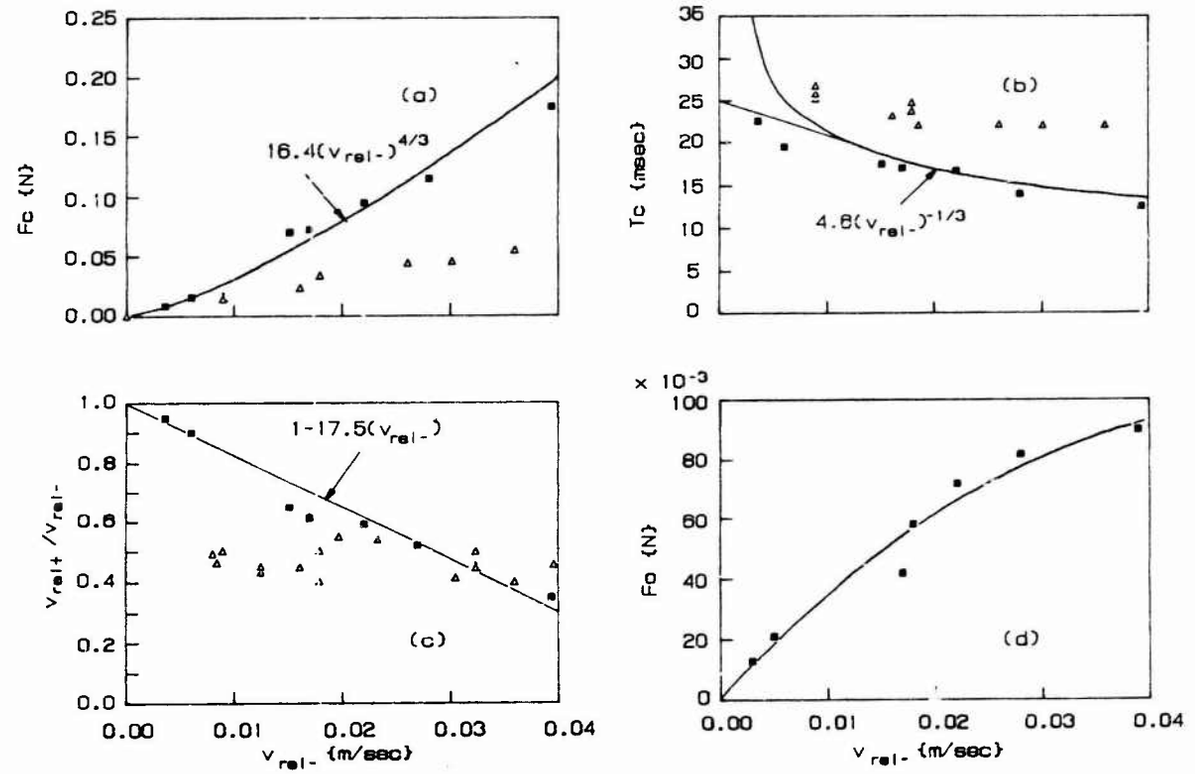

Figure 1. Variation of (a) Fc, (b) Tc and (c) vrel+/vrel- with vrel- measured in the pendulum (△) and in-situ damper tests (▪); and (d) variation of Fo with vrel- in the in-situ test alone.

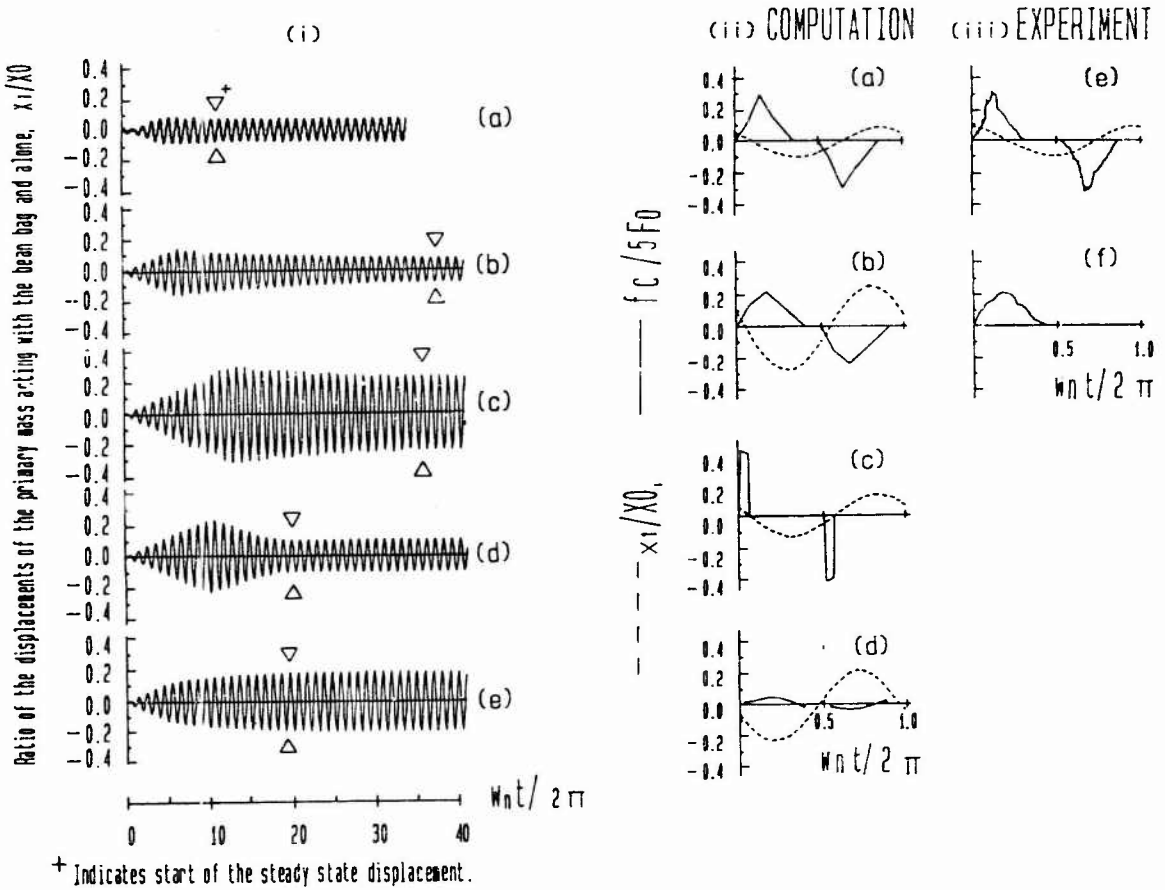

Figure 2. History (i) of the displacement ratio $x_1/X0$ which compares the primary system interacting with the bean bag and not at all. Steady state details, which occur after the arrows in (ia), are given in (iiie) for the in-situ experiment. Thereafter, the details are given in column (ii) in the same descending order as that presented in column (i) below (ib). The computer models are, in descending sequence, the semi-empirical model using first the contact force history measured in-situ and then in the pendulum test; the rigid plastic model; and the equivalent linear model.

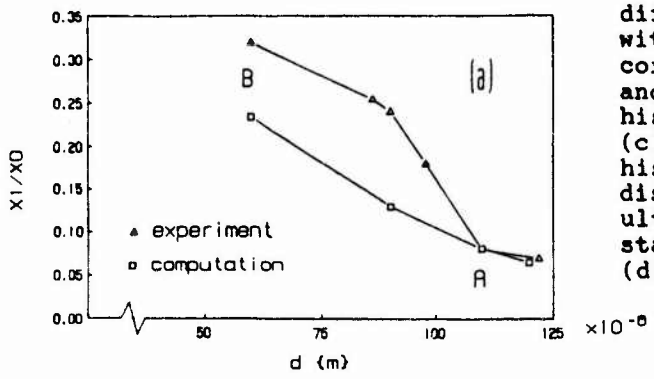

Figure 3. Showing (a) the steady state ratio X1/X0 of the primary mass for different clearances, d, with the bean bag and the corresponding (b) computed and (d) experimental histories at point B. The (c) and (e) give complete histories of the dispiacement ratio which ultimately attain the steady state character of (b) and (d), respectively.

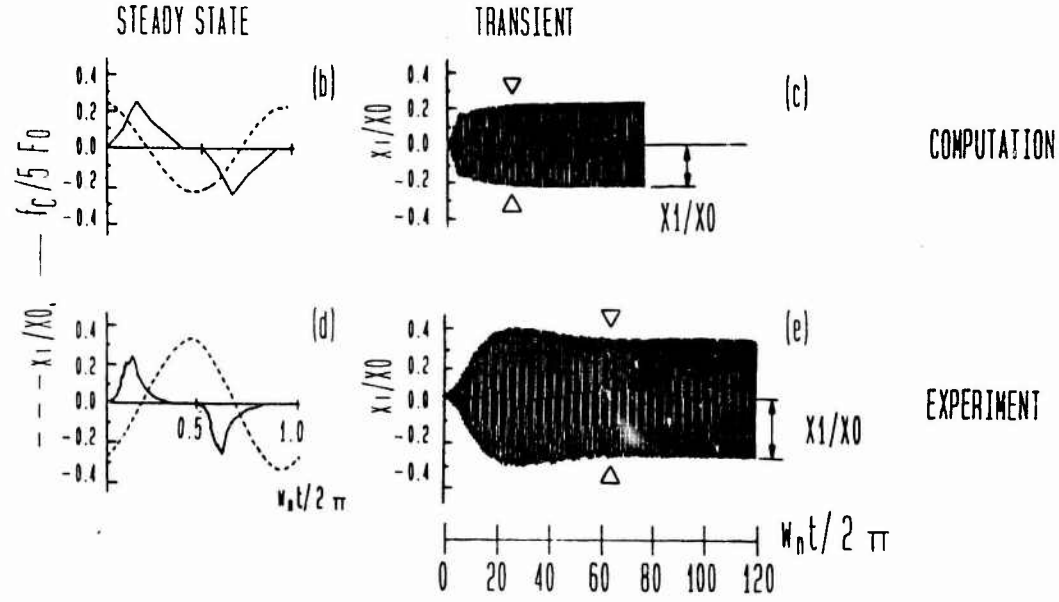

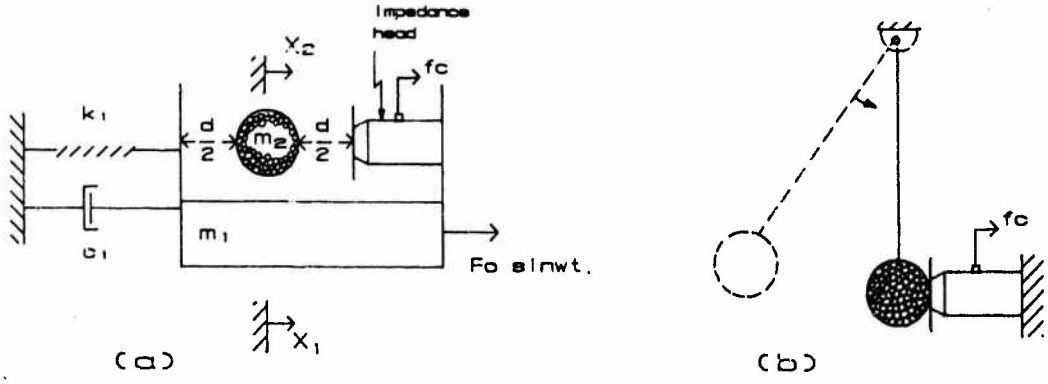

Figure 4. Showing the schematic of the setup for (a) the in-situ and (b) the pendulum measurements.

ANALYSIS OF COILS OF WIRE ROPE ARRANGED FOR PASSIVE DAMPING

M. A. Cutchins, J. E. Cochran, Jr., K. Kumar
N. G. Fitz-Coy and M. L. Tinker

Aerospace Engineering Department
Auburn University, AL 36849-5338

1. INTRODUCTION

Space activities have revitalized the importance of damping investigations. There has been a significant increase in the number of papers on the topic in the literature and a number of research investigations have been initiated. Long of interest to many, damping is receiving increased attention due to a variety of actual and potential applications; among them: large space structures, space structures with stringent pointing requirements, computer controlled flexible structures, flexible manufacturing systems, composite materials, swept-forward wings, SDI structural dynamics, and others.

One means of providing isolation or passive damping [1,2] is to arrange coils of wire rope in such a manner that portions of the coils are attached to one part of a structure, while other portions of the coils are attached to another part of the structure or the base. In between, the wire rope is free to respond and, as relative deflections take place, relatively high damping occurs. This phenomenon is not well understood, but is thought to be associated with interfacial slip of the various strands which make up the wire rope.

The primary interest of this investigation centers on vibration dampers constructed with multiple loops of wire rope. Such wire rope devices have been known to have good damping and isolation characteristics for some time, but have not been analyzed to a thorough enough degree to be yet used in space applications [3,4]. This lack of analysis is at least partly due to the difficulty in modeling the dynamics of wire rope. Due to the complex geometry and interaction of multi-strand wire rope, this modeling process is difficult (even when the rope is not coiled).

Wire rope is, from the basic point of view, simply several strands of wire twisted, or wound, together. Some types are commonly called "cable" and are used in many practical ways with which the reader is familiar. A less obvious, but equally important, use of wire rope is in shock and vibration isolation devices [3,5]. The structure of multi-strand wire rope provides many interfaces at which a portion of the relative motion of strands of wire is converted by friction into heat, thereby dissipating vibrational energy [6]. Furthermore, the rigidity of wire rope structures can be tailored to provide support and restoring forces. Stiffness and damping are adjusted by varying wire diameter, the number of strands, pretensioning and the arrangement of lengths of the wire rope. Commonly, helical coils of ropes are fixed in clamps (see Fig. 1) to form individual shock and/or vibration isolators. The isolators are used to support and isolate communications equipment in vehicles which are subjected to large magnitude, short-term accelerations; i.e., "shocks." In addition to absorbing shock, the internal, or system, damping [3] of the wire rope devices provides vibrational isolation over wide ranges of frequencies and amplitudes.

The damping characteristics of devices such as have been described are not well understood from the theoretical standpoint. Apparently, the design of individual isolators is accomplished by experimentation by engineers with considerable experience in applications of these devices [3,4]. Realistic mathematical models of wire rope isolators would be useful in the design process and perhaps would allow the achievement of the confidence levels in isolator characteristics needed for more applications, especially those in space, in which damping rates and dynamic response must be very accurately known to prevent resonance and control interaction problems. It is understood, though yet unconfirmed, that a French satellite is planned to contain some type of wire rope device.

2. LITERATURE DISCUSSION

2.1 Dynamic

Rogers [7] and others have shown that the use of passive damping devices plus active damping schemes results in a reduced number of active control components and reduced energy and power requirements. A combination of the two types of damping, as opposed to one type alone, can lead to more robust and reliable systems and less expensive systems. These attributes are especially desirable for in-space damping applications.

The most significant paper found in the literature which relates to wire rope damping is that by Pivovarov and Vinogradov [8]. Their study, however, was limited to excitation of straight wire rope which suspended a mass in pendulum fashion. Experimental hysteresis loops (shapes only) are given and several single nonlinear differential equations are solved (as we have done, to be discussed later) in an attempt to simulate the phenomena. LeKuch and Silverman [9] discuss wire rope damping in a designer notebook setting--a guide to isolator selection, and Kerley [1] just mentions wire rope "complex cable arrangements" as one type of passive damping device.

Perhaps the best recent source which summarizes damping considerations is the new book by Nashif, Jones, and Henderson [10], although again, no mention of wire rope damping is made therein. Their emphasis is on single degree of freedom hysteretic; i.e., $k(1+i\eta)$, damping. To date our studies have leaned towards Coulomb damping being more typical than hysteretic for wire rope dampers.

2.2 Static

One cannot discuss wire rope research without recognition of the long standing and exemplary work of Costello, [11] being just one example of a survey nature. Velinsky [12], one of Costello's former students, has made significant contributions. Kumar [13,14] has determined a number of closed-form solutions which hold promise for dynamic applications in the current study. Works by a number of other investigators are referenced in [11] and [14].

It is useful here to refer to two figures from [13] and Cutchins, et al. [15]. Figure 2 shows a typical arrangement of a wire rope cross section and a view of a segment which is typical of the types of rope used in wire rope isolators. Note especially the lay angle, α, and the typical six-wires-around-a-core arrangement. The symbol, m_1, is used to denote

each strand (i=1,2,...). The use of a fibrous core assumption greatly simplifies the analyses, but they are still quite complicated.

Figure 3 is typical of the kind of results documented by Kumar and Cochran [13] for special static loading cases. In this illustration, β=0 refers to a straight cable segment subjected to extension and twist with ends which are constrained against rotation (twist). The M=0 case refers to a similar straight cable segment which has ends free to rotate. Note the excellent agreement between previously published numerical results by Costello and Phillips [16] and the closed form results referred to above.

3. PRELIMINARY MODELS

3.1 Dynamic

For a particular candidate wire rope isolator, made for NASA and shown in Fig. 4, both experimental and analytical studies have been performed to determine the frequency response characteristics. Its average stiffness is approximately 175 N/cm.

The view of the isolator shown in Fig. 4(a) is a side view. Note that the z axis is an axis of symmetry. Figure 4(b) is an isometric view of one set of the wire rope loops for this candidate isolator only. Various arrangements (number of loops, size of rope, different types of rope, etc.) are possible, some more optimum than others.

One application of such an isolator--actually, three-paired sets of isolators--might be as in Fig. 5. Shown are top and side views of a rotating device. The use of the three pairs of isolators at R_0, R_1 and R_2 would serve to isolate undesirable vibrations.

One of the major intents of this research has been to explore the why and how of damping of this specific isolator and relate experimentally obtained data to analytical results of simple models. One simple experimental arrangement consisted of exciting the base in the z direction. A plot of the experimental data for the motion of the isolator base and center of mass appears with analytical curves discussed later.

Two models which were thought to have characteristics appropriate to modeling at least the uniaxial (z-direction) response of the isolator of Fig. 4 are shown in Figs. 6 and 7. The base excitation equations of motion for these two models are, for the Coulomb damper model

$$M\ddot{z} + K(z-u) + \mathrm{sgn}(\dot{z}-\dot{u})\, F_f = 0 \qquad (1)$$

and for the elastically connected Coulomb damper model

$$M\ddot{z} + K(N+1)(z-u) = 0 \qquad \text{(No sliding in damper)} \qquad (2)$$

$$M\ddot{z} + K(z-u) + \mathrm{sgn}(\dot{z}-\dot{u})F_f = 0 \qquad (NK = F_f\text{; damper sliding}) \qquad (3)$$

where z is the coordinate describing the response of the mass, F_f is a Coulomb friction force which always opposes the motion, and u is the base excitation. An undamped spring damper model, of course, would be governed by only the first two terms of equation (1).

Equation (1) has been solved using the Advanced Continuous Simulation Language (ACSL) [17] on a PC in preparation for solving more involved model equations, especially as nonlinearities are considered. A listing of the program to solve equation (1) with variable friction force is shown in Table I. As a first approximation, it was assumed that the friction force was constant for all frequencies. Using a constant friction force of 10.0 N, the mass displacement response for most of the frequency range was not in good agreement with experiment. These results led to the investigation of frequency dependence of the friction force F_f. It has been found that for low frequencies the analytical mass response is not as sensitive to changes in the friction force F_f as it is at higher frequencies. Using the values of F_f shown in Fig. 8 the frequency response shown in Fig. 9 was obtained, still using equation (1). This response is in much better agreement with experiment than the model which assumes no frequency dependence of the friction force.

Typical analytical hysteresis loops, generated by the ACSL model with variable friction force, are shown in Fig. 10 for frequencies of 40 and 100 Hz. The areas of these loops, of course, represent the damping at their respective frequencies.

The insensitivity of the Coulomb-damped model to changes in F_f at low frequencies suggests that the isolator might be even better modeled as an elastically connected Coulomb damper system. Problems with the acceleration response of the variable friction force model, which in contrast to the displacement does not agree very well with experiment, suggests the same. Equations (2) and (3), therefore, are currently being investigated using an ACSL simulation. Initial results indicate that the model is too lightly damped with Coulomb friction alone, and that another damping mechanism, probably viscous, needs to be incorporated into equations (2) and (3).

3.2 Static and Dynamic

Our primary success in this area has been with straight wire rope segments subjected to two loads, axial and torsional. Extension to more involved cases is in progress. A brief summary of closed form solutions obtained to date [13,14,18] follows. The expressions relating the applied tensile force, F, and the applied torsional moment, M, with axial strain ε and torsional strain β have been derived in the following convenient linear form:

$$\bar{F} = F_\varepsilon \, \varepsilon + F_\beta \, \beta \tag{4}$$

$$\bar{M} = M_\varepsilon \, \varepsilon + M_\beta \, \beta \tag{5}$$

where

$$\bar{F} = F/(AE)$$

$$\bar{M} = M/(\pi E R^3)$$

A = metallic area of cross-section; $\sum_i (m_i R_i^2)$

E = modulus of rigidity of the cable material

and the expressions for the force and moment derivatives, i.e., F_ε, F_β, M_ε and M_β have been evaluated separately in two different situations:

Case 1: Single strand cable with fibrous core, wrapped around by an arbitrary number of helical wires for which the expressions for F_ε, F_β, M_ε, M_β can be written as follows:

$$F_\varepsilon = a \sin\alpha$$

$$F_\beta = [b-(1/4)(1-)\sin^4\alpha \cos^2\alpha \sin^2\pi/m]\sin^2\alpha \cos\alpha$$

$$M_\varepsilon = (r/R) \cos\alpha[a-(1/4) \sin^2\alpha \sin^2\pi/m (1-\nu_f \cos^2 2\alpha)]$$

$$M_\beta = (r/R) \sin\alpha[b \cos^2\alpha + (1/4)(1+c) \sin^4\alpha \sin^2\alpha]$$

$$a = 1-(1+\nu) \cos^2\alpha -(1+\nu)(\cos^2\pi/m-\nu) \cos^4\alpha$$

$$b = 1 + (\cos^2\pi/m-\nu) \cos^2\alpha + (1-2\nu) \cos^4\alpha$$

$$c = \nu_f \cos 2\alpha + (1+\nu) \cos^2\alpha \sin^2\alpha$$

$$\nu_f = \nu/(1+\nu) \text{ where } \nu \text{ is Poisson's ratio}$$

R, r, α = radius, helix radius and helix angle of helical wires, respectively

m = number of helical wires

Case 2: Single strand cable with metallic core and an arbitrary number of layers for which the results are:

$$F_\varepsilon = \sum_i [m_i R_i^2 \sin\alpha_i(\sin\alpha_i - \nu \cos^2\alpha_i)]/\sum_i [m_i R_i^2]$$

$$F_\beta = \sum_i [m_i R_i^2 (r_i/R)\sin^2\alpha_i \cos\alpha_i]/\sum_i [m_i R_i^2]$$

$$M_\varepsilon = \sum_i [m_i \bar{R}_i^3 \cos\alpha_i \{(r_i/R_i)(\sin^2\alpha_i - \nu \cos^2\alpha_i) -(1/4)(R_i/r_i)\}]$$

$$M_\beta = \sum_i [m_i \bar{R}_i^4 \sin\alpha_i \{(r_i/R_i)^2 \cos^2\alpha_i + (1/4)(1+\nu_f \sin^4\alpha_i \cos 2\alpha_i)\}]$$

where R_i = radius of the helical wires in the ith layer

R = cable radius, $\bar{R}_i = R_i/R$

m_i = number of helical wires in the ith layer

and other symbols are as defined in Case 1.

We have successfully demonstrated the usefulness of the analytical results by applying these to study some important static as well as ...namic extensional and torsional stiffness characteristics of wire ropes. ... example, if one considers a vertically hanging cable of length ℓ clamped at the upper end and carrying a weight, W, at its free end, the differential equations governing the cable extension and twist oscillations can be written as

$$\frac{d^2\varepsilon}{dt^2} = -\frac{AEg}{W\ell}\left[F_\varepsilon\varepsilon + F_\beta\beta\right]$$

$$\frac{d^2\beta}{dt^2} = -\frac{R^4Eg}{I\ell}\left[M_\varepsilon\varepsilon + M_\beta\beta\right] \qquad (6)$$

Here, the I is the torsional moment of inertia of the tip mass. Also, the cable weight is neglected. The expression for the natural frequencies of coupled oscillations can now be written as

$$\omega^2 = \frac{1}{2}\frac{Eg}{\ell}\left[AF_\varepsilon/W + R^4 M_\beta/I \pm \left\{(AF_\varepsilon/W - R^4M_\beta/I)^2 + 4rR^3 F_\beta M_\varepsilon/(WI)\right\}^{1/2}\right] \qquad (7)$$

4. ADVANCED DYNAMIC MODELS

4.1 Fundamental NASTRAN Models

In order to explore the phenomena of wire rope damping, several NASTRAN models have been developed. Fig. 11 shows a schematic of these models and some of their features. The "one-loop" model is shown in Fig. 12, a NASTRAN-generated view. It is being used for comparison with an experimental one-loop arrangement, a loop which can be loaded perpendicular to its plane with realistic constraints on each boundary of the minor axis.

The "one-loop" model can also be placed into a "three-loop" arrangement with the loops shown in Fig. 13; one loop loaded out of plane as previously described, one loaded in-plane in extension, and one loaded in-plane in a "roll" deformation. The center block to which the force is applied also has to be guided along a minimum friction axial constraint, and has to prevent rotation of the wire rope boundaries at A, B and C.

Returning to Fig. 11, another fundamental model is the "two-strand" model. It and the "seven-strand" model (to be described in the next section) share many of the same features.

Details of the "two-strand" model are shown in Fig. 14. This model consists of a maiden strand around which a single strand is wound, each subdivided into 276 elements and requiring 1932 grid points for definition. The hexagonal cross section of each strand consists of six triangular segments composed of "pie-shaped" NASTRAN PENTA elements like that shown in Fig. 14. Strands are connected by scalar elastic elements (springs), which have been incorporated to model the normal forces acting on each strand (see Section B-B of Figure 14).

4.2 Advanced NASTRAN Models

Similar to the "two-strand" model, a "seven-strand" model has been developed. A cross section is shown in Fig. 15. Note the springs between all strands. While space does not permit a thorough discussion of the results from this model here, its use is two-fold. First, complete normal mode analysis yields the mode shape vectors, ϕ_j. typical (though very involved) mode shape plots, and the contact forces normal to the strands, f_{ij}. Secondly, equation (8) for the jth vibrational mode has been derived [15] using a Lagrange approach

$$M_j \ddot{q}_j + d_j \dot{q}_j + K_j q_j + \underline{K}_{g_j}^T \underline{q} = Q_{c_j} \qquad (8)$$

where M_j, d_j, and K_j are the generalized mass, damping coefficient and stiffness coefficient, respectively, for the jth vibrational mode. $\underline{K}_{g_j}$ is the jth row of the gravitation stiffness matrix $\underline{\underline{K}}_g$, and Q_{c_j} is the jth element of the generalized Coulomb damping vector $\underline{Q}_c$.

Unit tangent and binormal vectors are used to derive expressions for the normal forces (normal to each strand).

One means for solving problems with the most arbitrarily shaped wire rope is to use a NASTRAN model to generate the mode shapes ϕ and normal forces. If the friction forces can then be related to the normal forces and some realistic assumption made concerning the viscous damping present, the ϕ's output from NASTRAN can be used to find the rest of the terms in equation (8), which then can be solved for the response, q.

5. CONCLUSIONS

Some inroads have been made into solving the very complex problems associated with wire rope damping as found in typical isolator coil arrangements. The various models described in this paper are illustrative of a range of investigation that varies from fairly simple models to those which are extremely complicated. Perhaps the major conclusion is that the latter models are not as useful as one might expect without the insight into the physical phenomena provided by the simpler models.

6. ACKNOWLEDGEMENTS

The support of this research by NASA/MSFC under Research Grants NAG8-532 and NAG8-647 is gratefully acknowledged. The encouragement of the Technical Monitor, Stan Guest, has been very instrumental.

REFERENCES

1. J. Kerley 1984 Concepts and effects of damping in isolators, paper in Rogers (1984), L-1 through L-15.

2. L. Rogers (Ed.) 1984 Vibration Damping 1984 Workshop Proceedings, AFWAL TR-84-3064 (held at Long Beach, California, February 1984).

3. J. Silverman 1985 Aeroflex Lab, Plainview, N. Y., private communication, March 22.

4. R. Jewell 1984 NASA/MSFC private communication, December 19.

5. Gilbert/Commonwealth 1976 Transmission Line Reference Book, Wind-Induced Conductor Motion: Electric Power Research Institute, Palo Alto, California.

6. C. M. Harris and C. E. Crede (Eds.) 1976 Shock and Vibration Handbook (2nd Ed.): McGraw-Hill Book Company, New York, N. Y., Chapter 30.

7. L. Rogers (Ed.) 1986 Damping 1986 Proceedings, AFWAL-TR-86-3059, Vols. 1 and 2 (Held at Las Vegas, Nevada, March 1986).

8. I. Pivovarov and O. G. Vinogradov 1985 Proceedings of the AIAA/ASME/ASCE/AHS 26th Structures. Structural Dynamics, and Materials Conference, Part II, 232-237, Orlando, Florida. The phenomenon of damping in stranded cables.

9. H. LeKuch and G. Silverman 1983 Astronautics & Aeronautics, 30-32. Selecting shock and vibration isolators.

10. A. D. Nashif, D. I. G. Jones and J. P. Henderson 1985 Vibration Damping. New York: John Wiley & Sons.

11. G. A. Costello 1978 ASME Applied Mechanics Reviews, 897-900 Analytical investigation of wire rope, (This was the feature survey article which included 30 references; none address wire rope damping, however).

12. S. A. Velinski 1987 Design and mechanics of multi-lay wire strands. Boston, Mass. 13th ASME Design Automation Conference.

13. K. Kumar and J. E. Cochran, Jr. 1987 Proceedings of the AIAA/ASME/ASCE/AHS 28th Structures, Structural Dynamics, and Materials Conference, Part I, 88-92. Monterey, California. Analytical solutions for static elastic deformations of wire ropes.

14. K. Kumar and J. E. Cochran, Jr. 1987 Journal of Applied Mechanics 54. 898-903. Closed form analysis for elastic deformations of multilayered strands.

15. M. A. Cutchins, J. E. Cochran, Jr., K. Kumar, N. G. Fitz-Coy, and M. L. Tinker 1987 Final Report: NASA Research Grant NAG8-532, Aerospace Engineering Department, Auburn University, Alabama, Submitted to Marshall Space Flight Center, Huntsville, Alabama.

16. G. A. Costello and J. W. Phillips 1976 Journal of Engineering Mechanics Division, ASCE. 102, 171-181. Effective modulus of twisted wire cables.

17. Advanced Continuous Simulation Language Reference Manual (4th Ed.) 1986 Mitchell and Gauthier Assocs., Concord, Mass. 01742.

18. K. Kumar, J. E. Cochran, Jr. and M. A. Cutchins, Contact stresses in cables due to tension and torsion (in preparation).

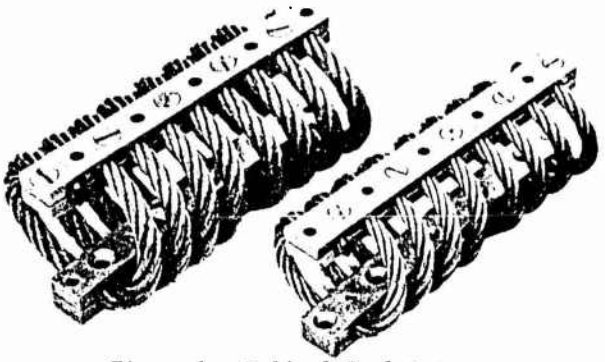

Figure 1. Helical Isolators

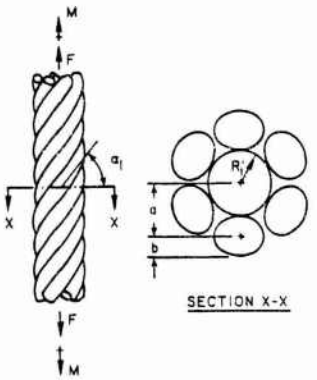

Figure 2. Typical wire rope geometry and loading.

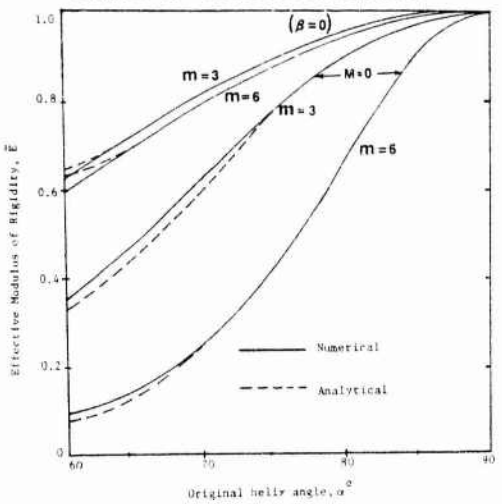

Figure 3. Plots comparing the analytical and numerical values of effective modulus of rigidity of wire rope for the practical range of α.

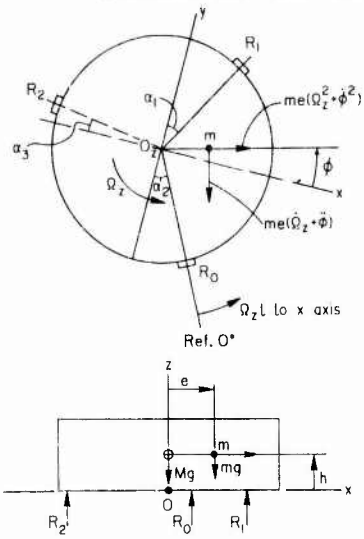

Figure 5. Typical application of wire rope isolators.

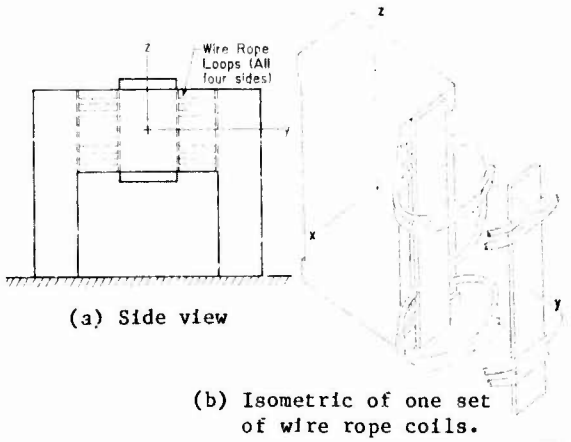

(a) Side view

(b) Isometric of one set of wire rope coils.

Figure 4. Candidate isolator.

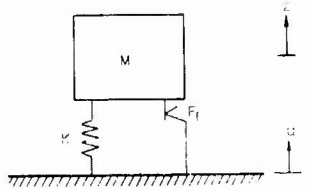

Figure 6. Coulomb damper model.

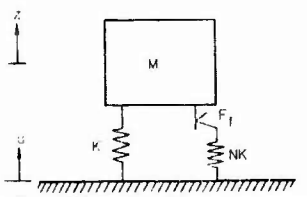

Figure 7. Elastically connected Coulomb damper model.

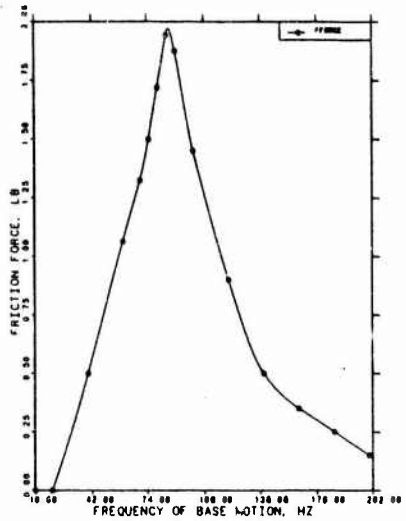

Figure 8. Variation of friction force in isolator.

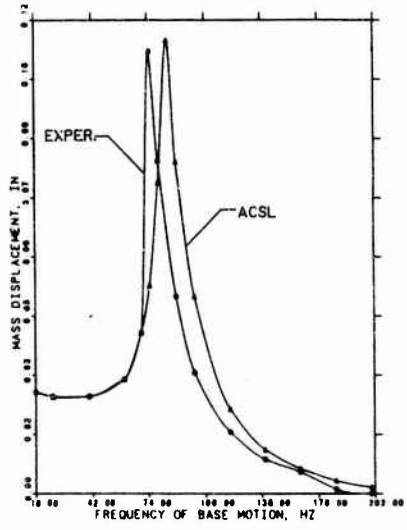

Figure 9. Isolator frequency response.

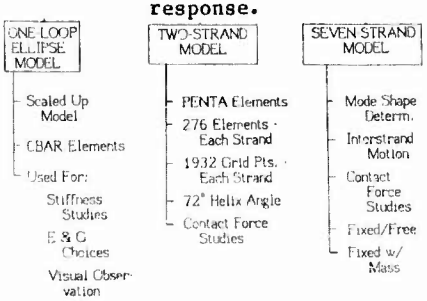

Figure 11. Features of NASTRAN dynamic models.

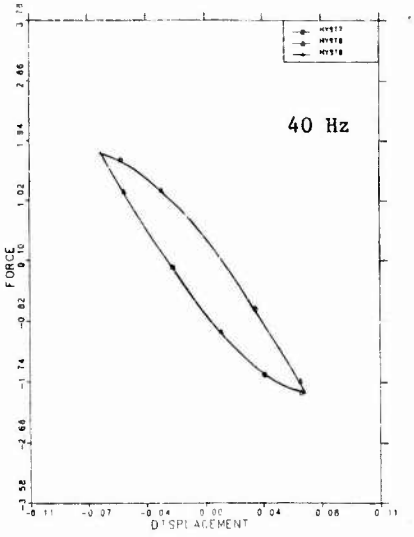

Figure 10. Typical hysteresis loops generated using ACSL, 40 Hz (above; 100 Hz (below).

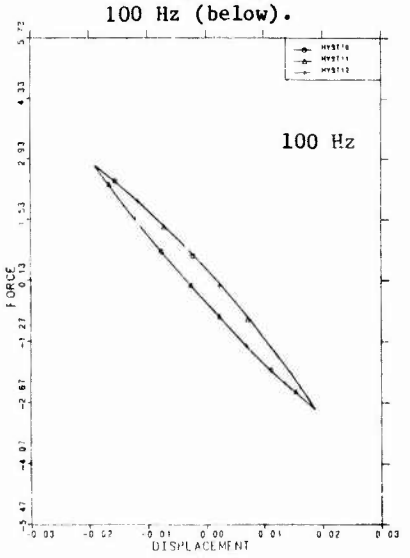

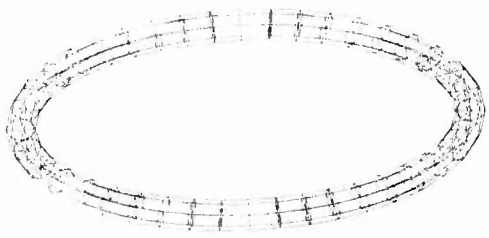

Figure 12. NASTRAN "one-loop" model.

Table I. Typical ACSL program with variable friction force and variable base motion.

```
PROGRAM CFMVF1
   CONSTANT WT=.1359    ,  G=386.4    ,  SLOPE=97.7
   CONSTANT TDEL=0.0    ,  PI=3.1416  ,  PHASE=0.0
   CONSTANT TSTP=2.0    ,  ZO=0.0     ,  ZDO=0.0
   CONSTANT OMEGA=40.0
   TABLE FF, 1, 14 ...
         /    10.0,   20.0,   40.0,   60.0,   70.0 ...
         ,    75.0,   80.0,  100.0,  120.0,  140.0 ...
         ,   160.0,  180.0,  200.0,  250.0          ...
         ,    0.75,   0.85,   1.25,   0.15,   0.10 ...
         ,    0.10,   2.25,   1.45,   0.50,  0.005 ...
         ,   0.007,  0.007,  0.004,  0.004          /
   TABLE FU, 1, 14 ...
         /    10.0,   20.0,   40.0,   60.0,   70.0 ...
         ,    75.0,   80.0,  100.0,  120.0,  140.0 ...
         ,   160.0,  180.0,  200.0,  250.0          ...
         ,   0.302,  0.170,  0.084,  0.051.  0.033 ...
         ,   0.028,  0.034,  0.024,  0.016,  0.012 ...
         ,   0.008,  0.006,  0.004, 0.0025          /
INITIAL
   W = 2.*PI*OMEGA
END $"OF INITIAL"
DYNAMIC
   CINTERVAL CINT=0.002
   TERMT (T .GT. TSTP)
 DERIVATIVE
   U = FU(OMEGA)          ...
       *HARM(TDEL,W,PHASE)
   ZDD = -G/WT*(SLOPE*(Z-U) ...
   + FF(OMEGA)*SIGN(1.0,ZD-UD))
   ZD = INTEG(ZDD,ZDO)
   UD = DERIVT(0.0,U)
   Z = INTEG(ZD,ZO)
 END $"OF DERIVATIVE"
END $"OF DYNAMIC"
END $"OF PROGRAM"
```

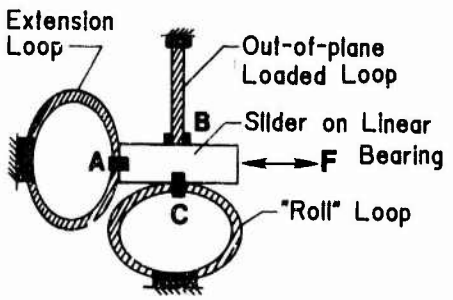

Figure 13. 3-loop arrangement.

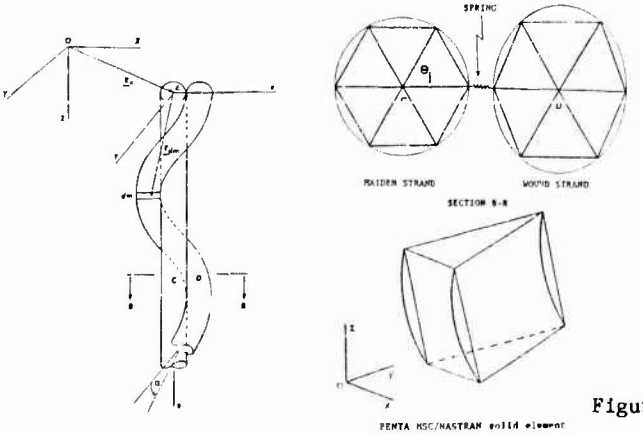

Figure 14. NASTRAN "two-strand" model.

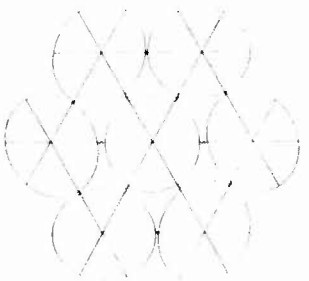

Figure 15. Section through NASTRAN "seven-strand" model.

STABILIZING THE NEGLECTED DYNAMICS IN ACTIVE CONTROL OF VIBRATION

André PREUMONT
Professor of Applied Mechanics

Free University of Brussels,
Avenue F.D. Roosevelt, 50
B - 1050 Brussels (Belgium)

Eva CZAJKOWSKI & Raphaël T. HAFTKA
Graduate Research Professor

Aerospace & Ocean Engineering Department
Virginia Polytechnic Institute & State
University, VA 24061, Blacksburg (USA)

1. INTRODUCTION.

Linear Quadratic Gaussian (LQG) [1,11] techniques provide a systematic way of designing well conditioned linear state feedback controllers which are optimal with respect to a quadratic performance index

$$J = E\,[x'Qx + u'Ru] \tag{1}$$

for given noise statistics, (W_1,W_2), where W_1 is the plant noise intensity matrix and W_2 is the measurement noise intensity matrix. The structure of Q is related to the required performances of the output, while R is related to the cost of the control. The relative magnitudes of Q and R are adjusted to obtain the desired compromise between performance and control requirements. LQG techniques are well suited for low order systems. Their application to active damping of vibration requires the truncation of the system model to the most significant modes. The uncontrolled modes are simply ignored in the controller design, although many of them are known with reasonable accuracy. It is well known that the uncontrolled dynamics may become unstable as a result of their interaction with the control system (spillover instability [2]).

The most straightforward way of alleviating spillover is to increase the passive damping of the residual modes. The same effect can be achieved by supplementing the modal control with direct velocity feedback with colocated sensors and actuators [5]. Alternative techniques have also been suggested.

Balas [3] proposed that a feedthrough component be added to the control, that restitutes the original stability margin to a selected number of residual modes. Sesak et al. [17] proposed the MESS (Model Error Sensitivity Suppression) method which desensitizes the control system to a given set of neglected modes. Gupta [9] introduced the concept of frequency dependent weighting matrices which increase the penalty for the high frequency components of the control. This reflects the fact that input in the frequency range where the model is poor, is undesirable. Non-linear modifications of the control in the vicinity of the equilibrium have also been suggested [15], to make the composite system (regulator, observer, and residual modes) benefit from the inherent stability properties of the open loop system.

Low order controllers insuring the stability of the full order system have been investigated by Kwakernaak and Sivan [11] and applied to flutter control by Mukhopadhyay et al. [13] and Newsom and Mukhopadhyay [14]. This method can be used to control a limited set of modes while keeping the others barely stable. Finally, Ridgely and Banda [16] suggested that spillover stability could be achieved by the Loop Transfer Recovery (LTR) technique by designing a regulator which satisfies a robustness test and making the controller "recover" the loop transfer matrix of the regulator assuming the noise enters the plant at the input.

There are certain restrictions and limitations on all the above methods.

This paper considers the stabilization of the neglected dynamics of the higher modes of vibration. It aims at designing modal controllers with improved spillover stability properties. It is based on the premise that the structural dynamicist will be able to predict more vibration modes than would be practical to include in the design of the controller. The proposed method calls for designing the observer so as to improve spillover stability with minimum loss in performance. It is based on optimizing the noise statistics used in the design of the Kalman-Bucy Filter (KBF).

2. STABILITY ROBUSTNESS TESTS.

In this section, we analyse what are the modes which are potentially critical from the point of view of spillover. To do that, we consider a stability robustness test based on singular values [7]. Let $\ell_m(\omega)$ be an upper bound to the maximum singular value of the multiplicative uncertainty at the plant output (Fig. 1) :

$$\bar{\sigma} [L(\omega)] \leqslant \ell_m(\omega) \qquad (2)$$

When $\ell_m(\omega) \gg 1$, the closed loop system is guaranteed to be stable in presence of uncertainty if the maximum singular value of the loop transfer matrix satisfies :

$$\bar{\sigma} [GK] < \frac{1}{\ell_m(\omega)} \qquad (3)$$

It is a sufficient, but not necessary condition for stability. Alternative tests exist (e.g. [10,12]) ; they are all conservative because they do not take into account the structure of the uncertainty. They are based on a worst case which is not necessarily allowed by the structure of the system.

A typical plot of $\bar{\sigma} [GK]$ and $\frac{1}{\ell_m(\omega)}$ is shown in Fig. 2. The magnitude of the troughs in the uncertainty curve is governed by the damping ratio of the uncontrolled modes. Due to the low structural damping expected in large space structures and the relatively slow decay rate of $\bar{\sigma} [GK]$ at high frequency, robustness test (3) cannot in general be satisfied by the uncontrolled modes in the transition region just outside the bandwidth of the controller (unless there is a gap in the natural frequencies of the structure). The modes which are in that transition region are candidates for destabilization and must be considered carefully. Amongst the uncontrolled modes, we distinguish :

- the marginal residual modes which do no satisfy the robustness test or have only a small margin ;
- the control-system-robust-residual modes (called robust modes hereafter) which satisfy the stability robustness test and are guaranteed to be stable.

Only the controlled and the marginal residual modes will have to be considered in the remaining of this study ; the latter will be called residual modes.

Note that an upper bound to the maximum singular value of the multiplicative uncertainty $L(\omega)$ can be obtained from that of the additive uncertainty $\Delta G(\omega)$ as follows :

$$G(\omega) [I + L(\omega)] = G(\omega) + \Delta G(\omega)$$

$$L(\omega) = G^{-1}(\omega) \Delta G(\omega)$$

It follows that

$$\bar{\sigma}\,[\,L\,] \leqslant \bar{\sigma}(G^{-1})\;\bar{\sigma}(\Delta G)$$

or

$$\bar{\sigma}\,[\,L\,] \leqslant \frac{\bar{\sigma}(\Delta G)}{\underline{\sigma}(G)} \qquad (4)$$

where $\underline{\sigma}$ stands for the minimum singular value. The spectral developments of $G(\omega)$ and $\Delta G(\omega)$ are readily obtained, in terms of the controlled and uncontrolled modes, respectively.

3. OBSERVER DESIGN.

The noise environment is defined by the noise intensity matrices W_1 and W_2. Often we do not know W_1 and W_2 accurately, and, even if we do, it may be advantageous to use different noise matrices in the design of the observer. Let V_1 and V_2 be, respectively, the plant noise and measurement noise intensity matrices used in the design of the Kalman-Bucy Filter (KBF). When V_1 and V_2 are different from W_1 and W_2, the resulting KBF is no longer optimum with respect to the given noise environment, (W_1,W_2). However, typically the performance index (equation (1)) is not overly sensitive to the choice of (V_1,V_2) for a wide range of values, i.e., the optimum is rather flat. Therefore, it is reasonable to select V_1 and V_2 so as to suppress spillover instability, as long as the performance of the KBF is not overly compromised.

In a previous study [6], the influence of the structure of the plant noise intensity matrix of the KBF on the stability margin of the residual modes was demonstrated. An optimization procedure was developed which used information on the residual modes to minimize spillover (i.e., maximize the stability margin) of known residual modes. This procedure selected the optimum plant noise intensity matrix to maximize the stability margin of the residual modes and properly place the observer poles. The optimization procedure demonstrated that it only required a small number of design variables in order to produce excellent results.

That study incorporated the performance implicitly by imposing a maximum stability margin on the observer (a minimum stability margin can also be enforced on the observer by means of Anderson and Moore's α shift procedure [1]). It offered no way to include the actual noise statistics, (W_1,W_2), in the design, even if they are known with some accuracy. This paper is expanding the optimization procedure to include an explicit measure of the performance and to incorporate the actual plant and measurement noise statistics of the system.

4. OBSERVER PERFORMANCE.

The performance index of the stochastic linear quadratic regulator (LQR) in equation (1) can be evaluated from the solution of a n x n Lyapounov equation. When the LQR is implemented on the reconstructed state from an observer, there is an additional penalty resulting from the imperfect knowledge of the state. The new value of the performance index, J, can be evaluated by solving a 2n x 2n Lyapounov equation. The following ratio can be taken as a measure of how well the observer works

$$F_{performance} = \frac{J - J_{LQR}}{J_{LQR}} \geq 0 \qquad (5)$$

J and J_{LQR} are evaluated with the actual noise statistics (W_1,W_2), and not those, (V_1,V_2), taken in the design of KBF, so that $F_{performance}$ represents the performance deterioration for the actual noise statistics, or at least those believed to be the closest.

5. OPTIMIZATION OF NOISE INTENSITY MATRICES.

The observer is obtained as the KBF whose plant noise intensity matrix, V_1, is the solution of the following optimization problem

Find V_1, δ such that

$$\min F = (\delta - t)_+^2 + \mu F_{performance} \qquad (6)$$

subject to the constraint

$$Re(\lambda_i) < \delta \qquad (7)$$

The two terms in the objective function (6) represent the spillover and performance contributions, respectively. The parameter μ is used to weight the objectives of spillover stability and performance. t is the minimum stability margin that one wishes to achieve, and the final value of δ is the actual stability margin. The sign (+) indicates that $(a)_+ = \max(a,0)$, therefore, the spillover part does not contribute to the objective function if the real parts of all the poles are smaller than t. In that case, the design is based on performance only.

In the above procedure, the measurement noise intensity matrix, V_2, can be taken either according to the MESS method [17], to minimize the observation spillover, or simply equal to W_2, the actual noise.

Note that if t is set to a large value so that the spillover part does not contribute to the objective function, and if $V_2 = W_2$, then the optimal solution will correspond to $V_1 = W_1$, the actual plant noise intensity matrix. This means that the optimum observer will be the KBF corresponding to (W_1,W_2) which minimizes J in equation (5). The same conclusion holds for μ being extremely large to cause the performance term to be dominant in equation (6) and the spillover term to be negligible.

In this formulation, the number of design variables is equal to $n^2 + 1$, but can be reduced by making assumptions about the structure of V_1. For example,

$$V_1 = \text{diag}(V_i^2) \qquad (8)$$

$$V_1 = aa' \qquad (9)$$

$$V_1 = HH' \qquad (10)$$

where H is an n by m arbitrary matrix. The foregoing choices lead, respectively, to n + 1, n + 1, and nm + 1 design variables. For MIMO systems, this number can be further reduced by assuming that the noise enters at the input:

$$V_1 = B_c \, V \, B_c^T \qquad (11)$$

where B_c is the input matrix of the controlled modes and V is a square matrix assuming one of the forms (8) to (10).

6. BEAM EXAMPLE.

The beam example used by Balas [2] to demonstrate spillover is used to demonstrate the proposed method. The beam is controlled by one actuator located at the 1/6 position and a displacement sensor located at the 5/6 position. The state variables in the problem are the modal amplitudes and modal velocities. The first three modes are controlled by a LQR based on the reconstructed state obtained by a KBF, while the fourth mode acts as the known residual mode. The regulator is the same as in [2] and [6]. It is assumed that the actual noise statistics are $W_1 = I$ and $W_2 = 0.02$.

The NEWSUMT-A programme [8] was used for optimization and the L-A-S programme [4] for control calculations.

The results for the observer design based on optimizing the matrix V_1 assumed of the form (8) or (9) are given in Fig. 3. The figure shows, for various values of the weighting parameter μ in equation (6), the values of the stability margin δ and the performance index J. The initial values for V_1 were respectively :

$$V_1 = I \quad \text{and} \quad V_1 = aa' \quad \text{with } a' = (1 \quad 1 \quad 1 \quad 1 \quad 1 \quad 1)$$

Tracing was used when decreasing μ (i.e., the optimum V_1 for one value of μ was used as initial solution for the next value of μ).

Although the KBF corresponding to the actual noise statistics leads to a stable residual mode in this case, it can be seen that, by decreasing μ, a substantial improvement of its stability can be obtained without a great performance deterioration.

Fig. 4 shows the evolution of the closed loop poles for the diagonal case.

7. SUGGESTED DESIGN PROCEDURE.

(1) Once the controlled modes have been selected, design a LQR to achieve a reasonable compromise between performance and control requirements, and a KBF with the best available noise statistics.

(2) Apply a robustness test as indicated in Section 2, where the uncertainty curve includes all the uncontrolled modes and corresponds to a reasonable value of the structural damping (this can be done easily using equation (4) and the spectral developments of G and ΔG in terms of the modes).

(3) Identify the uncontrolled modes which either fail the robustness test or have a small margin. These modes (residuals) are candidates for spillover destabilization. If there are none, the design is completed.

(4) Apply the foregoing optimization procedure to the design of an observer which stabilizes the modes identified at step 3 with respect to spillover.

(5) Apply the robustness test to the new controller to check that it is satisfied by all the robust modes of the original controller. If it is, the design is completed, if it is not, go back to step 4 with the new set of residual modes.

8. CONCLUDING REMARKS.

(a) The foregoing procedure aims at designing controllers with improved spillover stability properties. It is not guaranteed to produce a stable design, but if it does not, the final value of δ gives the minimum values of structural damping required to stabilize the system.

(b) The elements of the observer gain matrix K_c can be substituted to the elements of V_1 as design variables in the optimization problem of Section 5. The resulting observer is no longer a KBF, but the procedure does not require multiple solutions of the Riccati equation within the optimization process (only Lyapounov equations must be solved in this case). This alternative approach is currently being pursued.

9. REFERENCES.

[1] ANDERSON, B.D.O. and MOORE, D.L. (1971).
Linear Optimal Control.
Prentice Hall.

[2] BALAS, M.J. (1978).
Active Control of Flexible Systems.
Journ. Optim. Theory and Applic., Vol. 25, n°3, July, 415-436.

[3] BALAS, M.J. (1980).
Enhanced Modal Control of Flexible Structures via Innovations Feedthrough.
Int. J. of Control, 32, N°6, 983-1003.

[4] BINGULAC, S.P. , WEST, P.J. and PERKINS, W.R. (1985).
Recent Advances in the L-A-S Software Used in CAD of Control Systems.
IFAC Symposium on CAD, Copenhagen, July.

[5] CANAVIN, J. (1978).
Control Technology for Large Space Structures.
AIAA paper 78-1691, Conf. on Large Space Platforms, Los Angeles, September 27-29.

[6] CZAJKOWSKI, E. and PREUMONT, A. (1987).
Spillover Stabilization and Decentralized Modal Control of Large Space Structures.
SDM Conference, Monterey, April.

[7] DOYLE, J.C. and STEIN, G. (1981).
Multivariable Feedback Design : Concepts for a Classical/Modern Synthesis.
IEEE Trans. on Automatic Control, Vol. AC-26, 1, February 4-16.

[8] GRANDHI, R.V., THAREJA, R. and HAFTKA, R.T. (1985).
NEWSUMT-A : A General Purpose Program for Constrained Optimization Using Constraint Approximations.
ASME J. of Mechanics, Transmission and Automation in Design, Vol. 107, pp. 94-99, March.

[9] GUPTA, N.K. (1980).
Frequency-Shaped Cost Functional : Extension of Linear-Quadratic- Gaussian Design Methods.
AIAA J. of Guidance, 3, N°6, November-December, 529-535.

[10] KOSUT, R.L., SALZWEDEL, H., and EMAMI-NAEINI, A. (1983).
Robust Control of Flexible Spacecraft.
AIAA J. Guidance, Control and Dynamics, 6, n°2, March-April, 104-111.

[11] KWAKERNAAK, J., and SIVAN, R. (1972).
Linear Optimal Control Systems.
Wiley-Interscience.

[12] MUKHOPADHYAY, V., and NEWSOM, J.R. (1982).
Application of Matrix Singular Value Properties for Evaluating Gain and Phase Margins of Multiloop Systems.
NASA Technical Memorandum 84524, July.

[13] MUKHOPADHYAY, V., NEWSOM, J.R., and ABEL, I. (1982).
Reduced Order Optimal Feedback Control Law Synthesis for Flutter Suppression.
AIAA J. Guidance, Control and Dynamics, 5, n°4, July-August, 389-395.

[14] NEWSOM, J.R., and MUKHOPADHYAY, V. (1981).
Application of Constrained Optimization to Active Control of Aeroelastic Response.
NASA Technical Memorandum 83150, June.

[15] PREUMONT, A. (1987).
Spillover Alleviation in Active Control of Flexible Structures.
AIAA Journal of Guidance and Control (to be published).

[16] RIDGELY, D.B. and BANDA, S.S. (1985).
Introduction to Robust Multivariable Control.
AFWAL-TR-85-3102, Wright-Patterson Air Force Base, Dayton, OH.

[17] SESAK, J.R., LIKINS, P. and CORADETTI, T. (1979).
Flexible Spacecraft Control by Model Error Sensitivity Suppression.
Proc. VPI & SU/AIAA Symp. on Dynamic and Control of Large Flexible Spacecraft, Blacksburg, VA.

* * *

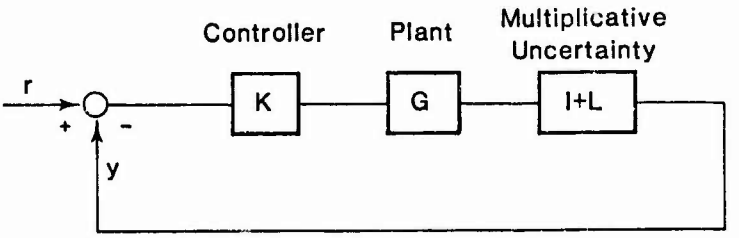

Figure 1 :

Multiplicative uncertainty at the plant output

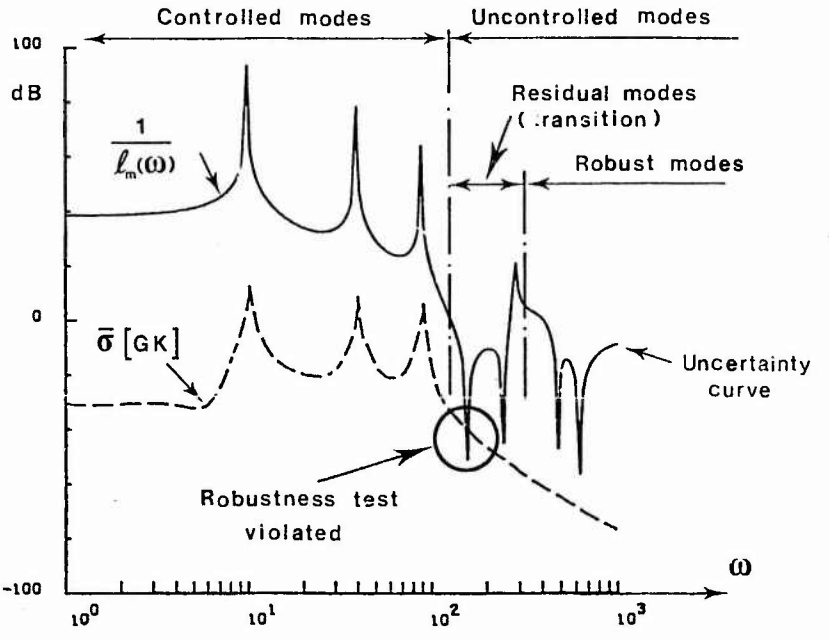

Figure 2 :

Robustness test based on singular values

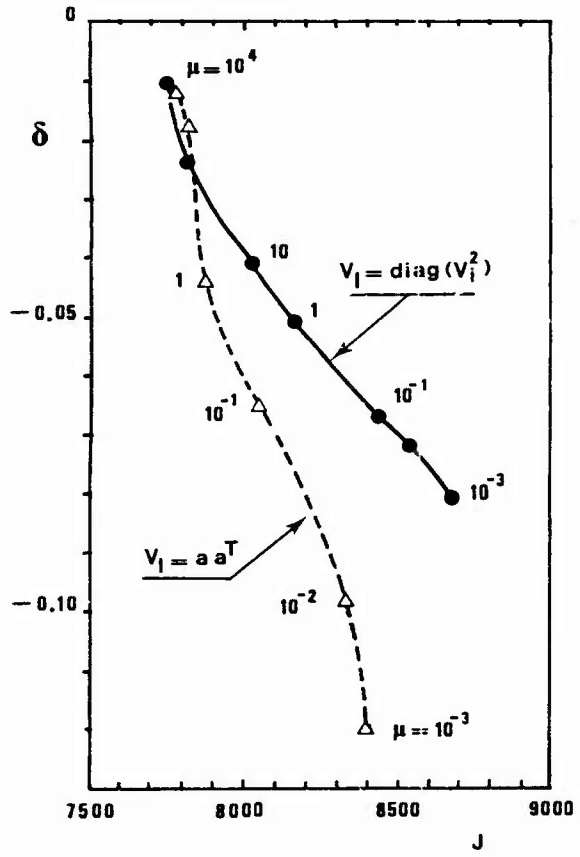

Figure 3 :
Stability margin δ vs. performance index J for different structures of V_I

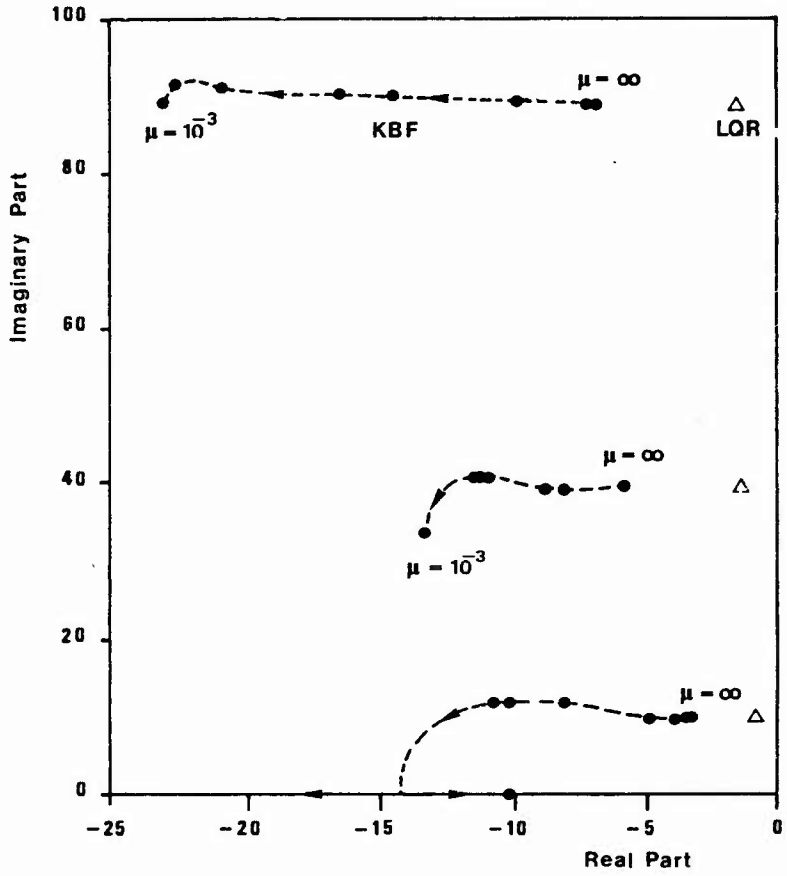

Figure 4:
Evolution of the closed loop poles as functions of μ (only the upper half plane is shown)
μ = ∞ corresponds to the stochastic optimum.

VIBRATION PROBLEMS IN COALMINE HAULING SYSTEMS

R. U h r i g

University of the Armed Forces of the Federal Republic of Germany in Munich, W. Heisenberg-Weg 39, 8091 Neubiberg,FRG

1. INTRODUCTION

Vertical hauling of coal has been practised since last century by hauling systems consisting mainly of one or two cages or buckets and one or more hoisting ropes. Since the end of last century a lower rope is added to the upper one for weight compensation. This shape of hauling system is known as "Köpe-System" [1] and is used today all over the world (s. Fig. 1).

To reduce transversal movements of the bucket during hauling it is equipped with front- and rear-wheels, which are elastically connected with the bucket following a vertical track. Because of irregularities of this track transversal vibrations are induced into the hauling system especially since the hauling speed was raised remarkably during the last twenty years.

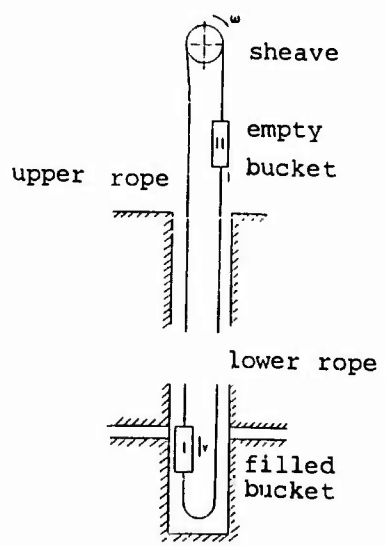

Fig. 1 Hauling system
System "Köpe"

Additional vibrations are induced into the system when the hoisting rope is passed over the sheave. Bending waves travel along the rope with kinetic effects given to the whole system.

Both phenomena described here are the source of kinetic stresses causing fatigue damage in the strand wires of the rope. The result is a reduction of its tensile strength and at the end of its lifetime complete destruction of the rope can be observed.

Because, until now, no save prediction of the lifetime of the hoisting rope is possible, intensive observation of the rope during its lifetime is necessary. Therefore theoretical and experimental research has been done during the last years to obtain a better basis for lifetime predictions.

Contributions can be divided into those which consider the hoisting rope alone under static or kinetic forces (s. for example [2]) and those which analyse the kinetic behaviour of the bucket alone moving along a track with irregularities. Contributions which consider both, the hoisting rope, the bucket and the lower rope as a complete hauling system are rarely to be found in literature (s. for example [3]).

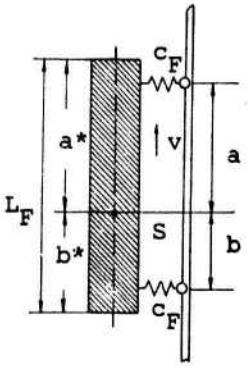

Fig. 2 Bucket with elastically connected wheels

The present contribution will develop a refined model to describe the transversal motion of the complete system by introducing time varying length of the upper and lower rope and additional bending stiffness of it. The model includes the bucket as a rigid body with rotary inertia (Fig. 2).

We shall find the solution of this problem in three steps.

2. KINETIC BEHAVICUR OF THE HOISTING ROPE

The equations of transverse motion of the rope under constant tensile force H are:

$$\begin{bmatrix} \bar{w} \\ \bar{\psi} \\ \bar{M} \\ \bar{V} \end{bmatrix}^{\nabla} = \begin{bmatrix} 0 & 1 & 0 & 0 \\ 0 & 0 & 1 & 0 \\ 0 & \lambda_K^2 & 0 & 1 \\ -\lambda_B^4 \partial^2 & 0 & 0 & 0 \end{bmatrix} \begin{bmatrix} \bar{w} \\ \bar{\psi} \\ \bar{M} \\ \bar{V} \end{bmatrix} + \begin{bmatrix} 0 \\ 0 \\ 0 \\ -\bar{p} \end{bmatrix} \qquad (1)$$

It is:

$$\left.\begin{aligned} &\bar{w} = -w && \text{the transversal displacement,} \\ &\bar{\psi} = l\,\psi && \text{the rotation of a cross section,} \\ &\bar{M} = M\,l^2/EI && \text{bending moment,} \\ &\bar{V} = V\,l^3/EI && \text{transverse shearing force,} \\ &l && \text{is the length and} \\ &EI && \text{is the bending stiffness of the rope,} \\ &\bar{p} = p\,l^4/EI && \text{time dependant external force.} \end{aligned}\right\} \qquad (2)$$

The parameters are with μ the mass per unit length and the tensile force H:

$$\lambda_K^2 = H\,l^2/EI\,, \qquad \lambda_B^4 = \mu\,l^4/EI$$

The meanings of the operators ∇ and ∂ are:

$$\nabla \hat{=} d(\ldots)/d(x/l)\,, \qquad \partial \hat{=} d(\ldots)/dt$$

It should be noticed that shear deformation and rotary inertia of the rope is neglected. No internal and external damping is considered.

From equations (1) we obtain by elimination technique the equation of motion ($\dot{} \triangleq d(...)/dt$):

$$\bar{w}^{\nabla\nabla\nabla\nabla} - \lambda_K^2 \bar{w}^{\nabla\nabla} + \lambda_B^4 \bar{w}^{\cdot\cdot} = - \bar{p} \qquad (3)$$

Exact solutions of equations (1) or (3) can be found only if the parameters are constant, i.e. if the length of the rope is constant. But this is not given in our case.

We therefore change from the rope with continuously distributed mass to a lumped system having concentrated bodies an massless elastic elements (s. Fig. 3).

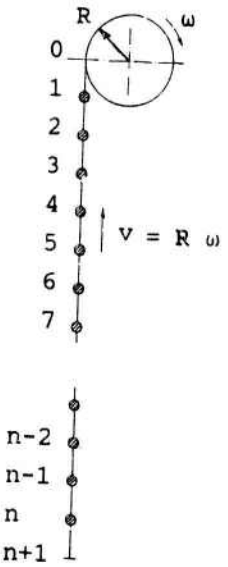

Fig. 3 Lumped system

The equations of motion in matrix notation then are:

$$^tA\ ^t\mathbf{u}^{\cdot\cdot} + ^tC\ ^t\mathbf{u} = ^t\mathbf{r} \qquad (4)$$

$^t\mathbf{u}$ is the vector of displacements and rotations of the discrete bodies at time t,

^tA is the matrix of inertias at time t which is a diagonal matrix here,

^tC is the matrix of force-influence coefficients, normally called global stiffness matrix at time t,

$^t\mathbf{r}$ is the inhomogeneous part.

The upper boundary conditions are described by:

$$w(0,t) = 0,\ \psi(0,t) = 0,\ \psi^{\nabla} = 1/R \qquad (5)$$

with R being the radius of the sheave.

The conditions at the lower boundary can be described by time dependant displacements:

$$w(n+1,t) = w_{n+1}(t),\ \psi(n+1,t) = \psi_{n+1}(t) \qquad (6)$$

$w_{n+1}(t)$ and $\psi_{n+1}(t)$ can be harmonic or randomly distributed functions.

The boundary conditions (5) and (6) yield a right-hand-side of equation (4) in the form:

$$ {}^{t}r = {}^{t}C_D \begin{bmatrix} w_{n+1} \\ \psi_{n+1} \end{bmatrix} + {}^{t}c_B \, (1/R) \qquad (7) $$

The matrix ${}^{t}C_D$ and the vector ${}^{t}c_B$ are:

$$ {}^{t}C_D = \begin{bmatrix} 0 & 0 \\ 0 & 0 \\ 0 & 0 \\ 0 & 0 \\ \vdots & \vdots \\ S_{12} & \end{bmatrix}, \qquad {}^{t}c_B = \begin{bmatrix} s_1 \\ s_2 \\ 0 \\ 0 \\ 0 \\ \vdots \\ 0 \end{bmatrix}. \qquad (8) $$

$s_1 = - EI[3/2 - \lambda_k^2/40]/l^3$, $s_2 = EI[1/2 - \lambda_k^2/40]/l^2$.

The solution of equation (4) is found by numerical integration using Wilson-θ-method (s. [8]). At the end of time-step Δt we obtain the displacements, velocities and accelerations of the lumped system which is kept constant during Δt.

Before starting the next time step the equations of motion at time $t+\Delta t$ have to be rearranged considering the reduced length of the rope and the changement of the right-hand-side of equation (4).

Results will be presented during the conference as computer—videos for three characteristical examples:

a) The hoisting rope is excited by $w_{n+1}(t)$, $\psi_{n+1}(t)$ only,

b) Bending of the rope at the upper boundary is considered only,

c) Both influences are considered.

The S_{12} is a submatrix of the order 2*2 of the stiffness matrix S which can be approximated by the elastic stiffness matrix

$$ S_E = B \begin{bmatrix} 12 & -6\,1 & -12 & -6\,1 \\ & 4\,1^2 & 6\,1 & 2\,1^2 \\ \text{symmetric} & & 12 & 6\,1 \\ & & & 4\,1^2 \end{bmatrix} \qquad (9) $$

$B = EI/l^3$, and the geometric matrix considering the influence

of the tensile force H on the element-stiffness:

$$H\ S_G = H \left[\begin{array}{cc|cc} A^{(0)} & -B^{(0)} & -A^{(0)} & -B^{(0)} \\ & C^{(0)} & B^{(0)} & -C^{(0)} \\ \text{symmetric} & & A^{(0)} & B^{(0)} \\ & & & C^{(0)} \end{array}\right] \qquad (10)$$

$A^{(0)} = 6/(5\ 1)$, $B^{(0)} = 1/10$, $C^{(0)} = 2\ 1/15$.

From equations (9) and (10) the global stiffness matrix ${}^{t}\mathbf{C}$ is built up under consideratio· of the principles of the matrix displacement method.

3. KINETIC BEHAVIOUR OF THE BUCKET MOVING ALONG A TRACK

The bucket with equal front and rear wheels with equal stiffnesses c_F moving along a track with irregularities is shown in Fig. 4. The lengths used in the equations of motion can be taken from Fig. 3. In matrix notation we obtain:

$$\mathbf{A}_F\ \ddot{\mathbf{u}}_F + \mathbf{C}_F\ \mathbf{u}_F = \mathbf{C}_T\ \mathbf{u}_T + \mathbf{Q}_F\ \mathbf{p}_F \qquad (11)$$

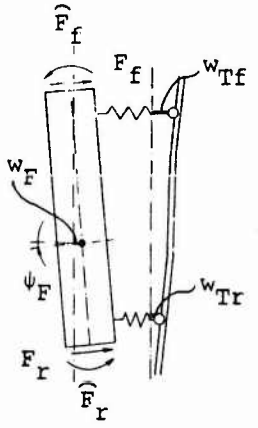

Fig. 4 Bucket with displacements and forces

It is:

$$\mathbf{u}_F = \begin{bmatrix} w_F \\ \psi_F \end{bmatrix}, \quad \mathbf{u}_T = \begin{bmatrix} w_{Tf} \\ w_{Tr} \end{bmatrix},$$

$$\mathbf{p}_F = \begin{bmatrix} F_f \\ \hat{F}_f \\ F_r \\ \hat{F}_r \end{bmatrix} \qquad (12)$$

The matrices are:

$$\mathbf{A}_F = \begin{bmatrix} m_F & \\ & \hat{m}_F \end{bmatrix},$$

$$\left.\begin{aligned} \mathbf{C}_F &= c_F \begin{bmatrix} 2 & (b-a) \\ (b-a) & (a^2+b^2) \end{bmatrix}, \quad \mathbf{C}_T = c_F \begin{bmatrix} 1 & 1 \\ -a & b \end{bmatrix}, \\ \mathbf{Q}_F &= \begin{bmatrix} 1 & 0 & 1 & 0 \\ -a^* & 1 & b^* & 1 \end{bmatrix} \end{aligned}\right\} \quad (13)$$

w_F, ψ_F are the displacement and rotation of the bucket, w_{Tf},w_{Tr} are the front and rear irregularities of the track and F_f,$\hat{F}_f$,F_r,$\hat{F}_r$ are the front and rear external forces and moments (s. Fig.3). m_F, $\hat{m}_F$ are the mass and rotary inertia of the bucket.

The solution of equation (11) can be found by numerical integration using Wilson-θ-Method.The irregularities of the track are assumed to be linearly varying during a time step Δt.

Results will be presented as computer-videos for the following characteristic situations:

a) A special coalmine bucket filled with coal will move along a track with different hoisting speeds v finding one short irregularity,

b) The track has randomly distributed irregularities

In both cases external forces are set to zero.

4. KINETIC BEHAVIOUR OF THE COMPLETE HAULING SYSTEM

Using the matrix displacement method developed in Chapter 2 and 3 a computer simulation of the complete hauling system can be done.

The vector of displacements at time t is a combination of the vectors of displacements of the upper rope, the lower rope and of the bucket:

$$ {}^t\mathbf{u}^T = \{ {}^t\mathbf{u}_{up}^T \quad \mathbf{u}_F^T \quad {}^t\mathbf{u}_{lo}^T \} \quad (14)$$

(^{T} means transposition of the vector.)

The matrix of inertia at time t is found from the submatrices of the upper and lower rope and the bucket:

$$ {}^t\mathbf{A} = \begin{bmatrix} {}^t\mathbf{A}_{up} & & \\ & \mathbf{A}_F & \\ & & {}^t\mathbf{A}_{lo} \end{bmatrix} \quad (15)$$

In the same manner the global stiffness matrix is built up:

$$ {}^{t}C = \begin{bmatrix} {}^{t}C_{up} & & \\ & C^{*}_{F} & \\ & & {}^{t}C_{lo} \end{bmatrix} \qquad (16) $$

The submatrices used here are overlapped in the described manner.

The equations of motion of the complete system at time t will become similiar to equation (4) by using the notations (14) to (16). And the right-hand side of equation (4) will be written as:

$$ {}^{t}r = {}^{t}C_{Tc}\,{}^{t}u_{Tc} + {}^{t}c_{Bc}\,(1/R) \qquad (17) $$

where the index c means: matrix or vector of the complete system.

After having found the solution at time t+Δt a rearrangement has to be done. The reduction in length of the upper rope and the enlargement of the length of the lower rope have to be considered.

Three characteristic examples of a coalmine hauling system will be presented at the conference:

a) The bucket moves at different hauling speeds and the system is excited by rope bending only.

b) Excitation is introduced by track irregularities only,

c) Both effects are considered.

5. CONCLUSION

Contribution demonstrates the influences of rope bending and track irregularities on the kinetic behaviour of a coalmine hauling system. It may be considered as the basis for further analysis of the influence of kinetic stresses on the lifetime of the hoisting rope.

6. REFERENCES

1. H. Arnold 1981 Schachtfördertechnik, Essen: Verl. Glückauf

2. J.W. Philipps, G.A. Costello 1985 Analysis of Wire Ropes with Internal-Wire-Rope Cores, Trans. ASME, Vol. 52, p. 510-516

3. R. Uhrig 1984 Theoretische Untersuchung des kinetischen Verhaltens von seitlich an Spurschienen geführten Fördergefäßen des Kohlebergbaus während der Fahrt, Ber. 84/4 Inst. f. Mechanik u. Statik - Baustatik- , Univ. d. Bundeswehr München

5. K.-H. Raabe u. R. Uhrig 1987 Zur Bestimmung des wirklichkeitsnahen kinetischen Verhaltens von Vertikalfördersystemen des Kohlebergbaus, Ber. 87/3 Inst. f. Mechanik u. Statik - Baustatik-, Univ. d. Bundeswehr München

6. S. Timoshenko, D.H. Young, W. Weaver Jr. 1974 Vibration Problems in Engineering, IV. Ed., New York,London ...:J. Wiley & Sons

7. L. Frýba 1972 Vibration of Solids and Structures under moving Loads, Groningen:Noordhoff Int. Publ.

8. K.-J. Bathe 1982 Finite Element Procedures in Engineering Analysis, Englewood Cliffs: Prentice-Hall

ALTERING THE VIBRATIONAL BEHAVIOUR OF AN I.C. ENGINE AS A PRELIMINARY STEP FOR NOISE REDUCTION

F. D'Ambrogio A. Sestieri P. Salvini

Dipartimento di Meccanica e Aeronautica
Universita' di Roma "la Sapienza"
Via Eudossiana 18 - 00184 Roma

1. INTRODUCTION

Control of noise radiated by I.C. engines is nowadays an imperative request made to the automotive industry.

The problem would require a global design devoted to this goal since its preliminary stage, but this is not usually permitted because the thermodynamic and kinematic parameters as well as the main architecture of the engine and its operating conditions are considered unchangeable characteristics. Therefore the possibility of action for the acoustician is quite limited and a reduction of few decibels is usually considered a successful result.

The main noise sources in a I.C. engine are the combustion process and the mechanical sources: piston slap, which is efficient at low speeds, bearing impacts and injection pump (for Diesel engines), important at high speeds. None of these sources can be modified, as shown in [1], to give more than a 5 dBA reduction in the sound radiated, without strongly hindering the operational efficiency of the engine.

On the other hand the sound radiated by any vibrating surface is highly dependent on the velocity and the radiation efficiency of the surface itself. Therefore, in order to achieve the goal of noise control without acting directly either on the combustion or mechanical noise sources, one may devote his strength towards the possibility of modifying the noise transmission paths through the engine structure, by altering, in some way, their vibrational behaviour. In other words, once the noise radiated by the engine surfaces has been computed or measured in running conditions by means of special techniques such as strip-tease, multi-coherence or near field methods, the object of the study transfers from the acoustic field to the transmission paths of vibrational energy. Such paths concern vibration transmission from the combustion chamber to the engine block and oil pan (through other elements of the engine) or the vibrations generated by mechanical components.

Starting from this point, the way in which one may change the vibrational behaviour of the engine is limited to a structural modification of the elements composing the transmission path. Considering that such elements are not amenable to complex modifications, for the reasons previously discussed, the means to bring about the vibration control can be reasonably obtained through local variations of mass, stiffness and/or damping, lumped on a limited number of positions of the path. The use of local lumped modifications is not of academic interest here, because it is one of the few ways to get beneficial results without actually changing the main architecture of the system, especially if these modifications involve only the static elements of the path such as the engine block, engine head or oil pan.

2. ABOUT STRUCTURAL MODIFICATIONS

The vibrational behaviour of an engine transmission path can not be easily computed theoretically and it is preferable to determine experimentally its frequency response function (FRF). This is usually obtained by measuring a FRF matrix which correlates excitation and response in a number of positions.

Most of the structural modification programs, which start from measured FRF, require the identification of modal and/or physical parameters. The identification of physical parameters of continuous structures is a hardly ill conditioned problem, while this is not the case for modal parameters. However, as shown by several authors [2,3,4], the approach derived from modal identification often causes negative effects on structural modifications: source of errors on the modification values and modal synthesis are the truncated modes, modal scaling, estimate of rigid body modes, etc. Moreover modal identification is usually performed through a curve fitting procedure whose efficiency depends on the accuracy of measurements and the characteristics of the tested system. Complex structures often present close modes and high modal densities which usually make the identification of modal parameters inefficient or almost impossible.

Unfortunately this is the situation for the kind of elements we are considering. Therefore structural modification is often severely limited by modal identification: surely this is what happens for the engine.

To avoid the pitfalls of modal identification, a method has been developed to modify the vibrating response of the engine in some way previously established, without requiring the knowledge of modal parameters. Raw - yet obviously accurate - frequency response data are only necessary. Because of the unneeding of modal identification, the only major trouble which the method presents is the necessity of measuring the whole FRF matrix, whilst one row or column is usually sufficient with other modification approaches.

On the other hand the method performs an optimization procedure, i.e. it minimizes an objective function subjected to some constraints in order to get the best solution as wished by the designer (or acoustician) within established limits of cost and technological convenience.

3. MATHEMATICAL BACKGROUND

As said, the method establishes the optimal modification to achieve a desired result. The goal of the structural modification may be explicited in different ways.

First we can minimize the difference, in a frequency band of interest, between a desired FRF and the one derived from the modified system, with technological constraints which define the range of variation for the physical parameters. In the developed procedure these parameters are a combination of mass, stiffness and damping, lumped on a number of points where the FRF was previously determined. This approach leads to a highly non-linear optimization problem, which can be simplified by expanding the modulus of the modified FRF into a power series. However it requires a mathematical constraint to provide a convergency condition for the power series expansion, giving rise to an iterative solution of the optimization problem [5].

Alternatively [6], we may express the objective function as a weighted sum of the squared physical parameters (decision variables), involved in the structural modification. In this way we make the marginal cost of a single modification proportional to the modification itself. The

main requirement of the optimization problem is here imposed by means of the constraint; i.e. at a specified number of frequencies (eventually encompassing the frequency band of interest), we demand that the modulus of one or more elements of the FRF matrix lie within a lower and an upper bound. Explicitly, the problem is formulated as follows. Find:

$$\min \Sigma_i \; w_i \cdot x_i^2 \tag{3.1}$$

subjected, at a specified number of frequencies (and FRFs), to the constraints:

$$| H_{ijL} | \leq | H_{ij}(\Delta \mathbf{B}(\underline{x})) | \leq | H_{ijU} | \tag{3.2}$$

and to other possible technological constraints. Here it is:

$\underline{x}$	the vector of decision variables;
w_i	possible weight accounting for design requirements;
$\|H_{ijL}\|, \|H_{ijU}\|$	lower and upper bounds for the expected FRF element;
$H_{ij}(\Delta \mathbf{B})$	modified FRF, which is an element of the modified matrix:

$$\mathbf{H} = (\mathbf{I} + \mathbf{H_0} \Delta \mathbf{B})^{-1} \mathbf{H_0} \tag{3.3}$$

$\mathbf{H_0}$ is the original FRF and $\Delta \mathbf{B}$ the matrix of structural lumped modifications, whose elements depend on the kind of modifications permitted. Expression (3.3) can be equally used to determine the new FRF as a result of the optimization process, or the differential or finite difference sensitivities of $|H_{ij}|$ with respect to a single modification [6].

Both formulations presented avoid the knowledge of modes, but the second one, involving a cost objective function, seems more efficient since it does not require least square regression to determine the physical modifications, and is finally numerically faster. Therefore this is the formulation used to change the vibrational behaviour of the engine.

4. VIBRATION ANALYSIS OF THE ENGINE

The engine examined is a small 2-cylinder, air cooled, gasoline engine, largely used in Italy and having limited performances (about 22 Kw at 5500 r.p.m).

4.1. Preliminary analysis

The noise radiated by the engine was measured in a reverberant room in one-third octave band from 100 to 10000 Hz, and a detailed analysis was performed to estimate the amount of power radiated by the individual surfaces [7]. The engine was divided into 6 surfaces and the sound power radiated by each surface was measured independently by a "near field" technique [8]. The strongest noise source was estimated to be the right side of the block. Having identified the surface dominating the noise emission, the paths of vibration to this surface were studied on the non-running engine to determine possible means of reducing the surface vibrations and the overall radiated noise. Since the cylinder pressure is usually considered as one of the dominant internal noise sources, we focused the vibration analysis on the transmission paths from the head of the piston to the right block side surface. As known, these vibrations propagate through two principal paths: a direct one and a kinematic one. The kinematic path corresponds to the piston-connecting rod, crankshaft and engine block. The direct path is through the cylinder head and the engine block. For both paths we considered the block as the most responsible element of acoustic emission, as it results from previous analysis carried out on the same engine.

For the study of the kinematic path we estimated its behaviour from the experimental knowledge of the FRF of the individual components, connected in series, by means of a simple method derived from building block analysis and used in [9]. In the method only forces are accounted for, but not moments. This is a reasonable statement for the kind of connections considered.

The first aim of this analysis was to identify the path component on which to perform structural modifications as those previously described (lumped masses and stiffnesses), in order to reduce the vibration transmission. Logical considerations show that the engine block is the most appropriate element to modify, since it is the sole element designed with merely static criteria. This practical indication is supported by observation of fig.1, which compares the FRF of the individual components of the kinematic transmission path with the FRF of the assembled components. It focuses that the engine block FRF is quite similar to the FRF of the whole path, whilst this is not the case for the other two components (piston-connecting rod and crankshaft). Therefore we can argue that the vibrational behaviour is largely controlled by the engine block, from now on identified as the component on which to act to reduce the whole response of the kinematic path to exciting vibrations. Very similar considerations might be done for the direct path.

4.2 Structural modification research

As a consequence of the previous considerations, a more detailed study of the block was developed. 12 points were considered on it, and the FRF matrix was experimentally determined between these points (fig. 2). These were also the points on which to locate the lumped modifications. Among them, only positions 1 and 12 (corresponding to the journal bearings) were considered not amenable to modifications. (We recall that the permitted modifications were only local addition of masses and/or introduction of springs between points of the block and an external fixed position).

In order to reduce the computation burden of the optimization algorithm and avoid the analysis of points having a poor effect on the considered FRF, a sensitivity analysis with respect to both masses and stiffnesses was performed on the 10 points of the block. Some results are presented in fig. 3. This figure presents a rapidly variable trend of differential sensitivities vs. frequency, showing that, in the frequency band under consideration, single modifications of mass and stiffness alter the FRF modulus in a quite complex way. However we can sort out modifications which do have some effect on the FRF modulus from the ones having almost no effect at all. This task could be performed by means of a looking inspection, but it seems more appropriate to consider, as a significant quantity, the RMS value of the sensitivity in the band of interest, which gives a global idea of the effectiveness of a specified modification (Table 1). It can be observed that only points 3,4,7,8,9,10 present a significant sensitivity either to mass or stiffness variations.

The FRF to change was H_{8-1}, with the input on the journal - 1 - and the response on the zone of the block most seriously vibrating - 8 -. At this point the optimization problem can be formulated as follows. Find:

$$\min \sum_{i \in S_M} (x_i)^2$$

x_i are the decision variables, corresponding to mass and/or stiffness variations, S_M is the index set of permitted modifications, with constraints:

$$x_i \geq 0 \qquad i \in S_M$$

$$| H_{8-1}(\Delta B(\underline{x})) | \leq | H_{8-10} |$$

in the frequency bend of interest.

The frequency bands of interest here considered were two, in order to estimate in which frequency band modifications of mass or stiffness were more convenient: the first one encompassed the range between 900 and 2000 Hz, the second one 2600 ÷ 3700 Hz.

In the following, results concerning modifications of mass and stiffness are presented.

4.2.1 Mass modification

In the lower frequency band, mass modifications are quite effective to reduce $|H_{8-1}|$. Fig. 4 compares the original FRF with results obtained by synthesis of the modified system, for different values of the upper bound constraint. When decreasing this value, the reduction of the modulus improves to the detriment of the cost of modifications, as shown by the value of the objective function (see Table 2). In the higher bandwidth results are still better (fig. 5). This can be reasonably explained considering that the high frequency range is mass controlled.

4.2.2 Stiffness modification

This kind of modification does not give a significant FRF reduction in any of the examined frequency bands, although the amount of stiffness introduced is quite large. In the higher bandwidth, stiffness modification gives still more negligible results.

4.2.3 Mass and stiffness modification

In this case too, the solution shows that masses play the major role in both bandwidths considered. However the modified FRF reaches, obviously, a lower amplitude.

4.2.4 Mass modification of two FRF elements

The response at a point of the block is controlled by the FRFs between the two block bearings and this point. In fig. 6 the results obtained by synthesis on the FRF H_{8-12} (between the other journal bearing and the same point 8 on the block), by modification of H_{8-1} only is shown. A very satisfactory reduction is achieved also on the second FRF. However, since the problem of considering more constraints (relative to two or more FRFs) does not require any additional hard computation (matrix inversion), we considered together the reduction of both moduli H_{8-12} and H_{8-1}. Figures 7 and 8 illustrate the improvement obtained. A comparison between figures 6 and 8 shows that a negligible improvement is obtained on H_{8-12} when considering the two paths H_{8-1} and H_{8-12} (fig. 8) instead of H_{8-1} only (fig. 6). This can be explained by asserting that the severe limits imposed to the most effective transmission path give modifications that immediately satisfy the constraints on the second path. In fact the single mass modifications are quite similar in both cases.

4.3 Experimental verification

In order to check the computed results, the modified engine block, as determined from the mass optimization with upper modulus constraint equal to 0.4 kg^{-1}, was experimentally tested. The prescribed values were

obtained by means of lead masses bolted on the established positions of the block. Of course these masses do not respond exactly to the scheme of lumped masses used in the computation of $\Delta \mathbf{B}(\underline{x})$. The real masses have rotational inertia and present some amount of elasticity, especially with respect to their connection to the block: these effects, not considered in the computation, can change the system response in an unexpected way. However the agreement between the computed modified system and the experimental one is quite satisfactory (fig. 9), validating the effectiveness of the method and encouraging to proceed with further developments.

In fig. 10 the reduction on the direct transmission path by modification of the kinematic path only is shown. A good result is achieved also for this path, confirming the correctness of choosing a modification of the engine block.

Finally, in fig. 11, the modified kinematic transmission path, obtained by synthesis, is presented in one-third octave band, on the whole range of frequency, to give an idea of the overall vibration reduction.

It is worthwile to point out that the block, within the level of excitation considered, presents a linear behaviour, and, consequently, the elements of the FRF matrix are almost symmetric, as proved by preliminary tests. Therefore, in our computations, we used indifferently the symmetric elements, as derived from the most convenient tests carried out on the structure. This could explain some of the small differences observed between the experimental and numerical tests.

5. CONCLUSIONS

A method to change the vibrational behaviour of an engine is here presented. If the combustion and/or mechanical forces are determined or measured and the radiation efficiency is known, the method can be successfully used to control the noise. The method finds an optimal structural solution in a permitted class of modifications, restricted to lumped variations of mass, stiffness and damping. Since the engine is a very complex system, its behaviour is experimentally determined. Starting from these measured data, a modification is performed on a specific component of the vibrational energy paths. In fact the engine presents the advantageous circumstance that the most radiating part of the system (the engine block) is also the most suitable element on which to perform modifications, either because it is a static element or because it is large enough to allow for several interventions.

On the other hand, the engine presents a high modal density which makes a modal identification difficult to work. Consequently modal synthesis processes, sensitivity analysis, or, in a word, structural modification, are very difficult to fulfill with techniques using modes of vibration. On the contrary, modal problems do not affect the optimization procedure, because the method uses only experimental raw data. It applies as well either to shifts of resonance values or to a reduction of the vibration amplitude in a frequency bandwidth. The computed results are quite satisfactory and the experimental tests carried out on the modified system agree very well with the results derived by synthesis of the modified model.

ACNOWLEDGEMENT

This work was supported by the National Research Council (C.N.R.) through grant n. 85.00187.93 "Progetto Finalizzato Trasporti".

REFERENCES

1. E.C. GROVER, N. LALOR 1973 Journal of sound and Vibration n. 28(3). Review of low noise engine design at ISVR.

2. S. BRAUN, Y.M. RAM 1987 Proc. 5th IMAC (London). On structural modification in truncated systems.

3. M.L. WEI, R.J. ALLEMANG, D.L. BROWN 1987 Proc. 5th. IMAC (London). Modal scaling considerations for structural modification applications.

4. J.C. O'CALLAHAN, C.M. CHOU, P. AVITABILE, C.H. WU 1987 Proc. 5th IMAC (London). Consistent scaling of rigid body and experimental flexural modes.

5. A. SESTIERI, W. D'AMBROGIO, E. DE BERNARDIS 1987 Proc. 5th IMAC (London). Optimal lumped modification of continuous vibrating structures.

6. W. D'AMBROGIO, A. SESTIERI 1987 Proc. 12th Int. Conf. on Modal Analysis (Leuven, Belgium). Skipping modal identification in performing structural modification.

7. W. D'AMBROGIO 1983 Degree Thesis. Universita' di Roma. Comportamento strutturale acustico di un motore a combustione interna bicilindrico. Caratterizzazione acustica.

8. M.J. CROCKER SAE Paper 810694. The use of existing and advanced intensity techniques to identify noise sources on a Diesel engine.

9. R. DE JONG 1976 Ph.D. Thesis, M.I.T.. Vibrational energy transfer in a Diesel engine.

Table 1. RMS sensitivity values in the frequency range 900 ÷ 2000 Hz

i	2	3	4	5	6	7	8	9	10	11
$\delta\lvert H_{8-1}\rvert/\delta m_i$ [1/kg²]	.047	2.094	3.031	.040	.890	4.052	8.760	2.320	3.645	.310
$\delta\lvert H_{8-12}\rvert/\delta m_i$ [1/kg²]	.046	2.193	1.134	.033	.175	1.648	3.563	0.917	1.517	.101
$\delta\lvert H_{8-1}\rvert/\delta k_i$ [m/kg·N]·10⁸	.037	2.703	2.547	.045	.738	3.376	7.377	1.932	3.018	.239
$\delta\lvert H_{8-12}\rvert/\delta k_i$ [m/kg·N]·10⁸	.331	2.603	1.030	.035	.205	1.386	3.253	0.738	1.301	.109

Table 2. Cost function and modification values relative to different upper bound constraints.

Upper bound [1/kg]	Cost function	Mass 3 [kg]	Mass 4 [kg]	Mass 7 [kg]	Mass 8 [kg]	Mass 9 [kg]	Mass 10 [kg]
.2	1.263	.274	.199	.620	.147	.252	.823
.3	0.747	.215	.162	.506	.150	.114	.620
.35	0.339	0	.140	.328	.157	.143	.409
.4	0.274	0	.106	.290	.162	.136	.365

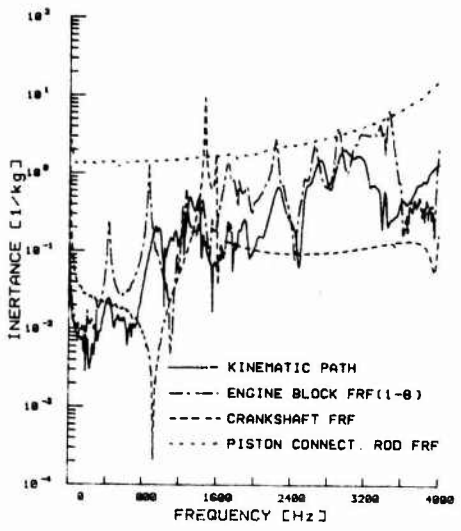

Fig. 1. Kinematic path: FRF of whole path and individual components.

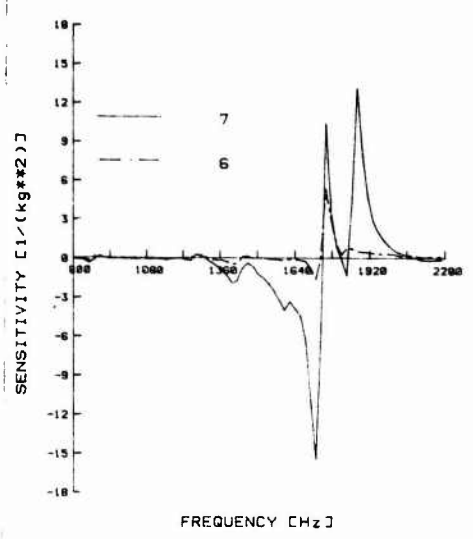

Fig. 3. Sensitivities of $|H_{8-1}|$ to mass modifications on point 6 and 7.

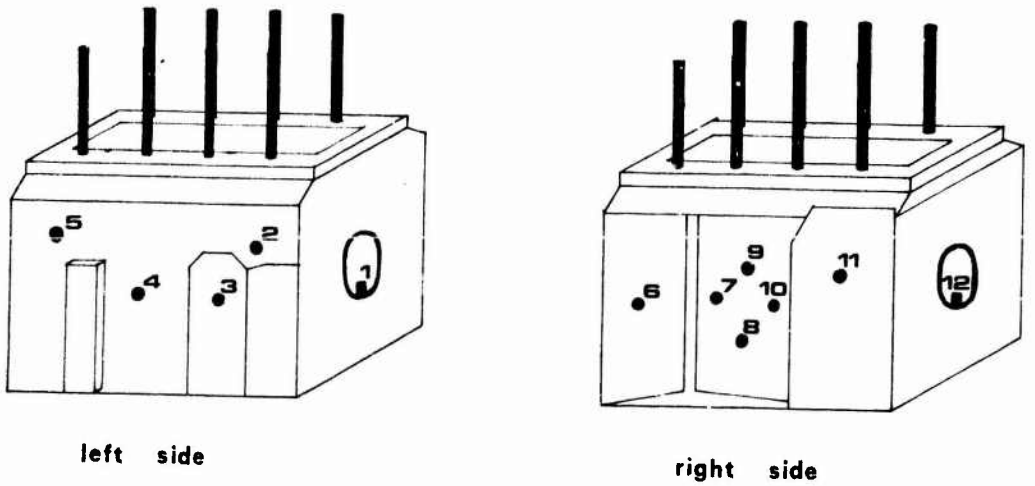

Fig. 2. Measurement points on the engine block.

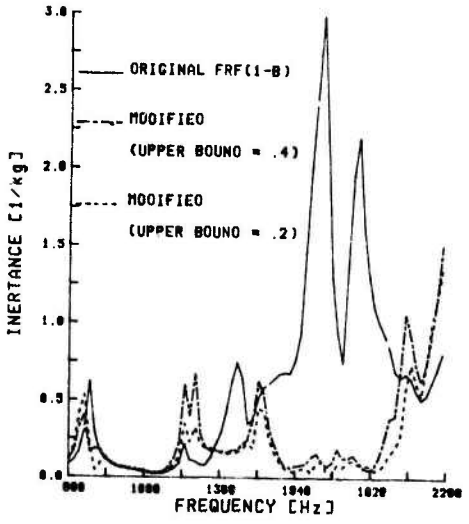

Fig. 4. Original and modified FRFs for different values of the upper bound constraint.

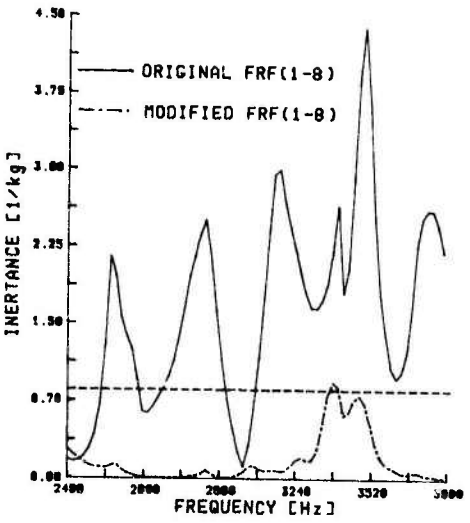

Fig. 5. Original and modified FRF in the frequency band 2400 ÷ 3800 Hz.

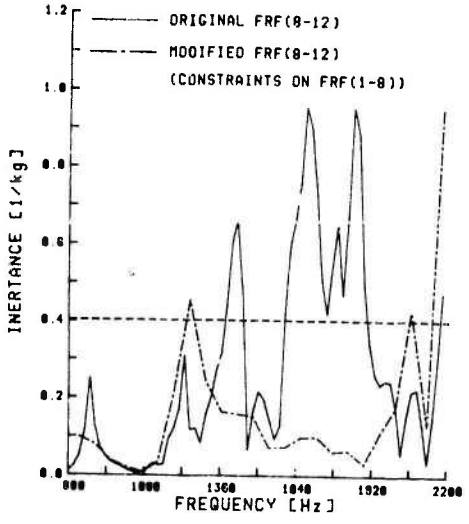

Fig. 6. Original and modified $|H_{8-12}|$ for constraints imposed to $|H_{8-1}|$ only.

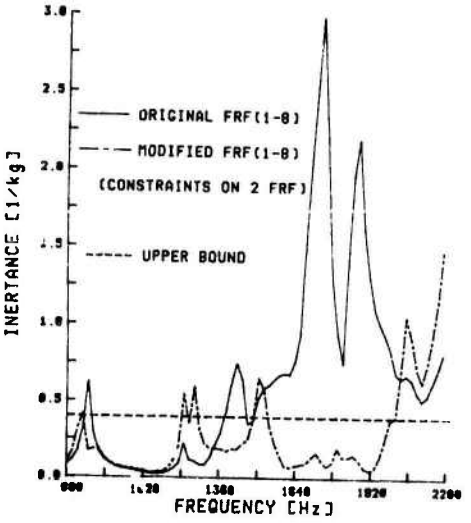

Fig. 7. Original and modified $|H_{8-1}|$ for constraints imposed to both $|H_{8-1}|$ and $|H_{8-12}|$.

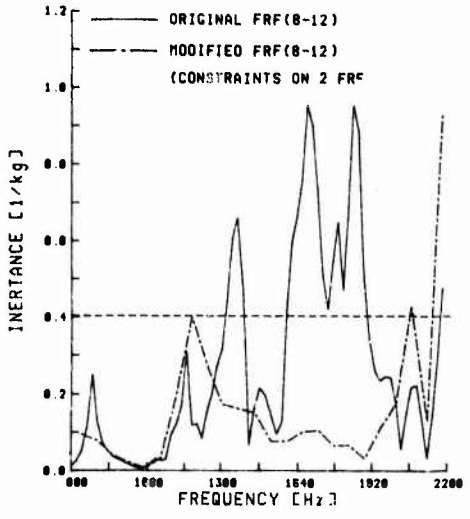

Fig. 8. Original and modified $|H_{8-12}|$ for constraints imposed to both $|H_{8-1}|$ and $|H_{8-12}|$.

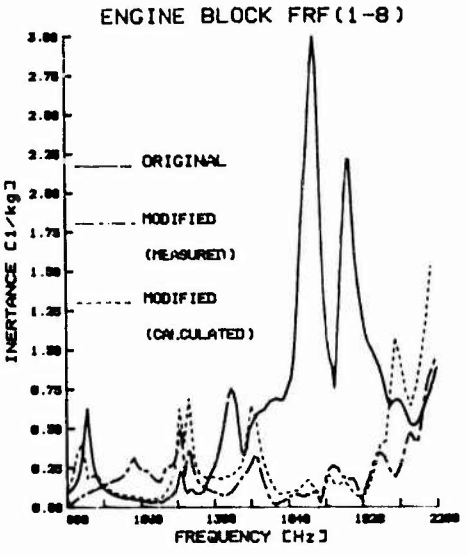

Fig. 9. Comparison between computed and measured modified FRF.

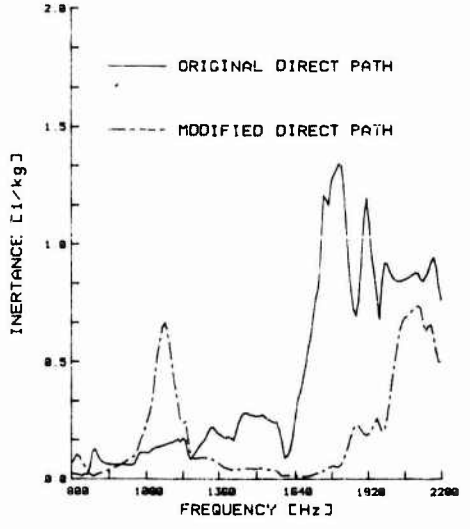

Fig. 10. Original and modified direct transmission path as a by-product of the changes imposed to the kinematic path.

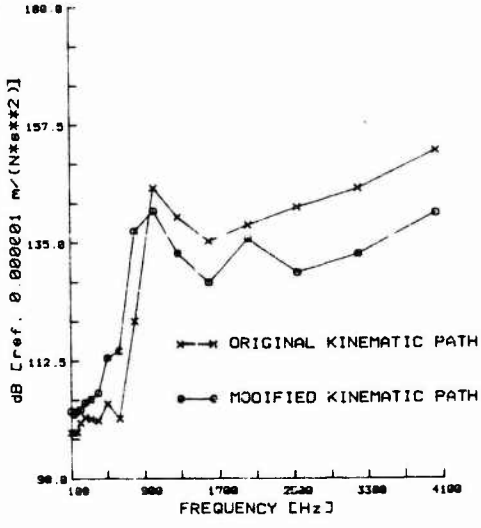

Fig. 11. Original and modified kinematic transmission path (one-third octave band).